RAL-89-045

Science and Engineering Research Council
Rutherford Appleton Laboratory
Chilton DIDCOT Oxon OX11 0QX

Science and Engineering Research Council Central Laser Facility

Annual Report to the Laser Facility Committee 1989

Central Laser Facility
Rutherford Appleton Laboratory

RAL-89-045

Science and Engineering Research Council

"The Science and Engineering Research Council does not accept any responsibility for loss or damage arising from the use of information contained in any of its reports or in any communication about its tests or investigations"

PREFACE

The Central Laser Facility provides advanced lasers for use by UK University and Polytechnic research workers. It is funded by the Science Board of SERC and operated by SERC's Rutherford Appleton Laboratory. Access to the lasers is through a competitive peer review process for research in the Science Board's area. Use of the facilities by other organisations is undertaken on a contract basis.

Work at, or in association with, the CLF in the year to 31 March 1989 is reported here at a scientific and technical level. A more condensed description is given in the annual report of the Rutherford Appleton Laboratory.

The three main facets in the programme of the CLF comprise: operation for users' experiments of a 5 TW neodymium glass laser facility, VULCAN; development and use for experiments of a prototype high power krypton fluoride laser, SPRITE; the Laser Support Facility with a laser loan pool and CLF based equipment for multidisciplinary research, particularly in nanosecond and picosecond spectroscopy.

The last year has been notable for major policy decisions determining the future of the CLF. The CLF Review Panel, chaired by Professor Challis, reported to the Science Board in September 1988. The report concluded that the CLF would continue to have a strategic role throughout the next 10 years and recommended that its funding be continued at the present level. In recommending also the construction of a new high performance KrF laser facility, SUPERSPRITE, which would significantly out perform VULCAN for a similar capital cost, and replace it in the mid 1990s, the Panel initiated radical change in the high power laser programme which offers exciting opportunities for the future.

The Panel was impressed by the quality and growing scale of the work of the Laser Support Facility and recommended a modest increase in its funding to permit enhanced capital investment and improved staff support.

The Science Board accepted these recommendations in principle and made provision for continued funding at the present level. The enhanced LSF activity and KrF laser development work will consequently be funded by a fairly severe reduction in the operations budget of VULCAN, which will restrict experiments during the development of the new KrF laser facility to those not requiring significant changes in equipment

The Science Board also linked its policy on SUPERSPRITE to the recent initiative of a group of five European research agencies which has established a scientific and technical study of the case for a European High Performance Laser Facility. The EHPLF concept is also included in the new Corporate Plan of the Council of SERC. The R&D phase of SUPERSPRITE development will be pursued for two years and will then be reviewed in the light of the European discussions. The prospect for high power laser users is therefore very encouraging in that they should either gain access to a new national facility, SUPERSPRITE, or to a superior European facility.

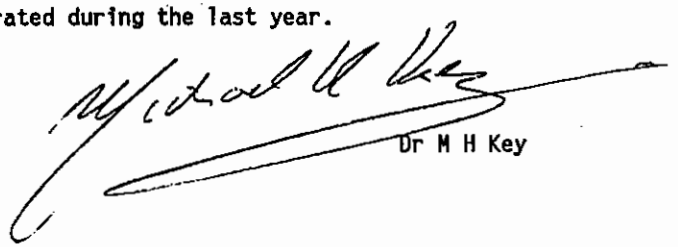
The scientific work of the CLF has been active and productive during the year. Section A (plus a late papers Appendix) highlight the broad programme of work with high power lasers, including notable achievements in interaction physics with the new induced spatial incoherence and random phase plate techniques producing more uniform focal spot characteristics, a CLF record for neutron yield in experiments applying thermonuclear sources to probing of Rayleigh-Taylor instabilities, significant progress in X-ray laser research with the first production of a well defined XUV laser beam, first observations of laser-driven beatwaves in a plasma at high relativistic γ, progress in use of pulsed X-ray laser sources to study transient changes in crystals and in biological microscopy, and developments in the study of dense plasmas by EXAFS.

Section B reviews the work on KrF laser development and emphasises proof of principle experiments on the new optical multiplex and

Raman beam combining architecture for high power KrF laser operation which is being developed using SPRITE.

Section C covers the extensive multidisciplinary scientific work with the smaller lasers of the LSF. The topics range from jet cooled spectroscopy through Raman scattering from organometallic catalysts, kinetics of DNA damage repair, multiphoton physics and X-ray generation to the deposition of thin films of high T_c superconductors and nonlinear optics materials.

It has been an interesting year especially because of the new prospects which have opened up for the future. There are major challenges ahead and I am confident that the staff and users of the CLF will rise to the occasion in the future in the same effective way as they have operated during the last year.



Dr M H Key

CONTENTS

		Pages
PREFACE		
Introduction		3-7
A	VULCAN OPERATIONS AND EXPERIMENTS	8-182
B	SPRITE OPERATIONS AND DEVELOPMENT AND SUPERSPRITE	183-230
C	LASER SUPPORT FACILITY	231-421
D	PUBLICATIONS	423-437
ACKNOWLEDGMENTS		
E	APPENDICES	

INTRODUCTION

W T Toner

The Central Laser Facility (CLF) is funded by the Science Board of the Science and Engineering Research Council and the programme is managed by the Laser Facility Committee (LFC) whose membership is given in Table 1. The LFC delegates responsibility to the Director of the Rutherford Appleton Laboratory for the operations of the facility.

The allocation by the Board to the CLF for the period covered by this report, April 1988 to March 1989, was £3.0M. Fifty four man years of effort were used and the staff costs and overheads amounted to 51% of the allocation. Seventy eight percent of the resources was devoted to the operation and minor development of the CFL laser systems for scheduled experiments by research workers in UK Universities and Polytechnics; twelve percent was used on the Phase I programme of capital facility development and ten percent was used in research and development on high power KrF lasers.

The major facilities provided by the CLF and their principal scientific applications are listed in Table 2. The Nd Glass laser VULCAN is the main facility for experiment using high power and about 53% of the resources was used to support its operation and the experimental programme of the users.

The KrF Sprite laser was reconfigured during the year to enable a thorough investigation of the optical multiplexing and Raman beam combining architecture which it is proposed to use in a future system, SuperSprite, which could replace VULCAN in the mid 1990's.

The Laser Support Facility and small scale R&D work some of which is supported by other funding sources, accounts for almost 25% of the Science Board allocation. The programme covers all areas of research supported by the Science Board and the experiments are frequently multidisciplinary in character. A target preparation service, engineering support group and a small group giving theoretical support by maintaining computer codes service all CLF activities.

Figure 1 shows the present divisional and group structure of the CLF.

Use of the CLF by UK research workers in HE1's is free of charge to those successful in a peer review process. The cost of travel to the facility and some incidental costs of the research are borne by the CLF out of its allocation from the Board. The costs of ressearch assistants and expenditure in HE1 laboratories may be sought by application to the SERC for a research grant. The Laser Facility Committee funds users wholly or mainly using the CLF with an annual committment allocation of £390 K. Grant holders may bid for time on the facilities of the CLF by application to one of the two selection panels (High Power Laser Panel, Laser Support Facility Panel) whose members are listed in Table 3. The panels meet three time a year to determine the relative priority of the bids for a specific four month schedule period. A small proportion of the time may be allocated by the Panels to applicants without grant support. Following the recommendation of the Panels as to priority, and taking account of logistical factors, schedules are prepared by CLF staff which are then discussed, modified as necessary and approved by open committees of facility users.

The SERC encourages use of the CLF by industry or other organisations on the basis of payment for the full cost of laser time. Such use is limited to 10% of available laser time.

International collaboration in the research programme is extensive though collaborative participation in approved experiments of UK University groups and through agreements negotiated with the CLF and SERC.

TABLE 1

Membership of the Laser Facility Committee 1988/89

Prof G J Pert (Chairman) (till Dec 88)
Dept of Physics
University of York

Professor R J Donovan FRSE (Chairman) (from Dec 88)
Dept of Chemistry
University of Edinburgh

* Dr K Burnett
Clarendon Laboratory
University of Oxford

Professor R N Dixon FRS
Dept of Theoretical Chemistry
University of Bristol

\+ Professor M G Haines
The Blackett Laboratory
Imperial College of Science and Technology

\+ Dr T A King
Atomic Molecular and Polymer Physics Group
Schuster Laboratory
University of Manchester

Dr M J Lamb
Dept of Pure and Applied Physics
Queen's University Belfast

* Dr W E Martin
Principal: Sowerby Research Centre
British Aerospace
Filton, Bristol

\+ Professor D Phillips
Department of Chemistry
Royal Institution

* Dr P D Roberts
MoD AWE
Aldermaston

Dr D C Robinson
Culham Laboratory
Harwell

* Professor M G Rusbridge
Dept of Pure and Applied Physics
UMIST

Professor W Sibbett
Dept of Physics
University of St Andrews

\+ Dr M Vaughan
Procurement Executive
Royal Signals & Radar Est MoD
Gt Malvern

Dr C W Wharton
Dept of Biochemistry
University of Birmingham

\+ until 31 August 1988
* from 1 September 1988

TABLE 2

Major Facilities and Programmes at the CLF

Nd glass laser facility	Laser Support Facility	High Power KrF Laser Facility
VULCAN	LSF	SPRITE
Laser plasma interactions and energy transport	Photochemistry Photobiology Nonlinear optics	Ultra high intensity pico-second laser source
Laser compression of matter and dense plasmas	High field atomic physics Laser Loan Pool Raman facility	Applications of high brightness laser produced plasma X-ray sources
XUV lasers and applications of laser produced plasma sources	Picosecond laser High repetition rate X-ray source	Short pulse laser plasma energy transport processes
Target Preparation Service Theoretical support service		

TABLE 3

Laser Support Facility Panel 1988/89

Professor R N Dixon FRS (Chairman)
Dept of Theoretical Chemistry
University of Bristol

Dr K Burnett
The Clarendon Laboratory
University of Oxford

Professor M C W Evans
Dept of Botany and Microbiology
University College London

Dr J J McGarvey
Dept of Pure and Applied Chemistry
Queen's University Belfast

Professor I W M Smith
Dept of Chemistry
University of Birmingham

Dr R N F Thorneley
Institute of Plant Science Research
University of Sussex

High Power Laser Panel 1988/89

Dr D C Robinson
Culham Laboratory
Abingdon

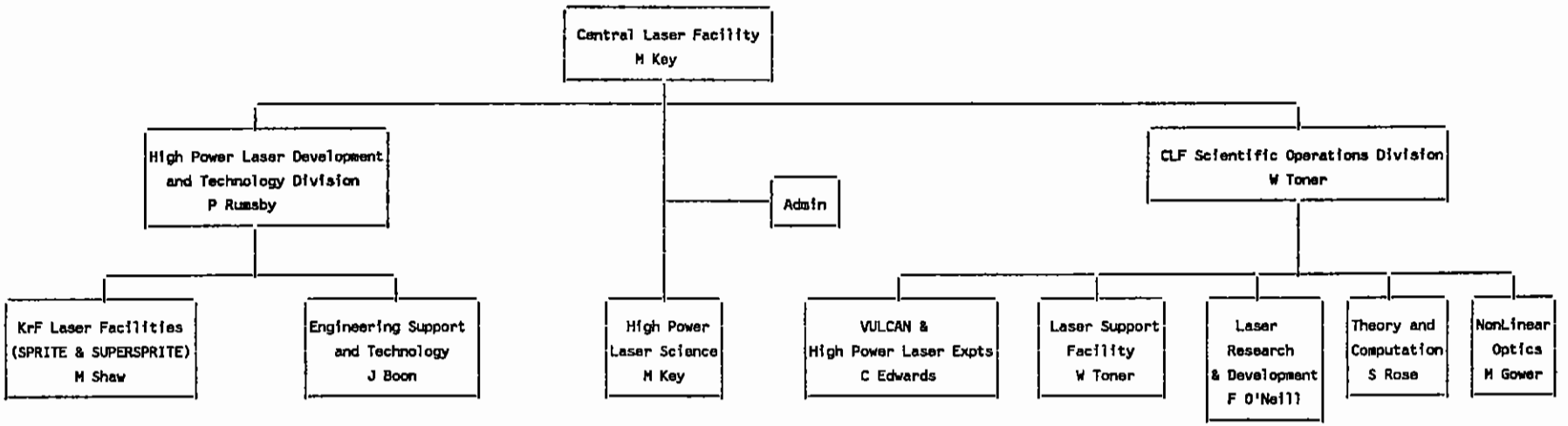
Dr H C Barr
University College of Wales
Bangor

Dr D A Brown
Department of Physics
Royal Holloway and Bedford New College

Mr A E Dangor
The Blackett Laboratory
Imperial College of Science and Tehcnology

Dr T A Hall
Dept of Physics
University of Essex

Dr M J Lamb
Dept of Physics
Queen's University of Belfast



Divisional and Group Structure of the Central Laser Facility

May 1989

A	VULCAN OPERATIONS AND EXPERIMENTS	Pages
A1	XUV & X-RAY LASERS AND OTHER APPLICATIONS OF LASER PRODUCED PLASMAS	13-49
A2	LASER PLASMA INTERACTION AND ENERGY TRANSPORT	50-66
A3	LASER COMPRESSION WITH DENSE PLASMAS	67-79
A4	THEORY AND COMPUTATION	80-129
A5	VULCAN OPERATIONS AND DEVELOPMENT	130-154
A6	INSTRUMENTATION	155-182

Section A

INTRODUCTION

There was some loss of experimental time in the period immediately after the VULCAN upgrade due to re-commissioning and staffing problems but thereafter the year has been very productive.

Six-beam energies of 1.7 kJ in the infra-red and 800 J in the green can now be produced. Smooth focal profiles can be generated using Induced Spatial Incoherence (ISI) and Random Phase Plates (RPP). The flexibility of the system has been demonstrated in such different non-standard configurations as the beat wave and short pulse X-ray laser experiments. The introduction of a target area 'set-up' week has resulted in a longer data taking period for each experiment.

The increased energy was used to good effect in a series of experiments (see appendix) with non-uniformly, irradiated, high aspect ratio, D-T filled glass shells provided by collaborators in Japan and Russia. An order of magnitude increase in neutron yield, (up to 5 x 10^8) was obtained on a reproducible basis and the implosions were used as α-particle sources to measure the stopping power of an aluminium plasma and the growth of Rayleigh Taylor instabilities in laser accelerated planar plastic foils.

The use of a RPP to improve the laser beam profile reduced the levels of Stimulated Rayleigh Scattering and Stimulated Brillouin Scattering in long scale length preformed plasmas by over an order of magnitude; with ISI the reduction was almost a factor 1000.

An important step forward in the X-ray laser programme was the demonstration of high gain, high power, collimated output from collisionally pumped Ge XXIII at 236 Å, opening up the way to future applications studies. XUV multilayer mirrors, fabricated at Reading, were used for the first time in these experiments. In addition, preliminary work has been carried out on short pulse pumping of Na XI Balmer-α and the technique of point projection absorption spectroscopy has been used to study the expansion and absorption characteristics of stripe targets. There has been theoretical work on isoelectronic scaling and the modelling of the Li-like Al scheme has been greatly improved. Contrary to earlier expectation it is now thought that the trapping of the L_α line plays little role in limiting the peak gain attainable in the hydrogen-like recombination scheme.

In the beat wave experiment (see appendix) beat waves were observed as sidebands in scattered probe light for the first time. The project - which is a collaboration between RAL, IC, Ecole Polytechnique and the University of Paris - has recently received increased support through EEC sponsorship. Theoretical work has been done on the effects of non-parallel pump waves and self-focusing in beat wave excitation.

The first direct measurement of crystal lattice spacing during shock breakout has been made using diffraction of X-ray pulses from a laser produced plasma and code predictions of density now agree well with improved EXAFS measurements of a laser driven shock compressed plasma.

Restricting the radiation from a laser produced plasma to the water window improved the contrast and resolution obtained in the contact microscopy of biological specimens. It has also been demonstrated that hypervelocity impact damage in metal and glass can be simulated using a focused high power laser beam.

Instrumentation developments include a novel method of measuring the reflectivity of XUV multilayer mirrors, new designs of crystal spectrometer, an orthogonal slit camera for the imaging of a plasma which is much longer in one dimension than another, photometric calibration of CCD streak cameras, α-particle imaging with coded aperture masks and an improved method of processing densitometer data.

Computer modelling has been carried out on Stimulated Raman Scattering from a density maximum in a laser-produced plasma, Rayleigh Taylor instability in the presence of self-generated magnetic fields and heat transport in laser produced plasmas. A 3D code has been developed for the simulation of non-uniformly irradiated implosions.

S A Ramsden

A1	**VULCAN OPERATIONS AND EXPERIMENTS**	Pages
A1.1	OBSERVATION OF EFFICIENCT PRODUCTION OF HIGH GAIN, HIGH POWER AND COLLIMATED BEAM IN A Ge XXIII XUV LASER	13-18
A1.2	DEMONSTRATION OF GAIN IN BALMER-α TRANSITIONS Na XI and Mg XII	18-25
A1.3	ENHANCED EFFICIENCY AND SHORTER WAVELENGTH F O R RECOMBINATION LASERS DRIVEN BY SHORTER (20 psec) PULSES	25-27
A1.4	1s-2p TERM STRUCTURE IN ALUMINIUM	27-32
A1.5	FIGURED SOFT X-RAY MULTILAYER MIRRORS: A METHOD OF MEASURING NORMAL INCIDENCE REFLECTIVITY	32-36
A1.6	INVESTIGATION OF THE EXPANSION OF SHORT PULSE (< 100PS) EXPANDING PLASMAS USING THE TECHNIQUE OF POINT PROJECTION ABSORPTION	36-45
A1.7	SOFT X-RAY CONTACT MICROSCOPY OF BIOLOGICAL SPECIMENS: DETERMINATION OF THE EFFECT OF IRRADIATON OUTSIDE OF THE WATER WINDOW	45-49

A1.1 OBSERVATION OF EFFICIENCT PRODUCTION OF HIGH GAIN, HIGH POWER AND COLLIMATED BEAM IN A Ge XXIII XUV LASER

C L S Lewis, D Neely, D O'Neill and J Uhomoibhi (Queens University Belfast)
S A Ramsden and A Rogoyski (University of Hull)
M Grande, M H Key, A McPhee and G J Tallents (RAL)
E A McLean (Naval Research Lab)
A M H Al-Arab and B Evans (University of Reading)

Collisional pumping of 3p-3s population inversions of neon-like ions in plasmas produced from thin film targets by 5 TW, 0.5 nsec, 0.53 μm laser pulses has created high gain length products giving near saturated laser action (gl ∿ 15) in Se XXV at wavelengths 20.6/20.9 nm [1]. A significantly greater efficiency of gain production (gl/P)[3] has been demonstrated with 1.06 μm irradiation of slab targets for Ge XXIII at 23.2/23.6 nm[2]. The 1.06 μm pulse length of 2 nsec in the latter work also suggested the possibility that the duration of gain, which was not measured, might be significantly larger than in the thin foil experiments, with interesting possibilities for multi-pass and resonator experiments using multi-layer XUV mirrors.

An experiment was designed for the VULCAN facility to test the possibility of obtaining high gl and to measure the duration of the gain. Ge targets up to 34 mm long were irradiated at 1.06 μm in a 200 μm wide line focus by 0.5 or 1 nsec laser pulses at energies up to 200 J cm^{-1}.

The experimental arrangement is illustrated schematically in Fig A1.1. Off-axis tilted mirrors are used to create line foci as in previous work[4]. Three ∿ 12 mm line foci were combined to produce irradiated lengths up to 34 mm. Targets were Ge stripes of (a) 0.5 μm thickness x 200 μm width on 35 μm CH (effectively slab targets) or (b) 0.05 μm Ge thickness x 200 μm width on a 0.1 μm CH base (thin film targets). A flat field grating spectrometer[5] with a 14 μm entrance slit recorded spectra emitted axially from the plasma. Time integrated spectra were recorded on film (Kodak 101) and time resolved spectra using a streak camera. A similar spectrometer recorded spectra emitted at 28° to the plasma axis. A crystal spectrograph was used to spatially resolve the neon and fluorine-like germanium resonance lines along the plasma, giving valuable information on the uniformity of irradiation along the line focus. X-ray images of the emission along the plasma line focus were also recorded to monitor uniformity.

Laser action was observed on the five transitions shown in the spectra of Fig A1.2. The J = 2-1 doublet transitions at 23.2/23.6 nm became strongly dominant in the spectra at the longer lengths. Intensity increased exponentially with length with g ∿ 3 cm^{-1} deduced from Fig A1.3, where the functional form appropriate to high gain amplified spontaneous emission[6] is fitted to the data. The single transit gain exponent reaches gl ∿ 10. The ratio gl/P of 15 TW^{-1} is somewhat lower than the value 30 TW^{-1} inferred in the earliest slab target experiments with lower gl values[2], but is still significantly above the 5 TW^{-1} recorded with 0.53 μm 0.6 nsec irradiation of thin foil targets for Se XXV[1].

With gl ∿ 10 amplified spontaneous emission narrows to a beam angle of the order of the width/length of the amplifying plasma column[7] and this was confirmed directly in the experiment from the photographically recorded spectra which showed intensity varying along the spectral lines of the laser transitions (fig A1.4); the position along the spectral line is directly related to angle of emission and Fig A1.4 shows the beam divergence to be 14 mrad. The beam is not parallel to the target surface but is deflected by 20 mrad, presumably by refraction. It is interesting to note that the refraction angle increases with wavelength of the gain line.

The power within the beam was estimated at 100 kW from the absolute sensitivity of the film and the known instrument and filter transmission characteristics (Fig A1.5).

The duration of the laser action and its timing were determined by streak camera recording of the spectra, as illustrated in Fig A1.6. The laser emission peaks in the latter half of the laser pulse

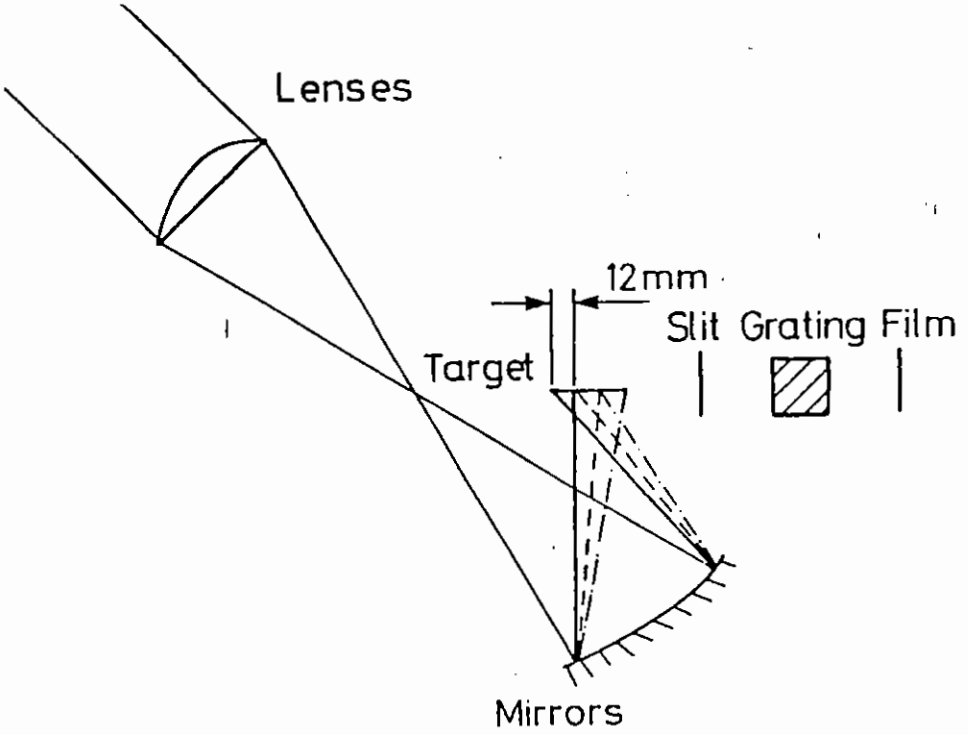


Fig A1.1 *Schematic plan view of the experimental arrangement for the collisionally pumped X-ray laser experiment. Three line-minor combinations produce an irradiated length of plasma up to 34 mm. The axial spectrometer (viewing down the plasma line) is also shown.*

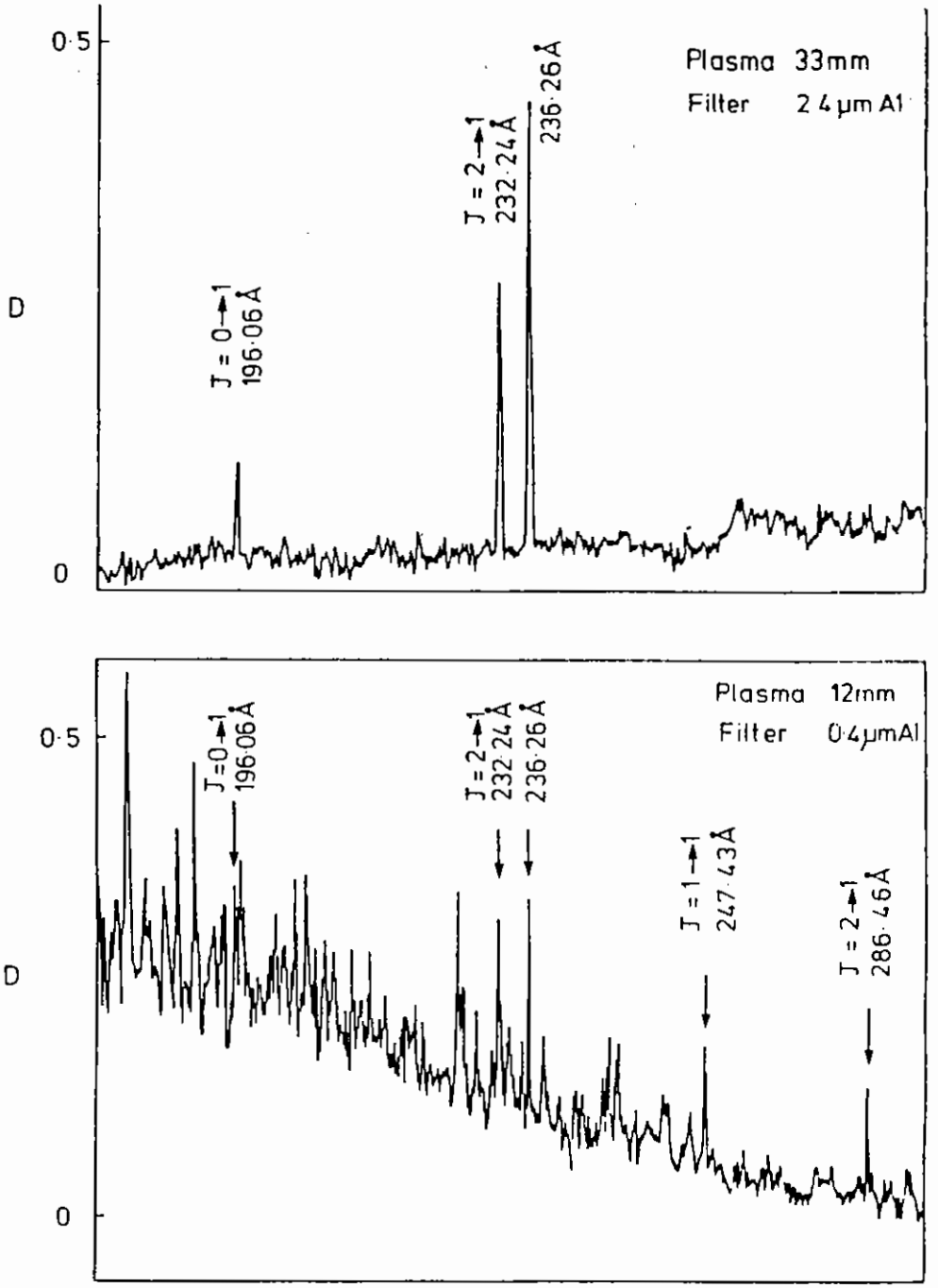


Fig A1.2 *Axial spectrum from two lengths of irradiated plasma. The five gain lines observed are marked on the lower densitometer trace (12 mm plasma length). The upper densitometer trace shows how gain lines increase in intensity much more than other spectral lines with increased plasma length (33 mm). Filtering was increased from 0.4 μm of aluminium on the lower trace to 2.4 μm on the upper trace in order to stop the upper spectrum gain lines becoming saturated.*

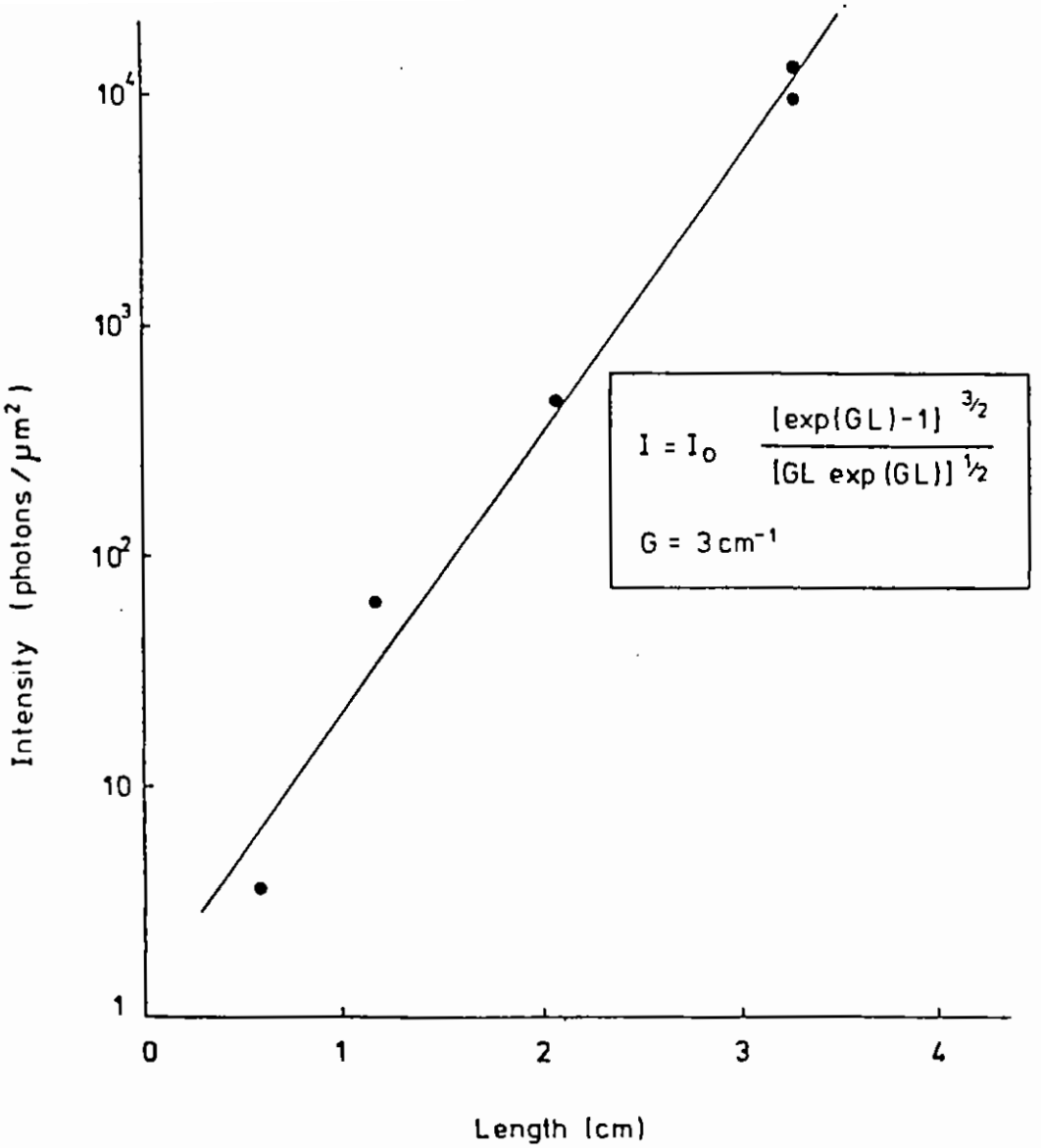


Fig A1.3 *Intensity scaling of the J = 2 → 1 236 Å line recorded on film in the axial spectrometer as a function of plasma length. The solid curve shows the intensity variation for amplified spontaneous emission with a gain of 3 cm⁻¹.*

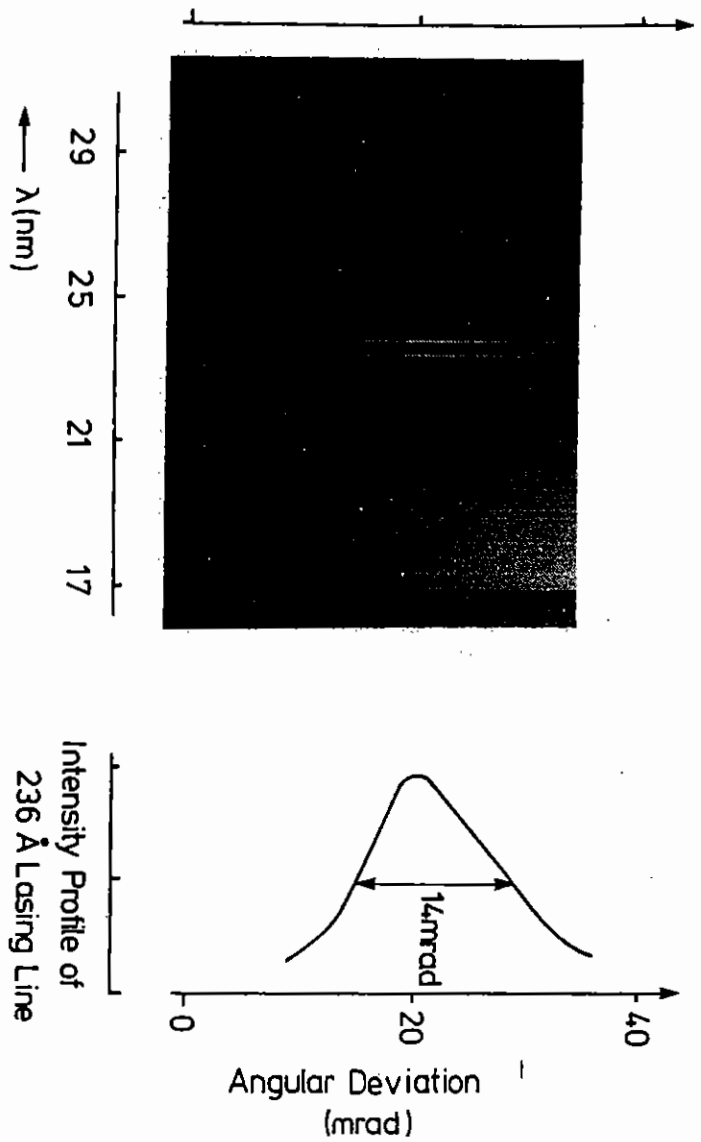


Fig A1.4 *Axial spectrum showing the angular deviation of the lasing lines.*

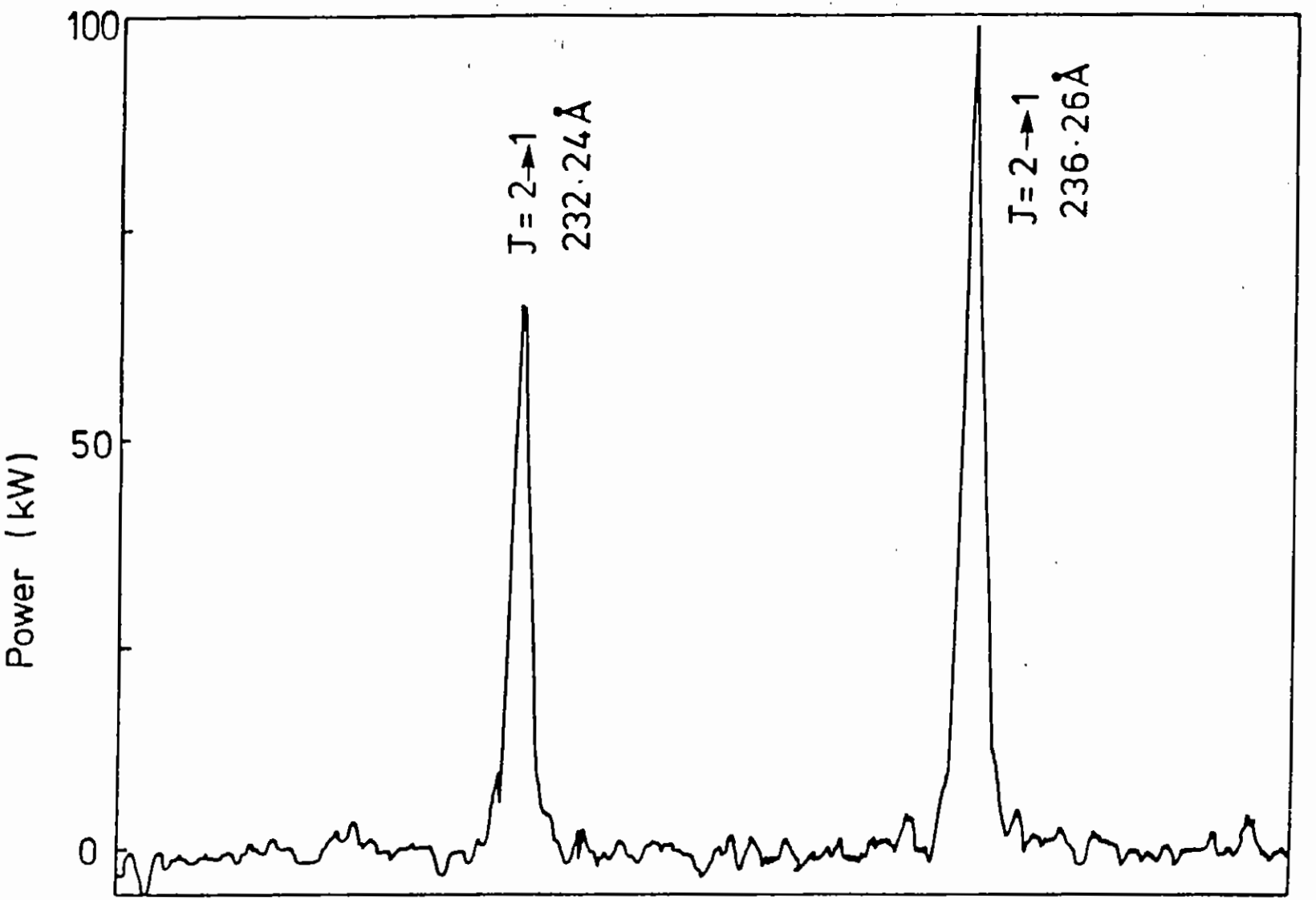
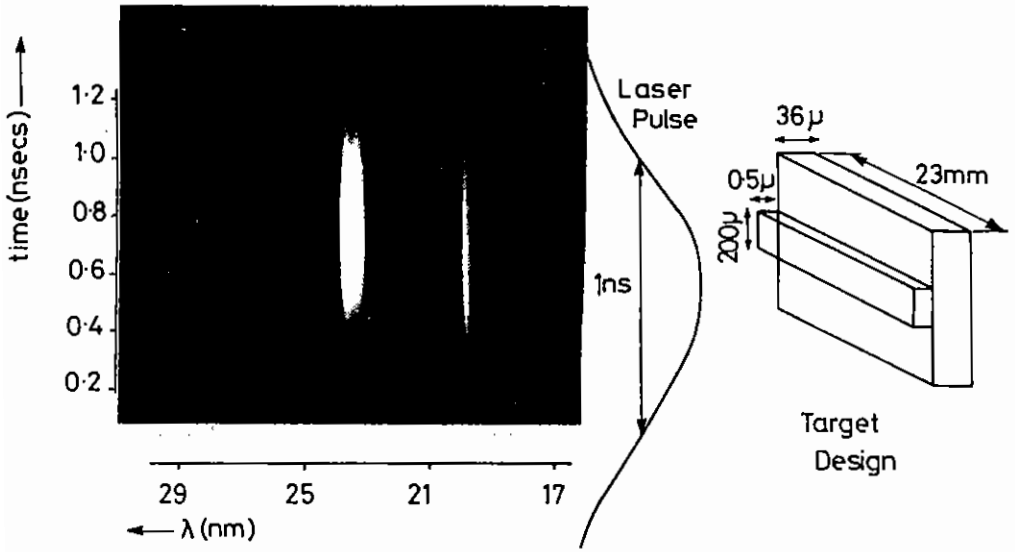


Fig A1.5 *Axial spectrum for an irradiated target of length 32 mm near two lasing lines connected for film nonlinearity with an approximate laser power scale shown.*



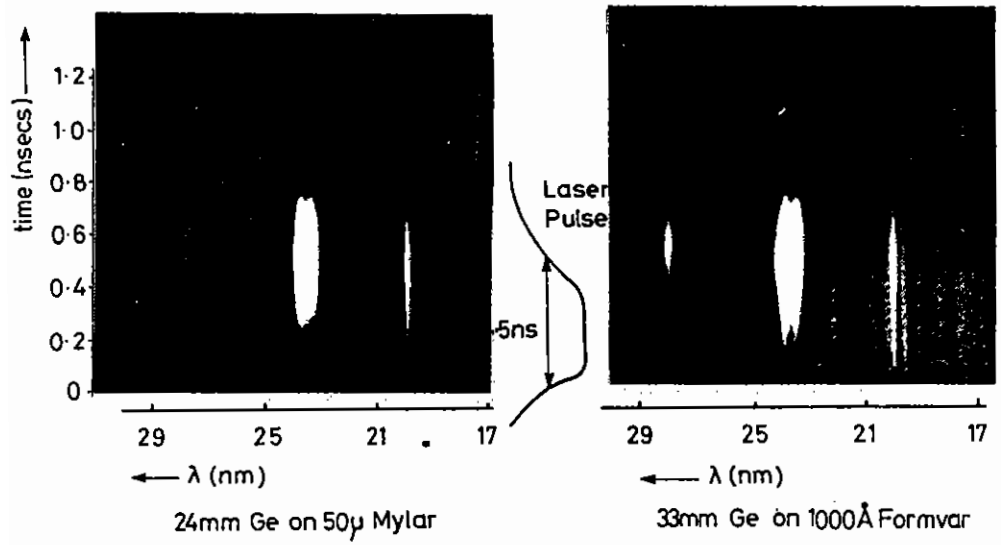
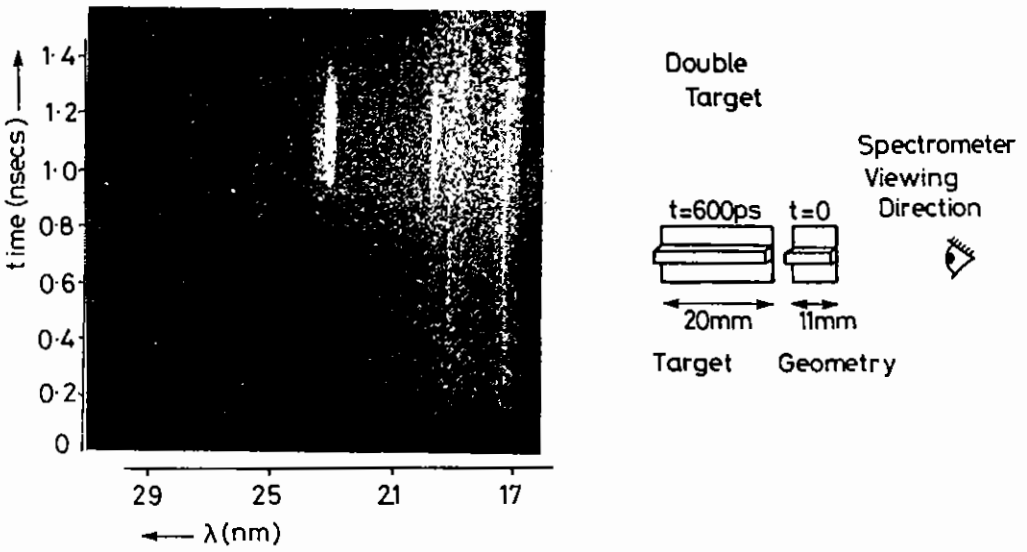


Fig A1.6 *Streak records of axial spectra.*



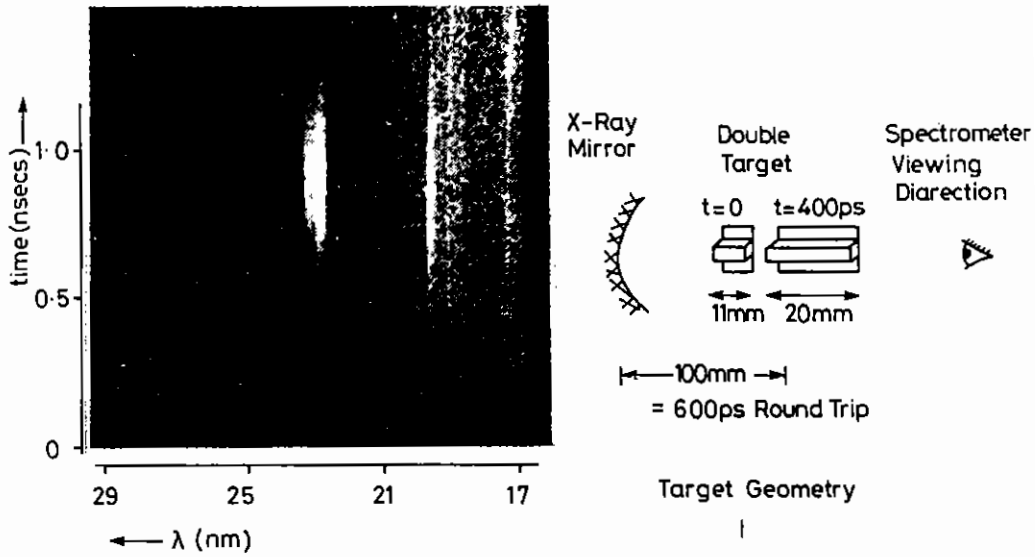


Fig A1.8 *Streak record of axial spectra with multilayer mirror and different timings along the target length.*

and for the longer 1 nsec pulses (Fig 6(a)), it is significantly shorter than the laser pulse, suggesting that long duration of gain is not obtained with long pulses. Comparison with a thin film target showed a similar duration of laser action.

Preliminary tests were carried out with an XUV mirror of 10 cm radius of curvature placed with its centre of curvature in the centre of the plasma. The mirror reflectivity was ∿ 6.5% (see Section A1.5). Because the duration of the gain is insufficient for the 600 psec transit time of radiation to and from the mirror, the plasma was subdivided into a 12 mm length (one beam) and a 24 mm length (two beams) with different timing. Fig A1.7 shows a streaked spectrum with a 600 psec delay of the 24 mm length with the spectrum observed after transmission though residual plasma from the 12 mm length, with no mirror. The 23.6 nm line appears to be strongly attenuated by the decaying plasma. With a mirror, (Fig A1.8), the absorbed spectrum shows a similar attenuation of the 23.6 line suggesting that the recorded emission originates in the 12 mm plasma, is reflected from the mirror and is then attenuated by the decaying 12 mm plasma and amplified by the 24 mm plasma. If correctly interpreted this is the first observation of time delayed amplification used to compensate for the short gain duration of a 3p-3s laser.

Conclusion

Preliminary analysis of the data from the recent experiment shows good potential of the 3p-3s Ge XXIII laser with slab targets at 1.06 μm radiation for development of techniques of XUV laser beam manipulation and for early work on applications. More detailed analysis is underway.

References

1. D L Mathews et al, Phys Rev Lett 54, 110-3 (1985).
   D L Mathews et al, J Opt Soc Am 4 588 (1987).

2. T N Lee, E A McLean and R C Elton, Phys Rev Lett 59 1155 (1987).

3. M H Key, J Mod Opt 35 575 (1988).

4. C Chenais-Popovics et al, RAL 87-041, Annual Report p6-12 (1987).

5. G P Kiehn, O Willi, A R Damerell and M H Key, Appl Opt 26 425 (1987).

6. G J Linford, E R Peressini, W R Sooy and M L Spaeth, Appl Opt 13 379 (1974).

A1-2 DEMONSTRATION OF GAIN IN BALMER-α TRANSITIONS Na XI and Mg XII

Y Kato, M Yamanaka, H Daido, T Tachi, E Miura, H Nishimura, H Shiraga, P R Herman[a], H Takabe, T Jitsuno, M Takagi, S Nakai and C Yamanaka[b] (Institute of Laser Engineering, Osaka University)
M H Key, G J Tallents, S J Rose, P T Rumsby (RAL)

Abstract

The first demonstration of soft x-ray gain in Balmer-α (H_α) transitions in NaXI at 54.2 Å and Mg XII at 45.5 Å is reported. Planar stripe targets were irradiated with intense, line-focused

351 nm laser light at an intensity of up to 5×10^{14} W/cm². The observed gain coefficients for the N H_α and Mg H_α transitions are 1.7 ± 0.6 cm^{-1} and 1.5 ± 0.6 cm^{-1}, respectively. Time evolution of the gain for the Na XI H_α line is also presented. These experimental results are compared with theoretical evaluations.

Extension of soft x-ray lasers to shorter wavelengths is being pursued at many laboratories. By creating population inversion with electroncollisional excitation[1], amplification of soft x-ray radiation at 50.3 and 56.1Å due to 4d-4p transitions in Ni-like Yb ions has been observed[2]. For the recombining plasma scheme where population inversion is created transiently during collisional-radiative cascade decay to lower levels[3,4], amplification has been observed at wavelengths as short as 80.9Å from the Balmer-α (H_α) transition of the H-like F ion[5,6], and at 83.2Å from the 4f-3d transition of the Li-like Cl ion[7].

Isoelectronic scaling of the H_α recombination laser has been studied[8,9] to determine prospects for shorter wavelength lasing, with broad conclusions that higher Z targets should be irradiated with shorter wavelength and shorter pulses of higher intensity.

Both high intensity and short wavelength laser irradiation of targets was provided by the frequency-tripled GEKKO XII glass laser. A laser pulse of 130 ps duration and 351 nm wavelength was focused to a line of 7 mm length and 30 μm width. The laser was operated with one beam up to the energy of 150 J corresponding to a maximum intensity on target of 5×10^{14} W/cm². Most of the data were taken with stripe targets[10] where the laser material was coated with 1μm thickness and 30 μm width on a stretched 0.13 μm-thick and 6 mm wide plastic CH foil. This coating thickness exceeds the calculated ablation depth of 0.4 μm at $I = 5 \times 10^{14}$ W/cm². A split-field imaging microscope system[11] was used to position a target to within ±5 μm and ±1 mrad accuracy and the same tolerances were achieved for laser focus alignment onto the target at 351nm. The whole 6 mm length of the target was irradiated from the coated side with the 7-mm lng line-focused laser beam. The laser materials tested for observing amplifcation in Na, Mg, and AI were, respectively, NaF and $Na_2B_4O_7$, MgF_2, and A1. The $Na_2B_4O_7$ was studied as a "diluted" target material which might provide higher gain than NaF due to reduced Ly_α trapping[8,9].

Two XUV spectrographs with varied-space gratings for flat-field recordings of spectra[12] were used for gain determination. One spectrograph was aligned onto the x-ray laser axis and another was positioned 60° off-axis. The XUV spectra were recorded either with films for high spectral resolution of 0.2 Å at around 50 Å, or with streak cameras for time resolved measurement with a reduced spectral resolution of 0.5 Å. A third spectrograph gave a survey XUV spectrum over a broad spectral range. A slit camera provided an x-ray image of the irradiated target surface with higher magnification perpendicular to the line focus.

Gain was determined from the line intensity ratio for the axial and transverse emissions as $I_a / I_t = (\exp(gl)-1)/(gl)$, which is valid for small $gl \leq 4$, where g is the gain coefficient and 1 is the gain length[5,7,13]. In order for this method to be used, the relative sensitivity of the two spectrographs has to be accurately calibrated. In this experiment, a grazing-incidence spherical mirror formed a 10:1 reduced astigmatic image of the source onto the horizontally-positoned entrance slit of each spectrograph[6,14]. Both slits were opened wide (500 μm) and the spectrographs were carefully positioned in order to ensure that the source images were completely contained within the widths of the slits. The relative sensitivity of the two spectrographs was determined by recording spectra from a carefully designed cross calibration target which produced identical emissions to both spectrographs. The frequency dependent relative sensitivity[20] was thus determined to an accuracy of ± 25% over 33-88 Å. The characteristic response curve of the Kodak 101-07 film used for the time-integrated spectral recordings was calibrated in an independent experiment. The observed H_α line is composed of 3 fine structures (neglecting the splittings due to Lamb shift). The gain

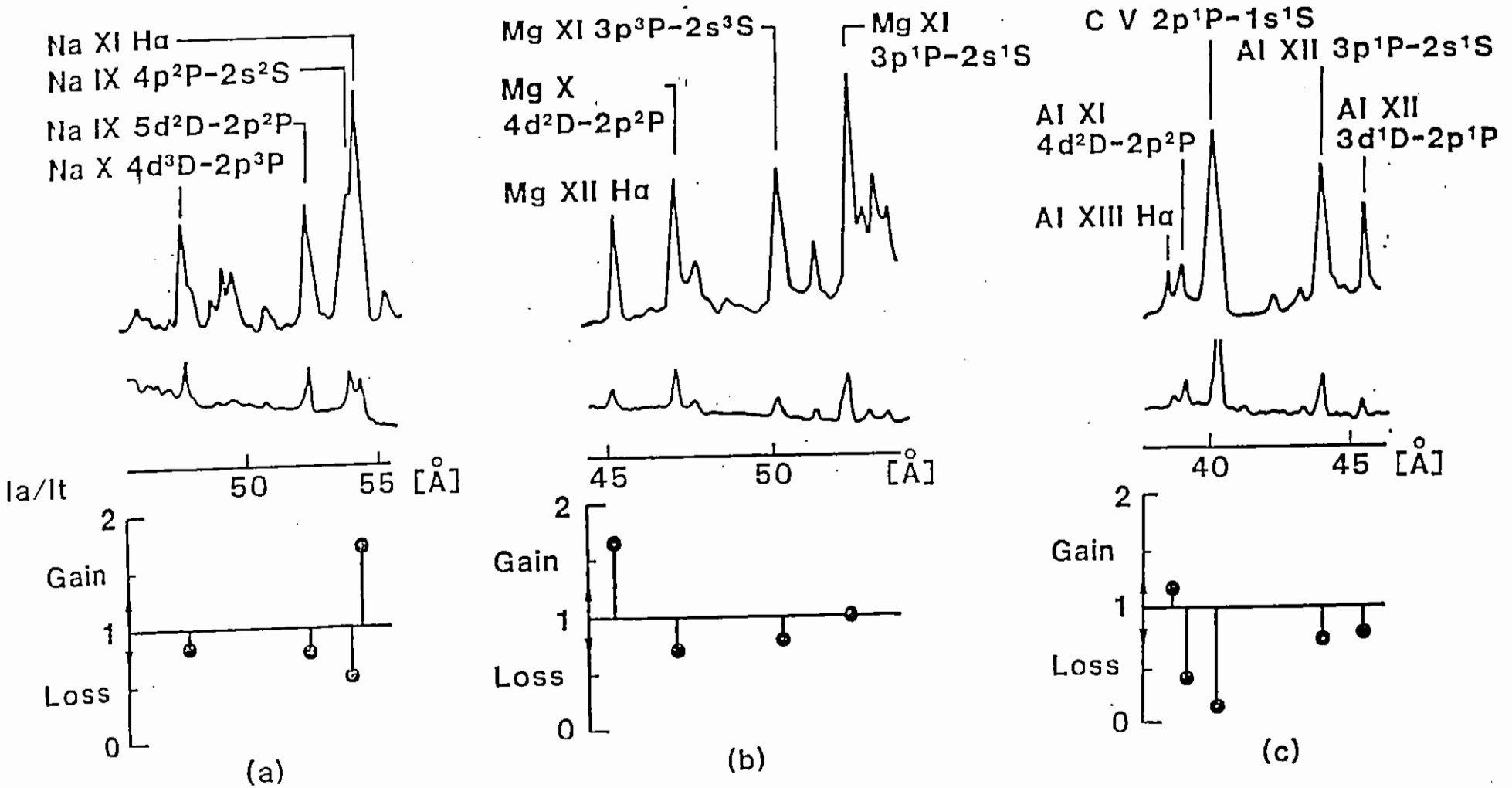


Fig.A1.9 *The axial and transverse spectra (upper traces and lower traces, respectively), and the normalized intensity ratios I_a/I_t produced by (a) NaF, (b) MgF_2, and (c) Al targets. The wavelength scale is in angstrom unit.*

was determined for the strongest component of the Ha line, ie. $3d^2D_{5/2} - 2p^2P_{3/2}$, after deconvolution of the fine structure and other blended weaker lines[15] using a least-squared curve fitting program[16].

The present experimental procedure for gain determination is particularly suitable when the gain-length product is small, since the gain is determined with one data shot once the cross calibration is made. In this way the determination of the gain value is not affected by shot to shot variation in irradiation conditions. The major emphasis of the experiment was placed on demonstration of gain in Na H_α both in time-integrated and time-resolved measurements. After confirming the reproducibility of the data and the reliability of the procedure with Na Ha, the experiment was extended to Mg H_α and Al H_α in order to test amplification at shorter wavelengths.

Time-integrated axial and transverse spectra and the normalized intensity ratios I_a/I_T of several lines near the H_α transitions of Na, Mg and Al are shown in Fig A1.9. The intensity ratio I_a/I_t is greater than 1 for the Ha lines of Na XI, Mg XII, showing definite gain; for Aℓ XIII the ratio appears to exceed unity but is close to error limits. On the other hand, I_a/I_t is less than 1 for all other lines including the blended lines such as Na IX 4p 2p - 2s 2s and Al XI 4d ^2D - $2P^2P$ which therefore show absorption along the plasma axis. [It is important to note that the sensitivity ratio of the two spectrometers changes rapidly with frequency because they had different diffration gratings and because the film response is nonlinear]. Table 1 summarizes the irradiation conditions and the gain values. The gain coefficients of the $3d^2D_{5/2} - 2p^2P_{3/2}$ transition obtained with the time-integrated measurements for the Na XI, Mg XII and Al XIII are 1.7 ± 0.6, 1.5 ± 0.6 and 0.3 ± 0.6 cm^{-1}, respectively. The inaccuracy of the gain value arises mainly from cross calibration and deconvolution of the lasing line from the overlapped lines.

As is observed in Table 1, the laser intensity was increased with Z^4 from Na to Mg in accordance with the theoretical conclusions for isoelectronic scaling[9]. However for Al XIII, it was not possible to increase the intensity above that used for Mg XII. The ionization balance was estimated from the intensity ratio of 2p-1s transitions of H-like and He-like ions, which were 0.1 for Aℓ compared with 0.9 for Mg and 0.7 for Na. From these intensity ratios and the transition probabilities for these lines, the time-averaged ratio of fully-stripped to hydrogenic ions, n^Z/n^{Z-1}, is approximately 0.2, 1.8 and 1.7 for Al, Mg and Na, respectively. In Table 1, the observed gain coefficient decreases with Z as expected[9] but the indeterminate gain value for Al H_α should be mostly ascribed to the insufficient laser intensity. In the case of the NaF stripe, an increase of laser energy from 73 J to 136 J resulted in a slight reduction of gain to 1.2 cm^{-1}, indicating that the plasma may be overheated at the higher intensity. The diluted $Na_2B_4O_7$ target resulted in a gain value of 0 ± 0.6 cm^{-1} in contradiction to our preliminary theorectical evaluation.

Time-resolved measurements using the streak cameras were made for the Na H_α transition. Cross calibration as well as data shots were repeated as described previously. The time-resolved spectrum observed from the axial direction is shown in Fig A1.10. The emission due to Na H_α lasts until ∿1 ns after laser irradiation. Contributions of the lines blended with H_α were subtracted based on recordings of the time-resolved as well as time integrated spectra. Figure A1.10b shows the time dependence of the gain coefficient of the Na H_α line thus derived for a NaF stripe target irradiated with 133 J of laser energy. The gain begins ∿80 ps after the peak of the laser pulse, becomes a maximum at 150-200 ps and decays to zero at ∿600 ps. As is expected, the measured maximum gain coefficient of 2-4 cm^{-1} is higher than the time-intergrated data of g∿1.2 cm^{-1}.

Analysis of the gain characteristics of the H_α laser in a recombining plasma of a stripe target is presented in Fig A1.11. A set of thin solid lines shows contours of reduced gain $g/Z^{7.5}$ as a function of the reduced density n_e/Z^7 and the reduced temperature $T_e/Z^{2.9}$ These gain contours are obtained by evaluating the

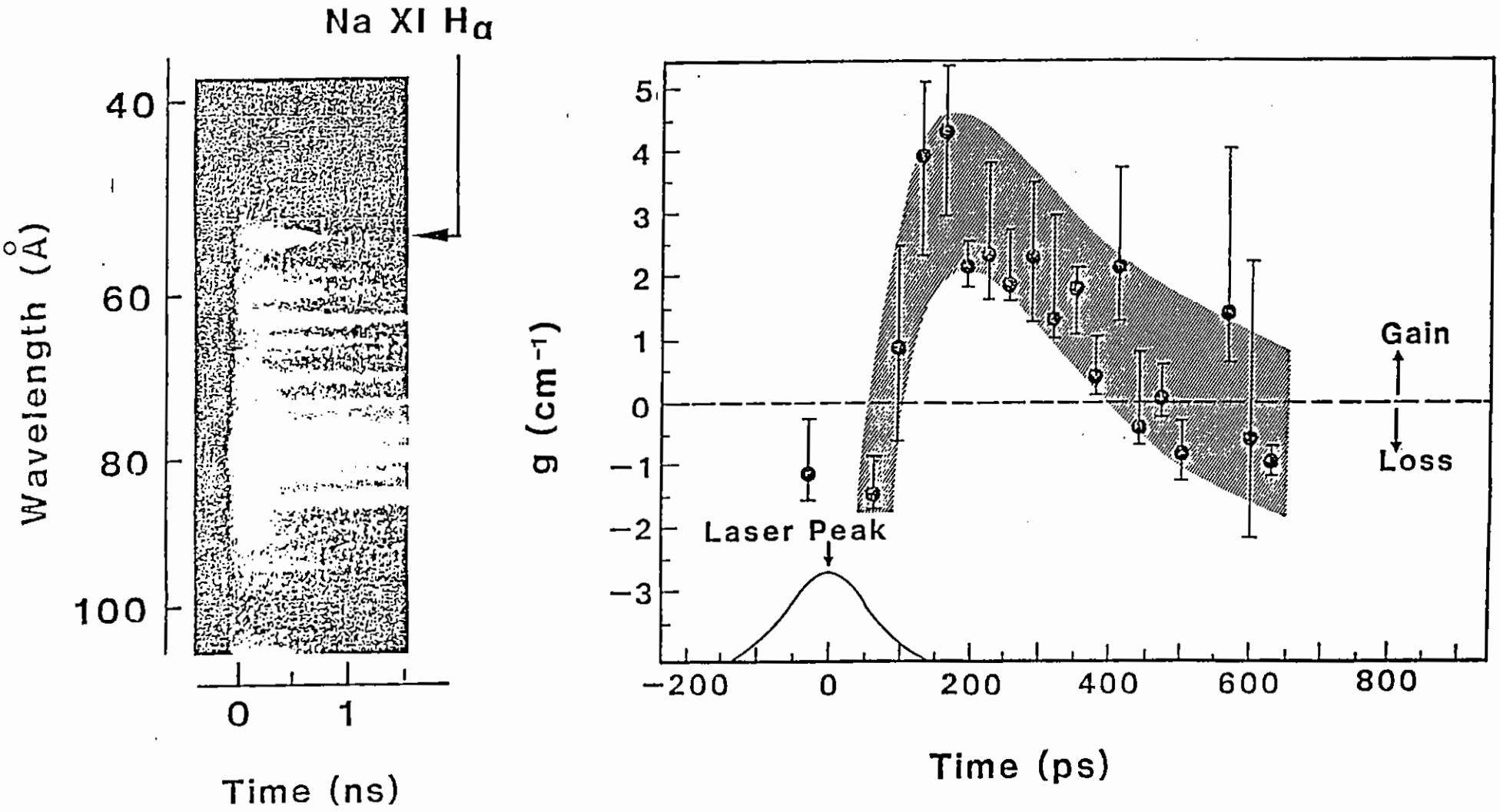


Fig.A1.10(a) A time-resolved spectrum for the NaF target.

(b) Time dependence of the gain coefficient of the Na XI Ha line determined from the time-resolved axial and transverse spectra.

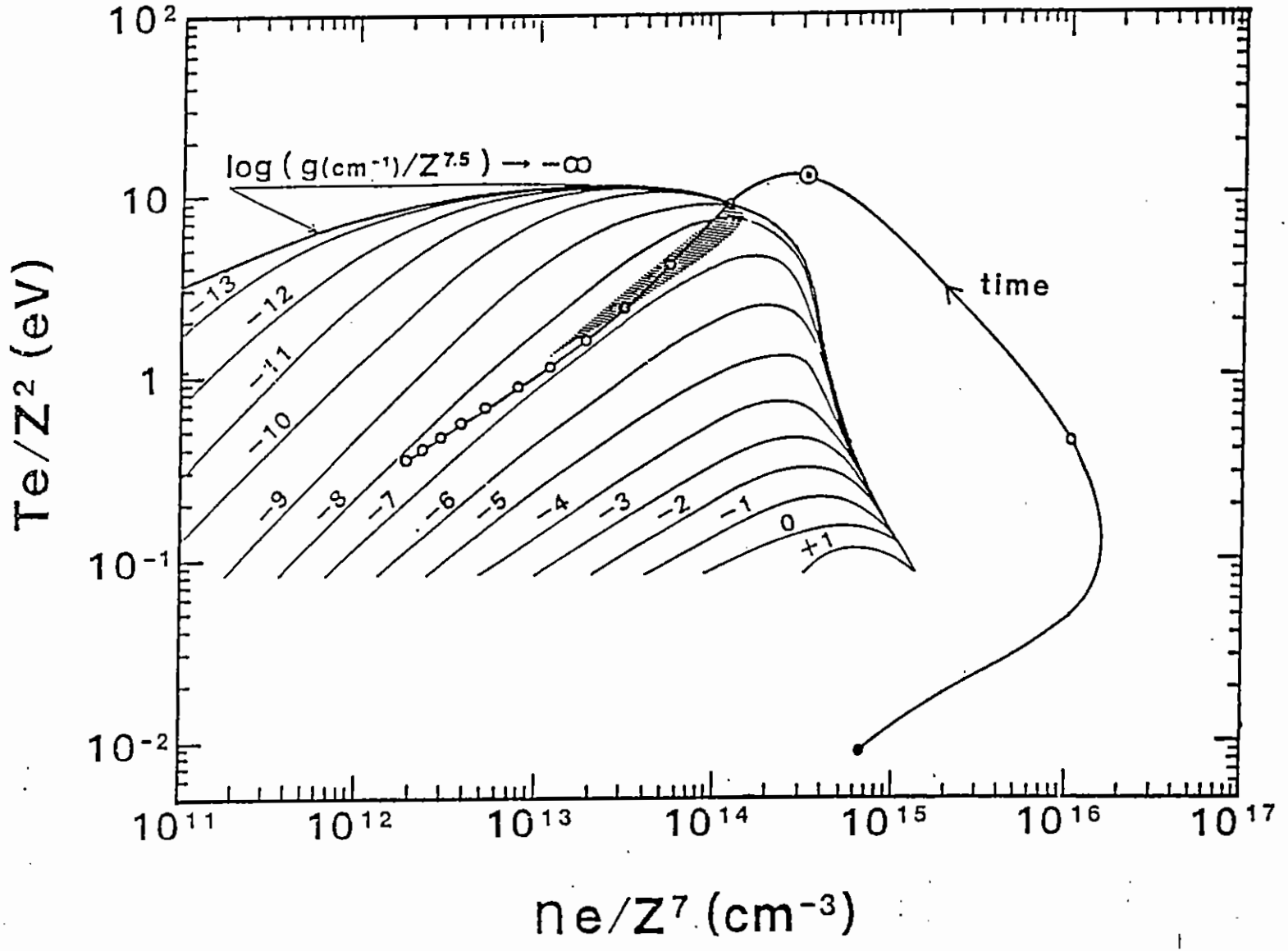


Fig.A1.11 *Theoretical evaluation of the gain characteristics. Thin solid lines represent gain coefficient g in terms of T_e and n_e, all in reduced units. Temporal variation of the plasma parameters for a NaF target for a plasma element with an initial depth of 1000Å from the surface is given by the thick solid curve. The gain region determined from the time-resolved measurement is shown as the shaded area.*

population inversion from the excited state populations determined by collisional radiative rate constants[17,18]. These are maximum possible gains obtained when the ions are fully stripped at the initial plasma formation and remain predominantly as bare nuclei during rapid cooling. The time variation of the plasma parameters was evaluated using a two-dimensional Lagrangean hydrodynamic code ILESTA-2D[19]. The result for a 1-μm thick NaF stripe irradiated by a 130 J, 130 ps laser pulse of 351 nm wavelength is shown in Fig A1.11. The thick solid curve show the result for the plasma element initially 1000 Å deep from the surface. A time step of 100 ps is shown by the open circles with the peak of the laser pulse marked by a double circle. This initial depth is approximately optimum for producing the highest gain. A plasma element closer to the surface is overheated resulting in lower density and a deeper element does -not reach to a sufficiently high temperature for complete ionization. At the peak of the laser pulse, T_e=1.5 keV and $n_e=6.4\times10^{21}$ cm^{-3} for this optimum plasma element, suggesting a sufficient ionization balance of $n^{Z-1}/n^Z=0.04$ for H-like ion relative to bare nuclei. After this time, T_e decreases faster than the adiabatic rate of $T_e \propto n_e^{2/3}$ due to thermal conduction to the cold region inside the target. The gain starts at 100 ps and reaches to a value of g$\sim$ 3 cm^{-1} at t $\sim$ 200 ps after the laser peak. At t = 200 ps, this plasma element is $\sim$80 μm away from the original position of the target surface. The gain value obtained from the time-resolved measurement is shown by the shaded area in Fig. 3. Calculations show[9] that collisional excitation from the n=1 to the n=2 state of the hydrogenic ions becomes negligible at t$\sim$100 ps. However Lyα trapping, which in numerical modelling significantly affects the gain until t$\sim$200 ps, seems to become negligible at somewhat earlier time judging by the observation of early onset of gain in Fig.2.

In summary we have demonstrated gain in the H_α lines in Na XI and Mg XII at the wavelengths of 54.2 Å and 45.5Å respectively. Time evolution of the gain was determined for the Na XI Ha line. These experimental results are generally consistent with the analytical as well as numerical evaluations. Higher gain for these transitions is expected in irradiation with a reduced pulse width.

We would like to thank technical support given by the staffs at the Institute of Laser Engineering and the Rutherford Appleton Laboratory including N.Miyanaga, M.Grande and A.R.Damerell. financial support by the Japan Society for the Promotion of Science to M.H.Key and P.R.Herman and by the Inoue Foundation for Science to P.R.Herman are gratefully acknowledged.

Table 1 Gain coefficient for the $3d^2D_{5/2}$-$2p\ ^2P_{3/2}$ transition obtained with stripe targets

	Na XI H_α	Mg XII H_α	Al XIII H_α
Wavelength (Å)	54.194	45.533	38.793
Target material	NaF	MgF_2	Al
Laser energy (J)	73	147	152
Gain coefficient(cm^{-1})	1.7±0.6	1.5±0.6	0.3±0.6 (indeterminate)
Time dependence (a)	g=2-4 cm^{-1} at 150-200 psec	———	———

(a) Time dependence of the gain for NaXI H_α was measured with the laser energy of 133J.

References

(a) Present address: Department of Electrical Engineering, University of Toronto, Toronto, Ontario, Canada, M5S 1A4.

(b) Present address: Institute for Laser Technology, Utsubo-honmachi, Nishi-ku, Osaka, 550 Japan

1. D.L.Matthews et al., Phys. Rev. Lett. 54, 110 (1985). D L Matthews et al, J Opt Soc Am 4, 588 (1987).

2. B.J.MacGowan et al., Phys. Rev. Lett. 59, 2157 (1987).

3. G.J.Pert, J.Phys. B9, 3301 (1976), and 12, 2067 (1979).

4. C.Chenais-Popovics et al., Phys. Rev. Lett. 59, 2161 (1987).

5. O.Willi et al., SPIE 688, 2 (1986).

6. P.R.Herman et al., to be published in IEEE Trans. Plasma Science 16, (5) (1988).

7. G.P.Kiehn et al., SPIE 831, 270 (1987).

8. A.K.Dave and G.J.Pert, J. Phys. B17, 4953 (1984).

9. M.H.Key, Rutherford Appleton Lab. Annual Rept., RAL 87-041, 100 (1987) (unpublished); M.H.Key, unpublished.

10. D.C.Eder et al., J.Opt. Soc. Am. B4, 1949 (1987).

11. I.N.Ross et al., Appl. Opt. 26, 1584 (1987).

12. T.Kita, T.Harada, N.Nakano, and H.Kuroda, Appl. Opt. 22, 512 (1983); G.P.Kiehn, O.Willi, A.R.Damerell, and M.H.Key, Appl. Opt. 26, 425 (1987).

13. D.Jacoby, G.J.Pert. S.A.Ramsden, L.D.Shorrock, and G.J.Tallents, Opt. Commun. 37, 193 (1981); D.Jacoby, G.J.Pert, L.D.Shorrock, and G.J.Tallents, J.Phys. B15, 3557 (1982).

14. Y.Kato et al., SPIE 831, 299 (1987).

15. R.L.Kelly, J.Phys. Chem.Ref.Data,16,Suppl.No.1~3 (1987).

16. Detailed aspects of the observed spectra will be reported elsewhere.

17. R.W.P.Mcwhirter and A.G.Hearn, Proc.Phys.Soc.2,641(1963).

18. T.Fujimoto, J.Phys. Soc. Jpn. 47, 265 (1979); T. Fujimoto, I. Sugiyama and K.Fukuda, Memo. Faculty Eng. Kyoto Univ.34, 249 (1972).

19. H. Takabe, unpublished.

20. M Daido et al, RAL-88-042, 9 (1988).

A1.3 ENHANCED EFFICIENCY AND SHORTER WAVELENGTH FOR RECOMBINATION LASERS DRIVEN BY SHORTER (20 psec) PULSES

M H Key, S J Rose, G J Tallents, M Grande (RAL)
D O'Neill, D Neely, C L S Lewis (Queen's University Belfast)
S A Ramsden, A Rogoyski (Hull)

Introduction

Iso-electronic extrapolation of hydrogenic recombination lasers to shorter wavelength is helped by the fact that gain increases as the plasma density at which the maximum temperature reached in the heating/cooling cycle increases. The theoretical basis for increased gain with increased density has been considered in numerical modelling of a homogeneously heated plasma[1] and more recently analytically and numerically for a plasma produced by ablation (see theory section A4). Increased plasma density can be obtained by using a shorter wavelength in the heating laser or a shorter pulse. The effect of shorter laser pulses has been seen in experimental studies and numerical modelling of 20 psec, 0.53 μm irradiation of targets with VULCAN (see A2.3).

Building on these ideas numerical modelling of 7 μm diameter fibre target irradiation was undertaken to estimate the optimum irradiation intensity and maximum gain for Na XI using 20 psec 0.53 μm irradiation with VULCAN. Table 1 summarises the principle parameters for the optimum conditions of the plasma from the numerical modelling.

Table 1 Computed Optimum conditions for gain with different experiments

Laser Wave-length (μm)	Pulse-length (ps)	Laser Energy (Jcm^{-2})	Laser Intensity (Wcm^{-2})	Peak Temp (eV)	Density at peak Temp. (cm^{-3})	Density at time of peak gain (cm^{-3})	Gain g (cm^{-1})
0.53	20	13	2.9×10^{14}	650	8×10^{21}	8×10^{20}	11
0.35	70	100	2.6×10^{14}	700	2.5×10^{21}	1.7×10^{20}	1.3

The table also shows for comparison resonator parameters for 70 ps 0.35 μm irradiation computed for the experiment described in Section A1.2. The difference between the two calculations is striking. The short pulse gives 7x higher efficiency of producing gain gℓ/P, where P is the absorbed power.

The calculations for fibre targets define an absorbed intensity at which the heating/cooling cycle is optimised in the ablated plasma and can (with some restriction) be applied also to the irradiation of narrow stripe targets at the same absorbed intensity. For example 2D hydrodynamic simulations suggest that the expansion from a 30 μm wide planar stripe target is similar, after a short time, to a quadrant of expansion from a fibre with circumference 4 x 30 μm (see A1.2). Stripe targets have the advantage of greater coupling of energy from a line focused laser beam. For example, 7 μm fibres absorb typically 10% of incident power in the ∿ 25 μm wide line focus produced by the VULCAN facility, while a 30 μm stripe can absorb over 50% at 6×10^{14} Wcm^{-2} incident to give the required 3×10^{14} Wcm^{-2} absorbed.

The VULCAN facility is capable of 0.5 TW/beam at 0.53 μm. With 70% transmission to target on a 30 μm wide stripe, 3 beams can irradiate 6 mm at the required intensity (> 6×10^{14} Wcm^{-2}). Alternatively, with 10% coupling to a 7 μm fibre and six beams the irradiated length could be 3 mm.

Experiment

An experiment was set up to investigate the gain obtained in Na XI using NaF coated fibres and 30 μm wide stripes of NaF on 100 nm CH films. The angles in the six beam line focus system were adjusted to produce a ≈ 3mm line focus. The laser was operated with second harmonic conversion and a nominal 20 psec pulse duration. Careful relative timings are needed; the super-position was accomplished within ± 5 psec for 3 beams from one side with the stripe targets. The actual pulse length was measured at ∿35 ps. Soft x-ray slit camera measurements showed the production of a 2.3 mm long, 50 μm wide focus. The work concentrated on NaF stripes 25, 50 and 100 μm wide on both thick (2 μm mylar) and thin (2000Å Formvar) substrates.

Several practical problems were encountered and only a limited data set was obtained. Best estimates of typical experimental parameters are as follows. Energies on target were 15 → 20J (2ω) or intensities of 3 → 4×10^{14} for the case of 25μ stripes, similar to the calculated required intensity level - although based on an assumed green conversion efficiency (in the absence of calorimetry on the 2 ω beams). The data obtained suggests that the actual conversion efficiencies were lower.

Figure A1.12 showns a typical time integrated spectrum taken on the axial spectrometer with the 2400 lines/mm flat field grating for a 25 μ NaF stripe on a thin substrate. The spectrum was recorded on KODAK 101-01 VUV film and resolution of between 0.3 Å and 0.5 Å was obtained over the range shown.

From the ratio of H-like to He-like resonance lines seen with the transverse spectrometer a low initial fraction of bare nuclei of Na is deduced. The observation of strong Na X and Na IX resonance lines also suggests that the plasma in this experiment was too cool to achieve laser action. The longer than expected pulse length may have been the cause of the cooler than expected conditions. In the case of the successful Osaka experiment reported in A1.2, comparable H and He-like populations were seen.

The Na XI Hα line at 54.14Å overlaps with a Na IX line (53.86Å) which is itself blended with the FIX line at 53.53Å. In the cooler plasma conditions obtained, both these lines have significant intensity. However, their individual contributions are difficult to quantify with the resolution available. The equivalent FIX Hα line (80.91Å) was also recorded. It too has line overlap with Na IX lines at 81.18 and 81.35Å. Again quantitative measurements may prove unreliable. Preliminary estimates for both lines indicate that they were approaching optically thin conditions rather than amplifying.

A limited amount of time resolved data was also obtained but little conclusive evidence of gain was observed.

In dealing with these low gl systems it is extremely important to be able to reliably and accurately normalise the response of the axial and transverse instruments before gain can be inferred with a high degree of confidence. A suitable cross calibration target for this region of the spectrum - $Na_2 B_4 O_7$ - was used. By placing the target at an angle, it is possible to arrange for identical illumination of both spectrometers. This should prove useful for future experiments at similar energies.

The deduction of gain has been complicated by the uncertain calibration of Kodak 101 film used in this experiment. The film used was several years old and there is evidence[2] that the calibration is varying between manufactured batches and with time. A small section of the film has been kept and will be calibrated by Max Planck Institut fur Quantenoptik.

Conclusion

NaF stripes on thick and thin substrates were irradiated at up to ~4×10^{14} Wcm^{-2} on 40 psec time scales. Observed ionisation levels were lower than predicted possibly due to technical problems. Preliminary analysis suggests that Hα and F Hα lines became at least optically thin in the axial direction, but more analysis is needed. In particular an accurate film calibration needs to be made.

References

1. A Dave and G J Pert, J Phys B17, 953 (1984).

2. K Eidmann, personal communication, 1989.

A1.4 1s-2p TERM STRUCTURE IN ALUMINIUM

S. Davidson, C. L. S. Lewis, D. O'Neill (Queens University Belfast)
S. Rose, M. Grande (RAL)
J. M. Foster, C. C. Smith (AWE)

Introduction

The properties of hot dense plasmas have long been of importance in astrophysics and, of recent years, in laser fusion type plasmas.

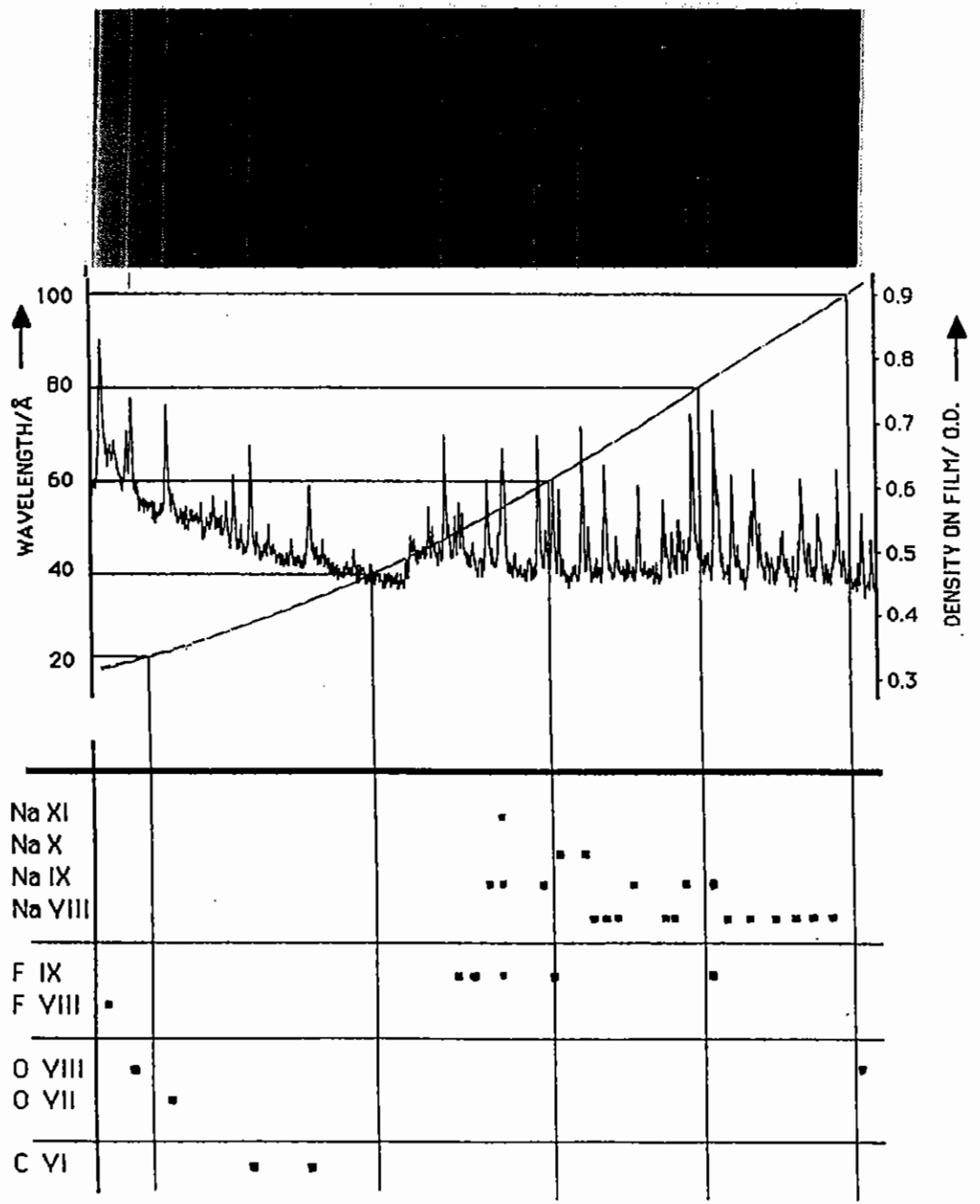


Fig A1.12 Time integrated axial spectrum of a Sodium Fluoride Target.

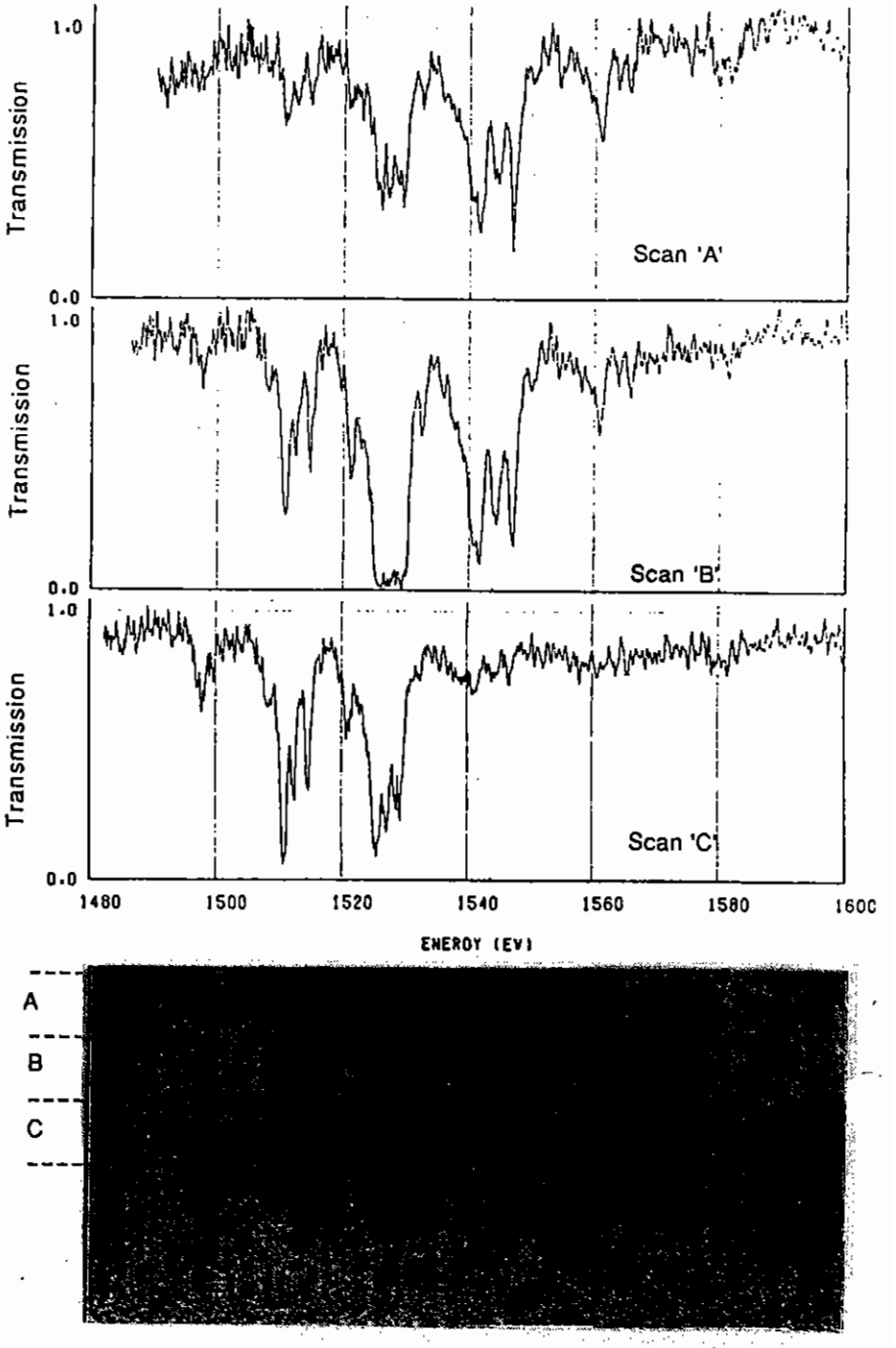


Fig A1.13 Reduced transmission data for shot 6240288 at three positions on the foil.

The calculation of the opacities of such plasmas in a reasonable time with finite computing resources often requires approximations to be made to the atomic physics. Even in the calculation of relatively low Z plasmas, term structure is often either omitted or approximated by a simple profile.

Calculated opacities are often used in situations such as laser plasmas which have large temperature and density gradients and often are far from equilibrium. In such circumstances it is difficult to separate the approximations involved in the calculation of the opacities from uncertainties in the simulation of the experiment.

The previous annual report[1] described initial results (Fig A1.13) from an experiment in which the technique of point projection spectroscopy was used to obtain absorption spectra of 1s-2p aluminium transitions. The data clearly showed structure due to transitions between the various terms of configurations present in the plasma. This report compares the data from the experiment with an ab initio calculation of the opacity.

The aluminium plasma used in the experiment was generated by soft X-rays from a second gold laser produced plasma. This resulted in a dense plasma with small density and temperature gradients and a well defined optical depth. Opacity can be directly inferred from the absorption data providing that saturated absorption of the backlighting X-rays does not occur.

Experimental results

The transmission results in Figure A1.13 were obtained on the VULCAN laser system configured to give two 0.53μm laser beams. The longer duration pulse, typically 40J in 600 pS, was focussed using f/2.5 optics onto a 500μm diameter, 1500Å thick layer of gold supported on a 1μm layer of Parylene 'N' plastic.

A 500Å tamped sample of aluminium mounted at the rear of the foil was heated by the transmitted X-rays. The sample was coated on both sides by 0.3μm of Parylene 'N' plastic which had the effect of tamping the foil expansion creating a more uniform density and temperature profile.

A laser beam typically 15J in 100pS and delayed by 600pS with respect to the first pulse, was used to produce a backlighting source of X-rays from a 20μm diameter carbon fibre coated with 1μm of samarium. This produced a point source of quasi-continuous M-band X-ray emission which was used to backlight the aluminium sample in a point projection geometry[4] configuration. The transmission data as a function of photon energy was obtained by converting to intensity the densitometered spectrum obtained from a PET crystal spectrometer and numerically taking the intensity ratio from the two regions of film corresponding to backlighting X-rays passing through and round the sample. The mean ionisation varied between different positions in the foil because of the 15° inclination of the sample foil relative to the gold heating foil.

Calculated opacity and comparison with experimental data

The calculation of the opacity follows that described previously[2] but differs in the treatment of the 1s-2p transitions. Multiconfigurational Dirac Fock (MCDF)[3] line positions and oscillator strengths were used in the calculation. Separate MCDF calculations for the inital and final configurations allowed all the term structure arising in the 1s-2p transitions to be accurately included.

Saha/Boltzmann distriubtions of lower state configurations $1s^2 2s^k 2p^\ell$ with k = 0,1,2 and ℓ = 0,1,...6. were used. The use of LTE statistics for the lower state populations has been shown to be a reasonable approximation by using the measured heating spectrum and the calculated density-temperature time history of the sample as input to the average atom, screened hydrogenic, rate equation solver code NIMP[5]. The absorption spectrum is largely independent of the upper state populations which couple more strongly to the radiation field and consequently depart more from LTE.

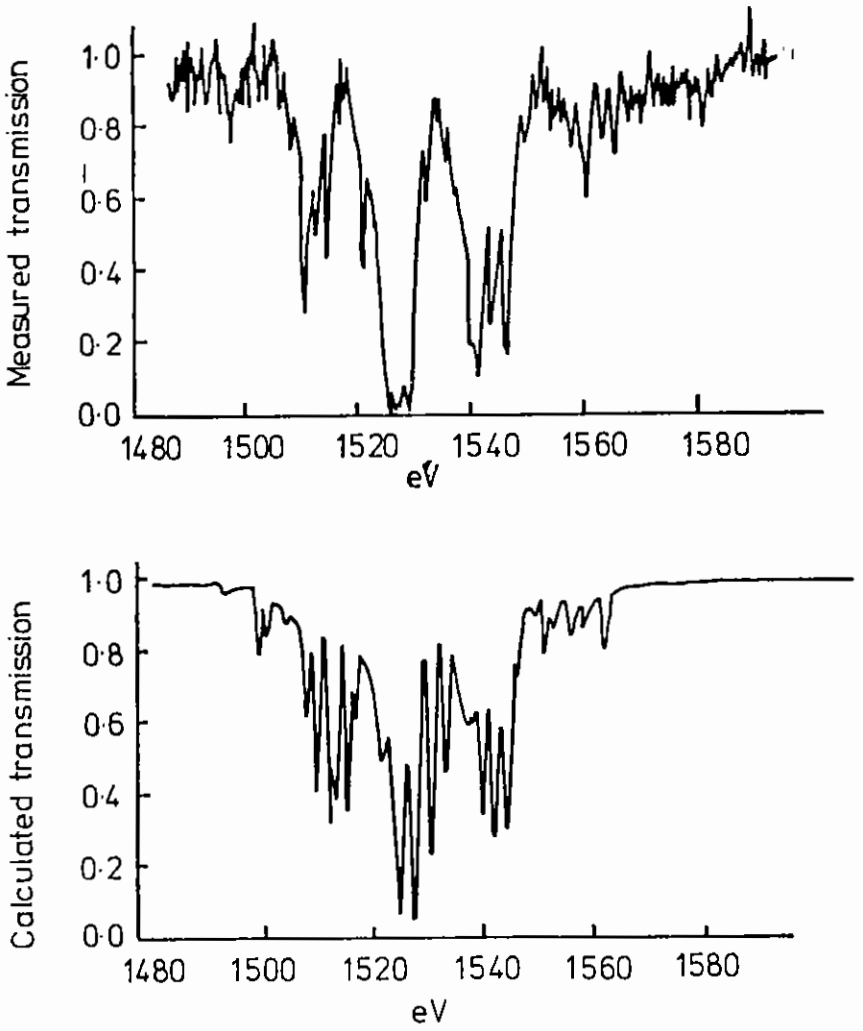


Fig A1.14 Comparison of measured and calculated transmission.

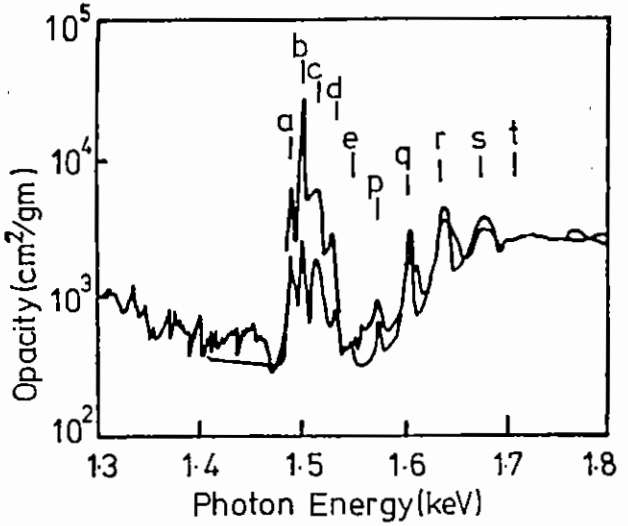


Fig A1.15 Previous measurement compared with calculation at 35 eV and 0.015 g/cc in which term structure is approximated by single (configurationally averaged) lines.

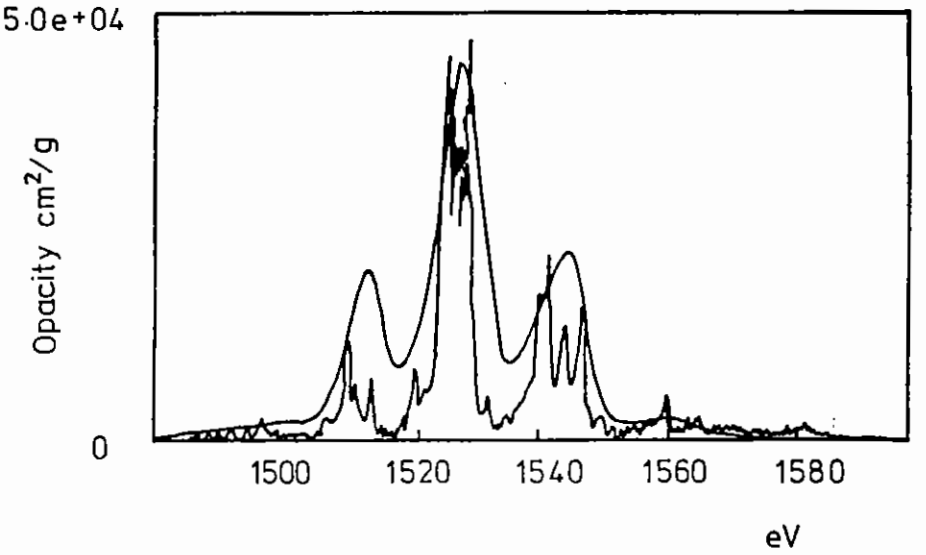


Fig A1.16 Recent measurements with improved resolution and thinner samples show better agreement with configurationally averaged calculation.

For the 1s-2p transitions, each individual allowed line transition between terms of the upper and lower configurations was treated as a Gaussian line of Doppler width in the calculation of the opacity. In this detail, the current calculation differs from that reported previously[2] where we averaged all of the 1s-2p lines of a given configuration, and represented their opacity as a single configuration average line of width equal to the greater of the variance of the term structure or the instrumental broadening. In the current calculation scaled configurational averaged lines are still used for configurations with an n=3 or n=4 spectator electron.

The absolutely measured intensity of the soft X-ray emission from the heating foil allows the flux at the surface of the sample to be estimated. This was used as a boundary condition in a hydro calculation of the sample expansion using the AWE hydro code NYM. Sample temperatures calculated in the hydro simulations were typically 40 eV at the end of the heating laser pulse, at which time the sample density was 0.005 of solid density.

Figure A1.14 shows a comparison of the present experimental data with the calculated absorption spectrum for an aluminium sample plasma with an electron temperature of 40 eV and a density of 0.014 g/cc. The effective solid thickness of 2000Å used in the calculation corresponded to the thickness in the direction of the absorption measurement when the 500µm sample was mounted at 15° to the plane of the heating foil.

Comparison with previously reported data

In the previously reported[2] low resolution data (Figure A1.15) we compared the measured aluminium opacity with a calculation in which for each lower state configuration, the 1s-2p term structure was approximated in a single (configurational average) line of appropriate width, as explained above. We noted a discrepancy between the calculated and measured opactiy in the 1s-2p lines, but found rather close agreement between measured and calculated 1s-3p lines.

We now believe that the discrepancy arose as a consequence of using a sample foil that was sufficiently thick (0.5µm) to provide large optical depth in each of the narrow, separated, but unresolved lines arising from the transitions from terms of each configuration. The large optical depth of the lines resulted in saturated absorption but because the lines were unresolved the saturation of the absorption was not evident in the measured absorption spectrum.

This explanation is born out in Figure A1.16, in which we compare the opacity obtained from the more recent data with the previous calculation (ie. the calculation using configurational averages for the 1s-2p lines). The new data is seen to be much closer to the calculation as a consequence of using an optically thinner sample.

Summary

The technique of point projection spectroscopy with a sample heated only by radiation from a laser plasma has been shown to be a powerful technique for the measurement of the opacity of high temperature, moderate density materials. Transmission measurements of partially ionised aluminium are consistent with the LTE calculations described. An anomaly between measured and calculated opacity in the 1s-2p lines which was evident in a previous experiment has been explained.

References

1. S. J. Davidson, C. L. S. Lewis, D. O'Neil, S. Rose, W. S. Shaikh, M. Grande A18 Annual Report to the Laser Facility Committee (1988)

2. S. J. Davidson, J. M. Foster, C. C. Smith, K. A. Warburton and S. J. Rose, Appl.Phys.Lett. 52, 847 (1988)

3. I. P. Grant, B. J. McKenzie, P. H. Norrington, D. F. Mayers and N. C. Pyper, Comp. Phys. Commun. 21, 207 (1980)

4. C. L. S. Lewis and J. McGlinchy, Opt. Comm. 53, 179 (1985)

5. S. Rose (Private Communication)

A1.5 FIGURED SOFT X-RAY MULTILAYER MIRRORS: A METHOD OF MEASURING NORMAL INCIDENCE REFLECTIVITY

M Grande, N Rizvi (RAL)
A M H Al Arab, B L Evans, S Xu (University of Reading)

Abstract

A method of measuring the reflectivity of concave spherical multilayer mirrors is described, which utilises the quasi-continuum soft x-ray radiation from a small laser-produced plasma. The small source size allows nearly on-axis imaging of the source and hence simultaneous direct comparison of the direct and reflected intensities. The method is applicable to concave multilayer mirrors of any radius of curvature.

Introduction

The fabrication of XUV multilayer mirrors has become widespread. One of the main driving forces for this research has been the goal of using figured XUV normal incidence optics in a variety of applications. As yet, however, very few direct measurements of the performance of figured XUV mirrors have been obtained, which is in part due to the difficulty of making such measurements. Many authors have, however, reported measurements on flat multilayers and the use of a low powered plasma source for plane multilayer assessment has recently been described [2].

We here report a new, simple and experimentally unambiguous method of assessing the reflectivity of concave spherical XUV multilayer mirrors, using a laser produced plasma as a point x-ray source. Some preliminary results using this setup have already been reported[1]; the aim here is to describe the experimental technique in more detail. It is hoped that this method, which is insensitive to the radius of curvature of the mirror (which may be as little as a few centimetres) will be used to assess mirrors for a variety of applications.

The immediate motivation for the present research was to produce cavity mirrors for an XUV laser scheme. (See eg. (3)) this places quite stringent requirements on the mirror. The scheme under investigation was the collisionally excited neon-like germanium scheme, where the laser plasma is pumped by a high powered (∿ 1TW) 1.06 μm wavelength laser, as developed at the Naval Research Laboratory (USA)[4]. The experiments performed in the XUV laser investigation will be described elsewhere (A1.1)[5]. Because of the short lived gain regime (≤ 600 ps) of the system, it is necessary to have a short transit time to the mirror and back; the bending of x-rays by the refractive index gradients in the column of laser produced plasma dictates that the mirror should be spherical and central on the mid point of the plasma column, giving a requirement for a radius 100 mm (or less) with a peak reflectivity, as high as possible, at 236 Å.

Mirrors were fabricated at the University of Reading, as a platinum silicon multilayer stack by the ion beam sputtering technique[6]. Platinum has proved an excellent material for multilayer fabrication. There is some interdiffusion of Pt and α- silicon[7], but this is not a major limitation in the EUV. Fig A1.17 shows the performance for an optimised PtSi multilayer structure, as calculated using the matrix method. It is interesting to note that at this wavelength platinum appears to give a higher reflectivity than molybdenum. However, there is evidence[8] that the optical constants may be misleading on this point. Although we are certain[7] that the silicon in our layer structure is amorphous, there is little good data on α - Si in this wavelength regime; we have used that of Hunter[9] for evaporated Si, which may be appropriate. The calculated peak reflectivity is 27% with a FWHM of 23Å.

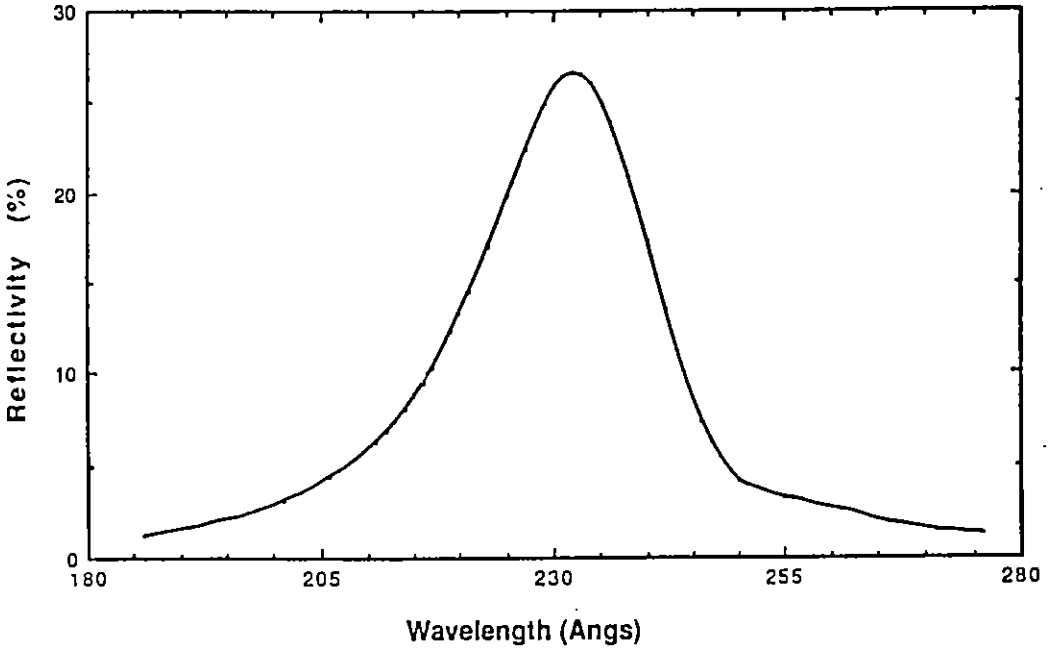


Fig A1.17 Calculated reflectivity of an optimised Pt/Si multilayer mirror as used in the experiment.



Fig A1.18 Print of a typical Kodak 101-0107 exposure. The upper spectrum is the source, the lower the reflection showing both liner and continuum within the reflected bandwidth. Note the low dynamic range of the film.

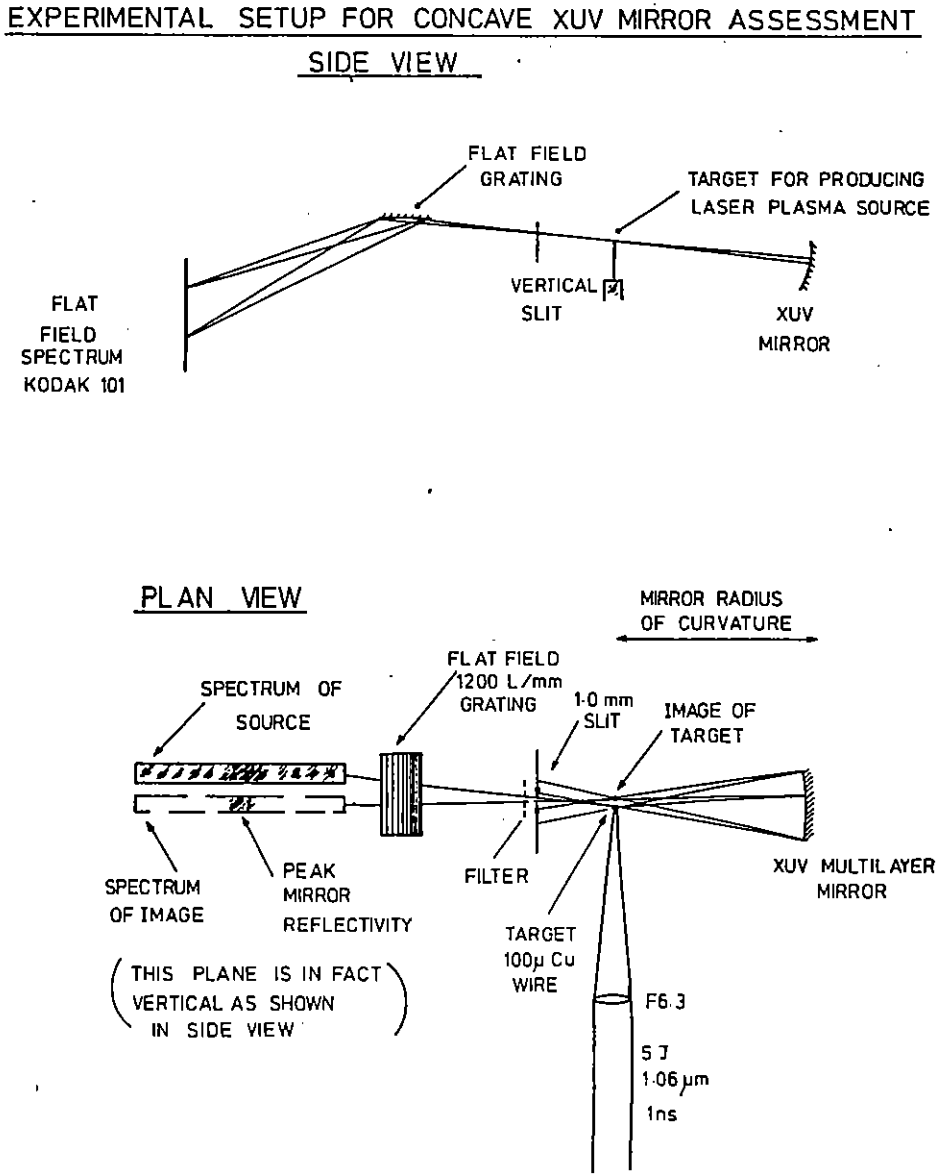


Fig A1.19 Experimental set up for concave XUV mirror assessment.

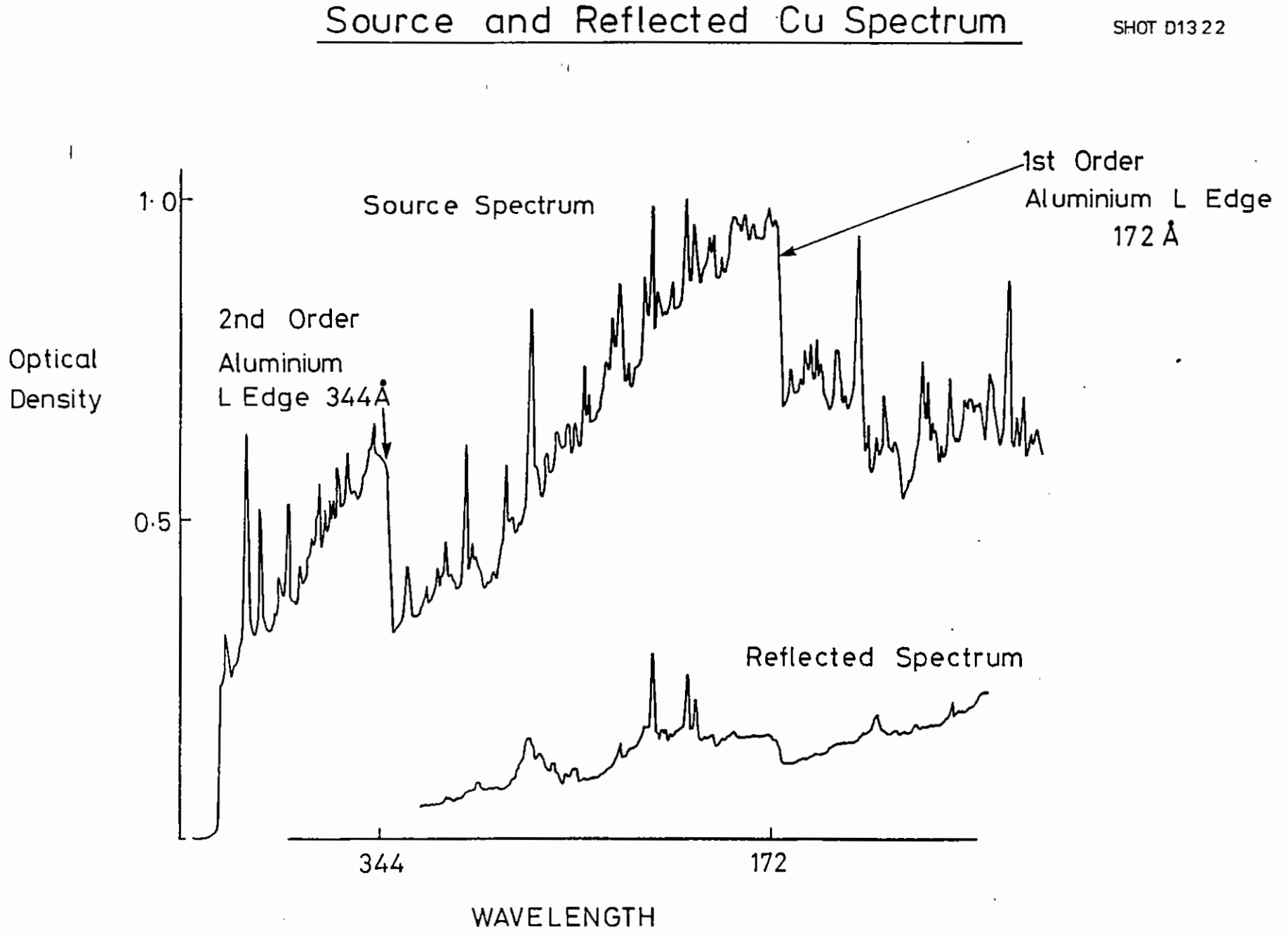


Fig A1.20 Densitometer analysis of the source and reflected XUV spectra.

The mirrors were evaluated in Target Area 4, a small parasitic single beam facility on the VULCAN high powered laser at the Rutherford Appleton Laboratory. The experimental set-up used is shown in Figure A1.19. The important feature is the mounting of the target which produces the laser plasma source at the centre of curvature of the mirror. By offsetting the mirror very slightly (typically 2°) a monochromatic XUV image of the source is produced very close beside the source itself.

The targets used were wires in the range 100 to 500 micrometres in diameter. The precise choice of diameter and target material depends on the wavelength of the mirror under test. For 236 Å we found a pulse, duration 1ns, wavelength 1.06μ, energy 5 J onto a 500μ copper wire gave an XUV flux ideally matched to the geometry and film response, so as to produce a source spectrum and its reflection within the useful film dynamic range on a single shot as shown in Figure A1.18 the result of a typical date shot; there is a strong continuum and several well resolved emission lines within the bandwidth of the mirror. In order to remove visible light contamination a 2000 Å aluminium filter was placed in front of the spectrometer. The absorbtion edge at 172 Å, seen in first and second order, provides a convenient wavelength calibration.

The small spatial extent of the plume of laser produced plasma means that when the source and its image are viewed with a spectrometer, the two are easily separated by using a space resolving slit on the input to the spectrometer, perpendicular to the direction of dispersion. The spectrometer therefore produces two separate side-by-side spectra, one direct from the source, and the other reflected via the mirror, with identical collection efficiency (since the reflection overfills the slit, as seen in figure A1.19). Thus we have a direct comparison of the incident and reflected spectra and hence a measure of reflectivity. The only assumption is that the x-ray emission from the plasma plume is symetrical about its axis, which is reasonable. The spectrometer was a flat field corrected grazing incidence type[10] using a non-uniformly ruled grating with an average 1200 times/mm[11]. Detection is this instance was via Koda 101-07 XUV film; a correction for non-linearity was made using calibrations obtained on the same film batch, since there seems to be appreciable batch to batch variation in response. The film was placed at the (flat) image plane, 472 mm from the source.

Although it is clearly desirable to test the mirrors in representative conditions, initially we had worried whether they would sustain damage or performance degredation due to the laser plasma blowoff during a shot. Repeated measurements were made but no significant degredation was seen. This is perhaps not surprising in view of the oblique geometry and low power incident; by contrast in an XUV laser environment obvious surface damage is seen on a single shot.

Results

Figure A1.20 shows a typical densitometer analysis for a mirror, illustrating a number of features. Although the nominal 2d spacing was chosen to give optimum reflectivity at 236Å, it is seen that the actual peak is around 10Å short of this. It was found that direct measurement of a figured mirror provided a very powerful feedback which resulted in the optimisation of our coating techniques. Two independent measures of reflectivity are obtained from each negative.

By comparison of the continuum levels we obtain a reflectivity measurement across the whole spectral range and hence the bandwidth can be estimated. However, the measurements can be contaminated by higher orders and background, which must be subtracted and hence are not appropriate for absolute reflectivity measurements. This is not a problem when comparing emission line ratios, but these are of course only available at discrete wavelengths.

It is very important to calibrate out the response of the film; our thanks to Dr Klans Eidmann of Max-Plank-Institute Fur Quantenoptik for supplying the reel of calibrated Kodak 101 film. The final measured reflectivity for the mirror shown in figure A1.20, is 6.7 ± 1.3%, very much lower than the calculated value; the bandwidth is ∿ 45Å, twice that predicted. Mirrors of higher reflectivity have been fabricated at nearby wavelengths, for

example the mirror shown in Fig 1.18 has the expected FWHM and a reflectivity above 10%, although the exact figure is subject to some uncertainty due to the use of non calibrated film in this measurement. It is nevertheless clear that further optimisation of the mirror coating parameters is possible, and that this experimental technique provides a powerful tool in the process.

References

1. M Grande, B L Evans, A M H Al Arab, N H Rizvi, Shi Xu, SPIE Vol 984 pp 253 (1988).

2. J A Trail, R L Byer, T W Barbee Applied Phys Lett 52(4) p269, (1988).

3. N M Ceglio, D B Stearns, A M Hawryluk, T W Barbee, K Danzmann, M Kuhne, P Mueller, B Wende, M B Stearns, A K Petford-Long, C-H Chang, J Phys Colloq (France) Vol 447, C6, p277 (1986).

4. T N Lee, E A McLean and R C Elton, Phys Rev Lett 59; 1155 (1987).

5. Section A1.1, this report.

6. B L Evans and B J Kent, Sppl Opt, Vol 26 p4491 (1987).

7. B L Evans, J Al-Dabbagh, B J Kent, SPIE Vol 984, p103 (1988).

8. T W Barbee, S Mrowka, C Hettrich, Appl Opt, Vol 24, No.6, p883 (1985).

9. W R Hunter, private communication quoted by D F Edwards in Handbook of Optical Constants of Solids, edited E D Palik Acad Press (1985).

10. G P Keihn, T Garvey, R Smith, O Willi, A Damerell and J Westcaue, SPIE, Vol 831, 150 (1987).

11. N Nakano, H Kuroda, T Kita, T Harada, Appl Opt Vol 23 No.14 p2386 (1984).

A1.6 INVESTIGATION OF THE EXPANSION OF SHORT PULSE (< 100PS) EXPANDING PLASMAS USING THE TECHNIQUE OF POINT PROJECTION ABSORPTION

D O'Neill, C L S Lewis, D Neely, S Davidson (Queens University, Belfast), S Rose (RAL)

Introduction

The technique of point projection spectroscopy (pps) has previously been applied to the study of temporal and spatial characteristics of both coronal[1] and LTE[2] plasmas produced by irradiation with laser pulses typically of 1 ns duration. For the first time this successful technique has been applied to the study of Al and F plasmas generated by sub-100 ps (2w) pulses.

Some data was also obtained on the absorption of a Be-like Mn line (12.643 Å) by an expanding F plasma relevant to the X-ray laser photopump scheme studied in January 1988[3].

Experiment

A line focus produced with a cylindrical/spherical lens combination was used in the standard pps geometry[4]. Aperturing the optics so that only the central region of the lenses was used produced a uniform line focus down to approximately 100μ with intensities up to a few 10^{13} Wcm^{-2}. In the vertical dimension the line focus was apertured down to approximately 1.3 mm - sufficient to encompass all required probing angles.

This plasma was backlit using 20μ Cu wires built up with plastic and overcoated with U to give a final dimension of 25μ (spectral resolution limit). These quasi-point, quasi-continuous plasma sources were irradiated with typically 20 → 25J (2w) in 70 → 100 ps using an f1.5 lens at tight focus.

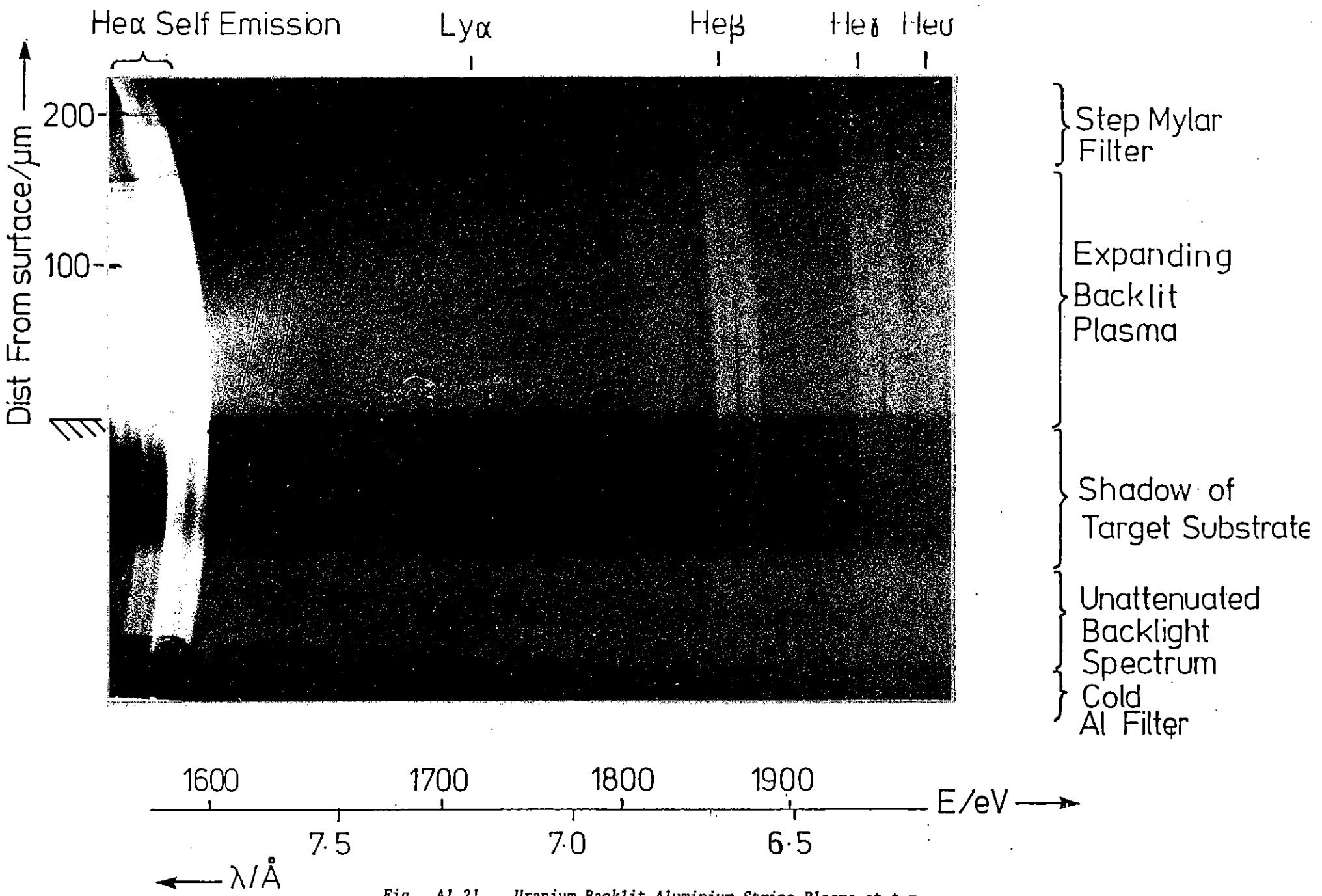


Fig A1.21 Uranium Backlit Aluminium Stripe Plasma at t = 100ps.

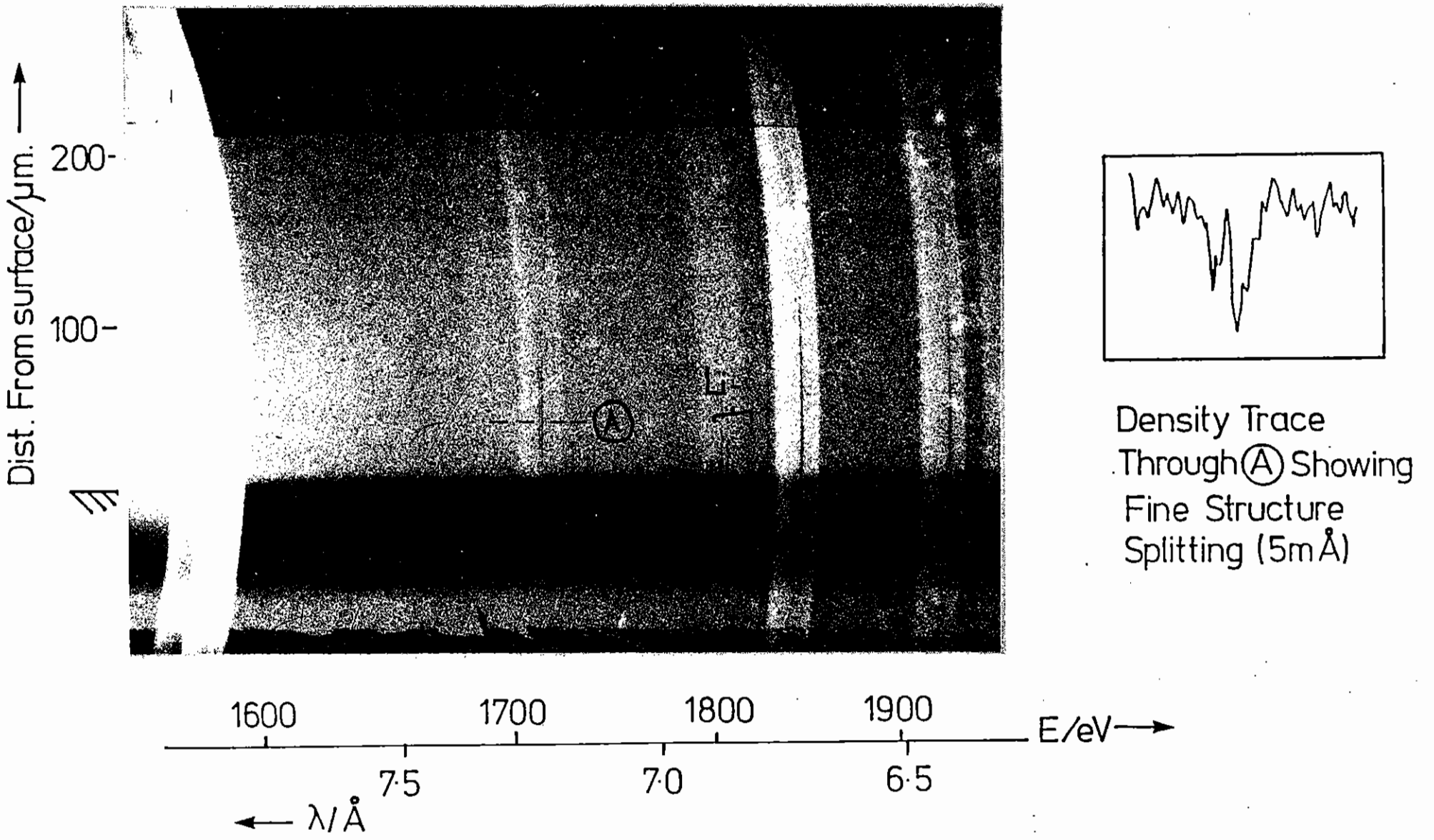


Fig A1.22 Uranium Backlit Aluminium Stripe Plasma at t = 200ps.

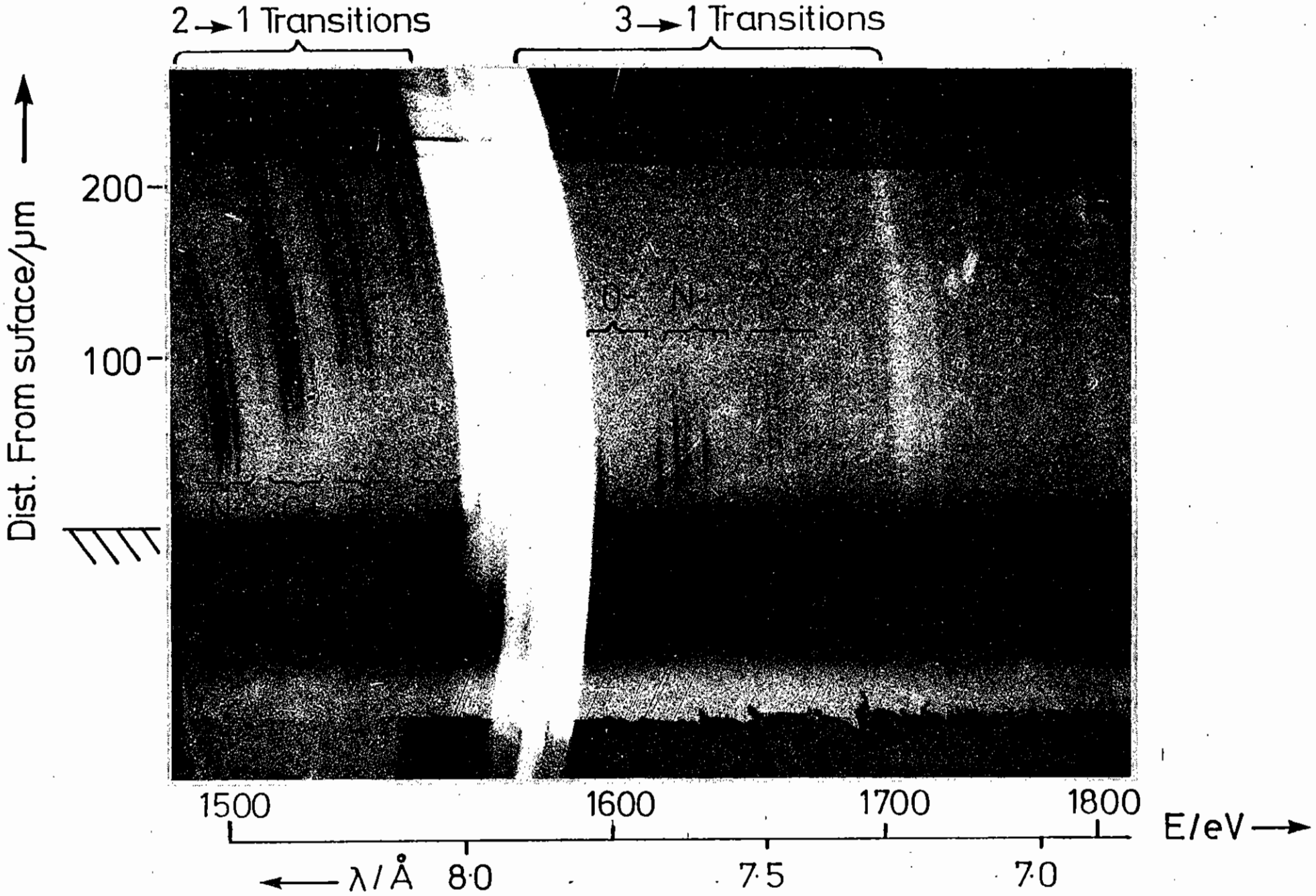


Fig A1.23 Uranium Backlit Aluminium Stripe Plasma at t = 1,000ps.

The targets were pre-aligned to a high degree of accuracy thus allowing very high magnification (up to x 120) backlighting of the plasma.

A PET crystal (resolving power ∿ 2000) was used to look at the Al plasmas while TlAP was employed in the study of F. In both cases the spectra were recorded on Industrex C film.

Aluminium Data

Al stripes 0.5μ thick were coated onto 12μ plastic substrates in two widths: 500μ and 100 → 150μ. The 500μ stripes were found to be too optically thick to yield any quantitative data. Reducing this dimension to between 100 & 150μ allowed us to obtain unsaturated data on these plasmas up to 1 ns after the peak of the incident pulse in 100ps intervals. (see fig A1.21 → A1.23).

The figures show 100 ps "snapshots" of the expanding Al plasma at 100, 200, and 1,000 ps after the peak of the pulse.

The resolution of the instrument was determined from the observation of the Ly_α splitting in fig A1.21 and A1.22.

The broad bands of emission surrounding the resonance absorption lines in all the pictures are monochromatic images of the probed plasma (they arise from self emission). These give a very good indication of the uniformity in the vertical dimension of the plasma. A further check of plasma uniformity are the pinhole camera images obtained.

The step mylar filter yields a density-intensity calibration as a function of wavelength while the cold Al filter gives a fixed wavelength marker at the K-edge.

Fig A1.21 shows the fine structure splitting of the Ly_α absorption feature ($2p_{3/2} \rightarrow 1s_{1/2}$ and $2p_{1/2} \rightarrow 1s_{1/2}$) extending out from the target surface to approximately 80μ. The He_β and He_α resonance lines are also observable.

100ps later (fig A1.22) it is clear that the Ly_α feature has become detached from the surface by about 20μ as the very hot plasma boundary moves away from the target surface. Further evidence of the relatively lower temperatures close to the surface is seen in the appearance of some Li-like satellites on the long wavelength side of the He_β.

At later times the He resonance lines can be seen to detach in the same way and progressively cooler ion stages are observed close to the surface. Figure A1.23 is an example which is particularly interesting in that it shows 3 → 1 and 2 → 1 (long wavelength side of He_α) transitions simultaneously. It also very effectively demonstrates the temperature gradient of these plasmas with hotter ion stages displaced spatially outwards from the surface.

One problem with these stripe targets is that the substrate itself obstructs probing closer than ∿ 10 → 15 μ from the surface. This is not the case in the wire targets also studied where tangential probing angles allow observation right up to the surface.

As a first approximation to the 8 μ coated fibres used in X-ray laser experiments, a 25 μ Al wire was irradiated and backlit in the same way as the stripes. These provided enough optical depth for absorption to be observable but unfortunately due to the poor quality of the line focus below 100 μ, the irradiance on target was low and only the 2 → 1 transitions were observable.

Fig A1.24(a) shows the cylindrical nature of the expansion with symmetrical lower ion stage absorption features suggesting similar optical depth on both sides of the wire for this low temperature plasma. However, fig A1.24(b) - the He_α absorption line - clearly demonstrates a major difference in the high temperature plasma expansion.

From the spatial extent of the absorption on film it is estimated that the speed of expansion of the front surface plasma is of the order of 5 x that of the rear surface (∿ 5 x 10^7 and ∿ 1 x 10^7 cms^{-1} respectively). This is consistent with the doppler width of the lines along the line of sight. Fig A1.25

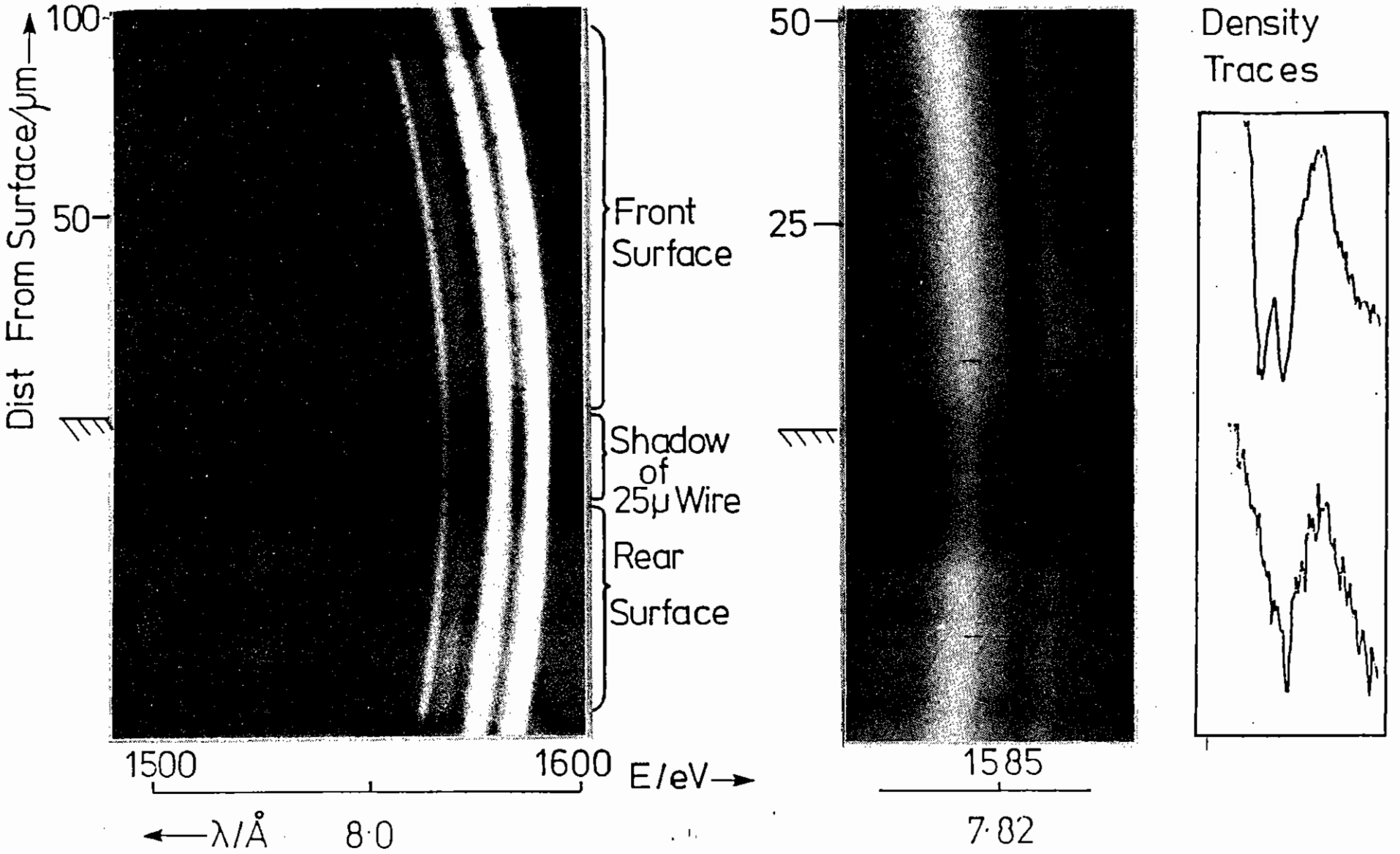


Fig A1.24(a) Uranium Backlit Aluminium Wire (25 μ) at t = 200 ps.

(b) Structure of He_α absorption feature.

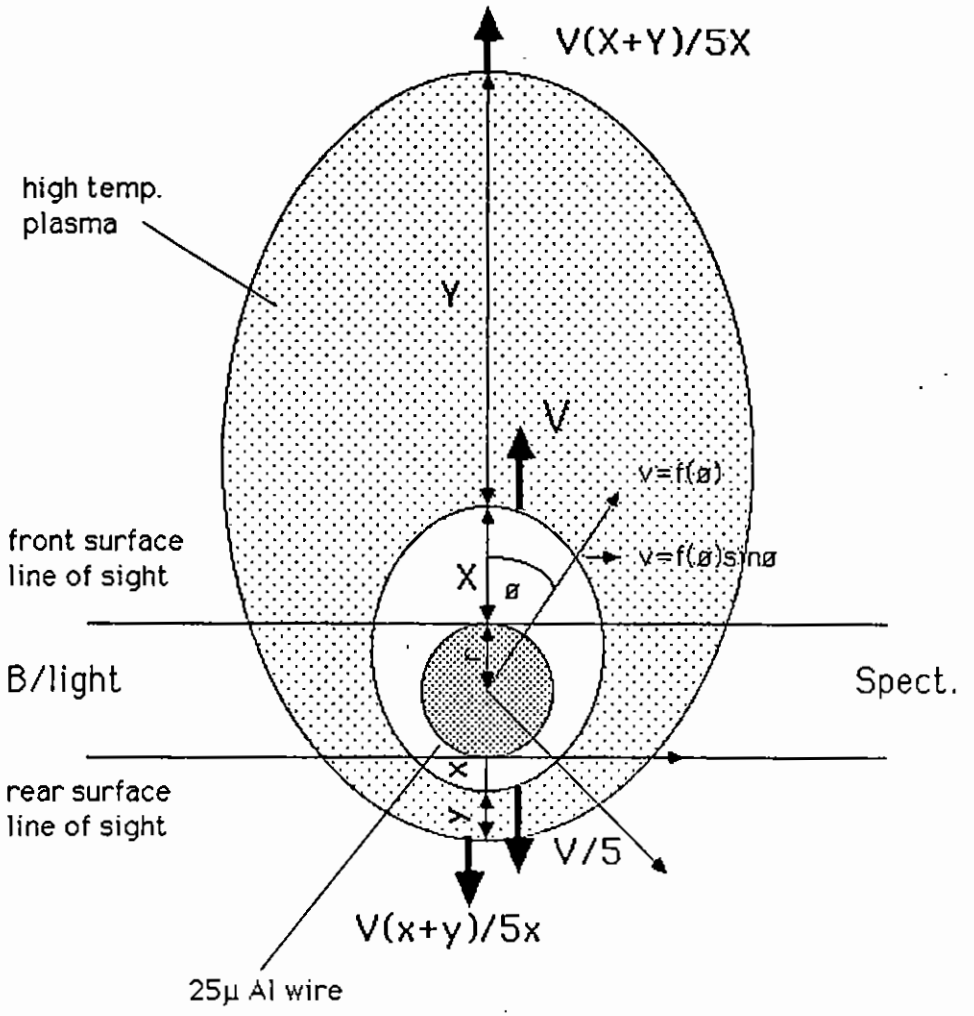


Fig A1.25 Non uniform expansion for a one-sided illumination of 25 μ Al wire.

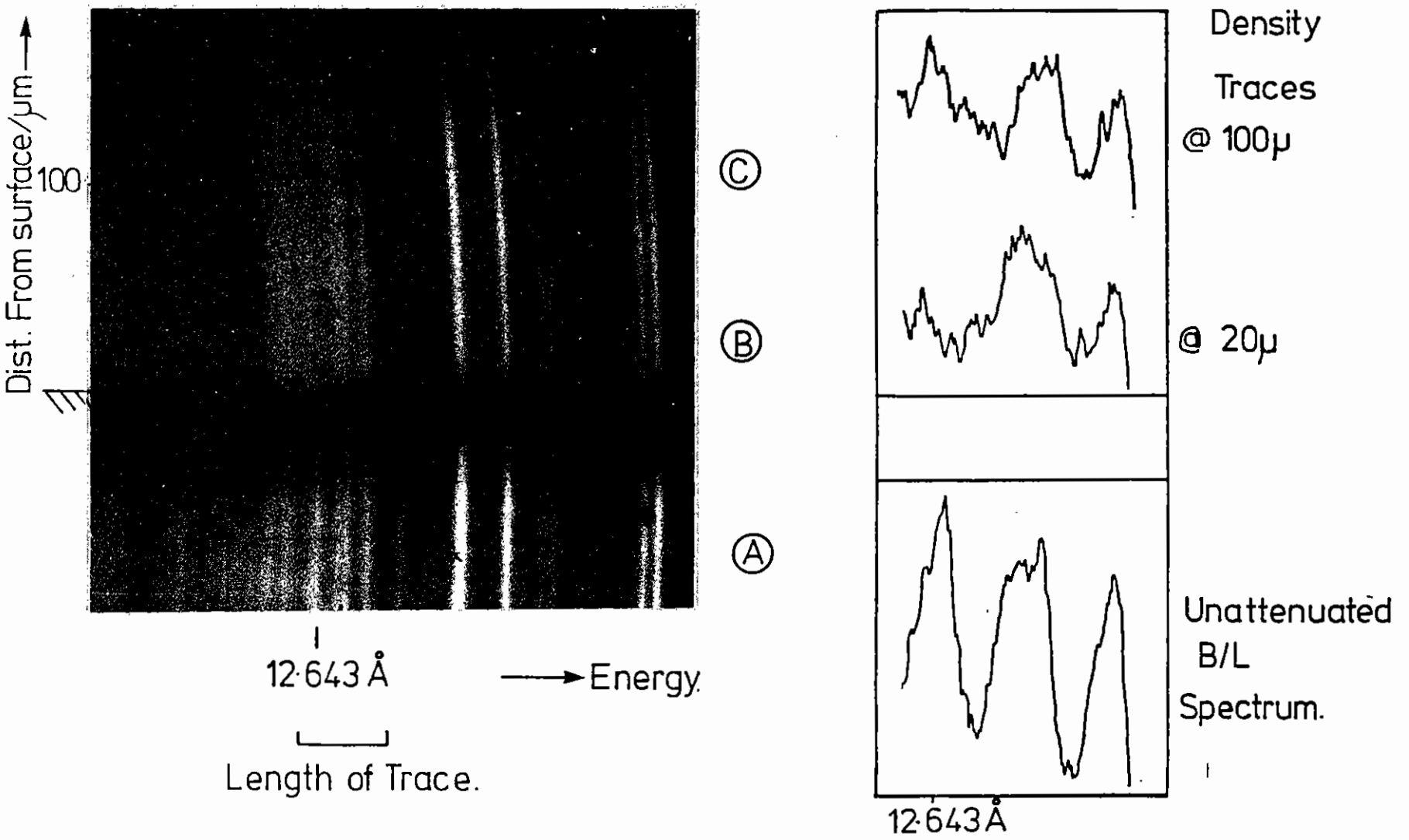


Fig A1.26 Absorption of 12.643 Å Be-like Mn Line in Fluorine Plasma at t = 150ps.

illustrates the type of expansion suggested by the observed structure in the He_α line.

It is clear that for this type of expansion there is a lack of absorbing ions moving perpendicular to the line of sight close to the surface. For the same probing direction there are relatively large numbers of ions absorbing at energies shifted from line centre by their direction of motion giving rise to the observed split line.

Progressing outwards spatially increasing numbers of unshifted ions (relative to those shifted by large amounts) are encountered. This would lead to a narrowing of the feature (see Fig A1.24(b)).

On the rear side of the wire close to the surface the optical depth of the motionally doppler shifted ions appears to be less than our detection threshold and so no absorption is observed close to the surface. Further out, where the bulk of the material is, the doppler shifts are clearly much less severe than those observed for the same distance away from the front surface and this is reflected in a relatively narrow (3 → 4 mÅ) absorption line (ie close to/on the limit of instrumental resolution).

Obviously this is an extreme case of non uniform illumination and the grossly non-cylindrical nature would be greatly improved with the addition of a relatively small number of beams.

The typical X-ray laser cylindrical expansion is further helped by the use of smaller diameter (∿ 8 μ) fibres. However, in the case referred to below[3] where fibre illumination is constrained to be one sided and the line overlap depends on some broadening/shifting processes then the above observations should be considered.

It should be noted that a full analysis of the measured opacities taken together with frequency shifts can lead to a complete 2-D description of the hydrodynamics of the absorbing ion plasma cloud around a thin wire.

Attempts to irradiate Al coated 8 μm C fibres proved unsuccessful.

Mn-F Data

In January 1988 an experiment was undertaken as part of the X-ray laser program to investigate the possibility of pumping the Ly_β transition in an expanding, cylindrical, recombining F plasma using a suitably matched transition in Be-like Manganese to augment the 3 → 2 inversion.

As a further study of this scheme, expanding F plasmas were looked at. Sm and U were tested as possible backlighters in the region of the F resonance lines (up to ∿ 1 KeV). However, both were found to be 2nd order dominated at these energies.

Backlighting the F plasma with a F coated wire proved unsuccessful due to poor brightness (combined with the lower resolution of TIAP)

Absorption of the relevant line was successfully demonstrated using a large (∿ 70μ) Mn backlighter as a source fig A1.26. The traces cover the 12.643 Å and the 2 lines to the higher energy side. Note that even at 100μ from the surface the line of interest has not recovered its full intensity with respect to the other 2 lines.

The F target was 1.2 mm x 500 μ stripe coated on 12 μ CH and was irradiated at ∿ 10^{13} Wcm^{-2}. Unfortunately time prevented progress to smaller Mn sources.

Analysis

Detailed analysis of these results is ongoing. Self consistent fitting of the resonance line absorption features will yield spatially and temporally resolved temperature and density profiles thus providing a very thorough check on theoretical simulations of such plasmas.

The results of this work will be reported in more detail at a later date.

Summary

Good data has been obtained for the expansion of ∿ 100μ Al stripes at intensities of ∿ 2 x 10^{13} Wcm^{-2} up to 1ns after an initial 80 → 100 ps pulse.

Some interesting observations have been made on the nature of a "cylindrical" expansion produced using single sided illumination.

Sm and U were tested as possible quasi continuous backlighters in the sub-Kev region and found to be 2nd order dominated.
Finally absorption of the Be-like Mn line (12.643 Å) was observed in an expanding F plasma although with somewhat reduced resolution.

References

1a) C L S Lewis & J McGlinchey Opt.Comm., 53, 179 (1985).

b) J Balmer C L S Lewis, R E Corbett, E Robertson, S Saadat, D O'Neill, J D Kilkenny, C A Back and R W Lee. To be published Phys Rev A 1989.

c) C L S Lewis, R E Corbett, E Robertson, D O'Neill, M J Lamb, S Sadaat, T Afshar, S Rose, J P Mosnier & E Kennedy, Annual Report to LFC 1987 Sect. A1, 5.

2a) S Davidson, C L S Lewis & D O'Neill et al. Annual Report to LFC 1987, SEct. A1,8.

b) S Davidson, C L S Lewis & D O'Neill et al. Proc. of 19th Eclim, Madrid (to be published).

3. C L S Lewis, D Neely, D O'Neill et al. Annual Report 1987, Sect. A1.5

4. See Annual Report 1987, Sect. A1.5.

A1.7 SOFT X-RAY CONTACT MICROSCOPY OF BIOLOGICAL SPECIMENS: DETERMINATION OF THE EFFECT OF IRRADIATON OUTSIDE OF THE WATER WINDOW

T W Ford, A D Stead, (Dept of Biology, RHBNC)
C P Hills, (Dept of Physics, King's College London)
R J Rosser and N Rizvi (RAL)

Introduction

It is claimed that the optimum wavelengths for the imaging of biological specimens by soft x-ray contact microscopy (SCCM) are within the so-called "water window" as this offers the best potential contrast between proteins (mainly carbon-containing) and water (Cheng et al., 1986). In previous studies we have shown that wavelengths longer than those of the "water window" (2.2 - 4.4nm), ie far u/v, do not contribute significantly to the process of image formation (Stead, et al., 1988a), however no attempt was made to discriminate between the effects of hard and soft X-rays on the quality of the image. In previous studies at RAL (Rosser et al., 1985; Eason et al., 1986) and elsewhere (Mochizuke et al., 1986) it has been shown that under the conditions used for soft X-ray contact microscopy using laser-produced plasmas at RAL there is considerable radiation produced outside the "water window". It is therefore important to investigate the effects of hard X-rays, as wavelengths shorter than those of the "water window" region may either decrease the potential resolution, or decrease the contrast of the image due to the greater mobility of the photoelectrons which are created by hard X-rays in the photosensitive resist.

In this study we have attempted to filter out either radiation of lower energy than that of the "water window" (vanadium filter), leaving soft and hard X-rays; or filter out u/v and soft X-ray irradiation, to leave only hard X-rays (beryllium filter). The quality of the images produced have been compared for each of the filter arrangements. In addition X-ray pin diodes were used, with similar filters, to measure the energy produced in the soft X-ray region under the standard conditions employed for specimen imaging.

Materials and Methods

In a series of experiments images of the filamentous cyanobacterium Anabaena cylindrica were obtained using TA4. The specimens were all critical point dried to avoid any differential absorption by varying thicknesses of water. The laser-produced plasmas were generated from a gold foil target with a laser energy of approximately 2J (IR) but, unlike previous studies (Stead et al., 1988a; 1988b) this was not frequency doubled. The specimens were mounted behind a broken Si_3N_4 window, except for those images without filters in which case the Si_3N_4 window was intact, and held at approximately 18mm from the target and at 30° to the target normal. The filters, 0.5µm vanadium on a 0.1µm formvar film or a free standing 25µm beryllium film, were placed over the front aperture of the specimen holder. The X-ray pin diode was placed in a similar position to the specimens and identical filters were positioned over the front of the diode. The resist material used to record the images was polymethylmethacrylate (PMMA) and development was with 50:50 iso-butyl methyl ketone (MIBK) : iso-propyol alcohol (IPA). Images were recorded by light microscopy (Leitz dialux) using reflected light interference optics.

Results and Discussion

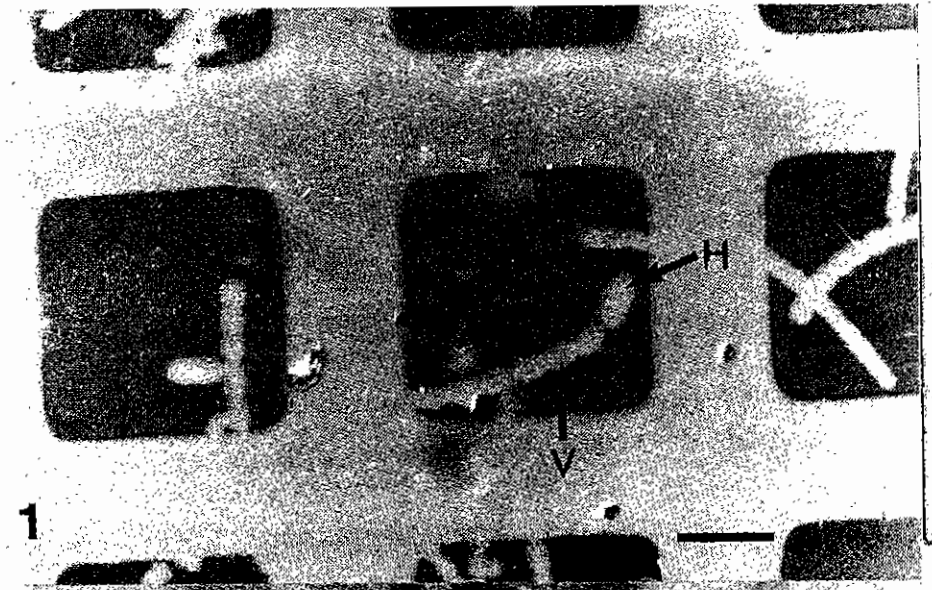
After chemical development of the PMMA resist it was possible to obtain images of the filament of A.cylindrica regardless of whether the cells were imaged behind a Si_3N_4 window alone, or in the presence of either beryllium or vanadium filters. This implies that contact images of biological specimens on PMMA may result from exposure to irradiation outside of the "water window".

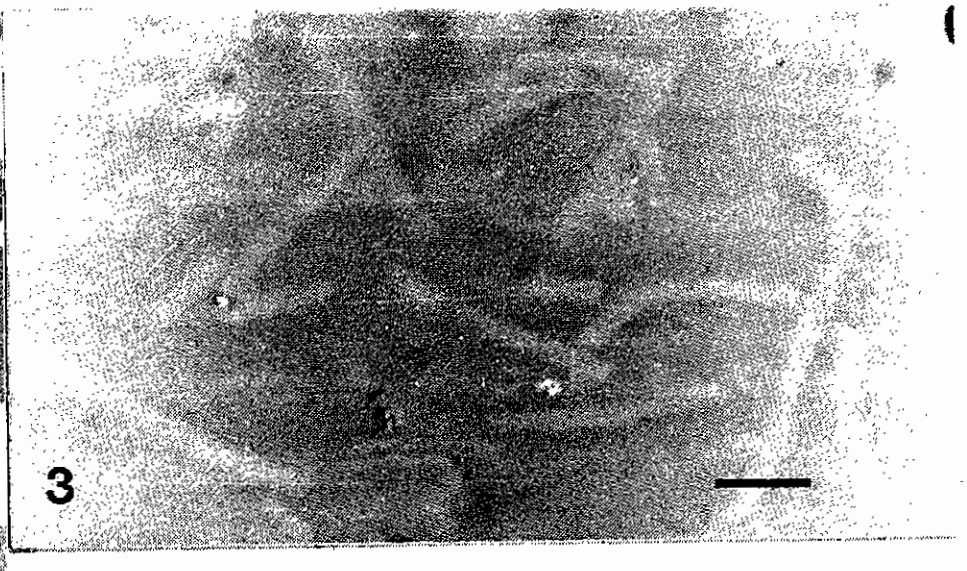
When imaged behind a Si_3N_4 window without filtering both cell types, heterocyst and vegetative cells, can be clearly differentiated in the developed image of the Anabaena filament (Fig.A1.27). Interferometry showed that the depth of development was less than 40nm, but the development time was only 5 mins and further development may therefore be possible. Excessive development however, can distort SXCM images and rather than improve resolution, can result in loss of information (Cheng et al., 1986).

The addition of a vanadium filter restricted radiation to the X-ray region (<5nm) (Fig. A1.28) and produced better quality images than in the absence of any filtering (Fig. A1.27(2)) in that internal detail is visible in the image of the heterocyst. The beryllium filter was used in the absence of a Si_3N_4 windown and therefore is transparent only to harder X-rays, ie wavelength <2nm (Fig. A1.28). Whilst images of Anabaena filaments are visible in the developed resist (Fig. A1.27(3)), there is a significant reduction in contrast resulting in no obvious distinction between heterocysts and vegetative cells. This low contrast is presumably due to the lack of radiation with a significant C:O edge discrimination, ie soft X-rays in the "water window". Furthermore the long development time needed to produce this image (8min) indicates that the resist is not particularly sensitive to hard X-rays.

Calibration of the X-ray pin diode showed that the response followed closely that calculated from data of Kuckuck (DATE). The diode's response is, as expected, much greater in the hard, rather than soft, X-ray region (Fig. A1.28). This difference in response has been folded into the filter function data (calculated from Henke et al., 1981) and the difference between the two responses taken as a measure of the X-ray flux in the "water window" region, with only a small contribution from wavelengths shorter than 2.2nm or longer than 4.4nm (Fig. A1.29). These measurements indicated that the X-ray flux in the band between 2 and 8nm was approximately 0.5mJ/cm², although the majority of the radiation falls within the "water window" region (fig. A1.29).

As a check on the validity of this measured X-ray flux we have constructed a model which yielded a given development depth for a given X-ray flux and development time. This model has employed a scaling law for development rates (Spiller and Feder, 1977; verified by Haelbeich et al., 1984) and this model gave good agreement with the measured development depths.





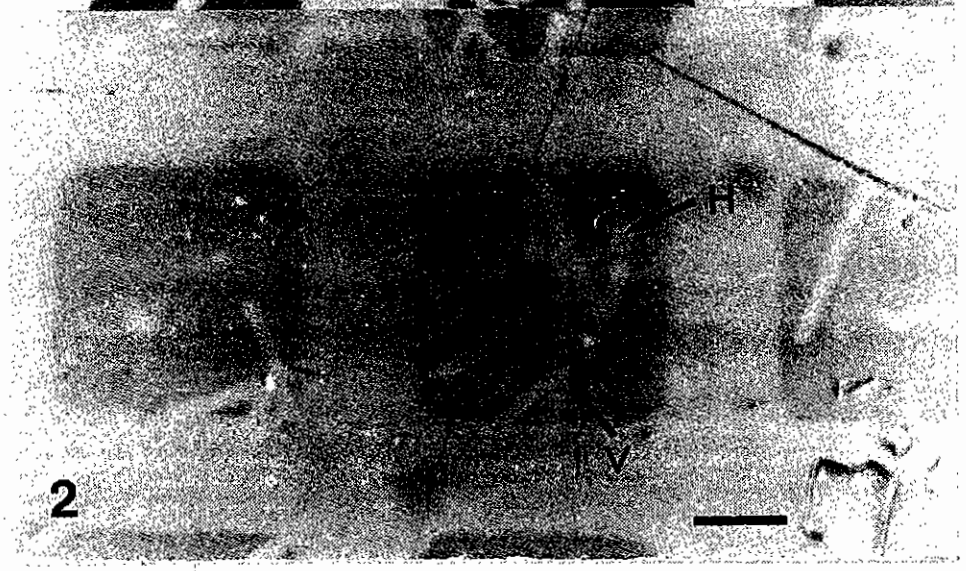


Fig A1.27 *Images of Anabaena cylindrica cells obtained by SXCM on PMMA photoresist. All images are light microscope images.*

(1) image obtained behind a Si_3N_4 window;

(2) as above but with a filter of 0.5μm vanadium on 0.1μm formvar;

(3) image obtained behind a 25μm beryllium filter.

H - heterocyst V - vegetative cell

Scale bar = 10μm

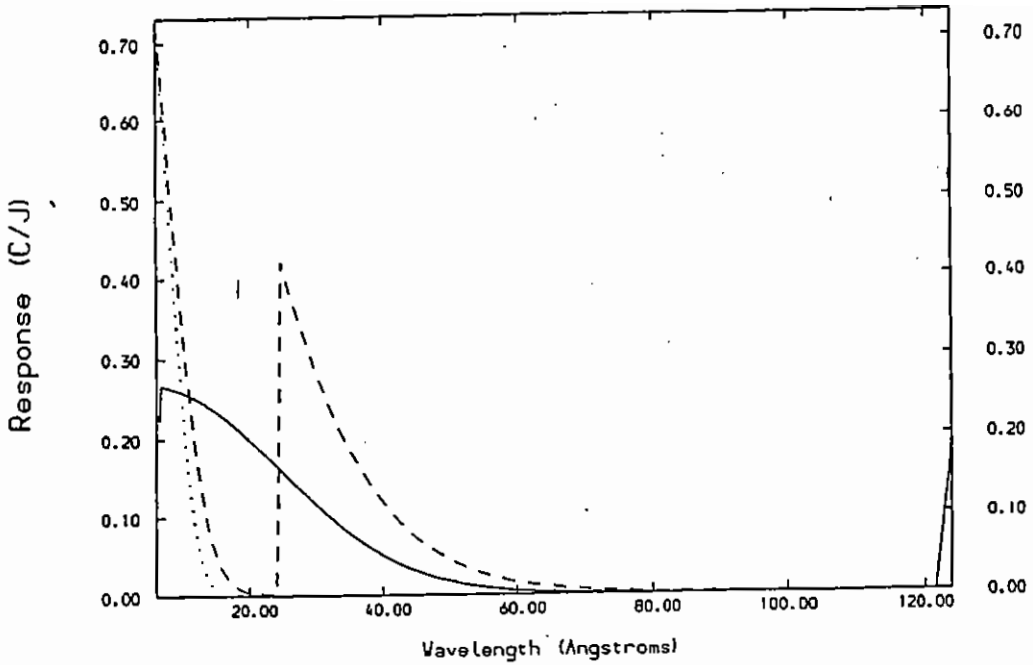


Fig A1.28 *The calculated response of the X-ray pin diode ( ) and the transmission spectrum for vanadium (0.5μm on 01. formvar) ( ) and beryllium (25μm) ( ).*

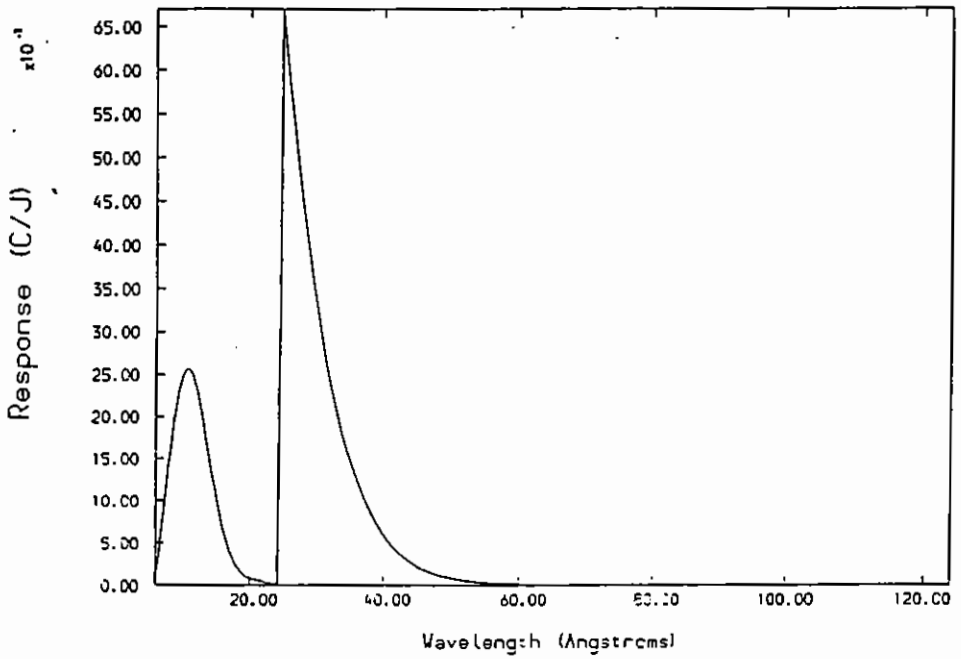


Fig A1.29 *The theoretical difference spectrum for the response of the pin diode used in conjunction with a beryllium filter (25μm) and a vanadium filter (0.5μm on 0.1μm formvar).*

The images obtained emphasise the benefits of imaging in the "water window" and the enhanced contrast and resolution resulting from elimination of hard X-rays and extreme UV from the imaging process. Filtering of the radiation produced by the laser plasma is therefore desirable, particularly with regard to the extreme UV which appears to detract from the image quality. The exclusion of hard X-rays from the imaging process seems less critical as the photoresist appears to have a low sensitivity to such radiation. There is of course a further advantage if the filtering is accomplished by coating the Si_3N_4 windows as these will then survive many more laser shots (Stead et al., 1988a).

The use of two X-ray pin diodes, one with a beryllium the other with a vanadium filter, on each shot will in future permit an accurate measurement of the X-ray flux for each specific shot. This measurement is essential if the process of resist development is to be simplified to the point where the technique of SXCM is to be widely available to the biological community.

Acknowledgements

This work was supported by SERC (grant no GR/E 36944) and the Central Research Fund, University of London (provision of a grant towards the cost of a light microscope and interferometer).

References

1) P.C. Cheng, R. Feder, D.M. Shinozaki, K.H. Tan, R.W.Eason, A.G.Michette and R.J. Rosser, Nucl. Instrum. Meth. Phys. Res. A 246, 668-674. (1986).

2) R.W.Eason, P.C.Cheng, R.Feder, A.G.Michette, R.J.Rosser, F.O'Neill, Y. Owadano, P.T.Rumsby, M.J.Shaw and I.C.E.Turco, Optica Acta, 33, 501-516 (1986).

3) E.Spiller and R.Feder, In X-Ray Optics, Ed. H.HJ.Quesser, pp. 35-92 (1977).

4) R.P.Haelbich, J.P.Silverman, J.M.Warlaumont, Nucl.Instrum. Meth. Phys. Res. A 222, 291-301 (1984).

5) B.L.Henke, P.Lee, T.J.Tanaka, R.L.Shimabukuro, B.K.Fujikawa, In Low Energy X-Ray Diagnostics, Eds. D.T.Attwood and B.L.Henke (1981).

6) R.W.Kuckuck. Lawrence Radiation Laboratory Report 51011. (19AA).

7) T.Mochizuke, T.Yabe, K.Okada, M.Hamada, N.Ikeda, S.Kiyokawa and C.Yamanaka, Physics Review A. 33, 525-539 (1986).

8) R.J.Rosser, K.G.Baldwin, R.Feder, D. Bassett, A.Cole and R.W.Eason, Annual Report to the Laser Facility Committee, Rutherfore Appleton Laboratory, A4.4 (1985).

9) A.D.Stead, T.W.Ford, J.A.Catcheside, C.P.Hills and A.Ridgeley. Annual Report to the Laser Facility Committee, Rutherford Appleton Laboratory, A1.15 (1988a).

10) A.D.Stead, T.W.Ford, C.P.Hills and N.Rizvi Annual Report to the Laser Facility Committee, Rutherford Appleton Laboratory, A1.16 (1988b).

		Pages
A2	**LASER PLASMA INTERACTION AND ENERGY TRANSPORT**	
A2.1	SUPPRESSION OF INSTABILITIES IN A LONG SCALELENGTH PREFORMED PLASMA	51-56
A2.2	THE PRODUCTION OF HOT NEAR SOLID DENSITY PLASMA BY ELECTRON ENERGY TRANSPORT IN A LASER-PRODUCED PLASMA	56-60
A2.3	HYPERVELOCITY IMPACT SIMULATION IN GLASS AND METAL USING A HIGH-POWER PULSED LASER	60-66

A2.1 SUPPRESSION OF INSTABILITIES IN A LONG SCALELENGTH PREFORMED PLASMA

S E Coe, T Afshar-Rad, M Desselberger, F Khattak and O Willi
(Imperial College)
A Giulietti (Instituto de Fisica Atomica e Molecolare del CNR)
Z Q Lin and W Yu (Shanghai Institute of Optics and Fine Mechanics)
C N Danson (RAL)

Proposed laser fusion targets will be surrounded by large, underdense, long scalelength coronal plasmas. Under these conditions the levels of various parametric instabilities such as Stimulated Raman Scattering (SRS) and Stimulated Brillouin Scattering (SBS) are predicted to be significantly higher than those previously observed in short scalelength plasmas[1,2]. High levels of these instabilites result in the preheat of the target core by hot electrons and significant losses of the incident laser energy. This is extremely detrimental for laser driven implosions and consequently it is vital that the levels of SRS and SBS can be controlled in such a plasma. It has been suggested that the levels of SRS and SBS can be significantly reduced by improving the uniformity of the laser beams used to drive implosions. However present day high power lasers are unable to produce sufficient beam quality to achieve this and consequently several beam smoothing techniques have been proposed to generate uniform illumination of the target with imperfect lasers. The two main approaches which have been used so far are the Random Phase Plate (RPP) technique[3,4] and the use of an Induced Spatial Incoherence (ISI) system[5,6]. The RPP technique breaks the incident laser beam up into a large number of individual beamlets which are then randomly shifted in phase. These beamlets are then overlapped onto the target by a focussing lens. The resulting interference pattern produced eliminates any gross long scalelength non-uniformities from the laser beam profile but introduces pronounced short scalelength intensity fluctuations which remain frozen in the focal spot distribution throughout the laser pulse. An ISI system is similar to this except that a broad band laser is used so that the coherence time of the laser, t_c, is shorter than the incremental delay between individual beamlets. This causes the instananeous interference pattern produced to be averaged out over times long compared to t_c, leaving a smooth focal spot profile. Recent results[7] have demonstrated that an ISI system can significantly reduce the level of SBS in a short scalelength plasma. Here, we report on an experiment which has been carried out at the Central Laser Facility, to determine the effectiveness of both a RPP and an ISI system to reduce the levels of SRS and SBS in a long scalelength preformed plasma similar to those which will surround proposed laser fusion targets.

A long scalelength plasma was generated by irradiating a thin foil stripe target by four frequency doubled (λ = 527 nm) beams of the Vulcan glass laser. The beams were focussed onto the target in two opposing pairs by a line focus geometry using an off-axis lens mirror scheme[8]. The length and width of the focal spot for each beam were 2.0 mm and 0.3 mm respectively. All the four beams were superimposed onto the target resulting in a typical irradiance of 10^{14} Wcm^{-2} in a 600 ps FWHM laser pulse. The targets consisted of an Aluminium stripe 300 µm wide, 700 nm thick and 0.8 mm long supported on a 100 nm formvar substrate. A delayed second harmonic, 600 ps FWHM laser beam was then interacted axially with this preformed plasma. Consequently the beam interacts with the plasma over a distance of about 800 µm along which the plasma temperature and density are approximately uniform. By varying the delay between the interaction beam and the heating beams it is possible to control the plasma conditions at the time of interaction. For the results presented here the interaction beam delay was 1.8 ns. For these conditions the model of Rosen and London[9] predicts a maximum plasma density of 8% of the critical electron density (N_{ec}) and a typical temperature of 500 eV.

The back scattered Raman and Brillouin signals generated by the interaction beam were imaged out via the incident focussing lens. The scattered light was then split into two separate channels and focussed down onto calibrated photodiodes and calorimeters to measure the scattered energy levels. In addition time resolved measurements were made of the SRS and SBS spectra by spectrometers coupled to optical streak cameras. The plasma conditions

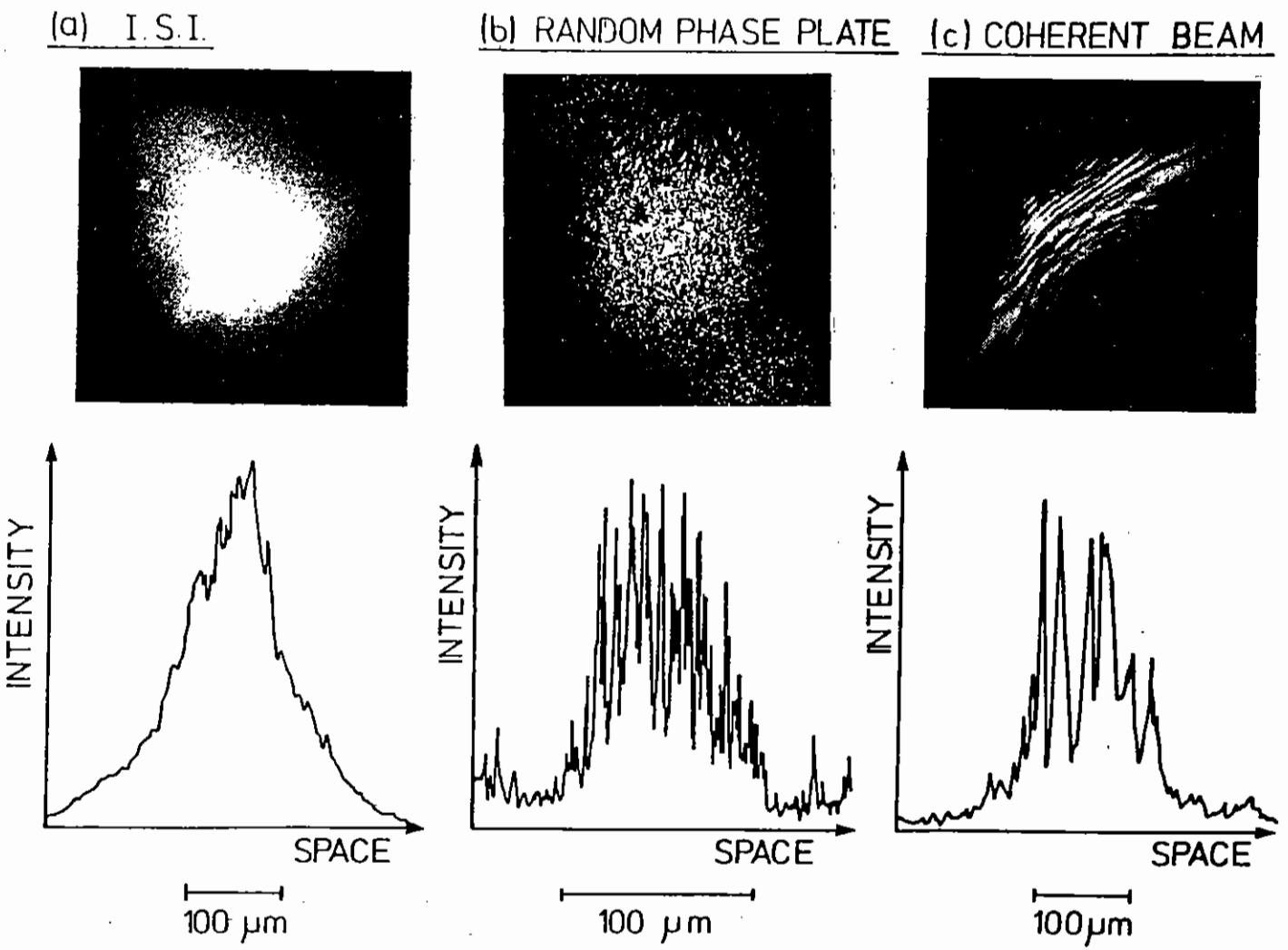


Fig A2.1 Typical focal spot distributions measured with the A2.1 equivalent plane monitor: a) broad bandwidth ISI beam (f/10 focussing lens), b) narrow bqandwidth beam with RPP (f/2.5 focussing lens), and (c) standard narrow bandwidth beam (f/10 focussing lens). Note that the magnification for the RPP image and densitometer trace is twice that of the other two cases.

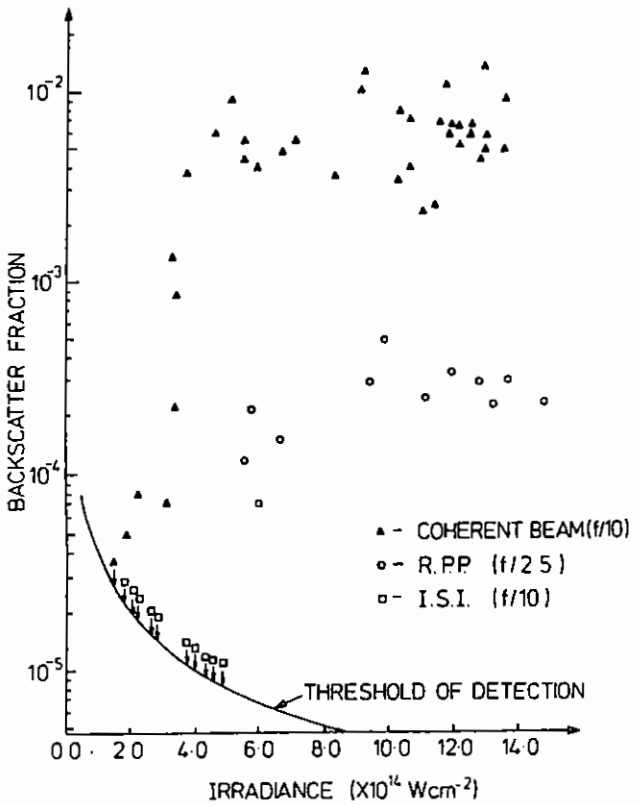


Fig A2.2 Variation of SBS backscatter fraction with average laser irradiance. An arrow indicates that the SBS signal was lower than the threshold of detection.

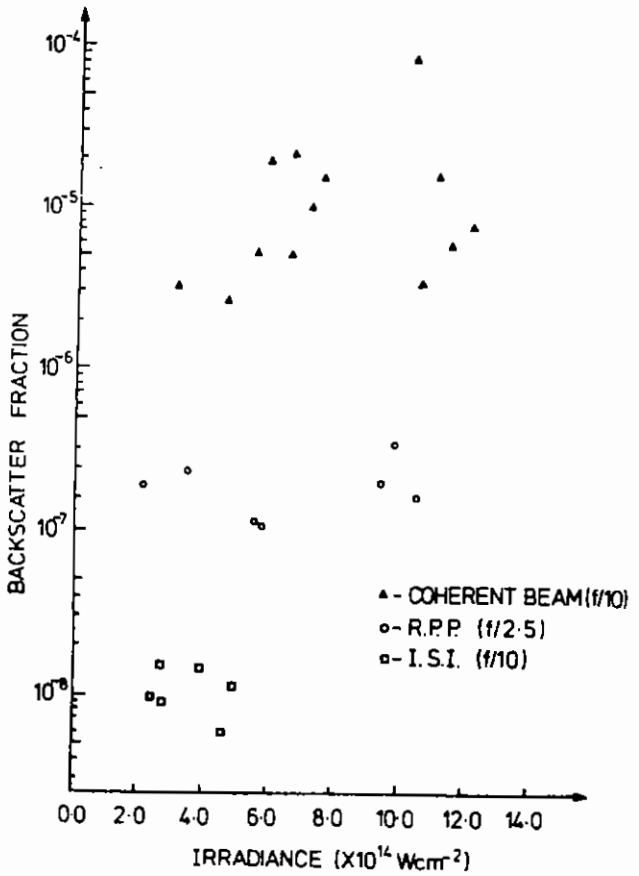


Fig A2.3 Variation of SRS backscatter fraction with average laser irradiance.

indicated by these spectra are consistent with the predictions of the Rosen and London model[9] for these experimental conditions. A detailed description of the spectra observed under similar experimental conditions is being published elsewhere[10,11]. An equivalent plane monitor recorded the incident interaction beam focal spot distribution at planes equivalent to a 200 μm separation throughout the length of the preformed plasma.

In the experiment three different situations were studied. Firstly a normal coherent narrow band laser pulse was used as the interaction beam and was focussed onto target by a f/10 aspheric singlet lens. This generated a focal spot of 120 μm diameter which was approximately constant along the length of the preformed plasma. Measurements were taken for irradiances up to 10^{15} Wcm^{-2}. Secondly these measurements were repeated but with a RPP placed in the interaction beam. This broke the beam up into approximately 2500 individual beamlets each 2mm by 2mm. These beamlets were then randomly shifted in phase by either 0 or π. When the RPP was used the interaction beam was focused onto target by an f/2.5 aspheric doublet so that the focal spot size was similar to that when the RPP was not present. From the equivalant plane monitor data the focal spot FWHM was found to vary between 70 and 140 μm along the length of the preformed plasma. Finally an ISI system was used to break up the spatial and temporal coherence of the interaction beam. The ISI system used was similar to that developed elsewhere[6] except that the echelons used to break the laser beams up spatially into individual beamlets were placed earlier down the amplifier chain of the laser instead of after the second harmonic generating crystals. This has the advantage of allowing a single pair of echelons to be placed in a high power laser system before the laser pulse is split into individual beams instead of requiring a separate echelon pair at the output of each beam. The transmission echelons used consisted of two perpendicular arrays of glass blocks which broke the laser beam up into a 5 x 5 array of individual beamlets. The incremental delays imposed between the beamlets was a minimum of 5 ps. The coherence time of the laser was 2 ps. This is less than the delay between the individual beamlets and so satisfies the requirements for temporal smoothing of the instananeous interference pattern generated in the focal plane of the beam. A more detailed description of the ISI system used in this experiment will be published elsewhere[12]. The interaction beam with ISI was focussed onto target with the f/10 aspheric lens and from the equivalent plane monitor no significant difference was found between the focal spot size and that obtained with the non-ISI beam.

Figure A2.1 shows images taken from the equivalent plane monitor for the far field of the narrow band laser beam, narrow band laser beam with random phase plate and the broadband ISI beam. For the non ISI beam without RPP pronounced structure with a typical scalelength of 15-25 μm causing intensity ratios of up to 5:1 can be seen. This gross structure is eliminated with the use of the RPP, but the interference pattern produced by the RPP results in a fine scale structure with pronounced intensity fluctuations on a 2-3 μm scalelength. It can be seen that the far field image for the ISI beam is observed to have very little structure compared with the other two cases.

Figure A2.2 shows the variation with irradiance of the level of SBS observed for the three cases considered during the experiment. It can be seen that the use of the RPP reduces the level of SBS by a factor of 10-20 and that for the ISI beam the level of SBS is reduced below the threshold of detection. For irradiances of 4.0-5.0 x 10^{14} Wcm^{-2} this corresponds to at least a drop of a factor of 500 in the level of SBS for the ISI beam. Unfortunately the laser output for the ISI beam was limited to 50-60 J of green energy and so it was not possible to take data for higher irradiance shots than this. For the non-ISI beam without the RPP there appears to be a threshold for SBS at about 2.0×10^{14} Wcm^{-2} and approaching irradiances of 10^{15} Wcm^{-2} the SBS level seems to saturate at a level of about 1%. Clearly in a real fusion solid target electron densities up to critical would be present, rather than just up to $\approx 0.1\ N_{ec}$ as in this experiment, and so much higher levels of SBS than this would be expected.

Figure A2.3 shows the variation of SRS level with irradiance for the three cases considered in this experiment. Similar reductions are observed due to the RPP and ISI as in the SBS case. However

the level of SRS observed with the ISI beam does not fall below the threshold of detection. A wide variation is observed in the level of SRS with the non-ISI beam without the RPP for a particular irradiance. We believe that this is because in this case the level of SRS depends critically on the scale and level of the hot spots present in the laser beam and this may vary on a shot to shot basis. Consequently it is difficult to observe if any threshold is present for SRS.

Since the preformed plasmas generated in this experiment have very long scalelengths in the direction of propagation of the interaction beam the thresholds for SRS and SBS should be significantly lower than those expected in other shorter scalelength experiments [1,2]. If the axial density profile of the plasma is assumed to be parabolic (ie of the form $n = n_0(1-x^2/L^2)$) then the threshold for connvective SRS can be calculated[13]. Assuming an electron density of $N_e/N_{ec} = 0.08$, a plasma temperature of 500 eV and a scalelength of 500 μm gives the threshold as 4×10^{13} Wcm^{-2}. For these experimental conditions the SBS threshold is determined by Landau and collisional damping rather than the density scalelength of the plasma. Consequently the homogeneous plasma threshold for SBS [14] can be used. This gives a threshold of the order of 10^{12} Wcm^{-12}. Therefore the irradiances used in this experiment are well above the theoretical thresholds for both SRS and SBS.

The observed reductions in the levels of SBS and SRS caused by the RPP or ISI are significantly greater than would be observed from simple intensity averaging of the hot spots in the non-ISI beam without RPP. One possible explanation for this is that the SBS and SRS are driven by filamentation which grows from hot spots in the initial laser beam rather than directly by the hot spots themselves. Both RPP and ISI should reduce filamentation under these experimental conditions. For the RPP this is because theory[15] predicts that filamentation will only grow on a scalelength larger than 6μm which is significantly greater than the 2-3 μm intensity variations produced by the RPP with f/2.5 focussing optics. This has been confirmed by numerical simulations[16]. For ISI filamentation should be suppressed since the instantaneous interference pattern is smoothed out over times greater than the laser coherence time which is significantly shorter than the growth time for filamentation. Also filamentation may explain the considerably higher than theoretically predicted threshold observed for SBS in fig A2.2. This is because the SBS threshold observed could be driven by the onset of ponderomotive filamentation which has a threshold of order 10^{14} Wcm^{-2} for the plasma conditions in this experiment.

Finally data was taken to determine the effectiveness of the ISI system with a f/2.5 focussing lens. It was found that the levels of SRS and SBS measured were similar to or higher than those with the ordinary coherent beam using f/2.5 focussing optics. The explanation for this is that with an f/2.5 lens the entrance plane of the preformed plasma is no longer in the far field of the interaction beam but is in the quasi-near field where the individual beamlets no longer significantly overlap. This gives rise to an extremely non-uniform focal spot which explains the high level of SRS and SBS. Therefore it appears essential with an ISI system to work in the far field of the laser.

To summarize, measurements have been made of the levels of SRS and SBS in a long scalelength preformed plasma generated by a novel experimental arrangement. It was found that the use of a RPP to improve the laser beam profile reduced the levels of SRS and SBSD by over an order of magnitude. For an ISI system these instabilities were reduced by nearly three orders of magnitude although it was found to be essential to work in the far field of the laser. This suppression was observed at irradiances well above the theoretical thresholds for both these processes. Consequently it seems that the levels of SRS and SBS observed in laser plasma experiments are completely dominated by the coherence and structure of the incident laser beam. Also it appears extremely promising that the levels of these instabilites can be controlled in future inertial confinement fusion implosions by the use of laser beam smoothing techniques.

References

1) K. Tanaka, L.M. Goldmann, W. Seka, M.C. Richardson, J.M. Soures and E. A. Williams, Phys. Rev. Lett. 48, 1179 1982).

2) A. J. Cole, J. Murdoch, S. M. L. Sim and R. G. Evans, Opt. Commun. 36, 51 (1981).

3) Y. Kato and K. Mima, Appl. Phys B29, 186 (1982).

4) Y. Kato, K. Mima, N. Miyanaga, S. Aringa, Y. Kitagawa, M Nakatsuka and C. Yamanaka, Phys. Rev. Lett. 53, 1057 (1984).

5) R. H. Lehmberg and S. P. Obenschain, Opt. Commun. 46, 27 (1983).

6) S. P. Obenschain, J. Grun, M. J. Herbst, K. J. Kearney, C. K. Manka, E. A. Mclean, A. N. Mostovych, J. A. Stamper, R. R. Whitlock, S. E. Bodner, J. H. Gardner and R. H. Lehmberg, Phys. Rev. Lett., 56, 2807 (1986)

7) A. N. Mostovych, S. P. Obenschain, J. H. Gardner, J. Grun, K. J. Kearney, C. K. Manka, E. A. McLean and C. J. Pawley, Phys. Rev. Lett., 59, 1193 (1987).

8) I. N. Ross, J. Boon, R. Corbett, A. Damerell, P. Gottfeldt, C. Hooker, M. Key, G. Kiehn, C. Lewis and O. Willi, Appl. Opt. 216, 1584 (1987).

9) R. A. London and M. Rosen, Phys. Fluids 29, 3813 (1986).

10) O. Willi, D. Bassett, A. Giulietti and S. J. Karttunen, to be published in Opt. Commun..

11) T. Afshar - Rad, to be published.

12) C. Danson, to be published.

13) H. Figueroa, C. Joshi, H. Azechi, N. Ebrahim and K. Estabrook, Phys. Fluids 27, 1887 (1984).

14) J. F. Drake, P. K. Kaw, Y. C. Lee, G. Schmidt, C. S. Liu and M. N. Rosenbluth, Phys. Fluids 17, 778 (1974).

15) W. L. Kruer, Comm. Plasma Phys. Contro. Fusion 9, 63 (1985).

16) A. J. Schmitt, Phys. Fluids 31, 3079 (1988).

A2.2 THE PRODUCTION OF HOT NEAR SOLID DENSITY PLASMA BY ELECTRON ENERGY TRANSPORT IN A LASER-PRODUCED PLASMA

G J Tallents and M H Key (RAL)
P Norreys and D Brown (Royal Holloway and Bedford New College)
J Dunn (University of Leicester)
H Baldis (National Research Council, Canada)

The process of energy transport and ablation when laser radiation is absorbed at a surface to form a plasma has been studied extensively for conditions where the hydrodynamic flow pattern approaches a steady state[1] and heating occurs at densities close to the critical density. However, when the laser pulse duration is less than the hydrodynamic response time, electron thermal conduction heats matter at close to solid density[2].

In X-ray laser research there is a need for plasmas with simultaneous high temperature, high density and high degree of ionisation[3]. Consideration of this requirement has lead us to undertake short pulse laser-plasma experiments with targets of a thin layer of aluminium buried beneath a confining plastic overcoat.

An experiment was carried out with 20 ps pulses from the VULCAN laser at 0.53 μm wavelength in a single beam at energies of 6-8 J focused to a 50 μm focal spot giving intensities of 1-2 x 10^{15} Wcm^{-2}. The energy transport was recorded using layered targets designed to show the following.

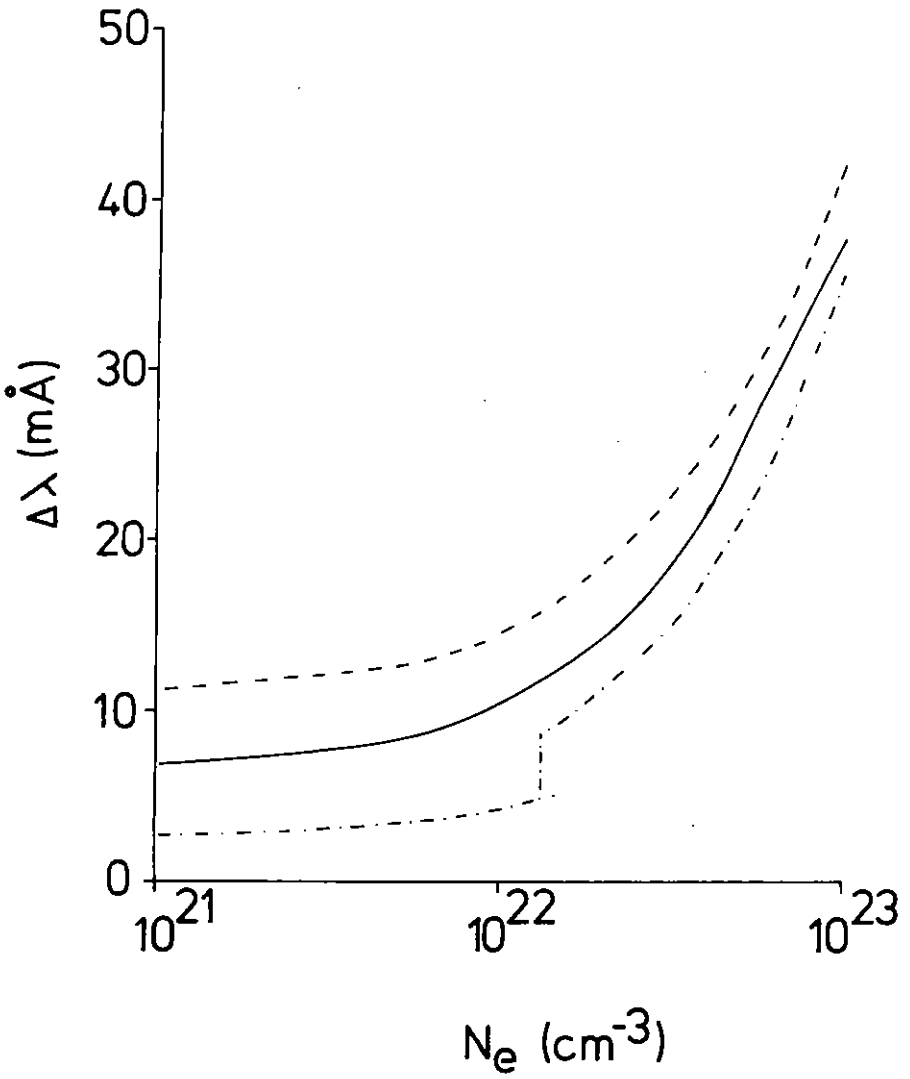


Fig A2.4 Calculated full-width at half maximum Δλ of the aluminium helium-like line $1s^2\ {}^1S_0 - 1s3p\ {}^1P_1$ as a function of electron density N_e. Doppler broadening is taken into account assuming an ion temperature of 500eV and instrumental broadening is taken into account assuming an instrument half-width of 10.7mÅ (broken curve), 6mÅ (solid curve) and zero (chain curve).

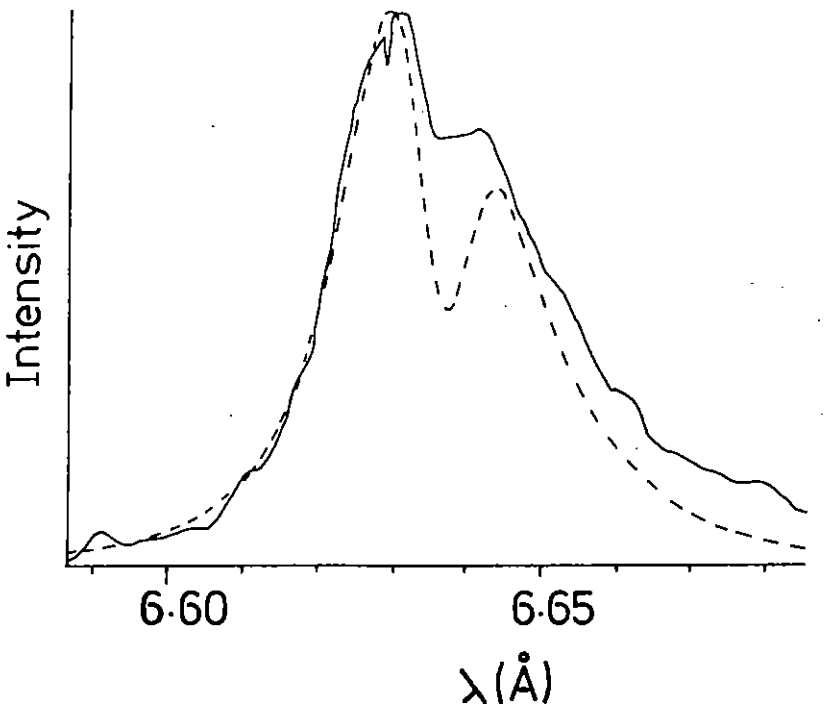


Fig A2.5 Experimental spectral line profile of AlXII $1s^2\ {}^1S_0$ - 1s 3p ${}^1P_1$ (solid curve) fitted with a theorectical profile (broken curve) assuming $N_e = 6 \times 10^{23} cm^{-3}$, an ion temperature of 500 eV and instrument broadening of 6mA. The experimental profile is emitted from an aluminium layer buried 0.5μm below a plastic overcoat.

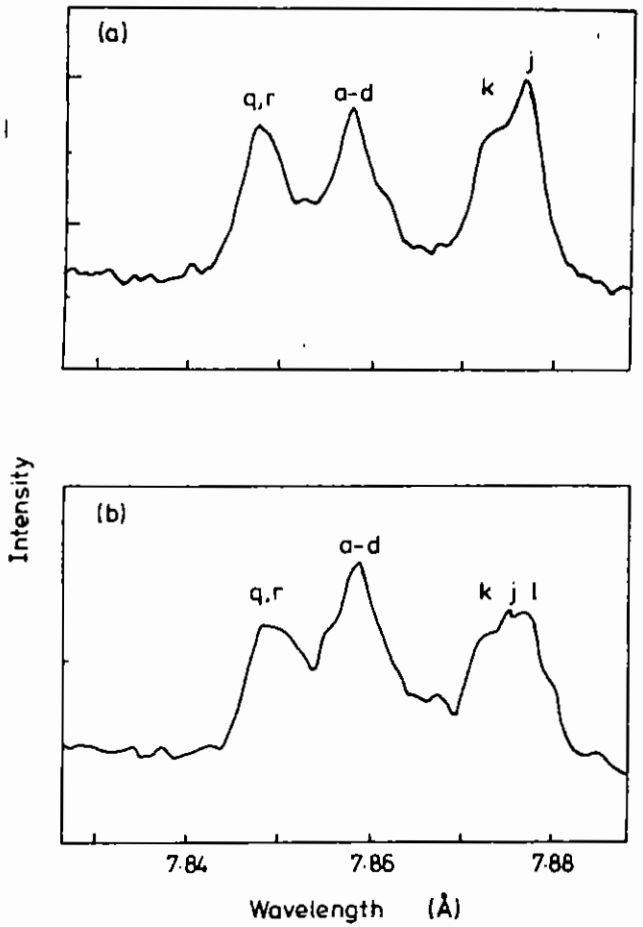


Fig A2.6 Satellite lines to the AlXII $1s^2\ {}^1S_0$ - $1s2p\ {}^1P_1$ resonance line labelled according to Gabriel[6] emitted from (a) an uncoated aluminium target and (b) and aluminium layer buried 0.5μm under plastic.

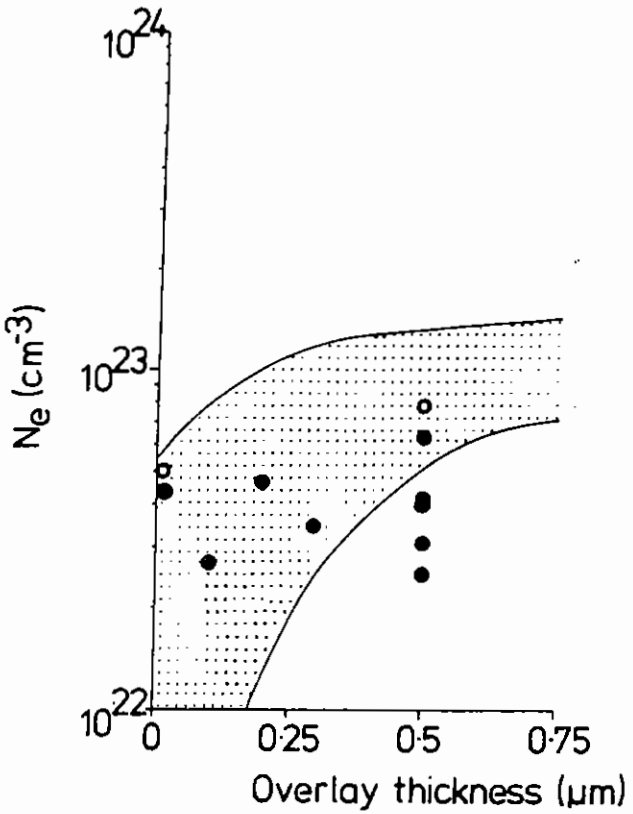


Fig A2.7 Electron densities measured (i) from the width of the AlXII $1s^2\ {}^1S_0$ - $1s3p\ {}^1P_1$ spectral line (solid circles and (ii) from the ratio of the intensity of the AlXII $1s^2\ {}^1S$ - $1s2p\ {}^1P_1$ satellites I(a - d + q,r)/I(j,k,l) (open circles) as a function of the thickness of plastic overlay on top at the aluminium layer. The shading shows the range of electron densities predicted by the MEDUSA code.

a) The penetration of heating into the solid evidenced by the emission spectrum of the Aℓ layer buried below the plastic layer. The aluminium layer was thin enough (0.2 μm) to permit measurement of a time averaged electron density and temperature from optically thin H-like and He-like Aℓ spectra features. All spectral lines except possibly for the Al H-like 1s-2p and He-like $1s^2\,{}^1S_0$ - $1s^2p\,{}^1P_1$ resonance lines are optically thin.

b) The penetration of hot electrons and their preheating effect from more deeply buried K_a fluors of KCℓ and CaF_2.

From the target surface to the inner layers, the target layer composition was: plastic (CH) ablator of thickness 0 to 1μm, Aℓ 0,2 μm, CH 2.5 to 5 μm, KCℓ 2 μm, CH 5 μm, CaF_2 2 μm with a substrate of 10 μm mylar. The targets were flat discs (lollipops) of 300 μm diameter.

Two X-ray spectrometers were used. A flat crystal spectrometer of moderate spectral resolution ($\lambda/\Delta\lambda \sim 7000$) was used to observe the n = 2 to n = 1 transitions of the He-like and H-like Al ions in the waveband 7.0 - 7.9 Å. The spectra were recorded on Kodak DEF X-ray film. Spectral intensities have been determined after converting the optical densities on film to intensities using the calibration given by Henke et al[4].

The Stark broadened spectral widths of the helium-like aluminium line AlXll $1s^2\,{}^1S_0$ - $1s3p\,{}^1P_1$ is a sensitive indicator of electron density for densities $\geq 10^{22}$ cm^{-3}. In figure A2.4 calculations using the code of Lee[5] are shown. The jump in the 'zero' instrument broadening curve of figure A2.4 is due to the double hump nature of the Stark line profile. For the flat crystal spectrometer, the expected instrument broadening is 6 mÅ (the solid curve of figure 1) caused primarily by the finite (≈ 50 μ) diameter of the plasma. Satellites to the hydrogen-like Lyman alpha line are expected to be broadened mainly by instrumental effects and indeed we have measured with the flat crystal spectrometer their full widths at half-maximum to be approximately 6 mÅ. Doppler broadening (provided the ion temperature is less than < 2 keV) does not significantly affect the measured line profiles with our instrument resolution.

Detailed comparisons of the Stark line shape predicted by Lee[5] and the experimentally measured line shape show excellent agreement (figure A2.5). In figure A2.5, the fit is optimised for the lower wavelength wing of the spectral line as there are satellite lines (in particular the intercombination line AℓXII $1s^2\,{}^1S_0$ - $1s3p^3P_1$) on the higher wavelength wing of the line. The electron density giving the best fit in this figure A2.5 example is 6 x 10^{22} cm^{-3}, a value significantly above the laser critical density of 4x10^{21}cm^{-3}. An aluminium plasma composed of fully stripped ions at solid density would have an electron density of 7.8 x 10^{23}cm^{-3}.

The intensity ratios of satellite lines to the helium-like aluminium line AℓXII $1s^2\,{}^1S_0$ - $1s2p\,{}^1P_1$ can also be used to deduce electron densities[7]. The satellites q, r, a-d and j, k, l, (labelled according to Gabriel[6]) emitted from an uncoated aluminium target and from an aluminium layer buried 0.5 μm under plastic are shown in Figure A2.6. The a-d satellite group show enhancement in the buried layer emission indicating[7] a higher electron density than for the uncoated aluminium emission. Using the tabulations of Jacobs and Blaha[7], the spectum (Figure A2.6a) from the uncoated target indicates an electron density of 5 x 10^{22} cm^{-3}, while the spectrum (Figure A2.6b) from the buried layer target implies an electron density of 8 x 10^{22}cm^{-3}.

Electron densities in the aluminium layer determined from the spectral width of the AlXll $1s^2\,{}^1S_0$ - $1s\ 3p\ {}^1P_1$ (deduced using the tabulations of Jacobs and Blaha[7]) are shown in Figure A2.7. The electron densities at the inner and outer boundaries of the aluminium layer at the end of the laser pulse predicted by MEDUSA[8] one-dimensional fluid-code simulations are also plotted on Figure A2.7.

Helium- and hydrogen-like aluminium spectra were produced with up to 0.75 μm overlay thickness, but the line widths and satellite line intensities and hence electron densities could only be accurately measured with overlay depths up to 0.5 μm because of the

low intensity of the lines with 0.75 μm overlay depth. The spectral intensities were approximately constant for all overlay depths up to 0.5 μm.

K_a emission of K and Cl was observed, but not of the more deeply buried Ca. This implies that the superthermal electron temperature is less than ∿ 10 keV[10]. The slope of the hard X-ray continuum between 5 and 20 keV measured by a filtered diode array indicated a temperature of 6 ± keV. The measured absolute flux of K K_a emission was = 2.5×10^{-7} Joules/steradian which using the analysis of Hares et al[10] implies that the total superthermal electron energy (temperature = 6 keV) was approximately 0.3 Joules. This is about 5% of the incident laser energy. Thermal electron temperatures in the aluminium layer have been determined from the slope of the He-like free-bound continuum measured by the flat crystal spectrometer. The temperatures are estimated to be ∿ 1 keV for all plastic overlay thicknesses from 0.1-0.5 μm. With larger overlay thicknesses, the intensity of the free-bound continuum was not sufficient for an accurate temperature measurement.

We have shown that hot(∿ 1 keV), dense (∿ 6-8 x 10^{22} cm^{-3}) and well- ionised plasmas can be produced from a layer buried under a plastic overcoat irradiated by short pulse (20 ps), high intensity (∿10^{16} Wcm^{-2}), 0.53μm laser light. The temperature and energy content of the superthermal electrons is small (6 keV and 5% of laser energy respectively). Our observation of a significant drop in emission from the buried layer plasma is produced by thermal conduction. Superthermal electron 'pre-heating' of the buried layer would fall-off more slowly with increasing overlay thickness.

References

1. Key, M H 20th Scottish Universities Summer School in Physics Laser-plasma Interactions (SUSSP, St Andrews) 1979 'Lectures on the Physics of the Super Dense Region'.

2. Murnane, M M, Kapteyn, H C and Falcone, R W, Phys Rev Lett 62, 155 (1989).

3. Dave, A and Pert, G J, J Phys B 17, A953 (1984).

4. Henke, B L, Uejio, J Y, Stone, G F, Dittmore, C H and Fujiwara, F G, J Opt Soc Am B3, 1540 (1986).

5. Lee, R W, J Quant Spect Rad Trans 40, 561 (1988).

6. Gabriel, A H, Mon Not R Astron Soc 160, 99 (1972).

7. Jacobs, V L and Blaha, M, Phys Rev A21, 525 (1980).

8. Christiansen, J P, Ashby D E T F and Roberts K V, Comput Phys Commun 7, 271 (1974).

9. Rosen, M D, Comments Plasma Phys Control Fus 8, 165 (1984).

10. Hares, J D, Kilkenny, J D, Key, M H,. and Lunney, J G, Phys Rev Lett 42, 1216 (1979).

A2.3. HYPERVELOCITY IMPACT SIMULATION IN GLASS AND METAL USING A HIGH-POWER PULSED LASER

David C Hill (Unit for Space Sciences, University of Kent)
Manuel Grande and Nadeem H Rizvi (RAL)

Introduction

Pulsed lasers, generating modest irradiances (∿10^{12}-$10^{14}$$W.cm^{-2}$), offer a unique, low-cost alternative means of simulating hypervelocity microparticle impact phenomena for a wide range of impactor mass/velocity combinations. For instance, a high-power laser can deliver significant energy (∿1 J) and momentum to a surface in a time (∿1 ns) comparable to that required by a hypervelocity microparticle to transfer its kinetic energy and momentum to a target. In vacuum, surface conditions similar to

those produced by the impact of a dust particle of mass ∿0.1 μg and velocity ∿ 7 km.s^{-1} are created.

From a space-technology/spacecraft materials stand-point it is precisely dust particles with these mass/velocity combinations that are significant. For an exposure time of 1 year and an orbital altitude of 500 km, between 1 and 10 dust particles with such mass/velocity characteristics will impact upon a square metre of space-exposed surface. Should this surface be a solar array or a power system radiator, significant irreversible, even catastrophic, damage may occur.

Glass/Ceramics

The impact damage in materials such as glass and dielectric laminar structures[1-5] is summarised in fig A2.8. Due to the brittle nature of glass and its low tensile strength, the shock related shear and release tensile stresses dominate the material strength over a longer time, resulting in more extensive damage.

At velocities below 3.5 km.s^{-1}, only a central, radially symmetric, pit is present. As the impact velocity is increased into the hypervelocity regime (fig A2.8(a)) the depth of penetration increases in the central pit and an outer spallation zone becomes evident where the impact induced shock front has fractured solid target material. Above 5km.s^{-1} the spallation zone increases in diameter and solid, fractured material is ejected due to the excess energy behind the shock front. The spallation zone is highly irregular in terms of shape, but the general morphology usually exhibits a variable number of concentric rings of surface spallation. Fractured material may remain partially attached to the target surface (fig.A2.8(b)). The depth with respect to the target surface of the spallation rings is inversely dependent on the radial distance from the impact axis. As the impact velocity is increased above ∿7 km.s^{-1} the central pit may be totally ejected if there is a sufficient excess of kinetic energy remaining after fracture and spall ejection, leaving no apparent crater but just spall damage.

Finally, fig A2.8(c) shows the typical damage to a laminated structure (e.g. solar cell or optical anti-reflection coating on a glass substrate). Single or multi-layer thin laminates are highly susceptible to impact spallation damage as the impact-generated shock front will interact strongly with each interface. At such interfaces, reflected rarefaction waves are generated, causing spallation, similar to release stress waves at the target surface, For glass itself (i.e. a homogeneous, randomly faulted material) the ratio D_S/D_C ∿4 with D_C being ∿3x the impactor diameter. For a stack of dielectric films or for a solar cell where there is a "fault plane" at each interface, the degree of spallation can be expected to be far greater than for a homogeneous material.

Laser Simulation

Laser simulation of microparticle impacts is based on three main tenets[6-9].

- the average laser-induced surface ablation pressure is equal to the 1-dimensional shock pressure generated by the hypervelocity impactor
- the impactor has a diameter equal to the focussed laser spot diameter
- the laser-induced impulse is equal to the impactor momentum.

Results

Work of this type has previously been undertaken at the CLF[10] using both VULCAN and SPRITE, to simulate the impact of micrometeorites on the DIDSY shield of the GIOTTO space probe. In the present investigation, we are interested in modelling the effects of meteorite strikes on glass, coated optics and solar panels. The facilities available in TA4 are well suited to the energy requirements. For example, a range of 1 to 5 joules into a 100 micrometer spot spans the regimes of contained impact to

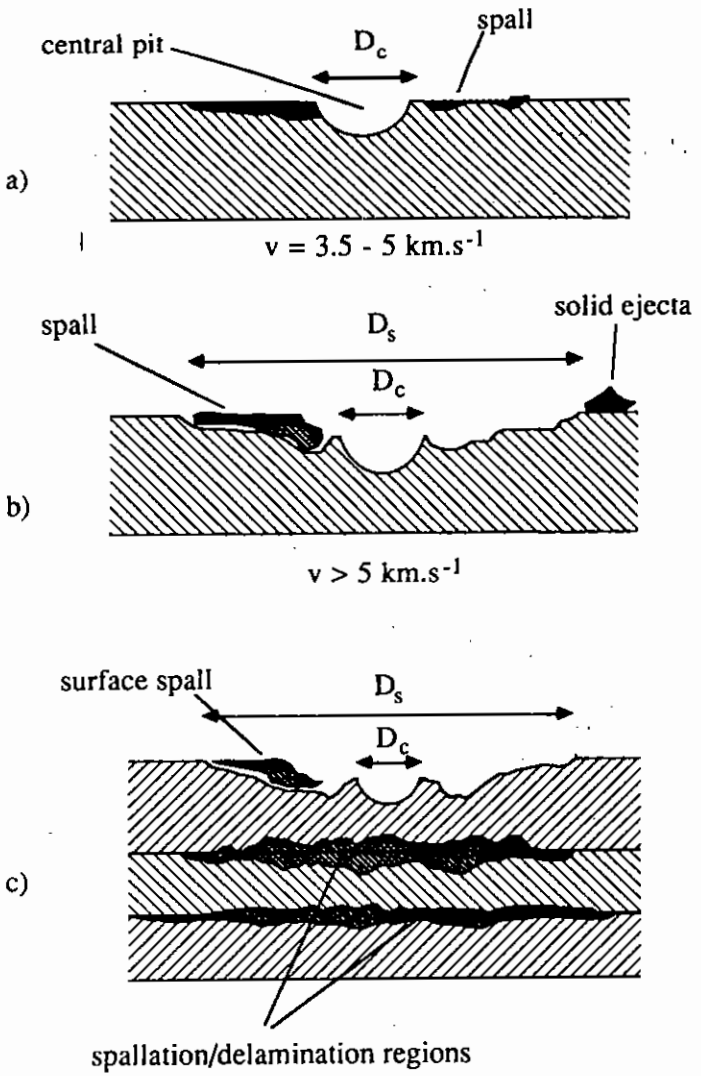


Fig A2.8 Schematics of impact damage (section) in (a, b) glass and (c) laminated glass/dielectric structures. The ratio D_S/D_C~4-5 where D_S is the spallation zone diameter and D_C is the crater diameter.

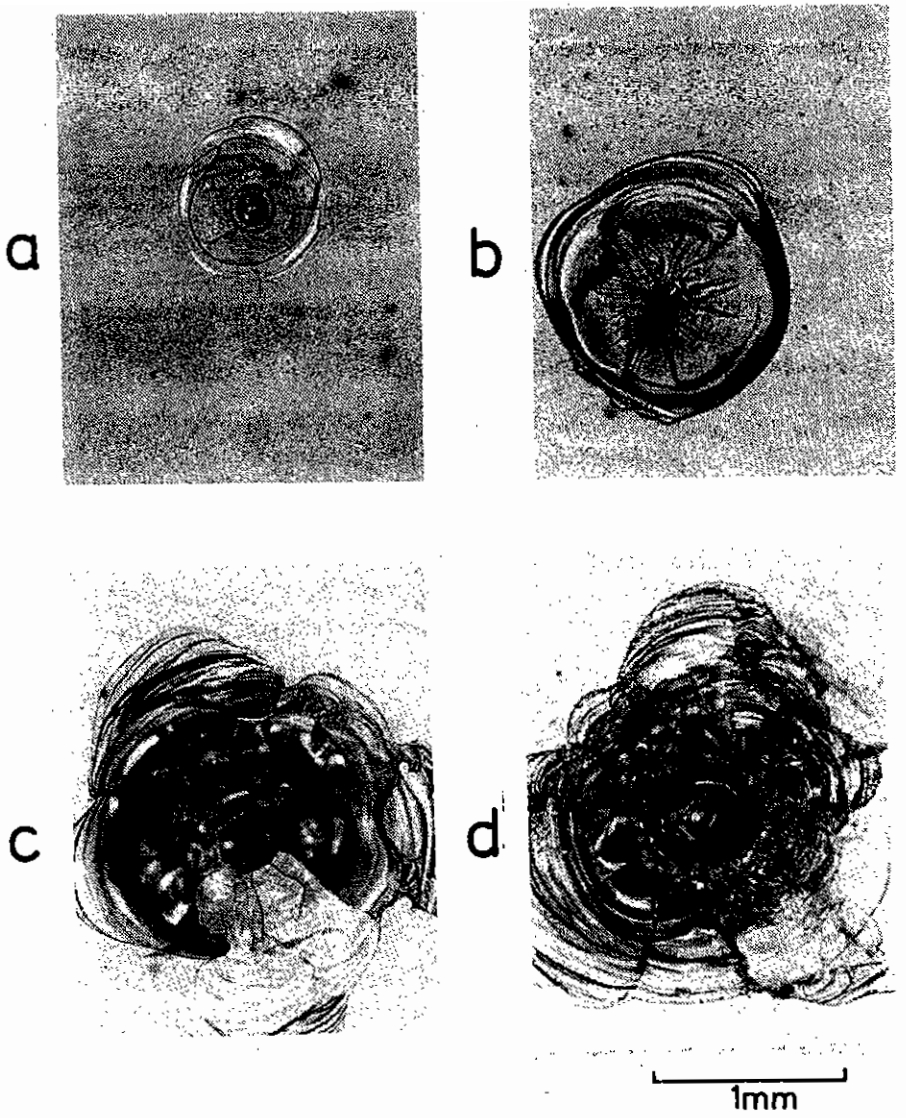


Fig A2.9 Laser impact sites in borosilicate glass. (a) Laser energy E = .46 J spall not ejected, (b) E = .5 J spall ejected, (c) E = .88 J spall ejected, (d) E = 3 J spall ejected plus large scale conchoidal fracture.

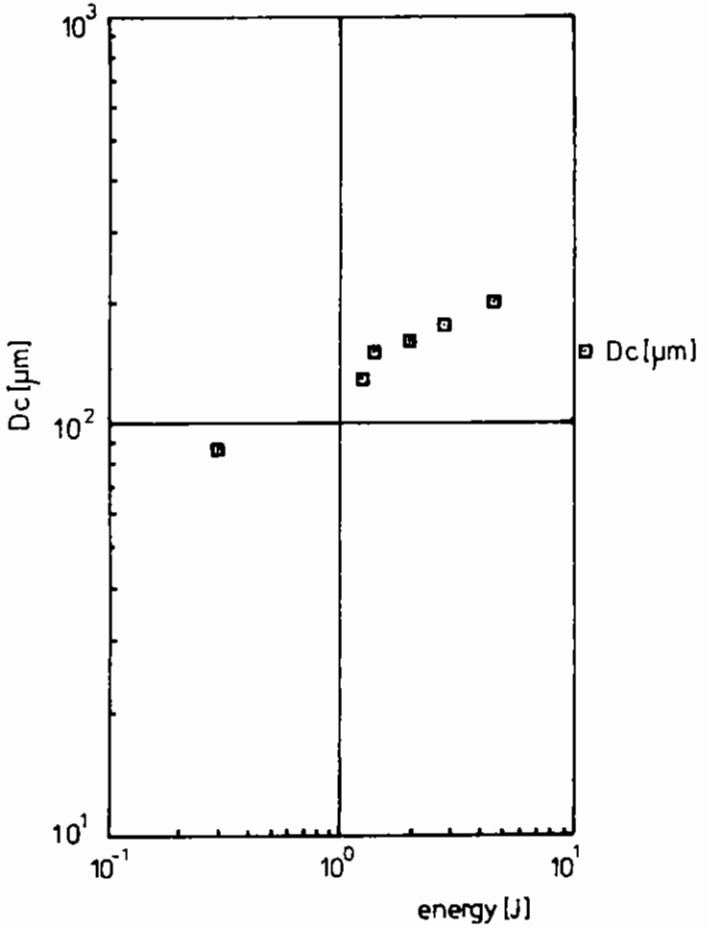


Fig A2.10 Crater diameter (D_C) vs Laser Energy (E) in steel. The best fit regression line (R = 0.99) is $D_C = 126E^{0.33}$ indicating excellent simulation of hypervelocity impact.

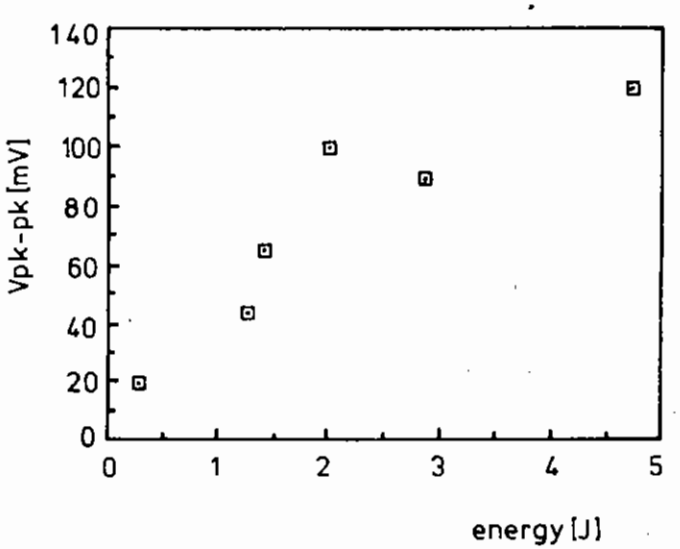


Fig A2.11 Correlation of momentum transfer with laser energy in steel for sub-perforation impacts.

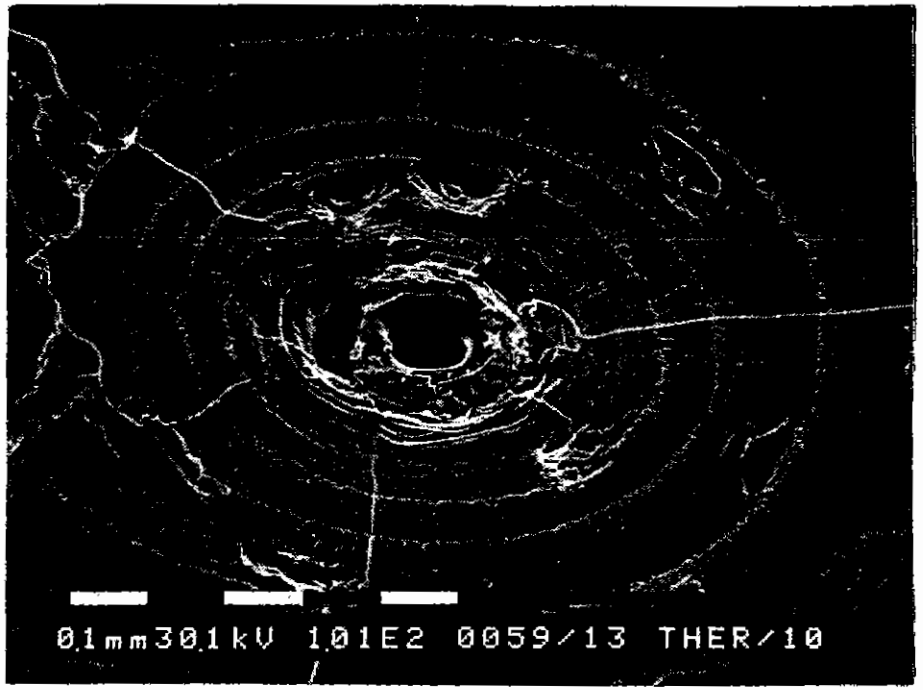


Fig A2.12 Laser impact in a layered glass target.

perforation on 150 micron thick glass specimens. Data sets were accumulated for 1mm thick borosilicate targets, 250 and 125 micron high purity silicon oxide, and 150 micron metalised thermal control mirrors. Data was also obtained on a range of metal targets, along with some momentum transfer measurements with a prototype detector. In total about 50 sites were generated; analysis is at a preliminary stage.

The impact sites generated in borosilicate targets were most promising. Morphology of these sites indicated that the simulation technique was faithfully reproducing hypervelocity impact phenomena. This is evidenced by the progression from a central crater with unejected spall (fig A2.9a) through partial spall ejection (fig A2.9c) to total spall ejection and increased spall zone (fig A2.9d). The morphology of these sites indicates that energies of $\sim$0.5J to 3J will correspond to hypervelocity impacts varying from velocities $\sim$2 km.s^{-1} upto $\sim$5 km.s^{-1}. Further work is necessary to quantify the impact site parameters (i.e. D_c and D_s) in terms of simulated impact velocity, simulated projectile mass and laser energy.

Using data from sites generated on a steel impact diaphragm (thickness 150µm) with an acoustic sensor (piezoelectric crystal) attached to the rear surface it is found that good correlation occurs between impact crater diameter and laser energy. For hypervelocity impacts, crater diameter (d) scales as $E^{1/3}$, where E is the impactor kinetic energy[11]. The best fit to the data presented here (as shown in fig A2.10) shows scaling as $E^{0.31}$, indicating excellent simulation of hypervelocity impact in steel, agreeing with similar experiments conducted on aluminium targets. Figure A2.11 shows the expected correlation between momentum transfer and laser energy in the impact regime below marginal perforation, suggesting a correlation between laser energy and simulated impact kinetic energy.

The layered targets indicated a distinctive morphology as evidenced in figure A2.12, suggesting that the impact process may be complicated by the interaction of shock fronts with the surface coatings, or the simulation technique, under these conditions, may be being affected by the spatial intensity profile of the focussed laser beam.

Conclusion

Although the analysis is at a preliminary stage, it is clear that we are successfully simulating hypervelocity impact damage in both metal targets (confirming previous work using aluminium but extending the technique to steel) and glass targets. Simulated impact sites in both types of materials exhibit correct crater morphology and extend the simulations into the perforation regime. The technique can obviously be fruitfully applied to further impact simulations on a variety of target materials and target configurations.

References

1) R E Flaherty, "Impact Characteristics in Fused Silica", AIAA Paper No.69-367, AIAA Hypervelocity Impact Conference, Cincinnati, (April 30th - May 2nd, 1969)

2) J F Vedder, "Microcraters in Glass and Minerals", Earth & Planetary Sci Lett 11 291-296, (1971)

3) J C Mandeville & J F Vedder, "Microcraters Formed in Glass by Low Density Projectiles", Earth & Planetary Sci Lett 11, 297-306, (1971)

4) J C Mandeville, "Profile and Depth of Microcraters Formed in Glass", Earth & Planetary Sci Lett 15, 110-112 (1972)

5) B G Cour-Palais, "Hypervelocity Impact in Metals, Glass and Composites", Int J Impact Eng 5, 1-4, 221-238,(1986)

6) J P Bibring, F Cottet, Y U Langevin & J P Romain, "Simulation laser d'impacts de particules de très grande vitesse", J Physique-Lettres, 44, 189-194 (1983)

7) A N Pirri, "Theory for Laser Simulation of Hypervelocity Impact", Phys Fluids, 20, 221-228, (1977)

8) P E Nebolsine, AIAA 14th Aerospace Sciences Meeting, Washington DC Paper 76-52, PSI SR-5, (1976)

9) P E Nebolsine, "Laser Simulation of Erosion", Adv Re-entry Aeromechs| Interim Sci Report, Vol3, PSI TR-29, Physical Sciences Inc Wakefield, Ma, (1975)

10) A Ridgeley in Laser Div. Annual Report 1985 RAL 85-047 C1.5

11) J Zucas, (Ed) "Impact Dynamics" John Wiley & Sons (1982).

A3 LASER COMPRESSION WITH DENSE PLASMAS Pages

A3.1 THE ANALYSIS OF IMPROVED ION CORRELATION EXPERIMENTS IN DENSE PLASMAS 69-75

A 3 . 2 SUB-NANOSECOND X-RAY DIFFRACTION FROM LASER-SHOCKED CRYSTALS 76-79

A3.1 THE ANALYSIS OF IMPROVED ION CORRELATION EXPERIMENTS IN DENSE PLASMAS

B Shiwai, A Djaoui, T A Hall (University of Essex)
S J Rose (RAL)

Introduction

In last years annual report[1] we described the improvements to ion correlation experiments on shock compressed plasmas. In this work we present the analysis of the data, with a view not only to measure the ion density but also to estimate the temperature during compression and subsequent heating of plasma. In section 2, the densities are measured using the EXAFS code and the band-structure calculations. In section 3, the plasma temperature is estimated. Finally, in section 4 a conclusion of this work is presented.

Density Measurements

As mentioned in the experiment conditions (see Ref 1), the EXAFS spectra were recorded on DEF X-ray film at various delay times between the main driving pulse (600 psec) and the backlighting pulse (70-100 psec). The procedure to extract the EXAFS data from the films is similar to those presented in Ref 2. Figure A3.1 shows the resulting absorption spectra above the aluminium K-edge as a function of energy taken at different times. At time 0.0 psec the shocks have not reached the aluminium layer, the EXAFS spectra are those of uncompressed, unheated aluminium. The vertical line on the figure represents the position of the first absorption minimum for uncompressed aluminium.

A small shift of the first minimum away from the K-edge can be noticed at +100 psec, whereas at +200 and +300 psec, a clear shift is observed. The +300 psec shows a large shift roughly twice the distance away from the K-edge but with a small EXAFS amplitude compared to the +200 psec. This can be explained as the aluminium temperature increases at the peak compression (see Fig A3.4) results in a decrease of the EXAFS amplitude. The shift of the peak is also observed at +400, +500 and +600 psec. This is a clear indication of compression within the aluminium. AT time +700 psec, where the plasma has expanded to densities lower than normal solid density we are still able to observe an EXAFS spectrum but at later times no EXAFS modulation was observable.

The EXAFS spectra shown in Figure A3.1 were analysed for density in two ways using the same approach as we have explained in Ref 2 first using the standard EXAFS analysis code[3]. Figures A3.2a-b show the experimental normalised EXAFS and their Fourier transforms corresponding to time 0.0 psec and +200 psec respectively. The fitted first shell corresponding to times 0.0 psec and +200 psec are shown in figures A3.3a-b, also table 1 shows the measured values of R_1, volumetric compression and densities. The last column shows the relative mean square displacement (σ_1^2) values as estimated from the fitting procedure. The quoted error bars are ±0.11 A° in R_1 due mainly to the atomic background subtraction procedure and the ±0.02 A°² in σ_1^2 is due to the fitting procedure.

In the second method of analysing this data, we used the band structure calculations[4] from which we are able to obtain a scaling for the second minima in the absorption spectra as a function of compression. The spectrum of cold uncompressed aluminium at 0.0 psec was used for calibration. Table 2 shows the estimated values of compression and density using this procedure. The error bars are calculated as follows; ±2 eV from the uncertainty in the K-edge position; ±4 eV from the position of the second minimum. This amounts to a total error bar of ±6 eV. The results using this method showed that there is a good agreement for density with the Fourier transforms results and with the MEDUSA[5] code predictions.

Figure A3.4 shows the MEDUSA code predictions of density as a function of time relative to the time of arrival of the peak of the main laser pulse. A range of densities through the aluminium layer are represented by the shaded region of the figure. The

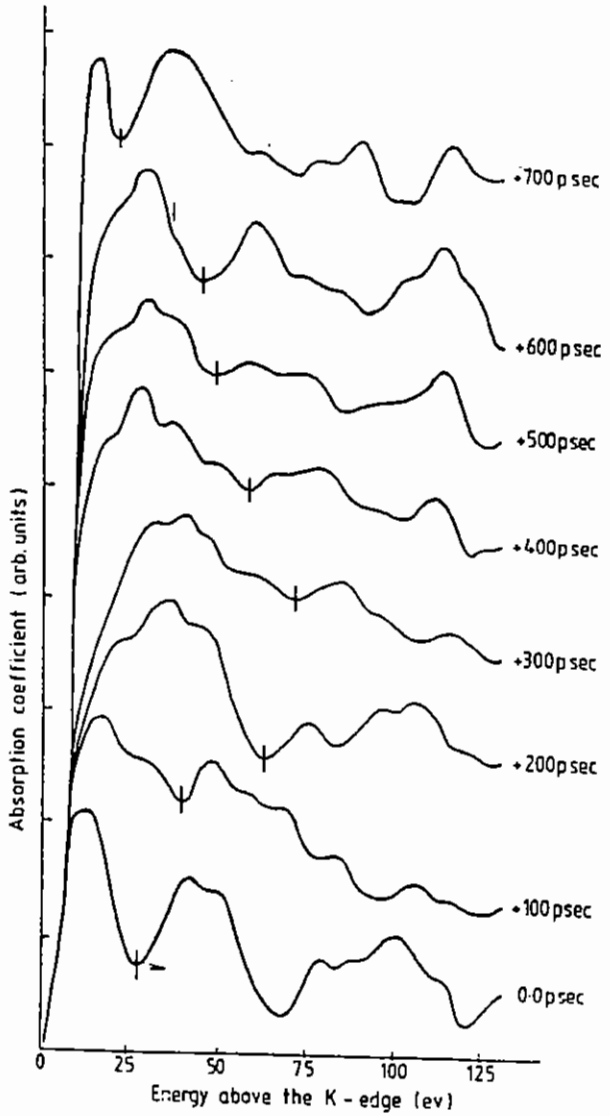
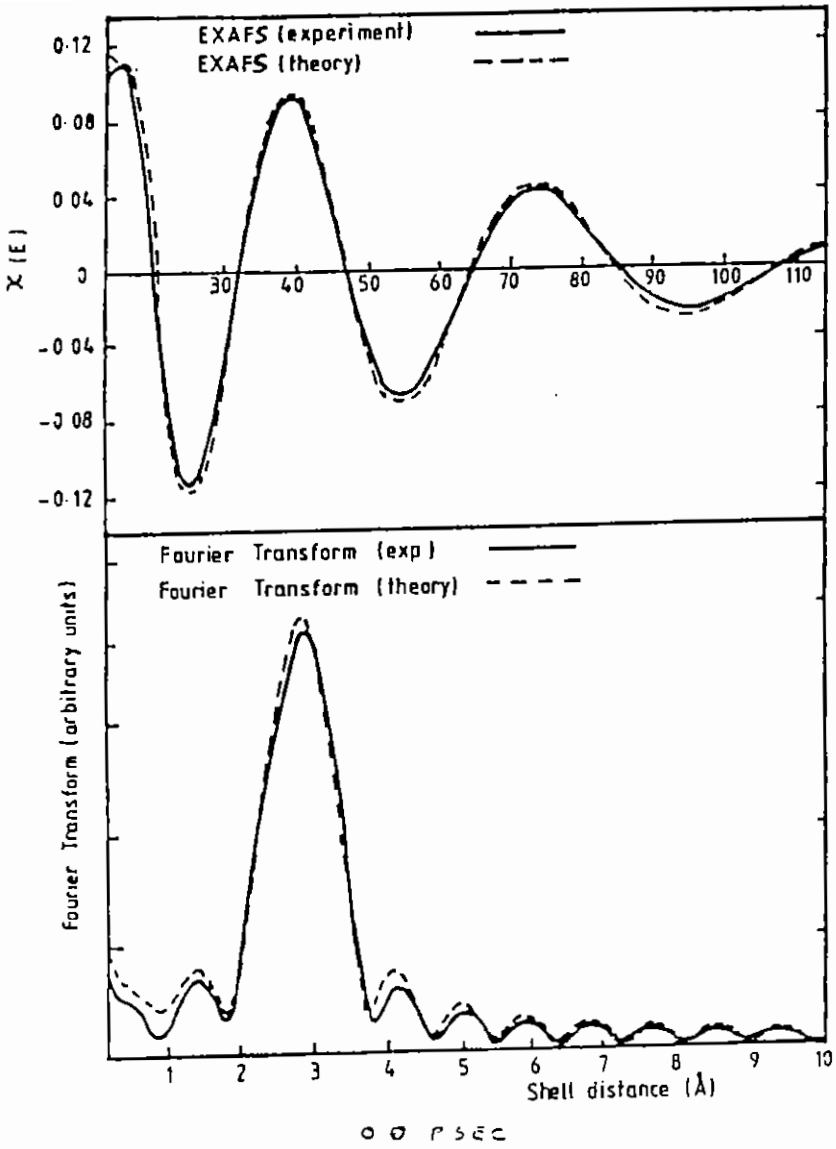


Fig A3.1 *Experimental absorption coefficient. The different curves are labelled with the relative time between the main drive pulse and the backlighting pulse. The vertical line represents the position of the first absorption peak for uncompressed aluminium.*



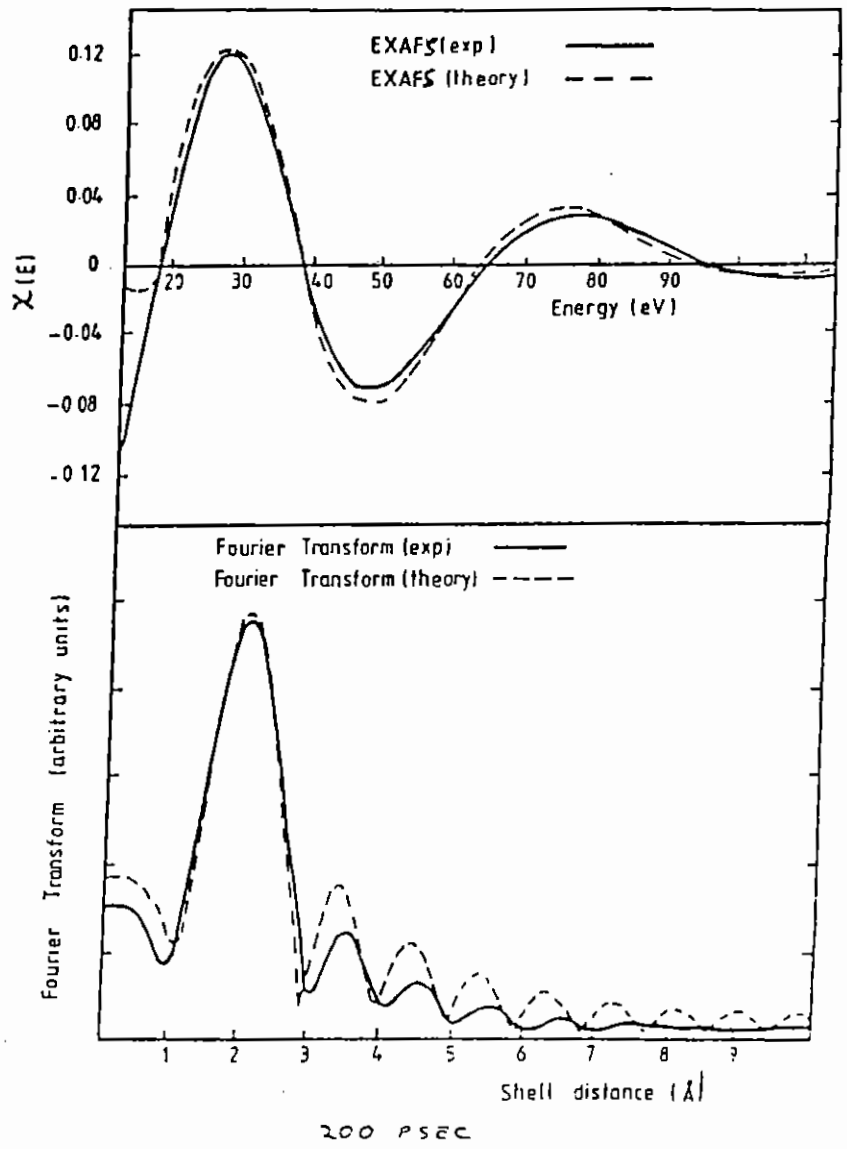
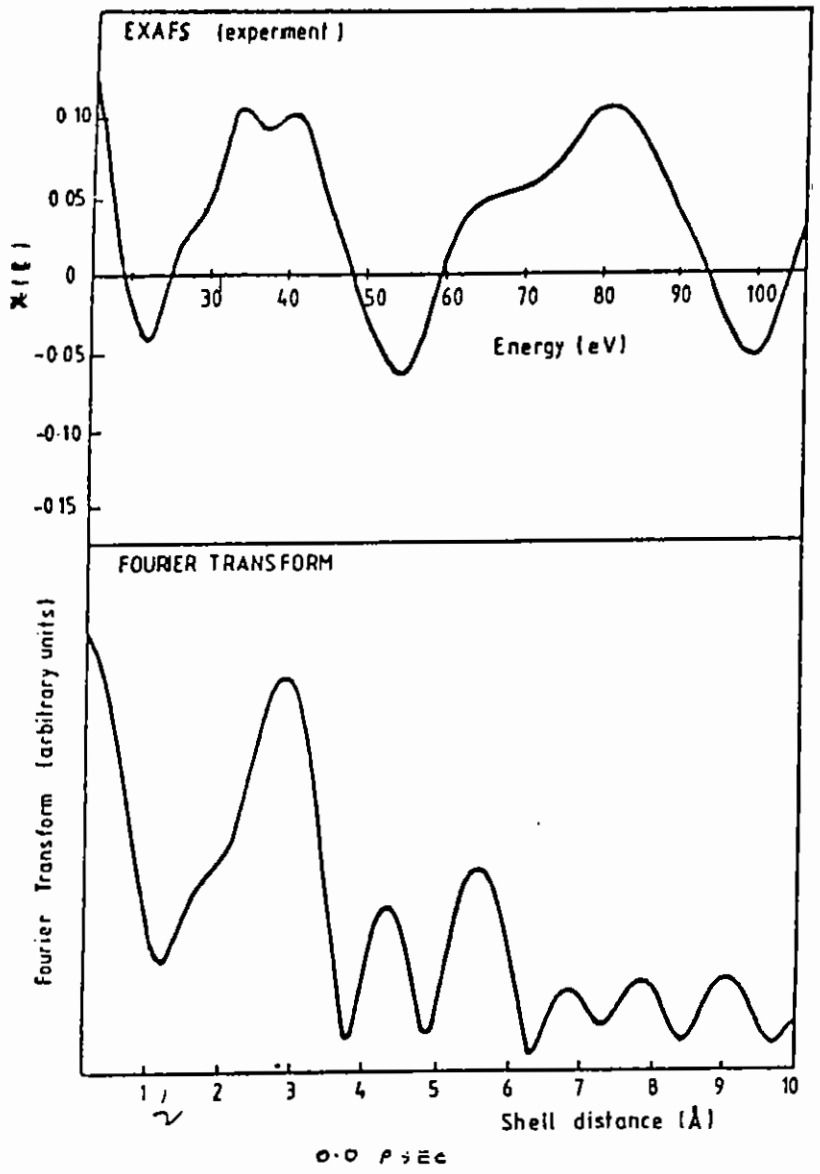


Fig A3.2 Experimental normalised EXAFS and their Fourier transforms corresponding to time 0.0 psecs and 200 psecs respectively.



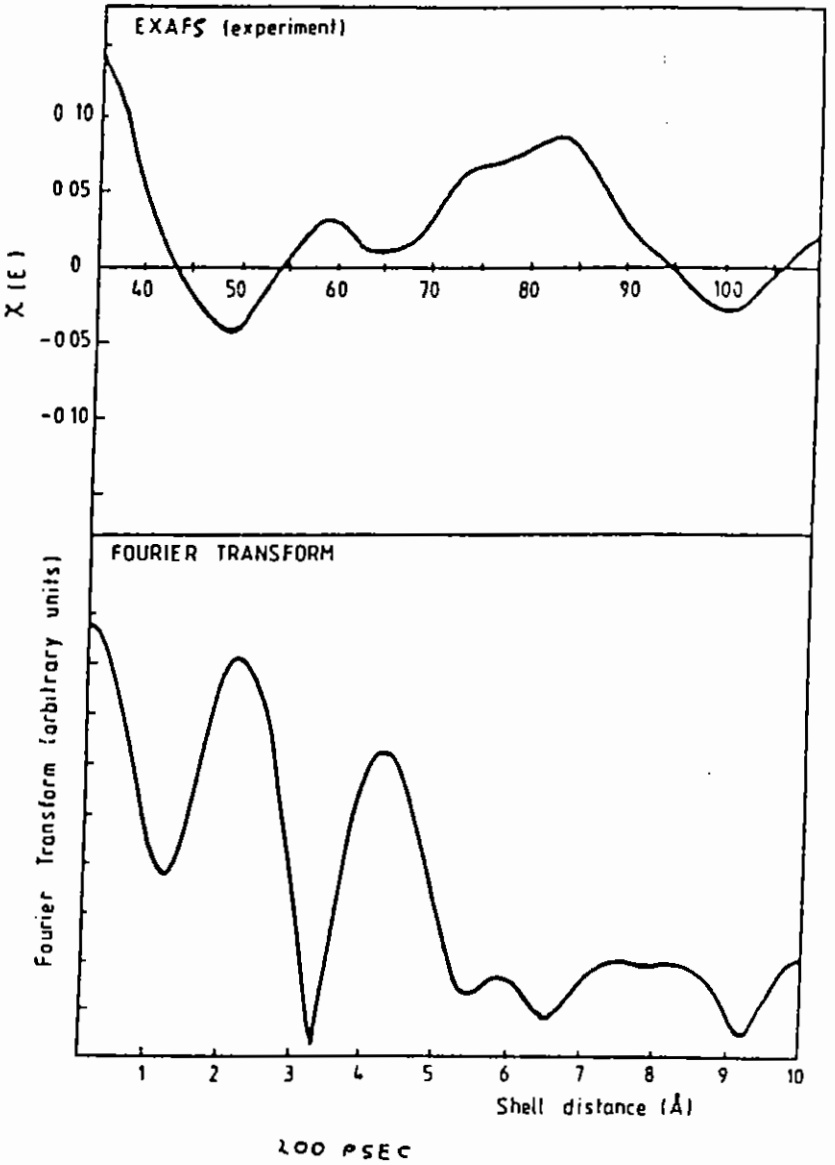


Fig A3.3 The fitted first shell corresponding to times 0.0 psecs and 200 psecs respectively.

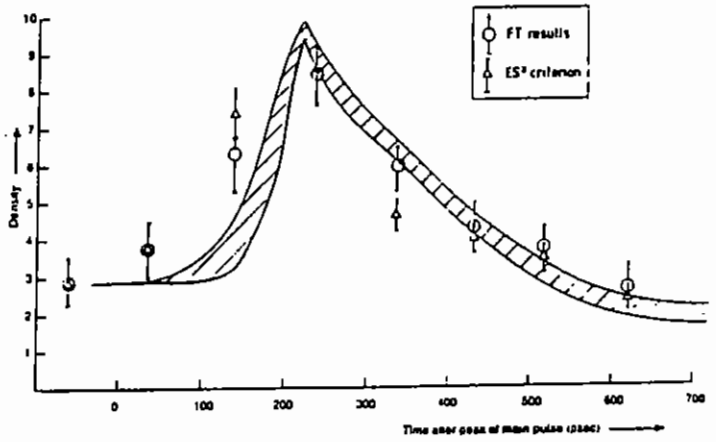


Fig A3.4 *MEDUSA code predictions of density as a function of time with respect to the peak of the main laser pulse (600 psec). The shaded region represents the range of densities through the aluminium trace layer. The experimental points are shown with error bars (circles as given by FT; triangles given by ES²): these experimental points have been moved 600 psec earlier in time (see text).*

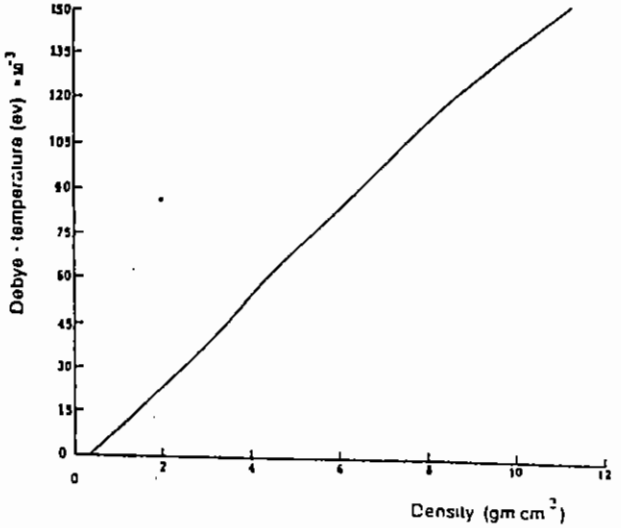


Fig A3.5 *The calculated Debye-temperature as a function of density for aluminium using Gauss model*

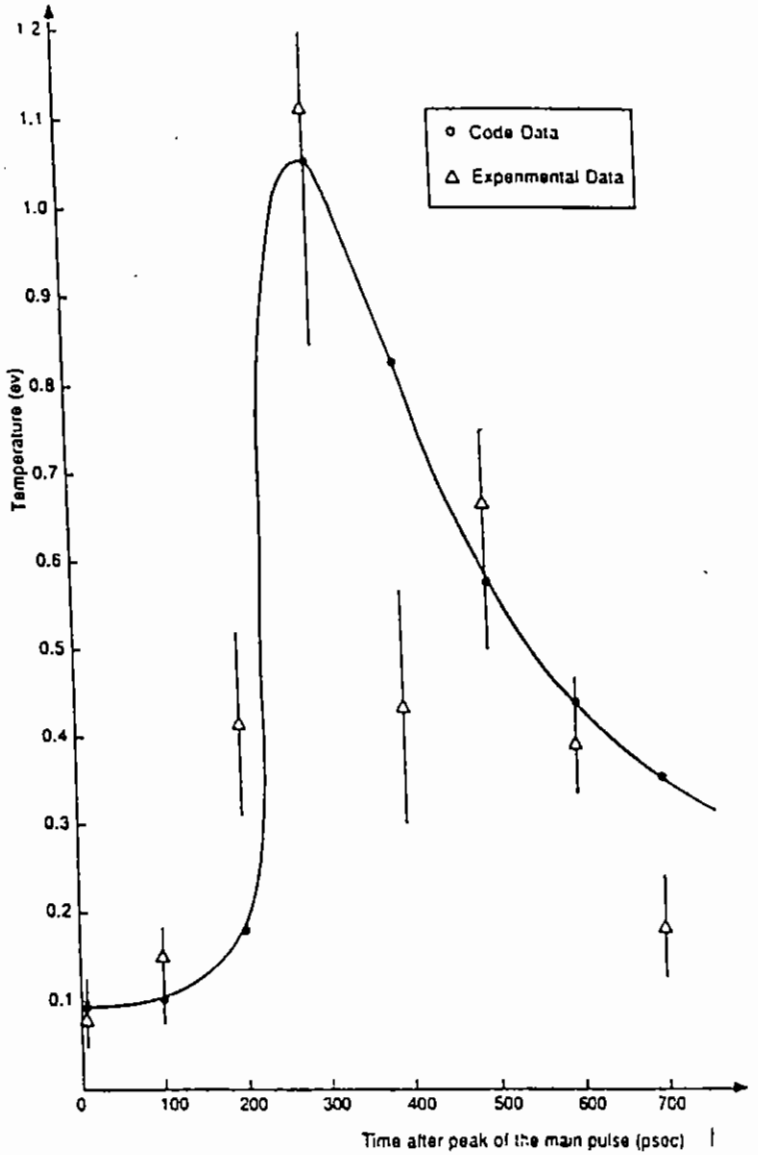


Fig A3.6 *MEDUSA code predictions of plasma temperature values as a function of time are shown (circle) together with the experimental value (triangles).*

experimental points are shown with error bars as given by the Fourier transform (circles), and as given by the band-structure calculations (triangles). Due to the unreliable measurement of the laser pulse shape at early times, the experimental points have been moved about 60 psec earlier in time to correspond with the peak compression in the code.

Plasma Temperature Measurements

In this section we attempt to measure the plasma temperature during compression of the aluminium foil target. In order to calculate the plasma temperature, we used the model of Beni and Platzman[6] which relates the relative mean square displacement σ^2 (see table 1) to the temperature.

$$T = \theta_D\left(\frac{M_p K_B \theta_D \delta^2}{3\hbar^2} - \frac{1}{4}\right) \qquad (1)$$

where ω_D is the Debye-temperature. M_p is the proton mass unit. the density dependence of σ^2 is included entirely through the Debye-temperature θ_D which is calculated by use of the Cowan model[7]. Values of θ_D as given by this model were compared by More et al[7] to experimental values throughout the periodic table. The agreement is quite good for most of the elements. Figure A3.5 shows calculated θ_D as a function of density for aluminium. Here one can observe that θ_D increases almost linearly with the density.

To estimate the experimental temperature from equation 1, two quantities are needed; σ^2 and θ_D. σ^2 was measured from FT and fitting procedure. θ_D is obtained by use of Cowan model together with the measured experimental density as given in table 1. Using equation 1 the results for temperature are listed in table 3 and compared with the calculated temperature from the MEDUSA code. In figure 6, we have plotted the temperature values (open circles) from the code as a function of time after the peak of the main drive pulse together with the experimental values (triangles). The agreement between code and experimental values are not as good as the density comparison because of the following:-

(1) The errors in experimental density measurements leads to an error in the calculations of Debye-temperature θ_D. The temperature in equation 1 is proportional to the square of θ_D which makes temperature very sensitive to errors in θ_D.

(2) The errors due to the method we used to estimate the relative mean-square displacement (σ^2) from EXAFS spectra.

The large error bars that result from these measurements inaccuracies make it difficult to comment on the degree of agreement between the experimental and the code results.

Conclusion

In this work, we have described results from improved measurements of EXAFS of laser driven shock compressed plasma. Compressions and densities measured in these experiments are higher and more accurate than those obtained previously[8,9]. The agreement between the code predictions of density and the experimental data is good. Also, the improved quality of these new results has enabled us to estimate the plasma temperature throughout the compression and expansion phase of the aluminium. However, the agreement between the experimental values and the code predictions of temperature is not so good and further refinement of the technique is necessary in order to make a critical comparison.

References

1. B A Shiwai et al, RAL Report No RAL-88-042, 1988, Annual Report to the Laser Facility Committee, Section A3.

2. A Djaoui et al, Plasma Phys Controlled Fusion 31, 1, pp111, (1989).

3. G N Greaves, private communication.

4. R C Allbers et al, Phys Rev B31, 6, pp 3435, (1985).

5. J P Christiansen et al, Comput Phys Commun 7, pp271, (1974).

6. G Beni and P M Platzman, Phys Rev, B14, 4, pp 1514, (1976).

7. R M More et al, Phys Fluid, 37, 10, pp3059, (1988).

8. T A Hall et al, Phys Rev Letts, 20, 60, pp2034, (1988).

9. B A Shiwai et al, Proc SPIE, Vol 913, 10-17, Los Angeles, (1988).

Time (psec)	$R_1(\AA)\pm 11$	Compression	p(gcm^{-3})	$\sigma^2+0.02A^{02}$
0.0	2.86	1	2.7	0.035
100	2.62	1.3±.14	3.5±.38	0.028
200	2.2	2.92±.4	7.85±.95	0.02
300	2	2.92±.4	7.85±.95	0.026
400	2.26	2.02±.24	5.47±.63	0.025
500	2.5	1.5±.17	4.04±.46	0.083
600	2.61	1.31±.13	3.55±.33	0.07
700	2.94	.92±.08	2.48±.22	0.09

Table 1 First shell radii, volumetric compression density p and σ^2 as determined by FT

Time (psec)	Second min ±6 eV	Compression	p(gcm^{-3})
0.0	54.4	1	2.7
100	65.5	1.3±.17	3.5±.45
200	102	2.56±.23	7.93±.63
300	112	2.94±.23	7.93±.63
400	75	1.61±.19	4.35±.5
500	68	1.4±.18	3.76±.5
600	63	1.24±.14	3.35±.37
700	49	.85±.15	2.30±.4

Table 2 Second minimum position volumetric compression and density p is determined by band-structure.

Time (psec)	θ_d(eV)	T_{exp}(eV)	T_{code}(eV)
0.0	0.035	0.088±.02	0.099
100	0.051	0.148±.06	0.1
200	0.1	0.42±.23	0.167
300	0.14	1.1±.48	1.04
400	0.091	0.43±.19	0.81
500	0.062	0.67±.16	0.6
600	0.052	0.4±.085	0.44
700	0.031	0.18±.035	0.36

Table 3 Calculated values of plasma temperature during the compression at different times in the experiment.

A3.2 SUB-NANOSECOND X-RAY DIFFRACTION FROM LASER-SHOCKED CRYSTALS

J S Wark (Clarendon Laboratory, University of Oxford)
G Kiehn (Imperial College of Science and Technology, London)
R R Whitlock (Naval Research Laboratory, Washington DC, USA)

Introduction

We have recently shown that it is possible to measure the interatomic spacings in a laser shocked crystal with sub-nanosecond bursts of x-rays emitted from a laser-produced plasma[1,2]. In these previous experiments a shock wave was driven into the crystal of interest by irradiation with a laser pulse of 1nsec duration at an irradiance of order 10^{10} Wcm^{-2}. A second laser beam, synchronous bu delayed with respect to the first, and of 100psec duration, was focused to a 50μm spot onto the surface of a medium Z (19 - 22) target. The resonance line of the helium-like ion was diffracted from the surface of the shock-compressed crystal, and the resulting spectrum recorded on x-ray film. The compression in the crystal is then extracted from the resulting shift in Bragg angle as given by a differentiation of Bragg's law:

$$\Delta(2d)/2d = -Cot\theta\Delta\theta$$

Thus in these previous experiments we obtain flash diffraction patterns of 100psec duration. For most of the experiment described here the x-ray producing pulse was increased in duration to 1nsec and the shift in diffraction recorded on an x-ray streak camera, allowing the whole event to be recorded at once. Time resolved data of the compression on the front surface of a compressed crystal were recorded, as well as data on the back surface (ie. during shock breakout) of a thin crystal. Simultaneous Bragg and Laue diffraction lines were also recorded, yielding information concerning compression in a direction running parallel to the shock front.

1. Diffraction from surface:

The experimental set up is shown schematically in Fig A3.7. A silicon (111) crystal was irradiated with 100J of 1.05μm laser light in 1nsec (FWHM) at an irradiance of 10^{11} Wcm^{-2}. A second beam, of the same duration, of 0.53μm light was focused to a tight spot (50μm diameter) onto a titanium target. The resultant plasma was an excellent source of the resonance line of helium-like titanium (2.63 angstroms). These x-rays were diffracted from the surface of the shocked crystal and the resultant spectrum recorded on an x-ray streak camera. A typical result is shown in Fig A3.8. As the crystal is compressed the x-ray radiation is diffracted at higher angles, the shift in angle being related to the compression by the formula given above. It can be seen that the peak reduction in the interatomic spacing at this irradiance is about 5%. It is interesting to note that the rise time of the compression follows that of the laser pulse, but that the subsequent decay is slower than the fall off of the laser. This is due to the fact that the surface of the silicon crystal had been coated with aluminium and plastic as in previous experiments[1,2]: the shock-driving laser passes through the plastic at these relatively low irradiances and deposits its energy in the aluminium. The aluminium plasma thus formed is therefore confined between the surface of the crystal and the plastic layer; this confinement thus increases the pressure pulse due to the storage of energy in the aluminium plasma.

2. Observation of expansion during shock-breakout

When a well-formed shock wave breaks out from a free surface the pressure drops to zero and the density of the material falls to a value very slightly less than that of the normal solid. If, however, as in these experiments, the shock front is not fully steepened and there is a ramp in compression, tension within the material can occur when the shock wave emerges from a free surface[3]. However, direct observation of the lattice spacing during such a process has not previously been observed. The

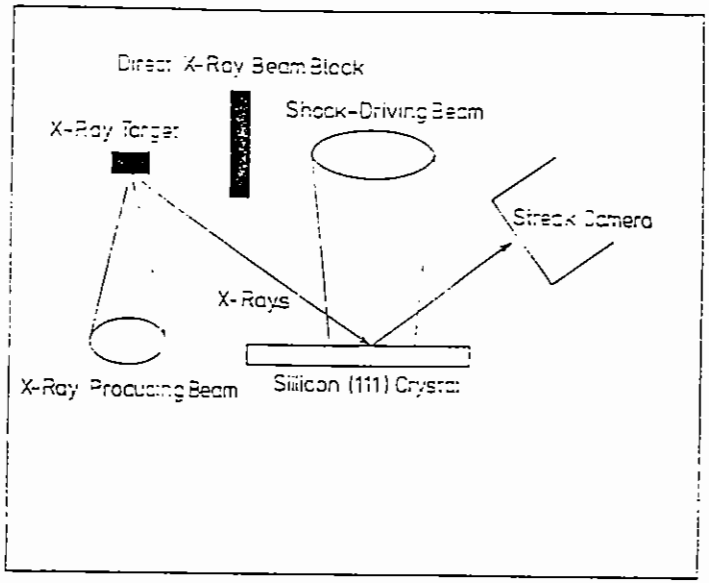


Fig A3.7 The experimental set-up for time-resolved observation of the compression of the front surface of a silicon crystal.

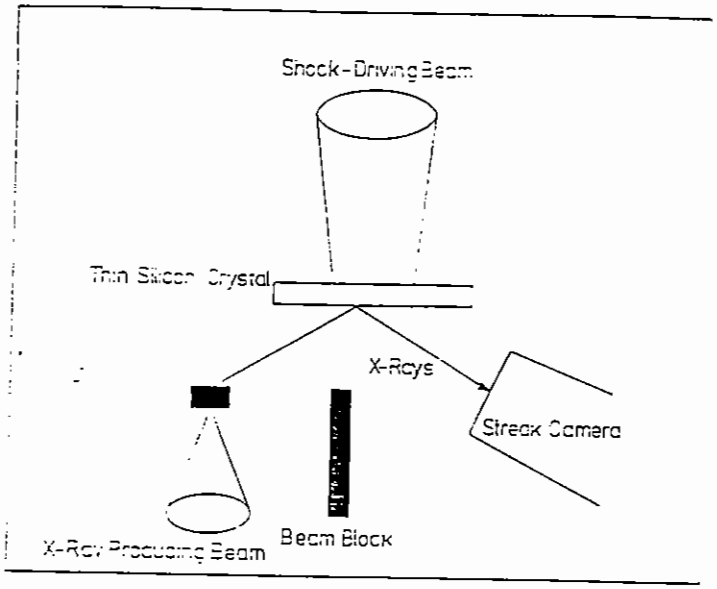


Fig A3.9 Experimental set-up for time-resolved observation of shock breakout.

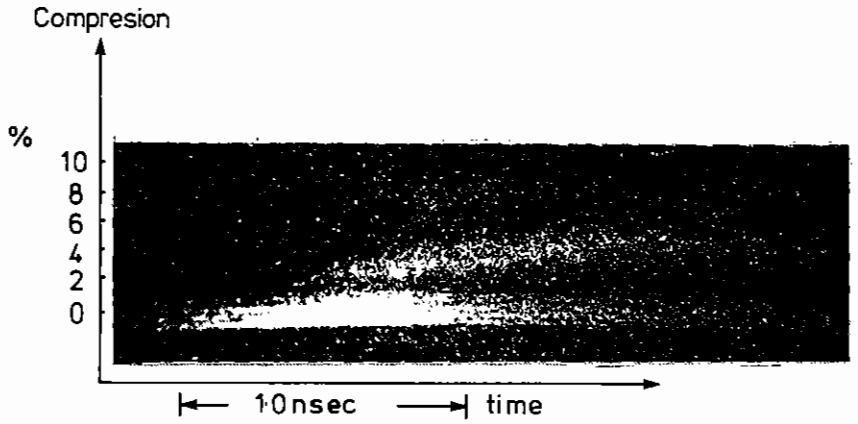


Fig A3.8 X-ray streak camera record of diffraction of the resonance line of helium-like titanium from the surface of the laser-shocked plasma.

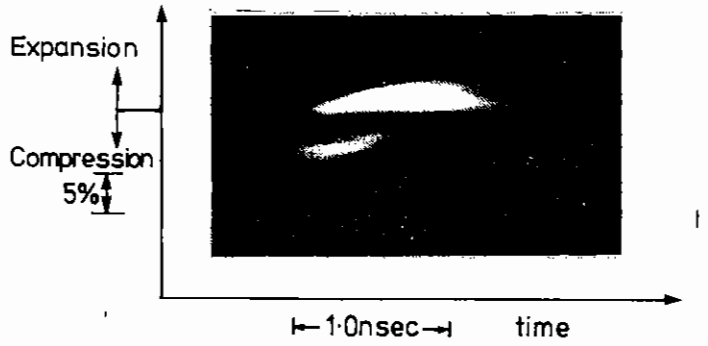


Fig A3.10 Time-resolved diffraction of the titanium helium-like resonance line from the rear surface of a thin silicon crystal during shock breakout.

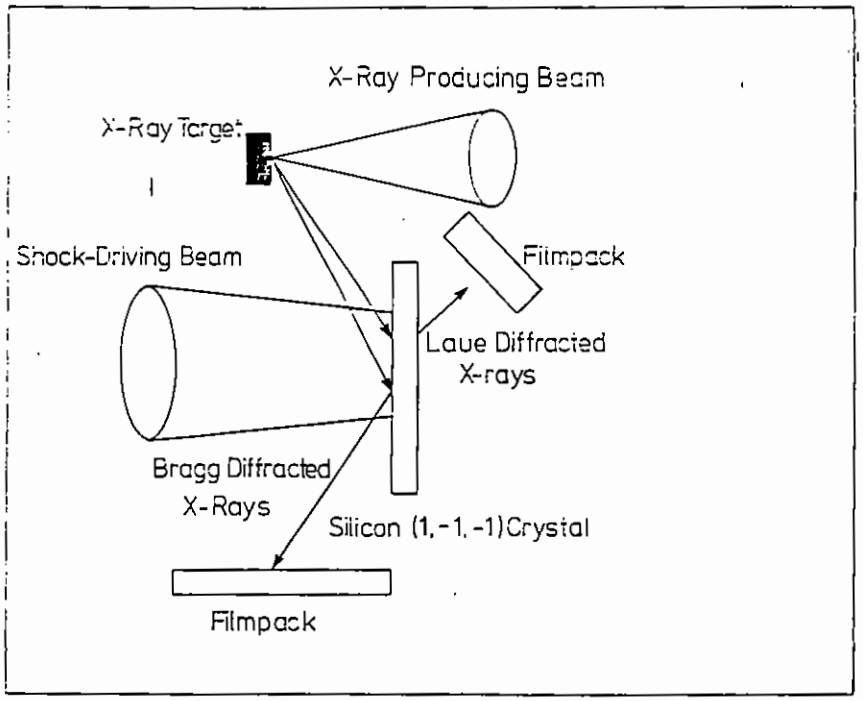


Fig A3.11 Experimental set-up for the simultaneous observation of Bragg and Laue diffraction from a laser-shocked lithium fluoride crystal.

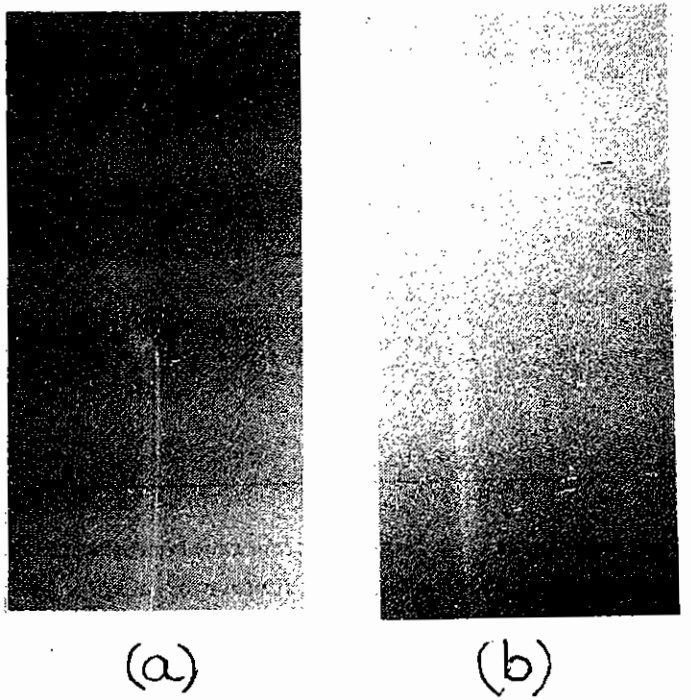


Fig A3.12(a) Bragg diffraction from the surface of the shocked lithium fluoride crystal, and
(b) simultaneous Laue diffraction through the crystal.

experimental set-up in this case is shown schematically in Fig A3.9 In this case the shock driving beam is incident on a piece of (111) silicon 40μm thick. At these relatively low compressions the shock speed is very close to the sound speed of 9μm per nsec, and thus the compression pulse takes several nonoseconds to traverse the width of the crystal. Helium-like titanium was again used as the x-ray source by focusing down the second laser beam to a tight spot on a 5μm thick titanium foil. For all elements above chlorine the helium-like resonance line lies below the K edge in energy, thus the titanium foil is transmitting to the helium-alpha lines, which are thus diffracted from the rear side of the crystal and recorded on the x-ray streak camera.

If we arrange the delays between the two beams such that the x-ray pulse arrives during shock breakout we observe the diffraction as shown in Fig A3.10. At early times in this picture we observe compression as the shock wave advances towards the rear surface. At the time marked on the diagram the shock wave breaks out of the free surface and it can be seen that we now observe diffraction to lower angles, corresponding to the crystal expanding and going into tension. This is the first time that a direct measurement of the lattice spacing has been made during shock breakout.

3. Simultaneous Bragg and Laue Diffraction

When a material is shock compressed above the Hugoniot elastic limit it starts to respond in a plastic rather than elastic manner. Little is known about the lattice dynamics of such a process in the high strain-rate environment of a shock wave. One means of investigating plasticity is to observe the response of the lattice in a direction parallel to the shock front. An experiment to investigate these lattice planes is shown schematically in Fig A3.11. A piece of 300μm thick (200) lithium fluoride was used as the target material. Perpendicular to the (200) planes are another similar set of planes. Thus in this experiment a 1nsec pulse of x-rays was Bragg diffracted from the (200) planes, and simultaneously the same x-rays were diffracted through the crystal (ie. Laue diffraction) from the perpendicular planes. In effect this gives us a unit cell measurement during the shock compression. Both spectra were recorded on x-ray film. The results are shown in Fig A3.12. The Bragg diffraction data shows compression of the planes with a reduction in interatomic spacing of 4%. However the perpendicular plane shows no apparent shift in the spectral lines, indicating an unperturbed lattice in the direction parallel to the shock front. This negative result is interesting for several reasons. It may mean that plasticity takes longer than the few nanoseconds duration of the pressure pulse in this experiment, or that plasticity does not initially manifest itself as a perturbation in the lattice parallel to the shock front. These questions can probably best be addressed by repeating the experiment at high laser irradiances, and thus higher compressions. It is obvious that at some point the material must tend to hydrostatic compression, which implies compression in all directions.

References

1. J S Wark, R R Whitlock, A Hauer, J E Swain and P J Solone, Phys. Rev. B Rap. Comm. 35, 9391 (1987).

2. J W Wark, R R Whitlock, A Hauer, J E Swain and P J Solone, Shock Waves in Condensed Matter, Proceedings of the American Physical Society Topical Conference, Monterey, California, 20-23 July 1987, edited by S C Schmidt and N C Holmes, p781-786, (1988).

3. Zel'dovich and Raizer, Physics of Shock Waves and High-Temperature Hydrodynamic Phenomena, Vol 2, p719-721, Academic Press (1967).

A4	**THEORY AND COMPUTATION**	Pages
A4.1	SCREENING EFFECTS ON THE ION COUPLING PARAMETER IN AN ALUMINIUM PLASMA	81-83
A4.2	EFFECTS OF NON-PARALLEL PUMP WAVES IN BEAT WAVE EXCITATION	84-86
A4.3	ATOMIC DATA FOR X-RAY LASER MODELLING SCHEMES	86-90
A4.4	STIMULATED RAMAN SCATTERING FROM A DENSITY MAXIMUM IN A LASER-PRODUCED PLASMA	90-96
A4.5	THREE DIMENSIONAL SIMULATIONS OF LASER DRIVEN IMPLOSIONS	96-98
A4.6	LASER SELF-FOCUSSING IN THE PRESENCE OF A BEAT-WAVE	98-100
A4.7	FOKKER-PLANCK SIMULATIONS OF ELECTRON HEAT FLOW	100-101
A4.8	MODELLING OF RAYLEIGH-TAYLOR INSTABILITY IN THE PRESENCE OF SELF-GENERATED MAGNETIC FIELDS	101-106
A4.9	MODELLING OF LITHIUM LIKE ALUMINIUM RECOMBINATION X-RAY LASER SCHEME	106-110
A4.10	THE CALCULATION OF GAIN AS DETERMINED EXPERIMENTALLY	110-114
A4.11	TRANSPORT IN LASER-PRODUCED PLASMAS	115-119
A4.12	A PHYSICAL MODEL OF THE EFFECT OF WAVELENGTH OF THE HEATING LASER IN ISOELECTRONIC SCALING OF XUV LASERS OPERATING BY RECOMBINATION	119-129

A4.1 SCREENING EFFECTS ON THE ION COUPLING PARAMETER IN AN ALUMINIUM PLASMA

A Djaoui, T A Hall (Essex University)
S J Rose (RAL)

The ion coupling parameter, Γ, in a plasma is defined as the ratio of average potential energy to average kinetic energy of the ions ($\Gamma = (Z'e)^2/(R_0 kT)$). Z is the effective ionic charge which determines the ion-ion interation, R_0 is the average ionic radius and T is the temperature. The effective ionic charge Z' is different from the ionization state (or valence Z) because even a highly degenerate electron gas (such as in Al,) is polarized by the ionic charge. This leads to the formation of a non-uniform electron distribution between ions, which modifies the ion-ion interaction by reducing the potential energy between them. The polarization of the electron gas depends on one dimensionless parameter $r_s = (R_0/a_0 Z^{1/3})$, where a_0 is the Bohr radius.

Extensive Monte-Carlo simulations of the thermodynamic properties of a plasma of point ions (OCP), embedded in a rigid, uniform, neutralizing background of electrons have been published[1]. The total energy and the Helmholtz free energy for $1 < \Gamma < 300$ have been calculated and the results fitted to simple analytic formulae[2]. The structure factors as a function of wavenumber have also been tabulated[3] for the liquid phase of the OCP $0.1<\Gamma<180$.

Galam and Hansen[4] used the OCP as reference system to calculate the properties of the screened Coulomb plasma by use of thermodynamic perturbation theory and a variational method based on the Gibbs - Bogoliubuv inequality. The method can be summarized as follows: one chooses a OCP reference system, which is appropriate to the plasma under consideration and has a free energy A_0; then the free energy of the actual system A_c is bounded above by the free energy of the reference system plus the difference in the potential energy between the actual system and the reference, averaged over all configurations of the reference.

$$A_c \leq A_0 + \langle U_c - U_0 \rangle_0 \qquad (1)$$

Figure (A4.1) shows the results,[4,5] for Z = 1 and r_s = 0.1, 1.0 and 1.5. At very high compressions ($r_s \leq 0.5$) we found that the screening effect, as calculated in the RPA approximation can be fitted by a simple expression $\Gamma' = \Gamma \exp(-r_s)$. This corresponds to an effective reduction of the ionic charge by a factor equal to $\exp(-r_s/2)$. At lower densities ($r_s > 1$) the screening is stronger and depends on Γ, as well as r_s. At these lower densities the RPA (Lindhart) dielectric function is not applicable and one should include exchange and Coulomb local field effects. These are seen to reduce even further the ionic charge as the points given by the Toigo-Woodruff (TW) and Utsumi-Ishimaru (UI) dielectric functions show. For the highest values of r_s = 1.5 and T = 160, there is a 20% difference between the TW and UI results.

By combining the pseudopotential theory of metals with this variational method[6] equation (1) can be extended to metallic plasmas to yield.

$$\frac{A_c(\Gamma,r_s)}{N k_B T} \leq \frac{A_0(\Gamma', r_s)}{N k_B T} + \frac{\Gamma}{\pi}\int_0^\infty f(q)\, S_0(1,\Gamma')\left(\frac{1}{\epsilon(q)} - 1\right)$$
$$+ \left(\frac{\Gamma - \Gamma'}{\Gamma'}\right)\frac{U_0(\Gamma')}{k_B T} + E_0 \qquad (2)$$

Z is the ionic charge or valence, $\epsilon(k)$ is an appropriate dielectric function, V is the ionic volume, U_0 is the total energy of the reference system and

$$f(q) = \left(1 - \frac{Q}{q^2 r^2/R_0^2}\right)\frac{q^2}{8\pi Z R_0^2}\Big)^2$$

$$E_o = \frac{QZ}{V}.$$

Q and V_c are the pseudopotential parameters for Aluminium[7].

If $Q = 0$, equation (2) reduces the screened OCP, and if $Q = 0$ and $\epsilon(q) = 1$, it reduces to the rigid OCP.

Γ' is varied in equation (2) until the RHS is minimized. As Γ' increases the first term on the RHS decreases, the second and third term increase while the forth term is constant. It is however the second term which explicitly contains the effect of screening through the dielectric function $\epsilon(q)$. In evaluating this term we use the UI dieletric function[5], $Q = 42.9$ and $r_c = 0.29$. Calculations were performed for Al (valence $Z = 3$, $r_s = 2.07$) at normal density (2.7 gcm^{-3}), and temperatures ranging from the melting temperature (933°K) to 2eV. For the structure factor $S(q,T)$ we used tabulated[4] values for 6 values of Γ from 2 to 160 and $0 < q < 20.4$.

Values of $S(q,\Gamma)$ for intermediate values were interpolated, certain values from reference (3) not being available. Table (1) shows the results of this calculation. It is interesting to note that, Al melts at a value of $\Gamma' \approx 156$, which is not too different from the OCP value of 170.

Even at 6 times the melting temperature (5600K), the effective ion coupling parameter has a high value (45). Compressed Al will have such high values of Γ' at even higher temperatures. This is an important result for XAFS (X-ray absorption Fine Structure) studies of dense plasmas, as this determines the highest temperatures for which XAFS can be obtained. Another important criterion for XAFS measurement is that their amplitude be above the experimental noise level.

TABLE 1 Screening effect on ion coupling parameter. T is temperature, Γ is the unscreened ion coupling parameter, Γ' the screened ion coupling parameter and A_c/Nk_BT is the minimal free energy. These results are for Al, Z=3 and $\epsilon(q)$ from reference (5).

T(°K)	933	1133	1733	2800	5600	11604	23208
Γ	1018	838	548	339	169	81.9	40.9
Γ'	156	118	109	53	45	16	13
$\frac{A_c}{Nk_BT}$	-734.39	-604.08	-393.77	-242.84	-120.28	-57.16	-28.02

References

1) J P Hansen, Phys Rev A8, 3096 (1973)

2) W L Slattery et al, Phys Rev A26, 2255 (1982)

3) F J Rogers et al, Phys Rev A28, 2990 (1988)

4) S Galam and J P Hansen, Phys Rev A14, 816 (1976)

5) Iyetomi et al, J Phys Soc Jpn 50, 3778 (1980)

6) M Ross et al, Phys Rev A24, 1016 (1981)

7) H D Jones, Phys Rev A8, 3215 (1973)

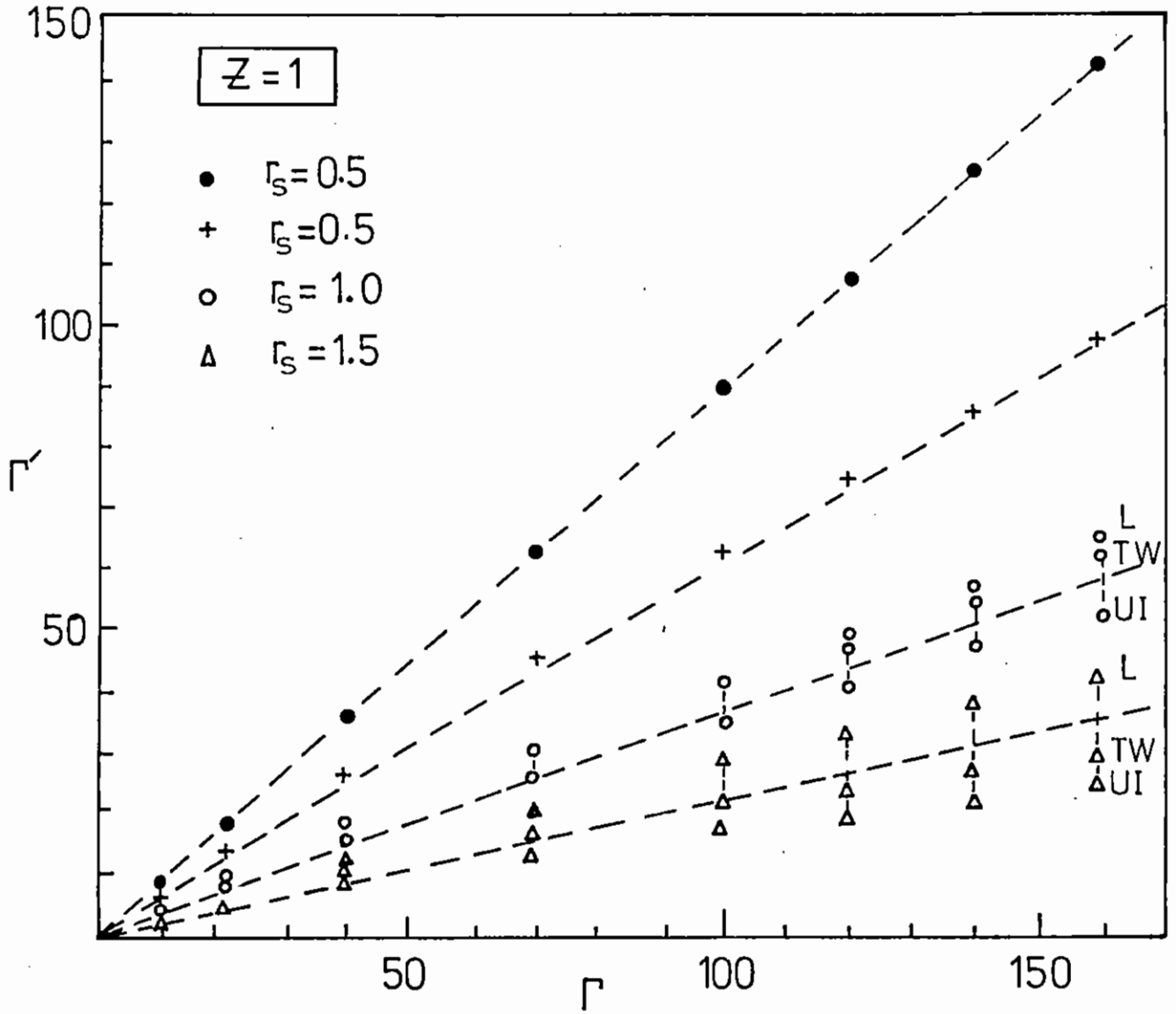


Fig A4.1 *Screened ion coupling parameter Γ' as a function of reference OCP Γ as given in reference 4 and 5. For r_s=1.0 and 1.5 three points are shown; the top corresponds to the use of the Lindhart (L) dielectric function, the middle to the Toigo-Woodruff (TW) and the bottom to the Utsumi-Ishimaru (UI) dielectric functions. The dashed lines are given by Γ' = Γ exp ($-r_s$).*

A4.2 EFFECTS OF NON-PARALLEL PUMP WAVES IN BEAT WAVE EXCITATION

R A Cairns and M R Amin (University of St Andrews)

During the past few years the process of resonantly exciting beat waves in plasmas from the nonlinear interaction of two high frequency intense electromagnetic waves (lasers), whose frequency difference matches the local plasma frequency, has been proposed as a means to: 1) diagnose the plasma density[1]; 2) study the ionosphere[2]; 3) heat a plasma[3,4]; 4) accelerate electrons to ultrahigh energies [5]; and 5) generate current in a tokamak[6]. Experimental databases for some of these applications now exist.

So far as we know all previous investigations on beat wave acceleration of particles have assumed that the pump waves are propagating in the same direction. However, it is our understanding that the pump waves in the RAL beat wave experiment[7] are incident with a small angle ($\sim 5^0$) between them, and we have investigated the effect of this. A major effect is that a small angle between the pump waves can produce a large change in the angle of the beat, simply because the beat wave wavenumber is small compared to the pump wavenumbers. This is illustrated in figure (A4.2).

We have developed a 2D code to investigate the effect of waves intersecting at an angle within a finite region, as shown in figure (A4.3). To begin we neglect the cascading of the wave modes. The equations describing the system in steady state are then

$$\underline{u}_1.\nabla a_1 = -\alpha_1 a_2 a_3 \qquad (1)$$

$$\underline{u}_2.\nabla a_2 = \alpha_2 a_1 a_3^* \qquad (2)$$

$$\underline{u}_3.\nabla a_3 + v_{eff} a_3 + i\delta a_3 - i\Delta|a_3|^2 a_3 = \alpha_3 a_1 a_2^* \qquad (3)$$

where the $\underline{u}_i$'s are the group velocities, v_{eff} is the effective damping of the beat wave, and $\delta=(\omega_p^2+3k_3^2v_{th}^2-\omega_3^2)/2\omega_3$ is the inhomogeneity detuning from the exact resonance $\delta=0$. The nonlinear term $\Delta|a_3|^2$ is the relativistic detuning, where $\Delta=3e^2/16m_e^2c^2\omega_p$, and the other parameters have their usual meaning. The coupling coefficients are given by[8,9].

$$\alpha_1=ek_3\,(\underline{e}_1^*.\underline{e}_2)/4m_e\omega_2 \qquad (4)$$

$$\alpha_2=ek_3\,(\underline{e}_1.\underline{e}_2^*)/4m_e\omega_1 \qquad (5)$$

$$\alpha_3=ek_3\omega_p\alpha_B\,(\underline{e}_1.\underline{e}_2^*)/4m_e\omega_1\omega_2 \qquad (6)$$

where

$$\alpha_B=(k_1-k_2)/k_3.$$

$\underline{e}_{1,2}$ are the unit vectors characterizing the wave polarization, and $\underline{E}_i=a_i\underline{e}_i$. $\underline{E}_{1,2}$ are the electric field vectors of the pump lasers. We assume identical polarization of the pump waves.

To solve the model equations numerically we apply an explicit finite difference scheme in a steady state situation, where the independent variables x and z now behave like time and position variables respectively. We consider finite spatial extent pumps, with initially Gaussian profiles

$$a_1(z,0)=a_1^{max}\exp(-(z+z_0)^2\sin^2\theta_1/l_1^2) \qquad (7)$$

$$a_2(z,0)=a_2^{max}\exp(-(z-z_0)^2\sin^2\theta_2/l_2^2). \qquad (8)$$

We arrange the direction of propagation, $\underline{k}_1$ and $\underline{k}_2$, of the pump laser pulses such that $\theta_2=\pi-\theta_1$ and $\theta=\theta_2-\theta_1$, where θ_1 and θ_2 are the

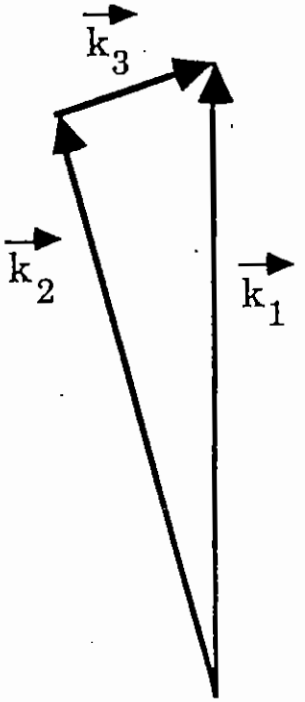


Figure A4.2 Wave vector matching in non-parallel pump waves.

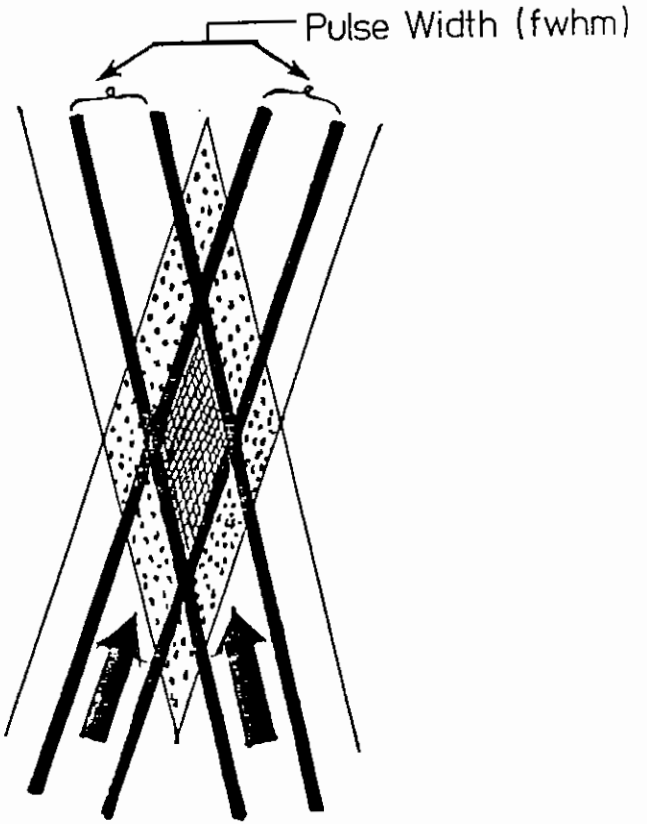


Figure A4.3 Interaction region in beat wave excitation.

angles which $\underline{k}_1$ and $\underline{k}_2$ make with the +z-axis, as shown in figure (A4.4). Since the coupling coefficients are positive, we assume[10]

$$\phi=\phi_1 - \phi_2-\phi_3= 0 \qquad (9)$$

where the ϕ's are the respective phases of the wave packets. It should also be noted that since the beat wave amplitude is initially zero, its phase is undefined. We can choose the initial phases to be anything we want which satisfy equation (9). We set the ϕ's at the beginning of the interaction to be

$$\phi_1=0, \phi_2=0, \text{ and } \phi_3=0.$$

We take the RAL beat wave experiment parameters to be[11]

wavelength of the pumps: $\lambda_1 = 1.053$ (μm), $\lambda_2 = 1.064$ (μm),

pump intensities: $I_1 = 1_2 = 2 \times 10^{14}$ (Wcm^{-2}),

pulse length: τ(fwhm) = 200 (ps),

pulse width: X(fwhm) = 330 (μm),

plasma frequency: $\omega_p=1.85x10^{13}(s^{-1})$,

plasma temperature: T_e= 50 eV.

For the moment we have neglected the relativistic detuning, but this and the cascading of the wave modes will be taken into account in future work. A typical solution of the coupled mode equations is shown in figure (A4.5) showing depletion of the higher frequency pump and generation of the beat wave. Although this work is still in progress, we can conclude that a small angle between the pump waves can produce a substantial change in the character of the beat. The latter propagates obliquely across a finite interaction region and its growth is limited by the size of the region.

References

1. N M Kroll, A Ron, and N Rostoker, Phys Rev Lett 13 83 (1964)
2. G Weyl, Phys Fluids 13, 1802 (1970)
3. B I Cohen, A N Kaufman, and K M Watson, Phys Rev Lett 29, 581 (1972).
4. M N Rosenbluth and C S Liu, Phys Rev Lett 29, 701 (1972).
5. T Tajima and J M Dawson, Phys Rev Lett 43, 263 (1979)
6. B I Cohen, Comments Plasma Phys Controll Fusion 8, 197 (1984).
7. A E Dangor et al, Proceedings 1987 New Developments in Particle Acceleration Techniques Workshop, Orsay, France.
8. V N Tsytovich, in Nonlinear Effects in Plasma, Plenum, New York, 36 (1970).
9. J A Heikinen, S J Karttunen, and R R E Salomaa, Nucl Fusion 28, 1845 (1988).
10. D J Kaup, A Reiman, and A Bers, Rev Mod Phys 51, 275 (1979).
11. P Gibbon and A R Bell, Rutherford Appleton Laboratory Annual Report RAL-88-042, 94 (1988).

A4.3 ATOMIC DATA FOR X-RAY LASER MODELLING SCHEMES

P G Burke, A E Kingston E M Robertson and M Terao
(Queen's University of Belfast).

In recent years the significant interest in laser produced plasmas as a suitable medium for obtaining lasing action in the X-UV and

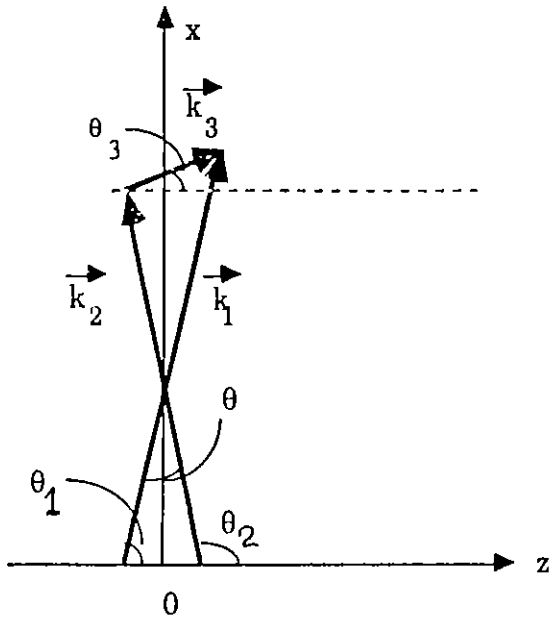


Figure A4.4 *Geometry of the direction of propagation of the wave modes.*

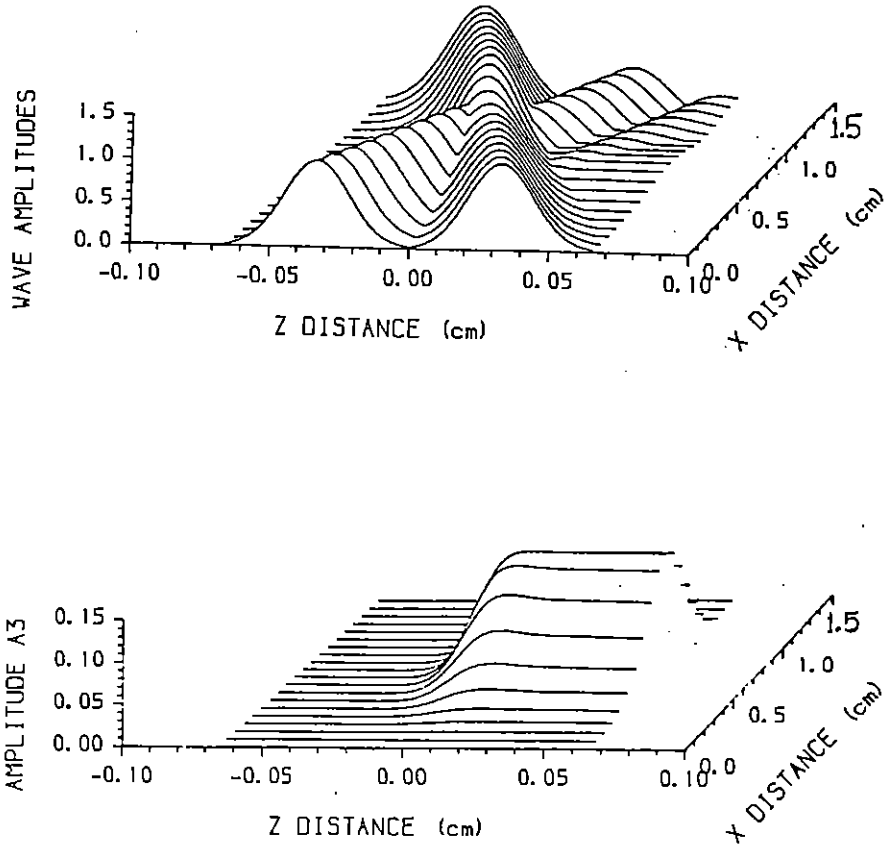


Figure A4.5 *(a) Evolution of the wave modes in nonlinear interaction. Angle between the pumps is 5^0. The amplitudes are normalized by the initial peak amplitude of the higher frequency pump.*

(b) Evolution of the beat wave. Angle between the pumps is 5^0. The amplitude of the beat wave is normalized by the peak amplitude of the higher frequency pump.

soft X-ray wavelength regions has stimulated the development of computer codes to model the hyrdodynamic and atomic processes in these plasmas. For these models to predict realistic values of laser gain it is necessary to have an accurate and complete understanding of the fundamental atomic processes which contribute to the overall population of ionized states within the plasma. The Belfast group are involved in the calculation of accurate atomic data to describe these processes. In the last year we have concentrated on two areas: (1) e-impact excitation collision strengths of Al^{10+}; and (2) dielectronic recombination rate coefficients of Al^{10+}.

Collision Strength Data for Transitions in Al^{10+}

Previous calculations of expected gain from Li-like Al recombination X-ray laser schemes[1,2] have used values of excitation collision strengths obtained from methods such as Mewe's Polynomial[3] and Van Regemorter's Formula[4]. Neither of these methods will give a complete and rigorous set of collision strengths for the different transitions of interest in the Li-like ion. In particular the $\Delta n = 0$ transitions were not included due to the absence of any known data, though these collisions may have an important effect on the population distribution between the $n = 3$ levels of the Li-like ions. These levels are the lower levels of the transitions from which we would expect to see gain[1].

The R-matrix method[5] has been used by us to obtain values for collision strengths of the Li-like Al. This method solves the integro-differential equations which describe the total wavefunction for an electron colliding with a target ion. A nine state calculation (including levels up to $n = 4$) was performed for energy values of the continuum electron between 2 and 30 Ryd. For the continuum electron values of the l quantum number up to $l = 10$ were included. The configuration interaction wavefunctions of the target ion were calculated using the CIV3 code of Hibbert[6].

Table (A4.2) shows values of effective collision strengths obtained using the R-matrix method compared with values calculated by analytical fits[7] ($\chi^{(n)}$ stands for $\chi \times 10^{n}$). In Table (A4.2) we also include transition strengths for transitions between the $n = 3$ states. It can be seen that these $\Delta n = 0$ collision strengths are not negligible. This data has been used by Pert and Henshaw in their most recent calculations (section A4.9 of this report). In the future we plan to look at Li-like Ca ions, the next ion in the isoelectronic sequence of interest to the study of recombination X-ray lasers.

Dielectronic Recombination Rate Coefficients of Al^{10+}

Dielectronic recombination must be taken into account in plasma models as it usually influences the ionization balance and ionic excited state distribution by competing with autoionisation:

$$e^- + Al^{10+}(1s^2 2s;\,^2S^e) \underset{}{\overset{\Gamma^a}{\leftrightarrow}} Al^{9+**}(1s^2 2pnl;\,^3,^1L)$$

$$\downarrow \Gamma^r$$

$$Al^{9+*}(1s^2 2snl;\,^3,^1L') + h\nu$$

In the isolated resonance approximation, α^{DR} is given by[8]

$$\alpha^{DR} = \left(\frac{2\pi}{kT}\right)^{3/2} \sum_d \frac{g_d}{2g_i} \frac{\Gamma_d^a \Gamma_d^r}{\Gamma_d^a + \Gamma_d^r} e^{-E_d/kT}$$

where i refers to the initial state of Al^{10+} and d to the intermediate decaying states Al^{9+**}.

A 2-state approximation has been chosen to describe Al^{10+}. The binding energies obtained for the $1s^2 2s$ and $1s^2 2p$ states are respectively -354.373 and -352.775 Ryd. The description of the collisional intermediate states Al^{9+**} includes $1s^2 2s^2$, $1s^2 2p^2$, $1s^2 2s2p$, $1s^2 2snl$ and $1s^2 2pnl$ configurations, with 20 continuum

transitions	C + M^{c}W	R-matrix
2s – 2p	2.43	1.38
2s – 3s	$7.26^{(-2)}$	$6.05^{(-2)}$
2s – 3p	$6.05^{(-2)}$	$5.52^{(-2)}$
2s – 3d	$1.40^{(-1)}$	$1.18^{(-1)}$
2p – 3s	$2.36^{(-2)}$	$2.16^{(-2)}$
2p – 3p	0.25	0.25
2p – 3d	1.08	0.88
3s – 3p	–	5.36
3s – 3d	–	$8.15^{(-1)}$
3p – 3d	–	6.63

Table A4.2 Collision strengths for Al^{10+} obtained using analytical fits (C + McW^{7}) and R-matrix.

L	$2S+1=3$				$2S+1=1$			
	$l = L-1$		$l = L+1$		$l = L-1$		$l = L+1$	
	μ	γ	μ	γ	μ	γ	μ	γ
0	–	–	$-6.11^{(-2)}$	1.42	–	–	$-9.20^{(-3)}$	2.92
1	$-1.28^{(-1)}$	$9.68^{(-2)}$	$-1.33^{(-2)}$	$5.24^{(-1)}$	$-1.16^{(-1)}$	1.55	$1.63^{(-1)}$	$4.44^{(-1)}$
2	$4.67^{(-3)}$	$2.70^{(-2)}$	$-7.18^{(-2)}$	$4.97^{(-2)}$	$-3.68^{(-2)}$	$7.16^{(-2)}$	$1.29^{(-2)}$	$2.97^{(-2)}$
3	$-3.43^{(-2)}$	$6.71^{(-2)}$	$4.60^{(-2)}$	$6.81^{(-3)}$	$1.10^{(-2)}$	$6.57^{(-1)}$	$5.11^{(-3)}$	$2.71^{(-2)}$
4	$-5.56^{(-3)}$	$5.08^{(-1)}$	$2.36^{(-2)}$	$5.70^{(-3)}$	$4.02^{(-2)}$	$6.77^{(-1)}$	$2.31^{(-3)}$	$1.00^{(-4)}$
5	$4.40^{(-4)}$	$6.15^{(-1)}$	$1.14^{(-3)}$	$6.96^{(-4)}$	$1.15^{(-3)}$	$6.19^{(-1)}$	–	–
6	$7.60^{(-4)}$	$4.39^{(-1)}$	–	–	$7.80^{(-4)}$	$4.40^{(-1)}$	–	–
7	$4.00^{(-5)}$	$2.60^{(-4)}$	–	–	$4.00^{(-5)}$	$2.60^{(-4)}$	–	–

Table A4.3 Energies and autoionisation widths of Al^{9+} resonance states $E = -10^{2}/(n + \mu)^{2}$, $\Gamma^{a} = \Upsilon/(n + \mu)^{3}$.

states nl for each partial wave $l(0 \leq l \leq 8)$. The K-matrix is calculated for e⁻-impact excitation of Al^{10+} using the R-matrix method[5]. The corresponding eigenphase-sum is then fitted to obtain the resonance widths and positions[9]. All the calculations have been performed in the L-S coupling scheme. Numerical values of the resonance quantum detects and widths are given in Table (A4.3). All energies are in Rydbergs.

The energy separation between the 2s and 2p thresholds in Al^{10+} is rather small and the lowest autoionizing states ($1s^2pnl$) are high Rydberg states (HRS), with n = 8 or 9. We can then identify the Γ_d^r of the Al^{9+**} ($1s^22pnl$) states with the Γ^r of the $Al^{10+}(1s^22p)$ state. We found $\Gamma^r = 3.7 \times 10^{-6}$ Ryd.

The total α^{DR} is shown in Figure (A4.6) as a function of the e⁻-energy. The first peak at very low energy is due to the lowest autoionizing states $1s^22p8l$ which happen to be very close to the 2s threshold. In the second peak, our results are about a factor 4 lower than Burgess' formula prediction[10] which is also shown.

As HRS give an important contribution to α^{DR}, spin-orbit interactions might have to be taken into account. This problem is under investigation.

References

1. G J Pert and M Henshaw, Rutherford Appleton Laboratory Report (RAL-88-042), 112-116 (1988)

2. P Jaeglé et al., JOSA B**4**, 563-574 (1987)

3. R Mewe, Astron. and Astrophys. J.,**20**, 215 (1972)

4. H Van Regemorter, Astrophys. J.,**136**, 906 (1962)

5. K A Berrington et al., Comput. Phys. Comm. **14**, 367-412 (1978)

6. A Hibbert, Comput. Phys. Comm. **9**, 141-172 (1972)

7. D M Cochrane and R W P McWhirter, Physica Scripta **28**, 25-44 (1983)

8. M J Seaton and P J Storey in Atomic Processes and Applications, Ed. P G Burke and B L Moiseiwitsch, 133-197 (North-Holland, 1976)

9. K Bartschat and P G Burke, Comput. Phys. Comm. **41**, 75-84 (1986)

10. A Burgess, Astrophys. J. **141**, 1588 (1965)

A4.4 STIMULATED RAMAN SCATTERING FROM A DENSITY MAXIMUM IN A LASER-PRODUCED PLASMA

H C Barr, T J M Boyd and A P Mackwood
(University College of North Wales, University of Wales, Bangor.)

Scalelengths in laser-produced plasmas approaching those projected for laser fusion targets are now produced routinely - but at a fraction of the cost in laser energy - by exploding thin foils[1]. These burnthrough targets are characterised by profiles having a subquarter-critical density maximum at some stage in their evolution. It is also likely that small scale localized density bumps may arise in experiments[1] using other than foil targets. such bumps have long been recognized[2] as sites for absolutely unstable stimulated Raman scattering (SRS). The optimist's view of these burnthrough experiments is that, by reproducing comparable 'local' conditions, their characteristics may be extrapolated to reactor-size targets. SRS characteristics however are frequently dependent on their 'global' environment.

The global features pertinent to SRS in any inhomogeneous plasma may be understood as a coupling of "Rosenbluth convective amplifiers"[2]. By this we mean the convective amplification of

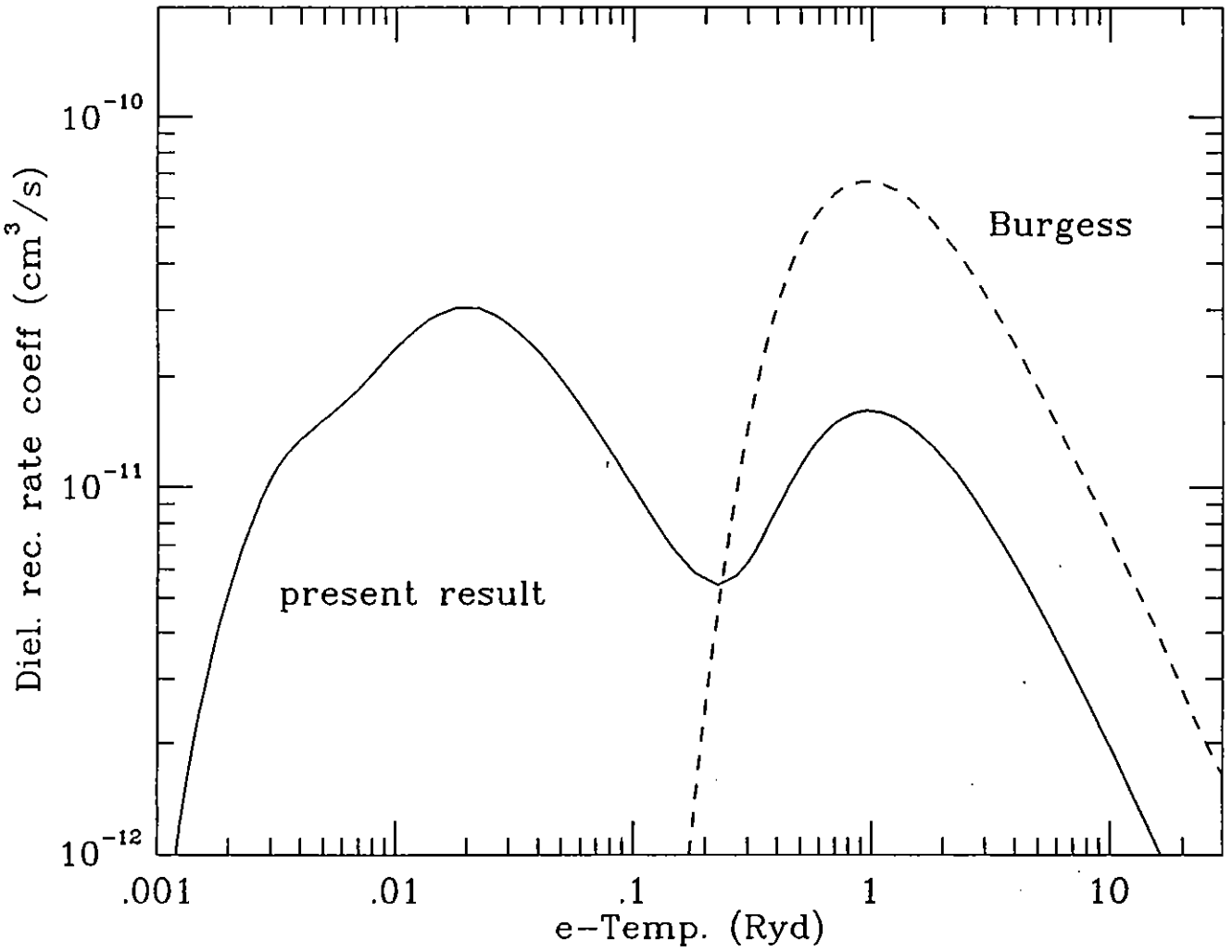


Figure 4.6 Dielectronic recombination rate coefficients of Al^{10+} as a function of e-temperature: —— present result, - - - Burgess' formula.

the scattered light signal of specified frequency as it propagates once through a localised resonance. The localisation is due to the wavenumber mismatch arising from wave propagation in the inhomogeneous medium. We assume the density profile to be locally linear. Other dependencies may be considered as limiting cases of this simple convective amplifier (CA). Treated as independent events, both backward and forward scattering are convectively unstable in such a monotonic profile[3] (referred to as the SRS-C regime). It has been recognised[4], of course, that in any given density profile two or more (backward or forward) convective amplifiers of common frequency may couple together through wave propagation and possibly the reflections of the daughter waves which may occur. Feedback between CAs makes possible temporal (absolute) growth. The Rosenbluth convective amplifiers may then be regarded as the building blocks from which an understanding of SRS in any density profile may be built. SRS from the quarter-critical density ($n_c/4$) or from a density extremum have long been recognised as absolutely unstable[2]. Each is a local event which may be viewed as the degenerate case of a nonlocal interaction between distinct resonances[5].

The qualitative features of scattering near an density maximum ($n_{max}<n_c/4$) are represented in figure (A4.7). Two distinct feedback loops occur depending on whether the plasma wave propagates through n_{max} (regime I) or is reflected from densities below n_{max} (regime II). The former consists of two backscatter CAs, at a common density on either side of n_{max}, coupled by the forward propagating plasma wave and the backscattered light wave. The lowest allowable ω_1 arises from the degenerate case mentioned above in which the two CAs merge at n_{max}. The maximum possible ω_1 in regime I arises when n_{max} is the plasma wave cutoff density. Regime I is therefore narrow band; it is the case studies originally by Rosenbluth[2] and recently re-examined by Williams and Johnston[6]. Before the plasma wave becomes evanescent through n_{max} forward scattering CAs appear near which can couple into the backsactter feedback loop. This has two effects. It strengthens the feedback loop thereby enhancing growth and reducing thresholds, though this is a weak effect given that forward scattering CAs are weaker than their backward scattering counterparts. More importantly, it allows the temporal growth of the forward scattered signal at the rates and with the thresholds determined for backscattering. In this regime (Ib), forward scattering is essentially parasitic to the backscattering feedback loop. This case has been considered by Villeneuve and Baldis[7], who observed thresholds for forward scattering much lower than expected from convective theory.

At scattered frequencies corresponding to regime II ($\omega_1>\omega_o-\omega_{pmax}$), forward scattering CAs are an essential component in the feedback loop which now couples two backward and two foward scattering CAs together. On each side of n_{max} backward and forward scattering CAs are coupled by distinct plasma waves. Backward (forward) scattering CAs are coupled by the backward (forward) scattered light waves.

The code which solves the full-wave SRS equations[7] was described in last year's annual report[8]. Here it is applied to scattering from a density bump modelled by a parabolic density profile $n_o(x) = n_{max}(1-x^2/L^2)$ where $n_{max}<n_c/4$. We seek regimes of absolute growth and hence solve the eigenvalue problem.

The numerically obtained eigenstates may be compared with the WKB theory of Rosenbluth[2,3], or the quasi-global theory of Williams and Johnson (WJ)[6] applicable to regime I. This latter theory follows the reasoning of Koch and Williams[4] in which "black box" CAs are coupled in such a way that the total phase shift around the feedback loop is an integral multiple of 2π with a loop gain of unity. Eigenvalues are shown in figures (A4.8, A4.9) for the parameter set: T_e=1.7KeV, $n_{max}=0.15n_c$ and $L=245c/\omega_o$. The plots of threshold v_o ($I\lambda_0^2=5.48\ 10^{18}(v_o/c)^2$W cm$^{-2}\mu$m^2 with our definition of v_o) against scattered frequency clearly exhibit the three regimes Ia, b and II. If we label the modes N=0,1,... starting from the lowest scattered frequency, modes N=0-13

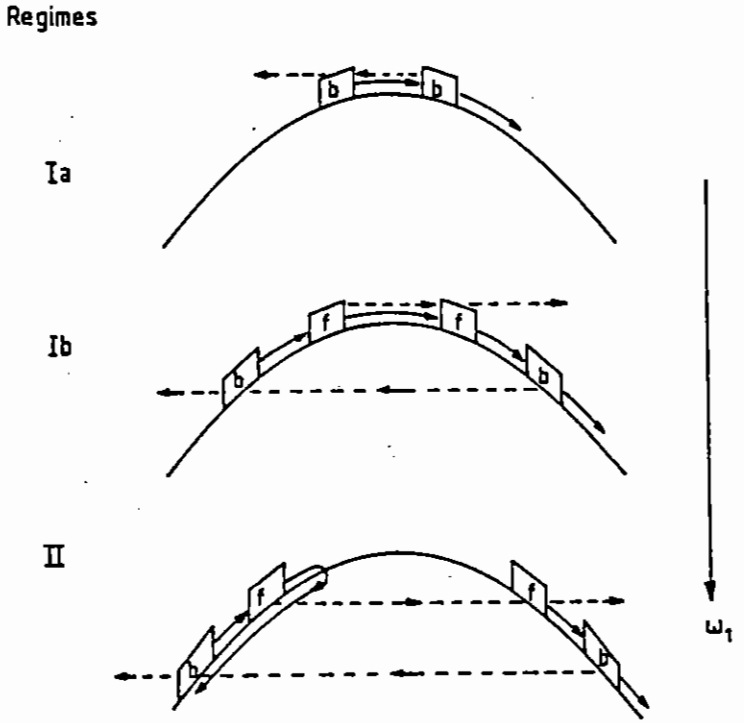


Figure A4.7 *Schematic of the feedback loop coupling back (b) and forward (f) scatter resonances. The arrowed solid (dashed) line indicates plasma (scattered) wave propagation.*

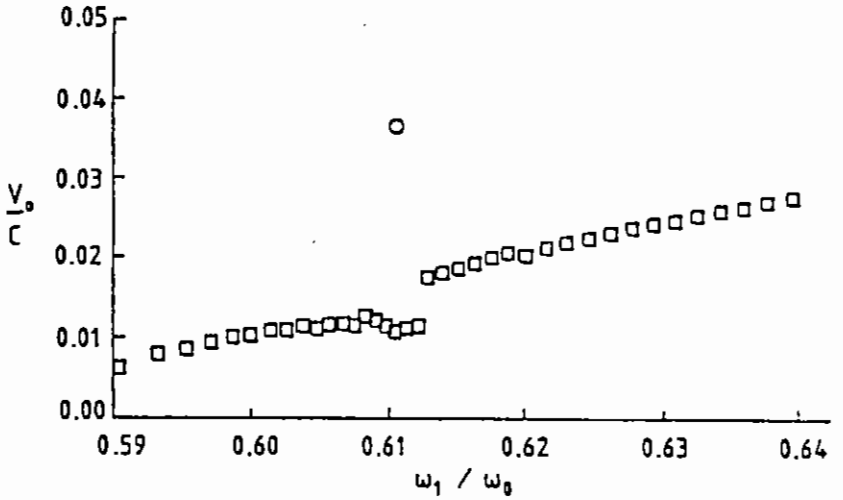


Figure A4.8 *Threshold v_o versus scattered frequency. The circle indicates the convective threshold for forward scattering from n_{max}.*

correspond to the narrow band regime Ia. These support the conclusion of WJ that the Rosenbluth result works well only for the ground state N=0. Indeed for this mode, it accurately predicts both the threshold and the growth rates at all laser intensities. For modes N=1-13, the WJ expression works well. Modes N=14-18 relate to regime Ib in which forward scatter CAs are located at or near n_{max} and are coupled into the backscattering feedback loop. The effect is a small reduction in the absolute backscattering threshold but a reduction by an order or magnitude in the threshold intensity for forward scattering from its value when treated as an independent convective amplifier. Forward scattering becomes absolutely unstable with backward and forward scattering having a common threshold. When the plasma wave is evanescent through n_{max} (regime II) there is a distinct jump at mode N=19 by a factor 3 in intensity after which the threshold v_o increases linearly with N (or ω_1) throughout this broadband regime. Threshold intensities scale at L^{-1} (compared with $L^{-2/3}$ for regime Ia) which can also be verified analytically by applying the method of Koch and Williams[7].

Above threshold the eigenvalues exhibit a complex scaling with laser intensity. Figure (A4.9) is representative of the two distinct patterns of growth rates which arise near threshold (Figure A4.9(a)) and well above threshold (Figure A4.9(b)). The ground state (black square in Figure A4.9) is accurately reproduced by Rosenbluth's expression at al laser intensities. Near threshold the ground state is strongly dominant as seen in Figure A4.9(a). The higher order modes N=1-13 are given reasonably precisely by the WJ expressions. Rosenbluth's formula fails badly for these higher order modes. The blip in figure A4.9(a) is the enhancement in growth expected in regime Ib when forward scattering occurs near n_{max}.

As the laser intensity rises well above threshold an unexpected pattern emerges, shown in Figure A4.9(b), with certain "high growth" eigenvalues scaling more rapidly with v_o while a second "low growth" group all but saturate or even reduce with v_o. Yet another "frequency locked" group line up below the ground state, producing the "tadpole" pattern of eigenvalues seen in figure A4.9(b). The distinction between regimes is now less clear since finite growth and finite v_o alter the dispersion characteristics of the waves; this is slight but measurable in the context of Figure A4.9(b). The tail of the tadpole corresponds to regime II and can be predicted by an application of the Koch Williams method to this particular pattern of resonances and for which both numerical and analytic results show growth to be independent of scalelength. At a fixed laser intensity, the ground state and the lowest growth mode at $\omega_1 \cong 0.6\omega_o$ are pivotal - they do not change with scalelength. The latter corresponds to forward scattering being only just possible at n_{max} and hence is a boundary between regimes Ia and Ib. The frequency locked side of the triangle corresponds to regime Ia, the low growth side the regime to Ib while the high growth side includes both - the transition being at a higher ω_1 than for the low growth side. As stated above, the tail is independent of scalelength except that its root moves to higher frequency as L increases. The tadpole head opens up accordingly with a corresponding increase (decrease) in the high (low) growth side of the head. Note that growth is no longer dominated by the ground state but by a group of eigenvalues corresponding to regime Ia. The differential in growth between the dominant mode(s) and those which involve forward scattering is now much less than when near threshold. This differential reduces with increased scalelength.

In conclusion, thresholds and growth rates for SRS from a density maximum have been obtained by solving globally the full-wave Raman equations. Near threshold the results lend support to the analysis of Rosenbluth, in the case of the ground state which is dominant, and to that of Williams and Johnston for higher order modes. Well above threshold Rosenbluth's theory still describes the ground state well but it is no longer dominant; scalings of growth with laser intensity arise which are neither apparent in nor anticipated from previous analysis.

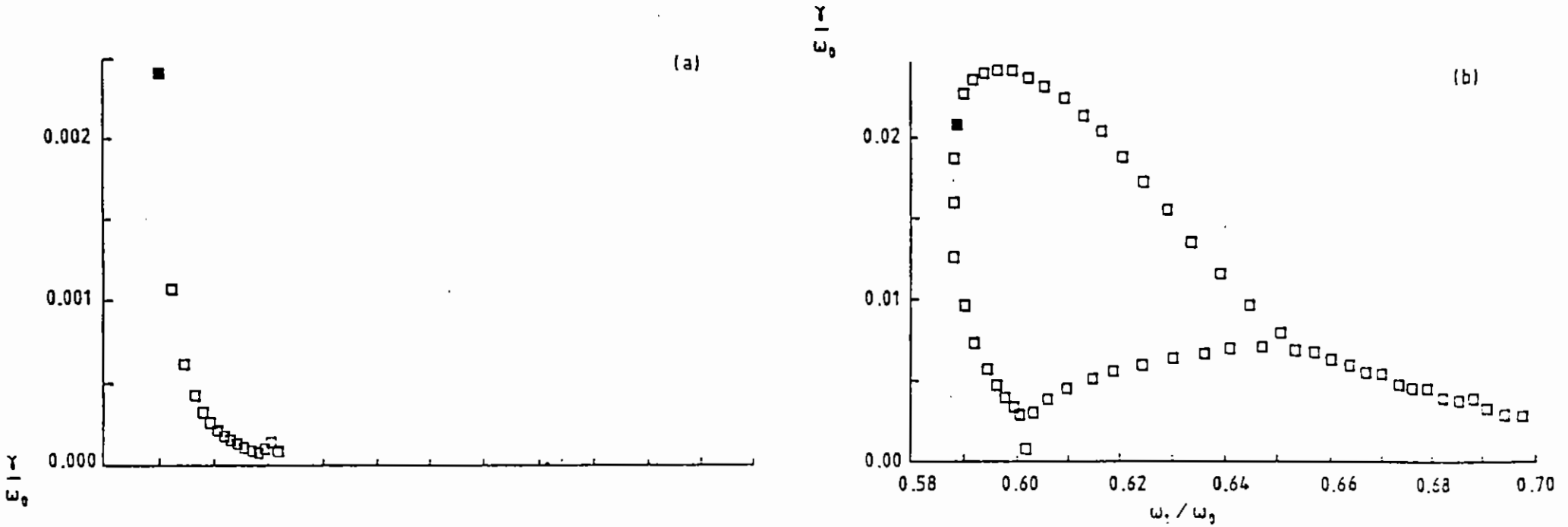


Figure A4.9 Growth rates versus scattered frequency (a) near and (b) well above threshold.

References

1. R P Drake et al.,Phys. Rev. Lett. 60, 1018 (1988); ibid, Phys. Fluids 31, 3130 (1988) and references therein

2. M N Rosenbluth, Phys. Rev. Lett. 29, 565 (1972)

3. C S Liu, M N Rosenbluth and R B White, Phys. Fluids 17 1211 (1974)

4. P Koch and E A Williams, Phys. Fluids 27, 2346 (1984)

5. H C Barr, T J M Boyd and G A Coutts, Phys. Rev. Lett. 60, 1950 (1988)

6. E A Williams and T W Johnston, submitted to Phys. Fluids

7. D M Villeneuve and H A Baldis, Phys. Fluids 31, 1790 (1988)

8. H C Barr, T J M Boyd and G A Coutts, Rutherford Appleton Laboratory Report (RAL-88-042), 93, (1988)

A4.5 THREE DIMENSIONAL SIMULATIONS OF LASER DRIVEN IMPLOSIONS

R P J Town and A R Bell, (Imperial College)

Inertial Confinement Fusion (ICF) targets can be characterised as going through three phases during the implosion[1]: acceleration, coasting and deceleration. Of paramount importance to the attainment of fusion conditions is the stability of the target throughout the implosion. Initially the shell is accelerated inwards, with the Rayleigh-Taylor (RT) instability on the outer ablation surface (seeded by non-uniform laser irradiation or defective target manufacture). Much work has been performed concerning this phase[2]. After the initial acceleration phase the shell coasts inwards at approximately constant velocity. Although the shell is no longer unstable the strong convergence can lead to a further growth in the asymmetries. The pressure inside the imploding shell grows causing the shell to decelerate. The shell is RT unstable again, but this time on the inner surface of the shell.

In order to realistically model the coasting and deceleration phases of the implosion, a three dimensional fluid code has been written using the Van Leer[3] advection algorithm as interpreted by Youngs[4].

Three dimensional codes require large amounts of memory and long run times. However, by exploiting the symmetry of the Rutherford 12 beam laser system it is possible to simulate the implosion dynamics.

Initial simulations have used as their basis the Rochester "High-density" target designs[5]. The shell is assumed to be coasting radially inwards at the experimentally observed velocity with an applied perturbation. The perturbation is a sixth-order Legendre polynomial summed over the centres of the laser beams. This is the lowest order perturbation to which a balanced 12 beam system would be susceptible.

The position of the inner (R_1) and outer (R_2) surface of the shell as a function of time is shown in figure A4.10. It can been seen that the shell is imploding fairly constantly and is in the thick shell limit as defined by Book and Bodner[1].

A measure of the perturbation amplitude of the shell can be obtained from comparing the normalised integrated density at the most strongly driven point to the weakest point. In figure A4.11 we have plotted this measure of the perturbation amplitude as a function of $R_1^{-1/4}$. This yields a straight line as R_1 decreases. This is in agreement with the analytic prediction of Book and Bodner.

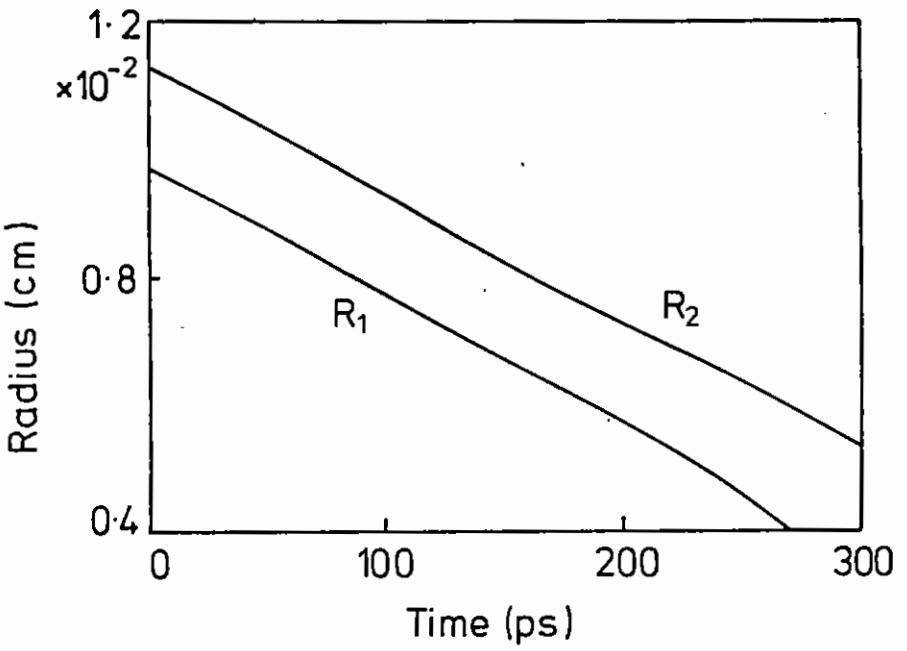


Figure A4.10 Plot of the inner (R_1) and outer (R_2) radius of the shell as a function of time.

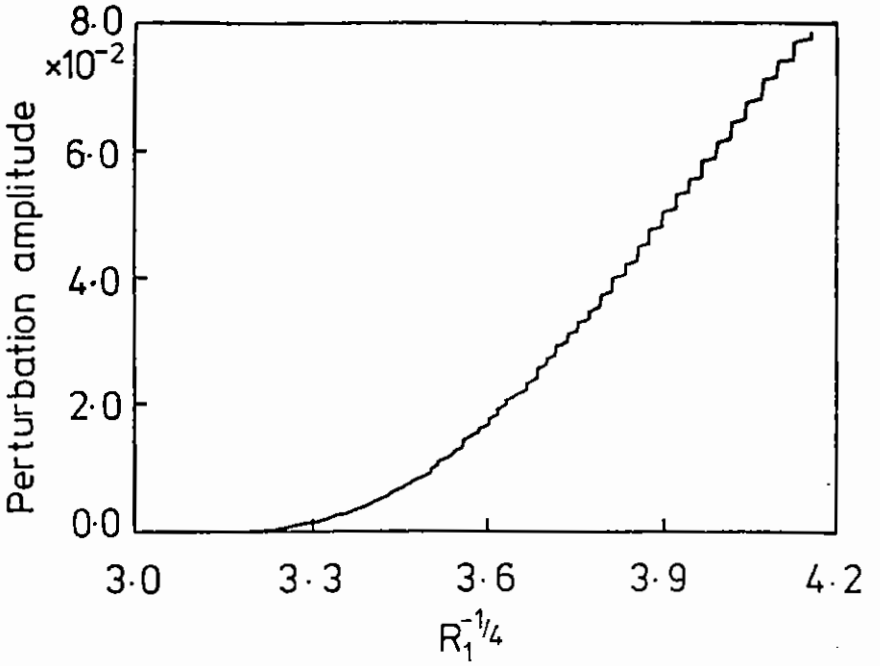


Figure A4.11 Plot of the perturbation amplitude as a function of $R_1^{-1/4}$.

Further simulations starting in the coasting phase through the deceleration phase to stagnation are currently being performed. It is hoped to simulate the NUHART[6] targets in order to investigate the unexpectedly large yield achieved.

References

1. D L Book and S E Bodner, Phys. Fluids 30, 367 (1987)

2. C P Verdon et al, Phys. Fluids 25, 1653 (1982)

   M H Emery et al, Phys. Rev.Lett. 57, 703 (1986)

   R G Evans et al, Phys. Rev.Lett. 49, 1639 (1982)

   M Henshaw et al, Plasma Phys. Cont. Fusion 29, 405 (1986)

3. B Van Leer, J. Comput. Phys. 23, 276 (1977)

4. D L Youngs, in Numerical Methods for Fluid Dynamics (K W Morton and M J Baines, eds) Academic Press, 273 (1982)

5. L L E Review (University of Rochester) 25, 7 (1988)

6. A J Cole et al, Rutherford Appleton Laboratory Report (RAL-88-042), 80 (1988).

A4.6 LASER SELF-FOCUSSING IN THE PRESENCE OF A BEAT-WAVE

P Gibbon (Imperial College)

One of the major constraints on the design of plasma-based accelerators is laser diffraction. The beam energy must be confined to a small region $O(5\text{-}10c/\omega_p)$ over a particle acceleration distance, but for typical parameters the latter is 10-100 times the Rayleigh diffraction length. Some means of laser self-focussing is therefore essential if these particle acceleration schemes are to be viable.

The disruptive effect of ion modulation instabilities at low irradiance rules out thermal and ponderomotive focussing mechanisms, both of which involve the formation of density channels on the ion timescale (ω_{pi}^{-1}). However, it has been suggested that relativistic focussing could be used at high irradiances[1]. This phenomenon occurs on a very rapid timescale ($\tau \ll \omega_{pe}^{-1}$): regions of high laser intensity (eg: the centre of the beam) increase the local refractive index of the propagation medium $n(\omega,a)=1-(\omega_p^2/\omega_0^2)+f(|a|^2)$, where $a=v_{osc}/c$, the normalised quiver velocity. The waves bend towards the region of high refractive index, further enhancing the intensity at the centre.

It has recently been shown[2] that the focussing threshold for two co-propagating waves of different frequencies (ω_0,ω_1) is reduced by a factor of 3. However, the situation is complicated by the presence of a Langmuir beat-wave $\omega_p=\omega_1-\omega_0$. The interaction between the pumps and the Langmuir wave produces a large spectrum of electromagnetic modes separated by the plasma frequency. The process can itself lead to focussing or divergence of the beam depending on the phase matching between the Langmuir wave and the electromagnetic pumps[3].

The physical mechanism for 'cascade focussing' is rather similar to relativistic focussing, except that the refractive index now depends explicitly on the Langmuir wave. By Fourier-analysing the wave equations for a scattered electromagnetic wave ω_s and the Langmuir wave, it is straightforward to show

$$n(\omega_s) = 1 - (\omega_p/\omega_s)^2 + \text{const}\ \frac{|a|^2}{(\Delta - |\delta n/n|^2)}$$

where $\Delta=(\omega_p^2-\omega^2)/\omega^2$, ω is the beat-frequency $\omega_1-\omega_0$ and $\delta n/n$

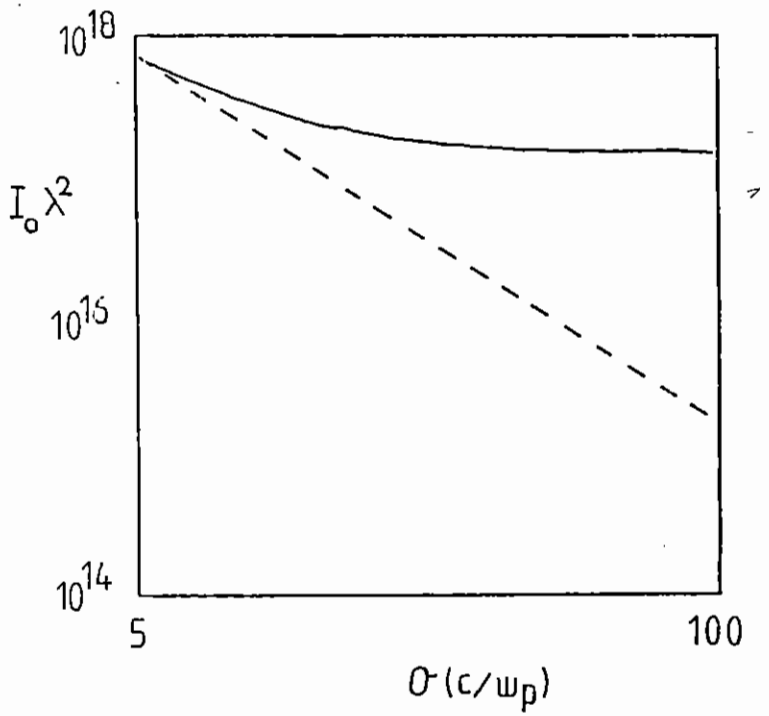


Figure A4.12 *Focussing threshold with resonantly driven Langmuir wave (solid line). The dotted line shows the 2-beam relativistic threshold of reference (2).*

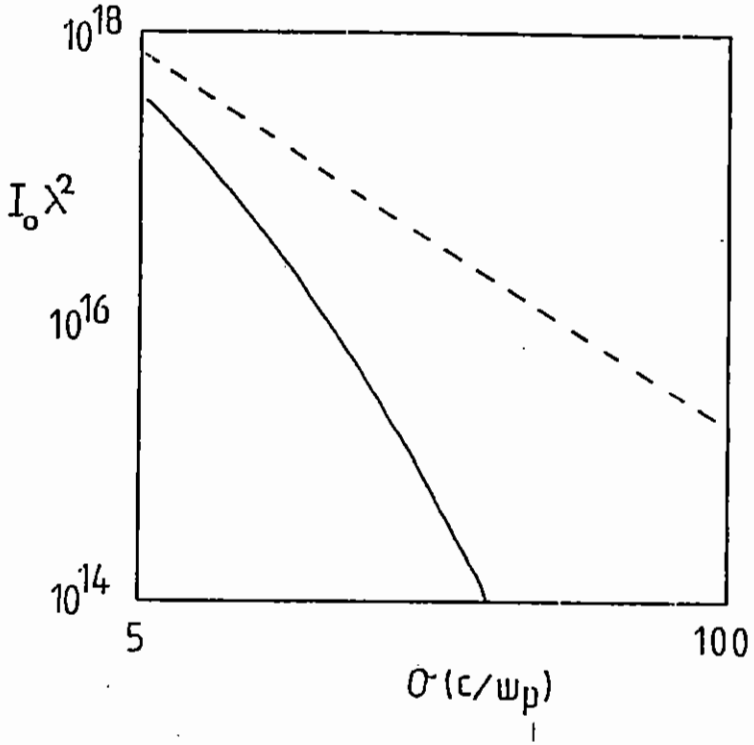


Figure A4.13 *Focussing threshold with detuned Langmuir wave (solid line).*

is the perturbed plasma wave density. The denominator of the 3rd term represents the total frequency shift of the plasma wave. If the Langmuir wave is driven sufficiently below the plasma frequency, the electromagnetic waves will focus[3], and can remain self-trapped over a particle acceleration distance[4].

We now consider the competition between the two focussing mechanisms described above. Firstly, we examine the relativistic focussing threshold in the presence of a resonantly driven Langmuir wave ($\Delta=0$). If the latter is non-linearly saturated by relativistic detuning, the refractive index will be reduced at the beam centre. The resulting threshold arises from the balance between relativistic focussing and enhanced divergence due to cascading. Namely: $|a|^2=\text{const}|\delta n/n|^2$, or $|a|^2=\text{const}$, since $\delta n/n \alpha |a|^2/^3$. Thus, instead of the usual power threshold for relativistic focussing, we now have an irradiance threshold - see figure A4.12. Consequently, we see that it is much more difficult to focus the wave in the presence of a large amplitude Langmuir wave.

If the Langmuir wave is driven off-resonance ($\Delta>0$), a very different picture emerges. The threshold is now below the relativistic one because of the additional focussing due to cascading - figure A4.13. The detuning in this case corresponds to a density mismatch of about 6% at $I\lambda^2=10^{16}$ $Wcm^{-2}\mu m^2$.

In conclusion, it appears that self-focussing is a promising means of confining laser energy to small spot sizes for the purposes of beat-wave acceleration, provided that the Langmuir wave is driven slightly below the plasma frequency. Driving the beat-wave resonantly will result in an irradiance threshold for focussing of about 2×10^{17} $Wcm^{-2}\mu m^2$.

References

1. P Sprangle, E Esarey, A Ting and G Joyce, Appl. Phys. Lett. 53, 2146 (1988)

2. C J McKinstrie and D A Russell, Phys. Rev. Lett. 61, 2929 (1988)

3. P Gibbon and A R Bell, Phys. Rev. Lett. 61, 1599 (1988)

4. P Gibbon, PhD Thesis, University of London (1988)

A4.7 FOKKER-PLANCK SIMULATIONS OF ELECTRON HEAT FLOW

G J Rickard, A R Bell, I R G Williams (Imperial College) E M Epperlein (Laboratory for Laser Energetics, USA)

The 1-D code SPARK outlined in the 1988 RAL Report[1] has now been extended to 2-D[2]. A standard fluid code using uninhibited Spitzer-Harm heat flow $\underline{q}_{sp}=-\underline{\nabla}T_e$[3] is also now used for comparison is both 1-D and 2-D with the Fokker-Planck (FP) codes. 2-D FP simulations have been made possible by the use of the diffusive approximation in configuration space, and integrating the equations with the ADI (Alternating Direction Implicit) method. This has brought 2-D FP simulations of laser ablation experiments within the bounds of present day computing capabilities.

Two areas have been explored with the 2-D FP code. The first[4] was an investigation of thermal smoothing arising from non-uniform laser energy deposition (0.35μm irradiation at $5.10^{14}Wcm^{-2}$). There it was shown that the non-local nature of electron transport resulted in less effective smoothing relative to that predicted by the fluid code, especially for small scale ($\leq 80\lambda_{mfp}$, where λ_{mfp} is the thermal electron mean free path) temperature modulations. The second[5] examined conditions applicable to short pulse laser-plasma experiments (0.25μm irradiation at $6.10^{15}Wcm^{-2}$, FWHM=3.5ps), and revealed non-classical heat flow both in terms of magnitude and direction, with differences in angle between the FP heat $\underline{q}$ and $-\underline{\nabla}T_e$ as much as 34°. However, this latter behaviour requires more simulations in terms of density scalelengths, intensities etc, before we can say whether this is a general

feature of 2-D heat flow or is just restricted to these short pulse experiments.

At present the 1-D FP code is being used to examine the scaling of ablation pressure with incident laser intensity for times less than 20ps. The 2-D FP code is also being used to model early time behaviour (≤50ps); in this case to look at thermal smoothing of non-uniform irradiation in the presence of a steep density profile (density scalelengths of the order of 3μm).

References

1. I R G Williams, G J Rickard, E M Epperlein and A R Bell, Rutherford Appleton Laboratory Report (RAL-88-042), 98 (1988)

2. E M Epperlein, G J Rickard and A R Bell, Comp. Phys. Commun. 52, 7 (1988)

3. L Spitzer Jr and R Harm, Phys. Rev. 89, 977 (1953)

4. E M Epperlein, G J Rickard and A R Bell, Phys. Rev. Lett. 61, 2453 (1988)

5. G J Rickard, A R Bell and E M Epperlein, submitted to Phys. Rev. Lett.

A4.8 MODELLING OF RAYLEIGH-TAYLOR INSTABILITY IN THE PRESENCE OF SELF-GENERATED MAGNETIC FIELDS

M J de C Henshaw and G J Pert (York University)

Self-generated magnetic fields of the order of megagauss have been observed in laser produced plasmas[1]. There has been quite a substantial amount of work done to analyse the sources and transport of these fields[2,3,4] and there has been speculation that growth of the Rayleigh-Taylor instability may be affected by them[5,6,7]. Theoretical considerations of laser accelerated targets indicate that the dynamics of an implosion are certainly changed when magnetic fields are included in the calculation; for instance, the ablation pressure is reduced because of the decrease in thermal flux from the critical surface, but resonant absorption is more efficient in a magnetised plasma. Pert[6] has commented that in the region where the initial Rayleigh-Taylor growth occurs (at the ablation surface) the magnetic fields are rapidly reduced by resistive diffusion. However, Nishiguchi et al[8] have drawn attention to the possibility of fields generated at the critical surface being advected to the ablation surface, and at the same time being amplified by up to 100 times, by Nernst convection.

The question of whether self-generated magnetic fields have a significant effect on Rayleigh-Raylor growth remains essentially unresolved and although various approaches have been used to examine the phenomena, few have treated the 2-D hydrodynamics and magnetic field generation self-consistently.

Computer simulation is clearly a most useful way of assessing the relevance of self-generated magnetic fields as the instability growth for a particular target-laser configuration may be compared directly for the cases of magnetic fields included and excluded.

The computer code MAGT has been described in detail by Pert[9,10]. It is a 2-D finite difference code, with grid rezoning, which models a fully ionised, two temperature plasma, accelerated by a cylindrically symmetric laser beam. Laser absorption is by inverse bremsstrahlung and a dump of 20% of the energy penetrating to critical density to represent anomalous processes; the code includes ion/electron equilibration and flux limited ion and electron thermal conduction. Magnetic fields may be included with the energy transport. The kinetic description of Braginski[11] is used throughout. Preliminary results presented below are for a 5μm CH target illuminated by 0.53μm light at 10^{14} Wcm^{-2}. Previous work on the Rayleigh-Taylor instability in laser targets[12] has highlighted the benefits of an efficient, and dynamic, mesh

generator for the rezoning procedure of the quasi-Lagrangian code. The technique of using a 1-D fully Lagrangian code to generate an "ideal" mesh reported previously[13] has been incorporated into MAGT. The absence of magnetic fields in the 1-D Lagrangian code is unimportant because it only contributes the form of the "ideal" mesh; it does not influence the calculation in any other way.

Initial tests have shown that for perturbations of short wavelength some effect due to magnetic fields is present (Evans[14] has also commented on this). It is thought probable that the effect is larger where the perturbation is applied to the laser intensity instead of to the target areal mass. This is due to changes in the transport between critical and ablation surfaces; further investigation into this is planned.

Preliminary simulations have used a mass perturbation applied as a sinusoidal variation in density at the laser surface. The perturbation has a short wavelength of 2.5μm and an initial amplitude of A_0=0.2μm; the target is a cylinder with its axis in the plane of the page. Figure (A4.14) shows the growth of the instability A/A_0 with $\sqrt{D}$ where D is the distance travelled. Clearly the growth is increased in the presence of magnetic fields. Density contour plots 600ps after the laser switches on are shown with magnetic fields excluded (Figure A4.15) and with magnetic fields included (Figure A4.16). The magnetic field contours are shown as dashed lines and reach a maximum of a few hundred kilogauss. Positive values of the field come out of the page, and negative values go into the page. The fields themselves form loops round the cylinder axis. An interesting feature is the inversion of the perturbation figure (A4.17) indicating the initial form. This is not yet fully explained but is possibly due to the ideal gas equation of state allowing fluid flow into the perturbation low density troughs before the laser has attained a very high power, i.e. a computational effect. When the perturbation wavelength is increased to 10μm the inversion does not occur, the growth itself is much reduced, and no change in growth due to magnetic fields is discernible.

Work is now in progress to investigate these effects more fully and to establish the regime in which they are of significance. In particular, the perturbation wavelength at which magnetic fields no longer affect Rayleigh-Taylor growth will be determined. It is possible, from the point of view of practical targets, that this cut off wavelength is so short that the effects due to self-generated magnetic fields are insignificant when compared to other laser-plasma effects. It is intended to further improve the model by including the improved Braginski coefficients of Epperlein and Haines[15] and a Thomas-Fermi equation of state.

References

1. J A Stamper and B H Rysin. Phys. Rev. Lett. 34, 138 (1975)

2. J A Stamper, Spontaneous magnetic fields: Phenomena and Measurements, in Handbook of Plasma Physics, Ed S Witkowski and A Rulenhick (North-Holland)

3. M G Haines, Can. J. Phys. 64, 912 (1986)

4. D G Colombant and N K Winsor, Phys. Rev. Lett. 38, 697 (1977)

5. A Nishiguchi and T Yate, ECLIM, London (1983)

6. G J Pert, in 'Transport, Interactions and Instabilities in Laser-plasmas,' CECAM (1983).

7. M G Haines, in 'Transport, Interactions and Instabilities in Laser-plasmas', CECAM (1983).

8. A Nishiguchi, T Yabe, M G Haines, Phys. Fluids 2, 3683 (1985)

9. G J Pert, J. Comp. Phys. 43, 111 (1981)

10. G J Pert, J. Comp. Phys. 49, 1 (1983)

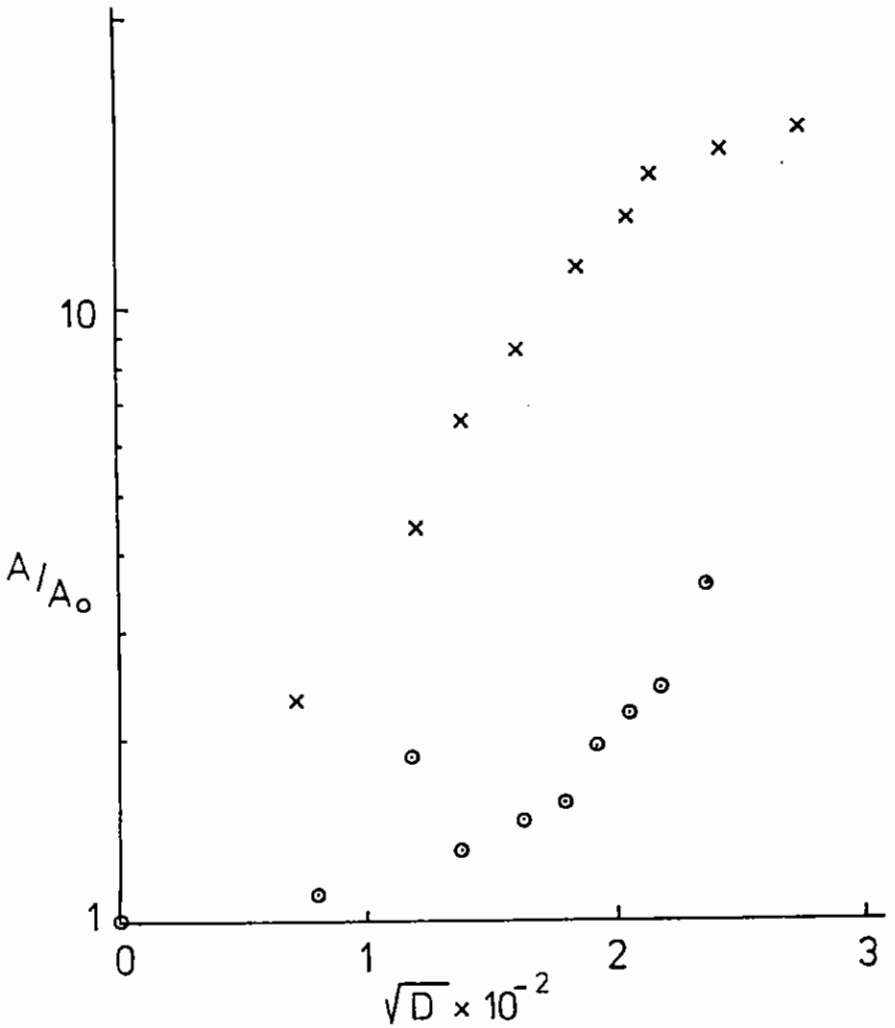


Figure A4.14 *Perturbation Amplitude (A/A_o) versus √(distance travelled) for instability growth at the laser surface of a 5μm foil. Calculation with magnetic fields included (x) and excluded (θ).*

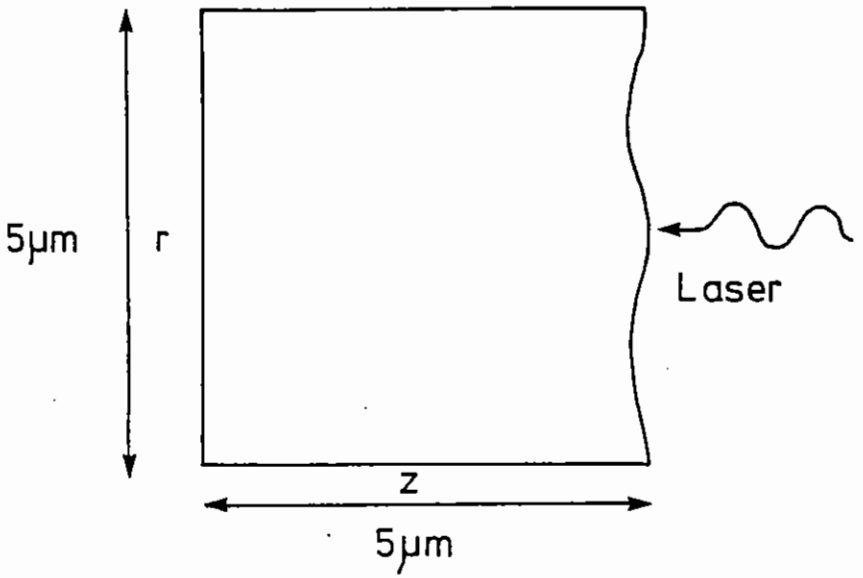


Figure A4.17 *Initial shape of CH foil.*

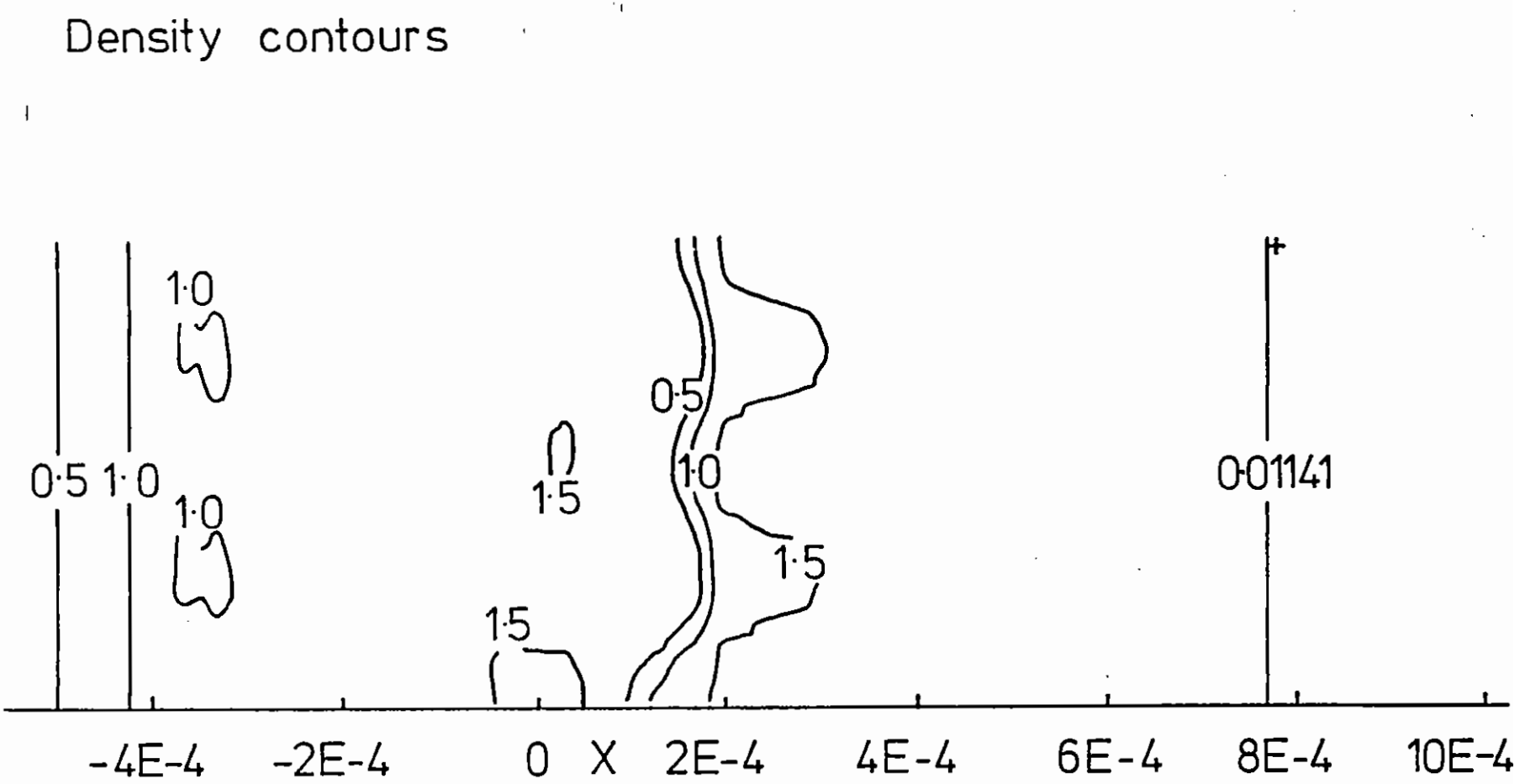


Figure A4.15 *Density contour plot at 600ps. Contour values 0.01141, 0.1, 0.5, 1.0, 1.5 gcm^{-3}. Magnetic fields excluded.*

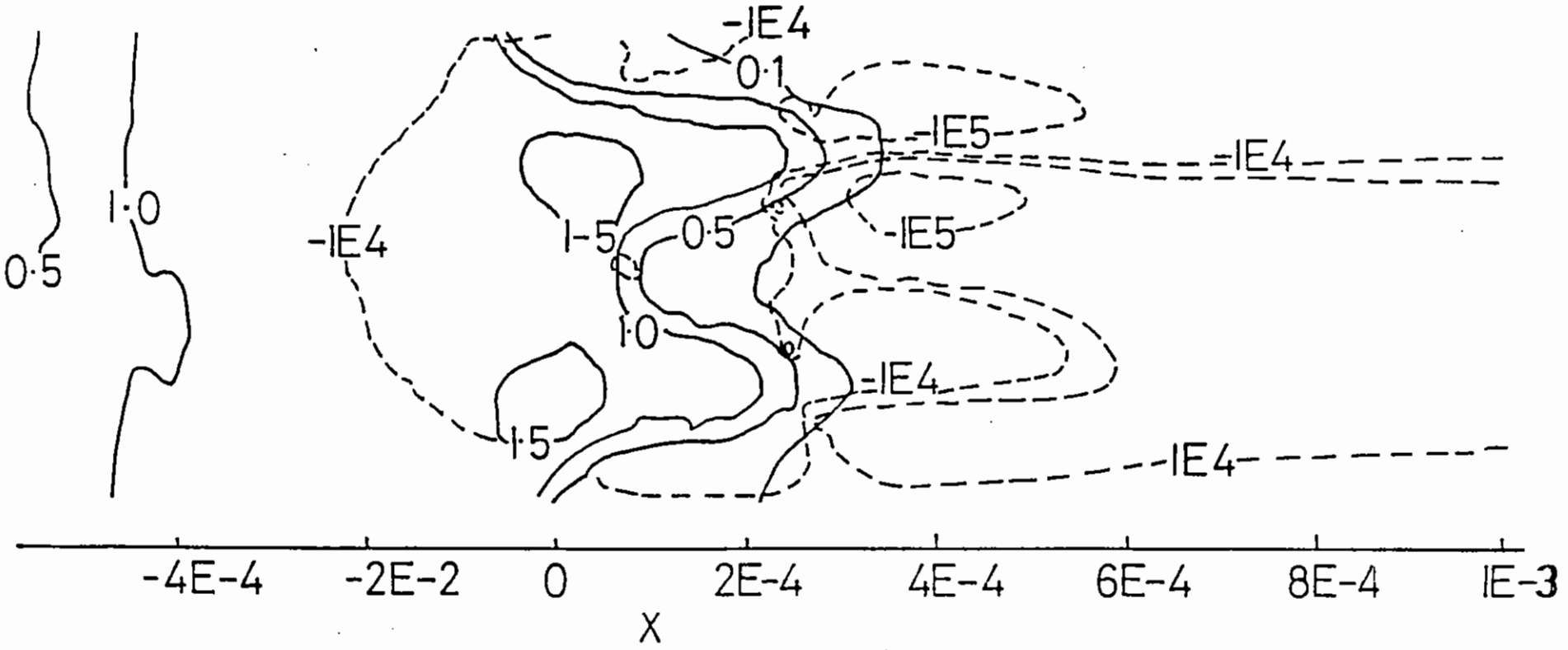


Figure A4.16 *Same as Figure A4.15 with magnetic fields included (contours (dashed): -10^5, -10^4, 10^4, 10^5 G).*

11. S I Braginski, in Reviews of Plasma Physics, Ed. M A Leontovich, 1, 205-311, (Consultants Bureau, New York)

12. M J de C Henshaw, G J Pert and D L Youngs, Plasma Phys. and Cont. Fus. 29, 405 (1987)

13. G J Pert, J D Crossland and M J Henshaw, Rutherford Appleton Laboratory Report (RAL-85-047), section A5.2.10

14. R G Evans, Plasma Phys. and Cont. Fus. 28, 1021 (1986)

15. E M Epperlein and M G Haines, Phys. Fluids 29, 1029 (1986)

A4.9 MODELLING OF LITHIUM LIKE ALUMINIUM RECOMBINATION X-RAY LASER SCHEME

M J de C Henshaw, G J Pert and P B Holden (York University)

During the last twelve months much work has gone into developing an improved understanding of experimental results of gain on the 3d-4f (154 Å), 3d-5f(105 Å), 3p-4d(150 Å) and 3p-5d(104 Å) transitions in lithium like aluminium plasmas[1]. Theory has also concentrated on this system, with further refinements to the computer model[2] being included and an increased effort to match the conditions of experiment. In addition, a detailed study has been carried out using a similarity model and scaling laws of the type developed for hydrogen like systems[3] have been formulated. Reasonable agreement with experiment has been obtained for the 3d-4f transition, but less good agreement for the 3d-5f transition; however, no gain, or only small gain in a restricted region of the plasma, is predicted for p-d transitions in marked contrast to experimental results. Efforts to account for this discrepancy have so far proved unsuccessful, although we note that there is less confidence in 3d-5f and d-p experimental results than in 3d-4f measurements, which were made using axial to transverse ratios as well as the axial measurements at different lengths common to all four transitions.

The useful gain on 3d-nf transitions relies on the fast radiative decay of the 3d level to 2p. This depopulates the 3d level sufficiently fast for it to become the lower level in a laser population inversion. It has been found, using the atomic model described in last year's report[2], that the relative populations of the n=3 levels are far from their Boltzmann statistical values, with both the 3p and the 3d levels being depopulated; the 3d level being furthest from its equilibrium value. From this data the 3p level cannot form such an effective inversion with 4d,5d as does the 3d with 4f,5f, unless it is rapidly depopulated by some mechanism not included in the calculations. Figure A4.18 shows the important transitions; it is noted that the oscillator strength (f) for 2p-3d is about twice that for 2s-3p. A plausible mechanism is collisional excitation from 3p to 3d levels allowing the 3p level to also depopulate via the rapid 2p-3d radiative decay (see figure A4.18).

The model now includes additional collision data, supplied by A E Kingston and E Robertson of QUB, which is in the form of polynomial fits[4] in the appropriate energy range for collisional excitation between all the levels from n=2 to n=4. Mewes' polynomial[5] is still used for collisions from 2s (ground state) to 5s, 5p, 5d, 6s, 6p, 6d; and Van Regemorters[6] formula between all the remaining allowed transitions up to n=6. Inclusion of these collisional rates brought the n=3 populations closer to their statistical values, although 3p and 3d were still depleted. Significant gain was still absent on the p-d transitions, and even artificially increasing the collisional excitation rate between 3p and 3d by up to 100 fold failed to bring the gain to the same order observed in experiment. In fact, the new collision data has not greatly affected the magnitude of the peak gain, although it has caused the 3d-4f gain to peak slightly later which is more in line with the experiment. The plasma is comparatively cool (∿28ev) when the gain first becomes positive, so it is perhaps not surprising that the collisions do not play a very important role during this time.

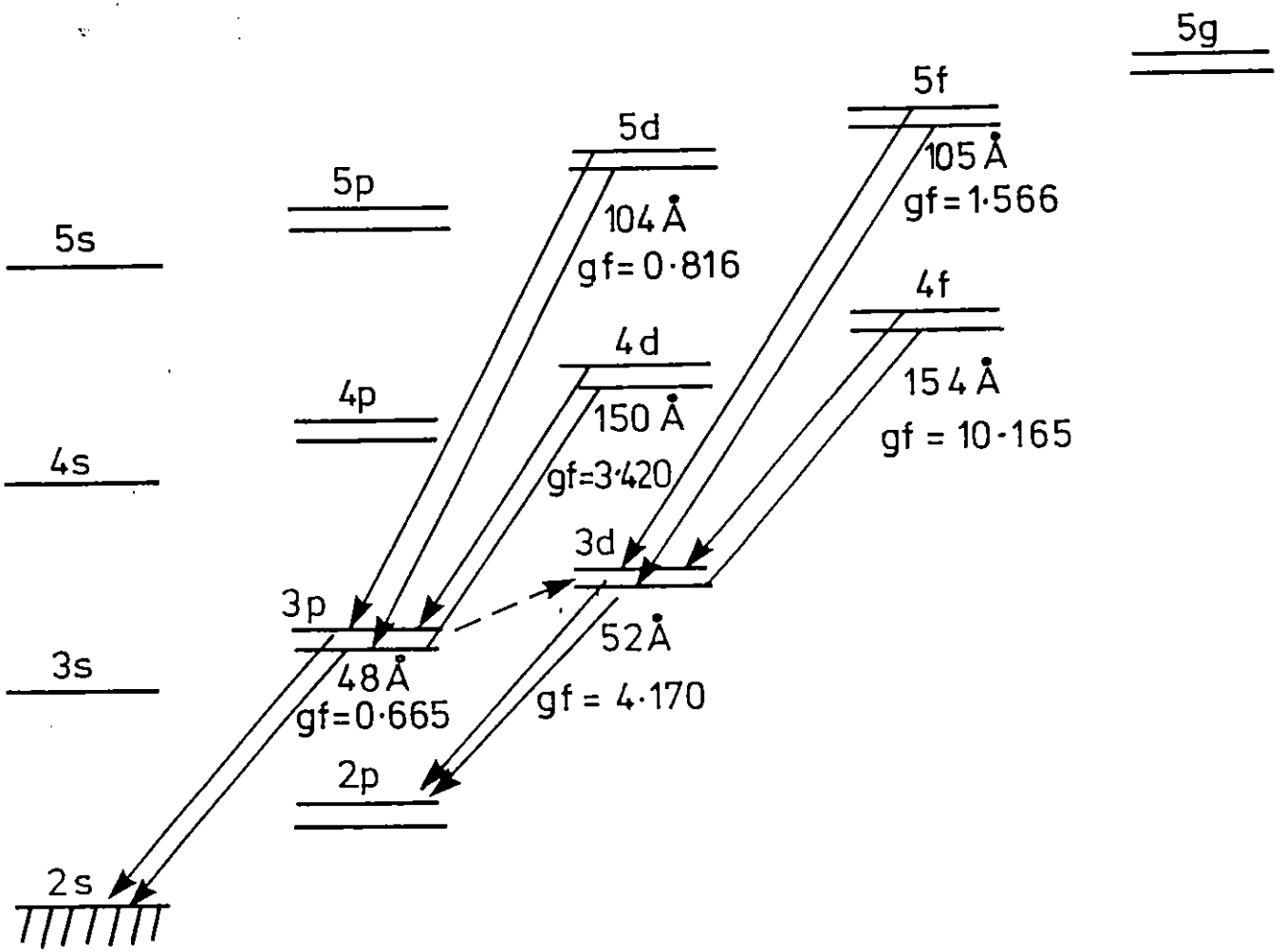


Figure A4.18 *Term scheme for lithium like aluminium showing important radiative transitions and collisional pump (broken line) 3p-3d.*

Previous results[4] had a multi-peaked profile for the peak gain at line centre versus time, the first peak occuring at ∿500ps (rather earlier than in experiment) being the largest. A refinement to the technique used to generate the initial computational grid has removed spurious peaks, in particular moving the maximum to a later time (∿800ps), see figure A4.19.

The code LAGR carries out a crude simulation with an initially uniform finite difference grid. The penetration of the burn wave is calculated and then the simulation is repeated with very fine zoning in an outer anulus of the fibre - which will form the recombining plasma - and coarse zoning in the central core, which is essentially undisturbed during the simulation. This process greatly improved the accuracy of the calculation. In the new model, the penetration of the burn wave is determined from the degree of conisation and not from the plasma temperature, as before. The spurious peaks in the gain profile, due probably to the peak gain moving from one computational cell to another, are smoothed out by this improved treatment of the hydrodynamics.

At present the importance of opacity effects has not been precisely determined; trapping is calculated in LAGR using an escape factor[3] chosen according to the dominant line broadening mechanism. The trapping may be turned off by setting the escape factor equal to unity; this has resulted in an approximate doubling of the peak gain. Experimental results of the 3d-4f gain lie somewhere in between trapping on and trapping off calculations.

A set of routines[7] have been added to the code which calculate the gain from the total intensities radiated in the axial and transverse directions; this combines the signals from various J split levels, where the splitting is small, to give a gain for the system equivalent to the experimentally determined values. Figure A4.20 shows the gain versus time for 3d-4f (154 Å) transition with trapping on and trapping off - the experimental graph is also shown. There is an absorbed energy of 4.2J from a 120ps FWHM laser pulse. The pulse and energy have not yet been optimised, a shorter pulse length (60-80ps) brings the peak gain into line with experiment when the trapping is turned off, but the peak is too early. Although the gain is too low, the peak occurs closer to experiment in time with the trapping on.

Scaling laws have been developed for the lithium like recombination scheme from a large number of simulations of aluminium plasma, using a model which excludes laser heating and treats the hydrodynamics of the expanding fibre as a self-similar expansion[3]. The plasma has an initial density of N_o particles per cc, radius: $R_o\mu m$, and energy: $\epsilon_T$ergs per particle. The peak gain on line centre for the $3d(^5/_2)$-$4f(^7/_2)$ transition has been found to maximise when these parameters are related by the optimising condition:

$$\frac{N_o^{0.53} R_o^{0.295}}{\epsilon_T} = 2.07 \times 10^{16} \text{ (ergs/particle cc}^{0.53} \mu m^{0.295})$$

The peak gain itself varies rather slowly with N_o and ϵ_T, but depends strongly on R_o, with the highest gain obtained for small initial radii. Only four values of Ro (in the range 10μm-40μm) have been tried, but the data at these values indicate that the peak gain scales as:

$$G(cm^{-1}) = 18.0\ e^{-0.08R_o}$$

The initial radius R_o relates to a particular adiabat along which the plasma expands, determined by the burn characteristics during the heating phase. This is primarily dependent upon the laser pulse, smaller R_o corresponding to shorter pulses.

A limited series of simulations has been carried out using LAGR (i.e. full treatment of laser absorption and one dimensional hydrodynamics) with the laser energy kept constant but the pulse

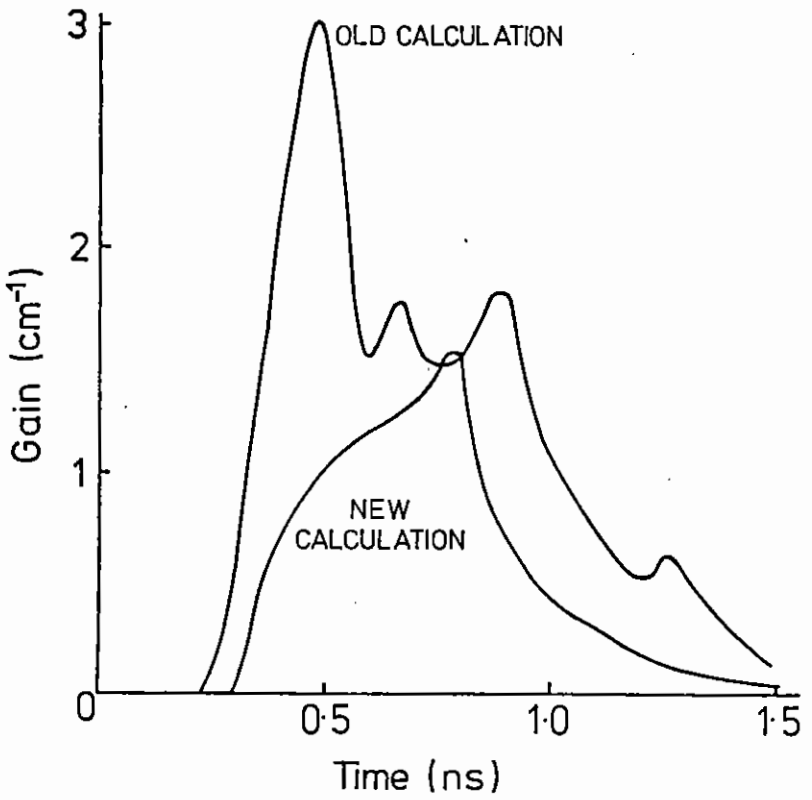


Figure A4.19 *Peak gain versus time at line centre of $3d(^5/_2)$-$4f(^7/_2)$ transition, illustrating effect of improved hydrodynamics modelling in LAGR.*

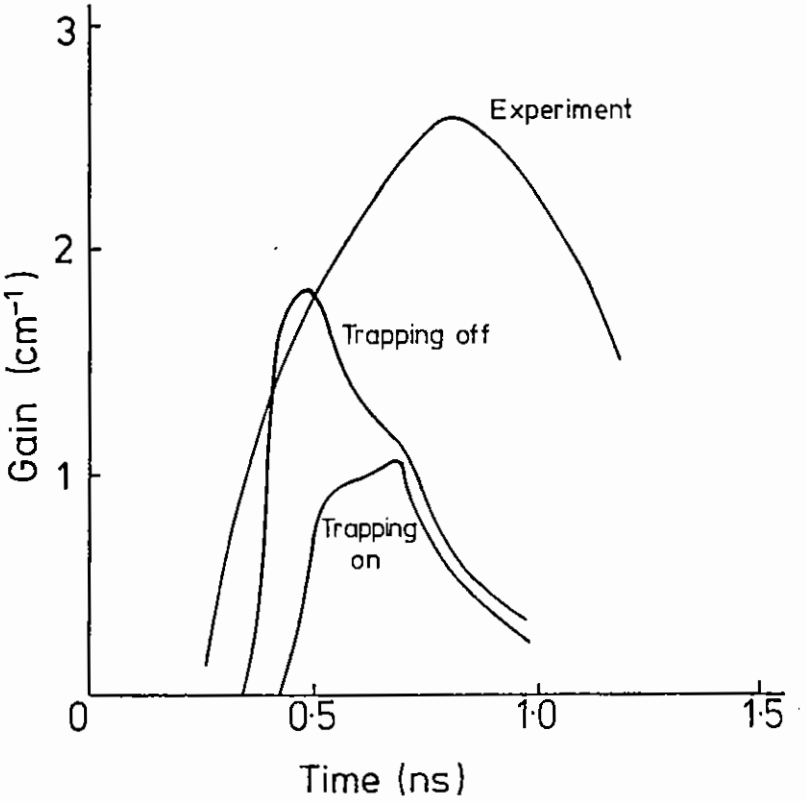


Figure A4.20 *Averaged gain versus time for 3d-4f (154 Å) line with trapping on and off.*

length varies; absorbed energy remained close to 5J. Using the plasma mass and dimensions at the time of maximum penetration by the burn wave a similarity radius equivalent to R_o has been calculated, and the scaling of the averaged 3d-4f gain (with trapping off) with R_o has been determined. Radii, R_o are in the range 2μm–17μm and these relate very approximately to the HWHM of the pulse by $R_o \sim HWHM/7.6(ps/\mu m)$. The pulse shape is not a pure Gaussian but a combination of a fast (10–60 ps) rise time and a Gaussian fall off. The gain scales as:

$$G(cm^{-1}) = \frac{12.28}{R_o^{0.777}}$$

The lower limit of R_o for which the above scaling laws are valid has not yet been determined, but it probably requires shorter pulse lengths than can be practically obtained with reasonable amounts of energy.

A scan of gain versus energy has indicated that for a 120ps pulse, and 7μm diameter fibre, the minimum absorbed energy for which gain is possible is about 1.5J. The optimal energy is between 2.5J and 6J, and the gain falls off slowly as the energy increases from 6J to 10J. The useful range of absorbed energy is fairly restricted because not enough will not ionise the plasma sufficiently and too much will create too many helium like ions which will not recombine through the lithium like state at a time during the expansion when the density is high enough to be useful. Our broad conclusion at this stage is that gain can be maximised by an appropriate amount of energy being absorbed in the shortest (practically) possible time. Matching the experimental conditions exactly in the simulation is hindered by a lack of knowledge of the precise laser pulse shape, a parameter to which the gain appears very sensitive.

References

1. C Regan et al, Rutherford Appleton Laboratory Report (RAL-88-042) 15 (1988).
2. G J Pert and M J Henshaw, Rutherford Appleton Laboratory Report (RAL-88-042) 112 (1988).
3. G J Pert, J. Phys. B9, 3301 (1976).
   G J Pert, J. Phys. B12, 2067 (1979).
4. W L Van Wyngarten, K Bhadra and R J W Henry, Phys. Rev. A20, 1409 (1979).
5. R Mewe, Astron. & Astrophys. 20, 215 (1972).
6. H Van Regemorter, Astrophys. J. 136, 906 (1962).
7. G J Pert (ibid).

A4.10 THE CALCULATION OF GAIN AS DETERMINED EXPERIMENTALLY

G J Pert (York University)

The experiments carried out at the CLF have measured gain in two independent ways. The most reliable is based on single shot two spectrograph measurements of the line intensity transverse and axial to directly determine amplification. The multi-shot axial length variation approach is less accurate and greatly affected by shot-to-shot variation. The simulation studies should thus attempt to reproduce both methods. The gain is inferred from the averaged gain-length amplification relation:

$$A = [e^{(\bar{G}l)} - 1]/(\bar{G}l) \qquad (1)$$

either directly or by an appropriate fit.

In fact equation (1) is strictly only applicable at a fixed frequency, and does not take the frequency variation across the line into account in calculating the averages. If this is done, the amplification is given by:

$$A = \int\{\exp[G_0 l\ f(\upsilon)]-1\}d\upsilon/G_0 l\int f(\upsilon)d\upsilon \qquad (2)$$

where $G_0 l$ is the gain-length product on line centre and $f(\upsilon)$ the line shape function normalised to $f(0)=1$.

For an isolated line the function is plotted in figure A4.21 for both a Lorentz and a Doppler profile, as a function of $G_0 l$, the gain-length on line centre. It is readily seen that values given by (2) are substantially less than those from (1). For a measured value of $(\bar{G}l)$ we may derive the value of $(G_0 l)$ from figure A4.22 for the overall values of gain measured the quoted values are about 20% too small.

For the hydrogen-like H_α line, the comparison is further complicated by the fine structure, which splits the line into two major components and five smaller ones. The accurate calculations of gain must take this into account.

In our computer model we have identified three modes of calculation:

i. The line width $\delta >> $ line splitting, $\Delta(\delta > 3\Delta)$ a single isolated line.

ii. The line width $\delta <<$ line splitting, $\Delta(\delta < \Delta)$ five separate isolated components (l-splitting is neglected).

iii. The line width $\delta \sim$ line splitting, Δ, a full numerical integration of the complete split and broadened (Voigt) profile.

For an isolated line of Doppler profile we may evaluate the integral in (2) in terms of a small order or asymptotic series with the following results:

$$A = \sum_{n=0}^{\infty} (G_0 l)^n / \sqrt{(n+1)(n+1)!}$$
$$[1+(3/8(G_0 l))+(^{65}/_{256}(G_0 l)^2)+\ldots]\exp(G_0 l)/(G_0 l)^{3/2}\ G_0 l \gtrsim 3 \qquad (3)$$

For a Lorentz profile the integral can be evaluated exactly:

$$A = e^{(G_0 l/2)}[I_0(G_0 l/2)-I_1(G_0 l/2)] \qquad (4)$$

where $I_0(x)$ and $I_1(x)$ are modified Bessel functions or order 0 and 1 respectively. For a Voigt profile no simple analytic form is available. Integration of equation (2) by the saddle point method gives the asymptotic value for large $(G_0 l)$:

$$A \simeq \phi(\Delta/\delta)\ \exp(G_0 l)/(G_0 l)^{3/2} \qquad (5)$$

where Δ and δ are the Lorentz half-half width and Doppler $^1/e$-half widths respectively. The value of ϕ is given in terms of the line shape function normalised to unit integral ($\int f d\upsilon = 1$) by:

$$\phi = \frac{(2\pi f(0)^3)^{1/2}}{|j(0)|} \qquad (6)$$

$$= \sqrt{\{2\pi f(0)^3/[2(1+2\Delta^2/\delta^2)/\delta^2 f(0)-(4/\pi)(\Delta/\delta^4)]\}}$$

The line shape function on line centre has the value:

$$f(0) = \frac{1}{\sqrt{\pi}\delta}\ \exp\ [\Delta^2/\delta^2]\ \mathrm{erfc}\ [\Delta/\delta] \qquad (7)$$

where erfc(x) is the complementary error function. Since ϕ has the limits:

$$\phi(0) = 1 \text{ and } \phi(\infty) = {}^1/\sqrt{\pi} \qquad (8)$$

for Doppler and Lorentz broadened lines respectively we may use ϕ to give an interpolation weighting function for the amplification

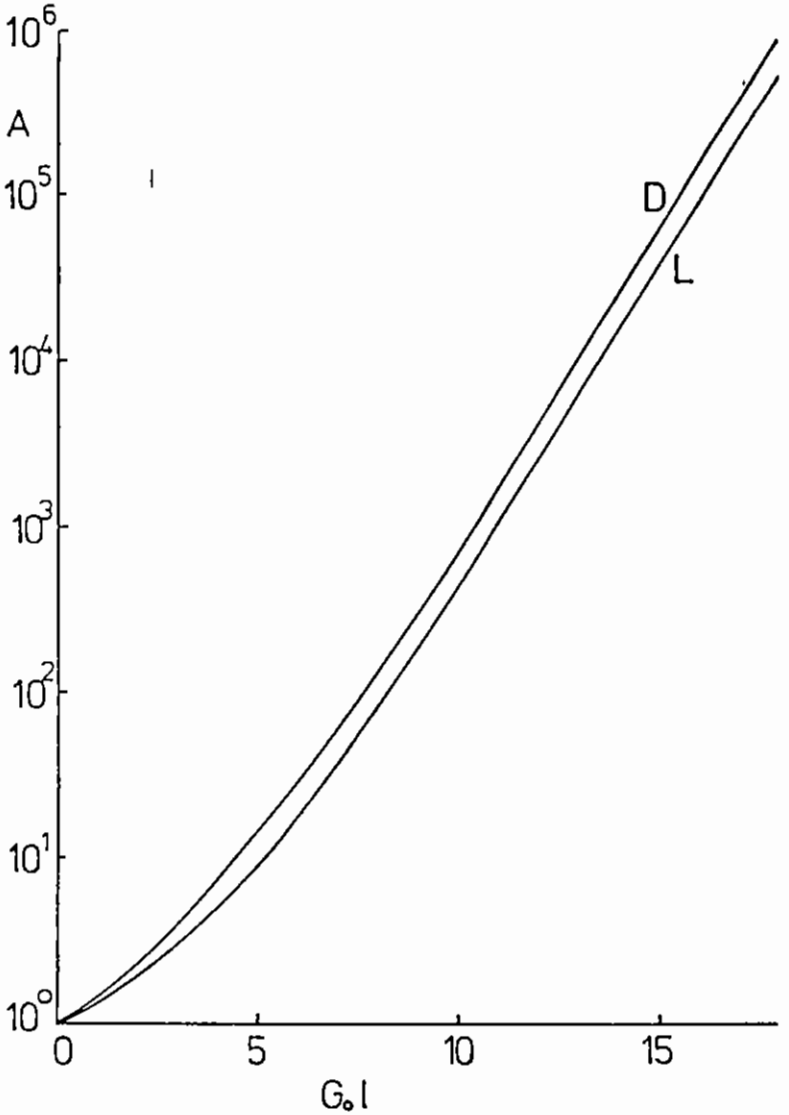


Figure A4.21 *Isolated line amplification versus gain on line centre for Doppler and Lorentz profiles.*

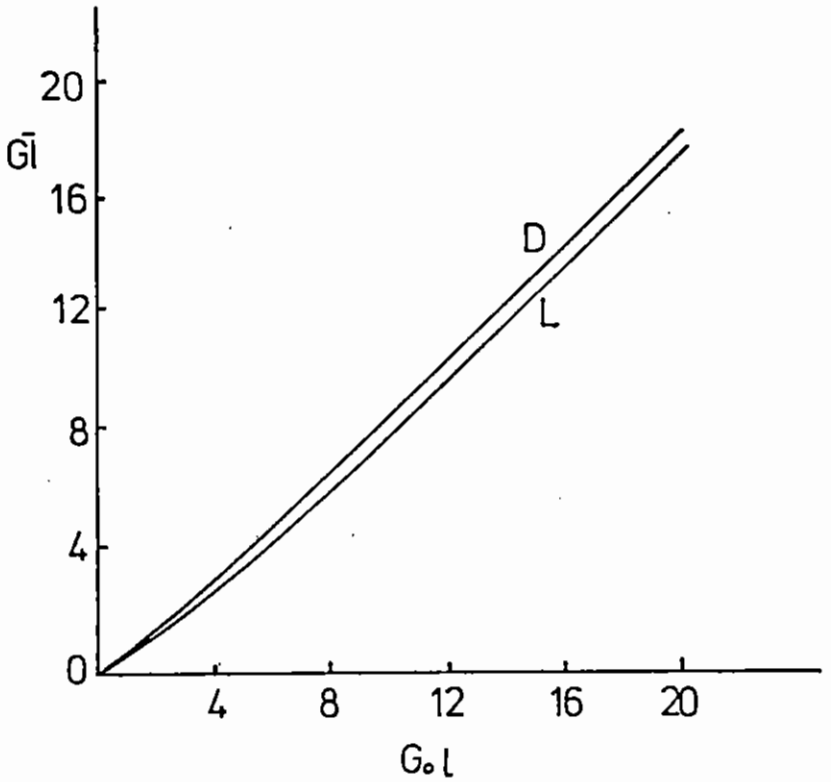


Figure A4.22 *Isolated line average gain-length versus gain-length on line centre for Doppler and Lorentz profiles.*

factor based on the values A_L and A_D for Lorentz and Doppler broadening respectively, i.e.

$$A = WA_L+(1-W)A_D \qquad (9)$$

$$W = \sqrt{\pi}\ (1-\emptyset)/(\sqrt{\pi}-1) \qquad (10)$$

The code LAGR has been modified to give signal amplifications from the above results. Calculations are done for a variety of lengths, typically, 0.2, 0.4, 0.6, 0.8 and 1.0cm, and for the transverse output. The axial/transverse gain for each length, and the axial length variation values are derived by fitting equation (1) to these values, the latter by least squares. We may note that for systems with positive gain these values may differ significantly from one another (due to line narrowing), the longest lines giving the largest values. Furthermore the axial fit also gives a value close to (dominated by) the longest line.

Calculations of Gains in Hydrogenic Carbon and Fluorine

The calculation of gain in expanding laser heated fibre targets of carbon and lithium fluoride has been carried out to compare with experimental data. The most extensive available set of data has been obtained for the H_α line of FIX, and is particularly suitable for assessing the reliability of various approximations made in the calculation. For example, the trapping factor used in the code is local, and overestimates the degree of self absorption. Its inclusion, therefore, gives a lower bound on the gain, similarly the absence gives an upper bound.

Another approximation which may be usefully tested concerns the 'rate of feed' of population into the uppermost state in the code. It is not difficult to show that direct recombination into the state cannot support the LTE condition qualitatively expected (at the least in the early stages of expansion). In fact, it is supported by cascade from higher levels - the diffusion term of the Fokker-Planck classical picture of recombination. Thus, a lower bound to this rate is given by the overall collisional cascade recombination feeding this level.

Figure A4.23 shows a comparison of these approximations with experiment. It can be seen that as expected the neglect of L_α trapping and inclusion of cascade effects (A) give the highest gain. The neglect of cascade (B) reduces the gain, and induces a more rapid fall-off of gain. Inclusion of L_α trapping (C) markedly delays gain onset and consequently gives much lower peak gain: cascade effects make relatively little difference in this case. The best agreement is found for curve (A) which accurately predicts the onset time, and slightly over estimates peak gain. The long tail (in time) to the gain is not seen in the simulations.

A similar pattern is seen in figure A4.24 with carbon. The code in this case significantly underestimates the value of the peak gain, but the general pattern and the timing are well reproduced in case (A).

Thus, we conclude that the cascade term is effective and more importantly, and controversially, that optical trapping of the L_α line plays little role in limiting the peak gain in these experiments. This latter conclusion has been further born out by simulations of AlXI, NaXI and MgXII experiments, where again conformity with experiments in only found if the trapping is small. This conclusion is in agreement with general rules for the design of XUV lasers enunciated in our earliest work, where we identified the switch role of L_α trapping, and the requirement that self absorption be absent at peak gain for effective operation. We may further point out that similar calculations by S J Rose with a different code are in satisfactory agreement when the differences are taken into account.

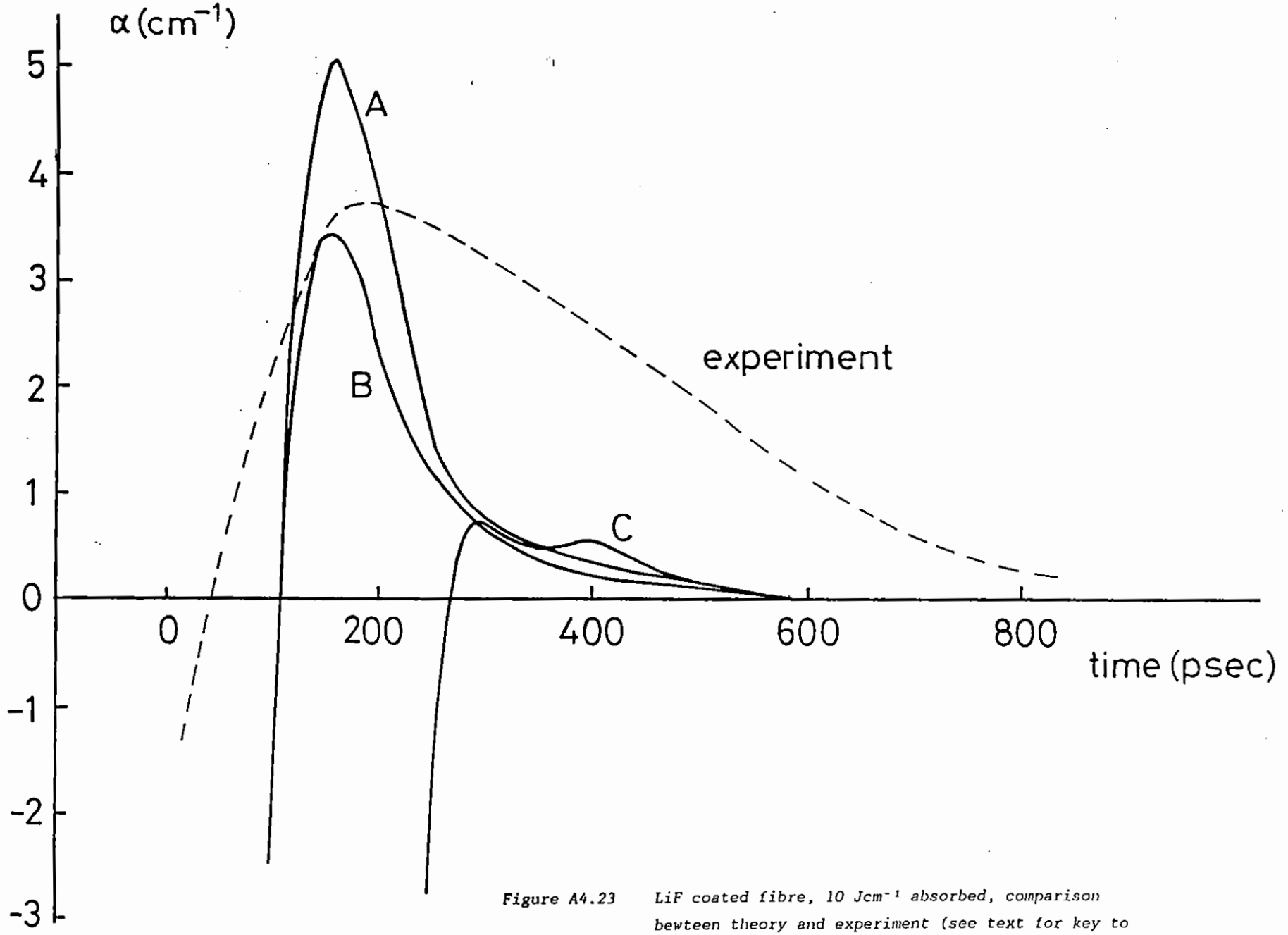


Figure A4.23 *LiF coated fibre, 10 Jcm⁻¹ absorbed, comparison bewteen theory and experiment (see text for key to A, B and C).*

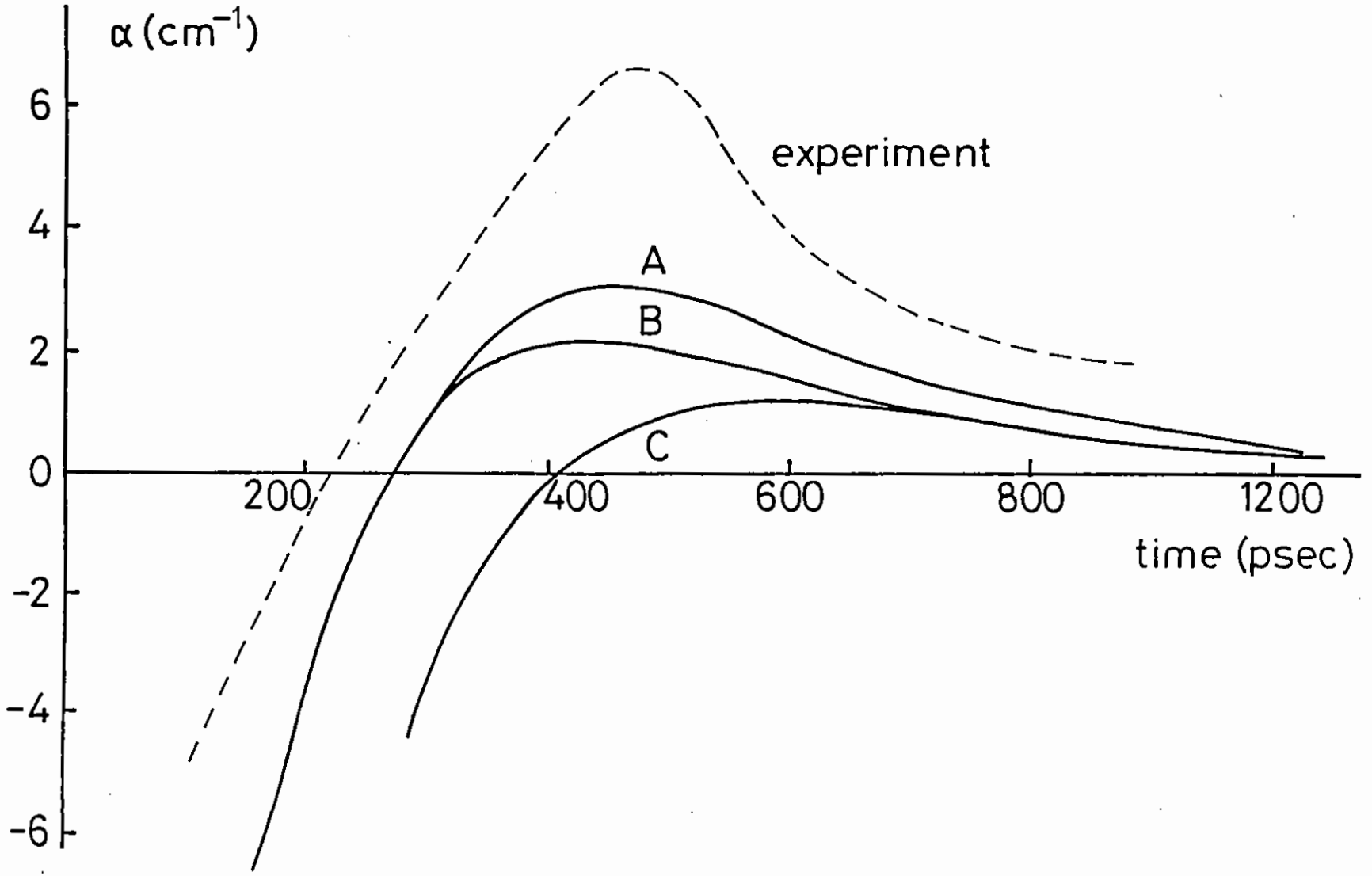


Figure A4.24 *Carbon fibre, 2.5 Jcm⁻¹ absorbed, comparison between theory and experiment (see text for key to A, B and C).*

A4-11 TRANSPORT IN LASER-PRODUCED PLASMAS

A D McGowan and J J Sanderson (University of St Andrews)

For several years it has been known that to accurately model electron transport in laser-produced plasmas, it is necessary to solve the electron Fokker-Planck equation. In most of the computer simulations carried out so far, it has been assumed that spherical effects and the anisotropic portion of the Rosenbluth potentials can be ignored. However, it was recently shown by Jorna and Wood[1] that these assumptions are not valid in certain regimes. We decided to study these two effects further.

A code has been written to solve the Fokker-Planck equation in spherical geometry (assuming azimuthal geometry) with the collision term solved in a similar way to that developed at the Livermore Laboratory[2]. The equation to be solved is

$$\frac{\partial f}{\partial t} + \frac{vu}{r^2}\frac{\partial}{\partial r}(r^2 f) + \frac{v}{r}\frac{\partial}{\partial u}(1-u^2)f$$

$$= \frac{\Gamma}{v^2}\frac{\partial}{\partial v}\left(Af + B\frac{\partial f}{\partial v}\right) + \frac{\Gamma}{v^2}\frac{\partial}{\partial u}\left(Cf + D\frac{\partial f}{\partial u} + E\frac{\partial f}{\partial v}\right) \qquad (1)$$

where f is the single particle distribution function, v is the total velocity, u is the cosine of the angle between the velocity vector and the radial vector, r is the radial distance and A,B,C,D,E are functions of the Rosenbluth potentials and the radial electric field.

The Rosenbluth potentials are represented by an expansion in Legendre polynomials.

$$g(v,u,t) = \sum_{l=0}^{l=l_{max}} \ln \Lambda_{ee} g_l(v,t) P_l(u) \qquad (2a)$$

$$h(v,u,t) = \sum_{l=0}^{l=l_{max}} 2 \ln \Lambda_{ee} h_l(v,t) P_l(u) \qquad (2b)$$

The derivatives of the potentials are done analytically within the Legendre polynomial representation.

The electron Fokker-Planck equation is solved by the method of fractional steps and without Chang-Cooper differencing of the velocity equation. The code conserved particles to 1 part in 10,000 and energy to within 1%. The advection equation is solved by the implicit Wendroff method and the radial electric field is calculated from Gauss's Law (with the inclusion of a time dilation factor).

To test the collisional part of the code, two tests were carried out which tested the velocity part of the code and the angular part of the code. The first test followed the relaxation of a high-energy Gaussian hump on a Maxwellian distribution. The results were compared to the work by Dolinsky[3] and the results, see figure A4.25a were in good agreement. The second test followed the relaxation of an anisotropic distribution. The agreement between the code and Spitzer's results [4] is excellent (see figure A4.25b).

To investigate the effect of curvature and the inclusion of the full Rosenbluth potentials, we considered the case of two concentric shell of radii r_1 and r_2 ($r_1 < r_2$), which are separated by a homogeneous plasma with fixed ions at a temperature T_0. The temperature at r_2 is ramped up to T_h, by injecting a half - Maxwellian, in such a way that no current is added to the plasma. The density of the plasma was $10^{21}cm^{-3}$ for the electrons and the ion charge was set equal to 5. Throughout the simulations, the width of the plasma was kept constant at 12μm. When studying the effect of curvature, the Rosenbluth potentials were assumed to be isotropic (ie only the first term in the Legendre polynomial expansion of g and h was considered) and r_1 was varied from 15μm to 300μm. When studying the effect of the full Rosenbluth potentials,

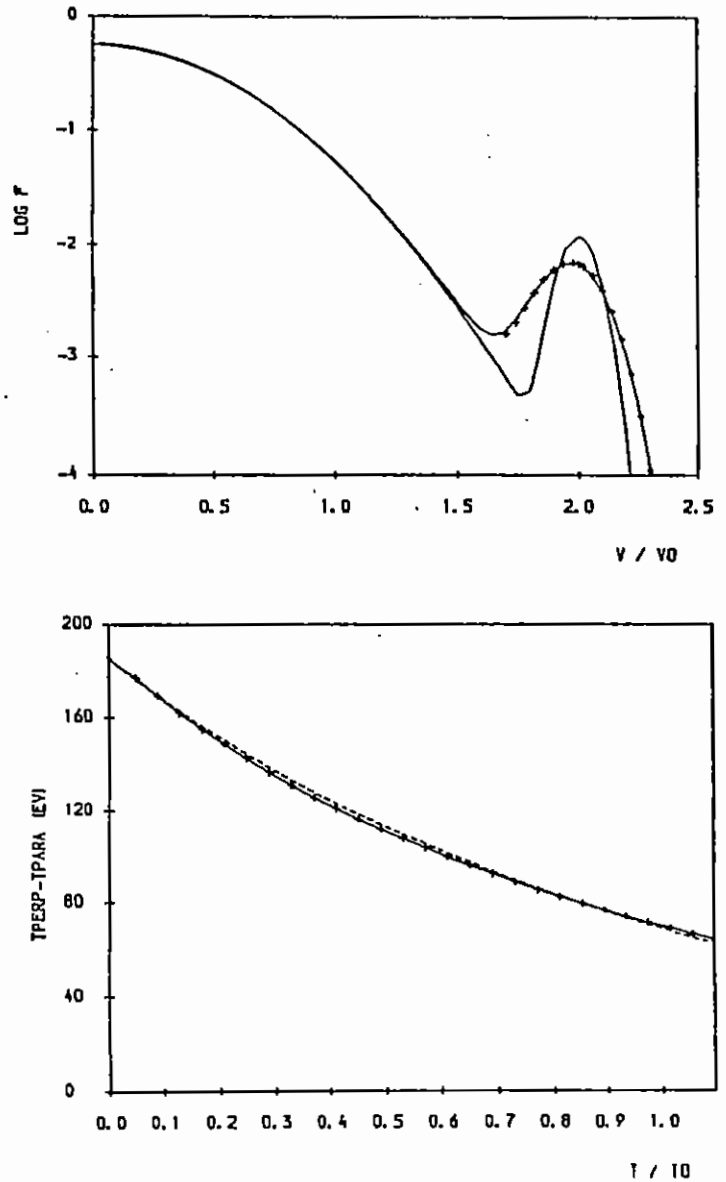


Fig A4.25a *Development of a Gaussian hump on a Maxwellian distribution for time t=0 and t=0.38t_0. The crosses show Dolinsky's results.*

Fig A4.25b *The relaxation of a small anisotropy. The background temperature is 1 kev. The dashed line shows Spitzer's results.*

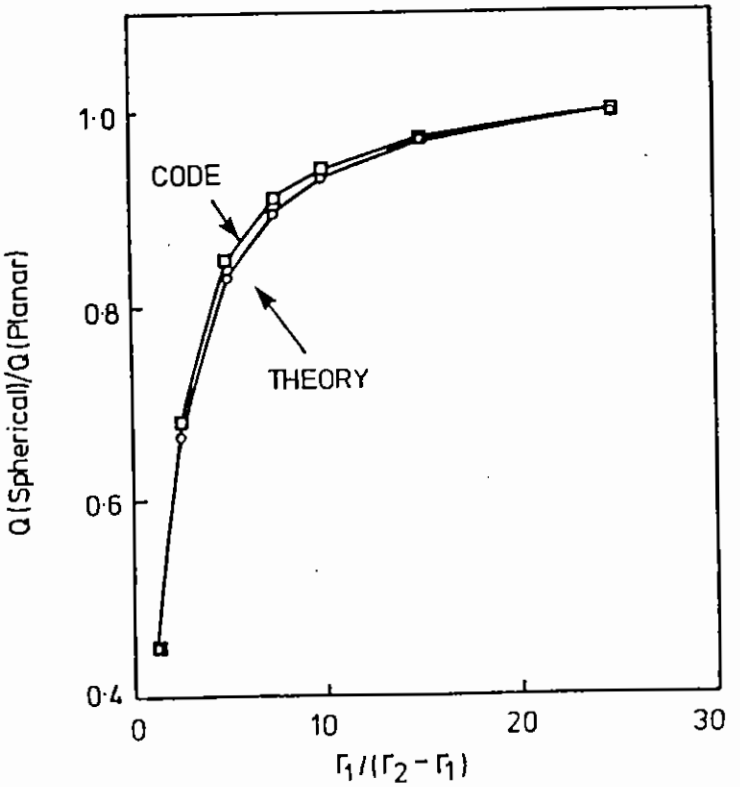


Fig A4.26 *The heat flux at r_1 after 0.35 t_0 against aspect ratio. The heat flux at r_1 is normalised to the planar case.*

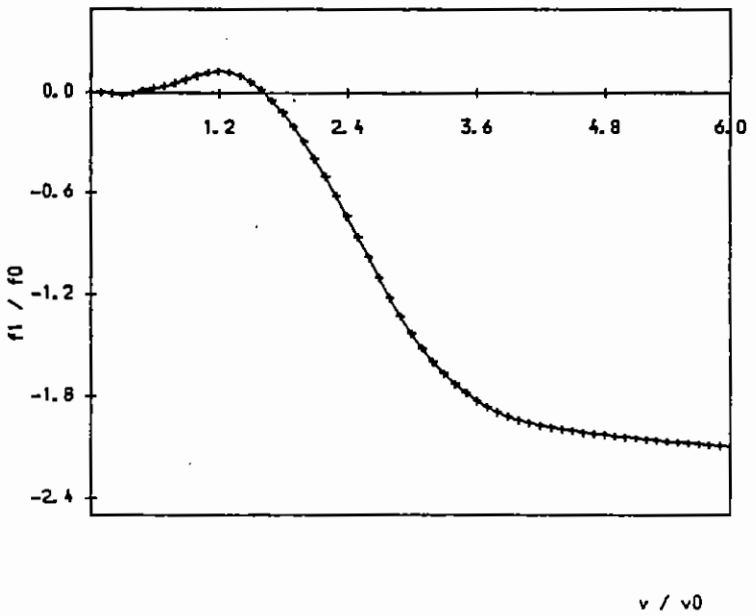


Fig A4.27a f_1/f_0 *against velocity after 0.35* t_0 *at the steepest part of the temperature gradient. The velocity is normalised against the thermal velocity* V_0.

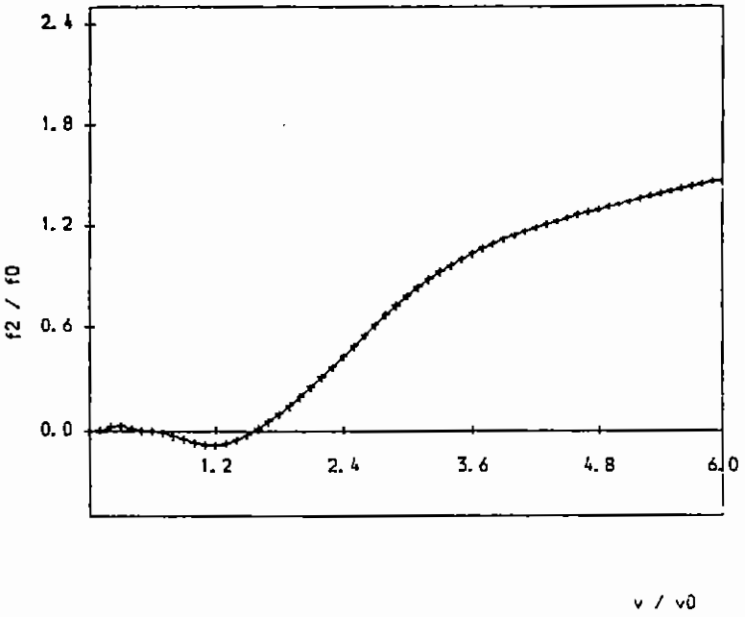


Fig A4.27b As figure A4.27a but for f_2/f_0.

r_1 was kept fixed at 120μm and the Rosenbluth potentials were calculated from the first four Legendre polynomials of f.

Figure A4.26 shows the heat flow at r_1 after 0.35 t_o, where t_o is the self collision time, for a number of different aspect ratios.

It can be seen that the effect of curvature can significantly reduce the heat flow at the inner boundary when the aspect ratio of the target is less than 15. The lower curve shows the predicted effect of curvature from purely geometrical arguments. The agreement is reasonably good. Similar results were obtained for more collisional systems.

To study the effect of including the full collision term, the plasma was heated at r_2 by a bi - Maxwellian heating distribution with $T_{par}/T_{perp}=2$. The results for the case with the full collision term were no different from those obtained when only the isotropic part of the Rosenbluth potentials were used. As can be seen from figure A4.27(a and b), the single particle distribution function can be highly anisotropic, but it is anistropic mainly at high velocities where the plasma is almost completely collisionless. Therefore, the Rosenbluth potentials are very close to being isotropic throughout the plasma. In fact, the maximum value of g_1/g_o and g_2/g_o is approximately 10^{-3} for the system concerned. Therefore, we conclude that in the regime covered by Jorna and Wood[1], it is not necessary to include the full Rosenbluth potentials.

The authors would like to thank Dr S Jorna for many useful discussions during the course of this work.

References

1. Jorna and Wood, Journal of Plasma Physics **38** 317-338.

2. McCoy, Mirin and Killean, Comput Phys Commun **24** 37 (1981).

3. Dolinsky, Phys Fluids, 8, 436 (1965).

4. Spitzer, Physics of Fully Ionized Gases (1962).

A4.12 A PHYSICAL MODEL OF THE EFFECT OF WAVELENGTH OF THE HEATING LASER IN ISOELECTRONIC SCALING OF XUV LASERS OPERATING BY RECOMBINATION

M H Key (RAL)

1. Isoelectronic scaling characteristics F IX to Na XI

Analytic modelling of the isoelectronic scaling characteristic of XUV lasers operating by recombination to hydrogenic ions has been a useful guide in earlier work[1], in which scaling from C VI (183 Å) to F IX (81 Å) was accomplished using fibre targets.

A similar analysis has been carried out for a new experiment aimed at further isoelectronic extrapolation, with the wavelength of the laser used to heat the plasma being considered explicitly, together with a better description of limits on gain due to trapping of Lyα emission.

Production of the plasma by laser irradiation

Plasma production by laser ablation from a solid target can be described, for self regulating absorption by inverse Bremsstrahlung, by the scaling relationships for mass ablation rate $\dot{m}$, ablation velocity v, ablation temperature T and sonic point density ρ as follows[2]:

$$\dot{m} \propto \lambda^{-4/9} I^{5/9} Z^{-2/9} \quad (1)$$

$$v \propto \lambda^{2/9} I^{2/9} Z^{1/9} \quad (2)$$

$$T \propto \lambda^{4/9} I^{4/9} Z^{-2/9} \quad (3)$$

$$\rho \sim \rho_c \lambda^{4/3} I^{1/3} Z^{-1/3} \qquad (4)$$

for absorbed irradiance I, ionic charge Z and laser wavelength λ, and critical density ρ_c.

In scaling from F IX to Na XI, temperature can be increased as $T \sim Z^2$, giving a ratio of number density of bare nuclei to hydrogenic ions in collisional radiative equilibrium. n^Z/n^{Z-1} which can be expressed in the form,

$$n^Z/n^{Z-1} \sim Z^{-4}\, S(T/Z^2, n_e/Z^7)/\alpha(T/Z^2, n_e/Z^7) \sim Z^{-4}, \qquad (5)$$

(The Z^{-4} change in ionisation ratio could be compensated by increasing T/Z^2 but, as seen later, this would not increase the gain)

From equation (1) we see that for $T \sim Z^2$,

$$I \sim Z^4 \lambda^{-1} \qquad (6)$$

and also from equation (4)

$$\rho \sim \lambda^{-1} Z \qquad (7)$$

Equation (7) is important because the number density at the initial temperature maximum, $n_{eo} \sim \rho$ is a major factor determining the gain.

Gain in the plasma medium

The gain scaling can be estimated from the relationship,

$$g \sim 1.1\times10^{-8}\, n(2)\left(\frac{n(2)}{g(2)}/\frac{n(1)}{g(1)} - 1\right) f_{u\ell}\, \lambda_\ell \left[\frac{M/1amu}{kT/eV}\right]^{\frac{1}{2}} \qquad (8)$$

which describes gain on a Doppler broadened transition of oscillator strength $f_{u\ell}$, ion mass M and laser wavelength λ_ℓ. The potentially available fractional inversion $f_i = (n(2)g(1)/n(1)g(2)-1)$ can be defined as that obtained when there is negligible population of n = 2 by collisions or reabsorption of resonance radiation from n = 1, ie negligible n(1).

This potential fractional inversion is a slowly varying function of reduced temperature T/Z^2 and reduced density n_e/Z^7 as shown in figure A4.28 which is derived from tabulated data[3].

The population density n(2) for negligible n(1) is given by [3]

$$n(2) = r_o(2)\, n_E(2) \qquad (9)$$

where $n_E(2)$ is the LTE population given by,

$$n_E(2) = 1.3 \times 10^{-21}\, n_e\, n^{Z+}\, (kT/1\ eV)^{-3/2} \exp(3.4Z^2/kT) \qquad (10)$$

$r_o(2)$ is a function of T/Z^2 and n_e/Z^7,[3] shown in figure A4.29. It is useful to introduce a fraction $f(Z^*) = Zn^{Z+}/n_e$ representing the fraction of bare nuclei remaining relative to a fully ionised plasma and with this to write,

$$n(2) \sim 1.3\times10^{-21}\, r_o(2) f(Z^*)\, n_e^2 Z^{-1} (kT)^{-3/2} \exp(3.4Z^2/kT) \qquad (11)$$

Returning to the gain equation (8) we can use (11) and (8) with $\lambda_\ell \sim Z^{-2}$ and $M \sim Z$ and consider only the 2s–3p component of H_α, with $f_{u\ell} \sim 0.64$ (for which half the n(2) population is relevant), to obtain,

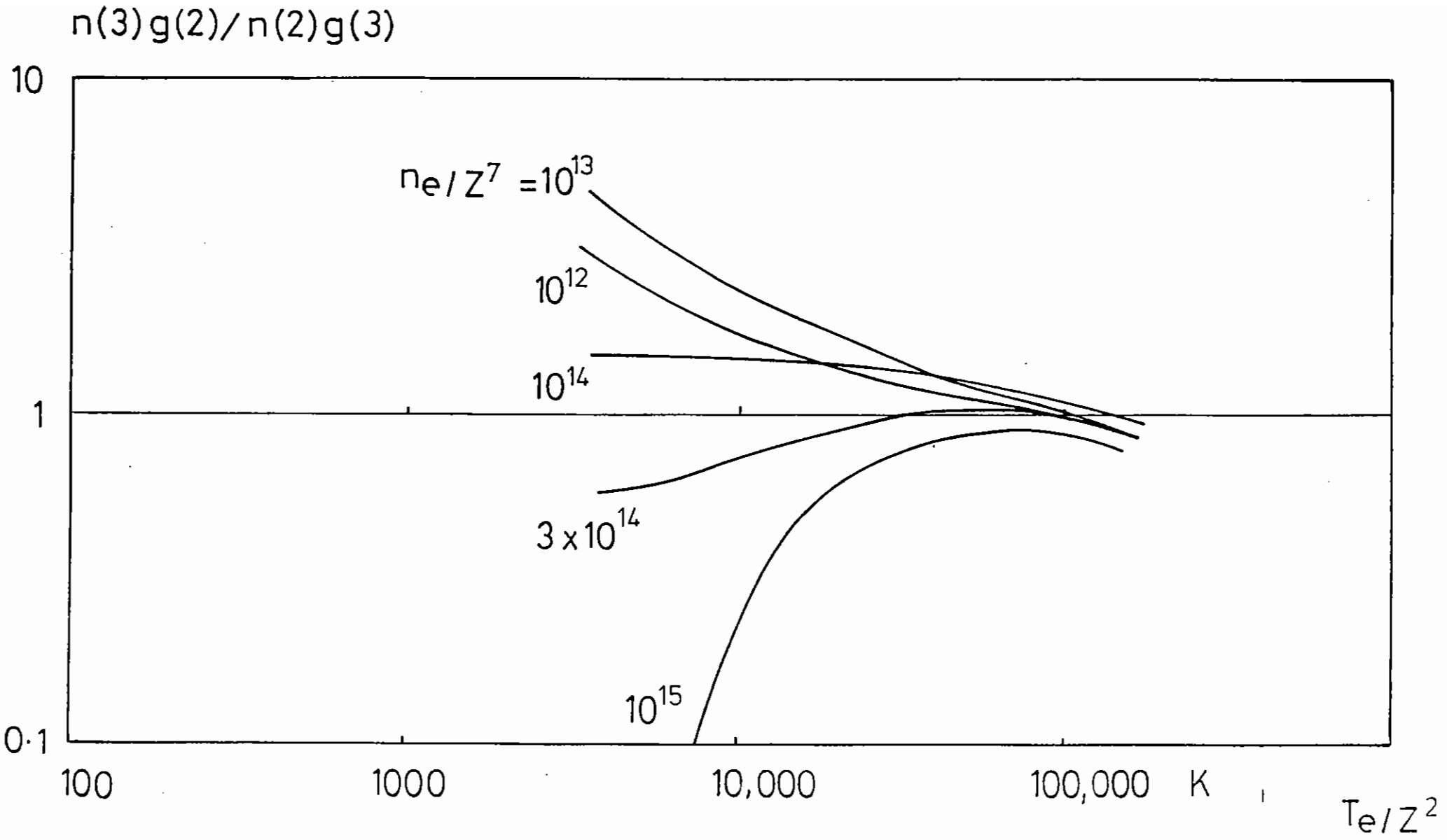


Figure A4.28 *Ordinate population ratio n(3)g(2)/n(2)g(3); abcissa reduced temperature, for various reduced electron number densities.*

$$g = 4\times10^{-34}\ r_0(2) f(Z^*)\ f_i Z^{7.5} (kT/Z^2)^{-2} (n_e/Z^7)^2 \exp(3.4Z^2/kT) \quad (12)$$

With equation (12) and the data for f_i and $r_0(2)$ shown in figures A4.28 and A4.29 contours of reduced gain $g/Z^{7.5}$ can be plotted which show the maximum possible gain, when $f(Z^*) = 1$ and $n(1)$ is negligible, as a function of the reduced n_e/Z^7 and T/Z^2, as shown in figure A4.30. This gain contour map can be helpful in understanding the isoelectronic scaling characteristics of the recombination lasers.

Figure A4.30 also shows the cooling adiabats for different hydrogenic ions when the plasma is produced by laser heating. The adiabat for C VI starting with $n_{eo} \sim 1.5\times10^{21}$ and $kT_0 \sim 200$ eV is based on computed initial conditions giving maximum gain in fibre targets[4]. Start points for higher Z are plotted using $kT \sim Z^2$ $n_{eo} \sim Z$, as discussed earlier.

It is interesting to note how the C VI scheme requires considerable expansion and cooling before reaching the region of potential gain, while for Na XI the start point is already in the region of potential gain.

Collisional excitation from n = 1

No gain can be produced on initial heating because of population of n = 2 by collisions from n = 1, which has a relatively high population in collisional radiative equilibrium or in any transient overheated state going towards equilibrium.

The effect is well described by the expression[3]

$$\frac{n(2)}{n_E(2)} = r_0(2) + r_1(2)\ \frac{n(1)}{n_E(1)} \quad (13)$$

where the coefficients $r_1(2)$ are available in tabulations[3] for reduced variables kT/Z^2 and n_e/Z^7.

The C VI laser requires a significant reduction of density after the initial heating to prevent LTE being established among the excited states. By contrast the Na XI laser requires only cooling to increase $n_E(1)$ to a level such that the ratio $n(1)/n_E(1)$ is small enough to make collisions from n = 1 a negligible factor in the population of n = 2. Fortunately $n_E(1)$ increases rapidly with reducing kT/Z^2, and figure A4.30 indicates at (a) the point on the adiabat at which, after modest cooling, gain becomes possible, and similarly the point at which there is negligible loss of gain due to collisions from n = 1, assuming that the initial n = 1 population was the CRE value. [The CRE value for the chosen condition is 1% hydrogenic ions for C VI and this increases as Z^4 for higher Z ions when $kT \sim Z^2$].

Trapping of resonance radiation

In practice gain may not be produced because of additional population of n = 2 by reabsorption of 2-1 resonance radiation. The approximate criterion for this to occur is when the opacity $\tau > 1$. The opacity of the Ly_α doublet is

$$\tau \sim 4.5 \times 10^{-9}\ \overline{n(1)}\, \ell\, \lambda_{12}\, \left(\frac{M/1amu}{kT/1ev}\right)^{1/2} \quad (14)$$

and the relevant depth of plasma is the smaller of the Doppler decoupling length and total depth of the plasma. With strong velocity gradient the former is usually smaller and is given by,

$$\ell \sim 2.3 \times 10^6\ \left(\frac{dv}{d\ell}\right)^{-1}\ \left(\frac{kT/1ev}{M/1amu}\right)^{1/2}\ \text{cm} \quad (15)$$

whence,

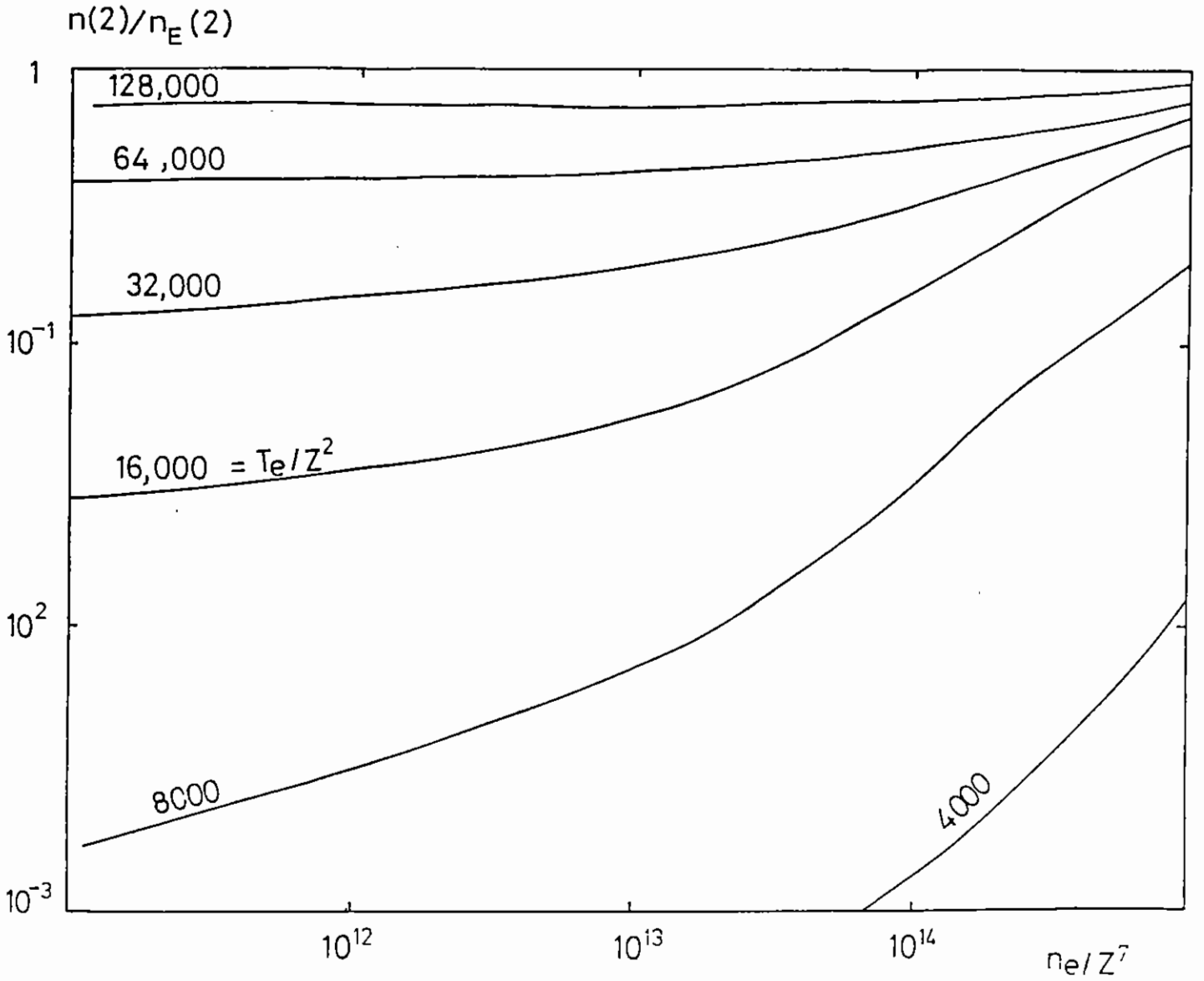


Figure A4.29 *Ordinate $r_0(2) = n(2)/n_E(2)$, abcissa reduced electron number density, for various reduced temperatures T_e/Z^2 in degrees Kelvin.*

$$\tau \sim 10^{-2}\, n(1) \left(\frac{dv}{d\ell}\right)^{-1} \lambda_{12} \qquad (16)$$

In the extensively studied case of the C VI fibre target there is only a small difference between the stage of expansion where collisional effects permit gain and the later stage where the opacity is low enough to permit gain. Scaling the C VI system to higher Z, with constant pulse length and fibre target size, gives a more serious limitation due to opacity, which can be seen as an analytic relationship, using equation (16)with $\lambda_{12} \sim Z^{-2}$, $\ell \sim \lambda_\ell^{-\frac{1}{2}} Z^{-5/2}$ from equations (1) and (6) and $v \sim T_0^{\frac{1}{2}} \sim Z$, the expansion velocity being determined by the initial temperature. Thus $\tau \sim n(1)\, \lambda^{-\frac{1}{2}} Z^{-11/2}$.

The density n(1) has no simple scaling because the physics changes with Z. One approximation is a constant ionisation fraction giving $n(1) \sim Z^6$, so that $\tau \sim \lambda_\ell^{-\frac{1}{2}} Z^{\frac{1}{2}}$ showing a weak increase with Z and with reducing λ. (The LTE criterion, $n_e \sim Z^7$, is a fair approximation for low Z (see figure A4.30) but breaks down for higher Z where reduced densities are lower).

Numerical simulations with $I \sim Z^4\lambda^{-1}$ and constant fibre size and pulse length show that for Na XI the onset of gain is considerably delayed along the cooling characteristics by the opacity constraint as illustrated in figure A4.30.

Recombination from bare nuclei to the H-like ground state

The population of ground state H-like ions and of bare nuclei are important parameters which depend on the initial heating and on the subsequent cooling characteristic. It is interesting to note that cooling adiabats are almost parallel to the contours of potential gain in figure A4.30, so that the actual gain is mainly determined by the fraction of bare nuclei remaining $f(Z^*)$ at the stage where gain quenching from n = 1 ceases.

The initial heating determines which gain contour is followed, eg for Na XI raising the initial temperature reduces the potentially available gain while raising the initial density increases it, figure A4.30 shows that for Na XI in the gain region the potential gain scales as,

$$g \sim n_0^2\, T_0^{-3}. \qquad (17)$$

The scaling $n_0 \sim \rho \sim \lambda^{-1}$ in equation (7) for ablative heating shows that reducing the wavelength of the plasma heating laser should give a significant improvement in potential gain with $g \sim \lambda^{-2}$. Any other effect which increases n_0 increases the potential gain, so that, for example, transient thermal conduction in short pulses may further improve the laser gain[5]. The actual n_0 in the ablation process is sensitive to the details of energy transport, linking closely the physics of energy transport in ablation and gain in recombination lasers.

Optimising T_0 in ablation implies varying I, with $T_0 \sim I^{4/9}$ and $n_0 \sim I^{3/9}$ from equations (3) and (4). The start point in figure A4.30 is thus a locus where $T \sim n^{4/3}$. Lower temperature gives greater potential gain at the expense of a lower initial fraction of bare nuclei and a more rapid loss of bare nuclei in the cooling process. There is a maximum gain for an optimum T_0 as discussed in[4].

The initial degree of ionisation is close to equilibrium which is given by,

$$\frac{n(Z^*)}{n(1)} \sim \frac{S}{\alpha} \qquad (18)$$

where S and α, the CR ionisation and recombination coefficients[6], are shown in figure A4.31 for the reduced variables T/Z^2 and n_e/Z^7. The time constant for equilibrium is of the order $1/n_e\alpha$, for a high ratio $n(Z^*)/n(1)$, and is similar to the inertial confinement time of the ablation plasma at peak temperature for fibre targets.

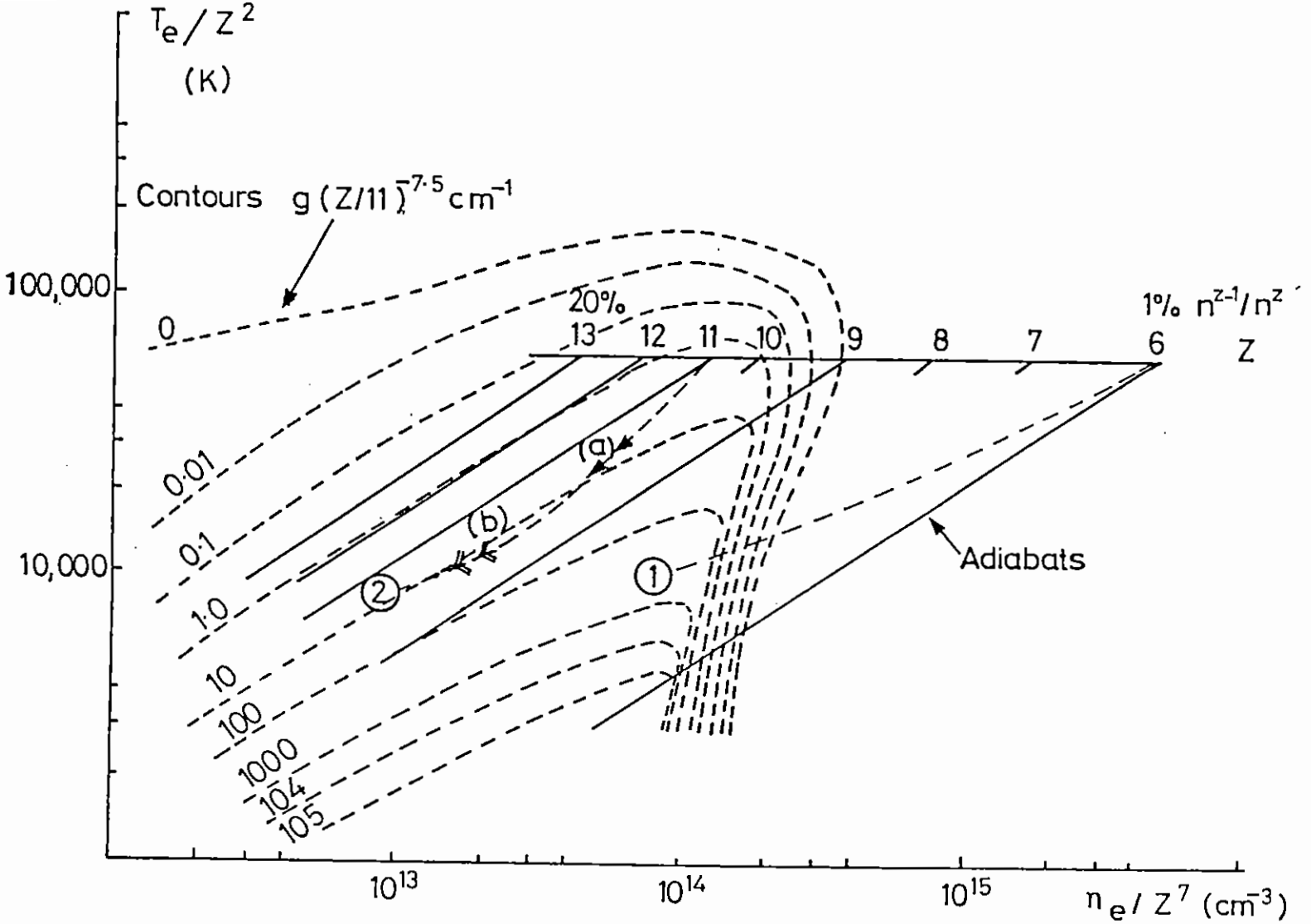


Figure A4.30 *Ordinate reduced temperature; abcissa reduced electron number density. Contours show reduced gain coefficient. Adiabats are shown from the initial temperature and density appropriate to lasers of varying atomic number Z from 6 to 13. The fraction of hydrogenic ions relative to bare nuclei varying from 1% at Z = 6 to 20% at Z = 13 is indicated as n^{z-1}/n^z. (1) and (2) are nominally computed cooling characteristics for Z = 6 and Z = 11. (a) and (b) denote cut off points for collisional quenching and trapping of resonance radiation.*

Numerical simulations illustrate this. In the Na XI fibre simulation with $n_{eo} \sim 5 \times 10^{21}$ cm^{-3}, kT_o 750 eV, figure A4.31 gives $n(1)/n(Z^*) \sim 0.18$ in equilibrium, while the numerical simulation gives 0.2. Variation of the initial temperature varies the ionisation rates but, provided the bare nuclei are initially a substantial fraction of the total, the more important question is the fraction surviving when the gain quenching from n = 1 ceases later on in the expansion.

Integration of the recombination using

$$\frac{\dot{n}(1)}{n(1)} = \alpha \left(\frac{n_e}{n(1)}\right) \frac{n_e}{z} - S\, n_e \qquad (19)$$

is easily carried out for any known time variation, n_e (t) and T_e(t) to show the build-up of H-like ground states at the expense of bare nuclei.

Optimum gain with a given timescale for expansion and cooling, is obtained with the lowest temperature adiabat for which a significant fraction f(z*) remains when gain quenching from n = 1 stops.

Numerical simulation

In earlier work numerical simulations were used to show the development of gain when 7 μm fibre targets were irradiated by 70 psec 0.53 μm laser pulses and optimum conditions were found first for C VI[7] and later for F IX[8]. Scaling the irradiance as $Z^4\ \lambda^{-1}$, equation (6), and changing from 0.53 μm to 0.35 μm wavelength, a simulation was made with 40 J cm^{-1} coupled to a Na fibre. Figure A4.32 shows the time variation of parameters in the plasma element producing most gain*. A significant feature is that the initial cooling is more rapid than adiabatic but later slower than adiabatic as illustrated also in figure A4.30. This is in contrast to C VI where recombination heating gives slower than adiabatic cooing at all times as shown also in figure A4.30. The initially more rapid cooling is tentatively attributed to increased thermal conductivity $K \sim T^{5\cdot2}/Z \sim Z^4$ at higher Z giving more rapid heat loss to the cold core when the laser heating stops.

There is an optimum depth below the surface of the target for a plasma element to produce gain. Plasma elements deeper in the target give less gain because of their lower peak temperature and small f(Z*) when trapping terminates, despite the higher potential gain of a lower temperature cooling characteristic. Elements nearer the surface reach their peak temperature too early in the laser pulse and stay hot as they expand on a low gain adiabat.

Dilution

Trapping can be reduced by diluting the concentration of laser ions with another ion species[9]. This suggests the possibility in the present context of gain at earlier times when the loss of bare nuclei f(Z*) is less serious, enabling gain to develop to higher levels in plasma elements with lower initial temperature.

The numerically modelled gain in the Na XI simulation was recalculated with various dilution factors to show this possibility as presented in figure A4.33.

For a particular level of irradiation, dilution gives higher gain for elements deeper in the target up to a point where the beneficial effect of a lower adiabat cannot outweigh the loss of (f/z*) due to enhanced recombination. The density gradient at the peak gain region is more severe however giving a limited gℓ value before refraction from the gain region. Variation of the irradiance to match the dilution would modify the latter problem.

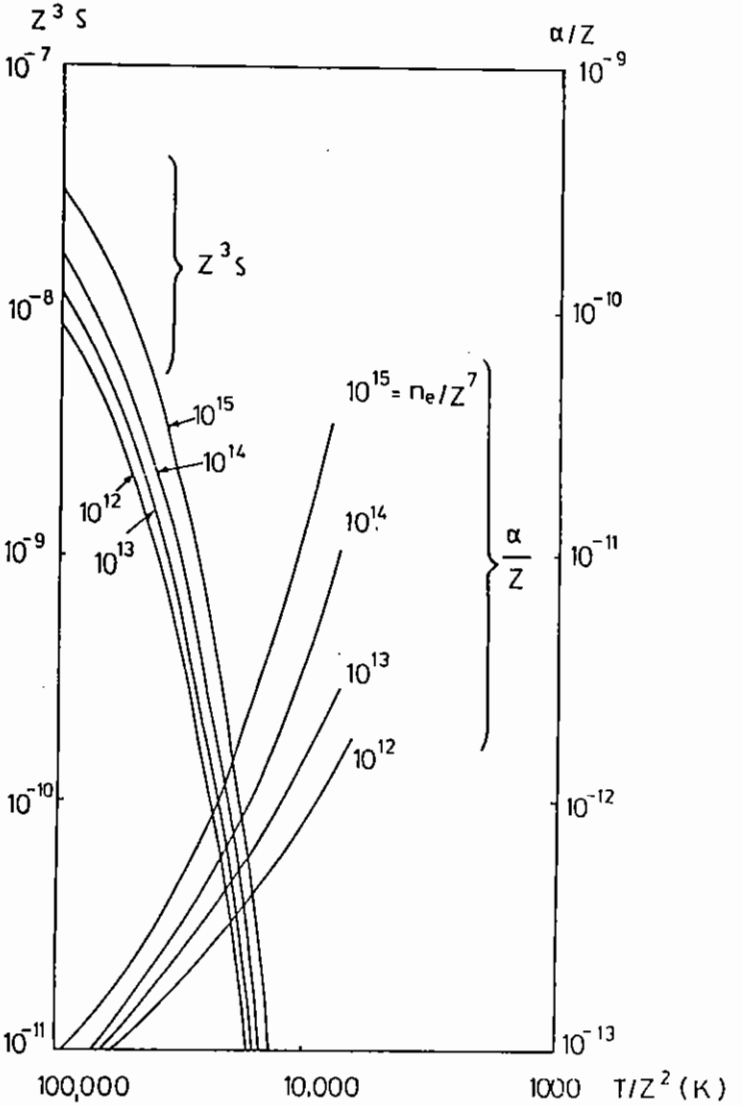


Figure A4.31 *Ordinates LHS reduced ionisation rate coeficient Z^3S RHS reduced recombination rate α/z. Abcissa reduced temperature T/Z^2, for various reduced electron number densities n_e/Z^7.*

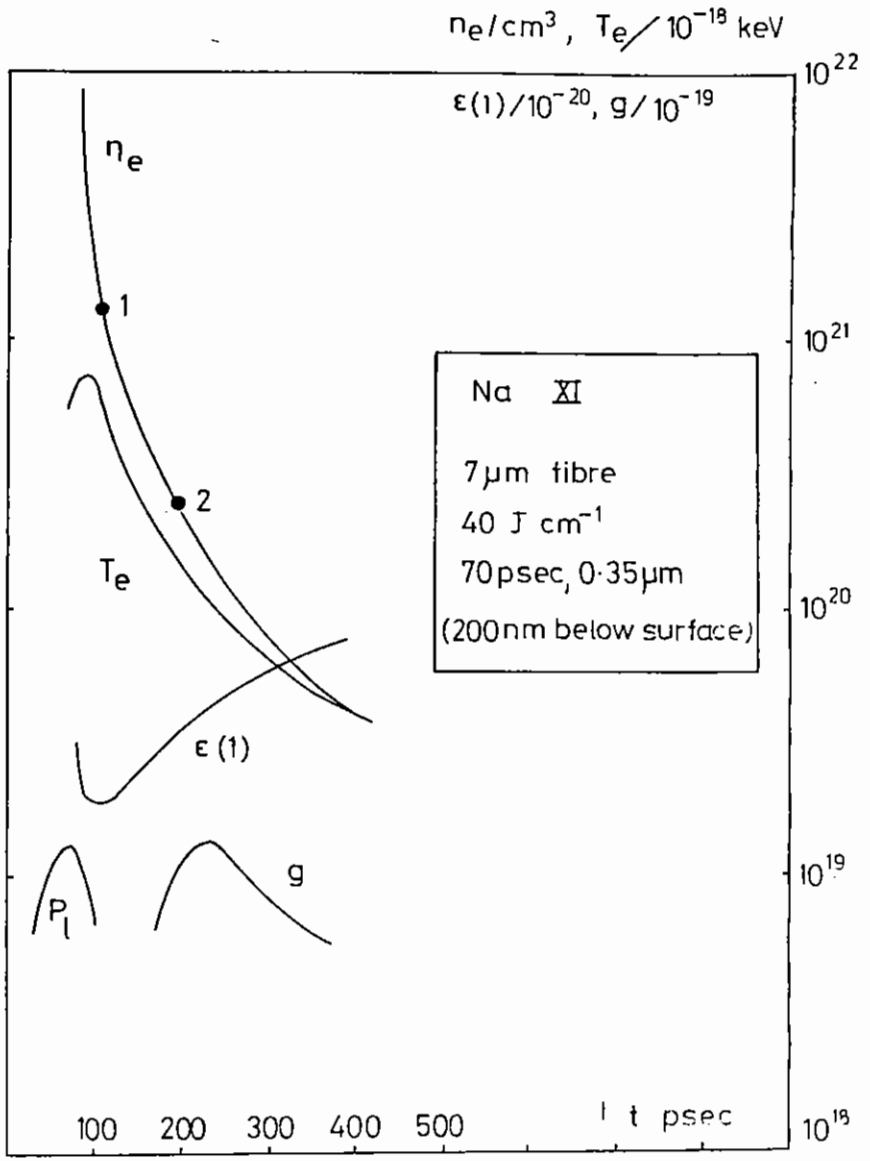


Figure A4.32 *Ordinates electron number density n_e cm^{-3}, temperature $T_e/10^{-18}$ keV, fraction of population in hydrogenic ground states $\epsilon(1)/10^{-20}$, gain coefficent $g/10^{-19}$ cm^{-1} and relative laser power P_l. Abcissa time in psec.*

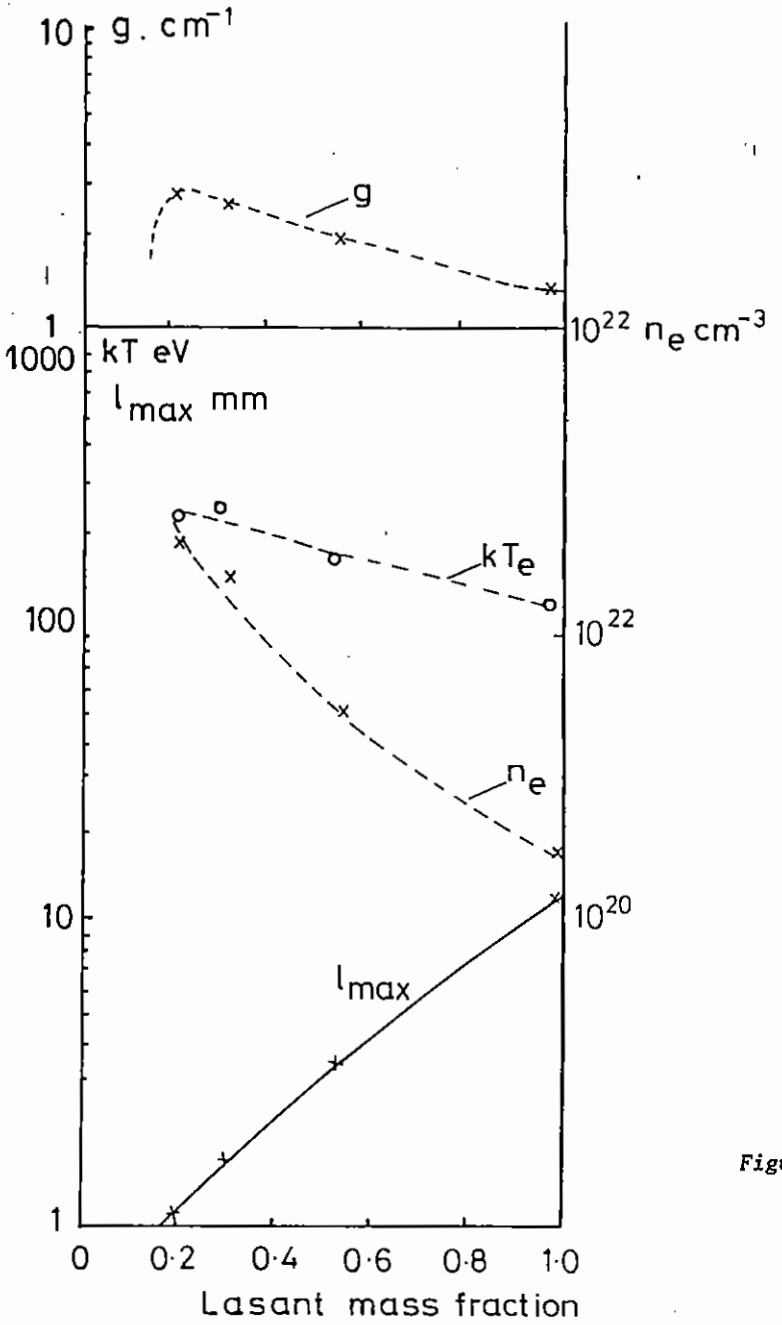


Figure A4.33 *Abcissa lasent mass fraction; ordinates peak gain coefficient g cm⁻¹, temperature and density at time of peak gain kT_e and n_e and minimum length before refraction out of the gain region. Numerically computed for target conditions as in Fig A4.32.*

Isoelectronic scaling

Extracting information from figure A4.30, the potentially available gain on adiabats starting with $T_o \sim Z^2$ and $n_o \sim Z$ is shown in table A4.4 for elements of interest viz Na XI, Mg XII and Aℓ XIII in the present context and F IX for comparison with previous work.

Table A4.4

Z =	9	11	12	13
$g_p \approx$	9	3	1.9	1.1
I_a	10^{14}	$2x10^{14}$	$3x10^{14}$	$4x10^{14}$

The potential gain falls rapidly with $Z^{-5.7}$ in table 1. The scaling is modified in numerical modelling by the trend to faster than adiabatic cooling for higher Z and slower than adiabatic cooling for lower Z, as shown in figure A4.30 for C VI and Na XI.

Conclusion

Analytic modelling gives a useful guide to the optimisation of gain in isoelectronic scaling of H-like recombination lasers to shorter wavelengths and shows the advantage of reduced wavelength in the plasma heating laser.

* Erratum: The values quoted in figures A4.32 and A4.33 were calculated before the discovery of errors in the numerical simulations involving the electron-ion heat exchange and thermal conduction processes. New simulations are being carried out.

References

1. M H Key, Rutherford Appleton Laboratory Report (RAL-87-041), 200 (1987).

2. M H Key et al, Phys Fluids **26** 2071 (1983).

3. R P W McWhirter and A G Hearn, Proc Phys Soc **82** 641 (1983).

4. M H Key and G J Pert, Rutherford Appleton Laboratory Report RAL-86-046, A5.38 (1986).

5. D Brown et al, Rutherford Appleton Laboraotry Report RAL-88-042, 58 (1988).

6. D R Bates, A E Kingston and R W P McWhirter, Proc Roy Soc, A267 (1962).

7. C Chenais-Popovics et al, Phys Rev Lett **59** 2161 (1987).

8. R A Smith et al, Rutherford Appleton Laboraotry Report RAL-88-042, 5 (1988).

9. A K Davé and G J Pert, J Phys **B17**, 4953 (1984).

A5	**VULCAN OPERATIONS AND DEVELOPMENT**	Pages
A5.1	INTRODUCTION AND OPERATION STATISTICS	131-133
A5.2	VULCAN UPGRADE	133-141
A5.3	GLASS LASER DEVELOPMENT	141-153
A5.4	COMPUTER CONTROL AND DATA ACQUISITION	153-154
A5.5	TARGET FABRICATION AND DEVELOPMENT	154

A5.1 INTRODUCTION AND OPERATION STATISTICS

C B Edwards and C N Danson (RAL)

The year began with an 11 week shutdown for the implementation of the Phase I upgrade. This involved the re-staging of VULCAN together with the installation and commissioning of the new capacitor room, the new 108 box disc amplifiers and the new design rod amplifiers. Details of the upgrade are presented in section A5.2.

Ease of alignment and operation of the system has significantly increased in the post upgrade period. The beam quality has been much improved allowing more energy to be delivered to the target areas. For six beam experiments infrared energies have been measured at 1.7 kJ, whilst green energies have been measured at 800 J. For single beam operation typical long pulse infrared energies are in excess of 250 J.

The experimental period immediately following the upgrade was unproductive, due to a number of factors which extended the re-commissioning of Vulcan; and target area staffing problems caused some loss of experimental time during the summer in TA West. With this exception, however, the post-upgrade period has been one of the most productive in terms of original experimental data and facility development.

Shot statistics for the period show a continued high shot rate and are summarised in Table 1. All three main target areas have been operational through the year with approx 1300 full disc shots delivered during experiments. For the first time TA4 has been fully operational over the year with approximately 500 target shots. Maximum Energy per pulse is 15 J. These have been used for X-ray microscopy, instrumentation development and for some small scale experimentation.

The flexibility of the system has been extensively tested with many different system configurations. These have included: a Beat-Wave experiment, the ISI experiments (discussed in detail in section A5.3.1 and A2.3), a short pulse X-ray laser experiment, and also the standard system configurations.

During the past year both staffing and operational aspects of the VULCAN target areas have been affected as a result of staff changes within the division. There is a greater emphasis than previously on the engineering aspects of operations, and this is now contributing to improved reliability of equipment in the Target areas.

Due to continuing problems with staffing levels, it has been necessary to authorise some facility users to act as target area duty operators to provide operator cover outside normal working hours. This system has worked very successfully to date, and has significantly increased the amount of facility time available to users.

A recent contribution to efficient operation is the introduction of a target area "set-up" week. In the past it had been found that target area staff had very restricted access to laser time for tuning, timing and pointing activities. During maintenance VULCAN is typically unavailable, whilst during the first week of an experiment users are understandably concerned with the particular experimental details relating to their experiment. This situation developed to the point at which it was impossible for target area staff to make anything but short-term solutions to long term problems.

The "set-up" week also gives valuable time to users for the optimisation of complex experimental arrangements, and smoothes the transition between experiments. To date this arrangement has proven very successful, resulting in a much longer data-taking phase during a run.

We are pleased to acknowledge the assistance by users during the "Set-up" weeks which has greatly contributed to the success of recent experiments.

Table 1

SHOT STATISTICS POST UPGRADE

485 disc shots into TA East
215 disc shots into TA West
622 disc shots into TA2
607 shots into TA4

Details of particular experiments are as follows:-

Date	Experiment	Comments
22 May 88	Ne like X-ray lasers	No useful shots (upgrade)
22 May 88	RT/particle radiog.	17 disc shots (upgrade)
19 June 88	Long scale length plasmas	97 disc shots
17 July 88	K edge spectroscopy	108 disc shots
17 July 88	Stellar opacity	85 disc shots
14 Aug 88	Beatwave	115 disc shots
4 Sept 88	Pulsed Exaffs of iron	21 disc shots
2 Oct 88	Ablation pressure and shock convergence	21 disc shots
2 Oct 88	Short pulse X-ray laser	46 disc shots
30 Oct 88	Hot matter stopping power	59 disc shots
30 Oct 88	Resonant photo-absorp.	134 disc shots
4 Dec 88	ISI experiment; scatt.	133 disc shots
15 Jan 89	Particle radiography	76 disc shots
15 Jan 89	Silicon diffraction	96 disc shots
19 Feb 89	X-ray laser	111 disc shots
19 Feb 89	Moire deflectometry	108 disc shots

Much time has been spent over the year on the detailed planning of the final phase of the laser upgrade, which is due to start in the last week of April 1989. The aim is to provide better beam imaging into TAE by the installation of six relay tubes, and to install the hardware and optics to carry 2 x 150mm beams into TAW. The system initially will be commissioned with 2 backlighting beams but only one will be expanded and amplified at 150mm diameter.

A5.2 VULCAN UPGRADE

A5.2.1 Vulcan Laser System

C N Danson, The Glass Laser Operations Group and the Mechanical and Electrical Support Group

Introduction

The beginning of the year was dominated by an 11 week shutdown (28 Feb- 15 May) for the implementation of Stage I of the Phase I upgrade. The Phase I upgrade was approved in 1983 and included the building of TAW and TAE together with an enhancement to the laser output. The target areas were completed some years ago and have been working effectively since then.

The enhanced laser design was finalised after 'hot operation' tests were completed in November 1986[1]. The design concept was to re-stage the laser such that good quality high output fluences would be obtained. The beam would then be slightly expanded and propagated to the target areas. The larger beam would reduce the possibility of damage to target area optics. To avoid the losses in propagating the beam to the target the optics associated with the target chamber would be anti-reflection coated. In operating a target area at these higher fluences it was realised that the areas would have to ensure that optics remained free from dust etc, therefore TAE and TAW were converted to clean areas.

The laser upgrade has been implemented in two independent stages. This was necessary as the funding limited what could be achieved in 1988, and it was considered desirable to reduce the overall system downtime. Stage II of the laser upgrade is planned for May/June 1989.

Stage I involved upgrading the main six beam output by installing the RAL design 108 mm diameter box amplifiers and new vacuum spatial filters to improve the relaying of the beam. At the same time the rod stages were totally reconfigured to provide a good input beam quality into the disc amplifiers. In preparation to upgrade the backlighting capabilities the existing capacitors were all transferred to the new capacitor room.

Stage II will involve the construction and installation of two 150 mm box type disc amplifiers with associated VSF's as an enhancement to the backlighting capabilities. In order to propagate these beams to the target areas it was realised that the switchyard would have to be significantly modified, this will include moving the timing trombones from the switchyard into TAE. For TAE to efficiently use the output power of Vulcan, beam relay optics will also be installed between the switchyard and the input to the area.

System Description

A schematic of the upgraded Vulcan laser system is shown in Figure A5.1. As can be seen the general layout is not dissimilar to the previous configuration; the main difference is with the staging of the system. To implement the changes every piece of hardware was removed from the laser areas apart from the oscillator bench and pre-amplifier stages, shown collectively in the diagram as "oscillators". By starting with a "clean sheet" as it were it allowed us to incorporate many of the add-on modifications, made to the system since the previous upgrade, in a more permanent manner. One of the main constraints in designing the upgrade was that the flexibility established for previous operations would not be compromised.

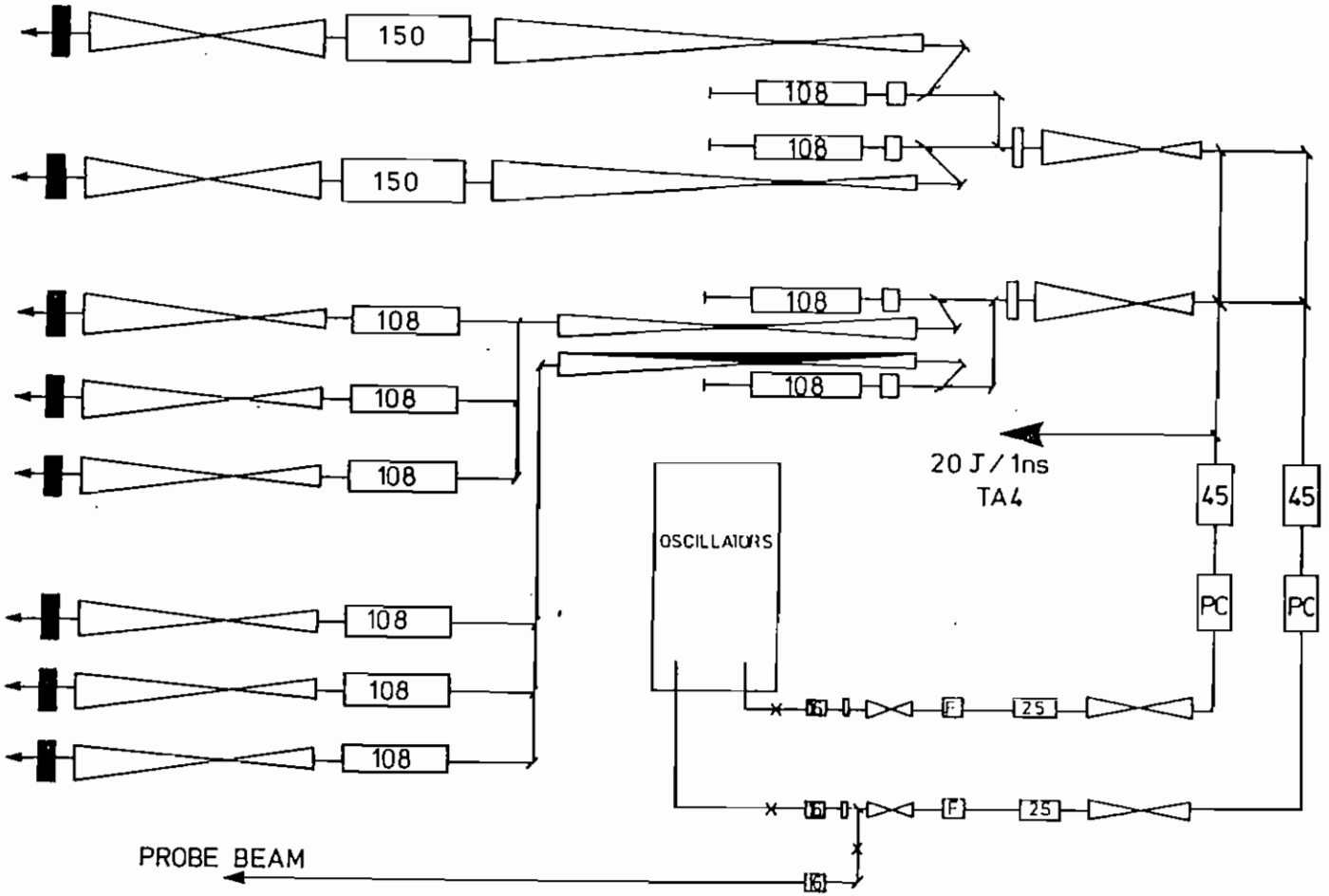


Fig A5.1 Schematic Layout of the Upgraded Vulcan Laser System.

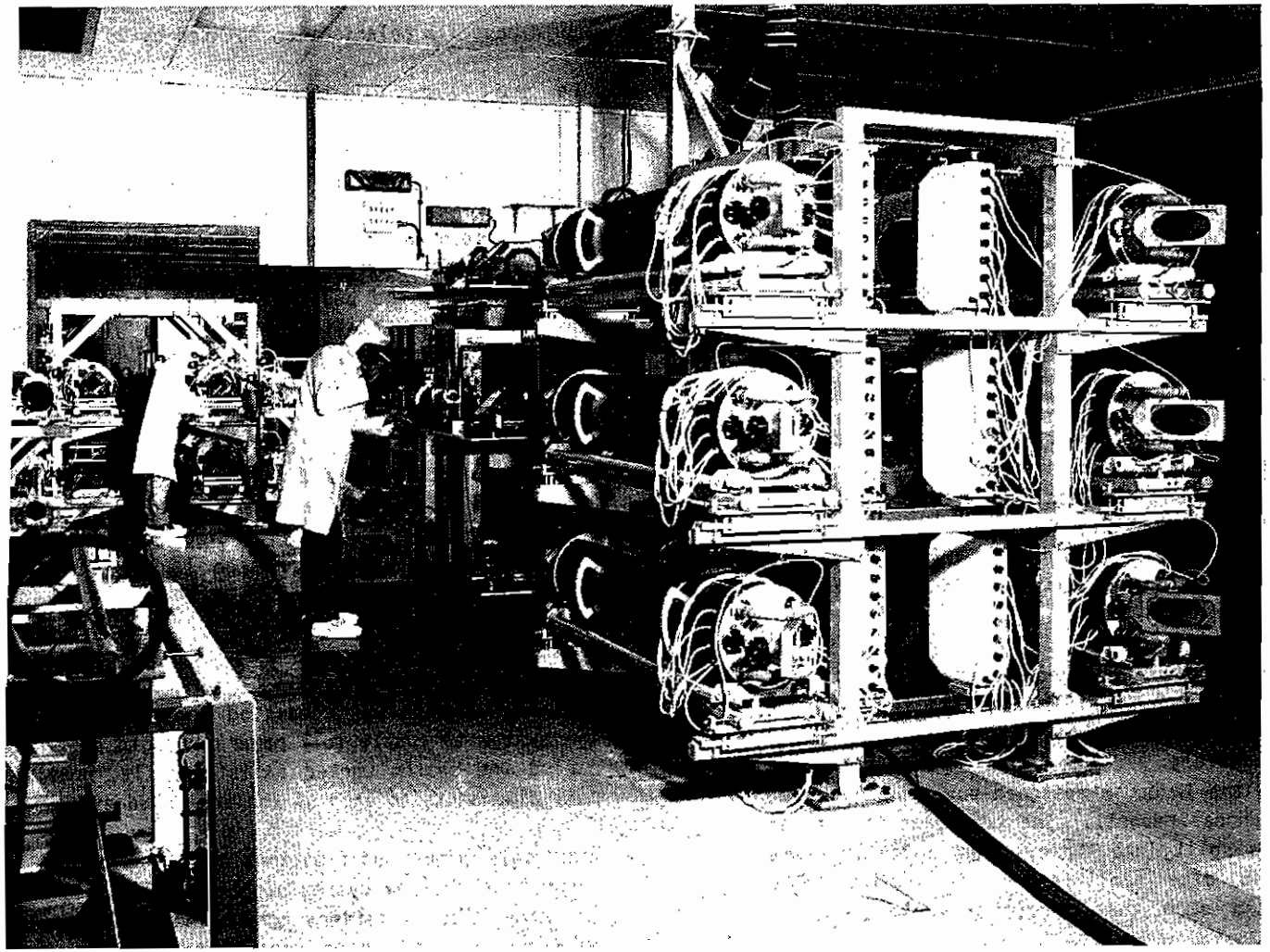


Fig A5.2 *Output Amplifying Stage of the Upgraded Vulcan Laser System.*

The optical pulses are amplified in two identical, but independent, rod amplifier chains. The two chains are referred to as the long and short pulse amplifier chains due to the standard laser configuration, but recently these chains can amplify any of the appropriate pulses for the experiment. After the pulse leaves the oscillator bench it is first passed through an air spatial filter and is then amplified through a 16 mm diameter rod, (all the rod amplifiers used in the upgrade are designed and built in-house and are described in detail in last year's annual report). After amplification the beam is apodized through a soft aperture and then spatially filtered. Following the spatial filter the beam is collimated and remains so through the rest of the amplification stages. There are two further stages of rod amplifiction each containing some degree of isolation: prior to the 25 mm diameter rod there is a Faraday rotator; and prior to the 45 mm rod there is a Pockels cell with a gate time of about 25 ns. To limit the growth of non-linear perturbations on the beam there is also a vacuum spatial filter between each of the amplifiers.

The energy at the output of the rod amplifiers can be 15 Joules in the long pulse and up to 4 Joules in the short pulse. The maximum total B-integral calculated through the rod amplifier stage is 3.0, while the maximum B-integral calculated for any one stage in the chain is about 1.3. This therefore should allow the generation of good quality short-pulse beams suitable for injection into the disc amplifier stages.

The two rod chain outputs can then be directed into either the six beam system or the "backlighting" arm. The beam to the six beam system is first split into two and these are then amplified in double passed disc amplifiers. (The disc amplifiers used throughout the system are the in-house designed box type described in detail in last years annual report). The two beams then enter LA2 where each of them is split into three, after which they are amplified in single pass disc amplifiers. To enable these amplifiers to be operated such that servicing would be at a minimum, it was decided to operate them with their discs mounted vertically. As the discs are operated at Brewsters angle it was therefore necessary to provide a laser beam which was horizontally polarised. The beams entering the six way split are vertically polarised, therefore the split was designed such that each beam would have its polarisation rotated by 90°.

The peak fluence in the system prior to the upgrade was at the output of the driver disc stage, since the six output beams were derived from a single disc driver stage. To enable the driver disc to be double passed it was necessary to use a polariser which was susceptible to optical damage. This therefore limited the output of the system to below the damage threshold of the polariser. With the upgrade the system output is still limited by damage to the polariser, but the peak fluence is now at the output of the six single pass disc amplifiers, allowing significantly higher output energies from the system. A view of the Vulcan laser area shown from the output of the six amplifiers is shown in Figure A5.2.

The "backlighting" beam following the Stage I upgrade consisted of a double passed 108 mm diameter disc amplifier with two stages of spatial filtering to relay the beam to the target area. During the Stage II upgrade the backlighting beam will be as presented in Figure A5.1. During the Stage I period the hardware for these modifications was installed.

System Performance

Once the upgrade was completed one month was taken commissioning the system to enable full power shots to be fired. Following this period the system worked satisfactorily, providing on average 85 full disc shots to each of the scheduled experiments.

With only minor modifications to the planned layout it has been shown that the new system has been relatively easy to operate. Of the nine disc amplifiers to be included in the Stage II upgrade only one has had to be removed to be maintained; this has given confidence in the reliability of the amplifiers. When the new rod

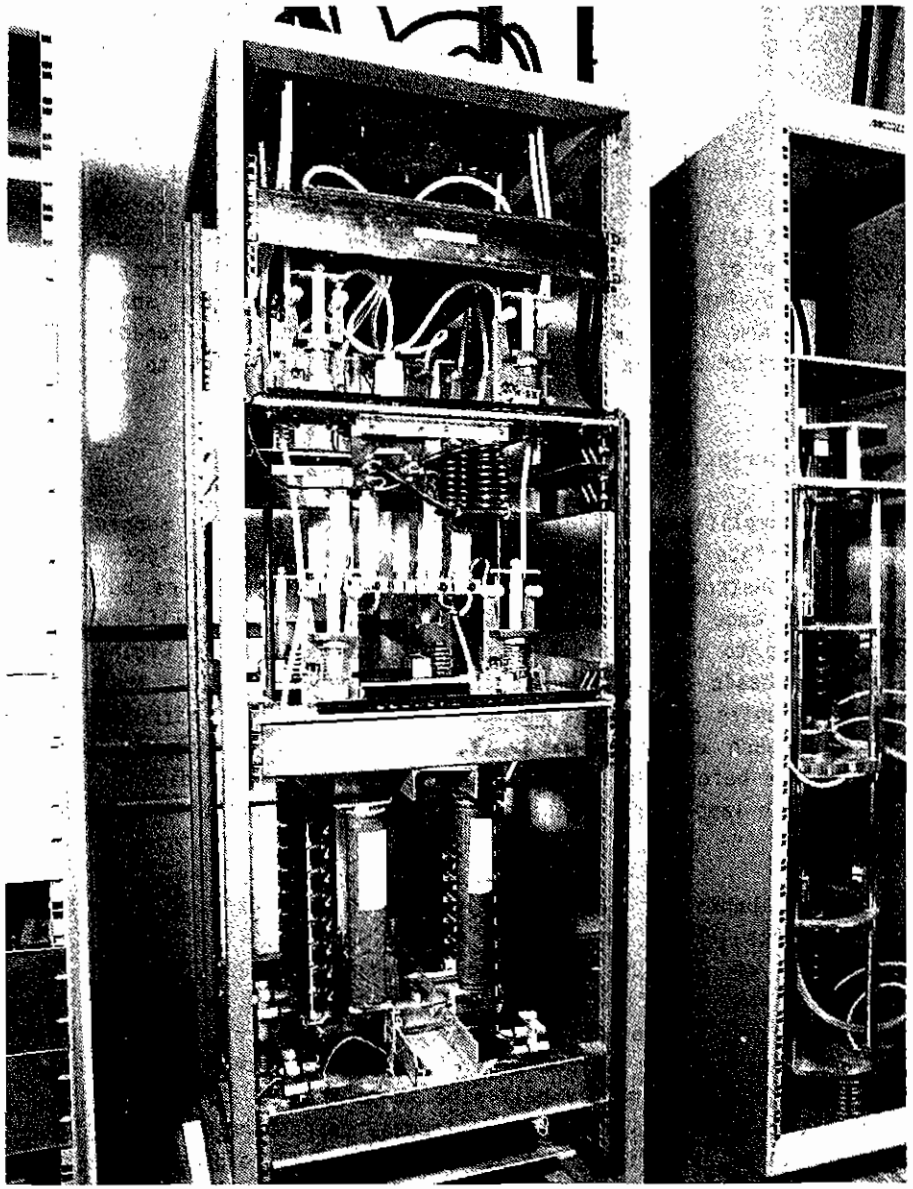


Fig A5.3 Disc Amplifier Selector Units.

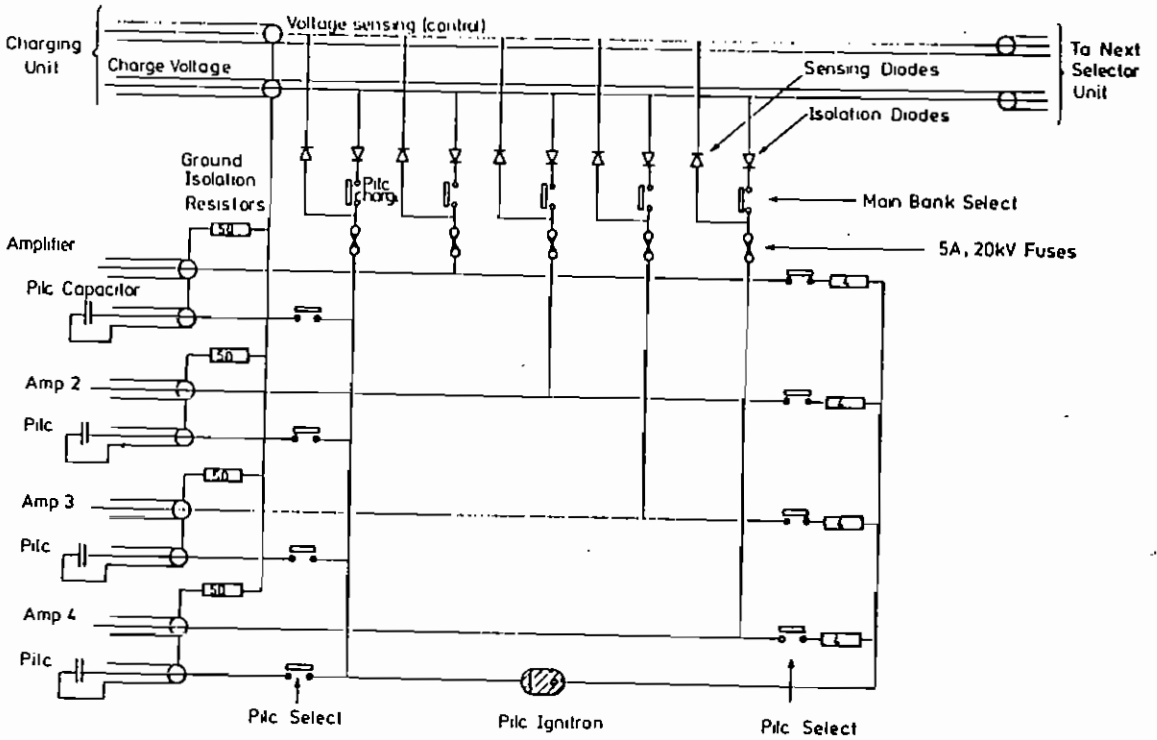


Fig A5.4 Disc Amplifier Selector Unit.

amplifiers were commissioned a problem was encountered with the lifetime of the flashlamps. The adhesive which held the electrode housing to the glass tubes was degrading over a few weeks operation. We have not seen any problems since a new adhesive was used by the manufacturers.

In summary the upgrade has proved very successful allowing good quality beams at nearly twice pre-upgrade energy levels to be delivered to the three main target areas. The highest infra-red energy shot was approximately 1.73 kJ while the highest green energies obtained were about 800 Joules. For normal operations we have observed no problems in operating the system at 1.5 kJ in the infra-red.

References

1. C B Edwards, RAL-87-041, Annual Report to the Laser Facility Committee 1987, Section C1.2 p 221.

A5.2.2 North Capacitor Room Design and Installation

P Gottfeldt, W Lester and D Pugh (RAL)

Overview

The rebuilding of VULCAN, based on new amplifier designs, required a complete re-configuration of the capacitor banks. The energy requirement for the 108 mm amplifiers was reduced from 200 KJ to 180 KJ and the number of flashlamps reduced from 20, 15 mm bore to 8, 25 mm bore. The 150 mm amplifiers similarly require 8 flashlamps but the energy requirement is 200 KJ. The entire capacitor bank was relocated in the North extension of R1 necessitating the design and construction of a new control system. Significant changes were also made to the method of amplifier selection. New Ignitron trigger amplifiers were designed based on SCR's, rather than Krytrons, and the timing system updated to accommodate the extensive use of fibre optics for transmission of synchronisation pulses. Furthermore the number of Ignitron switches was increased to provide one Ignitron per amplifier so that each amplifier could be individually timed relative to the laser-pulse. By deliberately mistiming the amplifiers fine tuning of the energy balance in the output beams could be achieved. Two more charging units were required for the increased storage capacity. The total charging capability is now 42 KJ/s for a total energy storage of 2.2 MJ. New capacitor racks were constructed with 7 levels instead of 5 to optimise the use of the space available. New racks were also constructed for the Faraday isolator capacitor bank but no significant changes were made to the system.

Functional Description

In operation amplifiers are selected by routing the charging supply to the appropriate capacitor banks using Ross HV relays. Selector units were constructed each controlling up to 4 amplifiers but provision was made for linking these where more than 4 amplifiers were connected to one supply. The units are depicted in Figure A5.3 and the basic circuit in Figure A5.4. It will be seen that the selector units also incorporate the lamp check (PILC) circuit. The lamps of each amplifier are tested for integrity by applying a 5 KJ discharge before the main 180/200 KJ pulse is applied. The current in each lamp pair is monitored via the CAMAC control system in both cases.

The capacitor banks for each amplifier are divided into 4 pulse forming networks (PFN). In the case of the 108 mm amplifiers each PFN consists of 225 μF capacitance, charged to 20 KV, and discharging into one flashlamp pair in series with a 220 μH inductor. For the 150 mm amplifier the capacitance is increased to 250 μF and the inductor is 200 μH. In both cases this gives a current pulse of approximately half sine shape and 450 μs duration at half height. The peak current amplitudes, corresponding to the 108 mm and 150 mm amplifiers, are 9.4 KA and 10.7 KA respectively.

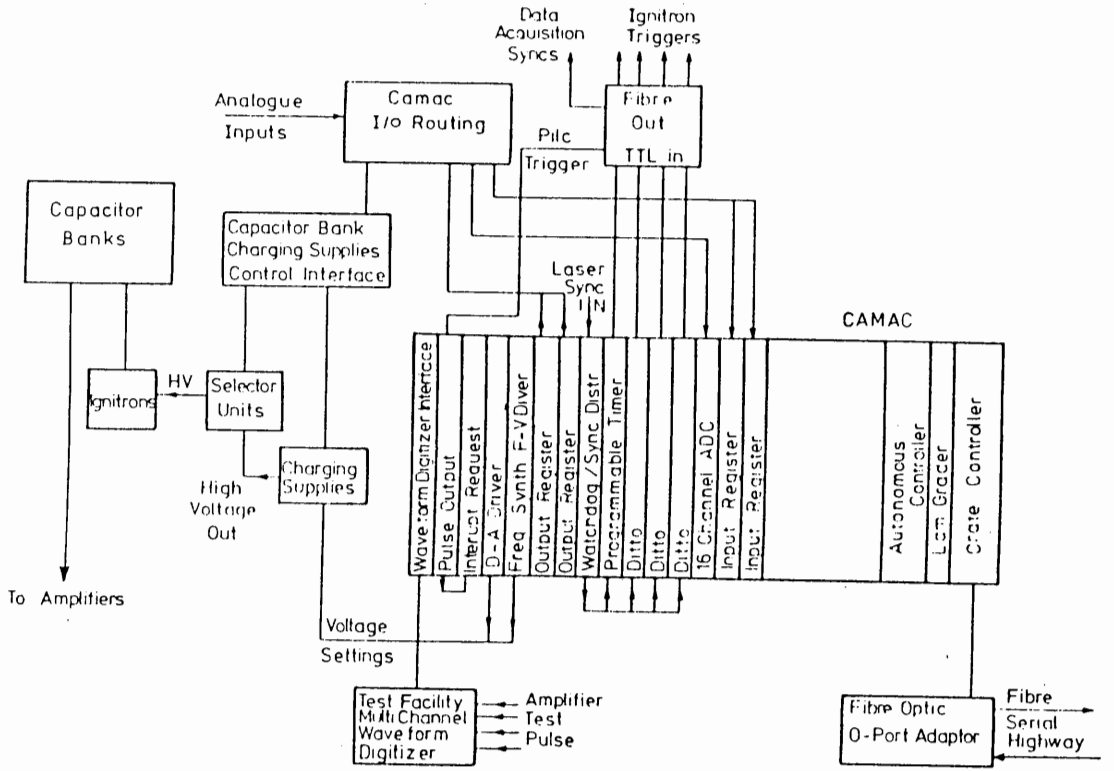


Fig A5.5 Disc Amplifier Energy Storage, Control and Instrumentation.

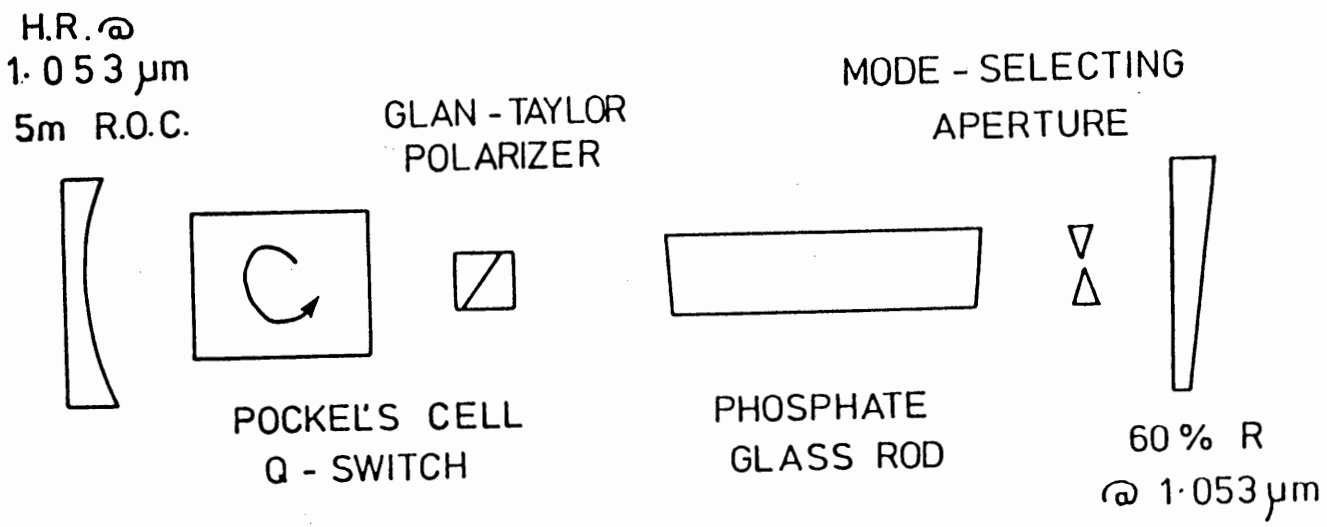
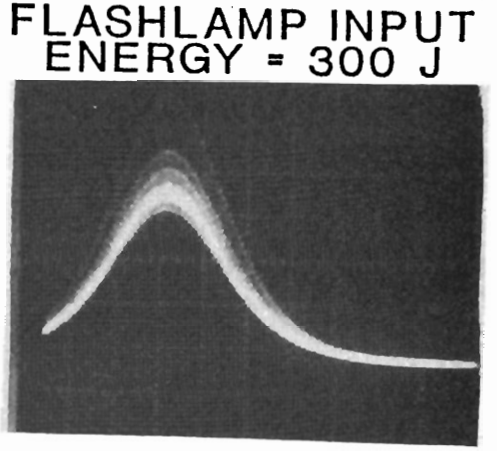


Fig A5.6 Schematic of the ISI Broad-Band Oscillator.



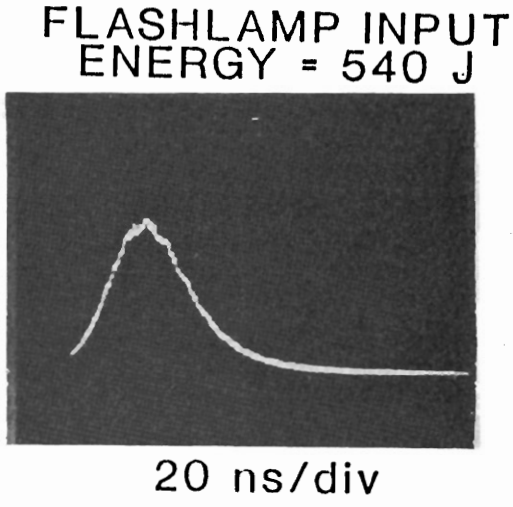


Fig A5.7 Temporal Profiles of the Q-switch Envelope from the ISI Broad-Band Oscillator.

The capacitors of the PFN are split into two sections with a 5000 KA fuse connecting them. This is to prevent all the stored energy from being released in a possibly faulty capacitor with the risk of rupturing the case. A 20 ohm resistor, in parallel with the fuse, ensures that the section of the PFN remote from the dump relay does not become isolated. The dump system is backed up by motor driven shorting switches to allow all capacitors to be short-circuited when access to the capacitor area is required or when work on an amplifier is necessary. Amplifiers are connected to the capacitor banks using RG217 cable. Because pulse currents are now so much higher, more than twice those of the old 20 lamp amplifiers, parallel cables have been used for the longer runs to reduce cable losses.

All the amplifiers are connected to building earth at one point in the laser area. To prevent large return currents flowing in cables other than those of the amplifiers in use, ground isolating resistors have been incorporated in the selector units. Such earth currents could be avoided altogether by earthing the system at the charging supplies but this was considered less safe from an operational aspect.

Control and Instrumentation

The capacitor banks and charging equipment are controlled using CAMAC. A single crate in the capacitor area is connected to the control room using the serial branch with optical fibre adaptors. The overall scheme is shown in Figure A5.5. Synchronizing pulses are also transmitted on optical fibres so that the control room is galvanically isolated from the HV equipment. Analogue inputs are isolated from CAMAC using isolation amplifiers while analogue outputs are isolated using optical isolators and driving digital to analogue convertors. A second system has recently been developed using a frequency synthesizer, built as a CAMAC module, driving a frequency to voltage convertor down an optical fibre. Simple I/O switching connections have, in general, been optically isolated although relays have been used in certain cases.

The autonomous controller (LSI 11/23 computer) is used at present to detect end of charge in correspondence with the pattern of amplifiers and Faraday isolators selected. It communicates with the main control computer, now being changed from a GEC 4080 to a network of PC compatibles, via a common register. A watchdog module has been built which is activated at the beginning of charge. If either the LSI 11/23 or the main control computer do not keep it active during charge it is assumed there has been a system failure, the charging system will shut down and the capacitor banks dumped. It is intended to extend the role of the LSI 11/23 in monitoring the system so that any malfunctions can be detected, and appropriate action taken, before damage occurs.

The operator interface uses the touch screen in the control room. A main menu is presented to the operator from which he can progress to sub-menus for selecting/de-selecting particular amplifiers and Faraday isolators. A regress touch position is provided to return to the main menu. Delay times and voltage settings are entered using a keyboard. Start of charge is signalled using a button switch.

A5.3 GLASS LASER DEVELOPMENT

A5.3.1 Induced Spatial Incoherence Studies

C N Danson, R Bann, D Pepler, N Rizvi, I Ross, P Rumsby, R Jackson (RAL)
S E Coe, T Afshar-Rad, M Desselberger and O Willi (Imperial College)

Introduction

Interaction experiments have generally suffered due to poor beam uniformity in the far-field of the laser beam. Most of these effects are as a direct result of the coherence of the laser. Several different methods have been employed in an attempt to produce optical smoothing. These have included: Random Phase

Plates (RPP)[1]; Induced Spatial Incoherence (ISI)[2]; Flys Eye Lens[3]; Broadband/Stack arrangement[4] and the Broadband/Fiber arrangement[5]. These methods can be grouped into two basic techniques:-

(i) The first method is to reduce the spatial coherence by introducing a random phase array across the beam, either by a RPP or a Fly Eye Lens. The far-field pattern is determined by the superposition of effectively many independent beams. This produces a high spatial frequency interference pattern across the focal spot. In most circumstances the plasma should be insensitive to these spatial frequencies.

(ii) The second method is to reduce the spatial coherence of the output of a broadband oscillator by introducing delay into one part of the near-field relative to another, the delay being significantly larger than the coherence length of the laser. The far-field distribution produces an interference pattern which is rapidly changing with time, smoothing out the optical distribution.

In order to provide the facility with smooth far-field profiles it was important to consider several constraints:-

(i) System flexibility - with more than one experiment operational at any one time, and the rapid change over in configurations it is important to maintain the flexibility of the system.

(ii) Cost - with a multi-beam system it would be impractical to provide output ISI echelons for the 12 beam and 6 beam target areas.

(iii) Focal spot requirements - with a broad based user community the focal spot requirements differ significantly from experiment to experiment. The final configuration should allow focal spot sizes of 25-1000 microns to be available.

These constraints led to a system which used a combination of the techniques described above.

A broadband oscillator was built and an ISI transmission stack was used to generate spatial incoherence on a scale length of 1mm. This was positioned prior to the final amplification stages such that only one device would be necessary for multi-beam experiments Unlike other ISI schemes the focal spot sizes available were limited as experiments have to be carried out in the far-field. One method of increasing the spot size would be to increase the number of elements in the ISI array. There is however a limit to the energy available with large arrays due to the onset of small scale self-focussing, making this unacceptable for most experiments.

To produce the larger focal spot sizes it is possible to go to longer focal length lenses, although space considerations place a limit on this technique. Therefore it was necessary to introduce another scheme. During the experiment in December a RRP was used both in conjunction with the broadband ISI beam and with a normal narrow-band beam.

Broad-Band Oscillator Development

The oscillator developed for the ISI experiments was of a design similar to that used for a broadband silicate oscillator[6]. A schematic of the cavity is shown in Figure A5.6. A high gain Phosphate glass rod was used to produce a bandwidth of 1-2 nm, necessary to produce a coherence length of about 2 ps. The cavity consists of a 5m radius of curvature HR mirror and a 60% reflector as an output coupler. To produce the high gain a 9 mm diameter rod is pumped by two flashlamps supplied with an electrical input energy of 540 Joules.

The oscillator is prevented from lasing by holding the cavity in a low-Q state using a Pockels cell Q-switched. At the peak of the fluorescence the cavity is switched to the high-Q state by removing

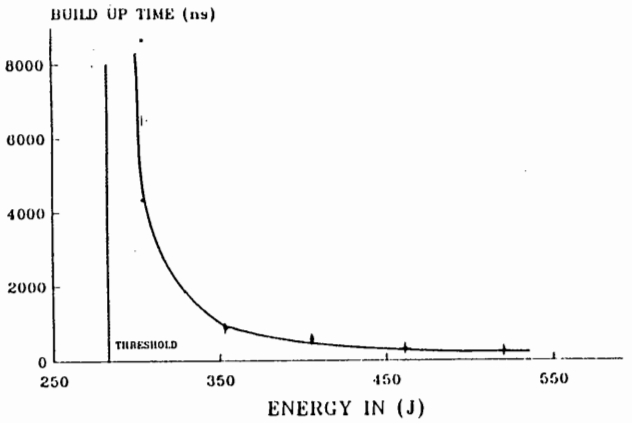


Fig A5.8 *Q-switch Build-Up Time for Varying Flashlamp Input Energy.*

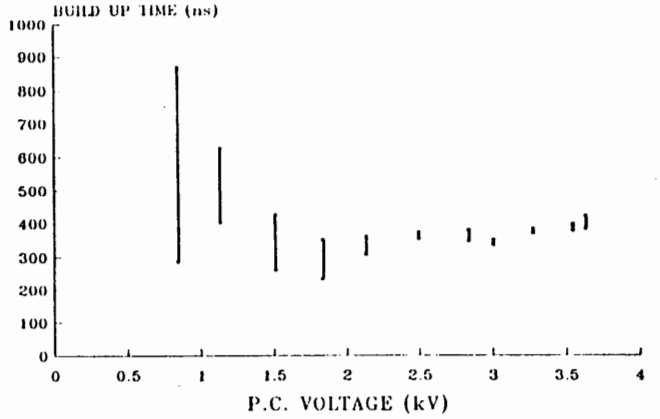


Fig A5.9 *Q-switch Build-Up Time for Varying Pockels Cell Voltage.*

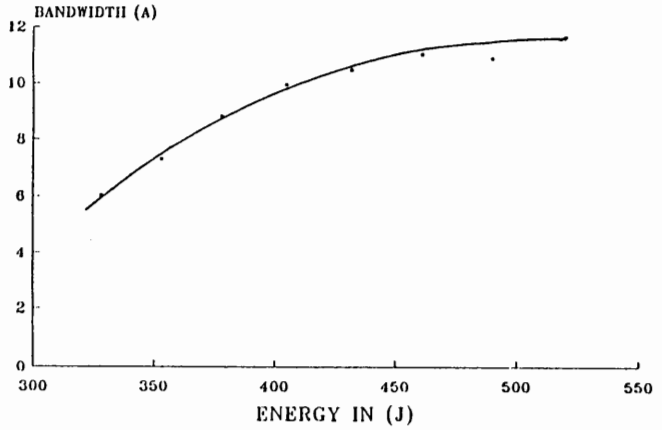


Fig A5.10 *Bandwidth Measurements for Varying Flashlamp Input Energy.*

ISI Broad-Band Oscillator Characterisation

the quarter-wave volts from the Pockels cell. This then produced a 40 ns Q-switched envelope which can be seen in Figure A5.7.

The two traces shown in the figure are the Q-switch envelopes produced at different flashlamp energies. With an input energy of 300 J, just above lasing threshold, a long 500 ns envelope is generated. The pulse has significant temporal noise present and shows poor stability from shot to shot. This is because there are few longitudinal modes present at these input energies. As the energy to the flashlamps is increased the Q-switch envelope becomes shorter, the temporal profile is much smoother and more consistent from shot to shot.

In order to synchronise the oscillator output to the rest of the pulse generation system on Vulcan it is necessary to have consistent Q-switch build-up times. Figure A5.8 shows the Q-switch build-up time as a function of input energy to the flashlamps. As the energy to the lamp is increased the build-up time decreases and becomes more stable. This can be seen as a reduction in the size of the error bars on the graph. At the operating flashlamp energy of 540 J the Q-switch build-up time was measured at approximately 300 ns with a standard deviation of 5 ns. With a 40 ns pulse this low jitter allows synchronisation with other stabilised oscillator systems.

The other variable within the cavity that was readily adjustable was the voltage applied to the Pockels cell Q-switch. The build-up time and jitter of the Q-switch envelope as the Pockels cell voltage was adjusted is shown in Figure A5.9. At low voltages a large jitter in the build-up time is observed. At a voltage of 3.2 kV a minimum jitter is seen. This voltage corresponds to the quarter-wave switching of the Pockels cell. In this state the cavity should not lase prior to the Q-switch. The oscillatory nature of the curve is associated with slight drifting of the cavity alignment, because this data was obtained using the oscillator in a laboratory which was not temperature stabilised.

To measure the bandwidth of the optical pulse the output of the oscillator was first expanded and collimated and was incident on a 1200 lines/mm diffraction grating. The first order diffraction pattern was focused using a one meter focal length lens onto a CCD camera. The signal from the camera was captured using an image framestore. The framestored image could then be analysed on an Apple II computer using in-house software. The system was calibrated by inserting a Fabry-Perot etalon into the oscillator output. The resolution of the system was limited both by the grating and the image processing giving a resoltuion of 0.03nm.

The bandwidth of the pulse was measured for various flashlamp input energies. The results are shown graphically in Figure A5.10. As the input energy was increased the bandwidth also increased. At the operating flashlamp energy of 540 J the bandwidth was measured at 1.2 nm. This should produce a coherence length of about 2.8 ps. A technique was established to directly measure the coherence length of the pulse by replacing one of the mirrors of a Michelson interferometer by a diffraction grating operated in littro configuration. The coherence length was measured by measuring the fringe visibility across the beam. Using this technique the coherence length was found to be 2-3 ps. This is in agreement with the calculated values using the bandwidth measurements.

It is believed that further work will produce bandwidths of 3-4 nm using techniques similar to those described in ref 6.

ISI Stack and System Performance

The 40 ns broadband oscillator pulse was injected into the Vulcan amplifier system in place of the normal 100 ps short pulse oscillator. A 1 ns pulse was sliced from the Q-switched envelope by using the Pockels cells in the synchronised switchout system. A schematic of the amplifying stages of Vulcan used for the experiment is similar to that shown in Figure A5.1. The pulse was propagated down the outer chain of rod amplifiers until the beam was 40 mm in diameter and had an energy of about 5 J. At this point in the system the beam was passed through the ISI stacks shown in Figure A5.11.

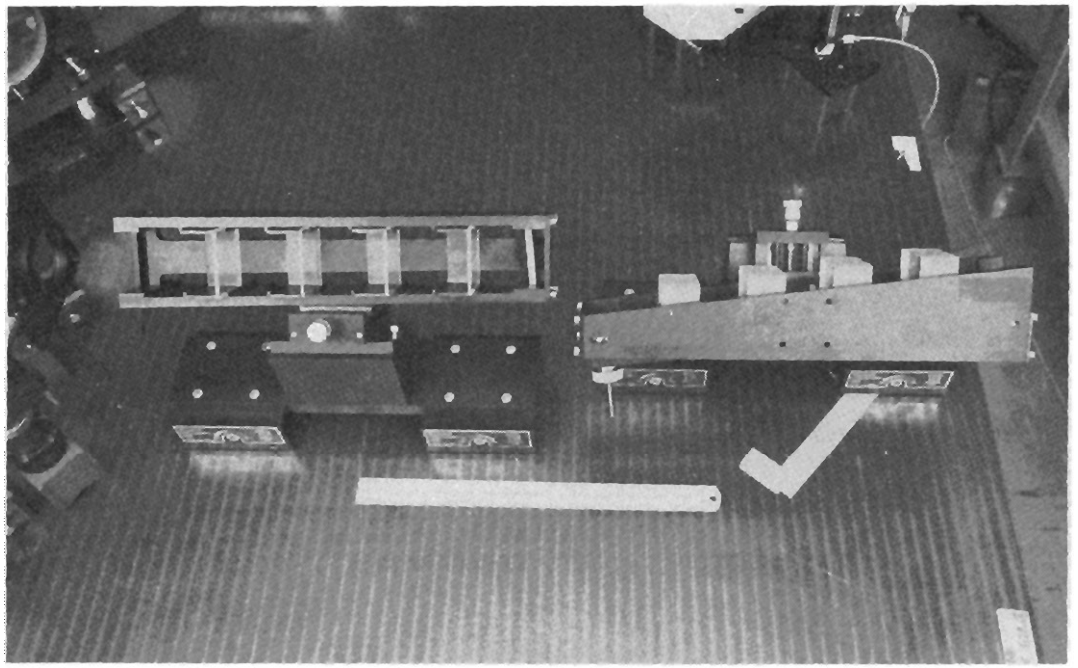


Fig A5.11 The ISI Delay Stack.

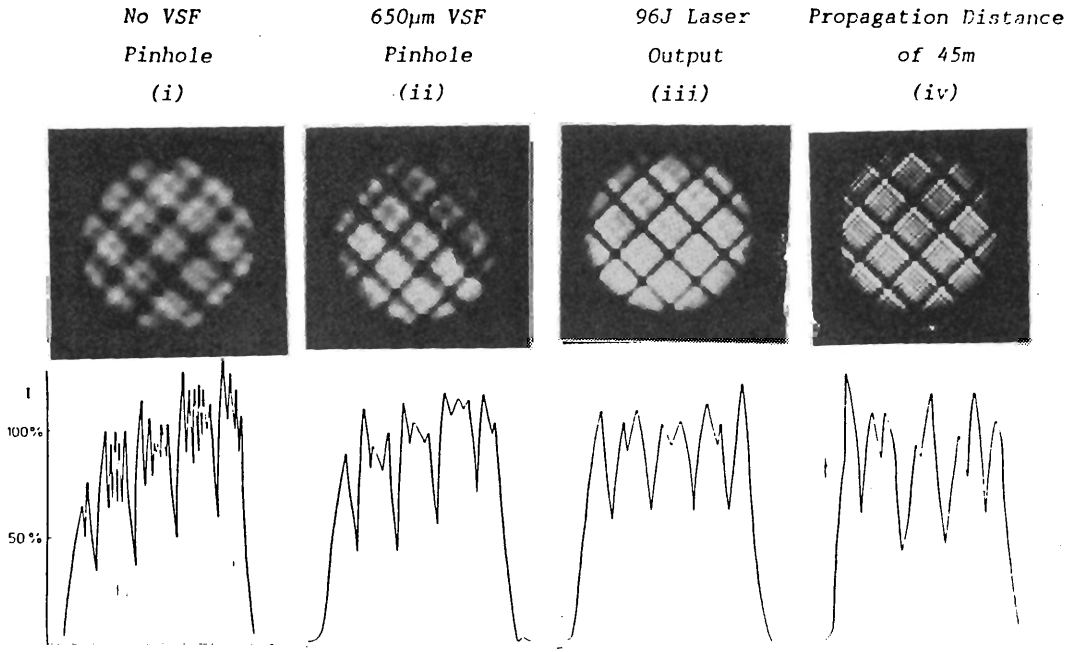


Fig A5.12 Beam Profiles at Various Stages of the Laser System.

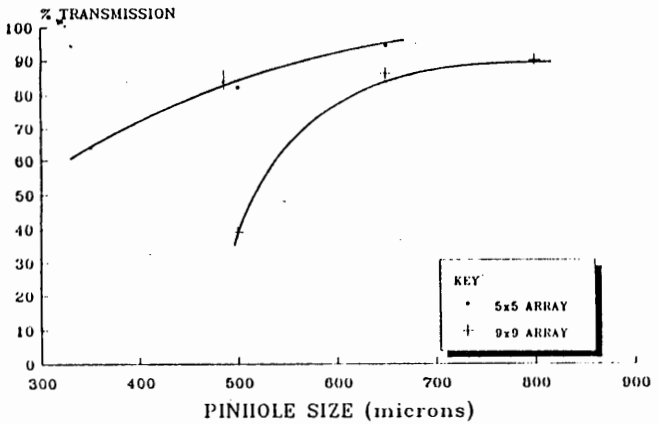


Fig A5.13 Transmission of Pulse Through Vacuum Spatial Filter Pinholes.

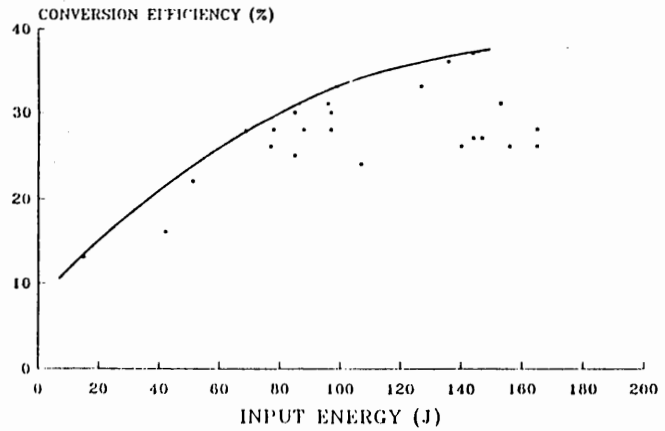


Fig A5.14 Disc Amplifier Gains for both Narrow-Band and Broad-Band Pulses

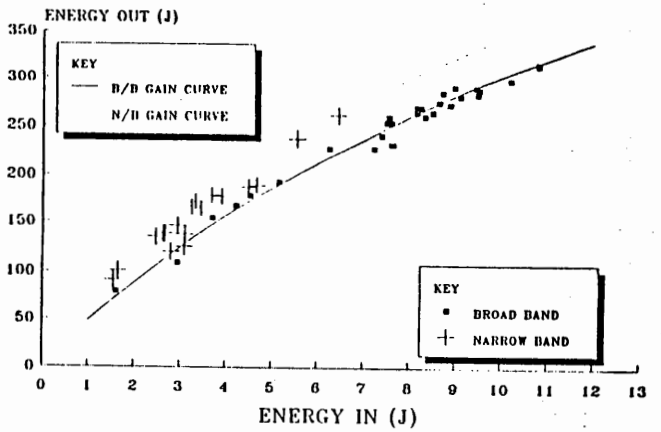


Fig A5.15 Green Conversion Efficiencies of the ISI Pulse.

Vulcan System Performance Using the ISI Pulse

Each delay stack could be loaded with between 1 and 9 glass blocks. All the blocks were anti-reflection coated to minimise the losses which would occur if the beam had to transverse 18 air-glass interfaces. Blocks of 2 thicknesses were used, 30 mm and 3 mm, to allow variable delays to be induced. Keeping the blocks normal to the beam, to minimise edge losses, they could be adjusted into a step formation so that different sections of the beam would pass through different numbers of blocks. Using two stacks in series with the step formations perpendicular to each other, a grid of small beamlets was produced. The first stack contained 30 mm blocks to produce steps separated by large delays, the second stack split these steps into square sections, each separated by a smaller delay generated by 3 mm blocks. In this way a grid of small beamlets, each with a different delay from any other in the beam, was produced.

The 30 mm and 3 mm blocks produced optical delays of 50 ps and 5 ps respectively. The minimum difference in time of propagation between any two beamlets was therefore greater than the coherence length of the pulse. A temporal broadening resulted from the induced delay so that for a 5x5 array of beamlets, the maximum delay time was 220 ps lengthening the pulse to 1.2 ns. This had the effect of smoothing the temporal intensity profile. Figure A5.11 shows the stacks loaded for the 5x5 array format which was used for the first series of experiments.

The grid structure can be seen on the unfiltered beam profile in figure A5.11(i). The assymetric diffraction pattern produced by the edge of each block was thought to be associated with the phase shifts induced by the anti-reflection coatings on the blocks. The scan of this unfiltered profile shows 50% intensity modulations on the beam. There is also high frequency spatial modulation associated with each beamlet. If amplified in this state, the high frequencies could bring about small scale self focusing effects producing hot spots and causing serious damage to the system. Therefore the beam was immediately spatially filtered and expanded up to 100 mm in diameter. Figure A5.12(ii) shows the higher spatial frequencies eliminated in the spatial filter to produce significantly smoother beamlets.

In this form the pulse was amplified down the backlighting arm of the system. This comprises a double passed disc amplifier followed by two stages of spatial filtering which also help to image relay the beam into the target areas. Figure A5.12(iii) shows the beam profile after amplification to the 96 J level. Saturation in the amplifiers helps to smooth out the modulated beam profile, reducing the 50% modulation down to 30% for this energy output. Figure A5.12(iv) shows the beam quality after propagation over 45 m. Diffraction of the higher spatial frequencies has broadened the modulation minima on the beam. This diffraction loss can be controlled by introducing image relaying into the system.

In the spatial filter immediately after the delay stacks, the focal spot of the beam consists of a central spot, centred on a cross of diffracted spots. The central spot contained the energy distributed in the lower spatial frequencies and so selective filtering of the cross pattern allowed the higher frequencies to be removed. Most of the energy was contained in the lower frequencies and so greater than 90% transmission could be obtained in passing through the VSF. A 650 micron diameter pinhole was found to be a good compromise when the system was run with a 5x5 array of beamlets but as figure A5.13 shows, 800 microns was necessary for a 9 x 9 array. Reduction of pinhole size beyond these values resulted in the removal of energy from the whole beam itself without a significant improvement in beam quality.

The gain of the double passed disc amplifier dropped to 80% of that seen in narrow band operation. This is thought to be due to the gain curve of the glass in the amplifiers being better matched to the lasing line of YLF than to that of the glass in the broad band oscillator. The associated gain curves are reproduced in Figure A5.14.

Vulcan Control System.

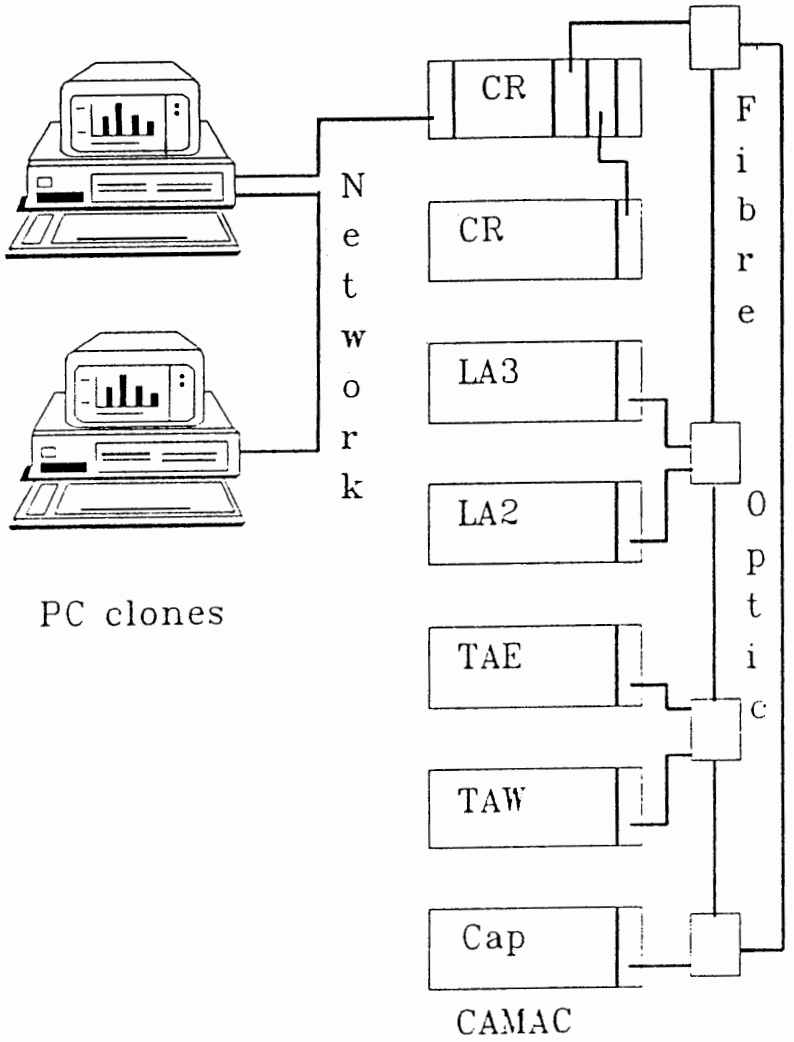


Fig A5.19

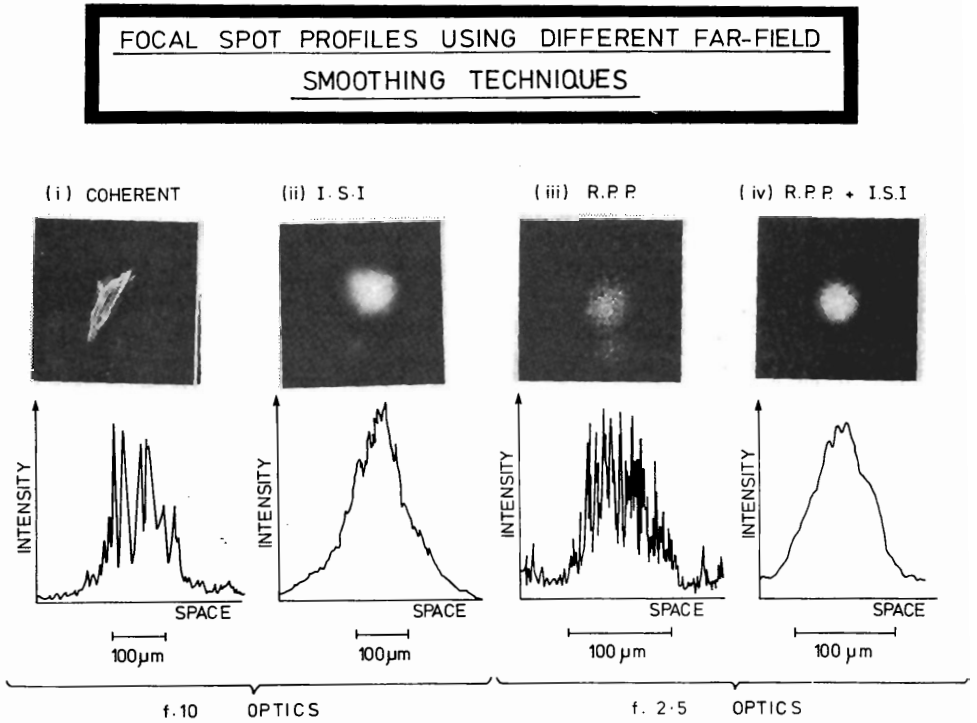


Fig A5.16

The change to broad band from narrow band reduced frequency doubling conversion by 20%-25% due to inefficient phase matching for all frequencies in the broad spectrum present. The 40% conversion achieved, shown in figure A5.15. would be enough to produce 0.5 kJ of green light into the target areas in a six beam experiment. Amplification and propagation of a well filtered >200 J pulse through the output stages of the system presented no new damage problems.

Random Phase Plate and Far-Field Analysis

In the target area an equivalent plane monitor was set up to examine the far-field of the laser beam under different operating conditions. A 4% sample of the main beam was focused using a 10 m focal length lens. A pair of air spaced etalons allows a scan of the focal plane and intensity in an array of spots such that it was possible to make an accurate measurement of the focal spot size. Focal spot images taken from the equivalent plane monitor are shown in figure A5.16. The first image shows the normal narrowband system output. The focal spot suffers from abberations producing a spot size which is about eight times diffraction limited. From the microdensitometer scan it is evident there are severe modulations present across the far-field.

Figure A5.16(ii) shows an equivalent plane picture of the far-field with the ISI system in operation. The focal spot size is approximately 1.7 times diffraction limited of the individual element size. It is evident from the microdensitometer trace that the focal spot quality is significantly improved from the narrowband case, with very little modulation across the trace. It was found that it was only possible to maintain this improvement in focal spot quality if the ISI beam was used in the far-field. The maximum focal spot size is therefore limited to approximately 100 microns, as the current target chamber configurations are limited to using f10 focusing lenses.

To obtain the larger focal spots a second method of smoothing was employed. This consisted of a Random Phase Plate (RPP) placed just prior to the final focusing lens in the target area. With RPP the beam was divided into small beamlets using a 2mm grid structure. A random distribution of these elements impose a half-wave phase-shift onto the beam. The intensity in the focal plane is determined by the random superposition of the deflected light from all the elements. The resulting intensity distribution is a high spatial frequency speckle pattern, the speckle size being dependent on the overall beam diameter. The focal spot size generated by using the RPP is given by:

$$D = \lambda f/d \text{ (FWHM)}$$

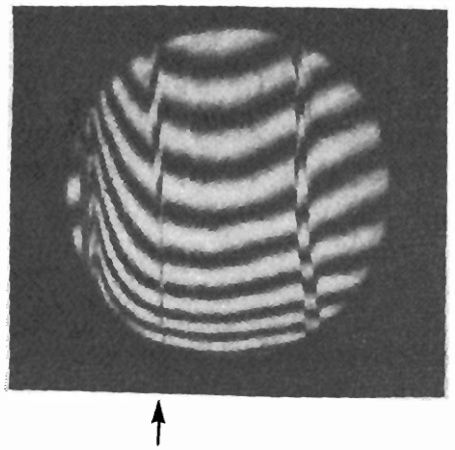
where: λ is the operation wavelength; f is the focal length of the lens; and d is the element size of the RPP.

The equivalent plane picture of the far-field using the RPP with the narrowband oscillator output is shown in figure A5.16(iii). the RPP employed for the experiment used a 2mm element size. Therefore with an f2.5 lens it was possible to produce focal spots of approximately 250 microns FWHM the experimental conclusions in comparing the three pulses described is given in detail in section A2.3.

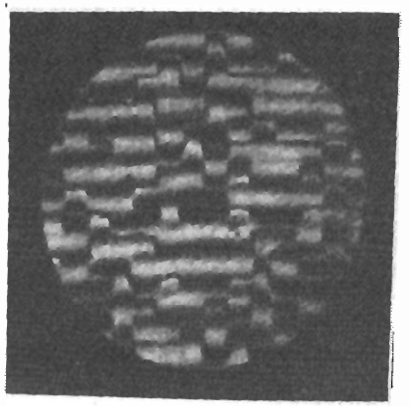
A configuration which was tested for focal spot quality but not used during the experiment was the combination of using the ISI laser beam together with the RPP. The equivalent plane image of this configuration is shown in figure A5.p (iv). As can be seen the focal spot size is very much the same as in the narrowband case with RPP although the modulation on the beam has been smoothed out.

Conclusion

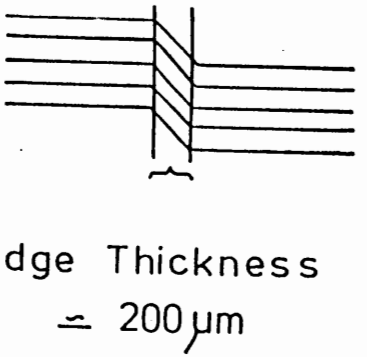
It has been shown that it is possible to generate smooth far-field distributions using the techniques described. With a number of different phase plates, which now seems practicable (see Section



Edge of Resist Seen in the Interferometer (i)



RPP Elements in the Interferometer (ii)



Tracing of Interference Microscope Image Showing Edge of A RPP Element (iii)

Fig A5.17 Optical Testing of the Random Phase Plates.

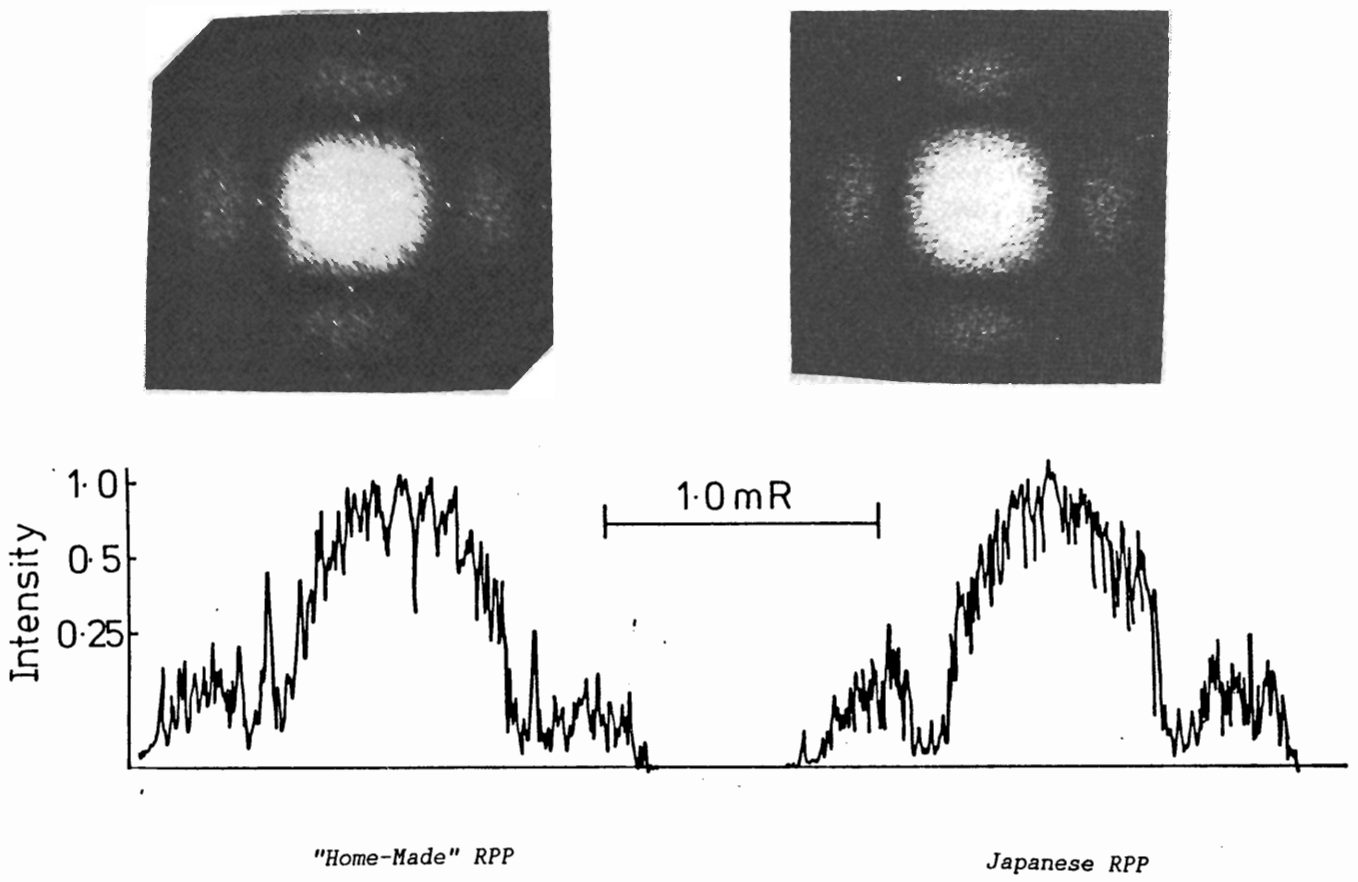


Fig A5.18 Far-field comparisons of Random Phase Plates.

A5.3.2), it should be possible to generate smooth focal profiles from 25-1000 microns FWHM.

References

1. Y Kato et al, Phys Rev Lett, Vol 53, No 11, 1984 p1057.

2. R H Lehmbrg and S O Obenschain, Opts Comm, Vol 46, No 1 1983, p27.

3. X Deng et al, App Opts, Vol 25, No 3, 1986, p377.

4. N Basov, A Danilov et al, Proc of the P N Lebedev Phys Inst of the Academy of Sciences of the USSR, 1987, Vol 178, p120-124.

5. D Veron et al, Opts Comm, Vol 65, No 1, 1988, p42.

6. I Aleksandrova, A Danilov etal, Kvantovaya elektronika, 1983, 10 (4), p892-895.

A5.3.2 Production of Random Phase Plates (RPP)

I Ross, R Bann, M Barraclough, C N Danson and D Pepler (RAL)

Introduction

Following a demand for Random Phase Plates for all beams with a performance similar to that of one externally purchased, it was decided to try a simple and inexpensive process of manufacture. If successful we would have a great deal of flexibility in design and be able to produce RPP's on a short time scale.

Specification

The RPP consists of a plate coated with squares of dielectric material, each giving a transmitted phase retardation of π at the operating wavelength and randomly distributed over the plate. The RPP should have high damage threshold at 0.526 microns. The squares should be 2 square mm giving the correct far-field distribution corresponding to a divergence angle of about 0.5 mrad. The backing plate need only be flat to less than $\lambda/10$ over the area of each square. The width of the edges of the squares should be less than 5% of the size of the square (100 microns for a 2 mm square).

Method

Conventional photolithography was used to produce the RPP. The chosen dielectric material was PMMA because of its high damage threshold in the visible. This is photosensitive at the ultraviolet wavelengths of less than 300 nm. It can give submicron resolution of an edge, is very tolerant to exposure and can be spun coated with good control of thickness and uniformity.

A UV transmitting mask is made by printing the appropriate computer generated pattern onto a thin sheet of PVDF. The mask is contact printed onto the PMMA coated plate using a UV emitting mercury lamp. Sufficient exposure is given to enable the exposed areas of resist to be completely stripped in development. The resulting plate is now ready for use.

Performance

Figure A5.17(i) & (ii) show interferograms of the unexposed PMMA plate with the coating stripped at one edge and of the exposed and developed plate, showing the coating thickness before the process and in the final RPP. Figure A5.17(iii) shows the edge of a square on the RPP using an interference microscope. The edge width is adequate at present but can be greatly improved. The PMMA measured thickness gave the required phase shift of π at 0.527 nm.

Figure A5.18 shows far-field distributions for our RPP along with that of the original bought RPP. Apart from the greater effects of the edges, which are not expected to affect the distribution seriously when using an imperfect illuminating beam, these distributions are equivalent.

Damage threshold measurements on our RPP at 1 micron gave a value of greater than 15-20 Joules per square cm in a 0.7 ns pulse. These RPP should not damage at normal operating fluences which are well below these damage thresholds. Evidence to date from target experiments suggest that the "home-made" RPP is working satisfactorily.

A5.4 COMPUTER CONTROL AND DATA ACQUISITION

C J Reason and D A Pepler (RAL)

The control and data acquisition system for Vulcan, comprising of a GEC 4080 computer, DEC computers and a CAMAC system, has given largely reliable service during the year. There were some problems with ageing equipment and part way through the year there were software problems on the DEC system. These were caused by the need to keep updating the software to reflect the changes in the target areas. The structure of the program had become fragmented allowing unexpected paths between sections of code. The problem was corrected by modifying some of these paths.

The GEC 4080 computer has now been controlling Vulcan for some 12 years and reached the limit of upgrades some time ago. In comparison with modern computers it is under powered and the maintenance charges are high for the computing power offered. It has therefore reached the end of its useful life, and our experiences with IBM PC clones (in particular Tandon PC's) show that these provide a suitable alternative to control Vulcan. The CAMAC system has been modified during the year to allow a PC with a CAMAC interface to work alongside the GEC 4080, and we have now reached the stage when the PC will fully take over the control of Vulcan. The GEC 4080 will stay in place for about one month and can be used at about two minutes notice to allow for any unforeseen problems. After that time it will be removed.

In specifying a PC system to control Vulcan, it has been necessary to evaluate where and when the computer is most active and to design a system to prevent bottle necks occurring. We have decided that two PC computers are needed and tasks and interfaces to the outside world should be split between them. The two computers are linked by a simple network giving each computer access to the others hard disk and RAM disk. Files written to RAM disk are used to pass small amounts of information between the computers at high speed and also act as a mechanism to synchronise code in the two computers. The hard disk is used to share large amounts of data acquired from various diagnostic devices. This network will be extended through a fibre optic link to a PC in the South Control Room, giving experimeters access to the data acquired from the laser and allowing archiving of data acquired by experimenters. The system is shown in Fig A5.5.

The first PC has an interface into the CAMAC system which is as before except that some user modules are no longer needed. It controls Vulcan through CAMAC, and the other computer through the synchronising files over the network. It also acquires data through the CAMAC system and makes it available on the hard disk. This computer also has an optical disk interface to allow for all data and information from all shots to be archived. The disk can store 200 Mbytes per side and can not be erased (write once, read many or WORM) and can be removed and stored when full.

The second PC controls the colour graphics system through a V24 serial port to display the layout diagram and charging diagram. It also controls a laser printer to produce a log after each shot comprising of text and graphics, totally describing the shot on one A4 sheet. Two framestore boards are included in this computer to read the image from the streak camera measuring the pulse lengths and the image from a fast scope monitoring the pre-pulse signal.

The number of PC's at the CLF has continued to increase, both for personal use and controlling specific items of equipment. The LSF has installed a number of these, in particular, one has been installed to control the DNA repair experiment (see section C2.2)

giving a faster turnaround of samples and increased reproducability of results. It is also proposed, in the light of our experiences with PC's on Vulcan, to install a similar system on Sprite, transferring it to Super-sprite as it becomes operational.

A5.5 TARGET FABRICATION AND DEVELOPMENT

C Brown, B Child, P Griffiths, F Lydon, N Prior, P Rumsby (RAL)

Despite a reduced number of experiments performed during the year, due to upgrades and developments to the VULCAN and SPRITE systems, the level of support required from the target production lab for high power laser experiments has increased.

Increased complexity of target structures, higher accuracy of target metrology and enhanced requirements for XUV instrumentation components such as streak camera cathodes and filters have contributed most strongly to this increase.

Considerable numbers of stripe and free standing ribbon targets of germanium, aluminium and bismuth and other materials have been fabricated for major experimental campaigns in both XUV laser development and long scale length plasma interaction studies.

Experiments probing both R-T unstable and radiatively heated foils by measuring alpha and proton energy losses have become a major part of the experimental programme during the year and have necessitated the provision of D_2 and DT filled shells of high aspect ratio. Quantities of high quality DT filled shells with aspect ratios of up to 400, diameters up to 680 µm and fill pressures up to 5 BAR have been supplied by ILE, Osaka and the Lebedev Institute, Moscow for use in collaboration experiments involving both of these establishments. The problems associated with the transport, storage and recovery of both mounted and unmounted shells have been solved with loss rates due to breakage reduced to the few percent level.

Development work during the year has concentrated on expanding the range of pure hydro carbon and doped polymer films available for incorporation into targets. A variety of metals have been incorporated into polyvinyl alcohol films at concentrations up to 10% by weight. Such films have been cast reproducibly in thickness between 1 and 10 µm and techniques developed to permit mounting in free standing form for subsequent coating. Laminates with alternate doped PVA and parylene N layers have been built up with up to 5 layers (thickness between 0.5 and 5µ) and mounted in free standing supports for radiation transport experiments.

A6	**INSTRUMENTATION**	Pages
A6.1	DESIGN AND FABRICATION OF MULTILAYER MIRRORS FOR USE IN THE EUV AND SOFT X-RAY REGION OF THE SPECTRUM	157-160
A6.2	PHOTOMETRIC CALIBRATION OF OPTICAL STREAK CAMERAS	160-163
A6.3	DEVELOPMENTS IN CRYSTAL SPECTROMETERS	163-172
A6.4	A SIMPLE ORTHOGONAL SLIT X-RAY CAMERA	172-176
A6.5	DENSITOMETER DATA REDUCTION	176-179
A6.6	ALPHA PARTICLE IMAGING WITH PSEUDO-NOISE PRODUCT (PNP) MASKS	179-182

A6.1 DESIGN AND FABRICATION OF MULTILAYER MIRRORS FOR USE IN THE EUV AND SOFT X-RAY REGION OF THE SPECTRUM

B L Evans, A M H Al-Arab, Shi Xu, Reading University.

In the EUV and soft X-ray regions of the spectrum the refractive index of a solid may be written as:

$$n = (1-\delta) - i\kappa \qquad (1)$$

where δ, κ are typically 10^{-3}. If a linearly polarised electromagnetic wave in a medium of refractive index n_1 encounters the plane interface with a medium of refractive index n_2 then the amplitude reflection coefficient at the interface is given by the approximate form of Fresnel's equations

$$r_{s,p} \quad \frac{(\Delta\delta + i\Delta R)}{2\ \mathrm{Sin}^2\emptyset_1}\ P(\emptyset_1) \qquad (2)$$

where $\emptyset_1$ is the glancing angle of incidence, $P(\emptyset_1) = -1$ or Cos $2\emptyset$, for r_S or r_p and

$$\Delta\delta + i\Delta\kappa = (\delta_1 + i\kappa_1) - (\delta_2 + i\kappa_2) \qquad (3)$$

The computed reflectivities $R_{s,p} = |r_{s,p}|^2$ and the vacuum-platinum and vacuum-carbon interfaces are given in Fig. A6.1 which shows that significant reflectivity occurs only at grazing angles ($\emptyset$ small). This effect has been the basis of the grazing incidence optics previously employed for X-rays. However, the small numerical aperture and off-axis distortions associated with grazing incidence optics makes them unsuitable for applications such as microscope imaging and laser cavity optics.

Following recent advances in the technology of thin film deposition it is now possible to fabricate multilayer stacks which utilise the near-normal incidence, in phase, reflections from a number of interfaces, as in the quarter-wave stack employed in conventional optics. Such a stack exhibits reflectivity maxima at wavelengths λ such that

$$2d\ \mathrm{Sin}\ \emptyset\ \{1 - \frac{\bar{\delta}}{\mathrm{Sin}^2\emptyset}\} = p\lambda\ (p\ \text{integer}) \qquad (4)$$

where $\bar{\delta} = \gamma\delta + (1-\gamma)\delta_2$; the layer thicknesses t_1 and t_2 are $t_1 = \gamma d$, $t_2 = (1-\gamma)d$ and d is the stack periodicity.

The materials composing layers t_1 and t_2 are chosen to give maximum $\Delta\delta$, $\Delta\kappa$, equation (2), while the thickness t_1 of the most strongly absorbing component layers is minimised to allow the maximum number of interfaces to contribute to the reflectivity. The minimum practical thickness of t_1 is approximately 5 atom diameters.

Multilayer fabrication consists of depositing alternating layers of non-reacting materials in the sequence ABAB etc on a smooth substrate. Each layer must be atomically smooth in order to produce a commensurate stack. The number of layers required (for appreciable normal incidence reflectivity) increases rapidly with decrease in operating wavelength i.e. from ca. 60 layers at λ = 30nm to ca. 500 layers at λ = 0.8nm.

Figure A6.2 shows the measured reflectivity of a 21/20 Pt-aSi multilayer ($t_p t$ = 1.13nm, t_{Si} = 13.87nm) at λ = 0.834nm in which the reflectivity maxima corresponding to p = 1---7, equation (4), are observed[1]. In this particular case, diffusion of Pt into the aSi layers reduces the performance of the multilayer at smaller t_{Si} (ie d-spacing) and this restricts the operation of the Pt-aSi multilayer to the EUV region. This restriction does not apply in the case of the Pt-aC multilayer[2] or in the Ni-aC multilayer now under development.

Figure A6.3 shows the image of a wire grid obtained at λ = 30.4nm using a Pt-aSi multilayer coated concave substrate (focal length 5cm) at 11° off axis[1]. Similar multilayer coated mirrors, exhibiting normal incidence reflectivities of ca. 20%, are currently being employed in laser plasma experiments at RAL[3].

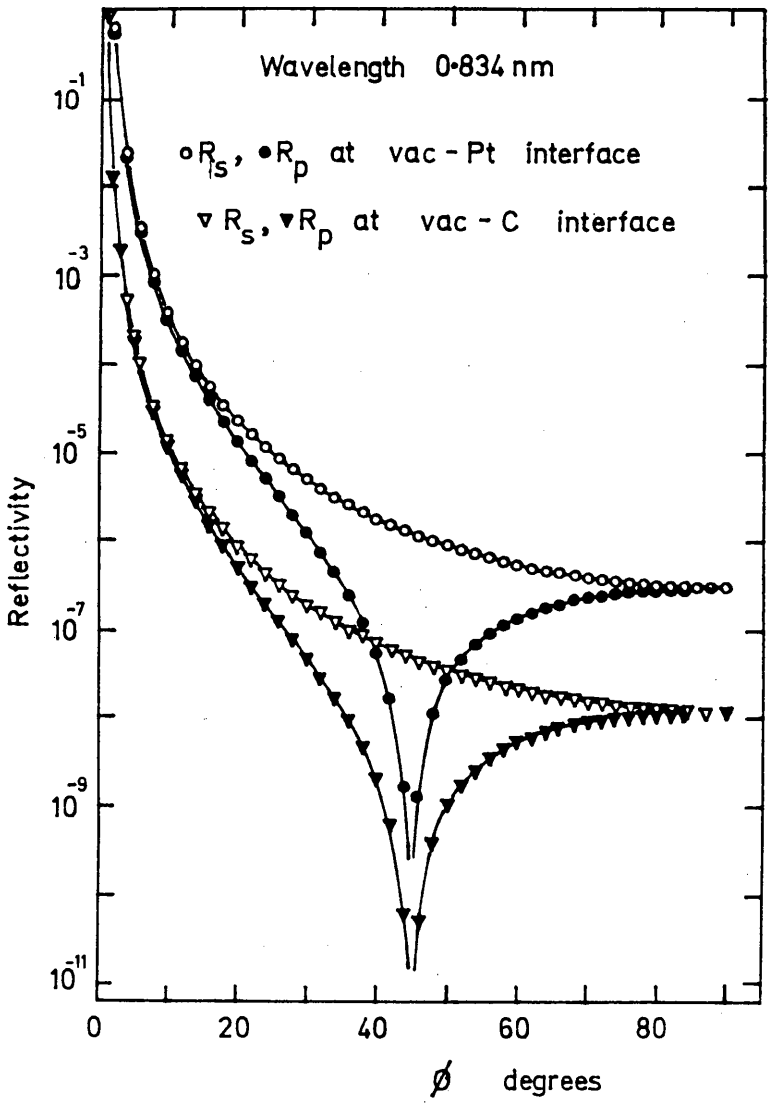


Fig A6.1 *Computed reflectivities $R_{s,p}$ at the vacuum-platinum and vacuum-carbon interfaces as a function of the glancing angle of incidence ϕ.*

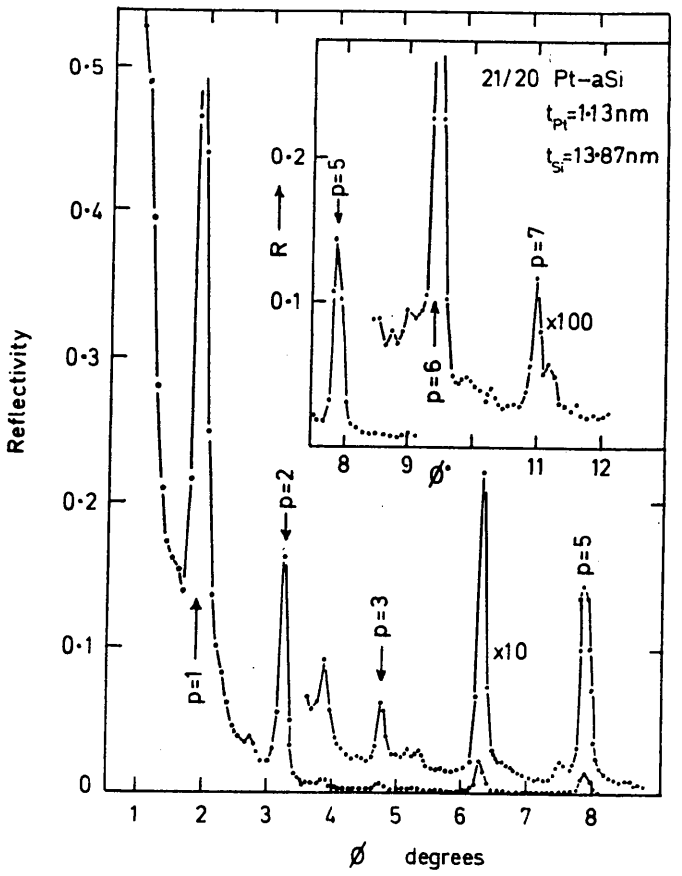


Fig A6.2 *The measured reflectivity at a plane 21/20 Pt-aSi multilayer (t_{Pt} = 1.13 nm, t_{Si} = 13.87 nm) at λ = 0.834 nm.*

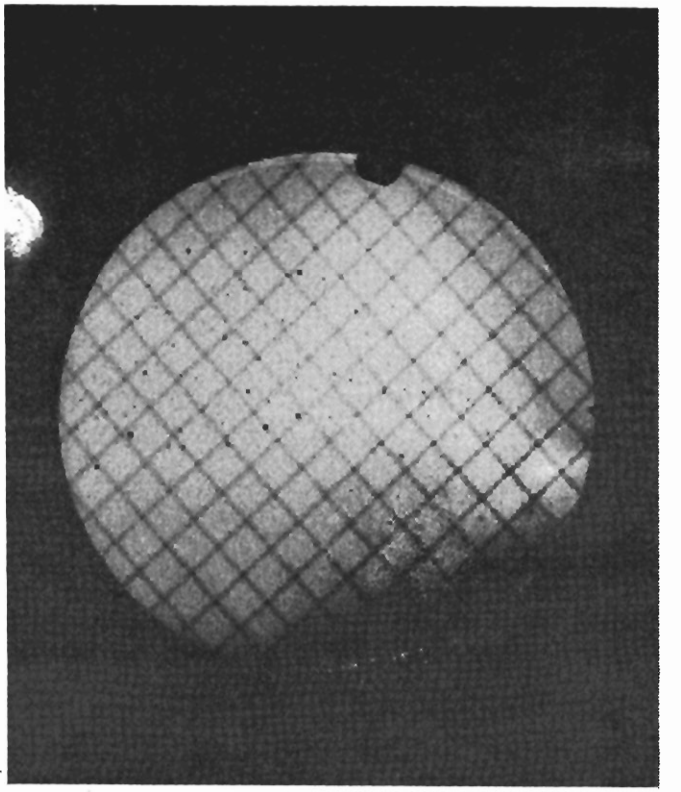


Fig A6.3 *The image obtained (using λ = 30.4 nm radiation) of a wire grid (28 wires/cm, wire width 24μm) using a Pt-aSi multilayer coated concave mirror (focal length 5 cms) at 11° off axis.*

References

1. "The soft X-ray to EUV performance of plane and concave Pt-Si multilayer mirrors". B L Evans, J Al-Dabbagh and B J Kent, J Mod Optics (1989) in press.

2. "Soft X-ray platinum-carbon multilayer mirrors". B L Evans and B J Kent (1987), Appl Optics 26 4491-7.

3. "Assessment of multilayer mirrors for XUV laser use". M Grande, B L Evans, A M H Al-Arab, N H Rizvi and Shi Xu (1988), SPIE 984 253.

A6.2 PHOTOMETRIC CALIBRATION OF OPTICAL STREAK CAMERAS

V Platonov, Y Serdyuchenku, S Majumdar, A Ridgeley.

Introduction

The possibility of using streak cameras as absolute photometric instruments with picosecond time resolution has been made realistic by the use of CCD cameras and image digitisation techniques in which we reported in 1987[1]. The present report describes the progress made in this area using the Dellistrique DSII streak camera[2] and a Peltier cooled CCD camera and analysis system, the LN-AT1 loaned by Delli Delti Ltd.

The Dellistrique DSII Streak Camera with an S-25 P-100 streak tube, coupled via a fibre optic reducer to a gated channel plate intensifier (Figure A6.4) was calibrated for absolute sensitivity and dynamic range in dynamic mode using the LSF picosecond laser system.

A peltier cooled CCD camera type PCCD/ATI was used to record the streak image which was stored into a computer for image processing and analysis. The system characteristics are also shown in Figure A6.4.

The CCD camera was practically identical with the one reported in[1] except the temperature of the sensor in the current instrument (Peltier cooled) was at -70°C as opposed to -125°C. This increased the system thermal noise to 0.3e/sec, compared to 0.5e/min. The linearity of the system was as reported earlier.

Experiment

The objective of the exercise was to explore whether we could establish:

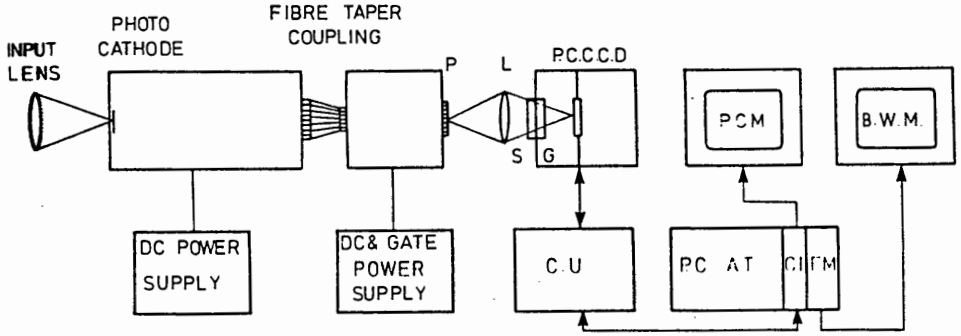
1. the input photon flux on a streak camera directly from the output counts in a cooled CCD camera;

2. the linear domain of the complete system at any specific time resolution setting of the streak camera;

3. the photometric sensitivity of the total system as shown in Figure A6.4.

We have already established[1] that the intensifier and streak tube combination has a useful linear range of greater than 200, when no sweep was applied to the streak camera.

In the current experiment, we have calibrated the sensitivity of the CCD camera at three different wavelengths, expressed in terms of photons per count, using a radiometer to measure energy absolutely. Table 1 below shows the CCD camera recording sensitivity:



P - OUTPUT SCREEN

L - LENS (TRANSMISSION 1·8%)

S - MECHANICAL SHUTTER

G - GLASS WINDOW

P.C.C.C.D. PELTIER COOLED CHARGE COUPLED DEVICE

C.U. - CCD CAMERA CONTROL UNIT

P.C. A.T. - PERSONAL COMPUTER

M - MONITOR

C.I - CCD CAMERA INTERFACE BOARD

F.M. FRAME MEMORY BOARD

Fig A6.4 Experimental arrangement for absolute sensitivity calibration.

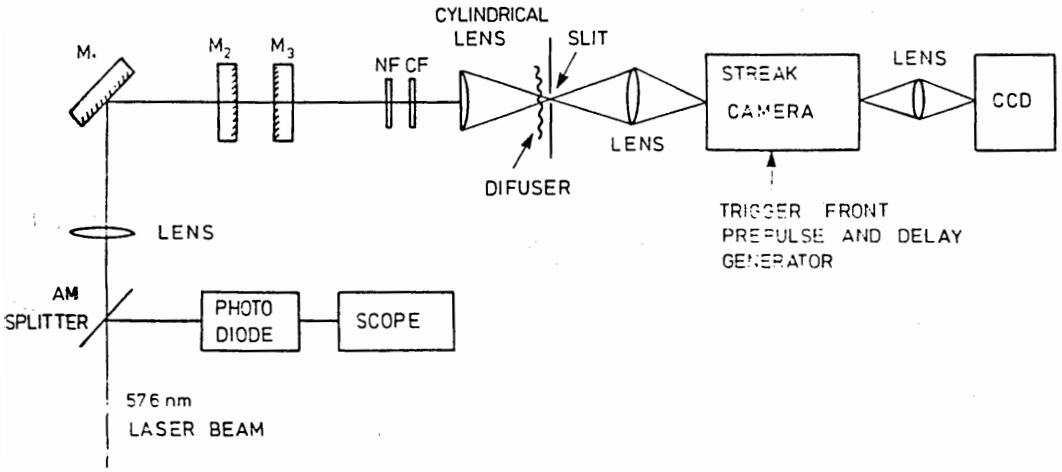


Fig A6.5 Experimental arrangement for calibration in dynamic mode.

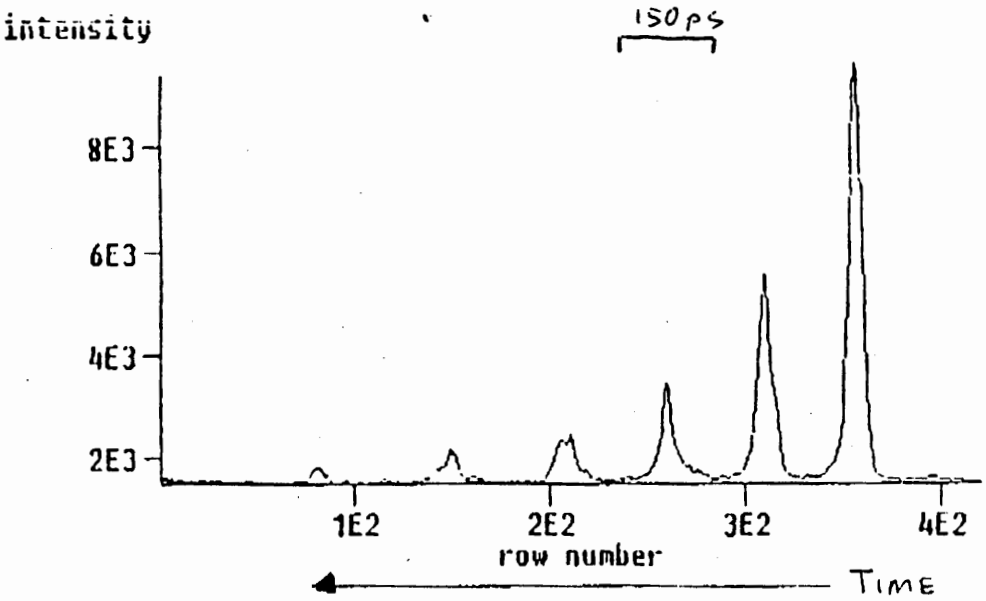


Fig A6.6 Measurement of dynamic range in dynamic mode.

Table 1

Wavelength	Sensitivity
540nm	74 photons/count
632nm	56 photons/count
820nm	54 photons/count

The sensitivities matched the manufacturer's spectral response curve (EEV).

The streak camera output is peaked at 550nm and by extrapolating the CCD sensitivity from the spectral response data of CCD sensor, the CCD camera sensitivity at 550nm was calculated to be 70 photons/count.

The system was next dynamically calibrated using the LSF picosecond laser at 576nm in the following way:

1. the CCD camera was first placed at the position where the streak tube photocathode would be positioned subsequently and the CCD readout was measured using a range of calibrated filters;

2. next the streak camera was placed in the position of the CCD sensor and the CCD sensor was now positioned to record the output of the streak camera through a F2.7 lens which had 1.8% collection at 550nm. The input energy was monitored by a photodiode.

3. the streak camera was now operated in a slow sweep mode (10ps/mm) so that the image of slit at output was of the same dimension as in the case of unswept or static mode.
4. the CCD signal at the output was then compared with that at the input to establish the streak camera sensitivity at 576nm in terms of input photons per count.

It is clear that the streak camera had a sensitivity of around one count per photon (or 20 counts per photo-electron,as the detective quantum of the photo-cathode at 576nm was 5%).

The system sensitivity was measured at two gain settings and shows saturation of the intensifier at the high gain setting, at an input light level equivalent to 1000 photo-electrons per resolution element (FWHM 80μm). This is equivalent to a total count of 20,000 at the CCD per resolution element (spread over 9 CCD pixels in our optical set up).

This linear range does not take into account any problems associated with the streak camera instrumental pulse broadening caused by excessive intensity of signal into the streak tube. The maximum intensity level for streak tube operation without instrumental pulse broadening at a sweep rate of 60ps/mm on the intensifier screen (equivalent to 9ps time resolution limit at the slit width used) is expected to occur at an intensity level lower than 1000 times the minimum (threshold) intensity level (2).

The streak tube was now used at a sweep speed of 60ps/mm, with a pair of etalons placed in the beam to generate a set of pulses of diminishing intensity and equal time separation of 20ps. Figure A6.5 shows the experimental set up.

The output of the laser fluctuated by up to 35% and the far field pattern was very non-uniform. This meant that pulse to pulse data output was not consistent in this single shot streak experiment.

The ratio of intensities of two successive pulses out of the etalon was 2.4, calculated from the reflectivity of the two surfaces.

The threshold level of detection is around one detected photo-electron, or 20 counts, over a group of CCD pixels. The image from a single photo-electron is spread over approx 5 pixels (90% of energy). This was just detectable above noise. The CCD

noise as less than 3 counts/pixel while the intensifier noise was even less than this figure in the gated mode of operation.

The system dynamic range at 10ps was greater than 130 using this system. Pulse broadening was observed clearly when the CCD counts went above 5000 counts, as can be seen from Figure A6.6.

References

1. RAL report RAL-87-041, Paper No. C58.

2. a) Majumdar 1978
   b) Hull et al 1982.

A6.3 DEVELOPMENTS IN CRYSTAL SPECTROMETERS

Increasingly, there is a need for versatility in the use of crystal spectrometer instrumentation and the limitations imposed by the standard trapezoidal mini-spectrometer crystal mount have been becoming more and more apparent.

In order to extend the versatility of instrumentation based on X-ray diffracting crystals a policy of buying crystals as fairly large blocks and subsequently cleaving them to size for particular specialist specifications has been adopted. This had enabled us to investigate a wider range of crystal based instrumentation without increase in cost.

This policy has so far resulted in the three spectrograph designs described below.

(a) A Convex Mini-spectrometer for use in Twelve Beam Geometry

A Ridgeley, E Madraszek (RAL)

Using the standard plane crystal spectrometers in the TAW target chamber it is difficult to get the spectrograph near enough to the target to achieve good magnification for space resolving. This problem can be solved by using a convex spectrometer, because a large range of Bragg angles can be accommodated for a small range of acceptance angles in the incoming beam. Referring to Figure A6.7, this effect is described by the relationship:

$$\Delta\theta = \Delta\Upsilon + \Delta\phi$$

Also using Figure 1, it is evident from the Sine rule that:

$$\frac{X}{\cos\theta} = \frac{L}{\sin\phi} = \frac{R}{\sin\Upsilon}$$

and this relationship can be used to optimise the parameters for any particular specification.

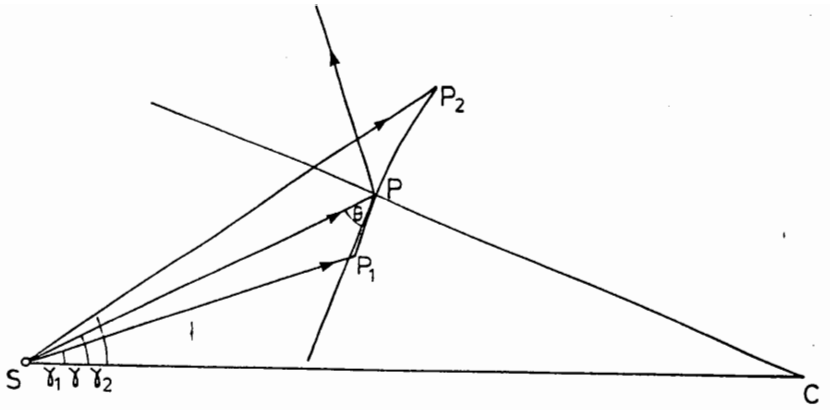
A spectrograph has been built with parameter values R = 150mm, X = 200mm, $\sin\theta_2 = 0.5$, $\sin\theta_1 = 0.9$.

The layout is illustrated diagramatically in Figure A6.8 and a photograph of the instrument is shown in Figure A6.9.

* This instrument achieves a spatial magnification of 4.5 at the designed 20mm slit-source distance.

* The entrance aperture is invisible from the film plane thus minimising fluorescence.

* The instrument is small enough to contemplate use of a vacuum interlock.



S = Source
C = Crystal Centre of Curvature
$P_1 P_2$ = Crystal Length
θ (Range θ_1 to θ_2) = Bragg Angle

SC = X
SP = L
CP = R

Fig A6.7 Convex crystal geometry.

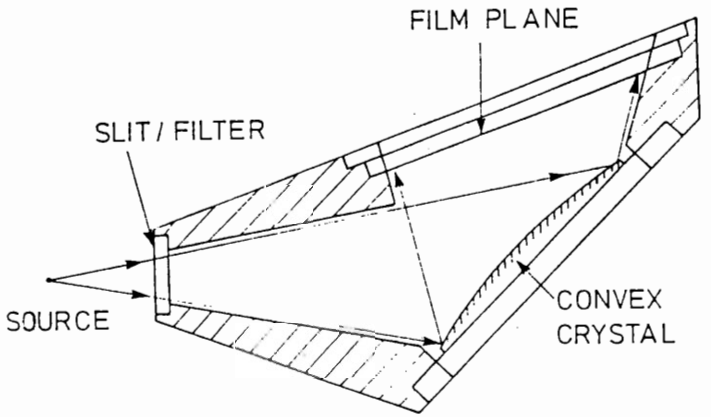


Fig A6.8 Schematic diagram of convex crystal minispectrometer.

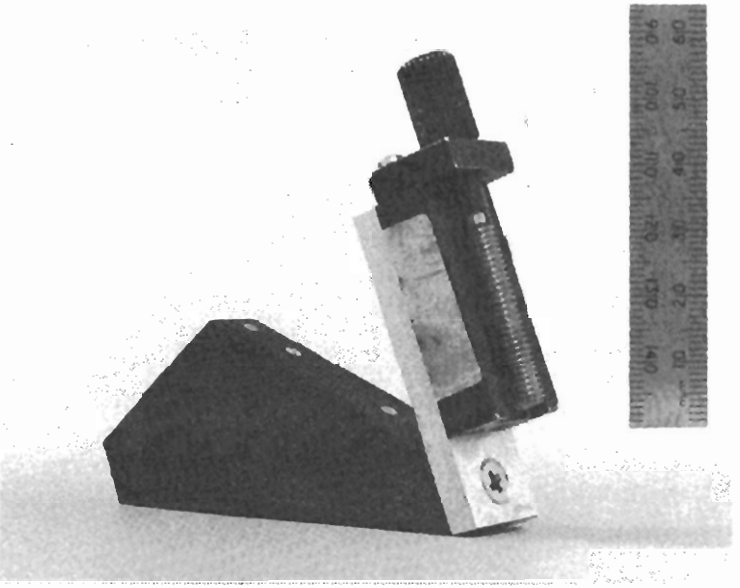


Fig A6.9 Photograph of convex crystal minispectrometer.

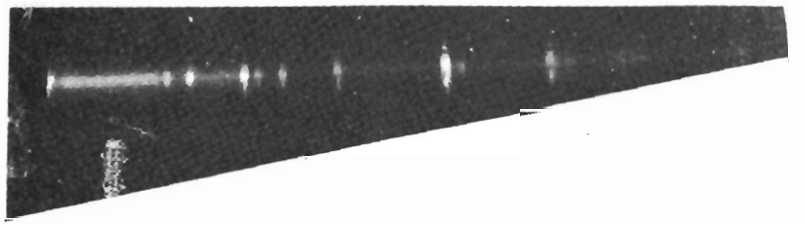


Fig A6.10 Spectrum obtained using convex crystal minispectrometer to diagnose a NUHART implosion. The strong silicon lines provide good monochromatic images of the plasma.

* The versatility exists to change the crystal radius of curvature (with perhaps a complimentary change in working distance). A flat or even concave crystal could be accommodated with reduced spectral coverage.

This instrument was used with a PET crystal in the particle radiography experiment in January 1989, and successfully produced spatially resolved spectra in the wavelength range 4.4Å-7.9Å. One spectrum is reproduced in Figure A6.10, in which good monochromatic images of a 12 beam NUHART implosion are seen, albeit with a 5x bigger magnification in one axis than the other.

(b) A Vacuum interlocked mini-spectrometer capable of spatial resolution of long plasma lengths

C Lewis, D Neely (Queen's University Belfast)
A Damerell, A Ridgeley (RAL)

Introduction

A new minature crystal spectrometer was designed to spatially resolve the emission from the Ne and F like states of a Germanium plasma of up to 33 mm length which was used in the February 1989 x-ray laser experiment. Both flat and convexly curved Mica crystals were used to examine different spectral regions and the magnification on film was adjusted from unity to .25 to suit varying target lengths from 33 mm to 6 mm.

Instrument

This new miniature crystal spectrometer was designed primarily to meet new diagnostic requirements of the X-ray laser program at RAL concerning experiments on the electron collisional excitationally pumped Neon like Germanium scheme. In this experiment the spectrometer was required to be capable of spatially resolving along a 6 to 40 mm length the emission from the Ne + F like (7-10Å) states of a Ge plasma so that information concerning the degree and distribution of ionisation states along the length of the plasma could be extracted. It was also considered advantageous that the instrument should be capable of travelling through a vacuum interlock so that between laser shots the chamber could be left under vacuum and hence facilitate a faster shot repetition rate.

Initial trial spectra were recorded at Queens, Belfast using typically a .56W I.R. laser pulse to irradiate Ge at an average power density of $\sim 3 \times 10^{12} Wcm^{6}$ so that the suitability of using either a Mica or TIAP crystal could be studied. Figures A6.11(a) and A6.11(b) show the densitometer traces of typical spectra where in both cases the similar spectral resolution obtained was limited by source broadening effects. From these initial results it was decided to use mica as the dispersive element primarily because of the ease with which mica can be cut, cleaved or brought into the desired shape and also because of the low replacement cost of a crystal should one become damaged.

Figure A6.12 is a schematic of the final instrument design showing both a section through the spectrometer from a side on view and also the positioning clip which is fixed onto the target holder so that the spectrometer is situated vertically above the target, and the entire assembly as shown in Figure A6.13 (consisting of the target holder, the spectrometer and the target) can be transported through the 46 mm diameter vacuum interlock device which was used in the experiment. The spectrometer uses a transverse slit to provide axial resolution along the length of the plasma . This slit must be positioned in one of two positions, either in position A between the crystal and the plasma to provide a magnification of unity which is suitable for short plasma lengths of below 15 mm or in position B between the crystal and the film to provide a magnification of .25 which is suitable for plasma lengths of up to 40 mm. To maintain an identical resolution using either magnification means that when using the lower .25 magnification then the slit width must be made = 2½ times smaller than when using a magnification of unity. The spectrometer was designed primarily for use with a 17 mm x 21 mm flat mica crystal which has a 2d of

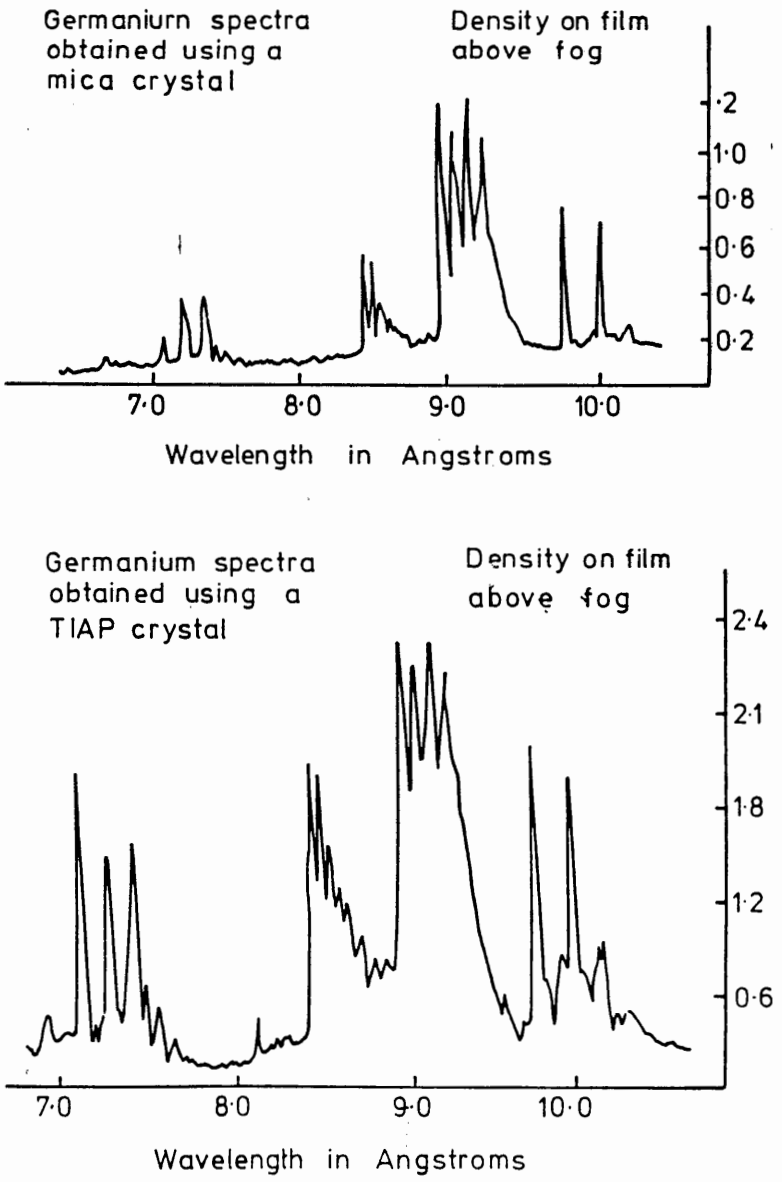


Fig *A6.11 Comparison of Ge spectra using TlAP and mica crystals.*

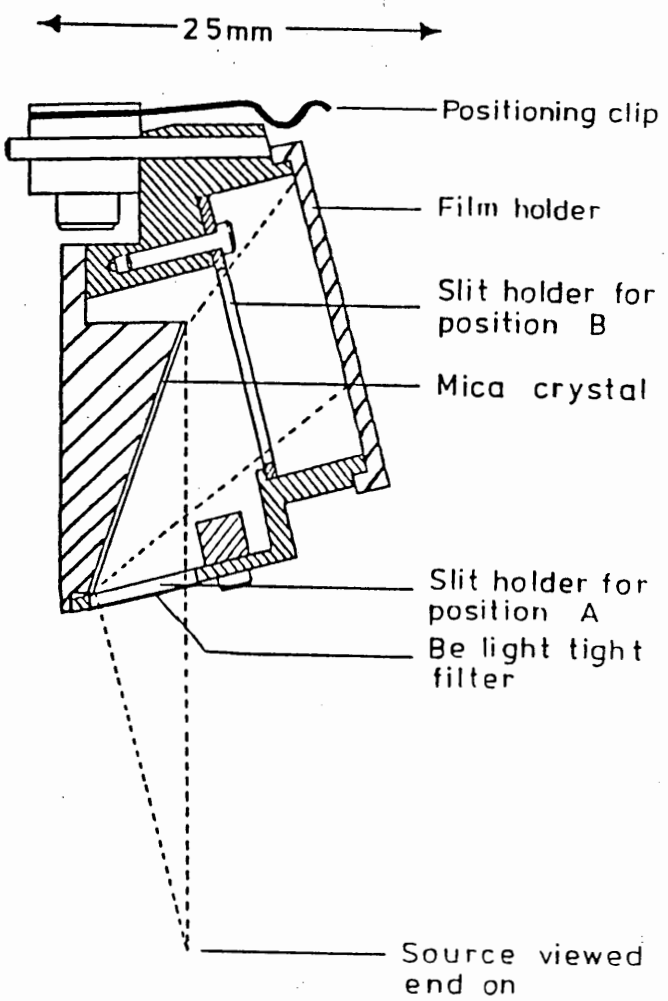


Fig A6.12 Schematic diagram of the vacuum interlocked minispectrometer capable of spatial resolution of long plasma length.

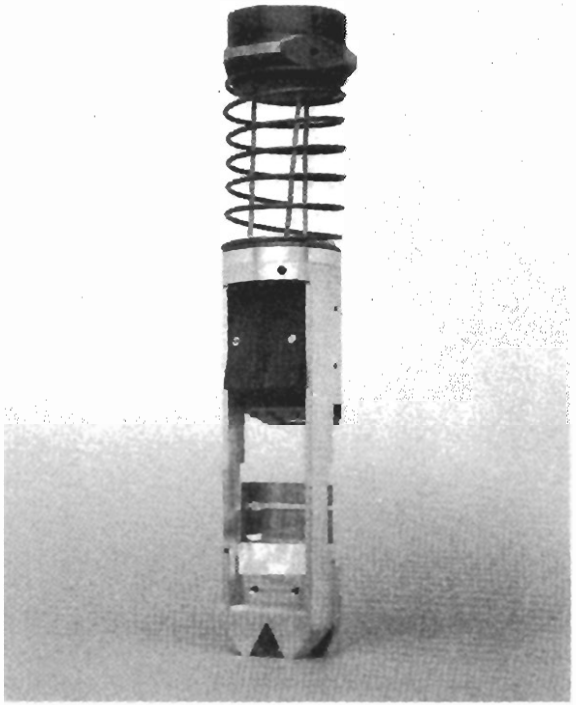


Fig A6.13 Vacuum interlock experimental assembly containing the minispectrometer.

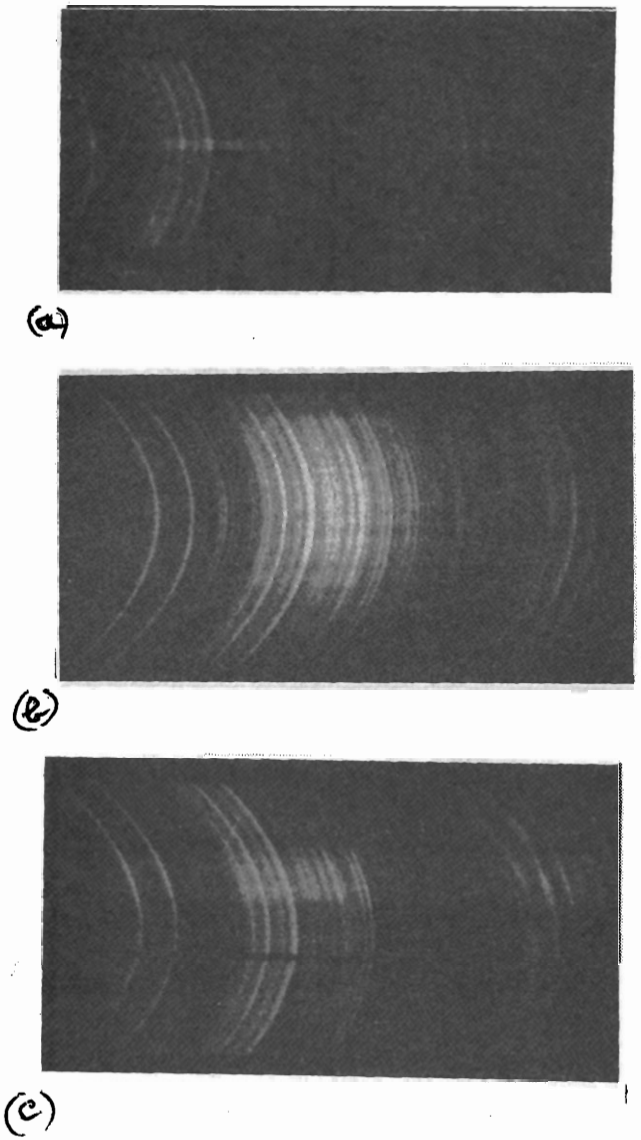


Fig A6.14 Spectra obtained using the vacuum interlocked minispectrometer.

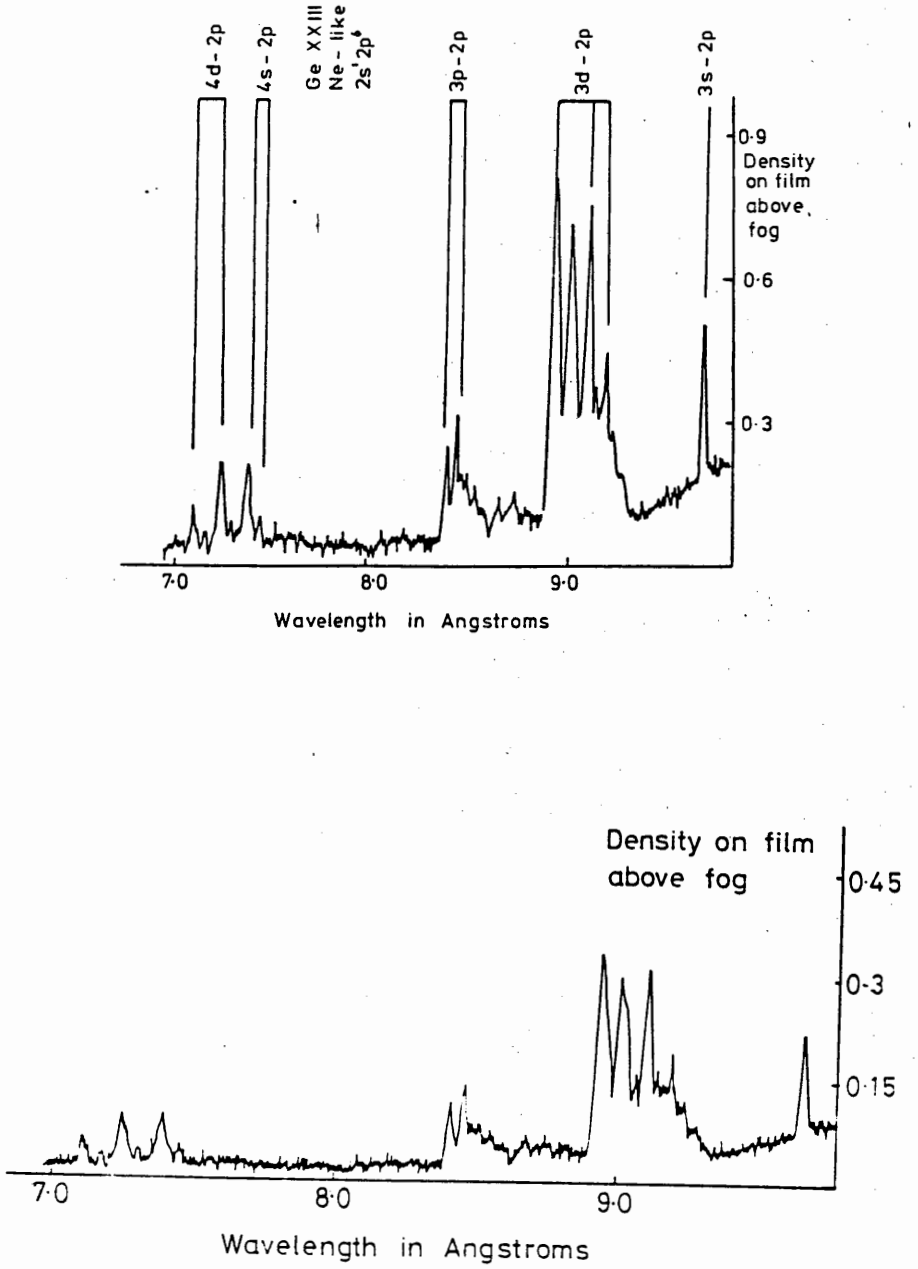


Fig A6.15 Densitometer tracings of spectra shown in Fig A6.15.

19.8A thus giving an average dispersion at the film plane of 350 mÅ/mm. The crystal is capable of accepting emission from the within an angular range ≈ 14° so that it is possible to examine in a single shot the wavelength range 6.5 Å to 10.8Å using a flat crystal or from 5.5 to 12.5Å using a convex curved crystal of radius ∿ 50 mm. The spectrometer was designed so that a slit could be mounted on a detachable internal plate making it relatively easy to mount cold k-edge absorption filters such as Mg(9.51Å) or Al(7.95Å) to give good wavelength markers with the advantage that, because they are internal to the spectrometer, the thin ≈ 5 μm filters are not damaged by plasma blow off and, being mounted on a detachable plate, they can be quickly and easily inserted or removed from the spectrometer.

Results/Discussions

The spectrometer functioned exceedingly well during the experiment with both flat and convex curved mica crystals being used. However, the extra spectral coverage of the curved crystal did not provide significantly more information and had a lower dispersion on film than the flat crystal so a flat crystal was used during the majority of the experiment. It was found that there were significant amounts of plasma and debri blown off even almost tangentially to the target surface which entailed the use of 25-50 Be filters to maintain a light tight seal over the spectrometer during the experiment. Because a thicker Be filter (25-50μm) than originally intended (8-12μm) was used, in order to maintain a reasonable density on film, wider slits had to be used which limited the spatial resolution of the instrument to ∿ 100μm in the axial direction.

Figure A6.14 show three examples of the spectra which the spectrometer produced during the February '89 run. Figure A6.15(a) shows a spectrum obtained during the early part of the experiment. In this shot two 12 mm long line focus are being used to irradiate a 22 mm long target. As the spectra clearly shows one of the two beams was not correctly masked resulting in an overlap at the target centre which clearly shows up as the bright band down the spectra. Figures A6.15(a) and A6.15(b) show two densitometer traces taken from the spectra with trace A6.15(a) taken through the overlap and trace A6.15(b) taken to one side of the overlap. To a good approximation trace A6.15(a) represents an irradiance of about twice that of trace A6.15(b) where the power density is estimated as ≈ 4×10^{12}W cm^2. Because of the good spatial resolution (∿100μm) along the length of the plasma this overlap distance was measured and the line focus adjusted to correct this mistake quickly. Figure A6.14(b) represents the typical spectrum obtained from a full length 33 mm plasma which shows an acceptable uniformity along its full length for a maximum energy shot. Figure A6.14(c) hows the spectra obtained from a single shot of two targets placed side by side. In this shot a short (11.5 mm) target is placed 1mm away from a longer 21.5 mm target, the shorter target is irradiated first and the longer larger 600ps later. Initial fears were that the gap between the targets might not have been large enough to stop damage occuring to the edge of the second target. However, as the spectra shows, the longer target has uniform emission right up to the sharp cut off therefore showing that no damage occurs before the second target is fired.

Further developments now planned for this spectrometer are the use of high surface quality crystals of higher reflectivity so that information concerning the transverse structure as well as the axial could be extracted. It is estimated ≈ 20μm transverse resolution and better than 40μm resolution axially can be obtained.

(c) An elliptical spectrometer for exafs measurements

T Hall, D Goodman (Essex University) and A Ridgeley (RAL)

Introduction

EXAFS studies of ion correlation effect in dense, laser driven, shock compressed aluminium have been very successful over the years and have resulted in many publications. In previous experiments a planar dispersing crystal has been used which has led to a

geometric arrangement requiring plasma shocks with a high degree of uniformity to be produced over a large area (∿ 1mm²) in order to obtain a reasonable range of angles into the crystal. It has been difficult to employ such an experimental arrangement, and the requirement of a large compression area has limited the strength of the shock, hence the compression that could be achieved.

A new technique, using an elliptical crystal spectrometer, has been developed which should overcome these difficulties, achieving a much smaller illuminated region on the target, which will, in turn, allow higher compression to be achieved.

Experimental Design

Figure A6.16 shows the experimental arrangement which is being developed. An X-ray dispersing crystal is bent to a concave elliptical contour. The backlighting source is placed at one focus of the ellipse and the EXAFS target at the other focus. Dispersed X-rays from the backlighter source pass through the EXAFS foil target and on to a suitable detector (film or photo-diode array). The EXAFS target is a thin metal, plastic coated foil and will be shocked by two opposed, long pulse laser driver beams. The backlighter target will be illuminated using the TAE six beam short pulse F/10 cluster. The time delay between the backlighting and drive beams may be varied to provide time resolved EXAFS studies.

The elliptical arrangement has several advantages:

- In contrast to the planar crystal arrangement the foil in only penetrated by the required diagnosing wavelengths, and is not exposed to direct polychromatic radiation from the backlighting source, with subsequent unwanted heating in the sample and deterioration in the EXAFS structure.

- The dispersed X-rays recorded by a plane crystal spectrometer have passed through different regions of the target, and in the process have probed different plasma conditions which result from non-uniformities in the drive beam and variations in the target thickness. The elliptical and cylindrical nature of the curved crystal, however, ensures a line focus at the convergent focus. Thus in any arbitrary horizontal phase the dispersed spectrum is derived from a single point on the compressed foil, i.e. from a plasma with almost uniform density and temperature.

- An additional advantage of the line focus from the elliptically curved crystal is that it is larger than the diameter of the compressed region. This allows the simultaneous recording of EXAFS from both compressed and uncompressed regions. It is expected that study of this boundary will yield valuable information concerning shockwave development in the transverse direction of the foil.

- The backlighting radiation within the elliptical spectrometer is much more spatially compact than within the plane spectrometer, enabling more effective shielding of the detector from the undispersed radiation. The fact that the detector is directly isolated from the source should result in a negligible background.

- The diagnosing radiation from the elliptical crystal is incident upon the foil at a shallower angle than is seen in the linear arrangement, thereby increasing the pathlength of the radiation within the target. Thus the transmitted flux may be optimised, to suit the detector, by use of a thinner foil, which has a correspondingly smaller longitudinal variation in density during compression.

Realisation of the Design

The parameters of the ellipse are determined by the upper and lower energies of the analysing radiation and the availability of crystal 2d spacings.

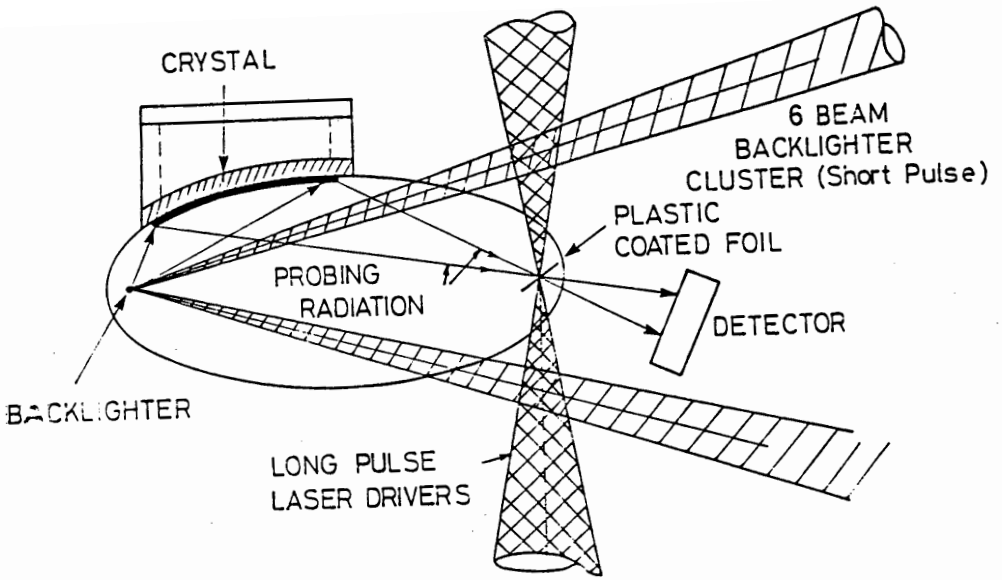
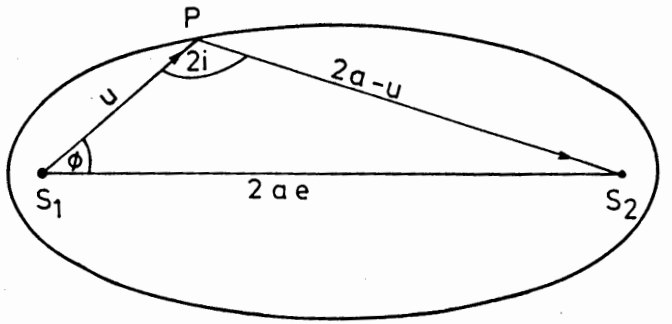


Fig A6.16 Schematic diagram of the proposed arrangement for an EXAFS experiment using an elliptical spectrometer.



EQUATION OF ELLIPSE

$$\frac{l}{u} = 1 - e \cos \phi$$

AND FROM PROPERTIES OF AN ELLIPSE

$$u = \frac{a(1-e^2)}{1 - e \cos \phi}$$

HENCE FROM SINE RULE

$$\sin 2\theta = \frac{2e\,(1-e\cos\phi)\sin\phi}{1 - 2e\cos\phi + e^2}$$

e = eccentricity of ellipse
l = semi - latus rectum
a = semi - major axis
i = angle of incidence
θ = Bragg angle = (90-i)

Fig A6.17 Elliptical crystal geometry.

The parameters of the ellipse are derived from the geometry indicated in Figure A6.17. For a given 2d spacing the lowest analysing wavelength determines the eccentricity of the ellipse ($\emptyset = \theta = \mathrm{Sin}^{-1}\ \lambda$ min/2d) and the minimum size of the ellipse is determined by the minimum radius to which the crystal can be bent at the λ max reflection point.

Of the various designs possible it was decided that an NH_4AP crystal used in second order (2d = 13 Å) with eccentricity 0.89 and with 10cms separation between the foil was optimum for aluminium EXAFS. NH_4AP has a high reflectivity in second order).

A technique for bending crystals to the required elliptical form has been developed at Essex University using an impregnated compression technique. For initial trial purposes ∿150μm cleaved slice from a 50mm x 10mm KAP (available) crystal has been curved to the above elliptical form. Flourine spectra have been recorded at the University of Essex using this curved crystal and a planar TlAP crystal. The two systems performed equally well in terms of dispersed spectral intensity. The width of the line focus at the far focus of the ellipse was approximately 200μm from a very broad source.

Work is now proceeding to produce an NH_4AP elliptically curved crystal in preparation for a full elliptical EXAFS experiment in TAE with ISI beams.

A6.4 A SIMPLE ORTHOGONAL SLIT X-RAY CAMERA

C Lewis, D Neely (Queens University)
E Madraszek (RAL)

Introduction

The advantages of using an orthogonal slit camera compared to a pinhole camera for spatially resolving both axially and transversely the Ne + F-like (1-2 keV) emission from a Germanium target of typical dimensions 33 mm by 0.2 mm as used in the Feb 1989 Neon-like X-ray laser experiment are discussed and a preliminary analysis of the data obtained using the orthogonal slit camera is presented.

Instrument

The orthogonal slit camera as shown schematically in Fig A6.18 consists essentially of two slits placed orthogonally to each other to image the plasma, a filter to select the energy band to be examined and a combination of phosphor, intensifier and film to record the image. By using a combination of three parallel slits and appropriate filters instead of just one front slit three simultaneous images were recorded and after allowing for different relative throughputs due to variations in the widths of the slits it was possible to examine only emission from the 6-10 Å region of the plasma.

The front slit consisted of three parallel slits each of dimensions 40 mm and 11 μm separated by .75 mm cut into a 20 μm deep copper substrate, with five 50 μm wide spacer bars along the length of each slit to hold it rigid. It is the front slit which provides transverse resolution and the main requirements for it are

(1) The slit must be sufficiently long in the axial direction that it allows radiation from all parts of the plasma to pass through it and onto the second slit.

(2) The slit must be sufficiently narrow in the transverse direction that it can provide high transverse resolution, and

(3) The slit must be placed as close as experimentally possible to the plasma and orientated parallel to it to obtain as high and uniform a transverse magnification as possible. The back slit is placed orthogonally to the front slit to provide axial resolution and by placing it much further back from the plasma, a lower axial magnification is obtained. Hence the instrument has the desired differential magnification. After the images pass through both slits they are filtered using various thicknesses of aluminium and

mylar before being recorded onto HP5 film using a phosphor and intensifier combination to convert from an X-ray to an optical image.

Theory

The magnifications in the axial and transverse directions M_n and M_T can be written in terms of the axial and transverse viewing angles α_n and α_T. The distances from the source to the front slit, back slit and phosphor D_2, D_2 and D_T respectively and the intrinsic magnification of the intensifier M_2 as

$$M_A = \text{Cos } \alpha_A \left(\frac{D_T - D_2}{D_2}\right) M_I \qquad (1)$$

$$M_T = \text{Cos } \alpha_T \left(\frac{D_T - D_2}{D_1}\right) M_I \qquad (2)$$

The orthogonal slit camera was designed to operate with slit positions in the range

$150 \text{ mm} \leq D_2 \leq 310 \text{ mm}$

$30 \text{ mm} \leq D_2 \leq 150 \text{ mm}$

and using a port with an $\alpha_A = 33°$ and $\alpha_T = 60°$ Eq(1) and (2) give
$2.5 \geq M_A \geq .86$

$9.0 \geq M_T \geq 1.5$

From this available range of magnifications further restrictions were imposed by experimental considerations and the final magnifications obtained were $M_T = 4.3$ and $M_A = .86$ with a transverse resolution of ≥ 175 μm.

The advantages of using the orthogonal slit camera compared to a pinhole camera are clearly shown by considering the case of a pinhole camera operated with an identical axial magnification and resolutions and contrasting the final image size and throughput of the instruments for a targets of typical dimensions 33 mm x .2 mm and noting that the two main features of the plasma which this diagnostic was designed to examine were

(a) The size and uniformity of the plasma when it is in the Ne and F-like state (of which the transverse measurement is of prime interest).

(b) Any misalignment of the three 11 mm long line foci used to create the 33 mm long plasma.

	Orthogonal slit camera	Pinhole camera
Axial Magnification	0.86	0.86
Transverse Magnification	4.3	0.5
Relative Throughput	8	1
Image Size	.86 x 29 mm	.1 x 29 mm

Table 1 showing the comparison between the Orthogonal slit and pinhole camera.

From examining the design requirements of the diagnostic (a) and (b) and considering the comparison as shown in Table 1, it is clear that the factor of eight greater throughput of the orthogonal slit camera will provide a greater freedom in the choice of filters and also since requirement (a) and (b) are concerned mainly with measurements of transverse structure along the axial direction of the plasma, then the much greater (a factor of 8) transverse to axial differential magnification obtainable with the orthogonal slit camera in the above where the transverse dimension of the

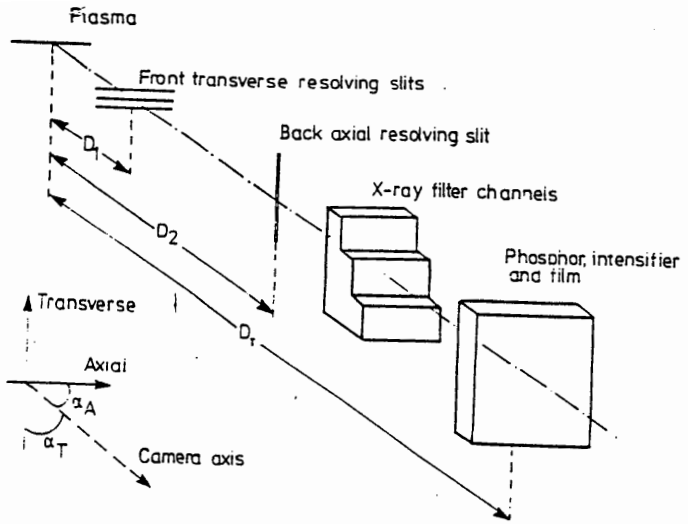


Fig A6.18 Schematic diagram of orthogonal slit camera arrangement.

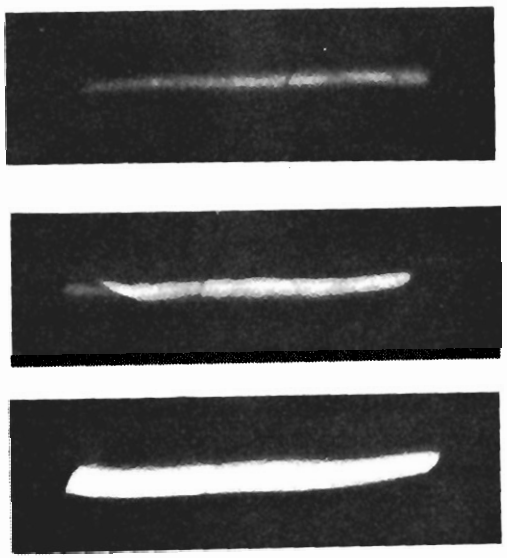


Fig A6.19 A typical set of images obtained using the orthogonal slit camera.

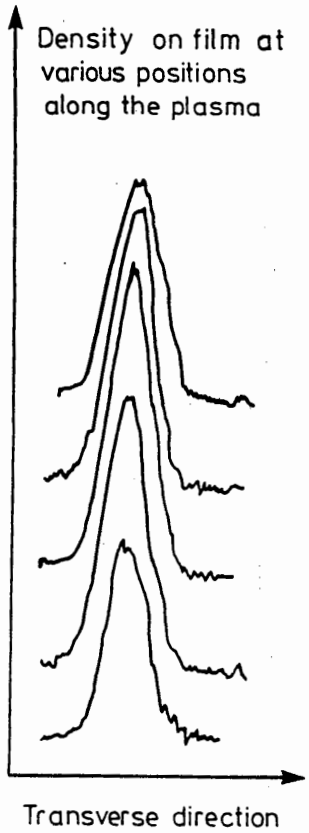


Fig A6.20 Densitometer traces taken at various positions along the length of an orthogonal slit camera image.

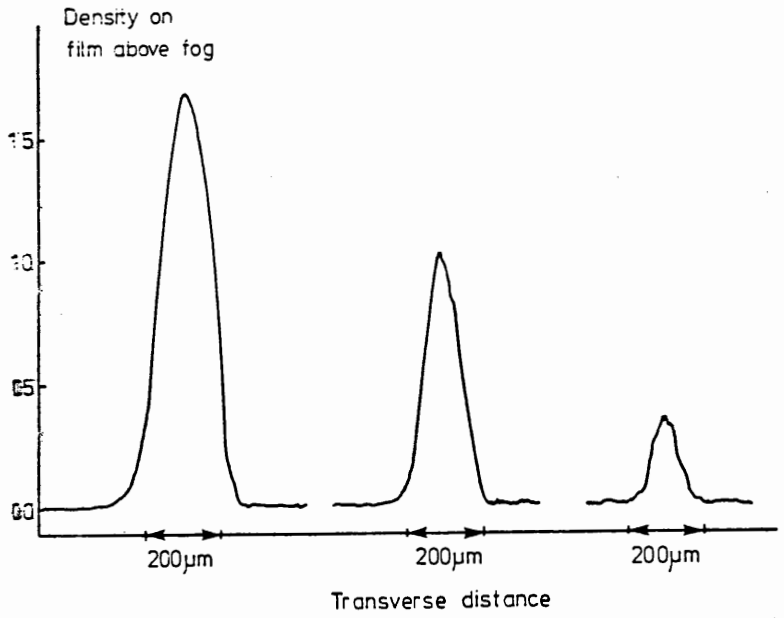


Fig A6.21 Densitometer traces at equivalent position in three orthogonal slit camera images.

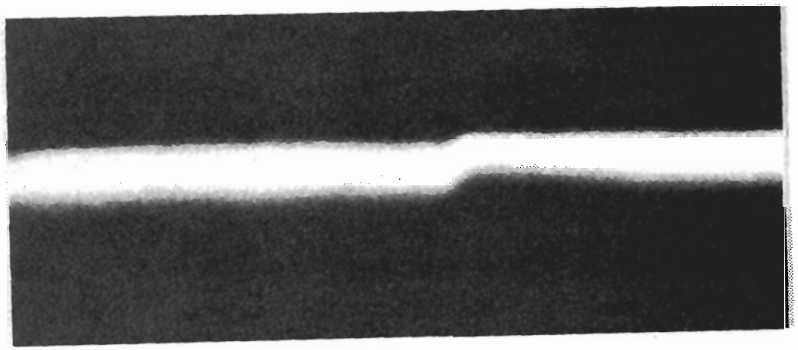


Fig A6.22 An image taken with the orthogonal slit camera showing misalignment of line foci.

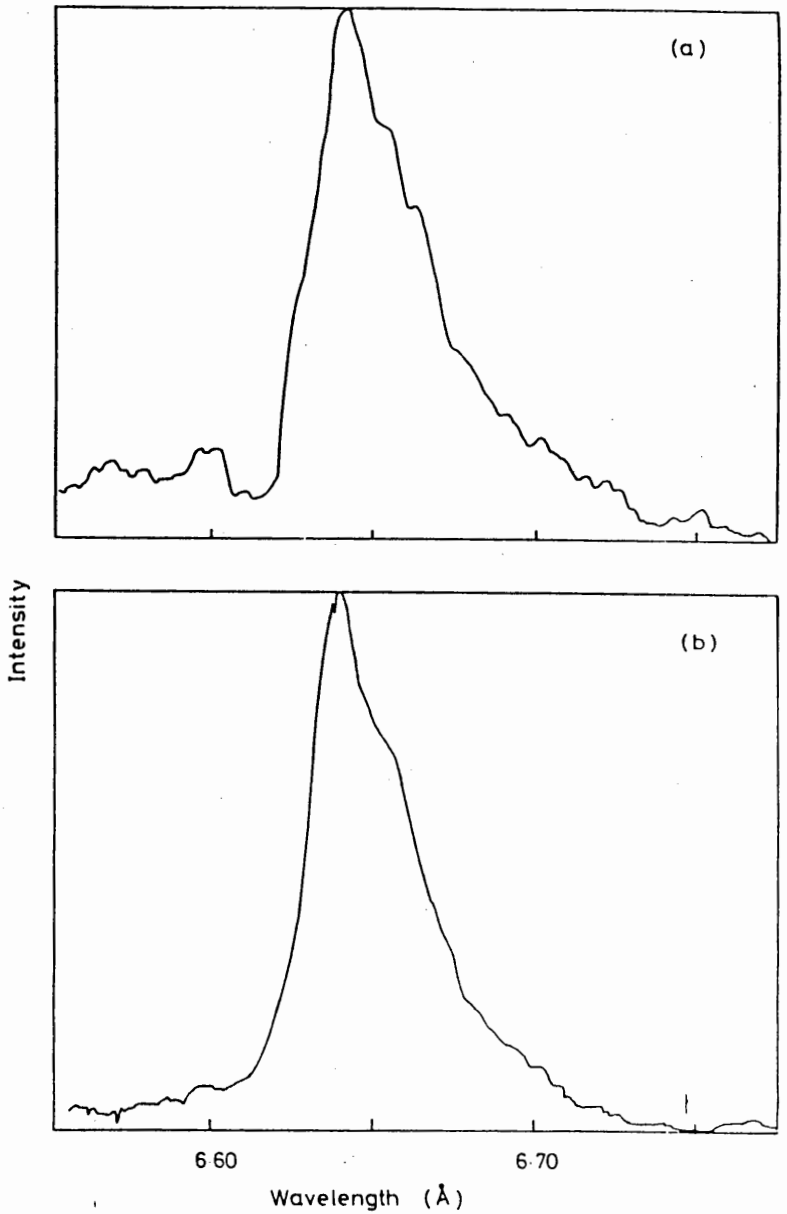


Fig A6.23 Spectral line profile measured (a) in a single densitometer scan and (b) by averaging six scans over the line at different positions on the film. The improvement in signal to noise ratio in (b) is apparent.

plasma are much smaller than the axial make the orthogonal slit camera the best choice of imaging device.

Results

A typical set of images obtained from a single shot of a 200 μm wide Ge target irradiated at 14 J mm^{-1} using a 1.8 ns IR pulse is shown in Fig A6.19 where the filters used have 1/e cut-offs at 1.0 keV, 1.25 keV and 2.1 keV respectively. From this set of images densitometer traces were taken both at various positions along each image as shown in Fig A6.20 and also traces were made at equivalent positions on each of the three images as shown in Fig A6.21. The traces were then converted from density to exposure plots and the transverse FWHM measured. Measurements show that the transverse FWHM is constant to with ± 6% over the full length of the plasma and was measured as 112 ± 7 μm. Fig A6.21 shows the traces from the same position on the plasma but filtered differently. When the FWHM is measured here again it lies in a similar range 110 ± 12 μm and initial calculations suggest that in the .5 ← → 3 keV region the emission from the 1-2 keV band dominates.

Fig A6.22 shows the 1.25 keV 1/e image obtained on shot #07030389 which was taken just after some adjustments to the line foci had been made. This image shows that one of the line foci was incorrectly aligned and the displacement between the centres of the FWHM measured on either side of the misalignment corresponds to 40 ± 4 μm. Measurements also show that the FWHM on either side of the misalignment changes by 26% indicating that part of one beam missed the target and fell on the plastic support as would be expected from a 40μm misalignment on a 200 μm wide target.

Discussion

The data obtained from the Orthogonal slit camera during the Feb 1989 X-ray laser experiment has enabled the easy measurement of transverse plasma structure along the length of the plasma, an estimation to be made on the time integrated emission profile in the .5 <> 3 keV region and any beam misalignment problems to be quickly observed and corrected.

For the direct imaging of a plasma which is much longer in one dimension than another the differential magnification obtainable from the orthogonal slit camera compared to the pinhole camera therefore makes it an ideal choice of imaging device.

A6.5 DENSITOMETER DATA REDUCTION

G J Tallents (RAL)

Spectra recorded on film are often the major diagnostic information produced in experiments at the CLF. The optical densities on the film usually need to be related back to the intensities of the radiation producing the exposure and the distances on the film in the dispersing direction need to be converted to wavelength or photon energy. A computer program to process densitometer data in this way has been developed and this is a brief report of what is available.

A computer controlled Joyce-Loebl microdensitometer is used for the x-y scans of film. The driving computer is a PC-clone and a program (MDEN written by C Reason) controls the densitometer and produces a file of 10 bit integers (plus header information), where each integer corresponds to a pixel in the scan and the value of each integer is proportional to the film optical density. This file is the input data for the program (called DENSDISP) discussed here. The program is written in TURBO PASCAL IV.

The densitometer scans should be made so that the +x direction is normal to any spectral lines in the direction of increasing wavelength. Each y position scan is read and processed separately by the program.

The integer numbers produced by the densitometer are converted to optical density using calibrations for the different densitometer wedges. These have been determined using KODAK WRATTEN filters. The density D above clear film of the exposure needs to be fixed by the user. If the scan extends onto clear film, for example, this will be D=0. Film calibrations for KODAK DEF and 101 X-ray and XUV film respectively are incorporated in the program following Henke et al (1,2).

For KODAK DEF, the optical density D is related to I the photon number/μm^2 producing the exposure by the thick emulsion formula

$$D = A \ln (1 + BI) \qquad (1)$$

where $$B = 1.728\ (1-\exp(-G\mu))\exp(-\mu_o/\sin\theta)\ \mu m^2 \qquad (2)$$

and μ is the absorption coefficient for Ag Br (see table 9 of Henke et al (2)), G is the film grain size (= 1.6μm), μ_o is the absorption coefficient for gelatine (see table 9 of Henke et al (2)), θ is the angle of incidence of x-rays onto the film. A is a parameter deduced from the table 1 calibration of Henke et al (1).

We set $A = 2/\ln (1+BI_{D=2})$, where $I_{D=2}$ is the intensity of photons/μm^2 producing an exposure of D=2. The table of $I_{D=2}$ for different photon energies given by Henke et al (2) is stored and interpolated by the code. The absorption coefficients μ and μ_o have been fitted by parameterised variations.

For KODAK 101, the optical density D is related to I the photon number/μm^2 producing the exposure by the thin emulsion formula

$$D = A_1(1-\exp(-B_1 I)) \qquad (3)$$

For all wavelengths longer than $\sim$20Å, Henke et al (2) have found that $A_1 = 1.957$ and $B_1 = .3128\mu m^2$. More recent batches of KODAK 101 film have been found to vary such that $A_1 = 1.2$ and $B_1 = .08\mu m^2$ (3). Values of A_1 and B_1 are selected by the user of the program.

A linear dispersion fit can be readily made to known wavelength spectral features using the program with a cursor option. Once the dispersion is known, it is possible to allow for the effect of any filters on the flux of x-rays. Absorption coefficient data μ (4) for beryllium, mylar, aluminium and silicon have been fitted by expressions of the form

$$\mu = C\ E^{-\kappa} \qquad (4)$$

where C and κ are constant between absorption edges for different photon energies E(keV) (see table 1).

If the spectrometer is a flat crystal instrument, the flux ϵ of x-rays in units of photons/Angstrom/steradian from a point source is given by

$$\epsilon = \frac{D\ D_{sp}}{W_c}\ I_f \qquad (5)$$

where D_{sp} is the dispersion in Å/mm say,
D is the distance of the film from the source along the path of the x-rays (in mm).
W_c is the crystal integrated reflectivity (in radians),
and I_f the photon intensity onto the film after taking account of any filter attenuation (in photons/mm^2).

The distance D of the film from the source can be found by simple geometry for a flat crystal spectrometer if the dispersion D_{sp} is known. We have

$$D = (1/D_{sp})\frac{2d\cos\theta}{\sin(\theta+\phi)} \qquad (6)$$

where d is the crystal atomic plane separation (in Å),

$\theta = \sin^{-1}(\frac{\lambda}{2d})$ the Bragg angle,

and ϕ is the angle between the plane of the crystal and that of the film.

The crystal integrated effectivity W_c varies with Bragg angle θ and on how "perfect" or "mosaic" the crystal is. For a perfect crystal (5), we have

$$W_c^{(p)}(\theta) = W_c(\frac{\pi}{4})(1+|\cos(2\theta)|)\tan\theta \qquad (7)$$

and for a mosaic crystal (5)

$$W_c^{(m)}(\theta) = W_c(\frac{\pi}{4})(\frac{\sin\theta}{\sin(\pi/4)})^3(\frac{1+\cos^2(2\theta)}{2\sin(2\theta)}). \qquad (8)$$

The integrated reflectivity $\theta = \frac{\pi}{4}$ needs to be defined by the user if $W_c(\theta)$ is to be absolutely specified.

Similarly, the code needs the perfect crystal contribution and the mosaic crystal contribution at $\theta = \frac{\pi}{4}$ specified. If the Bragg angle θ is close to $\frac{\pi}{4}$, both $W_c^p(\theta)$ and $W_c^m(\theta)$ do not vary greatly with θ and, consequently, the wavelength variation of the spectrometer sensitivity is minimised. Bragg angles $\theta \sim \frac{\pi}{4}$ are better for relative flux measurements at different wavelengths as the state of the crystal (perfect - mosaic) is less important.

The program allows the emissivity to be summed over a wavelength range and the x-ray energy emitted over this range to be calculated using equations (5) and (6). Various other calculations can also be made (see the menu in table 2). A useful facility is the ability to store a spectrum and then (i) to average the saved spectrum with a new spectrum (ii) subtract the saved spectrum from a new spectrum or (iii) divide the saved spectrum into a new spectrum. For example, option (i) is useful for averaging scans made at different y-positions on the film and can improve the signal to noise ratio (Fig A6.23).

In summary, a computer program to process densitometer spectra has been developed. The program can be used on the CLF microdensitometer computer or copies obtained from G Tallents. A technical manual will be prepared.

Table 1

Parameters to give absorption coefficients $\mu = C\,E^{-\kappa}$ in units of cm^2/g.

	C	κ
Beryllium	5.37×10^2	2.95
Mylar		
$\lambda > 43.66$Å	2.71×10^2	2.11
23.31Å $< \lambda < 43.66$Å	1.08×10^3	2.82
$\lambda < 23.31$Å	2.89×10^3	2.60
Aluminium		
172Å $> \lambda >$ 7.95Å	1.15×10^3	2.67
$\lambda <$ 7.95Å	1.49×10^4	2.69
Silicon		
124Å $> \lambda >$ 6.74Å	1.53×10^3	2.69
$\lambda <$ 6.74Å	1.75×10^4	2.69

Table 2

Menu available with DENSDISP program.

MENU

Press

W	Spectral line half-Width				
A	Add intensity above background				
R	change intensity and dispersion calibration				
L	intensities on a Logarithmic scale				
E	toggle from wavelength to Energy scale				
J	energy emitted (Joules/4pi)				
C	activate Cursor T change vertical limits				
S	change wavelength range plotted				
D	fit Dispersion I intensity calibration				
F	effect of Filters on spectrum				
B	Biology - calculate rads/joule				
G	adjust backGround intensity				
P	Print plot	M	arithmetic on graphs		
Y	plot saved graph	N	New continuum	H	Help
X	re-plot	Z	save graph	Q	Quit

References

1) B L Henke, J Y Uejio, G F Stone, C H Dittmore and F G Fujiwara 1986,
J Opt Soc Am B3, 1540.

2) B L Henke, F G Fujiwara, M A Tester, C H Dittmore and M A Palmer 1984

J Opt Soc Am B1, 828.

3) Dr K Eidmann 1989 Max-Planck-Institut fur Quantenoptik Private Communication.

4) E B Saloman, J H Hubbell and J H Scofield 1988 At Data and Nud Data Tables 38, 1.

5) N G Alexandropoulos and G G Cohen 1974 Appl. Spect 28. 155.

A6.6 ALPHA PARTICLE IMAGING WITH PSEUDO-NOISE PRODUCT (PNP) MASKS

M Grande, RAL
P Fews and M Williams, Bristol University
M Lamb and M Savage, Queens University, Belfast

Imaging by coded aperture masks based on uniformly redundant arrays (URA), has been applied to laser produced plasmas previously[1,2] both for α-particles and X-rays. However, until recently there was always a problem in producing the isolated free standing elements required in thses masks. However, this problems has been eliminated by the PNP mask. For a full description, the reader should consult the original paper by Gottesman and Scheid [3]. Essentially, their suggestion was that a two dimensional mask may be constructed from two one dimensional PN sequences (for example the Hademard sequences used to construct a URA) by the recipe

$$PNP = \begin{bmatrix} \overline{a_1 b_1} & a_1 b_2 & \cdots & a_1 \overline{b_n} \\ a_2 b_1 & \overline{a_2 b_2} & \cdots & a_2 b_n \\ \cdots & \cdots & & \cdots \\ a m b_1 & a m b_2 & \cdots & \overline{a m b_n} \end{bmatrix}$$

where a_1, a_2, ..., a_m and b_1, b_2, ... bm (a_i, b_j = 0 or 1) are the original sequences, which may be the same in practice.

Fig A6.24 shows such mask. It is seen that although the mark-to-space ratio is only about 25%, as opposed to about half for a conventional URA, this is compensated by ease of fabrication

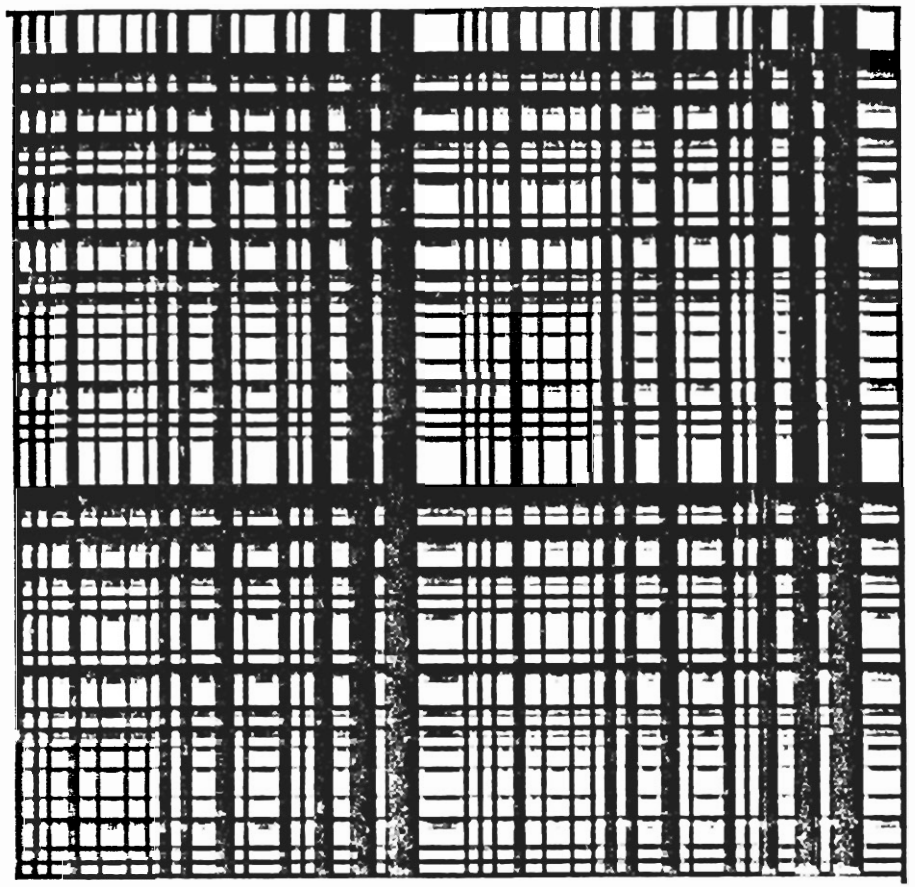


Fig A6.24 Design for a PNP mask.

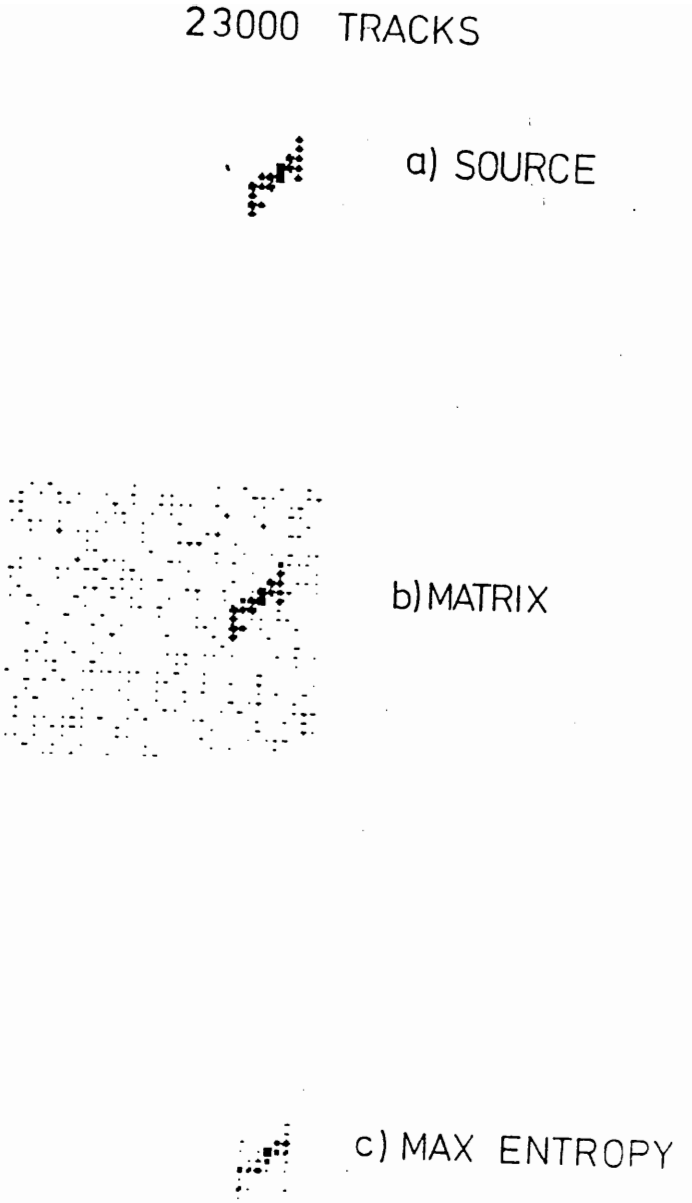


Fig A6.25 Reconstruction of a simulated PNP image. There are 23000 tracks in the image, a realistic number for the configuration used in TAW.

(a) source,

(b) analytical reconstruction by the method of Gottesman and Scheid,

(c) maximum entropy reconstruction.

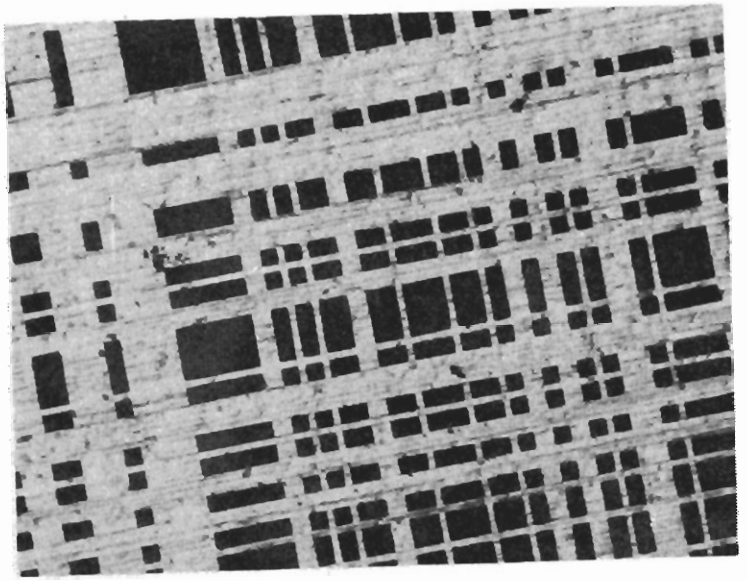


Fig A6.26 Detail from an actual mask.

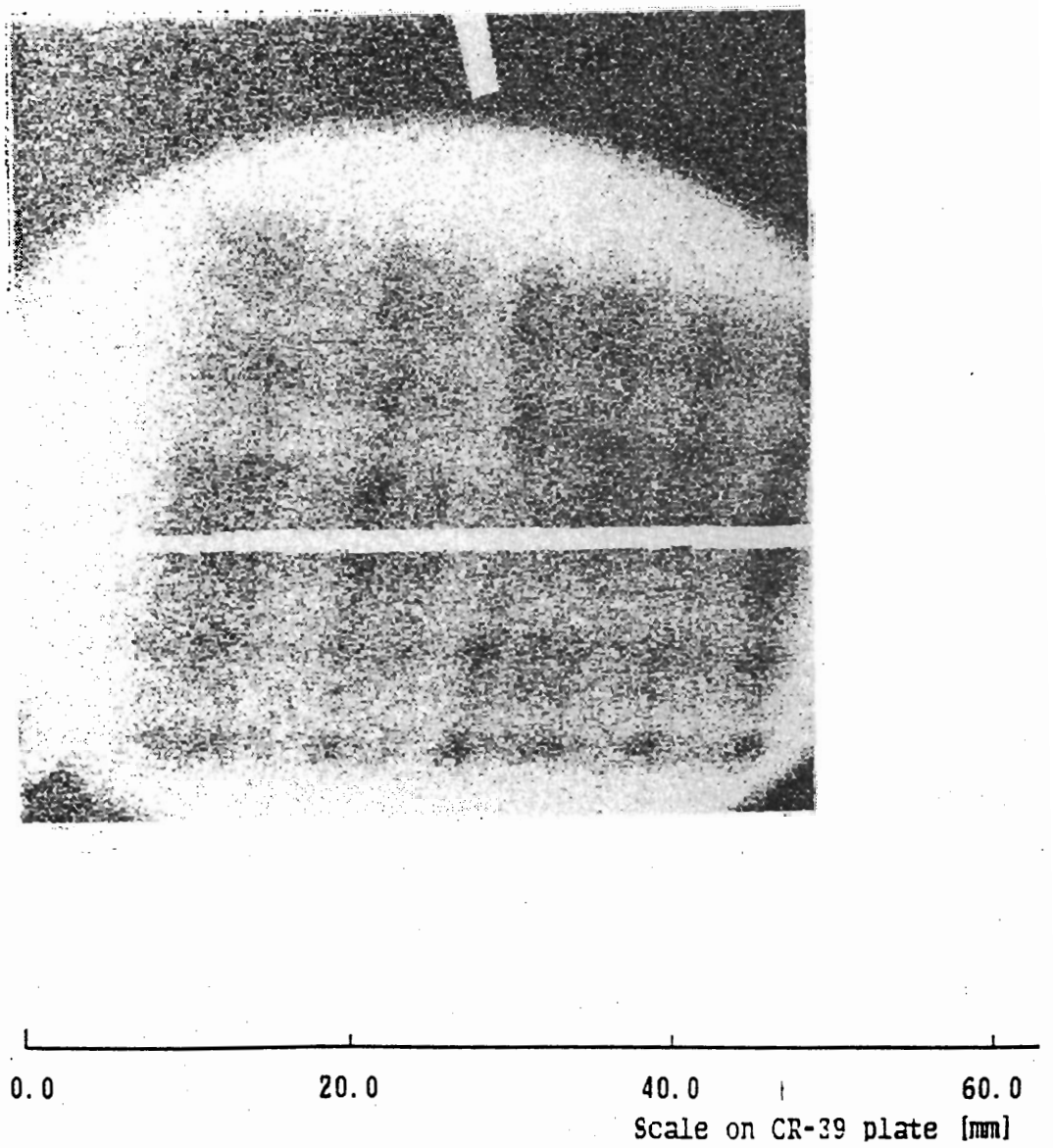


Fig A6.27 CR-39 image of a NUHART implosion seen through a PNP mask.

since it can be completely self supporting. Moreover, the analytical deconvolution of a source imaged thorugh such a mask is essentially simple[3] and will yield a signal to noise ratio much higher than either a pinhole of the same resolution, or a penumbral aperture of the same size. Fig A6.25 shows a reconstruction of a simulated source in a realistic configuration, using the mask in Fig A6.26. For comparison an unfolding using a maximum entropy method to analyse the image produced by the mask.

Similar (but slightly non-optimum) masks have recently been used fore α-particle imaging of NUHART implosion cores[4] using a grating of minimum period 15 μ, which should therefore be the spatial resolution limit. Fig A6.27 shows a detail from an actual mask*. Fig A6.28 shows the distribution of α-particle tracks observed through it, using a CR-39 plastic detector. Detailed analysis of the results obtained is in progress, and the technique appears to offer signficant advantages, particularly if the mask geometry can be very accurately defined with respect to that of the target.

The masks in 15 μm copper were produced by Graticules Ltd. Our thanks to John A Watkins for his assistance.

References

1. M Yamanaka et al, 18th ECLIM, Prague, 1987.

2. M Grande, T Tomie and E Fill, 18th ECLIM, Prague, 1987.

3. S R Gottesman and E J Schneld, IEEE Trans Nucl Sci **33**, 745, 1986.

4. A P Fews et al, section A3.5 in the appendix to this report.

B	**SPRITE OPERATIONS AND DEVELOPMENT AND SUPERSPRITE**	Pages
B1	SPRITE OPERATIONS AND DEVELOPMENT	185-224
B2	SUPERSPRITE DEVELOPMENT	225-230

B SPRITE OPERATIONS AND DEVELOPMENT AND SUPERSPRITE

Introduction

P Rumsby (RAL)

The SPRITE laser system has been used throughout the year to investigate that basic physics of Raman beam combination in the picosecond pulse duration transient regime. Section B1 lists experimental and theoretical work associated with this programme.

Work is now proceeding to develop the technology and specify system designs for two versatile high power, high energy ultraviolet laser systems based on Raman/KrF multiplexed architecture.

Detailed design and pulsed power development work is now active for the SUPERSPRITE laser facility which the recent CLF Review Panel recommended should be built to replace the existing VULCAN laser system in 5-6 years time. Performance of the proposed SUPERSPRITE system is shown in Table 1.

Section B2 below discusses initial work on generator development and establishment of costing models.

In addition architecture designs and costings for a 100 kJ, multi-Petawatt system for a scientific and technical study of options for a European High Performance Laser Facility are have recently been initiated.

SUPERSPRITE SPECIFICATION Table 1

Laser	
No of beams	12
Maximum energy	3.5 kJ
Maximum power	300 TWatt
Pulse duration	1 psec - 10 nsec
Wavelength	268 - 277 nm
Pulse Rep Rate	10 per hour
Target irradiation facilities	
a) 12 beam, longpulse, cluster or spherical.	
b) 12 beam, short pulse, high power, cluster or line focus.	

B1	**SPRITE OPERATIONS AND DEVELOPMENT**	Pages
B1.1	SPRITE DEVELOPMENT AND OPERATIONS	187
B1.2	KrF MULTIPLEXER DEVELOPMENT	187-191
B1.3	OSCILLATOR DEVELOPMENT	191-193
B1.4	CHARACTERISATION OF THE SPRITE RAMAN SYSTEM	193-204
B1.5	RAMAN AMPLIFIERS - A NUMERICAL APPROACH	204-215
B1.6	LIGHTGUIDES FOR RAMAN AMPLIFIERS	215-218
B1.7	DESIGN CONSTRAINTS FOR MULTI-STAGE RAMAN AMPLIFICATION IN OPTICAL AND RAMAN MULTIPLEXED KrF LASER ARCHITECTURES	218-224

B1.1 SPRITE DEVELOPMENT AND OPERATIONS

M. Shaw (RAL)

This year has seen the integration of the Sprite system as an amplifier of multiplexed picosecond pulses followed by Raman beam combination to form a single Raman shifted output beam. This process met with more difficulties than originally anticipated and target shooting runs scheduled for August 1988 which should have produced a few joules at 4 ps duration were not successful.

There has, however, been a rather intense period of laser development activity aimed at understanding the system more fully and over the year a total of some 2,300 shots have been fired. The main conclusions are as follows:-

The 4 ps experiments were not successful due to spectral broadening of the initial non-transform limited oscillator pulses. The broadening mechanisms (which occur in air and in the laser medium) depend not just on the intensity length product but on the bandwidth of the initial pulse. Details of experiments performed to investigate these and other non-linear processes in air and silica are given in section C3.1.

Spectrally narrow (transform limited) 40 ps pulses do not broaden significantly and have been successfully amplified in Goblin and Sprite and beam combined in the final Raman amplifier with efficiencies of around 50%. Pump intensity variations due to reflections at near grazing angles from the non flat lightguide walls were much worse than anticipated and lead to imprinting on the Stokes beam. This situation is aggravated by operating the Raman amplifiers at high stage gain without spatial filtration.

These points and others are discussed in more detail below. In section B1.2 the layout and performance of the Sprite KrF multiplexer system is discussed. In B1.3 the continuing development of the oscillator system is described. In B1.4 the characterisation of the Raman amplifiers is described and the development of a numerical code which can handle many of the parameters of Raman amplifiers in 1D is presented in section B1.5. In section B1.6 the question of flatness and reflectivity of the glass used in lightguide construction is considered in some detail. In B1.7 the design constraints imposed by some of the problems we have been encountering are discussed in the general context of large systems based on Raman beam combiners.

B1.2 KrF MULTIPLEXER DEVELOPMENT

M J Shaw, C J Hooker (RAL)
J E Andrew (AWE)
E Fujiwara (Osaka)

During this year the Sprite multiplexer system has been extensively modified so that multiple picosecond KrF beams can be amplified in the Goblin and Sprite lasers. The purpose of the work was to demonstrate beam combination in Raman amplifiers operating in the short pulse (transient) regime. The results from the Raman amplifiers is discussed in section B1.4. In this section we consider the multiplexer system.

Figure B1.1 shows a simplified schematic of the beam paths in the multiplexer room. The 248 nm KrF beam enters the room at an energy level of between 1 and 5 mJ and pulse duration of between 4 and 40 ps. After spatial filtration the beam is expanded and apodised to 20 mm diameter and a few hundred μJ are injected into the multiplexer. The multiplexer divides the beam by amplitude into 4 beams and inserts a delay of 5 ns between beams.

The four beams are injected into Goblin via the multibeam VSF as shown in Figure B1.2. The pinholes in the VSF were removed, so the purpose of the evacuated section was mainly to provide an image

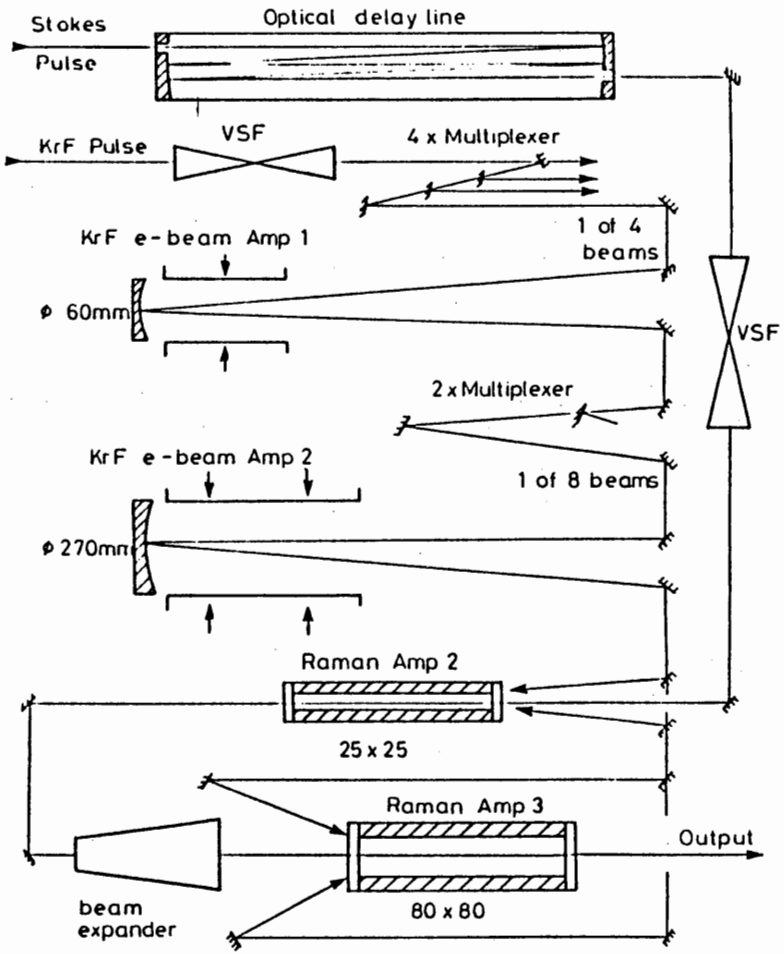


Fig B1.1 Optical layout of the Sprite multiplexer system showing multiplexed KrF beams and the Raman shifted beam line.

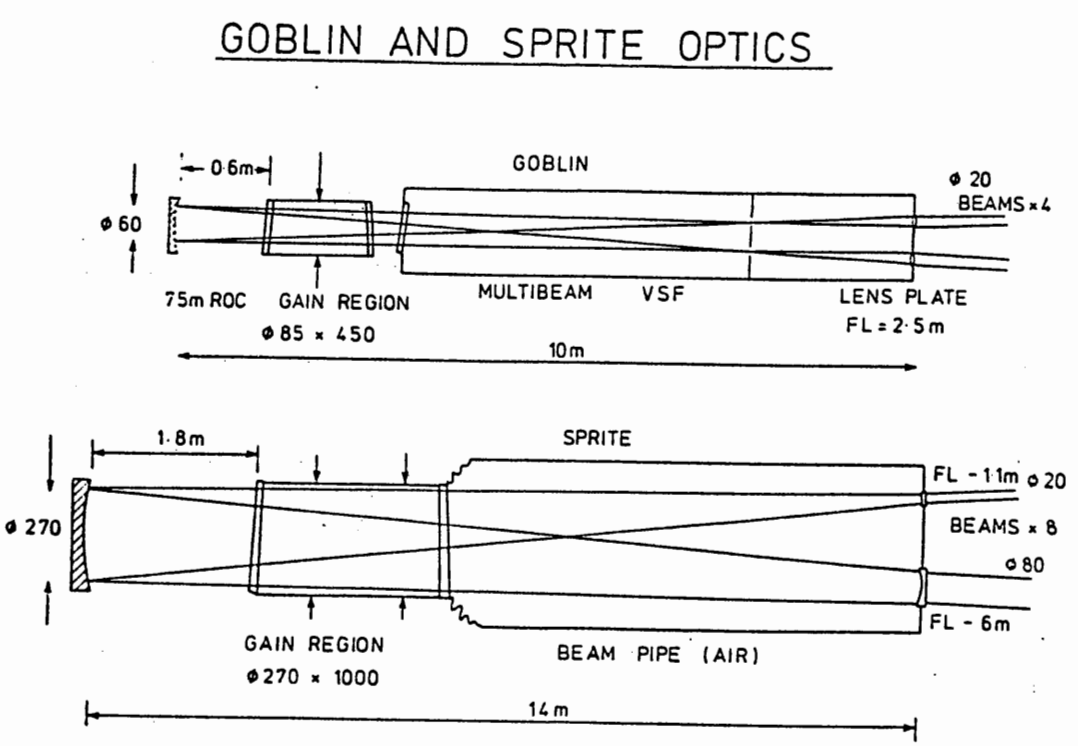
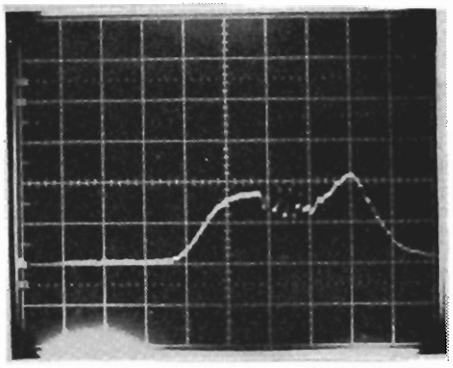
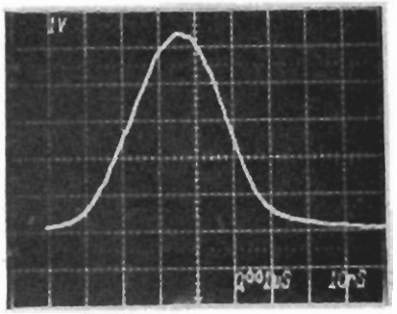


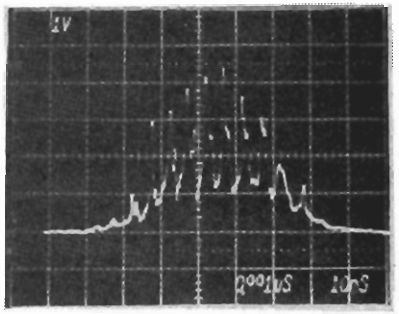
Fig B1.2 Details of the Sprite and Goblin optics used for short pulse multiplexing.



(a)



(b)



(c)

Fig B1.3(a) Axial ASE from Goblin depleted by amplification of 4 short pulses. (b) Axial ASE from Sprite with no depleting pulses. (c) As (b) but with 8 pulses being amplified. (a) at 20 ns/div. (b) and (c) at 10 ns/div.



Fig B1.4 View of multiplexer room. Sprite beam pipe is on the right delivering and output beams to the output mirror frame. De-multiplexing mirrors are in the foreground.

relay stage. With the input energy available, typically between 10 and 20 mJ per beam was obtained at the output of Goblin. The stage gain for Goblin is about 100 and the output only partially saturates the gain; 20 mJ corresponding to about ½ of the saturation fluence at the output window. Figure B1.3a shows depletion of axial ASE from Goblin by the passage of the 4 multiplexed beams through the amplifier.

The collimated output beams are then each multiplexed into 2 beams via a 50% splitter and a delay of 20 ns inserted into the split off beams. There are now thus 8 beams with a 5 ns spacing between pulses and a first to last pulse spread of 35 ns. These beams are then directed into the Sprite amplifier by the optical arrangement shown in Figure B1.2. The back mirror is situated 1.8 m from the gain region in order to reduce ASE depumping. This reduces the beam diameter at the output from 27 cm to 22 cm, however some of the beams are cut off and the effective beam area is quite a bit smaller than the 380 cm^2 calculated for non cut off beams. The maximum energy obtained on an individual beam was 1.5 J and the maximum total energy (8 beams) was 10 J. The maximum fluence obtained at the Sprite output window was 4 mJ/cm^2 corresponding to $2x\ E_{sat}$. Figure B1.3 b) and c) shows the axial ASE from Sprite respectively without and with a depleting pulse train. The pulses significantly deplete the gain although with this inter pulse spacing the gain repumps to close to its maximum value in the 5ns between pulses.

Figure B1.4 shows a view of the layout in the multiplexer room. One of the 8 output beams is split into 8 beamlets with a segmented mirror and pumps the 2.5 cm square lightguide of RA1 (Raman amplifier 1). The other seven output beams from Sprite are de-multiplexed by the mirrors on stands which are arranged at a common cone angle of either 2.5° or 5° to the axis of RA2.

B1.3 OSCILLATOR DEVELOPMENT

C J Hooker, I N Ross, J Lister (RAL)
E Fujiwara (ILE, Osaka University)

The oscillator development work over the last year has concentrated on converting the experimental Raman generator and amplifier[1] into a reliable front-end for the Raman amplifier chain. The 746nm dye laser, which is the source of picosecond pulses for the entire Sprite system[2] has remained essentially unchanged, although the introduction of a sapphire jet has increased its stability by providing an optically flat dye stream. The dye amplifier has been modified by removing the second stage, which was contributing very little to the overall gain and was causing some beam distortion. More recently, the pumping of this amplifier has been greatly improved by changing from the Lumonics XeCl pump laser to a Q-switched frequency doubled YAG. The new pump laser (made by Spectron UK) puts out 300mJ at 532nm in a 6ns pulse, a four fold increase in pumping energy over the Lumonics. The output of the third harmonic has increased from the previous 20µw (2.5µJ per pulse) to 160µw and the better temporal stability of the Spectron laser has greatly reduced the pulse-to-pulse fluctuation.

The major changes made to the oscillator are (a) the use of the EMG 103 KrF amplifier in double-pass and (b) a different Raman generator/amplifier layout. The present arrangement is shown in Figure B1.5.

The 249nm beam from the tripling crystal is spatially filtered, and sent on a skew path through the amplifier. The beam is 5mm in diameter and at the output the energy is typically 300µJ per pulse. 10% is split off by a quartz flat (QF) and sent through the spatial filter, whose 50µm pinhole is in a vacuum cell. The beam is recollimated at diameter of 17mm for the second pass of the amplifier, after which the energy per pulse approaches 10mJ. Part of this beam, which is a rectangle defined by the laser aperture, is split off spatially to serve as the seed pulse for the KrF chain, and the remainder is used to pump the Raman amplifier.

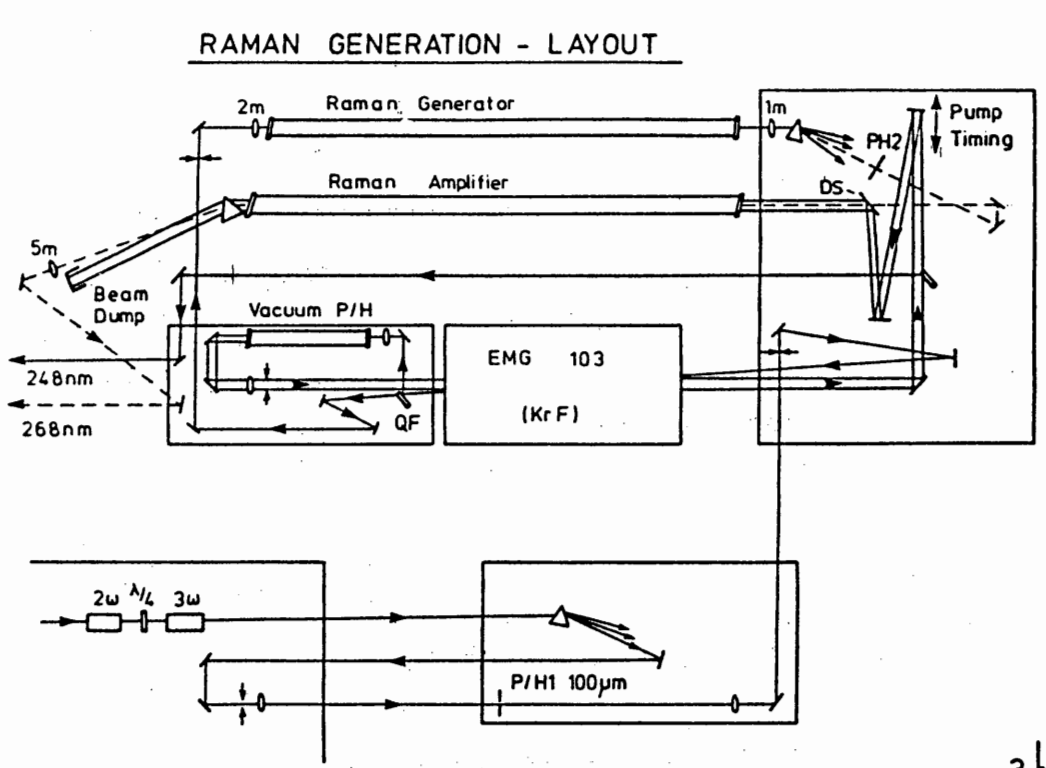
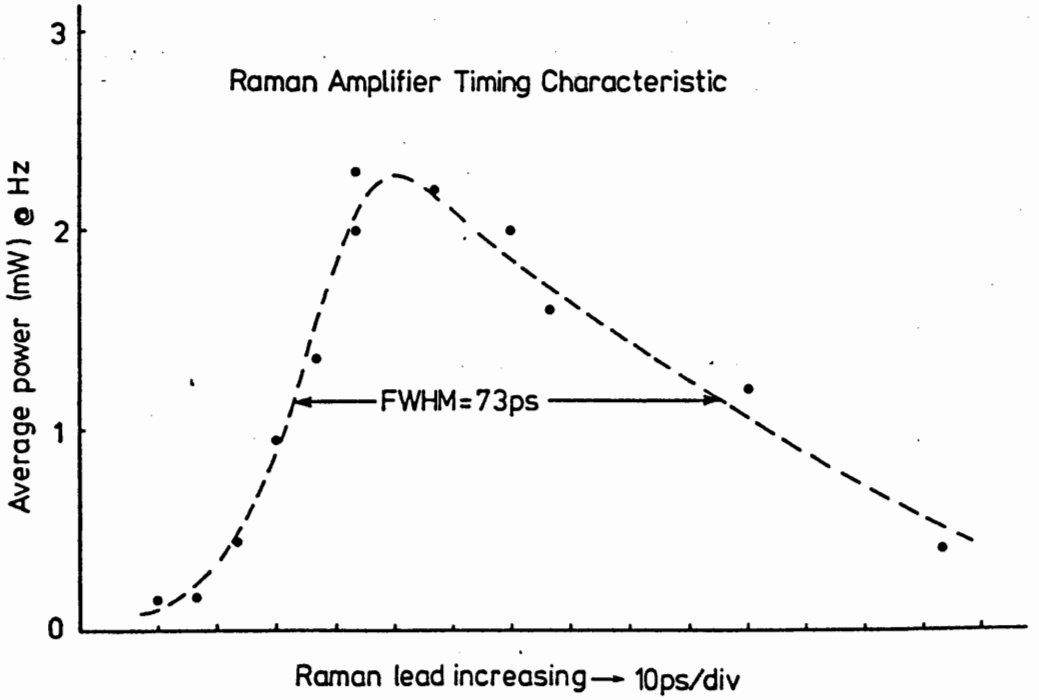


Fig B1.5 Beam layout for the first KrF amplifier (EMG 103), Raman generator and first Raman amplifier, RAØ.

Fig B1.6 Average output power from RAØ as a function of the relative time between pump and Stokes beams.



The main portion of the first pass beam is transmitted through the beamsplitter and steered to the Raman generator. The cell is a 2.7m length of stainless steel tubing, containing methane at a pressure of 3 atmospheres. The beam, which contains 250μJ per pulse, is focused into the cell by a lens of 2m focal length. At the output the beam is recollimated using a 1m fl lens, and the various frequencies separated using a prism, there being typically three or four Stokes and one or two anti-Stokes lines present. A 500μm pinhole (PH2) selects the central portion of the first Stokes, which is allowed to expand gradually through the amplifier until it is collimated by a 5m fl lens at the output.

The pump and Stokes beams are combined on the dichroic splitter (DS) which reflects 249nm while transmitting the 268nm first Stokes. The path lengths from the 10% splitter to this point are nearly equal and can be made exactly so by a sliding mirror which adjusts the pump beam path. The two beams propagate together through the amplifier cell, which is 3 metres long and is generally pressurised to 5 atmospheres with methane. The gain in the amplifier is typically 400x, giving a Stokes energy of 1mJ. At the output, another prism separates the two wavelengths, and the residual pump is rejected. In fact, the two beams are not exactly colinear, a slight skew angle between them serving to prevent the fringes on the pump beam becoming imprinted on the Stokes. This intensity averaging effect preserves the quality of the Stokes beam.

The output from the oscillator room consists of the two approximately synchronised seed pulses, the KrF with about 2-3mJ per pulse and the Stokes with typically 1mJ per pulse.

References

1. Annual Report 1988, A5-3, P124. Everall/Fujiwara.

2. Barr et al, Optics Comm 66, 127 (April 1988).

B1.4 CHARACTERISATION OF THE SPRITE RAMAN SYSTEM

C J Hooker, J M D Lister, J Radford, I N Ross and M J Shaw (RAL)
J E Andrew, AWE Aldermaston
G M Davis, NTT Opto-Electronics Laboratory
E Fujiwara, ILE, Osaka University

a) Introduction

During July and August 1988 the SPRITE Raman system was operated using nominally 10ps pulses, but its performance fell short of expectations. The highest energy obtained from the large Raman amplifier was 400mJ; more typical energies were 50-100mJ, with extraction efficiencies between 1% and 2%, and gains in the range from 10x to 20x.

In the smaller Raman amplifier, measured gains exceeded 10^4 on some shots, but its output appeared to be clamped at a maximum of 15mJ, despite pump energies of 1-1.5 Joules.

The overall behaviour was highly erratic, with shots that were identical with respect to Raman input and pump energies having outputs that varied by factors of 3.

Using etalons, the spectra of the 746nm oscillator and the amplified 3rd harmonic were examined, and found to fluctuate dramatically from pulse to pulse. The time-averaged spectrum at 746nm was very smooth, but individual pulses selectively amplified in the dye amplifier showed two or three peaks within the average envelope, and the 248nm light varied in a corresponding way.

It was found that the spectrum could be stabilised by installing an etalon (FSR=17cm^{-1}) in the dye oscillator cavity, at the expense of lengthening the pulse, and this arrangement was used subsequently for characterisation.

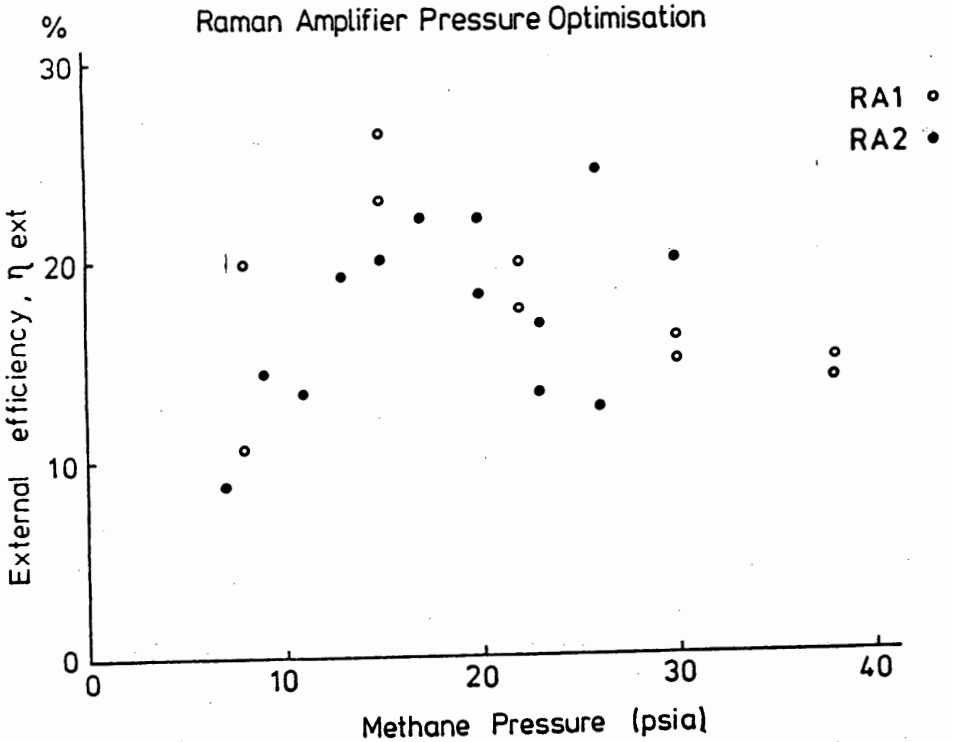
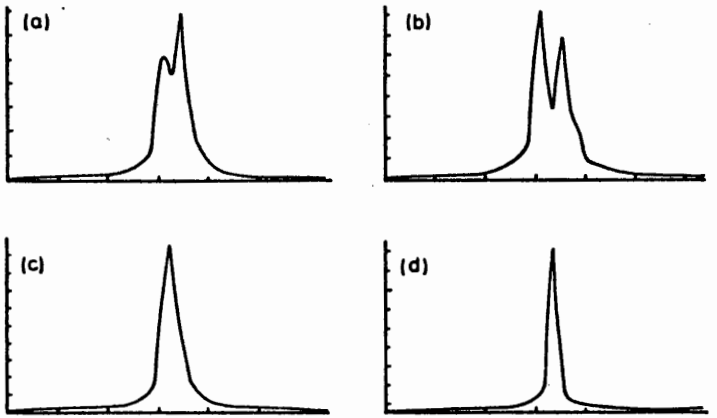


Fig B1.7 Extraction efficiency of RA1 and RA2 as a function of methane gas pressure.

Fig B1.8 OMA spectra of KrF output from the EMG 103 with the sync-pumped oscillator at (nominally) 3 ps pulse duration.



25 cm^{-1} per div.

(a), (b), (c) : Typical grating spectra of 3ps oscillator

(d) : Instrumental profile

FWHM max 18cm^{-1} min 10cm^{-1}

Central wavelength variation ± 6cm^{-1}

(b) **Preliminary Measurements**

With a 746 nm etalon incorporated into the dye oscillator cavity, the output pulses were wider than the time window of the autocorrelator. The FWHM of these pulses was estimated at 80ps.

The optimum relative timing of the Stokes and pump pulses in the Raman preamplifier changed significantly when the pulse length was changed. To find the new optimum, the average output power in the amplified Stokes beam was measured while scanning the delay of the pump beam; the results are shown in Figure B1.6.

The FWHM of the peak gives Stokes-to-Pump cross correlation measure of the pulse length, which at 73 ps is in reasonable agreement with the dye oscillator autocorrelation measurement. The actual delay between the pulses was not measured at this stage; however, during pulse-length measurements performed later, the Stokes and pump inputs to the second Raman amplifier were found to be separated by 80ps, with the Stokes leading. Similar timing characteristics to Fig B1.6 were observed for both the larger Raman amplifiers. The Stokes lead of about 1 pulse duration and the asymmetric time characteristic were also observed by Duncan et al[1] for Raman amplification in hydrogen.

For the remainder of the characterisation period the delays were adjusted to obtain peak gain from all three Raman amplifiers.

A second quantity requiring optimisation was the methane pressure in the two larger amplifiers. Both cells were fitted with 15mm thick windows, so the pressure could be varied above and below 1 atmosphere. As a measure of the amplifier's performance, the efficiency

$$\eta = \frac{\text{Stokes output energy}}{\text{Pump energy x Guide transmission}}$$

was used. Values of η obtained at pressures between 7 and 38 psia (0.5-2.5atm) are plotted in Fig B1.7 and shows good agreement between the two amplifiers. The best operating pressure for RA1 is 1 atmosphere, and for RA2 slightly higher, however, it was decided to operate RA2 at one atmosphere as well, using 2 mm thick Hoya windows to minimise two-photon losses.

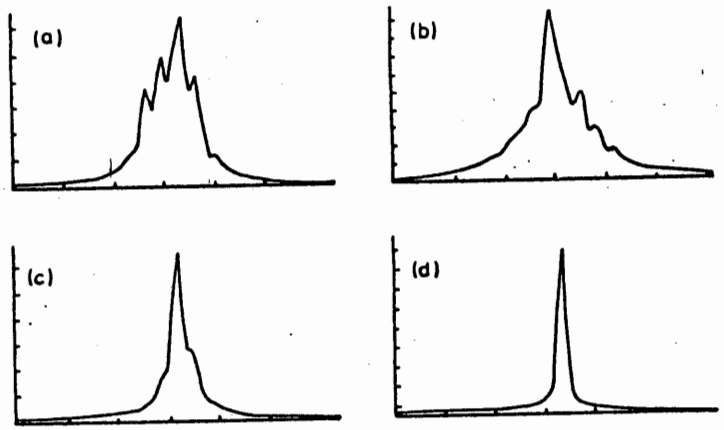
The relative timing of the seven pump beams to RA2 was set up by interference, using nominally 3ps pulses, at the start of the short pulse run in July 1988. Since that time no changes had been made to individual beams that were likely to alter the timing. Since the present experiments would use "long" pulses, it was considered unnecessary to repeat the timing check.

(c) **Spectral Measurements**

Two sets of spectral measurements were made. First, the spectra of the short-pulse oscillator at 3ps (free-running) and 10ps (etalon external to the cavity) were recorded using a 0.5 metre grating spectrograph with OMA output. These short-pulse spectra were too broad to use the etalons available. The 80ps pulse spectrum was recorded using an etalon with a spectral range of $1.1cm^{-1}$, the fringes being photographed on Type 55 Polaroid film.

The measurements were made in the multiplex room, using a portion of one of the SPRITE output beams which passes through the central hole of the RA1 segmented pump mirror. It was thus possible to record oscillator spectra alone, or to amplify in SPRITE and GOBLIN and look for any changes that occurred.

Figure B1.8 shows a sample of 3 ps oscillator spectra, which vary in structure, FWHM and central wavelength from pulse to pulse. The instrumental profile has a FWHM of $5cm^{-1}$ and was obtained using the 80ps oscillator. After amplification in GOBLIN alone, the spectra (Figure B1.9) are in general broader and show more subsidiary peaks, but the variation in FWHM is far wider. No spectra were



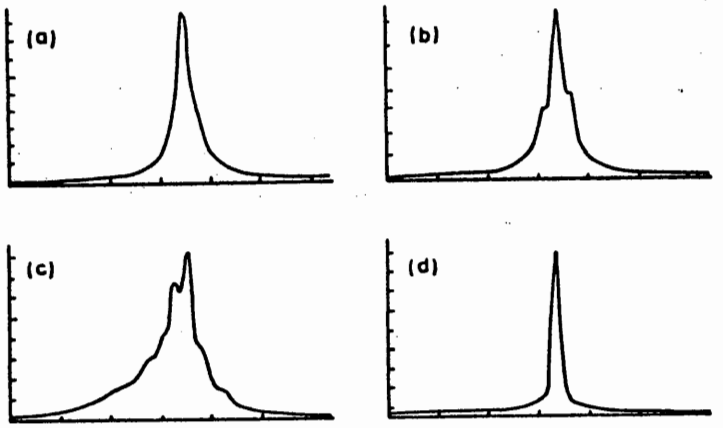
25cm^{-1} per div.

(a) - (c) : Spectra of 3ps pulses after amplification in Goblin

(d) : Instrumental profile

FWHM max 31cm^{-1} min 7cm^{-1}

Fib B1.9 OMA spectra of the KrF output after amplification in Goblin. 3 ps pulse duration.



25 cm^{-1} per div.

Spectra of 10ps pulses:

(a) Oscillator only

(b) After amplification in Goblin

(c) After amplification in Goblin and Sprite

(d) Instrumental profile

FWHM:		
	Oscillator	5 - 10 cm^{-1}
	After Goblin	5 - 10 cm^{-1}
	After Goblin and Sprite	10 - 18 cm^{-1}

Fig B1.10 OMA spectra of the KrF output from (a) oscillator (EMG 103), (b) Goblin, and (c) Sprite showing the effects of spectral broadening. 10 ps pulse duration.

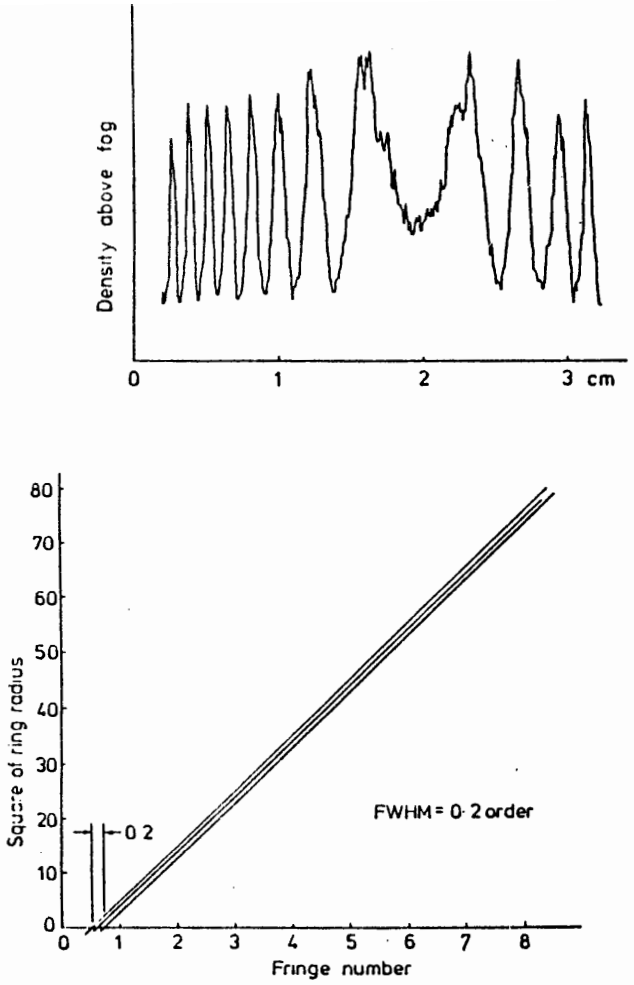


Fig B1.11(a) Densitometer trace of etalon spectrum of KrF oscillator (EMG 103 output) for nominal 40 ps pulse duration. (b) Ring analysis growing symmetric lineshape of 0.22 cm^{-1} (FSR = 1.1 cm^{-1}).

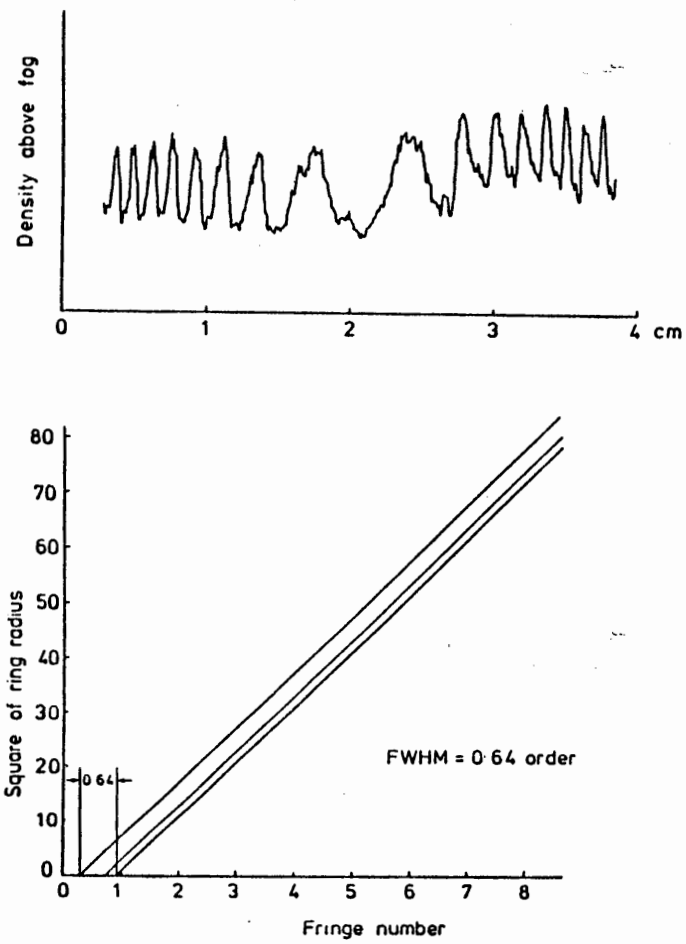


Fig B1.12 As Fig B1.11 after amplification in Goblin and Sprite FWHM = 0.7 cm^{-1} with broadening to the red.

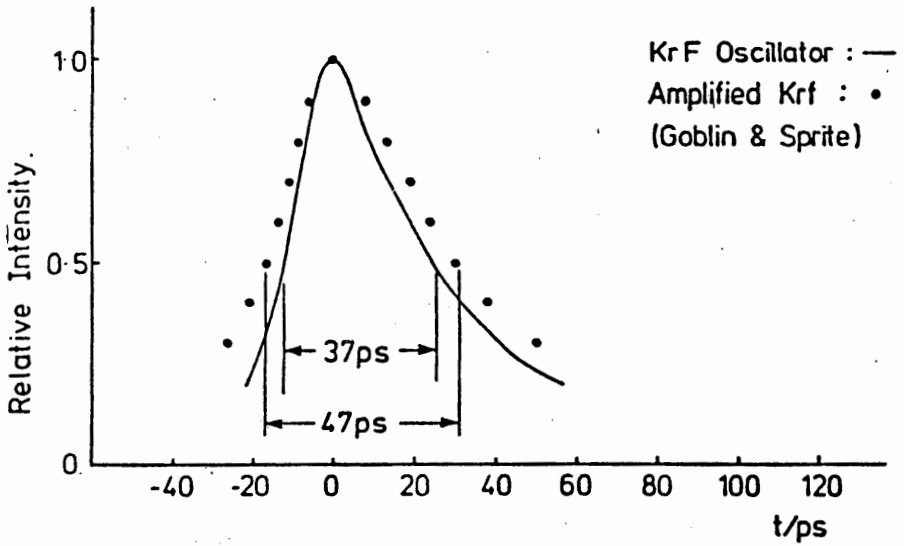


Fig B1.13 Pulse width as measured by streak camera for KrF oscillator and after amplification in Goblin and Sprite.

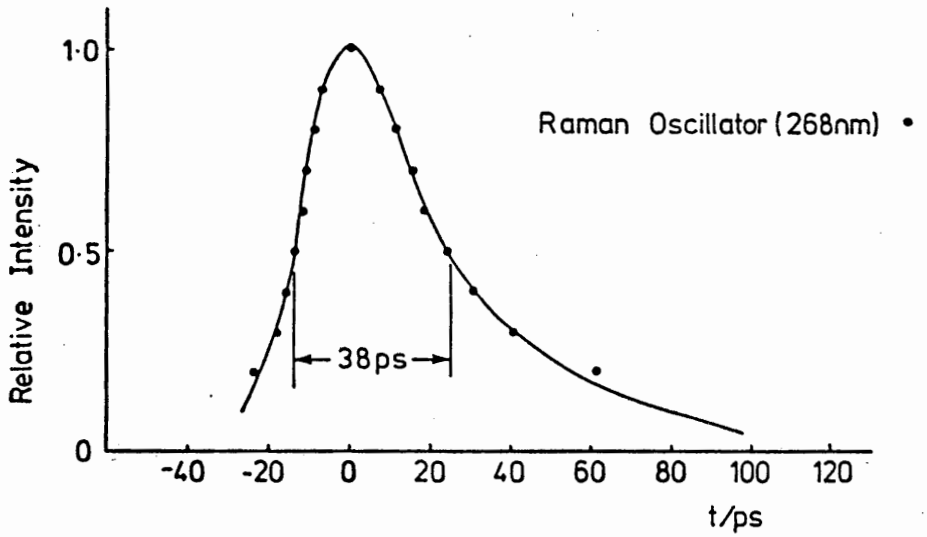


Fig B1.14 Pulse width as measured by streak camera for Raman pulse after amplification in RAØ. KrF pump pulse as in Fig B1.13.

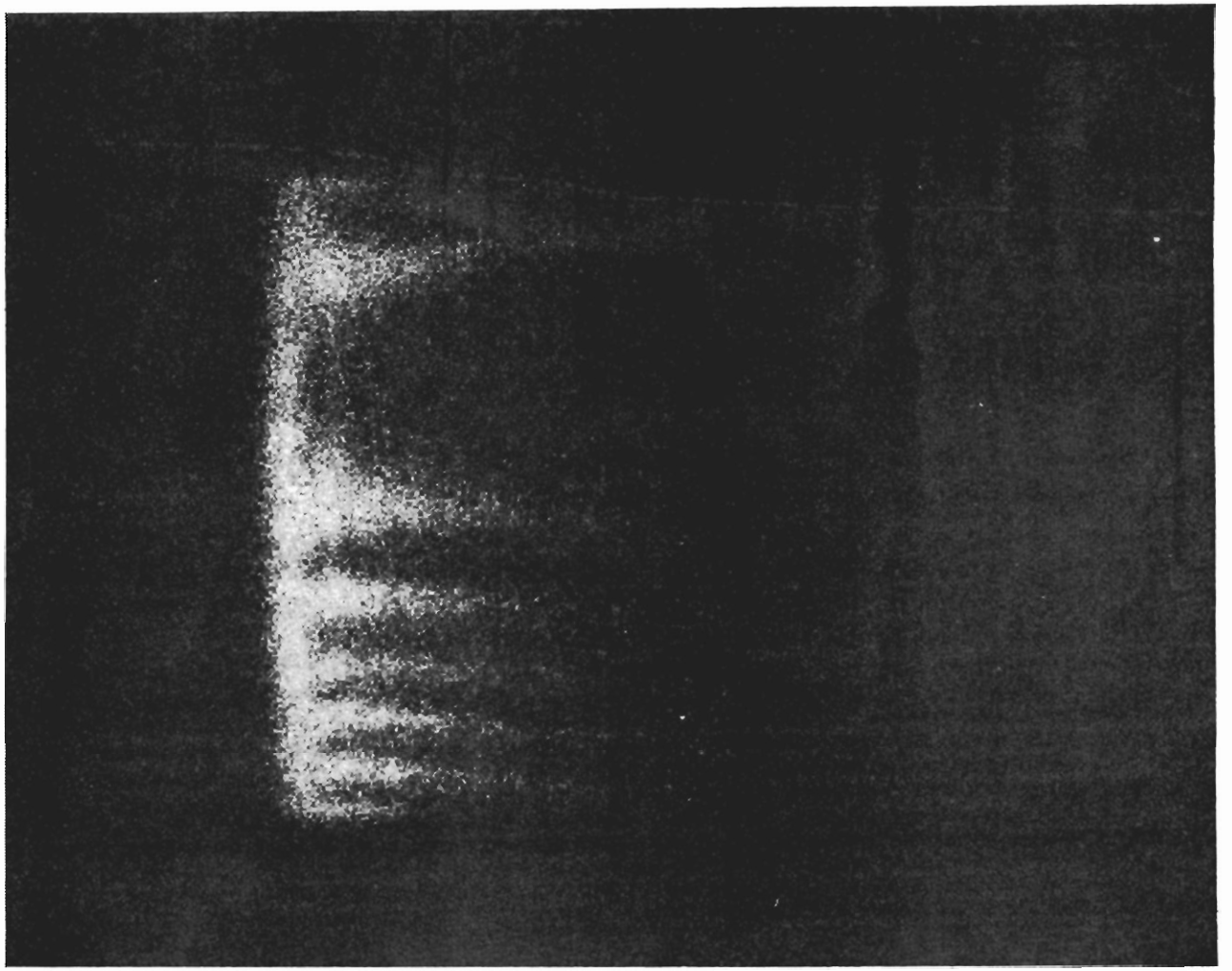


Fig B1.15 Streaked etalon spectrum of KrF output from the oscillator (EMG 103) nominal pulse width 40 ps and etalon FSR 1.1 cm^{-1}.

recorded after amplification in GOBLIN and SPRITE at 3 ps, but in Figure B1.10 a representative set of spectra of the 10 ps pulses is shown.

The 80ps oscillator spectrum could not be resolved by the grating spectrometer, so an etalon with a free spectral range of $1.1cm^{-1}$ was used. A densitometer trace across the Polaroid negative is shown in Fig B1.11(a) for the oscillator alone, while in Fig B1.11(b) are plots of (ring radius) squared against order for the centre and half-maximum points on the fringes. The intercept on the order axis shows the fractional order at the centre of the pattern for the wavelength in question. The FWHM of the oscillator spectrum measured from these data is 0.2 order or $0.22cm^{-1}$. The resolution of the etalon, which has a finesse of 14, is $1.1cm^{-1}/14=0.079cm^{-1}$; thus the oscillator linewidth is resolved.

Fig B1.12 shows corresponding results for the spectrum after amplification in GOBLIN and SPRITE. The linewidth has increased to $0.7cm^{-1}$, and in addition the line has become asymmetric, the red wing being broader than the blue. The shift in the central wavelength is probably not significant, since the two spectra were recorded on different days.

The broadening and asymmetry of the amplified spectrum are similar (though far less in magnitude) to those observed with 10ps and 3ps pulses. The mechanism of the broadening, and the reason why one wing of the spectrum is more prominent than the other, are not clear at present. However, most non-linear processes which introduce a frequency spread yield pulses in which the red component leads the blue and would be expected to see a larger gain, which is what is observed. Further study of the broadening is required.

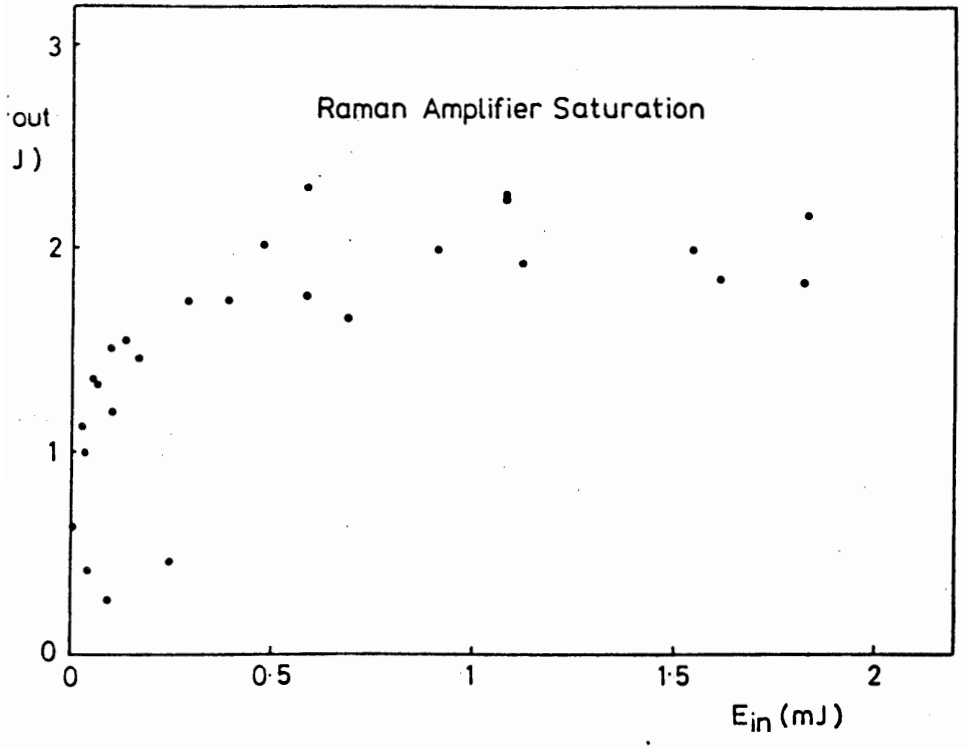
(d) **Temporal Measurements**

Pulse length measurements were made using an Imacon-500 streak camera with a UV sensitive photocathode. Raman and KrF beams were intercepted at the input to RA1, where they are coincident in space and timing. The streak speeds used were nominally 20ps/mm and 50ps/mm, but both were calibrated by streaking the two oscillator pulses and varying the Raman pulse timing using the dogleg delay. Streaks were recorded on HPS in the usual way and densitometered, and an H-D curve was obtained using the target areas film calibrator to enable correct pulse shapes to be determined.

Figure B1.13 shows pulse shapes for the KrF beam before and after amplification. The oscillator pulses recorded all had FWHM lengths between 35ps and 45ps, and similar shapes to that shown. The amplified KrF pulse in the Figure is the only one well enough exposed to enable a pulse shape to be obtained, so the shot-to-shot variation is unknown. However, any pulse broadening that may be produced by amplification seems to be very slight.

Figure B1.14 shows the pulse shape of the Raman beam from the preamplifier, which is practically identical to the KrF pulse. Similar variations in pulse length were seen in the Raman pulses. One amplified Raman pulse was recorded at the output of RA1, but this appeared to be anomalous in shape, with a very sharp cut off after the peak.

A few streaks of the KrF oscillator spectrum were recorded, using the same etalon as before, to see whether any frequency chirp was present. Figure B1.15 shows a streak image that was obtained, in which the fringes apparently spread out during the pulse in a way that would correspond to a shift of wavelength towards the blue. However, the same effect could be caused by pin cushion distortion in the streak camera. The image was densitometered at four different positions along the time axis, and r^2 versus order plots made, similar to those in Fig B1.11. The line slopes increase with time, indicating a change of scale which is typical of distortion, but the intercepts on the order axis are the same within the limits of measurement; thus, the entire effect is attributable to distortion rather than to a frequency shift.



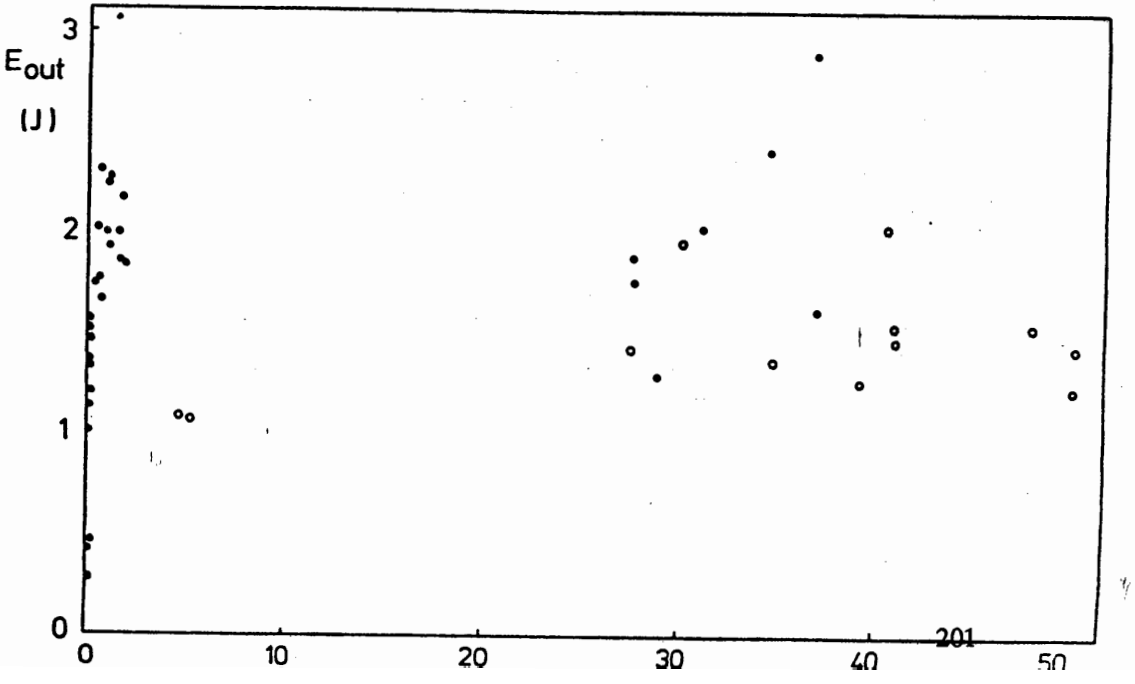


Fig B1.16(a) Extracted energy from the final Raman beam combiner (RA2) as a function of Stokes input in the small signal regime. (b) As (a) but with higher Stokes input energies. Open points taken from B1.7 scaled to 1 atmosphere pressure.

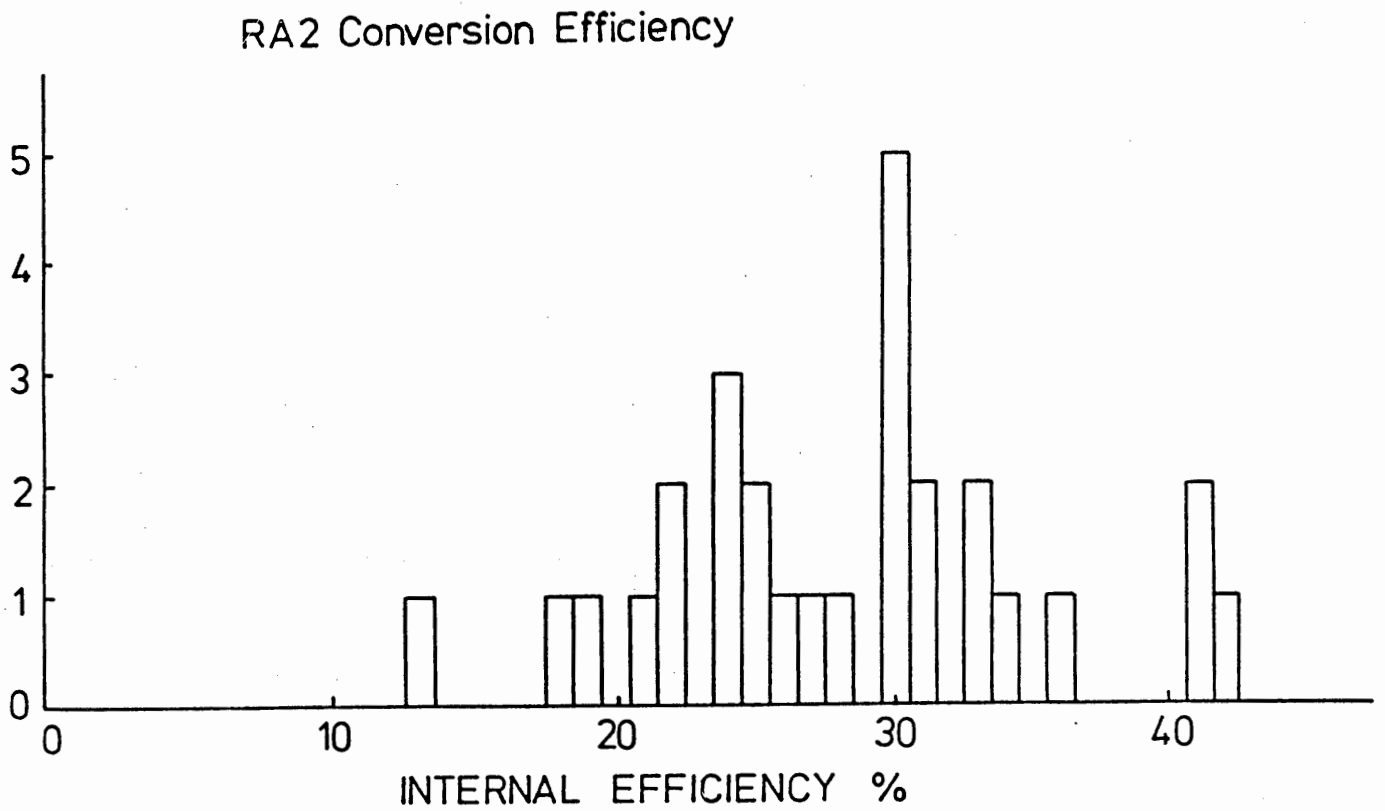


Fig B1.17 Histogram of number of shots vs conversion efficiency for beam combiner RA2.

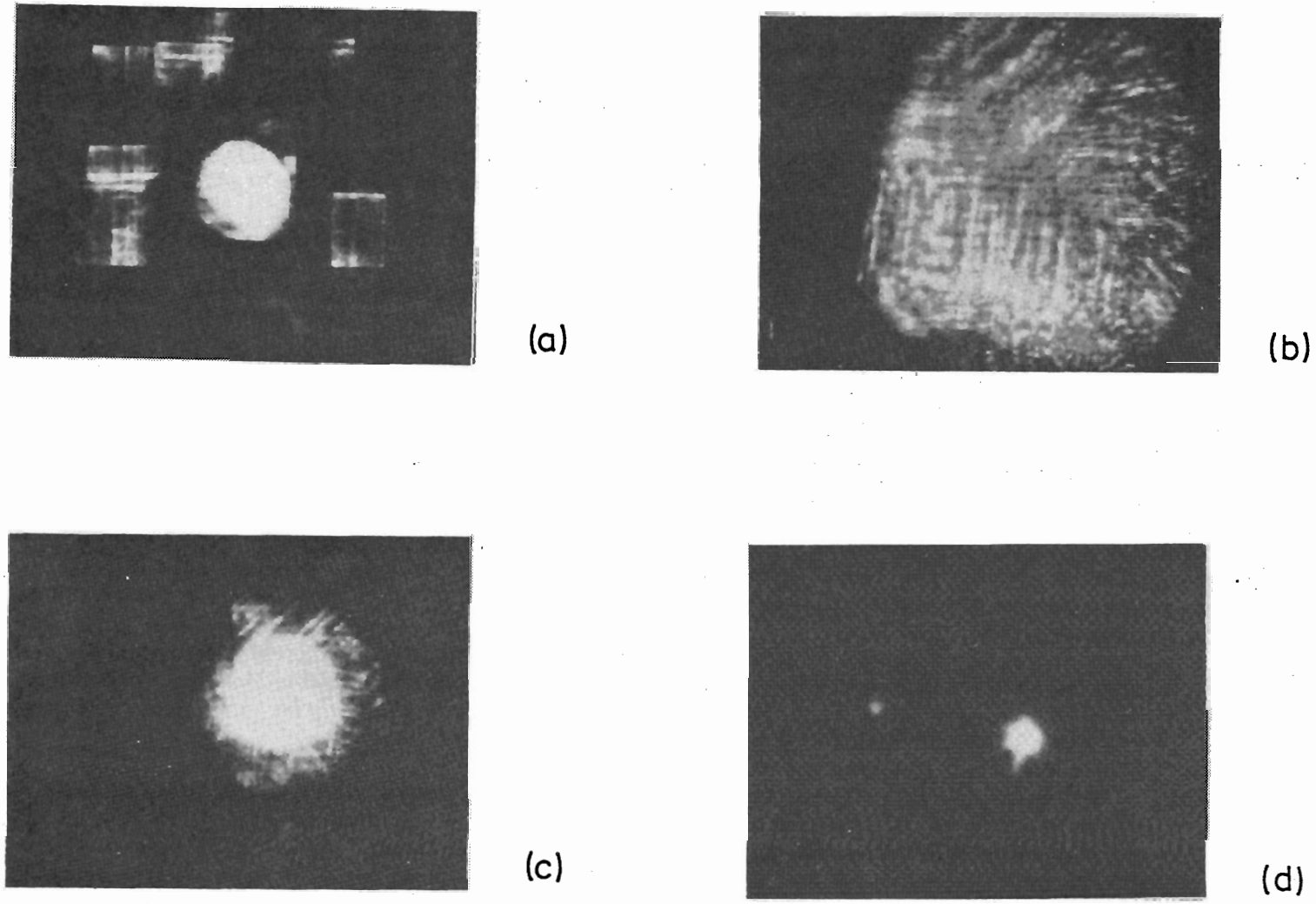


Fig B1.18 Stokes output beam profiles from RA2. (a) shows central Stokes output and also depleted pump beams. (b) gives Stokes near field. (c) shows non-focusing part of near field and (d) shows the far field, beam divergence ∿ 50 μrad.

(e) **Raman Amplifier Performance for 40 ps Pulses**

To measure the performance of RA2 a set of energy-monitoring diagnostics was installed to measure three quantities for each shot: the input Raman energy, the output Raman energy and the energy in the KrF beams pumping the amplifier. A variable attenuator (NO_2 gas cell) was inserted after RA1 to allow the input to RA2 to be varied over a wide range. This input energy was monitored by either an integrating photodiode (for small energies) or a calorimeter (for larger energies); these two devices were carefully cross-calibrated. A silica-plate splitter before the input window of the Raman amplifier provided a fraction of the pump energy to a 4-inch calorimeter, and the output Raman energy was recorded on a second 4-inch calorimeter about 2 metres from the exit window of the amplifier. None of the residual pump beams entered the output calorimeter.

Results are plotted as Figure B1.16 (a) shows the output saturation at low input energies up to 2mJ, (b) shows also the high input energy shots (with no attenuation). The open circles in (b) are data taken from the pressure of 1 atm. The quantities plotted are the Raman energies immediately before the input window and immediately after the output window of the amplifier. Pump energy for these results was approximately constant at 6J.

It is clear from (a) that the amplifier reaches saturation with an input of about 0.5mJ, which gives an output of 2J: a gain of 4000. There is a slight trend towards higher output energy with increasing input, but the main feature of the data is the large scatter in the output. The reason for this is not clear at present, though there are several possibilities: beam profile variations from shot to shot, self-generation of Stokes light as a result of focusing by the light-guide walls, or residual spectral fluctuations.

Efficiency of conversion from pump to Stokes inside the guide was calculated from the output data and the pump energies, both corrected for losses in the amplifier windows. A histogram of efficiencies is shown in Fig B1.17, and appears to be a symmetrical distribution centred at about 29%. Corrections for the presence of about 10% ASE in the pump beams, and for 20% losses in reflection from the light guide increase this average to about 40% and the peak efficiency to nearly 60%.

(f) **Beam Profiles and Prepulse**

Profiles of the output Raman beam were taken using a CCD camera to record the fluorescence from a glass plate in the beam. A framestore controlled by an IBM PC was used to capture the image and perform processing on it. A selection of profiles from near-field to focal spot is shown in Fig B1.18(a) shows the Stokes beam surrounded by the residual pump beams, in which the intense line foci due to ripples in the walls of the light guide can be clearly seen. The remainder of the figure shows three profiles of the Stokes beam, from near field to focal spot. There are two components: a good-quality beam which focuses to a small spot and a highly structured component which focuses more slowly. The focal spot (d) formed by a lens of 2 metre focal length is 50 microns in diameter, corresponding to a beam divergence of 25 microradians. The structured component (b), (c) is probably due to Stokes self-generation in the line foci formed by the guide wall ripples. Improved light guides are being constructed to overcome this problem.

A preliminary upper limit on prepulse levels can be obtained in the case of RA1 from one shot in which a filter was left out of the optical path. Any prepulse intensity was less than 1 part in 2×10^4.

B1.5 RAMAN AMPLIFIERS - A NUMERICAL APPROACH

P A Rodgers (RAL)

In laser pulse amplification by stimulated Raman scattering (SRS) the incident pump laser (electric field E_p and frequency ω_p) is coupled to the Stokes field (E_s and ω_s) by the non-linear polarization of the Raman medium. The coupling occurs via material excitations, or phonons, Q (frequency $\omega_p - \omega_s$).

The equations governing E_p, E_s and Q can be derived by treating the molecules as damped harmonic oscillators and expanding the polarizability in a Taylor's series as a function of inter-nuclear separation[1], or by using a three-level system model and the Rabi frequency techniques of quantum optics[2]. In both cases we must solve Maxwell's equations and make the slowly varying envelope approximation. For single mode plane waves the equations are:

$$\frac{\partial E_p}{\partial z}(z,t) + \frac{1}{v_p}\frac{\partial E_p}{\partial t} = -\frac{v_p}{v_s}\frac{\omega_p}{\omega_s} Q E_s$$

$$\frac{\partial E_s}{\partial z}(z,t) + \frac{1}{v_s}\frac{\partial E_s}{\partial t} = Q^* E_p$$

$$\frac{\partial Q}{\partial t}(z,t) + \frac{Q}{T_2} = C_1 C_2 E_p E_s$$

z is the distance travelled into the amplifying medium, v_p and v_s are the pulse velocities, both fields have been treated as single mode and we have neglected the transverse structure of the beams. C_1 and C_2 are proportional to the polarizability of the medium[1,2] and determine the strength of the interaction (and hence amplification) together with T_2 which sets the timescale. Transforming to a moving frame by the change of variables.

$$z' = z \; ; \; t' = t - z/v_p$$

we find

$$\frac{\partial E_p}{\partial z'}(z',t') = -\frac{v_p}{v_s}\frac{\omega_p}{\omega_s} Q E_s \qquad (1)$$

$$\frac{\partial E_s}{\partial z'}(z',t') + \frac{v_p - v_s}{v_p v_s}\frac{\partial E_s}{\partial t'} = Q^* E_p \qquad (2)$$

$$\frac{\partial Q}{\partial t'}(z',t') + \frac{Q}{T_2} = C_1 C_2 E_p E_s^* \qquad (3)$$

As a further approximation we assume $v_p = v_s$ and the second term on the LHS of (2) vanishes. We note from (1) that E_p decreases as E_s increases; from (2) that E_p causes E_s to grow with z and from (3) that the time taken for Q to peak is determined by T_2. Our initial conditions are given by the pulse shapes of the incident Stokes and pump lasers, i.e.

$E_p(0,t')$ = incident pump shape

$E_s(0,t')$ = incident Stokes shape.

We also assume that the Raman medium is initially unexcited - $Q(z',0) = 0$. Our problem is to find the Stokes field after the pulses have travelled through the medium, i.e. $E_s(z'=L,t')$, as a function of differing Stokes and pump input (eg intensity, duration, shape, relative timing, phase structure etc) and media (ie different C_1 C_2 and T_2 - usually varied by changing the Raman gas or pressure). From $E_s(L,t')$ we can integrate to find the energy of the outgoing Stokes pulse, $W_s(L)$. We usually express our results as either amplification (or gain), $W_s(L)/W_s(0)$, or

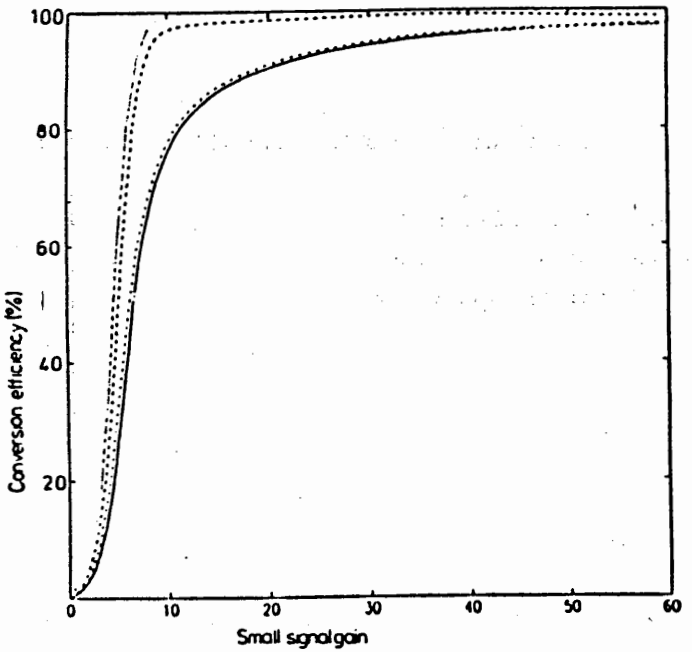
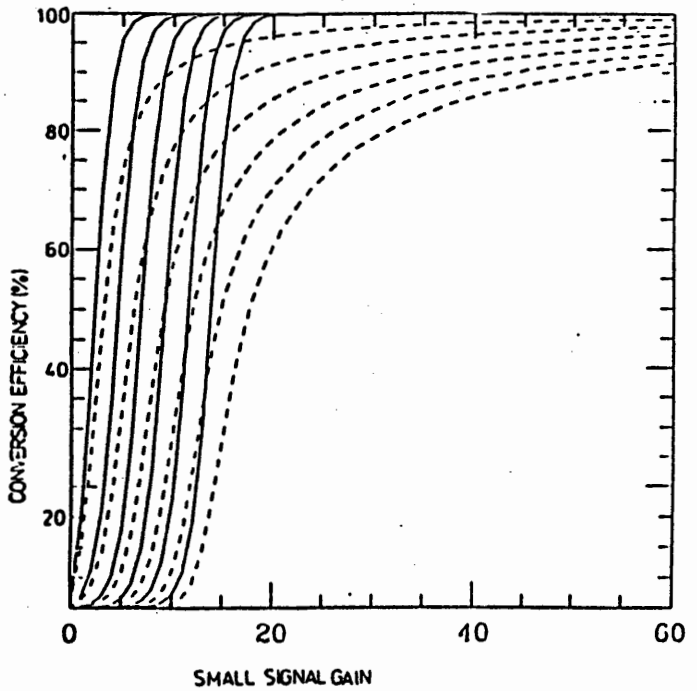


Fig B1.19(a) Conversion efficiency vs small signal gain. I_s = 10^{-3} I_p and T_2 = 30ps. Steady state square pulse (dotted), 1000ps square pulse code result (dashed), steady state Gaussian pulse (dot-dashed) and 1000ps Gaussian pulse code result (solid).



(b) Conversion efficiency vs small signal gain. From left to right I_s = 10^{-1}, 10^{-2}, 10^{-3}, 10^{-4}, 10^{-5} and 10^{-6} I_p. Square pulse (solid) and Gaussian pulse (dashed).

conversion efficiency, $(W_s(L)-W_s(0))/W_p(0)$. We have written an iterative and fully implicit finite difference computer code to solve equations (1) - (3). We represent the dependent variables as follows.

$$E_p(z',t') = E_p(m\Delta z', n\Delta t') = P^n_m$$

$$E_s(z',t') = E_s(m\Delta z', n\Delta t') = S^n_m$$

$$Q(z',t') = Q(m\Delta z', n\Delta t') = Q^n_m$$

Equation (3) can be solved implicitly at $(m\Delta z', (n+\frac{1}{2})\Delta t')$ if we represent

$$\frac{\partial Q}{\partial t'} = \frac{Q^{n+1}_m - Q^n_m}{\Delta t'}$$

Equations (1) and (2) reduce to a pair of linear algebraic equations in two unknowns if we solve explicitly for Q and implicitly for the electric fields using.

$$\frac{\partial E_p}{\partial z'} = \frac{P^n_{m+1} - P^n_m}{\Delta z'} \; ; \; \frac{\partial E_s}{\partial z'} = \frac{S^n_{m+1} - S^n_m}{\Delta z'}$$

This gives P^n_{m+1} and S^n_{m+1} for all n. We can now calculate Q^n_{m+1} from[3] and then recalculate P and S completely implicitly.

We iterate this procedure until all three quantities converge to within a user-defined limit.

We can test the code in two limits for which analytic solutions are known.

1. **Steady-state limit**

Here we neglect the $\partial Q/\partial t'$ term in[3] such that $Q = C_1C_2T_2E_pE_s$ Equations (1) and (2) can now be solved to give

$$I_s(z') = I_o \frac{I_R \exp(\gamma I_o z')}{1 + \frac{\omega_p}{\omega_s} I_R \exp(\gamma I_o z')} \qquad (4)$$

Where $I = \frac{1}{2}\epsilon_o v|E|^2$, $I_R = I_s(0)/I_p(0)$, $I_o = I_p(0) + (\omega_p/\omega_s) I_s(0)$ and $\gamma = 4C_1C_2T/v\epsilon_o$. In the non-depletion limit (ie initially the Stokes energy is much less then the pump energy and can be amplified by orders of magnitude without significantly lowering the pump energy) this reduces to

$$I_s(L) = I_s(0) \exp(\gamma I_p L)$$

This exponent - $\gamma I_p L$ - is termed the small signal gain (G) and is frequently used as a measure of the expected gain, even though it has been derived in the steady-state non-depletion limit.

In figure B1.19(a) we plot the conversion efficiency obtained from equation (4) vs small signal gain for steady-state square and Gaussian pulse envelopes (dotted and dot-dashed lines respectively). The code results for square and Gaussian pulses (dashed and solid lines) of FWHM 1000 ps and T_2=30$_{ps}$ (i.e. near steady-state conditions) are in excellent agreement with the steady-state curves for all small signal gains. The pump energy is 100 times the Stokes energy. We notice that the curves rise sharply for small $\gamma I_p L$ and approach 100% conversion efficiency; the square pulse curve rises more steeply and this is emphasized in figure B1.19(b) where we plot the exact curves for initial energy ratios ranging from 10^{-1} (leftmost curve) to 10^{-6} (rightmost). Here the square pulse is the solid line and the Gaussian pulse is dashed.

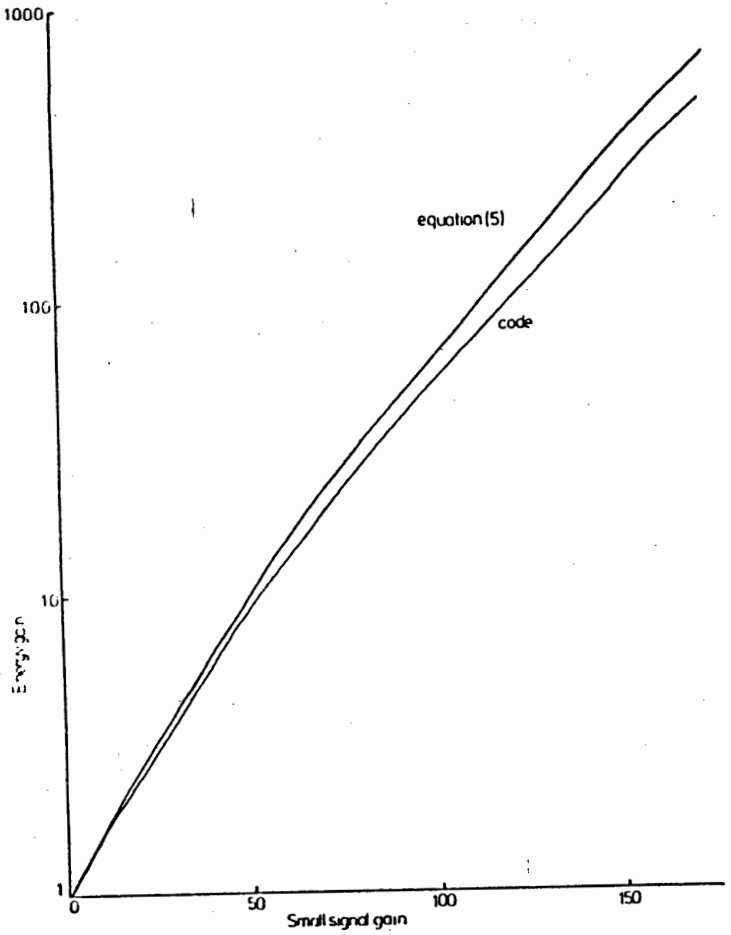


Fig B1.20 *Energy gain vs small signal gain for 10ps square pulses. T_2 = 100 ps and I_s=10^{-9} I_p. Approximation (eqn 5 - solid line) and code result (dashed line).*

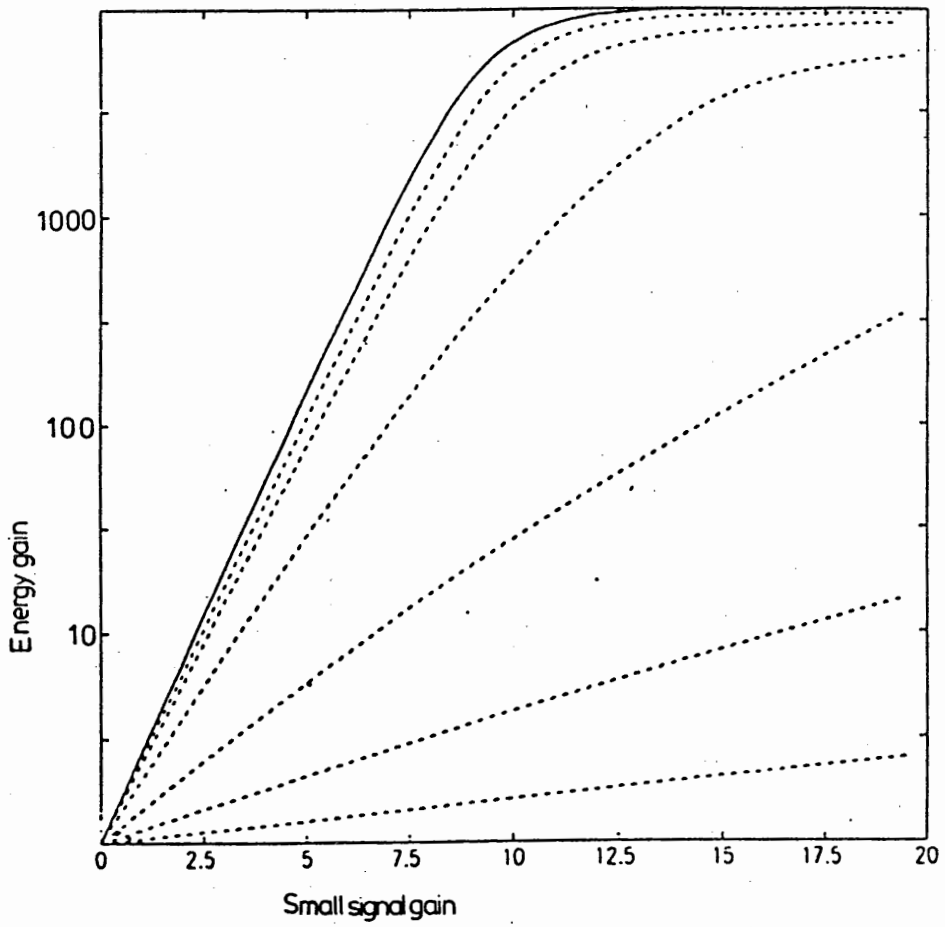


Fig B1.21 *Energy gain vs small signal gain. I_s= 10^{-4} Ip and T_2 = 30ps. Steady-state solution (equation 4-Solid line) and Tp = 1000 ps, 300 ps, 100 ps, 30 ps, 10 ps and 3 ps (dashed lines - left to right)*

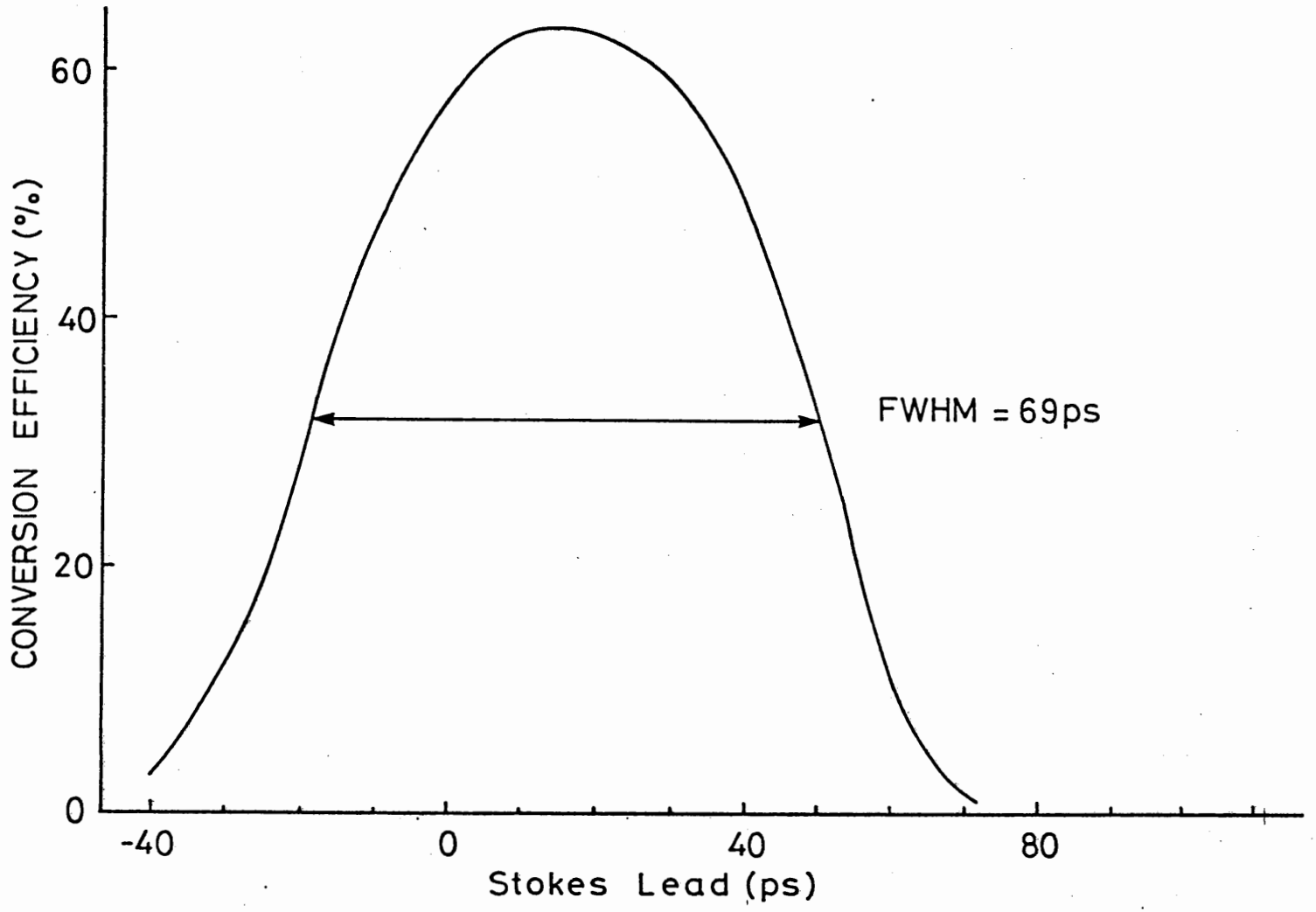


Fig B1.22 *Conversion efficiency vs stokes pulse lead for asymmetric Gaussian pulses. Tp = 37 ps; T_a = 27 ps and $\gamma I_p L$ = 35.*

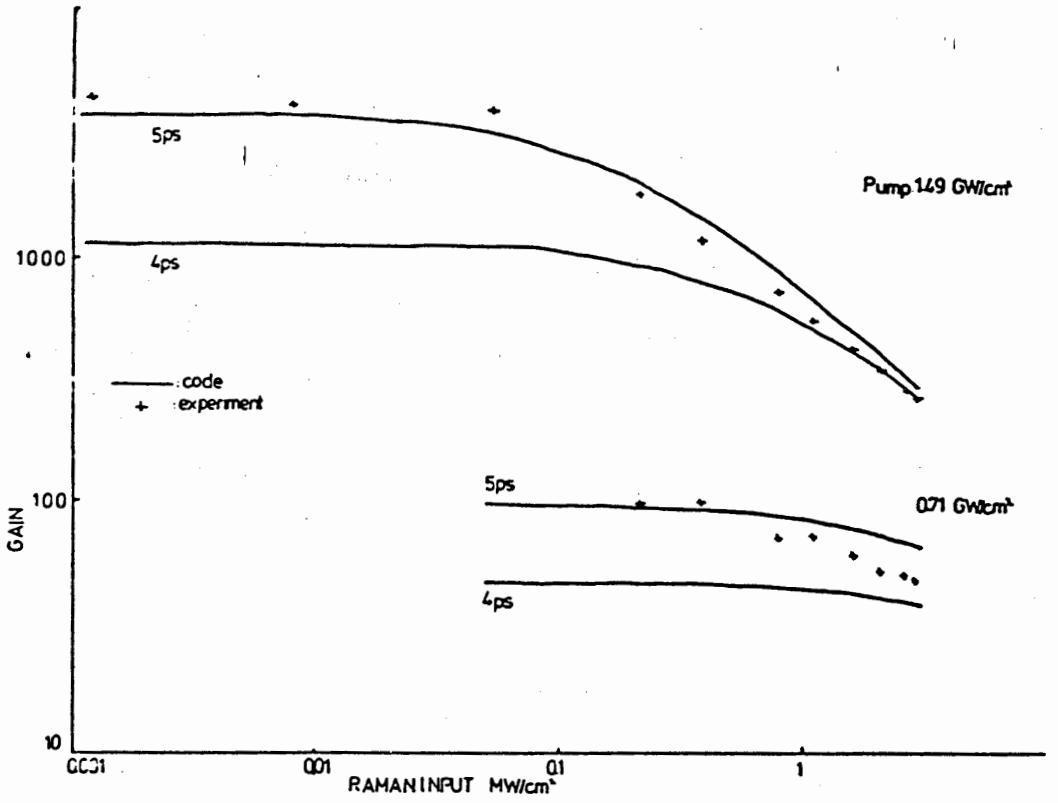


Fig B1.23 *Energy gain vs Raman input intensity for two different pump intensities: code (solid line) and experiment (crosses).*

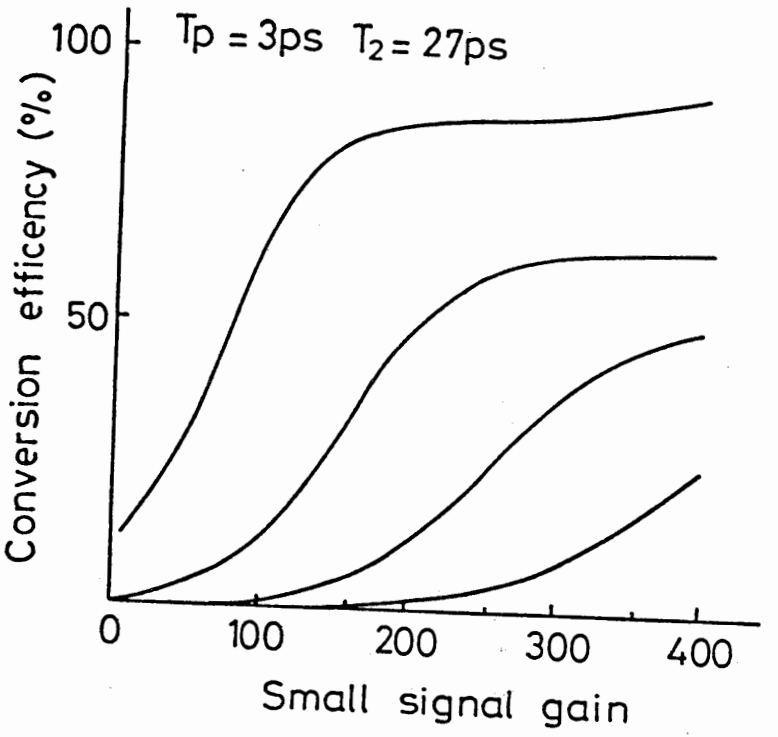


Fig B1.24 *Conversion efficiency vs small signal gain for optimally timed 3 ps Gaussian pulses. I_s=10^{-1}, 10^{-2} 10^{-3} 10^{-4} Ip (left to right). T_2 = 27 ps.*

2. Transient non-depletion limit

If we set $\partial E_p/\partial z' = 0$ in equation (1), equations (2) and (3) can be solved exactly in terms of modified Bessel functions[3]. In the limit $T_p < T_2$ (where T_p is the pulse length) the Bessel function arguments can be considerably simplified and the Stokes energy gain written as[4]

$$I_0^2(u) - I_1^2(u) \approx \frac{e^{2u}}{4\pi u^2}\left(1+\frac{1}{4u}\right) \qquad (5)$$

where I_0 and I_1 are modified Bessel functions and $u^2 = 8\,C_1C_2zW_p$. In figure B1.202 we plot $\log_{10}$(energy gain) vs small signal gain with $I_s=10^{-9}I_p$, $T_2=100_{ps}$ and $T_p=10_{ps}$. The code results are in good agreement with equation (5). (For small u the approximation in (5) is not accurate and we rely on the tabulated values of I_0 and I_1 which can be found in standard texts[5]). The agreement is best for small gains, when the pump depletion is lowest, as is expected.

The changes in behaviour on moving from the transient to near steady-state regime can be investigated by varying T_p for a fixed T_2 and either a) keeping the intensities constant or b) keeping the energies constant. In figure B1.21 we plot energy gain vs small signal gain for square pulses of equal intensity and pulse lengths varying from 3ps to 1000ps. The ratio of the initial energies is 10^{-4} and the steady-state curve is shown for comparison. In the steady-state case we see the gain is exponential for small γIpL (when there is very little pump depletion) and then saturates. Similar behaviour is observed in the transient regime but with reduced gains.

As the pulses become shorter their relative timing becomes important. This can be predicted from equations (1) - (3). To maximize the gain we require the product Q^*E_p to be a maximum but the maximum of Q depends on both E_p and E_s. In general we find the gain to be a maximum when the Stokes pulse enters the medium first.

For these calculations we used asymmetric Gaussian pulses (the HWHM of the front edge was half that of the rear edge). For T_p=37ps the maximum gain occurs for a Stokes lead of about 18ps. The full timing curve is shown in figure B1.22 and the maximum conversion efficiency of around 65% and FWHM of 69 ps are in reasonable agreement with a comparable experiment. However the optimal time delay as measured experimentally was much larger than predicted by theory.

In figure B1.23 we plot Stokes energy gain vs input Stokes intensity at two fixed pump intensities for short pulses ($T_p\sim$5ps, T_2=27ps). At low input Stokes intensities the gain is very sensitive to T_p and it is important to characterise the pulses properly. However for higher Stokes inputs - and hence lower energy gains - the agreement with experiment (crosses) is good.

An obvious motivation for solving the SRS equations numerically is to produce families of solutions in regimes where approximations are not known - for example in the short pulse saturation regime. In figure B1.24 we plot conversion efficiency vs small signal gain for optimally timed 3 ps pulses (T_2=27ps) for four initial energy ratios. We note that the 10^{-1} curve saturates in a conventional manner whereas the 10^{-2} curve saturates much slower. The 10^{-3} and 10^{-4} curves are less than 50% efficient for small signal gains as high as 400.

References

1) J P Partanen and M J Shaw, JOSAB3 1374 (1986)

2) M G Raymer, J Mostowski and J L Carlsten, Phys Rev A19 2304 (1979)

3) R L Carmen, F Shimizu, C S Wang and N Bloembergen, Phys Rev A2 60 (1970)

P REFLECTIVITY (AT λ = 248 nm) VERSUS ANGLE OF INCIDENCE FOR VARIOUS SURFACES

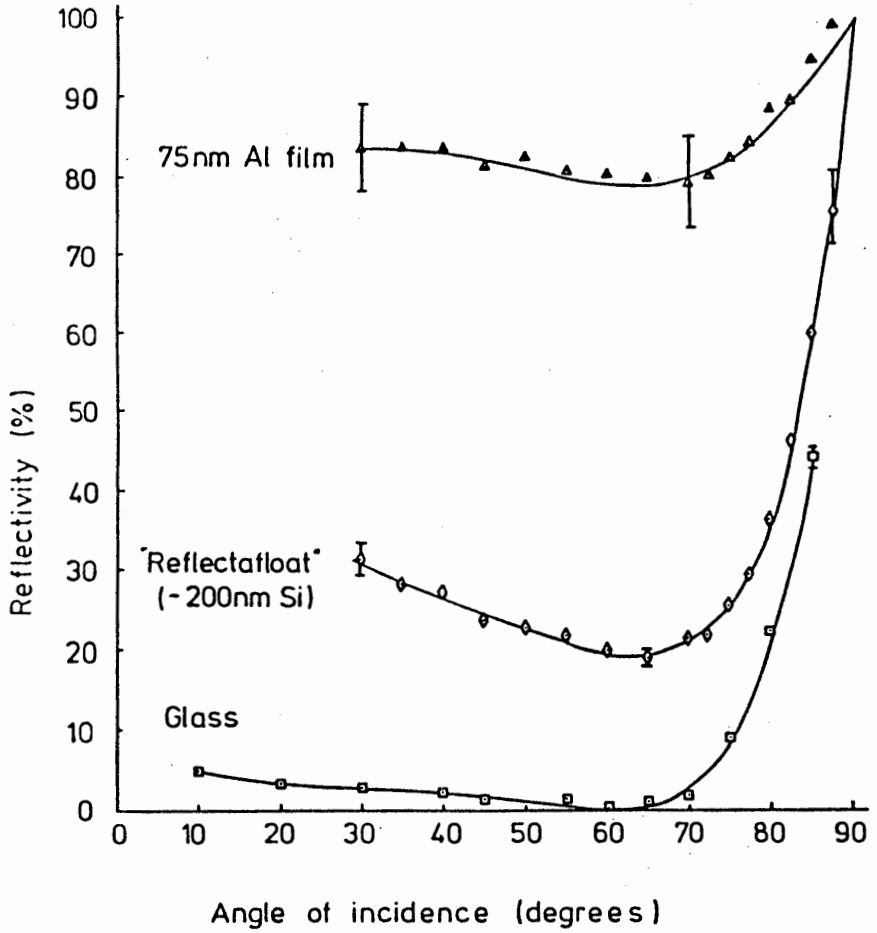


Fig B1.25 *Measured P reflectivity of bare aluminium, "Reflectafloat" and uncoated glass at 248 nm as a function of angle of incidence.*

S AND P REFLECTIVITY OF Al : MgF_2 SAMPLE

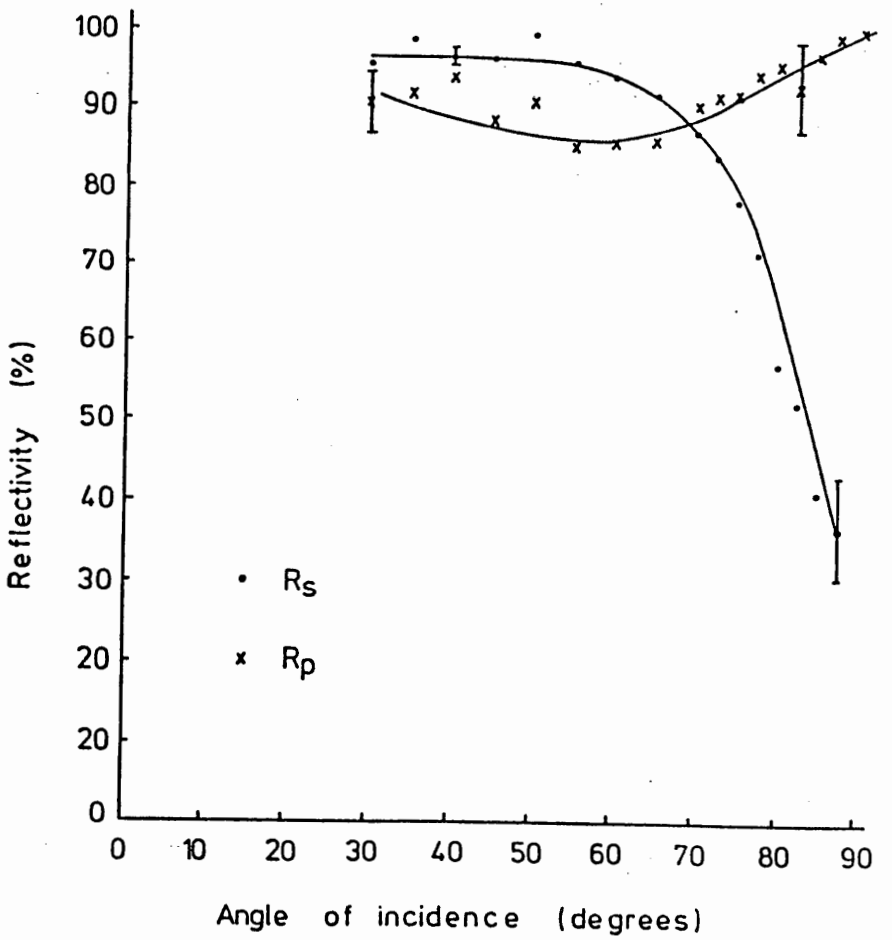


Fig B1.26 *Measured R_s and R_p for Kendall-Hyde MgF_2 overcoated Aluminium as a function of angle of incidence.*

S AND P REFLECTIVITY OF OCLI SAMPLE

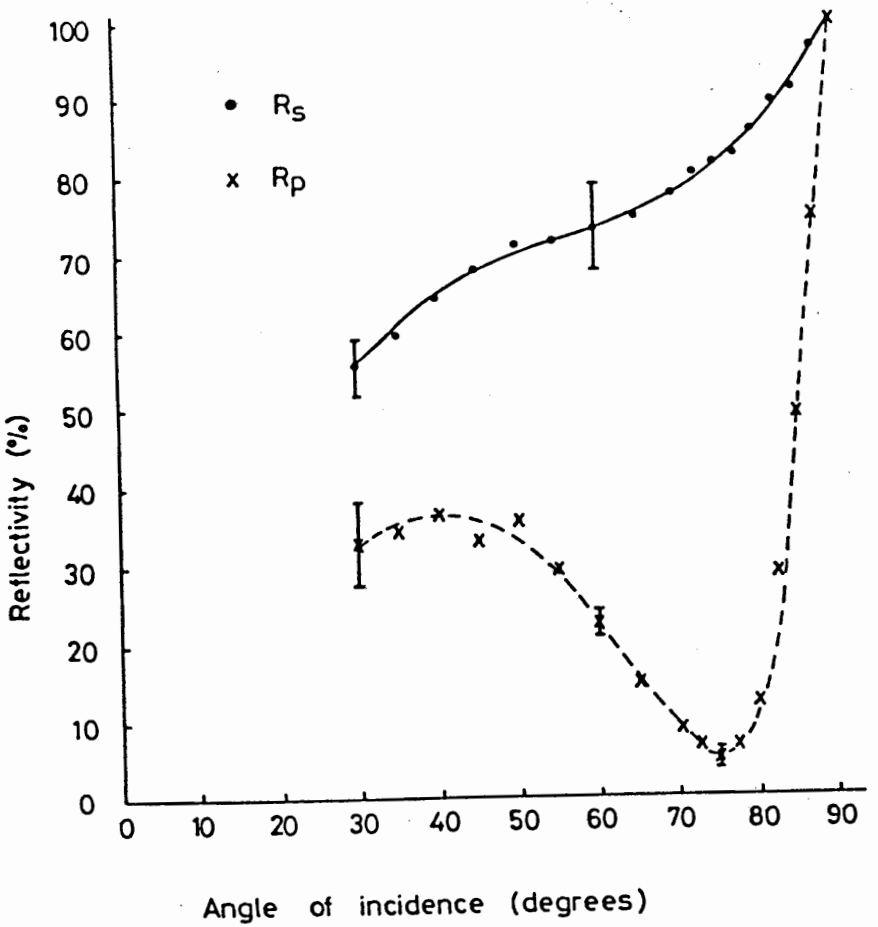
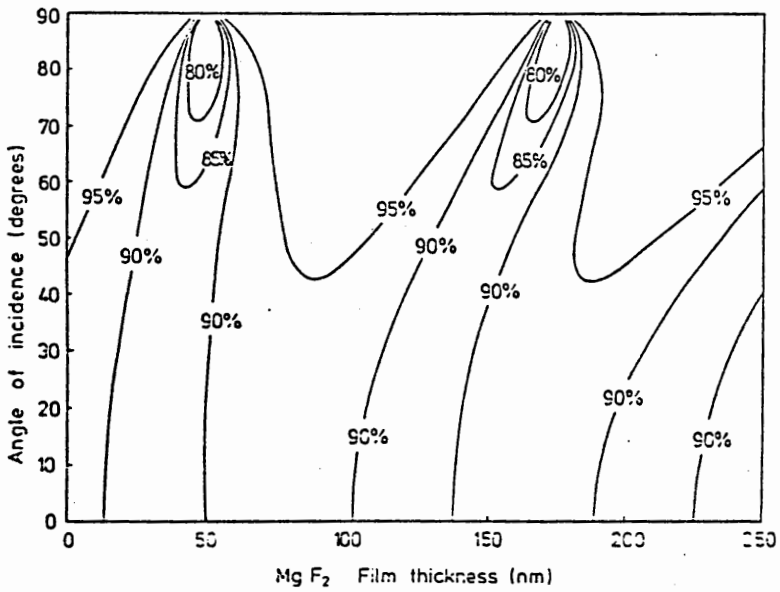


Fig B1.27 *Measured R_s and R_p for OCLI overcoated aluminium as a function of angle of incidence.*

THEORETICAL PREDICTIONS OF S REFLECTIVITY FOR MgF_2 COATED Al AS A FUNCTION OF MgF_2 THICKNESS AND ANGLE OF INCIDENCE

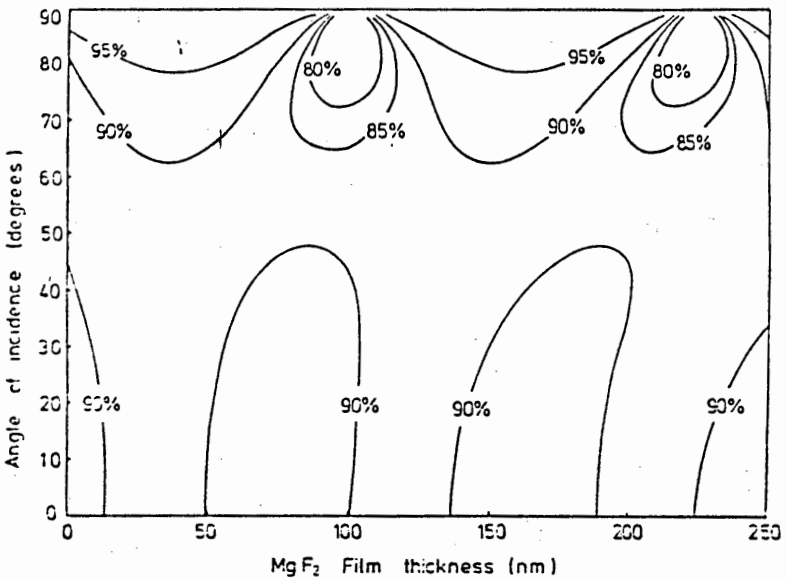


i	n_i	K_i
1	1	0
2	1·412	0
3	0·19	2·942

λ_1 = 248 nm

Fig B1.28 *Calculations of R_s as a function of angle of incidence for aluminium overcoated with a varying thickness MgF_2 layer.*

THEORETICAL PREDICTIONS OF P REFLECTIVITY FOR MgF_2 COATED Al AS A FUNCTION OF MgF_2 THICKNESS AND ANGLE OF INCIDENCE



i	n_i	K_i
1	1	0
2	1·412	0
3	0·19	2·942

λ_1 = 248nm

Fig B1.29 As 1.28 but for R_p.

S AND P REFLECTIVITY AT NEAR GRAZING INCIDENCE FOR MgF_2 COATED Al AT λ = 248 nm

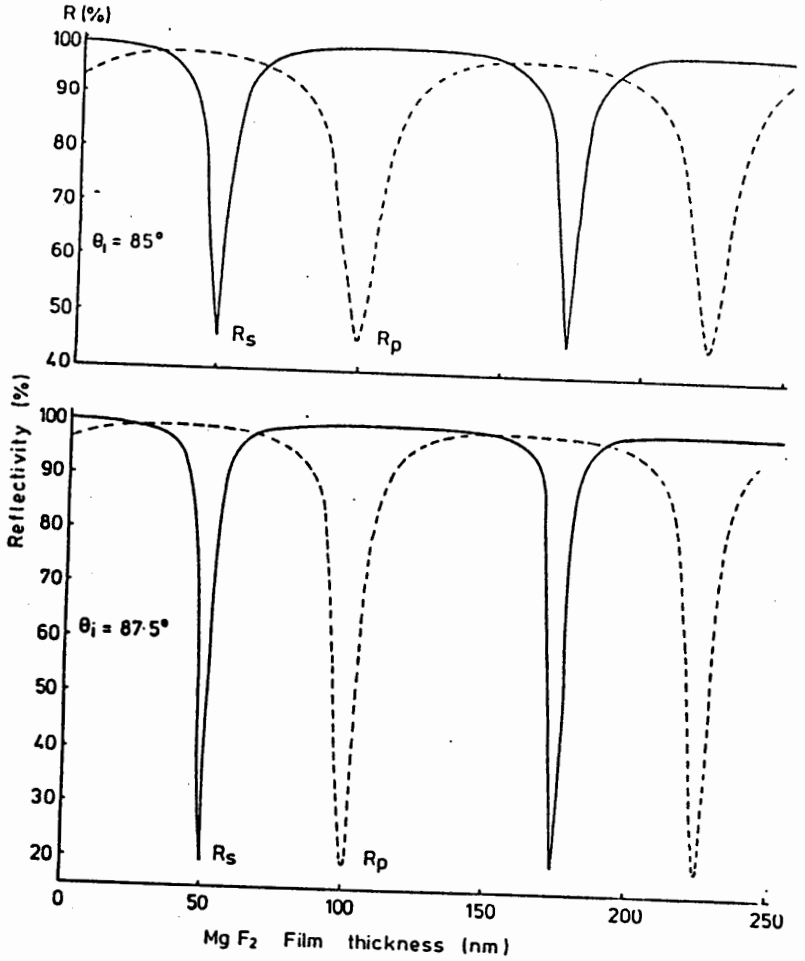


Fig B1.30 Calculations of R_s and R_p at 85° and 87.5° angle of incidence as a function of MgF_2 film thickness.

4) M D Duncan, R Mahon, L L Tankersley and J Reintjes, JOSAB5 37 (1988)

5) M Abramowitz and I A Stegun (eds) Handbook of Mathematical Functions (table 9-8) Dover (1964)

B1.6 LIGHTGUIDES FOR RAMAN AMPLIFIERS

J E Andrew (AWE, Aldermaston)

Introduction

Light guides for Raman Amplifiers at RAL have been fabricated from proprietary float or silicon coated glazing quality glass. The use of these materials at near grazing incidence has resulted in poor KrF pump beam transmission through the guide and insufficient averaging of the pump source. In order to improve both these factors a number of commercially available materials and coatings have been evaluated for their use as improved light guide walls.

Reflectivity

The pump beam transmission of the existing "Reflectafloat"[1] guide has been determined to be 75% and 35% at grazing angles of 2.5 and 5.0 degrees respectively. This represents an appreciable loss of pump power and it is desirable to increase this to a value in excess of 90% at the larger grazing angle. Figure B1.25 illustrates the reflectivity of P polarised light at the KrF wavelength for the materials used for the existing guide walls and a 75nm thick Aluminium film on a glass substrate. It is clear that the aluminised substrate has superior reflectivity at near grazing angles. This coating however is mechanically soft and degrades with time by oxidation and therefore commercially available "protected" Aluminium films were evaluated also. Figures B1.26 and B1.27 show reflectivities for two such films. The first sample (Fig B1.26) consisted of a 150nm Al film overcoated with MgF_2 optimised for high normal incidence reflectivity in the visible. It was observed that although the P reflectivity was high at grazing incidence the S reflectivity was low. The second sample, of unknown dielectric specification, shows the opposite behaviour with high S and low P reflectivity.

Using a computer program based on theory presented in Ref[2] it is possible to understand why such large differences in S and P reflectivity occur for MgF_2 coated Al films. Figures B1.28 and B1.29 show the reflectivity of MgF_2 coated Al as a function of angle of incidence and MgF_2 film thickness. It has been assumed that the light is incident in vacuum and the Al layer is optically thick. For most of the parameter space the reflectivity is in excess of 90% but at certain thicknesses of MgF_2 at near grazing incidence it drops markedly due to interference effects. Figure B1.30 illustrates the influence of dielectric film thickness on S and P reflectivity at two angles of incidence (θ_i). It can be seen that the minima in either reflectivity are periodic with film thickness and that the minimum value decreases with increasing angle of incidence. However there are regions of thickness with a width of $\sim$125nm where high reflectivity is maintained. It is therefore possible to specify a MgF_2 thickness which optimises either S or P reflectivity. Since the Raman amplifiers are pumped by a linear polarised source it is desirable to use separate S and P reflectors for the vertical and horizontal light guide walls respectively. The P reflector could be fabricated from the material of Figure B1.29 and the S reflector from that shown in figure B1.28 or Al overcoated with a MgF_2 thickness chosen to prevent poor reflectivity.

Surface Flatness

Glass for glazing purposes can be obtained in large sheets (3.2m x 6m) but its surface flatness is only occasionally quoted and rarely guaranteed. It is usually manufactured by a "float" process[3]

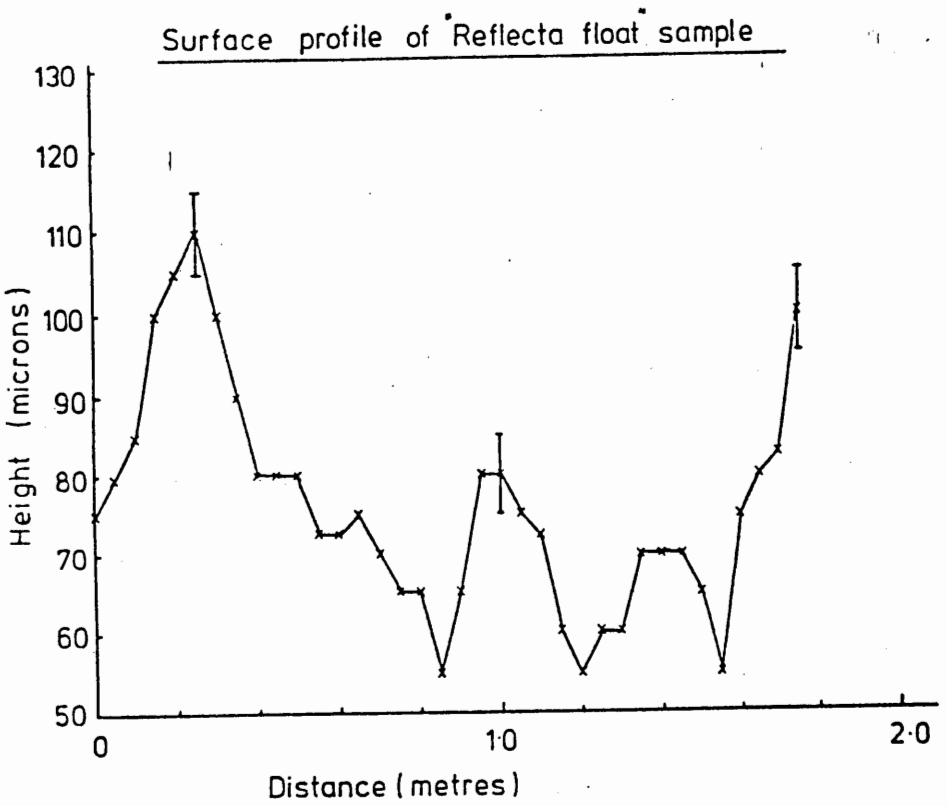


Fig B1.31 *Measured surface profile of the existing "Reflectafloat" light guide walls.*

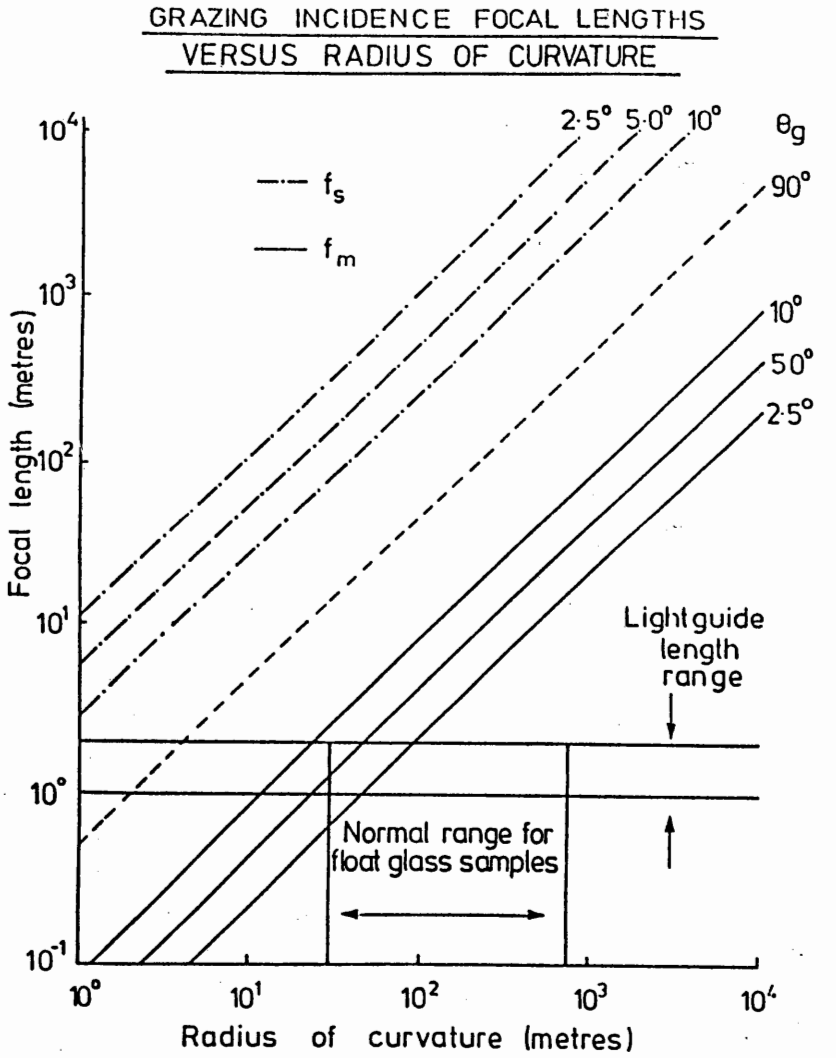


Fig B1.32 *Calculated sagittal, fs and meridional, fm focal lengths as a function of radius of curvature and grazing angle.*

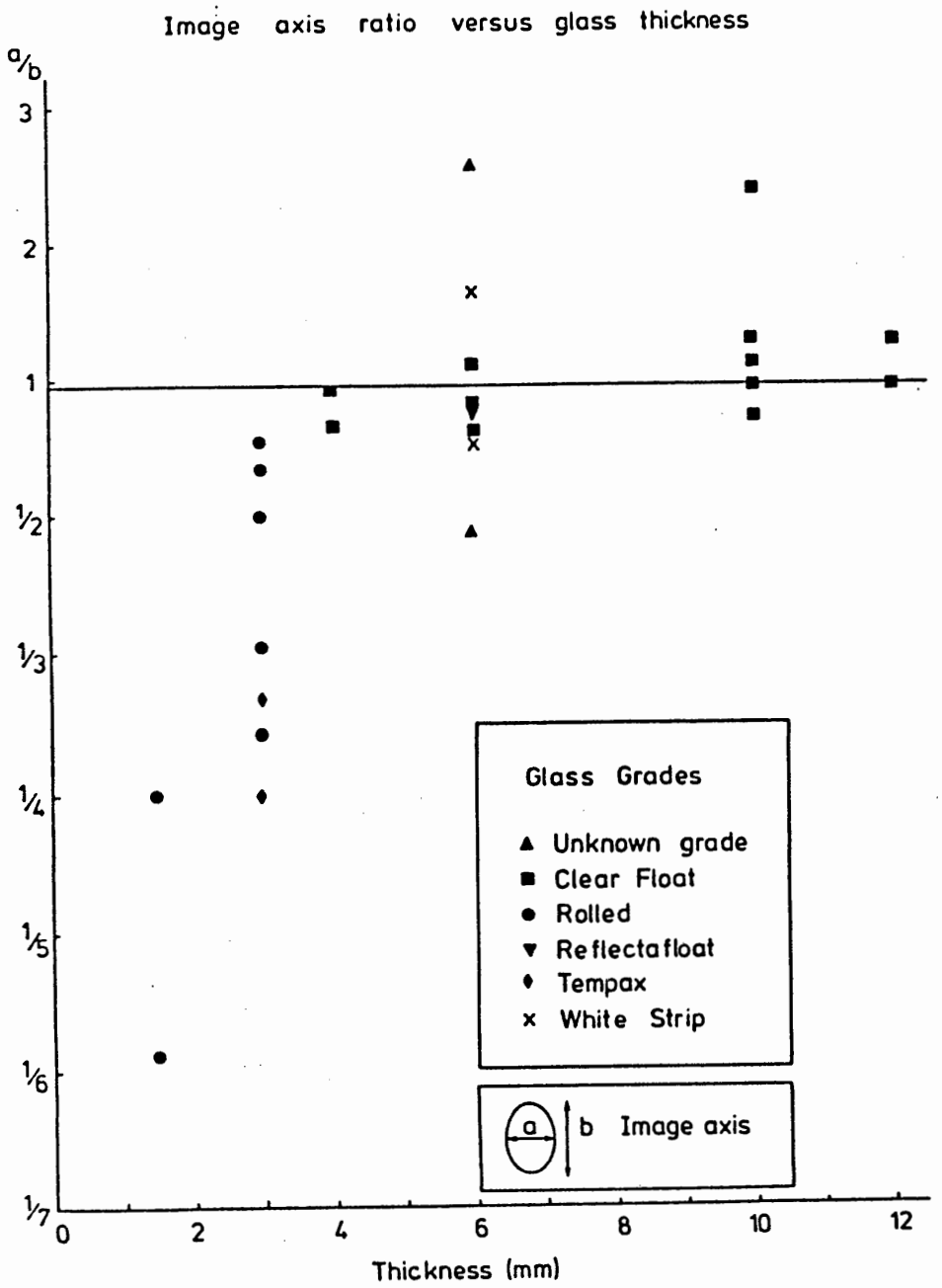
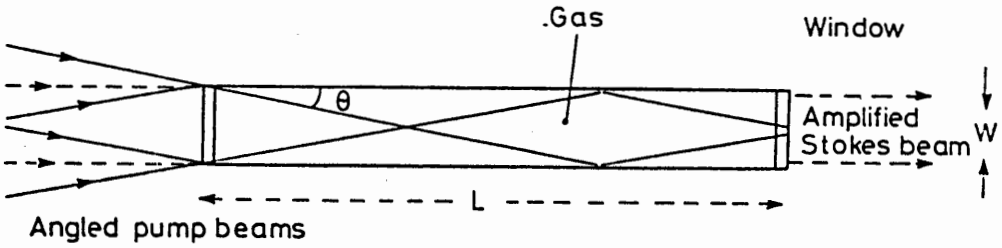


Fig B1.33 *Measurements of image distortion in grazing incidence reflection at 2.5° for various grades of flat glass.*



Schematic Raman Amplifier with Reflecting Walls.

Fig B1.34 *Schematic of a Raman amplifier with reflecting walls and pump beams incident at a grazing angle θ.*

although thin glass may be made by drawing and rolling. The surface profile of a strip of 6mm thick "Reflectafloat" is shown in Figure B1.31. Rippling of the surface arises from the manufacturing process and shows amplitudes of 20-50 microns and wavelengths of 0.4 - 1.5 metres. If these ripples are assumed to be spherical concave reflectors then their sagittal and meridional focal lengths are given by[4]:-

$$f_m = R.\sin\theta_g/2$$

and

$$f_s = R/(2.\sin\theta_g)$$

respectively, where R is the radius of curvature and θg is the grazing angle. At near grazing incidence the focal lengths due to these surface variations can be short as shown in Figure B1.32. If pump beam focusing within the guide is to be avoided then increased grazing angles or radii of curvature (i.e. better surface quality) is required. In order to evaluate a variety of materials for light guide substrates an apertured He-Ne laser beam was shone onto samples at large angles of incidence and the dimensions of the reflected beam were photographically recorded at a distance of ∿8 metres from the point of reflection. Typically, ovoid shaped beams were observed and their axis ratios were plotted as a function of glass thickness (Figure B1.33). Measurements were taken from both sides of a sample since the beam quality often depended on the surface used and in some cases the orientation of the sample also influenced the reflected beam shape. The line at an a/b ratio of 0.95 indicates the axis ratio of the reflected beam from a λ/10 polished mirror and is a reference for the ratio desired. This ratio was not unity due to the slightly non normal alignment of the beam with respect to the photographic imaging plane. In general the thicker samples of glass yielded better beam quality as long as the flattest side was used. The data also indicates that rolled glass should be avoided.

Conclusions and Future Work

Coatings have been identified which allow high reflectivity of the KrF pump beams at near grazing incidence. The substrates for these need to be selected carefully by inspection to ensure that appreciable focusing is not achieved within the length of the guide. New guide walls are currently being fabricated from selected 10mm float -glass and will be separately coated with the high S and P reflectivity coatings identified by this study to provide improved replacements for the existing Raman Amplifier light guides used in the SPRITE system.

References

1) Trademark of Pilkington Glass Ltd, St Helens, Lancs, UK

2) M Born and E Wolf, "Principles of Optics", Pergamon Press 6th ed. 1980.

3) H G Pfander, "Schott guide to Glass", Van Nostrand, 1983.

4) A Franks, Sci Prog Oxf pp371-422, vol.64, 1977.

B1.7 DESIGN CONSTRAINTS FOR MULTI-STAGE RAMAN AMPLIFICATION IN OPTICAL AND RAMAN MULTIPLEXED KrF LASER ARCHITECTURES

M H Key, RAL

Beam combining in forward Raman amplifiers has many potential advantages for high power KrF lasers. It is a basic feature of the design of the SUPERSPRITE system[1]. Optimisation of a chain of Raman amplifiers using multiple angled pump beams (fig B1.34) is therefore an important consideration for SUPERSPRITE and is also of more general interest.

Constraints which are relevant include:

- Self generation of Stokes power in hot spots of the pump beam pattern.

- Two photon absorption and small scale self focusing in window materials.

- Relative timing changes of pump and Stokes beams with angled pumping of reflecting waveguide amplifiers.

- The effects of anomalous dispersion at the Raman amplification resonance.

These constraints are considered in the following sections.

Self generation of Stokes power

The final output amplifier is required to operate with high conversion efficiency of pump power to Stokes power. Highly saturated amplification with the largest possible value of the small single amplification gain length product gl is therefore necessary. The threshold for self generation of Stokes power is gl $\geq$ 25. This will be reached first in line integrated hot spots of pump intensity for Stokes rays passing through the Raman amplifier. Super position of many pump beams in a reflecting waveguide Raman amplifier reduces the problem of hot spots. However, for cost effective laser architectures the pump beams will not have high quality optics or beam cleaning spatial filters, apodisers, etc. As a result, significant variations in pump intensity along Stokes ray paths can be anticipated. Consider the case where the ratio of the pump hot spot to the average is n:1. The Stokes beam is assumed to be of good quality with propagation via spatial filtering, optical relaying, apodisation, etc. It will have a smooth radial variation of intensity which can be characterised by a fill factor F relating the intensity at the beam centre to the intensity if the aperture were filled uniformly. The pattern of pump intensity seen by the Stokes rays will have small-scale fluctuations resulting from the superposition of many individually non-uniform beams in the reflecting waveguide structure.

A reasonable requirement for the performance of the principal output amplifier is 80% conversion of the pump to Stokes at the average power of the pump in the centre of the beam, together with a safety factor against self generated Stokes requiring that hot spot regions have a small signal gl < 17.

This requirement becomes a **limitation on the saturated gain** of a single amplifier stage. Numerical calculation of the saturated amplification of a gaussian shaped pulse in the steady state limit are presented in Section B1.5 ibid. It follows directly from these results in figure B1.19 that the ratio of the input Stokes intensity I_{so} to the pump intensity I_p in the Raman amplifier, is limited to values which are a function of the hot spot ratio n, as shown in Table 1.

Table 1

n	I_{so}/I_p
1.5	1/300
2	1/30
3	1/10
4	1/< 10

This simple analysis suggests that an efficient Raman amplifier should have a saturated gain of about 30 for a pump hot spot ratio of 2:1. In saturated amplification the intensity of the Stokes beam output will have the same pattern as the line averaged pump intensity. Unsaturated operation of the Raman amplifier is highly undesirable as fluctuations in the pump would be translated into

exponentially enhanced variations of the Stokes intensity through the small signal gain relationship $I_s = I_{so} \exp(gl)$.

This discussion is based on the saturation behaviour of gaussian pulses in the steady state limit. In the context of SUPERSPRITE operation we are concerned also with pulses in the transient regime ($t << T_2$) eg using CH_4 as the Raman amplification medium with T_2 = 30 psec, and pulse durations of interest for SUPERSPRITE from nanosecond to a few picoseconds.

Small signal gain in the transient regime is less than the steady state value $\gamma I_p \ell$ and for $t << T_2$ can be approximated as $(\exp(2u)/2\pi u^2)(1 + \frac{1}{4} u)$, where $u^2 = 2\gamma I_p \ell (t/T_2)$.

Numerical simulations comparing the saturation behaviour in the steady state limit with that in the transient regime for equivalent small signal gain are needed to extend this discussion to consideration of the transient regime. It is unlikely, however, that the essential conclusion that saturated stage gain should be limited to a value of the order of 30 will be different in the transient regime than in the steady state.

Two photon and small scale self focusing limit

The two photon absorption coefficient of fused silica at 249 nm is approximately 0.055 cm/GW while that of CaF_2 is 0.008 cm/GW. The small scale self focusing B integral is 0.1 $I/(1\ GW\ cm^{-2})$ $(\ell/1\ cm)$ for fused silica and 0.07 $I/(1\ GW\ cm^{-2})$ $(\ell/\ cm)$ for CaF_2. At the Stokes wavelength (266 nm for CH_4) two photon absorption in fused silica is 0.02 cm/GW and the B integral 0.09 $I/(1\ GW\ cm^{-2})$ $(\ell/1\ cm)$, measurements for CaF_2 are not available[2].

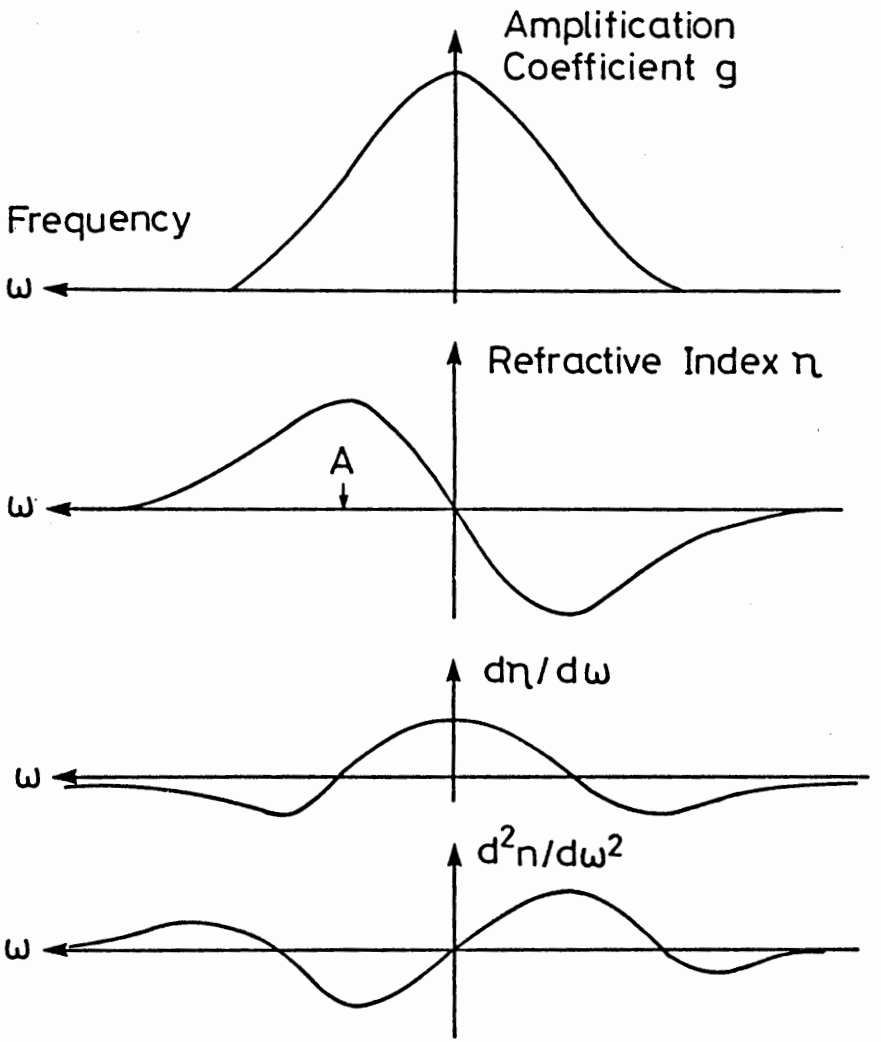
The power density on a fused silica entrance window is limited by two photon losses and, for example, requiring the loss not to exceed 10% in 1 cm thickness, gives a limit of 2 GW cm^{-2}. The corresponding B integral of 0.2 is small relative to the value 3 at which small-scale self-focusing becomes serious. At the output window two photon constraint gives 5 GW cm^2 and the B integral is relatively larger but still unimportant.

These nonlinear limits become relevant for very short pulses $t << T_2$ where high intensity is required to obtain sufficient gain. If atmospheric pressure is used in the Raman amplifiers, thinner fused silica windows or possibly CaF_2 windows can be used to raise the intensity limits.

Variations of relative timing of pump and Stoke pulses due to angles in the reflecting waveguide structure

If the pump radiation is incident in a reflecting waveguide, see fig 1, at angle θ to the axis and the Stokes beams travels on the axis, then for aperture W and with the pulses synchronous at the centre of the aperture, their timing difference at the edge of the aperture is given by $\Delta t_w = \sin\theta/c$. This limits the aperture which can be used without segmentation of the pump beam. For example, with a 10 psec pulse and a 2° angle, the maximum aperture is 8 cm, (corresponding to the output amplifier used presently in the prototype SPRITE system).

There is also a difference of propagation velocity for the pulses down the waveguide with a change in relative time in propagating through length L given by $t_p - t_s = L(1/\cos\theta - 1)/c$. Efficient extraction can be achieved when $t_p - t_s \leq 2\Delta t_w \leq \Delta t_p$ where Δt_p is the pump pulse duration. It follows that for small angles the aspect ratio for efficient extraction is $W/L \leq \theta/4$. Similarly the number of reflections of the pump in the guide is $N \leq 4$.
If the Stokes pulse duration is smaller than the pump pulse duration, it is possible for the Stokes pulse to move through the pump pulse and extract its energy by virtue of the different velocities of the pump and Stokes in the guide[1]. However, if this process is considered in the context of stability against self generation in the pump, a more severe constraint on the saturated



Gain and refractive index in a raman
Amplification resonance (schematic)

Fig B1.35 *Schematic variation of refractive index and dispersion terms in the region of a Raman resonance.*

energy gain is obtained. The interaction length L_i for a Stokes pulse of duration Δt_s is less than the full length of the Raman amplifier in the ratio $L_i/L = \Delta t_s/\Delta t_p$, whereas the constraint on small signal gain for the pump to prevent self generation applies to the small signal gain length product gL of the whole system. In addition, small signal gain of the Stokes pulse in the transient regime is less than that for self generation in the pump pulse because of the difference of pulse duration. In the strongly transient high gain limit, the gain coefficient scales as $\epsilon_p^{1/2}$, where ϵ_p is the pump energy in the time interval of a Stokes pulse. Thus, if the constraint $g\ell < 17$ is applied for self generation in a pump hot spot with intensity ratio n:1 and the ratio $\Delta t_p/\Delta t_s = m$ it follows that for the Stokes pulse we have

$g_s L_i = g\ell/m^{3/2}\, n^{1/2}$. For example with m = 5 and n = 2 we have $g_s L_i = 1$ and saturated gain would not be possible without violating the constraint on self generation of the pump. A further problem is that for lower effective gains the Stokes pulse broadens during interaction with the pump. Some mitigation of the constraint would be obtained through the temporal truncation of the pump pulse by saturated amplification of the Stokes pulse[1]. Nevertheless, the use of short Stokes pulse and longer pump pulse, while having some theoretical advantages, is subject to a problem with self generation of the pump.

Effects of Anomalous Dispersion in a Raman Resonance

The Raman gain resonance has associated with it an anomalous dispersion feature as with any amplifying or absorbing resonance. The magnitude of the refractive index disturbance is proportional to the magnitude of the gain and it occurs in a spectral width proportional to the width of the gain line, (fig B1.35). Thus Stokes radiation propagating in a Raman amplifier experiences anomalous dispersion effects proportional to the exponent of its saturated amplification $g_{eff}\ell$ in the amplifier. Similarly, the pump radiation experiences antisymmetric anomalous dispersion effects proportional to the exponent of its attenuation. If, for the reasons discussed earlier, the stage gain is limited to an exponent of the order of 3.5 and the attenuation of the pump is limited to an exponent of the order of -1.6, the dominant effect of dispersion will be on the Stokes beam. The magnitude of the dispersion resonance has been assessed experimentally by observing the focusing effect for a Stokes beam detuned to the peak of the change in refractive index (A in Fig B1.35) in a spatially gaussian pattern of pumping intensity with $gL = 2.7$[3]. Scaling from this observation, the peak change in optical path length for $g_{eff}\ell = 4$ is estimated at $0.8\ 10^{-4}$ cm.

Where the Stokes beam propagates at the centre frequency of the resonance and is in a transform limited pulse, when $t >> T_2$ the effect of the anomalous dispersion will be negligible but can possibly cause pulse broadening for $t \leq T_2$. The characteristic length for two-fold stretching of the pulse duration[4] can be expressed in the form

$$L_D = \Delta t_s^2/(d^2k/d\omega^2)$$

or, in terms of the change of refractive index,

$$L_D = \Delta t_s^2/((\omega/c)(d^2n/d\omega^2) + (2/c)(dn/d\omega)).$$

The frequency width of the CH_4 Raman line is $\Delta\omega = 7 \times 10^{10}$. Estimating $dn/d\omega$ and $d^2n/d\omega^2$ from the peak refractive index change and the linewidth, shows that for a 10 psec pulse and $g_{eff}\ell = 4$ there is negligible pulse broadening even if $d^2n/d\omega^2$ were constant across the pulse bandwidth, while fig B1.35 shows that it changes sign giving a reduced broadening effect.

Pulse chirping through the sudden saturation of the dispersion resonance is also possible. If the dispersion resonance is bleached in a time equal to the pulse duration we can estimate the

rate of change of optical path length experienced by the Stokes beam and hence the frequency shift. For a Stokes pulse duration giving a frequency width equal to the Raman linewidth (30 psec at transform limit in CH4) the maximum frequency change $\Delta\omega/\omega = 0.6\ 10^{-6}$ whereas the linewidth is 10^{-5}. Moreover the above estimate applies for a change in optical path which is experienced by all frequency components of the pulse. In the dispersion resonance and there are changes of opposite sign for up-shifted and down-shifted frequencies. The resultant effect is therefore smaller than the above estimate. From this it is concluded that chirping effects should also be negligible for gain length products $g_{eff}\ell \leq 4$ of interest here.

If a Stokes beam were propagating in a Raman amplifier with strong variations of the pump intensity across the beam and the pulse were already chirped, then focusing and defocusing of the up-shifted and down-shifted components of the pulse could occur as shown in Ref 3. This scenario is however unlikely because the chirping effect in the anomalous dispersion resonance is small as discussed previously.

It appears therefore that the anomalous dispersion resonance effects may be neglected.

Staging of a series of amplifiers

The foregoing discussion has shown that individual amplifier stages are best operated with saturated gain and with moderate gain per stage. It follows that, to obtain high power output, a staged series of amplifiers is required. The need for high conversion efficiency is paramount only in the final stage and some relaxation of the previously discussed constraints is possible in the feeder stages. An examination of the saturated gain behaviour, Section B1.5 ibid, shows that relaxation of the requirement for efficiency enables increase in the ratio of pump power to input Stokes power. For example, with hot spot ratio 2:1 and maximum gL = 17 in the hot spot, relaxing the required conversion efficiency from 80% to 50% relaxes the required ratio of Stokes input to pump from 1/30 to 1/300. These considerations suggest that the series of Raman amplifiers should have saturated gain in the output stage limited to about 30 for the reasons discussed earlier but that higher gain could be used in preamplifiers up to a few hundred times.

Practical example for SPRITE

It is required for a general purpose KrF laser facility that the Raman amplifiers operate at pulse lengths from the order of 1 nsec to a few picoseconds. Also, to allow use of thin windows, the gas fill pressure should be 1 atm. This suggests the possibility of using an active Raman gas with a buffer gas of small Raman gain making up the pressure to 1 atm. The feasibility of this procedure can be assessed with reference to a practical example.

The SPRITE laser has an output Raman amplifier of 8 x 8 cm cross-section and 2 m length. It is pumped by six pump beams which have a maximum individual energy in short pulses of 2 J. This energy is the saturated output of the 27 cm SPRITE aperture for pulses short compared to the upper state lifetime of KrF (<< 2 nsec). The Raman amplifier is required therefore to operate with constant energy input and variable pulse length. It is interesting to consider how this output amplifier could perform for eg 1,000 psec, 100 psec, 30 psec and 10 psec inputs.

1,000 psec

The steady-state Raman gain in CH_4 is γI_p where $\gamma = 2.3\ 10^{-10}$/W cm^{-2} bar. With 12 J pump energy in 64 cm^2 and a 2:1 hot spot ratio $\gamma I_p \ell = 17$ is obtained in 2 m length with 1 bar CH_4.

The small signal gain at the average pump intensity is $g\ell \sim 8.5$ and ~ 0.3 J Stokes input gives 10 J output.

100 psec

At this pulse length transient behaviour becomes non negligible and the small signal gain is reduced relative to the steady state value. Estimating the effect from numerical calculations, Section B1.5 ibid, suggests that gL = 17 for n = 2 is obtained with a CH_4 pressure of 0.2 bar in 2 m length.

30 psec

At t < 30 psec the nonlinear limits due to the entrance window become effective. For 0.25 cm fused silica the maximum intensity is 10^{10} W cm^{-2} which is reached in the beam centre for 30 psec 12 J with a fill factor F = 0.8. Again estimating transient small signal gain from numerical calculations gives a required pressure in 2 m length of 0.14 bar CH_4 for gℓ = 17 n = 2. The small signal gain at the average pump power is larger than in the steady stae at gℓ = 12, so that a Stokes input of 0.1 J is sufficient for 10 J output.

10 psec

Here the energy in the pump is restricted to 4 J to avoid nonlinear effects at the entrance window. Proceeding as before the required CH_4 pressure is 0.3 bar.

The output Stokes energy is limited to 3.2 J for an input of 0.03 J.

Further reduction of the pulse length at constant pump intensity would require increased CH_4 pressure for adequate amplification. Also the input pump energy would be reduced in proportion to the pulse length reduction.

These estimates suggest the possibility of operating a Raman output amplifier with constant pump energy and conversion efficiency ∿ 80% at pulse lengths from nanosecond to 10 psecs simply by varying the percentage CH_4 at 1 atm of fill pressure in the final output amplifier.

Practical Staging

Applying the previous arguments to the staging of a series of Raman amplifiers for SPRITE suggests apertures in the series 8 cm, 2.5 cm, 0.5 cm with gains 15, 150 and 250 and efficiencies of 85%, 80% and 75%.

Amplifying the Stokes pulse from microjoule levels produced in a dye laser harmonic conversion system to ∿ 10 J using saturated amplification of the Stokes beam, produces a situation where the intensity length product for the Stokes radiation is comparable to that of the pump radiation down the series of amplifiers but where no strong saturating signal is injected at the second Stokes frequency, consequently there is unsaturated small signal gain at the second Stokes frequency. This could lead to self generation of the second Stokes if the small gain length product were to exceed 25. Typically, the previous discussion has focused on small signal gain exponent per stage at the average pump intensity of 17/2. Three such stages could therefore give small signal gain for the second Stokes reaching the self generation threshold. A dispersive filter suppression of second Stokes at intervals of two or three stages is therefore indicated.

References

1. J R M Barr et al, SPIE 874, 60 (1988).

2. I N Ross (private communication).

3. A Owyoung, Appl Phys Lett 26, 168 (1975).

4. R Wilhelmi et al, Optica Acta 32, 1175 (1985).

B2	**SUPERSPRITE DEVELOPMENT**	Pages
B2.1	MARX GENERATOR DEVELOPMENT	227
B2.2	SUPERSPRITE ARCHITECTURE AND COSTING	227-230

B2.1 MARX GENERATOR DEVELOPMENT

E Madraszek, H T Medhurst, J Lister and M Shaw (RAL)

Due to a kind gift of 44 storage capacitors (1.35μF, 100 kV, 50 nH) from Sandia Laboratories (via AWE Aldermarston) it was decided to proceed with the development of a new compact, high energy Marx generator of the type which would be required for Supersprite and the succeeding generation of KrF lasers.

For these large aperture lasers the electron beam voltage will need to be increased from the 450 kV at present in Sprite to the region 700 - 900 kV This will require PFL voltages of 1.4 - 1.8 MV. From these considerations it was decided that a 12 stage (24 capacitor) Marx would be required. This is the same number as the Sandia Hermes III design which was known to be very reliable and so this design was followed fairly closely in our construction.

Figure B2.1 shows a general view of the Marx Generator during trial assembly. The two stacks of 12 capacitors are arranged in a low inductance configuration and are switched by a midplane triggered spark gap (Physics International type T508). The capacitors are charged alternately + - to the required charge voltage through a network of copper sulphate resistors shown in Figure B2.2. The spark gaps are all triggered via 2kΩ resistors and the complex arrangement of grounding resistors is designed to give minimum jitter on triggering.

The inductance and internal resistance of the Marx was measured by ringing it into a short circuit. In this test all of the spark gaps are shorted out by thick copper wire and the series stack charged to 350V. (All the normal charging resistors are removed for this test). A pin switch is used to provide a low inductance short and the current is measured by a Rogowski loop. The circuit and the ringing waveform is shown in Fig B2.3. The ringing frequency gives the Marx inductance of 5.0 μH and the decay time gives the series resistance of 0.73Ω. These are in good agreement with Sandia figures of 4.9 μH and 0.97Ω respectively where the latter contain the effective resistance of the spark gaps which is not measured in our test.

The Marx is due to be assembled inside its oil tank in R7 during May 1989 and the first high voltage shots should be in June 1989.

B2.2 SUPERSPRITE ARCHITECTURE AND COSTING

P T Rumsby (RAL)

Some flexibility exists in the choice of KrF output module aperture and number and size of multiplexer beam lines to be used in the Supersprite system. Since total system cost must be minimised the final design details will be influenced strongly by the scaling of all components with size and number.

Optics costs represent at least 1/3 of the total system cost and consequently a data base of fabrication and coating costs for all optical components required for Supersprite has now been established.

Two general conclusions of this exercise are that:-

(a) from a given vendor, costs of optically worked fused silica windows and dielectric mirrors scale closely as the cube of the aperture over the 100 to 1000 mm aperture size.

and

(b) that costs of both mirrors and windows are substantially cheaper at apertures less than 350 mm where a large number of potential vendors exist in the UK.

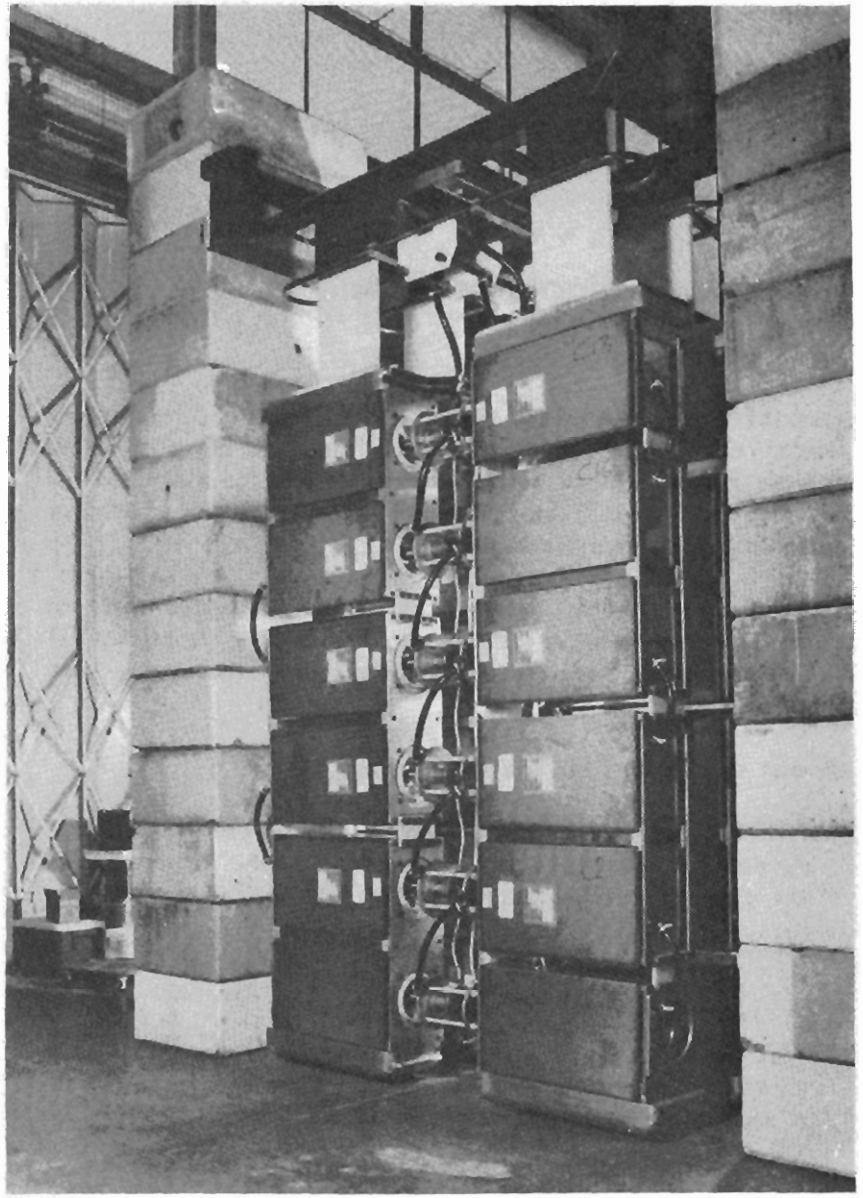


Fig B2.1 General view of Supersprite Marx generator during trial assembly.

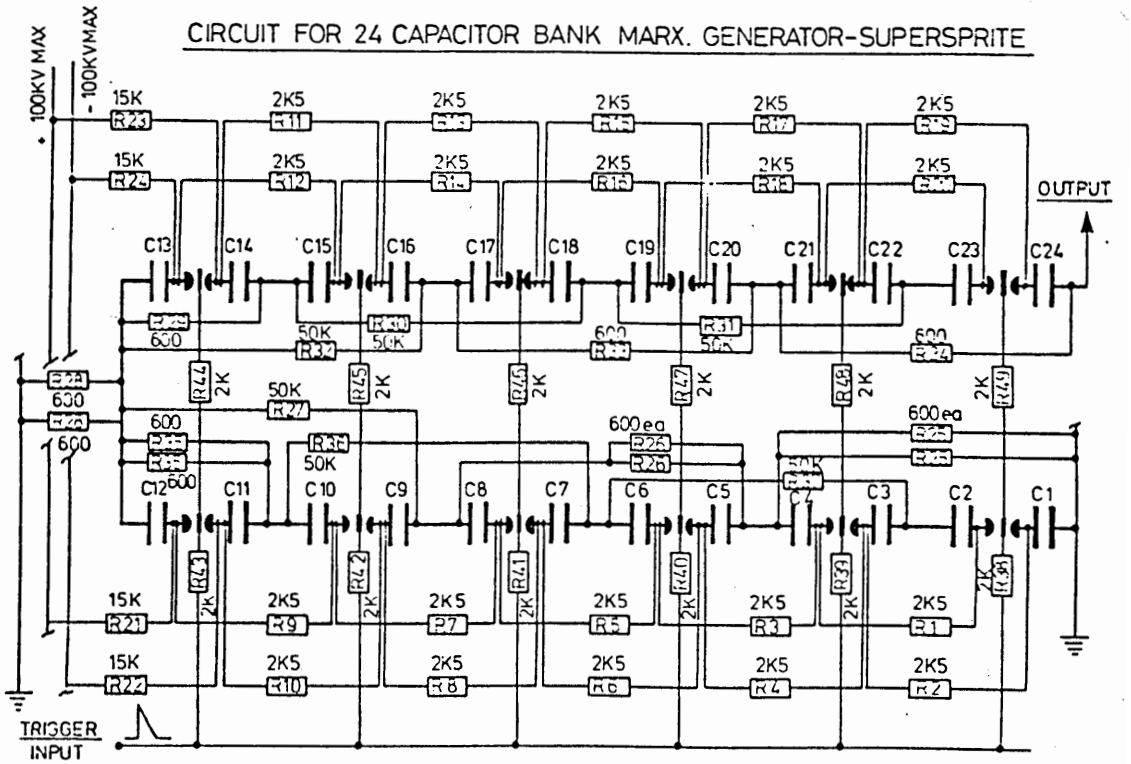
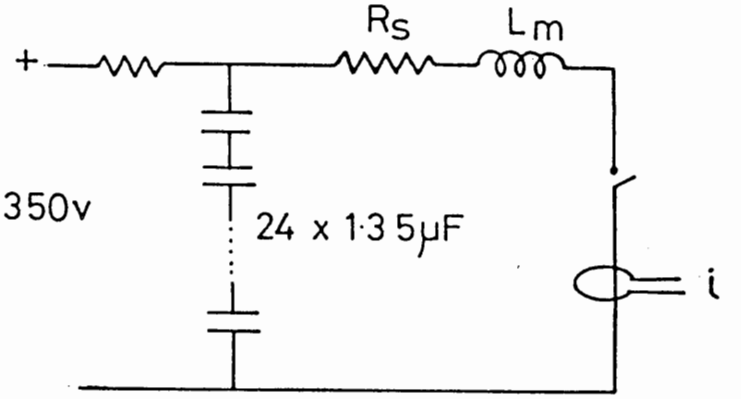
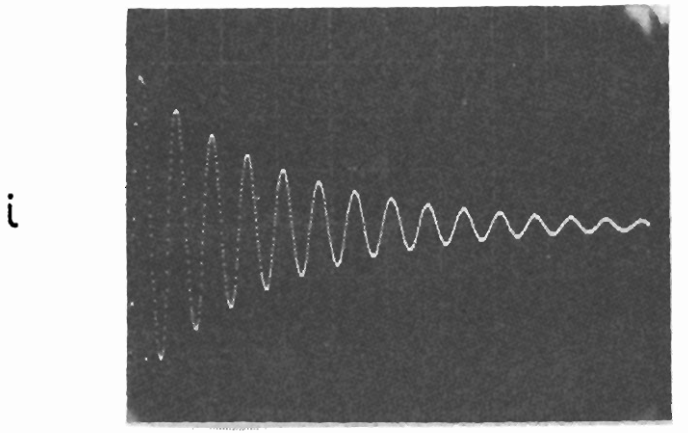


Fig B2.2 Electrical circuit diagram of Marx generator.





5μs per div

$f = 300\ kHz$

$L_m = 5{\cdot}0\ \mu H \quad \left(f = \frac{1}{2\pi\sqrt{LC}}\right)$

$R_s = 0{\cdot}73\ \Omega \quad \left(\ln\left(\frac{i_1}{i_2}\right) = \frac{R_s}{2fL_m}\right)$

Fig B2.3 Ringing waveform of Marx generator with all gaps hard wired as short circuits.

The data base is now being extended to include cost scaling of pulsed power and KrF e-beam module mechanical components such as spark gaps, water lines, capacitors etc, so that a complete system cost model can be derived to aid design of both Supersprite and future larger scale KrF systems.

The total output beam aperture of Supersprite (number of beams x individual beam area) is set by the safe operating fluence (J/cm^2) level on dielectrical coated mirrors. Hence for both cost saving and operational safety reasons there is a strong desire to increase the damage level of high power UV laser mirrors and splitters substantially above that available at present. In addition substantial system cost savings can be achieved if fluorine resistant dielectric coatings can be developed for use on the retro-mirrors associated with each double pass KrF amplifier, halving the number of large aperture fused silica windows required.

For both the reasons a programme of UV coating development and testing has been started involving a variety of coating vendors, CLF staff and the UV laser damage test facilities at Loughborough University. Using both conventional e-beam and new coating techniques such as ion beam sputtering, plasma plating and molecular beam deposition a variety of existing and new dielectric materials are being investigated to guide future specification of beamline high damage level mirrors and KrF module fluorine resistant mirrors.

C	LASER SUPPORT FACILITY	Pages
C1	CHEMISTRY	231-318
C2	BIOLOGY	319-337
C3	PHYSICS	338-368
C4	PLASMA X-RAY SOURCES/PSEC LASER DEVELOPMENT, NLO RESEARCH	369-418
C5	LASER SUPPORT FACILITY OPERATIONS	419-421

Section C

Introduction

This section describes work done in association with the Central Laser Facility using small lasers. Experiments using scheduled time at the Laser Support Facility and Loan Pool lasers are described in C1 (Chemistry), C2 (Biology) and C3 (Physics). Section C4 contains reports on work by the Laser Development and the Non-linear Optics groups some of which is funded from other than Science Board allocations (The Paul Fund of the Royal Society, Eureka, RAL Director's Fund). A brief account of LSF operations is given in C5.

This has been a vintage year both for contributions and for publications. The topics range from jet cooled spectroscopy through Raman scattering from organometallic catalysts, kinetics of DNA damage repair, multiphoton physics and X-ray generation to the deposition of thin films of high T_c superconductors. Such a spread cannot be summarised in a brief introduction.

W T Toner

C1	**CHEMISTRY**	Pages
C1.1	RYDBERG STATES OF THE SH(SD) RADICAL REVEALED BY MULTIPHOTON IONISATON SPECTROSCOPY	235-240
C1.2	EVIDENCE FOR THE EXISTENCE OF TRANSIENT GAS-PHASE COMPLEXES IN LASER FLASH PHOTOLYSIS STUDIES OF DIMETHYLSILYLENE	240-242
C1.3	UV RESONANCE RAMAN STUDIES OF INCLUSION COMPOUNDS	242-244
C1.4	INVESTIGATION OF ENERGY TRANSFER IN POLYCARBONATE FILMS USING PICOSECOND PUMP-PROBE LASER FLASH PHOTOLYSIS	244-248
C1.5	PRESSURE AND TEMPERATURE DEPENDENCE OF THE RATES OF SOME REACTIONS OF THE METHOXY RADICAL	248-249
C1.6	STATE DISTRIBUTIONS FOR BOTH PRODUCTS OF THE REACTION:H + NO_2→ OH = NO	249
C1.7	TIME-RESOLVED RESONANCE RAMAN SPECTROSCOPY OF PHOTOGENERATED TRANSIENTS IN METAL CARBENES: INTRAMOLECULAR REARRANGEMENT vs SOLVENT INTERACTION	249-253
C1.8	TR³ STUDIES OF REACTION INTERMEDIATES IN UBIQUINONE PHOTOLYSIS	253-259
C1.9	INTERFACIAL CHARGE-TRANSFER STUDIES ON COLLOIDAL SEMICONDUCTORS BY TIME-RESOLVED RESONANCE RAMAN (TR3) SPECTROSCOPY	259-263
C1.10	IN-SITU MOVPE DIAGNOSTICS: OPTICAL SECOND HARMONIC GENERATION - A FEASIBILITY STUDY	263-270
C1.11	IODINE ATOM DETECTION IN THE INFRARED PHOTODISSOCIATION OF CF_3I	270-271
C1.12	PHOTODISSOCIATION DYNAMICS OF JET-COOLED ALKYL THIONITRITES	272-276
C1.13	PHOTOFRAGMENTATION OF JET-COOLED CCl_3NO	276-281
C1.14	PICOSECOND SINGLE VIBRONIC LEVEL FLUORESCENCE SPECTROSCOPY	281-285
C1.15	DISPERSED FLUORESCENCE AND FLUORESCENCE EXCITATION SPECTROSCOPY IN A SUPERSONIC JET	285-291
C1.16	LASER EXCITATION SPECTROSCOPY OF TRANSITION ELEMENT HALIDES IN SUPERSONIC BEAMS	291-293
C1.17	LASER SPECTROSCOPY AND PHOTOPHYSICS OF INTRAMOLECULAR CHARGE TRANSFER SYSTEMS UNDER JET-COOLED CONDITIONS	293-301
C1.18	TR3 SPECTRA OF OCTACYANOTUNGSTATE ION IN AQUEOUS SOLUTION	301
C1.19	RAMAN SPECTRA OF NOCl and Cl_2: PHOTODISSOCIATION DYNAMICS	301-307
C1.20	DEVELOPMENT OF A STREAK CAMERA SYSTEM AND DATA ANALYSIS SOFTWARE FOR THE MEASUREMENT OF TIME RESOLVED LASER INDUCED FLUORESCENCE	308-313
C1.21	CHEMILUMINESCENCE AND ENERGY TRANSFER IN Mn ATOM REACTIONS	313-314
C1.22	NON-THERMAL LASER INDUCED DESORPTION AND ENERGY TRANSFER FOR MOLECULES ADSORBED ON DI-ELECTRIC SURFACES	314-318

C1.1 RYDBERG STATES OF THE SH(SD) RADICAL REVEALED BY MULTIPHOTON IONISATON SPECTROSCOPY

M N R Ashfold, B Tutcher and C M Western (University of Bristol)

Introduction

Multiphoton excitation methods, and the technique of multiphoton ionisation (MPI) in particular, are becoming increasingly important as means of detecting and characteristing reactive free radicals[1]. Such methods are of particular interest when applied to radicals for which conventional, one photon detection methods - most notably laser induced fluorescence (LIF) - are unsuitable, or lacking in sensitivity. The mercapto radical is one such species. Its first excited electronic state ($A^2\sum^+$) is predissociated, to an extent which increases with increasing levels of internal excitation[2]. Thus the fluorescence quantum yield of this state is not only small, but internal quantum state dependent. Consequently, there have been relatively few quantitative measurements of SH(X) or SD(X) radical concentrations using LIF on the A-X transition as the radical probe[3-5], and even fewer attempts at determining internal quantum state population distributions for these species[6].

Several higher excited (Rydberg) electronic states of SH (SD) have previously been identified by vacuum ultraviolet (VUV) absorption spectroscopy[7]. Analysis of the rotational fine structure accompanying these electronic excitations (which appears sharp in spectra involving the SD species but which shows clear evidence of lifetime broadening in the SH spectra) enabled derivation of the various excited state symmetries[7]; their electronic configurations have been discussed in the light of recent ab initio calculations of the vertical electronic spectrum of the mercapto radical[8].

The $X^3\sum^-$ ground state of the SH^+ ion is just one three states derived from the lowest energy configuration, $...5\sigma^2 2\pi^2$. The others ($^1\Delta$ and $^1\sum^+$) are observed[9] to lie, respectively , 1.28 eV and 2.39 eV higher in energy. Rydberg series will converge to each of these limits, resulting in a complex pattern of states in the energy range traditionally associated with one photon VUV wavelengths. The present paper reports the observation and partial characterisation of three of these Rydberg states each detected via the two photon resonance enhancement it provides to the overall MPI yield and each attributable to a $2\pi^2 4p^1 \leftarrow 2\pi^3$ electron promotion.

Experimental

Ground state SH(SD) radicals were produced by 193 nm photolysis of a pulsed molecular beam sample of $H_2S(D_2S)$, and subsequently ionised by two photon resonant MPI in the source region of a time-of-flight (TOF) mass spectrometer. The 193nm radiation (unpolarised) was provided by a Lumonics HE460 excimer laser operating on ArF and, of necessity, at a repetition rate of 100 Hz. Resonance enhanced MPI spectra of the SH(SD) radicals, in the wavelength range 265-317nm, were obtained using the frequency doubled output of an XeCl excimer pumped dye laser (Lambda-Physik EMG 201 and FL 2002 together with an Inrad 5-12 "auto-tracker"). The latter laser, and the pulsed valve, were operated at a 10 Hz repetition rate. Typical 193 nm pulse energies in the interaction region were in the range 1-5 mJ (beam diameter ∿3mm), whilst those of the frequency doubled dye laser were typically ∿0.3 mJ (focused using a 27 cm f.l. lens).

The experiment utilised a master oscillator to provide the 100 Hz trigger pulses for the probe laser and, through use of a decade divider, the 10 Hz trigger pulses for the probe laser and pulsed valve. These trigger pulses were suitably delayed so that every tenth photolysis pulse intercepted the pulsed molecular beam at its instant of maximum flux. The probe laser output was timed so as to interrogate the sample ∿1μs after photolysis. The choice of this delay represents a compromise: at shorter delays the concentration of the sought after neutral fragments within the probe volume is higher, but so too is the background ion signal (resulting from the photolysis laser alone) in the ion TOF spectrum. These TOF spectra were recorded by feeding the amplifier output from a channel electron multiplier (positioned at the end of the field free drift

region of the TOF spectrometer) into a fast digital oscilloscope (LeCroy 9400, 125 MHz bandwidth), the sweep of which was pre-triggered by the signal from a fast photodiode concident with the probe laser pulse. Signal averaging of these transients, and data storage, was accomplished via an IEEE interface to an Apple II microcomputer. MPI spectra associated with the formation of just one particular ion mass were obtained as a function of laser excitation wavelength using a boxcar (Stanford Research Systems, model SR250, operating in its linear gate mode with a 50 ns time window) to monitor just that fraction of the total ion yield which showed the appropriate time-of-flight. Dye laser wavelength calibration was achieved through the observation of 2+1 MPI resonances associated with the $3p^3np^1 \leftarrow 3p^4(n=4,5)$ $^3P_J \leftarrow {}^3P_J$ transitions of S atom photoproducts formed by multiphoton excitation and dissociation of the $H_2S(D_2S)$ precursors.

Results

MPI resonances associated with three band systems of the SD radical were identified in the wavelength range investigated. In the case of SH however, we were only able to discern fragmentary structure at two of the corresponding excitation energies. Fig. C1.1c shows the shortest wavelength feature identified in the MPI spectrum of the SD radical. It consists of two sub-bands, whose energy separation corresponds to the spin-orbit splitting of the ground $X^2\Pi$ state ($A_0"=-376.7_5 cm^{-1}$ [10]) if the spectrum is assumed to arise as a result of a coherent two photon resonance enhancement. The validity of this conclusion, which necessarily implies a small value for the excited state spin-orbit interaction parameter, is confirmed by rotational analysis.

This involved a number of stages. At the outset we calculated the likely form of the rotational structure accompanying all possible spin and symmetry allowed one colour two photon transitions from the $X^2\Pi$ ground electronic state.

Spectroscopic constants for the ground state were taken from the original analysis of Ramsay[10] and, for the purpose of these trial simulations, we assumed the excited state to have rotational constants typical of those determined for the previously characterised Rydberg states[7]. This exercise readily revealed that the experimental spectrum shown in Fig. C1.1c must arise as a result of two photon resonant excitation to a hitherto unobserved $^2\phi$ state from the zero-point level of the $X^2\Pi$ ground state. This conclusion is reinforced by our non-observation of any transitions to excited state levels with $J'<{}^5/_2$. Least squares fitting of the observed lines yielded the spectroscopic constants listed in Table 1. The correctness of these values is illustrated by comparing the line positions in the experimental spectrum with those appearing in the calculated spectrum (Fig. C1.1b), which assumes a 300K thermal distribution. Franck-Condon considerations imply that this must be an origin band.

Two other band systems were identified at longer wavelengths in these preliminary investigations of the MPI spectrum of the SD radical. Rotational analysis revealed the longer wavelength feature to be associated with a two photon resonant excitation to a $^2\Sigma^-$ state from the zero-point vibrational level of the $^2\Pi_{3/2}$ spin-orbit component of the electronic ground state; spectroscopic parameters for the $^2\Sigma^-$ excited state are listed in Table 1. The companion sub-band from the F_2 ($^2\Pi_{1/2}$) component of the ground state could not be identified in the present work because of the large yield of SD^+ fragment ions following 2+1 MPI via the $^1A_2(2b_1{}^14pb_2{}^1)$ Rydberg state of the parent D_2S at the relevant dye laser excitation wavelengths. The intervening features have so far defied detailed analysis but, based on our band simulations, we believe that this somewhat fragmentary structure must be associated with a $^2\Pi$-$X^2\Pi$ transition of the SD free radical. The origin estimated for this electronic transition is also included in Table 1.

The earlier VUV absorption work[7] revealed negligible isotope shift between the Rydberg states of SD and SH. Consistent with this the only MPI resonances attributable to the SH radical that we have detected to date occur at excitation wavelengths in the range 270-272 nm and at ∿312 nm, ie, at the equivalent wavelengths to the $^2\phi$-$X^2\Pi$ and $^2\Sigma^-$-$X^2\Pi_{3/2}$ transitions of SD. The structure observed is

reasonably sharp, but sparse, yielding insufficient lines for rotational analysis. Attempts at detecting MPI resonances in the region of the anticipated $^2\Pi$-$X^2\Pi$ transition of SH were unsuccessful.

Discussion

The ab initio calculations of Bruna and Hirsch[8] provide a wholly consistent rationale for these new spectroscopic observations. The electronic configuration of the mercapto radical in its ground state is

$$(5\sigma)^2(2\pi)^3 \qquad ^2\Pi$$

All of the transitions identified in the earlier VUV absorption studies[10] can be understood in terms of excitation to s or d Rydberg orbitals (ie, the transitions all satisfy the $\Delta\ell=\pm1$ Laporte selection rule, if the highest occupied (2π) molecular orbital in the ground state is presumed to have an essentially 'atomic'-like $3p_x$ nature.) The present results provide further support for the atomic-like nature of this 2π molecular orbital, in as much that the newly identified excited states are all attributable to electronic promotion to a p Rydberg orbital. (The two photon equivalent of the Laporte selection rule requires $\Delta\ell=0,\pm2$).

Rotational analysis demonstrates unequivocably that the lowest energy excited state observed in the present work has $^2\Sigma^-$ symmetry. The calculations of Bruna and Hirsch[8] indicate that the first three states of such symmetry will arise from the configurations $5\sigma^22\pi^2[^3\Sigma^-]6\sigma^1$ (where 6σ is an antibonding valence orbital), $5\sigma^22\pi^2[^3\Sigma^-]4s^1$ and $5\sigma^2\pi^2[^3\Sigma^-]4p\sigma^1$ respectively. The potential function for the first of these is calculated to be repulsive at all internuclear separations[8]. Excitation to the second gives rise to the well documented $B^2\Sigma^-$-$X^2\pi$ system, the origin transition of which shows well developed band heads in one photon absorption at ∿167.3 nm and ∿168.4 nm[7]. Since this B-X transition involves what is, at the atomic limit, a s ← p excitation, it is doubtful whether it would show a significant two photon resonance enhancement. By the same arguments however, excitation from the ground state to the third of these excited configurations would be predicted to be a one photon forbidden, but two photon allowed, process. The resulting $^2\Sigma^-$ state is calculated to lie at a vertical excitation energy of ∿7.82 eV above the ground state and, as with the $B^2\Sigma^-$ state, to have a bond length R_{S-D} = 0.137 nm, (equivalent to B_o = 4.68 cm^{-1}) greater than that of the ground state neutral or ion as a result of Rydberg ($4p\sigma$)-valence (σ^*) mixing[8]. Such predictions accord well with the spectroscopic constants listed in Table 2 for the newly identified $^2\Sigma^-$ state (T_o = 7.92 eV, B_o = 4.696 cm^{-1}), and we associate it with the leading electronic configuration $5\sigma^22\pi^2[^3\Sigma^-]4p\sigma^1$ accordingly.

Energetic considerations dictate that the $^2\pi$-$^2\pi$ transition identified at slightly shorter wavelength must be part of the same p-complex. However the ab initio calculations for this excited $^2\pi$ state reveal substantial Rydberg ($5\sigma^22\pi^2[^3\Sigma^-]4p\pi^1$) - valence ($5\sigma^1\pi^36\sigma^1$) configuration mixing and predict the resulting potential energy curve to include just a shallow minimum centred at an internuclear separation larger than that for a typical Rydberg state of the mercapto radical[8]. Such a result is consistent with the paucity of rotational structure evident in the spectrum of the SD radical and with our inability to detect the equivalent transition in the SH spectrum.

The first $^2\phi$ state expected in the vertical electronic spectrum of SH(SD) would arise from the configuration $5\sigma^22\pi^2[^1\Delta]4p\pi^1$ and, in view of its strong showing as a two photon resonance and the good agreement between its observed (9.14 eV) and calculated (9.16 eV [8]) term value, we assign our newly discovered $^2\phi$ state accordingly. The spin-orbit interaction parameter A in the $^2\phi$ state is found to have a small positive value. This accords with expectations based on Hund's rules in as much that the dominant contributions to this term should arise from coupling of the spin and orbital angular momenta of the single $4p\pi$ Rydberg electron.

Individual rotational lines in the SD($^2\Sigma^-$-$X^2\Pi$) transition show clear evidence of lifetime broadening. After deconvoluting the effective two photon laser bandwidth (0.8 cm^{-1} modelled as a gaussian lineshape), the observed linewidths indicate a lifetime

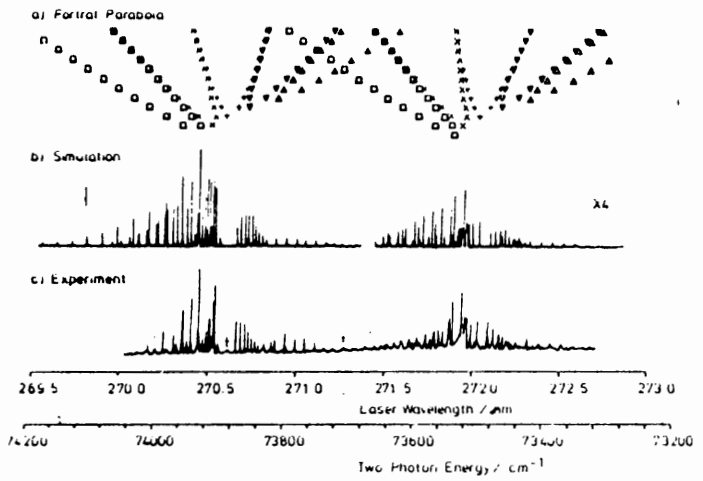


Fig. C1.1 Two photon resonance enhanced MPI spectrum of SD fragments (m/z = 34) following excitation in the wavelength range 270-273 nm (fig. 1c). The weak feature apparent at ∿270.65 nm (marked with an asterisk) is a doublet associated with the intense $^3P_{2,1} \leftarrow ^3P_1$ ($3p^3 5p^1 \leftarrow 3p^4$) two photon transitions of S atoms, 'breaking through' into the m/z = 34 time channels. The break in the experimental spectrum at ∿271.31 nm (also marked with an asterisk) coincides with the corresponding $^3P_J \leftarrow ^3P_2$ two photon transitions of the s atom. (b) displays the predicted form of this $^2\phi$-$x^2\Pi$ two photon transition derived using the appropriate spectroscopic parameters taken from Table 1 and assuming an effective two photon excitation bandwidth of 0.8cm^{-1} fwhm (gaussian) and a 300K thermal population distribution over the $X^2\Pi$ rotational and spin-orbit states. The corresponding Fortrat parabolae are shown in (a), with the various branches indicated from left to right S_{21} and S_1, x R_{21}, + Q_{21} and Q_1, ∇ P_{21} and P_1, Δ O_{21} and O_1, and similarly for the F_2 component of the ground state.

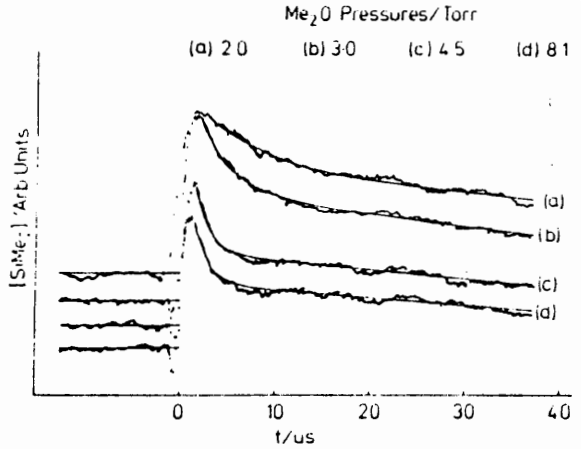


Figure C1.2 Concentration-time profiles for $SiMe_2$ in the presence of Me_2O at 295K.

for this $^2\Sigma^-$ Rydberg state of SD of ~2.5 ps. In contrast, the $^2\phi$-$X^2\Pi$ spectrum appears with laser limited resolution, thus suggesting that the $^2\phi$ state might be sufficiently stable for this $^2\phi$-$X^2\Pi$ transition to provide a possible laser induced two photon detection scheme for SD(X) radicals.

Acknowledgments

Equipment grants and studentship (to BT) from the Science and Engineering Research Council are gratefully acknowledged, as is the loan of the Lumonics HE460 excimer laser from the SERC Laser Support Facility. CMW would like to thank the Royal Society for the award of a 1983 University Research Fellowship. We are all grateful to Professor R N Dixon for his advice and encouragement at all times, to K N Rosser for his outstanding technical support and to J D Prince, for her help with the multiphoton line strength calculations.

Table 1

Spectroscopic constants (in cm^{-1}) for the zero point levels of the $^2\Sigma^-$, $^2\Pi$ and $^2\phi$ state of SD identified in this work. Quoted errors represent 1σ, except in the case of the band origins. For the $^2\Sigma^-$ and $^2\phi$ states the quoted errors in T_o reflect the uncertainty in extrapolating between the available calibration lines. The larger error on the $^2\pi$ state origin reflects our inability to carry out an unambiguous rotational analysis of the available spectrum. Rotational constants for the zero point level of the ground state neutral[10] and ion[11] are included for comparison.

Electronic State and Leading Configuration	T_o*	B_o	$D_o X10^4$	A_o	γo
$5\sigma^2 2\pi^3$ $X^2\Pi$	0	4.900	1.3_s	-376.7_s	0
$5\sigma^2 2\pi^2[^3\Sigma^-]4p\sigma^1$ $^2\Sigma^-$	63855.7(10)	4.696(1)	0.54(6)	-	-0.203(18
$5\sigma^2 2\pi^2[^3\Sigma^-]4p\pi^1$ $^2\pi$	64831 (5)				
$5\sigma^2\pi^2[^1\Delta]4p\pi^1$ $^2\phi$	73720.2(10)	4.828(8)	1.3(7)	8.14(20)	-0.2^+
$5\sigma^2 2\pi^2$ $X^3\Sigma^-$	-	4.73298	1.289	-	-0.08534 (λ_o=5.761)

*In accord with usual practice, T_o includes $B\Lambda^2$ but does not include $B[S(S+1)-\Sigma^2-\Omega^2]$ which is here included in the rotational energy.

+not floated in least squares fit.

$X^2\Pi$ rotational and spin-orbit states. The corresponding Fortrat parabolae are shown in (a), with the various branches indicated from left to right S_{21} and S_1, x R_{21} and R_1. + Q_{21} and Q_1, ∇ P_{21} and P_1, Δ O_{21} and O_1, and similarly for the F_2 component of the ground state.

References

1. J W Hudgens, "Advances in Multiphoton Processes and Spectroscopy", (edited by S H Lin), World Scientific, Singapore), 4, 171 (1988).

2. K P Huber and G Herzberg "Molecular Spectra and Molecular Structure IV: Constants of Diatomic Molecules", van Nostrand Reinhold, New York (1979).

3. J J Tiee, F B Wampler, R C Oldenborg and W W Rice Chem Phys Lett 82, 80 (1981).

4. G Black, R Patrick, L E Jusinski and T G Slanger, J Chem Phys 80, 4065 (1984).

5. R R Friedl, W H Brune and J G Anderson J Phys Chem 89, 5505 (1980).

6. W G Hawkins and P L Houston, J Chem Phys 73, 297 (1982) also J Chem Phys 76, 729 (1982).

7. B A Morrow, Can J Phys 44 2447 (1966).

8. P J Bruna and G Hirsch, Mol Phys 61, 1359 (1987).

9. S J Dunlavey, J M Dyke, N K Fayad, N Jonathan and A Morris Mol Phys 38, 729 (1979) also Mol Phys 44, 265 (1981).

10. D A Ramsay J Chem Phys 20, 1920 (1952).

11. J Rostas, M Brion, J Daumont and J Malicet Mol Phys 52, 1431 (1984).

C1.2 EVIDENCE FOR THE EXISTENCE OF TRANSIENT GAS-PHASE COMPLEXES IN LASER FLASH PHOTOLYSIS STUDIES OF DIMETHYLSILYLENE

J E Baggott, M A Blitz, H M Frey, P D Lightfoot and R Walsh (University of Reading)

Introduction

Silylenes, SiX_2, are thought to be intermediates in the thermal and photochemical decompositions of many silicon containing compounds. We have begun a programme of investigation of the kinetics of their reactions by time-resolved means and published the first gas-phase rate constants for the insertion of $SiMe_2$ into Si-H bonds[1], and the addition of $SiMe_2$ to unsaturated hydrocarbons[2]. These studies have provided substantial insight into the nature of these processes revealing that rates are controlled by a delicate balance between electrophilic and nucleophilic interactions in the activated complex[2,3].

If reactive substrates containing non-bonded lone pairs are chosen, we may anticipate a situation where the electrophilic interaction alone may lead to bond formation with the resulting generation of a donor-acceptor complex. In fact theoretical calculations have already been published[4] which indicate the likely importance of an initial donor-acceptor complex in the reaction of SiH_2 with NH_3, H_2O, HF, PH_3, H_2S and HCl. Matrix-isolation investigations have also suggested the formation of such complexes between diorganosilylenes and various ethers[5]. In the hope of obtaining further evidence for such species, we have undertaken the present study of the reactions of $SiMe_2$ with O-donor molecules. Part of this work has been published elsewhere[6].

Experimental and Results

$SiMe_2$ radicals were generated in the gas-phase in a static vessel by pulsed 193 nm photolysis (Oxford KX2 ArF exciplex laser) of pentamethyldisilane (PMDS) or octamethyltrisilane (OMTS). Typical pressures of ca 1.5 x 10^{13} molecules cm^{-3} of $SiMe_2$ were generated with pulse energies of ca 90 mJ and precursor partial pressures of 25 mTorr. $SiMe_2$ radicals were detected and monitored via their $\tilde{A}^1B_1 - \tilde{X}^1A_1$ visible absorption band at 457.9 nm using a Spectra Physics 2025 Ar^+ laser provided via the Laser Facility loan scheme. A multipass arrangement gave a total detection path length of ca 6m. Absorption signals were detected using a fast photodiode and concentration time profiles recorded on a transient recorder interfaced to a BBC microcomputer used as a signal averager.

Experiments were carried out for 11 different substrate O-donor molecules including both alcohols and ethers. Typical experiments employed partial pressures in the range 0-10 Torr with total pressures ca 10 Torr (made up with Argon). The majority of studies gave single exponential decays. In these cases bimolecular rate

coefficients were determined by measuring the pseudo first-order decay constants as a function of concentration of added reactant. The rate coefficients measured in this way are shown in the table.

More striking, however, were the decay profiles obtained with Me_2O and tetrahydrofuran (THF). These showed a characteristic biexponential appearance. Figure C1.2 shows a sequence of such profiles, with the fast component clearly becoming more rapid as the Me_2O pressure is increased.

Discussion

Kinetic analysis of the biexponential decays in the reaction of $SiMe_2$ with Me_2O suggests a mechanism in which a lone-pair donor-acceptor complex is formed reversibly in competition with $SiMe_2$ removal via reaction with its precursor, viz.

$$SiMe_2 + Me_2O \xrightarrow{1} Me_2\bar{S}i\text{-}\dot{O}Me_2$$

$$Me_2\bar{S}i\text{-}\dot{O}Me_2 \xrightarrow{2} SiMe_2 + Me_2O$$

$$SiMe_2 + P \xrightarrow{3} \text{products}$$

where P represents either PMDS or OMTS.

End product studies provide no evidence for re-arrangement of the complex (eg via $Me_2\bar{S}i\text{-}\dot{O}Me_2 \longrightarrow Me_3SiOMe$) but the kinetics suggest the complex may react further with something else in the system[6].

Other evidence supporting complex formation comes from the lack of significant isotope effect in the reaction of $SiMe_2$ with CH_3OH and CH_3PD (see Table 1). The close agreement in rate coefficients supports a rate-determining step prior to H or D migration. In the reaction of $SiMe_2$ with H_2O and D_2O, the uncertainties are too high to draw any significant conclusion. Although there is not direct evidence for complex formation in the other cases, there is a strong correlation between values of log k and the ionisation energies of the substrate molecules. This supports the idea that, as with the reaction of $SiMe_2$ with alkenes and alkynes[2], the electrophilic interaction dominates the kinetics. In the present case this interaction corresponds to the lone pair donation from oxygen into the empty p-orbital of $SiMe_2$. The overall process is illustrated in figure C1.2. This work to be published in full elsewhere[7], represents the first evidence for such complexes in the gas-phase. It is hoped in future studies to detect and monitor the complexes themselves and thus obtain more quantitative information about their stability and reactivity.

References

1. J E Baggott, M A Blitz, H M Frey, P D Lightfoot and R Walsh, Chem Phys Letts, 135, 39 (1987).

2. J E Baggott, M A Blitz, H M Frey, P D Lightfoot and R Walsh, J Chem Soc Faraday Trans 2, 515 (1988); see also SERC Central Laser Facility Annual Report 1988, p. 172.

3. R Walsh in 'Silicon Chemistry', Eds E R Corey, J Y Corey and P P Gaspar, Proc 8th Int Symp on Organosilicon Chemistry 1987 publ. Ellis-Horwood 1988, Chap 41, p447.

4. K Raghavachari, J Chandrasekhar, M S Gordon and K J Dykema, J Am Chem Soc, 106, 5853 (1984).

5. G R Gillette, G H Noren and R West, Organometallics, 6, 2617 (1987).

6. J E Baggott, M A Blitz and P D Lightfoot, Chem Phys Letts, 154, 330 (1989).

7. J E Baggott, M A Blitz, H M Frey and R Walsh, paper in preparation.

Table 1 Rate Constants for the Reactions of $SiMe_2$ with O-containing Molecules.

Reactant	$10^{12}k/cm^3$ molecule$^{-1}s^{-1}$
O_2	0.25 ± 0.02
CO	<0.05
H_2O	0.12 ± 0.05
D_2O	0.077 ± 0.005
MeOH	1.2 ± 0.1
MeOD	1.0 ± 0.1
Me_2O	ca 2.9
Oxirane	3.3-4.6*
Oxetane	34.3 ± 1.8
3,3-Dimethyloxetane	46.6 ± 2.4
Tetrahydrofuran	ca 5.5

*This data is pressure dependent (1-10 Torr).

C1.3 UV RESONANCE RAMAN STUDIES OF INCLUSION COMPOUNDS

J E D Davies and V A Tabner (University of Lancaster)

Introduction

Inclusion compounds are two component systems wherein a 'guest species' is enclosed in a void formed by the 'host'[1]. The shape and dimension of the void, the nature and the extent of the interaction between the host and the guest, and the degree of mobility of the guest are all dependent on the host used for a given guest species.

Vibrational spectroscopy, using both infrared and Raman techniques, has been used extensively to give information about host-guest interaction and the degree of mobility of the guest[2]. Previous Raman studies have been of the non resonant type, thus the extent of the host-guest interaction was obtained simply from the magnitude of the difference between the gaseous state and guest wavenumber values for the vibrational modes arising from the bonds assumed to be involved in the interaction.

Objectives of the Research

We wish to investigate whether UV excited resonance Raman spectra, combined with pre-resonant Raman spectra obtained at Lancaster, can yield detailed information about the nature of the interaction between the host and guest components.

The systems chosen for initial study were the inclusion compounds formed between quinol, $C_6H_4(OH)_2$, acting as the host and a variety of small guest molecules such as H_2S, SO_2, CH_3OH, CH_3CN and HCO_2H since many have been studied crystallographically. Furthermore the compound formed with SO_2 is unique in that it is the only coloured (pale yellow) inclusion compound formed by quinol. This could indicate a different host-guest interaction, most probably charge transfer (CT) in origin, in the quinol/SO_2 compound.

We have already carried out a pre-resonant Raman study of this compound using the visible region lines obtainable from the argon ion and dye lasers available in Lancaster. This study revealed a selective intensity enhancement of the band arising from the $\nu_1(A_1)$ mode of the SO_2 guest molecule and of some bands arising from the quinol host lattice. We wished to extend the study into the UV region to see whether these and any other bands are further enhanced.

Results and Discussion

The inclusion compounds of quinol are stable in the solid state only, and on our previous visits to the LSF we were able to optimise the design of the spinning solid sample holder provided by Ventacon[3].

Quinol itself and all of the inclusion compounds give an absorption

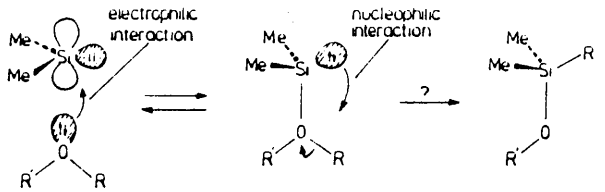


Figure C1.3 Representation of the reaction of $SiMe_2$ with an O-donor molecule (R OR) in terms of orbitals and specific interactions. Note that ultimate product formation depends on the migrating ability of the R-group in the intermediate donor-acceptor complex.

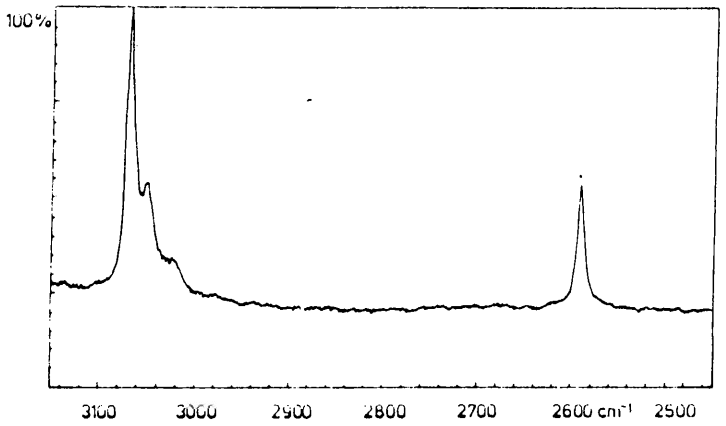
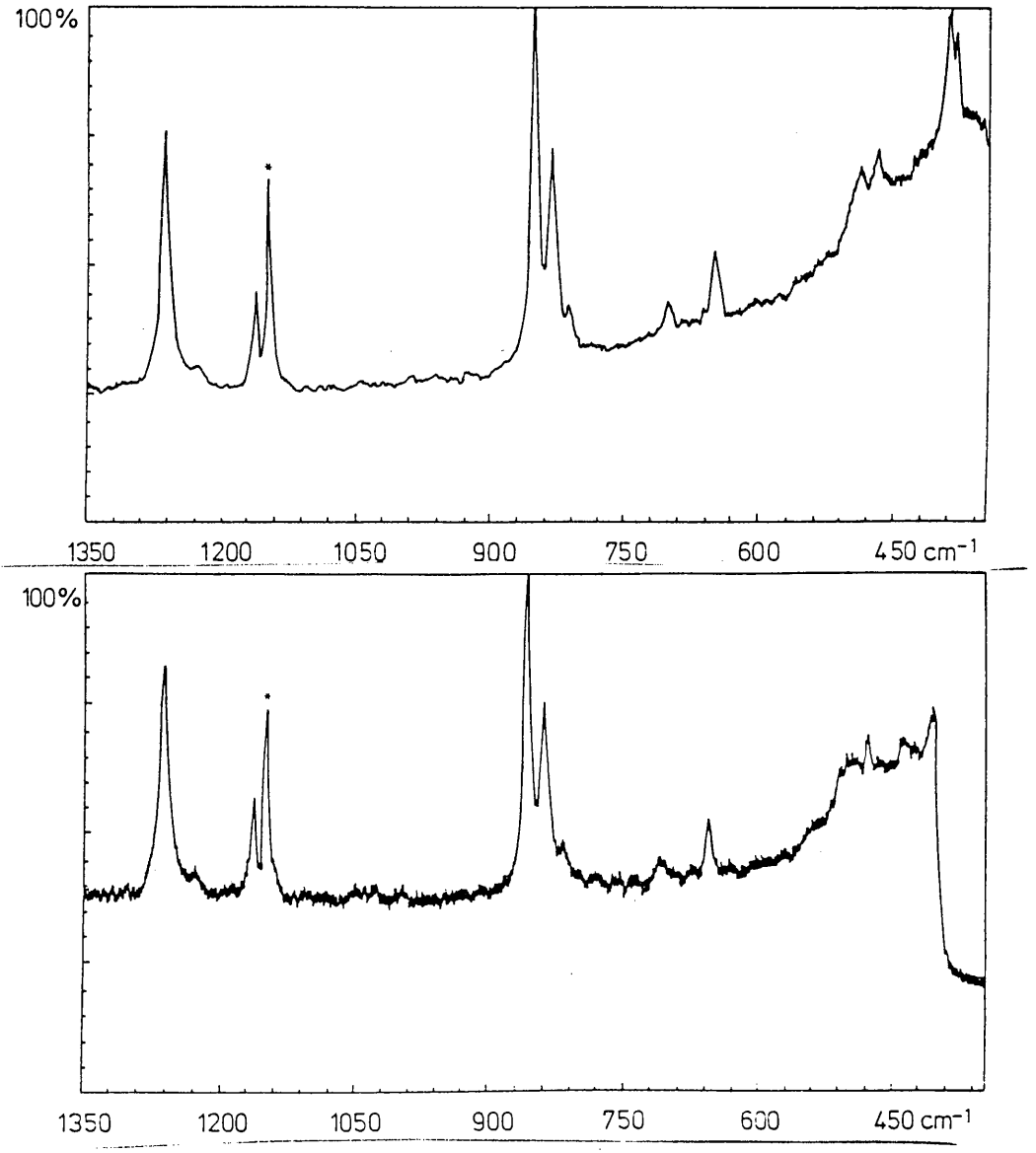


Fig C1.4 The Raman spectrum of the white quinol/H_2S inclusion compound using 360nm excitation, 3mJ pulse energy, 5Hz repetition rate. H_2S band marked with an asterisk.



Comparison of the Raman spectra of the quinol/SO_2 inclusion compound using:

Fig C1.5 a) 100mw cw Ar^+ 458nm excitation and

Fig C1.6 b) 455nm pulsed excitation, 0.2mJ pulse energy, 10Hz repetition rate. SO_2 band marked with an asterisk.

band with a λ_{max} value of 280nm. The SO_2 inclusion compound gives an additional absorption band with a λ_{max} value of 360nm which is unique to this compound, and thus arises from the CT band of the compound.

Excellent quality Raman spectra could be obtained from the white quinol compounds using 360nm pulsed excitation (DMQ) dye. The spectrum obtained from the quinol/H_2S compound is shown in Figure C1.4 where the band at 2589 cm^{-1} arising from the $\nu_1(A_1)$ mode of guest H_2S is marked with an asterisk.

Attempts to obtain the resonance spectrum of the SO_2 compound using 360nm pulsed excitation were unsuccessful irrespective of the laser energy and irrespective of whether the neat solid or samples diluted with KBr were used. Since good quality spectra had been obtained at Lancaster using cw Ar^+ 458nm excitation, a wavelength which is well within the absorption band contour, the use of pulsed 455nm excitation (Coumarin 2 dye) was investigated.

A spectrum could be obtained but under the rather specific conditions of using a defocused, attenuated laser beam with a pulse energy of about 0.2mJ. Using these conditions spectra could be obtained from the neat solid as well as from samples diluted with KBr. The S/N ratio of the spectra were however inferior to those obtained using cw Ar^+ 458nm excitation, as shown in Figures C1.5 and C1.6. The use of higher pulse energies resulted in immediate sample decomposition.

Future Work

Our experience suggests that obtaining the Raman spectra of highly absorbing solid samples using pulsed lasers is problematic in that the energy of the pulse seems to be critical.

The inclusion compounds formed by quinol are stable in the solid state only, but other hosts such as the crown ethers, the cyclodextrins and the cyclophanes form inclusion compounds which are stable in solution as well as in the solid state. We therefore now intend to concentrate on solution phase studies with the aim of obtaining information about the nature of the host-guest interactions.

References

1. J L Atwood, J E D Davies and D D MacNicol (Editors), 'Inclusion Compounds', Academic Press, London, 1984.
   a) Volume 1 - 'Structural Aspects of Inclusion Compounds formed by Inorganic and Organometallic Host Lattices'.
   b) Volume 2 - 'Structural Aspects of Inclusion Compounds formed by Organic Host Lattices.
   c) Volume 3 - 'Physical Properties and Applications".

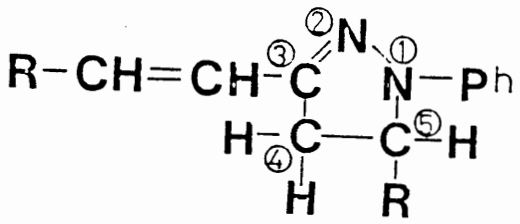
2. J E D Davies, Chapter 2 in Ref. 1c.

3. J E D Davies and V A Tabner, Annual Report to the Laser Facility Committee, 1988.

C1.4 INVESTIGATION OF ENERGY TRANSFER IN POLYCARBONATE FILMS USING PICOSECOND PUMP-PROBE LASER FLASH PHOTOLYSIS

F Wilkinson, G P Kelly, P A Leicester, D R Worrall (Loughborough)
R S Chittock (RAL)

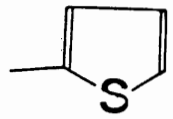
In attempts to assign the transient absorptions observed in diffuse reflectance following picosecond laser excitation of opaque microcrystalline 1,2 Pyrazolines[1], we investigated energy transfer from 1,2 Pyrazolines to an energy acceptor, disulfone magenta. In order to improve the quality of the data in the presence of strong fluorescence, these measurements were carried out using pump-probe techniques in transmission mode. The pyrazolines were dissolved within a polycarbonate matrix deposited as a thin film on a polyester base. Transient absorptions were observed for each of PYA, PYB and PYC (Fig. C1-7) at 590nm following excitation at 295nm. The observed decay kinetics could be fitted with a biexponential model, the lifetimes of the first and second processes being 5.5×10^{-12} and 1.7×10^{-10} seconds



PYA (R = Ph)

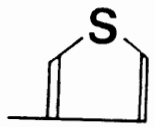
1,5-diphenyl -3-styryl -2- pyrazoline

PYB

R = 

1-phenyl -5(thien-2'-Yl) -3 [2"-(thien-2'- yl) vinyl]-2- Pyrazoline

PYC

R = 

1-phenyl -5 (thien-3'-yl) -3 [2"-(thien-3'-yl) vinyl]-2- pyrazoline

Fig C1.7 Structures of PYA, PYB and PYC.

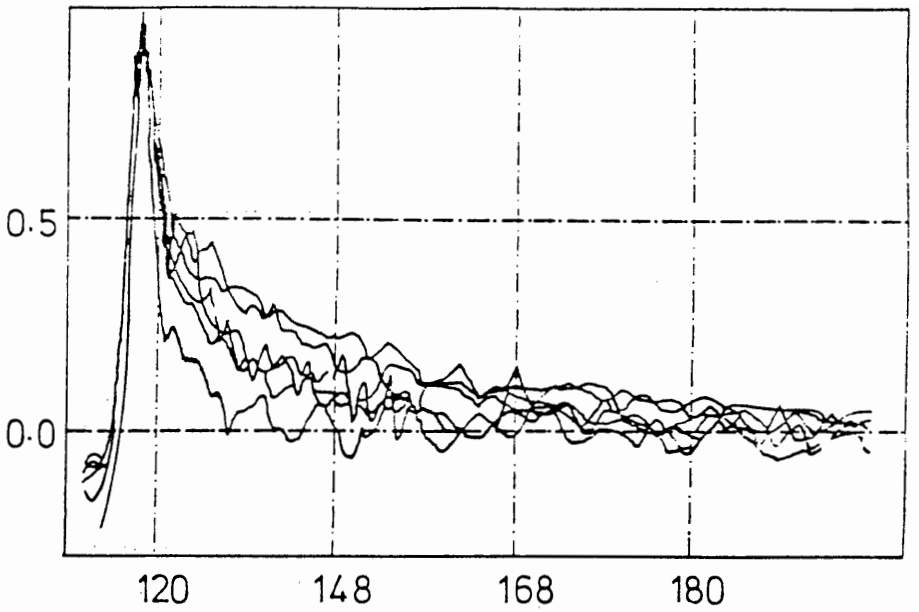


Fig C1.8 Transient absorption decays of PYA in the presence of varying DSM concentrations.

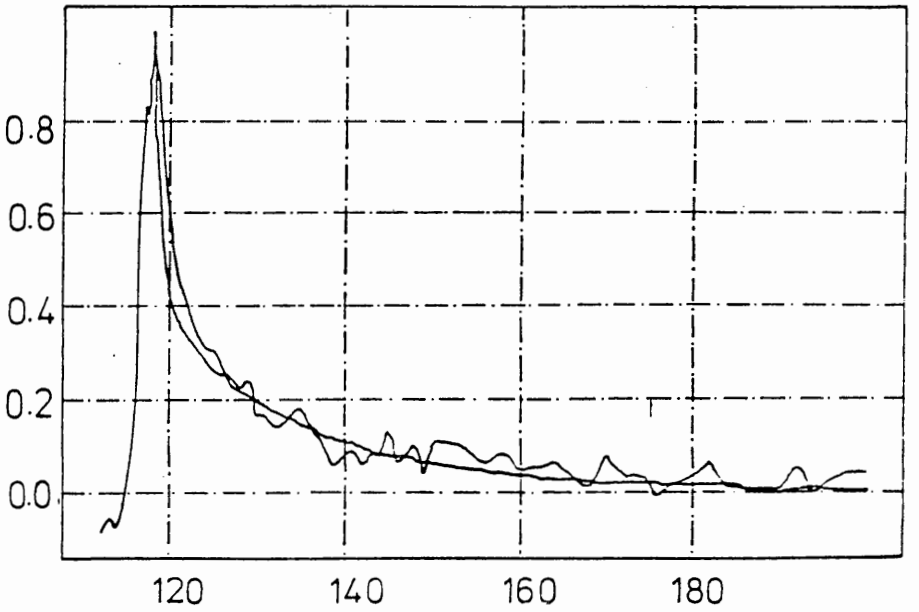


Fig C1.9 PY A in polycarbonate film. DSM concentration 0.37 wt %

respectively, ie. each is an order of magnitude faster in the polycarbonate film than in the microcrystalline solid.

A similar film to those used above, containing PYA with a trace amount (0.1% by mass) of disulfone magenta (DSM), demonstrated a more rapid transient decay than observed in the absence of DSM. A study was therefore made of the kinetics of the decay of the PYA transient absorption in the presence of a range of concentrations of DSM. It was observed that as the DSM concentration increased, the transient absorption decayed more rapidly, indicating that he DSM quenches the excited state(s) of these compounds. A film containing DSM (0.1 wt %) and polycarbonate only was seen to give no transient absorption signal when pumped at 295nm under identical conditions.

The transient absorption decays obtained for the thin films of PYA in the presence of DSM are reproduced in figure C1-8. The unquenched PYA decay is seen to fit, as mentioned earlier, a biexponential model. Based on results obtained in solution[2], it would be expected that quenching of the PYA singlet by DSM would be by long range energy transfer ie. by the Forster mechanism. The Forster radius has been determined in solution as being 55 Å.

From the Forster equation[3]

$$\frac{R_o^6}{(cm^6)} = \frac{9\ K^2\ 1n10}{128\ \pi^5\ N}\ \frac{\phi_d}{n^4}\ \frac{J_{da}}{(cm^6\ mol^{-1})}$$

where R_o is the Forster radius, ϕ_d is the fluorescence quantum yield, n is refractive index and J_{da} is the spectral overlap integral of donor emission and acceptor absorption, it can be seen that

$$R_o^6 \ \alpha\ \phi_d$$

Note that the unquenched lifetime of the S_1 state is approximately 3×10^{-9} s in solution, but is reduced to 1.7×10^{-10} s in polycarbonate film. Since the relationship

$$\frac{\phi_{d\ solution}}{\phi_{d\ film}} = \frac{k_f\ \tau_{o\ solution}}{k_f\ \tau_{o\ film}}$$

holds, a decrease in τ_o will lead to a decrease in the anticipated Forster radius. In addition,

$$n\ (dichloromethane) = 1.42$$
$$n\ (polycarbonate) = 1.58$$

and, since

$$R_o^6 \ \alpha\ n^{-4}$$

the increase in refractive index from dichloromethane to the Forster radius would be reduced in the polycarbonate matrix to polycarbonate will also reduce R_o. Thus it would be expected that about 30 Å.

The fitting of the data was performed using a manual iterative method, the initial approach being to take a Forster model in isolation and, using realistic values for the constants involved, to determine the value of R_o which gave curve shapes best fitting the experimental data. The model expression used in this instance was

$$\phi_t = \exp\ (-t/\tau_o - 2C/C_o\ (t/\tau_o)^{1/2})$$

where

$$C_o = \frac{3}{4\ \pi\ R_o^3\ N}$$

The value of τ_o used was that obtained for the second decay component in the unquenched PYA sample, and it was determined that the curve shapes best fitting the data were obtained using an R_o value of 25 Å.

Having determined these parameters, the biexponential model used to fit the unquenched data was modified to incorporate the possibility of long range energy transfer. Due to the rapid nature of the

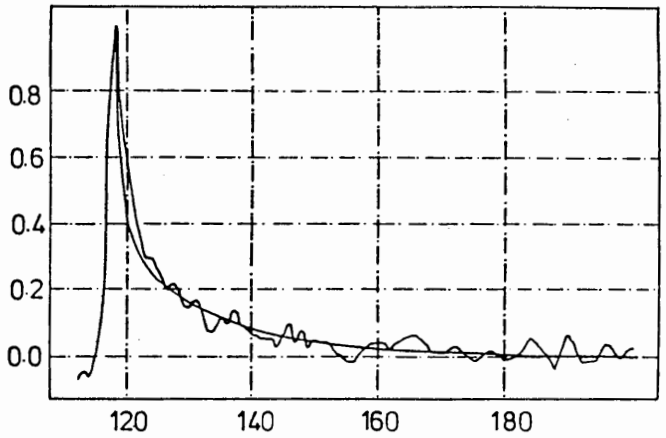


Fig C1.10 PYA in polycarbonate film. DSM concentration 0.45 wt %.

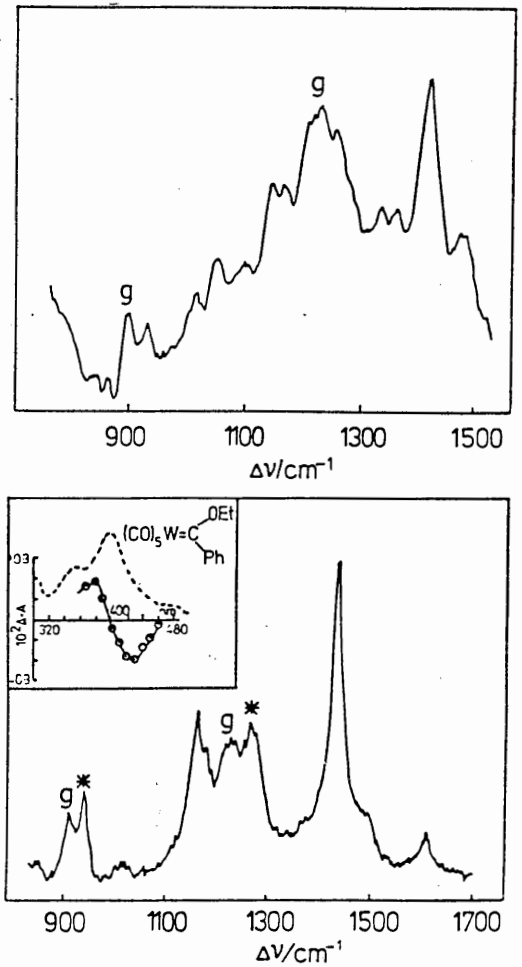


*Figure C1.11 Single colour resonance Raman spectra of $(CO)_5W = C(OEt)Ph$ (**1a**) in CH_2Cl_2.*
(a) CW excitation, 363.8 nm (Ar^+).
(b) pulsed excitation, 400nm (dye laser).
** : Transient features; **g** : ground state.*

*Inset: Absorbance difference spectrum (-0-0-0-) in CH_2Cl_2 of transient formed by pulsed laser photolysis of (**1a**) at 354.7nm.*
*(------): Ground state spectrum of (**1a**) (Arbitrary absorbance scale for the latter).*

first decay component, this will remain unquenched and as such its lifetime should be independent of DSM concentration. The second, slower component would, however, be quenched and so it is possible to formulate an expression of the type

$$\phi_t = a \exp(-k_1 t) + b \exp(-k_2 t - t/\tau_0 - 2C/C_0 (t/\tau_0)^{1/2})$$

where the second exponential term is modified by the Forster term. This model can be summarised as describing a mechanism whereby the initial excitation by the 295nm pulse is to the S_2 state, which decays rapidly to the S_1 state. The S_1 state then undergoes one of two processes;

(i) first order decay due to radiative and non-radiative relaxation to the ground state, and
(ii) long range, non-radiative energy transfer to a molecule of DSM.

The above model is seen to give a good fit to the experimental data, as illustrated in figures C1-9 and C1-10 for DSM concentrations of .37 and .48 weight percent, respectively. The constants employed here are considered realistic based on comparisons with solution work, and their use gives a global fit, using the proposed model, valid over all concentrations investigated.

Conclusions

In previous work we have observed a transient absorption, decaying biexponentially in the picosecond time domain, in microcrystalline samples of pyrazolines using diffuse reflectance geometry. The observed transient was assigned as being due to absorption by the S_2 state superimposed on top of absoption by the S_1 state. This assignment is confirmed using transmission geometry with the pyrazolines incorporated within a polycarbonate matrix, where a similar biexponential decay is seen although the lifetimes of the two states involved are decreased by an order of magnitude relative to those observed in the microcrystals.

Also investigated were the decay kinetics of PYA incorporated within a polycarbonate matrix in the presence of a range of concentrations of disulfone magenta. The mechanism proposed here to explain the observed kinetics involves decay of the initially produced S_2 state to the S_1 state, the rate of which is so rapid as to be unaffected by DSM concentration. This is followed by decay of the S_1 state to the ground state by both direct relaxation and by long range energy transfer to disulfone magenta.

References

1. G P Kelly, P A Leicester, F Wilkinson and L F V Ferreira, Annual Report to the Laser Facility Committee, Rutherford Appleton Laboratory, p.190, (1988).

2. G P Kelly, L F Vieira Ferreira and F Wilkinson, J Photochem. and Photobio.A: Chemistry, 45, 223 (1988).

3. Th. Forster, Ann. Physik, 2, 55 (1948).

C1.5 PRESSURE AND TEMPERATURE DEPENDENCE OF THE RATES OF SOME REACTIONS OF THE METHOXY RADICAL

M J Frost and I W M Smith
(School of Chemistry, University of Birmingham)

Although the methoxy radical (CH_3O) is an important intermediate in the gas-phase oxidation of methane, direct measurements on the rates of its reactions remain comparatively scarce. This despite the fact that it can be conveniently created by ultraviolet photolysis of CH_3ONO and can be observed by laser-induced fluorescence (LIF). The aim in our programme is to expand the kinetic data base for this important radical and to compare its behaviour with that of the well-studied OH radical to see whether similarities and differences can be ascribed to the natures and structures of the two radicals.

A Nd:YAG laser from the loan pool is used in its frequency quadrupled mode to photolyse CH_3ONO. LIF from the methoxy radicals is observed using a frequency-doubled, flashlamp-pumped, dye laser tuned to 298.5nm to excite the A^2A_1, $v' = 3 \leftarrow X^2E_1$, $v_3'' = 0$ band.

Both lasers fire at 10 Hz and the time between the pulses is varied using a scan delay generator.

During the current loan period we expect to complete measurements on the reactions of CH_3O with NO and with NO_2 over wide ranges of temperature and total pressures (the reactions proceed, at least in part, to produce CH_3ONO and CH_3ONO_2 by association). In addition, we shall perform preliminary measurements on the reactions of CH_3O with simple hydrocarbons. Some emphasis will be placed on the reactions with unsaturated hydrocarbons which have scarcely been studied before.

C1-6 STATE DISTRIBUTIONS FOR BOTH PRODUCTS OF THE REACTION: H + $NO_2 \rightarrow$ OH = NO

A M L Irvine, I W M Smith and R P Tuckett
(School of Chemistry, University of Birmingham)

The reaction between H atoms and NO_2 acts as a prototype for reactions between free radicals occurring via a strongly bound, transitory collision complex. Measurements on the nascent distribution of product species over their quantum states can reveal the nature of the reaction dynamics: for example, whether the collision complexes are sufficiently long-lived for the product state distributions to be essentially statistical.

We have now measured the distribution of both OH and NO over vibrational, rotational, spin-orbit and λ-doublet states in all levels up to v=3 in both molecules. This is quite the most comprehensive single study of this reaction to date. The v=3 level in OH is the highest which is energetically accessible and the information on NO(v=0-3) will allow us to estimate the full vibrational distribution via a surprisal analysis. The work on the NO state distributions has been made possible by loans of frequency-doubling equipment from the Laser Loan Pool. The equipment has enabled us to record LIF spectra for the (0,0), (1,1), (2,2), (0,2) and (1,3) bands of NO using single photon excitation. The spectra are recorded on computer and analysed by matching them with simulated spectra. This analysis is not complete but it is clear that the NO vibrational mode absorbs a substantial percentage (~10%) of the energy released in the reaction but the NO is less excited than the OH. This finding is consistent with reaction dynamics which are somewhere between the direct and long-lived complex limits. Preliminary measurements on the NO produced in the O + NO_2 and H + ClNO reactions have been made.

Two papers on our results for the H + NO→ reaction are being prepared. They have also been reported at the 19th Informal Conference on Photochemistry and at a meeting of the Gas Kinetics Discussion Group.

C1.7 TIME-RESOLVED RESONANCE RAMAN SPECTROSCOPY OF PHOTOGENERATED TRANSIENTS IN METAL CARBENES: INTRAMOLECULAR REARRANGEMENT vs SOLVENT INTERACTION

K C Gordon, J J McGarvey, D Rooney, K P Taylor, (Dept of Chemistry, Queen's University of Belfast)

Introduction

In earlier investigations at the LSF on the Fischer carbene complex $(CO)_5W = C(OCH_3)C_6H_5$ we obtained the first examples of two-laser pump and probe TR^3 spectra of photogenerated organometallic species[1,2]. During a two-week visit in the current reporting period we have extended these investigations. The results of the TR^3 studies described below, together with complementary laser flash photolysis and single-colour Raman experiments at QUB, suggest that the reactivity of the coordinatively unsaturated fragments produced by CO dissociation following irradiation in the ligand field bands of the class of metal carbenes,

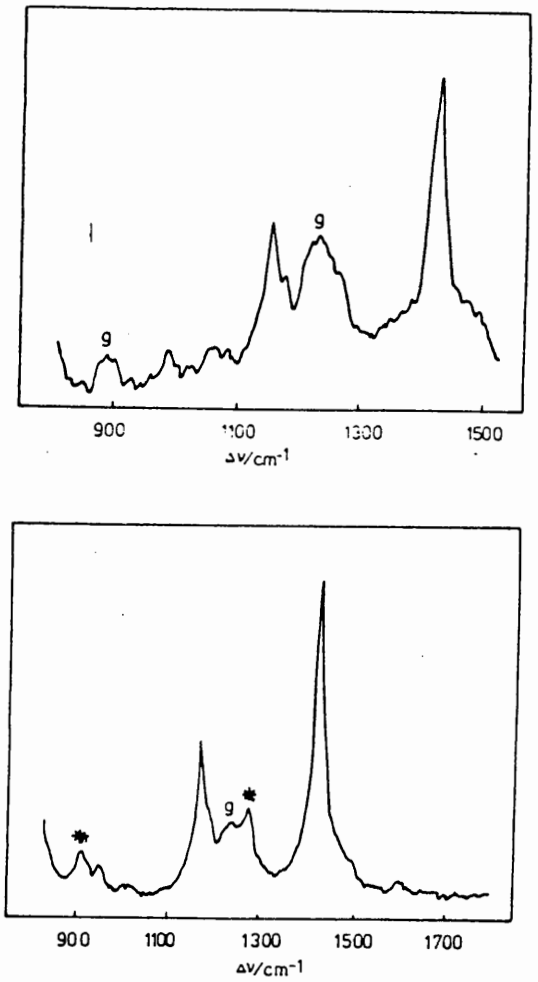


Figure C1.12 Single colour resonance Raman spectra of $(CO)_5W = C(OMe)p\text{-}CH_3\text{-}C_6H_5$ *(1b) in* CH_2Cl_2
(a) CW excitation, 363.8nm (Ar^+).
(b) pulsed excitation, 405nm (dye).
** : transient features; g : ground state.*

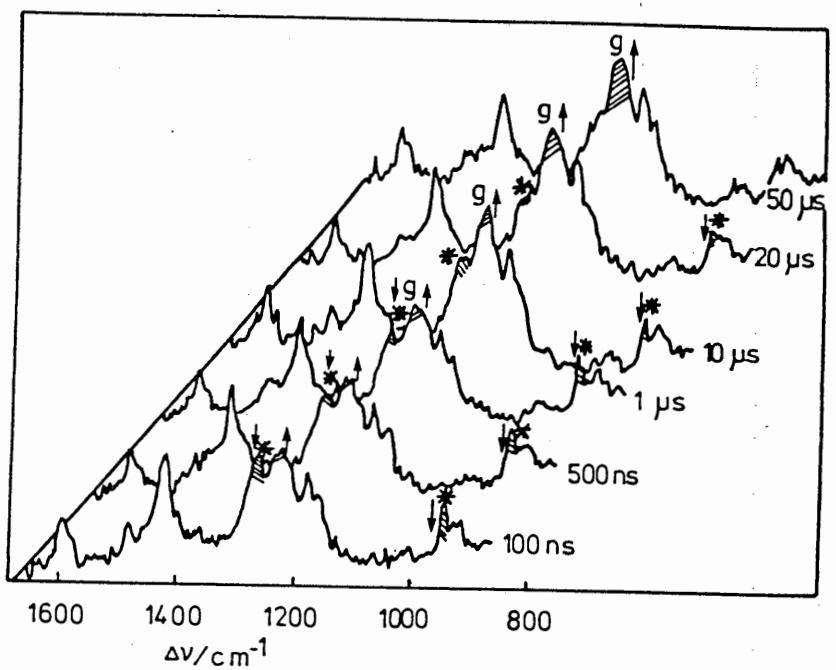
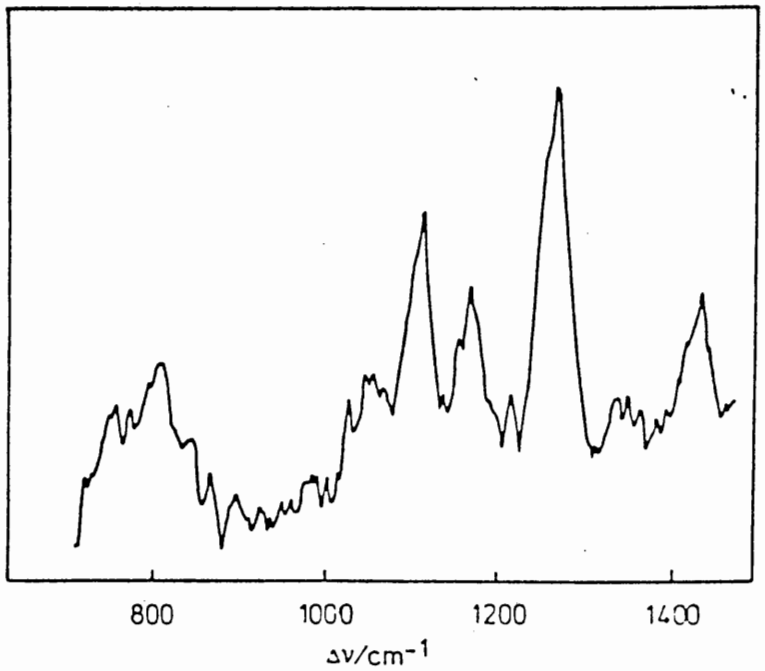


Figure C1.13 Two-laser pump and probe time-resolved resonance Raman spectra of (1a) in CH_2Cl_2 *at various time delays.*

λ pump: 351nm (EMG 150, broadband)
λ probe: 420nm (FL3002 dye laser, pumped by Lumonics HX 460)

** : Transient features; g : ground state.*



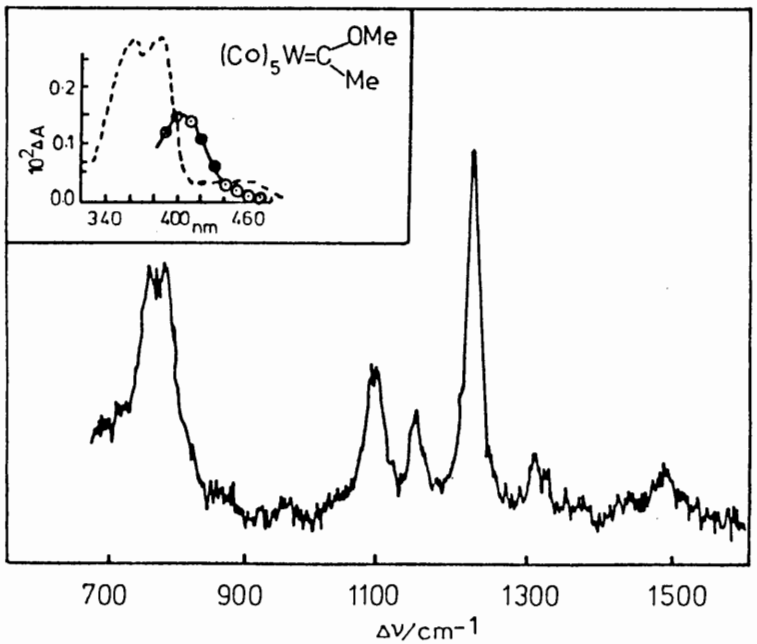


Figure C1.14 Single colour resonance Raman spectra of $(CO)_5W = C(OMe)Me$ (1c) in CH_2Cl_2.
(a) CW excitation, 363.8nm (Ar^+)
(b) pulsed excitation, 420nm (dye).

Inset: Absorbance spectrum (-O-O-O-) in CH_2Cl_2 of transient from pulsed laser photolysis of (1c) at 354.7nm. (------): ground state spectrum of (1c) (arbitrary scale).

$(CO)_5W = C(OR)R'$, is markedly dependent upon the nature of the group, R'.

Experimental

The two-laser arrangement used for the pump and probe studies was similar to that described in earlier reports[1]. Careful monitoring and control of the energy of the probe beam was necessary in order to minimise the effects of secondary pumping. It was important to ensure that both beam energies remained constant throughout a series of runs. For the pump excimer beam this was done by monitoring the energy directly. For the probe beam a more convenient procedure was to check periodically the number of counts from a standard sample of cyclohexane, with the spot size of the beam held constant during the experiment. A bipolar pulse generator was used to control the delays between the pump (EMG 150) and probe (FL3002 dye) lasers. CW-excited resonance Raman spectra were generated using an Ar^+ laser (Coherent Innova 90).

Argon-purged solutions of metal carbene in the appropriate solvent (ca. 10^{-3} mol dm^{-3}) were flowed through a quartz capillary. A 90° scattering geometry was used throughout and all spectra were recorded using the Spex Triplemate spectrometer (1200 grooves/mm grating) and the OMA III detection system.

Results and Discussion

Single colour experiments were carried out on the carbene complexes $(CO)_5W = (OR)R'$ (**1a:** R = OEt, R' = Ph; **1b:** R = OMe, R' = p-CH_3Ph; **1c:** R = OMe, R' = Me) at several excitation wavelengths.

For complexes **1a** and **1b**, ground state Raman spectra recorded under CW excitation at 363.8nm are compared with pulse-excited spectra in Figures C1.11 and C1.12. The additional features (*) which appear in the pulse-excited spectra are reminiscent of the pattern previously reported[1,2] for the Fischer complex[2], $(CO)_5W{=}{=}C(OCH_3)C_6H_5$, and suggest similar behaviour as a result of pulsed laser irradiation, with CO dissociation followed by rapid intramolecular rearrangement to an "internally solvated" ["agostic"[2]] species. In line with this, the ΔA spectra (e.g. Figure C1.11. (inset) for C1.11a show a blue shift (with respect to the ground state) analogous to that reported[2] for (2) and the transient lifetimes (τ) derived from the ΔA decay traces show a moderate solvent dependence. That the species observed in the single pulse (pump + probe) Raman experiments is the same as that recorded in the laser flash photolysis (ΔA) experiments is demonstrated by two-laser pump and probe studies. The results for complex **1a** are shown in Fig C1.13. Although the S/N ratio is inferior to that obtained in the single-colour experiments (due in part to the fact that the probe wavelength 420nm, chosen so as to minimize the effects of secondary pumping of the sample, is off maximum resonance with the transient spectrum), the evidence is clear cut and the same transient features as in the single-colour studies are present here at the shortest time delay (1200ns) between the pump and probe pulses and decay on a microsecond timescale, in accord with the ΔA data. As far as we are aware, Figure C1.13 and our previously published spectrum[2] are the only reported examples of two-laser TR^3 spectra of photogenerated organometallic transients.

The results for complex **1c** are in some contrast to the above data. The CW- and pulse-excited Raman spectra (Figure C1.14) are virtually the same in the frequency range examined despite the fact that a transient is populated under the pulsed excitation conditions (Figure C1.14, inset shows the ΔA spectrum). The transient is suggested[3] to be a solvent-coordinated species, $(CO)_4W[S]{=}{=}C(OR)R'$[3], formed in a fast step after initial CO loss. Consistent with this, the lifetimes are much more solvent dependent than those associated with **1a** and **1b**, being longer in more coordinating solvents[3]. Experiments in which the laser fluence and excitation wavelength were varied[3] confirm that the Raman spectra shown here (Figure C1.14) are assignable to the transient. The similarity to the CW-excited spectrum in the (800-1300) cm^{-1} region suggests that transient formation is accompanied by minor perturbation of the carbene chromophore, consistent with the proposed species[3].

$$=C\begin{matrix}\nearrow OR\\ \searrow R'\end{matrix}$$

Thus the Raman spectra show that the nature of the transients formed following primary photo-induced loss of CO in these metal carbenes, $(CO)_5W = C(OR)R'$, is dependent upon the nature of R'. In cases where R' is an aryl group (e.g. C_6H_5-, $pCH_3-C_6H_5$), the predominant species present after CO loss is the rearranged ("agostic") entity[2] and its formation is signalled by frequency shifts in the features assignable to the carbene moiety, as shown here and in previous work[2]. On the other hand, formation of species such as (3), with R' = CH_3 or C_2H_5 involves no intramolecular rearrangement and thus minor changes in carbene-associated modes‡. The reasons for this distinction in behaviour appear to involve both steric and electronic factors and a full report is in preparation.

The present experiments provide a further demonstration of the ability of TR³S to probe transients showing subtle structural differences and extent of interaction with the solvent medium, where the latter may function as a "token ligand"[4]. This type of information is important because of its relevance to an understanding of homogeneous catalysis in solution, where it appears that structurally similar or even identical intermediates (to those formed photolytically) may be involved in thermally induced catalytic reactions. Laser flash photolysis coupled with TR³S provides one promising way of creating and structurally probing such species. The studies are currently being extended to lower frequencies and to some novel, $SiPh_3$-containing carbenes.

---

‡ The formation of species such as (3) may however involve changes in W-C-O bending modes. Studies of the low frequency region, <650 cm^{-1}, are now in progress and appear to be promising.

Acknowledgements

We wish to thank Dr A W Parker and Miss S Tavender for much valuable assistance in setting up the TR³ experiments. We thank SERC for support of the work.

References

1. J J McGarvey, S E J Bell and K C Gordon, Annual Report to the Laser Facility Committee, RAL-87-041, **B1.4**, 128, (1987).

2. S E J Bell, K C Gordon and J J McGarvey, J. Am. Chem. Soc., **110**, 3107, (1988).

3. D Rooney, K C Gordon, J J McGarvey and S E J Bell, unpublished work; manuscript in preparation.

4. G R Dobson, P M Hodges, M A Healy, M Poliakoff, J J Turner, S Frith and K J Asali, J. Am. Chem. Soc., **109**, 4218, (1987).

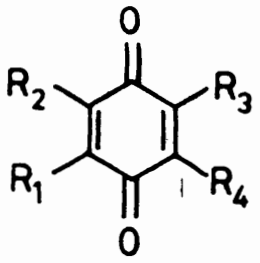
C1.8 TR³ STUDIES OF REACTION INTERMEDIATES IN UBIQUINONE PHOTOLYSIS

A W Parker (Rutherford Appleton Laboratory)
D Phillips (The Royal Institution)
R E Hester and S Umapathy (University of York)

Introduction

Ubiquinone (I), UQ, is a methoxy substituted benzoquinone. The naturally found ubiquinones have an isoprene sidechain at ring position 6 of 6 - 10 units in length. It is a constituent of the electron transport system of mitochondria and of the chromatophores of photosynthetic bacteria. Ubiquinones are also present in the plasma membranes of certain bacteria. The electronically excited states of UQ give rise to semiquinone radicals which lead to additional single-electron transport processes or to the formation

of other products which affect the systems in which they are found.



I ubiquinone, $R_1=R_2=OCH_3, R_3=CH_3, R_4=H$

II duroquinone, $R_1=R_2=R_3=R_4=CH_3$

III benzoquinone, $R_1=R_2=R_3=R_4=H$

This work extends previous time-resolved resonance Raman (TR^3) studies on quinone compounds (for example see Ref 1) and examines the photochemistry of UQ in the solvents water, ethanol, and cyclohexane. UQ gives a much lower triplet quantum yield ($\phi_T \sim 0.1$)[2] than does benzoquinone or duroquinone ($\phi_T \sim 1.0$)[2a].

Experimental Details

A Lambda Physik EMG-150 excimer laser was used for photolysis at 248 nm (KrF, 25 ns pulse width). Raman spectra were obtained using an excimer-pumped dye laser (Lumonics, Hyperex 460 and Lambda Physik FL3002, 8ns pulse width, line width $<0.1cm^{-1}$). The pump and probe beams were combined co-linearly using a 45° dichroic mirror and focussed vertically from below into the sample. An open flowing jet of the sample solution was aligned horizontally, perpendicular to the entrance slit of the triple spectrometer (Spex Triplemate), i.e. a 90° collection geometry was employed. The detector was a Spectroscopic Instruments IRY700 intensified diode array and was gated (∿ 50 ns width) in synchronisation with the probe pulse in order to improve the signal-to-noise ratio. The timing of the lasers and gating was controlled using a pulse delay generator which allowed independent control of each laser; the pulse repetition rate of the lasers was 10 Hz. Wavenumber accuracy of spectra is ± $5cm^{-1}$ and temporal jitter between lasers was ± 10 ns. Laser energies were typically 2 mJ/pulse at the sample for both pump and probe lasers. UQ was obtained from Aldrich, sodium nitrite from BDH, and both were used without further purification. Ethanol was 99.9% pure (Burroughs) and water was BDH purified grade.

Results and Discussion

Ubiquinone in ethanol

Previous flash photolysis studies[2] using 265 nm laser radiation of ubiquinone in pure ethanol showed a transient species at 430 nm with a lifetime of 3.6 μs. This transient was not quenched by oxygen and therefore was not assigned to triplet ubiquinone (^3UQ).

The TR^3 spectra of UQ in ethanol (1.0×10^{-3} mol dm^{-3}) show two clear bands, (see Figure C1.15), one very prominent at 1618 cm^{-1} and another less intense at 1515 cm^{-1}. Although kinetic analysis of both bands gave similar lifetimes (viz.1618 cm^{-1}, 0.67±0.03 μs and 1515 cm^{-1}, 0.70 ± 0.02 μs), the addition of a small amount of sulphuric acid to the solution quenched only the 1618 cm^{-1} band (see Figure C1.16). Accordingly, the bands are assigned to two different species. Furthermore, in view of the long lifetime for both the species, the triplet state can be ruled out and the bands are attributed to an electron or hydrogen transfer adduct formed from the reaction triplet ubiquinone (^3UQ) with the solvent.

Two mechanisms for the reaction of ^3UQ with ethanol involve either hydrogen atom transfer viz.

$$^3UQ + CH_3CH_2OH \rightarrow \dot{UQ}H + CH_3\dot{C}HOH \quad (1)$$

followed by

$$CH_3\dot{C}HOH + UQ \rightarrow CH_3CHO + UQ^{\dot{-}} + H^+ \quad (2)$$

or electron-transfer, viz.

$$^3UQ + CH_3CH_2OH \rightarrow UQ^{\dot{-}} + CH_3\dot{C}H_2\overset{+}{O}H \quad (3)$$

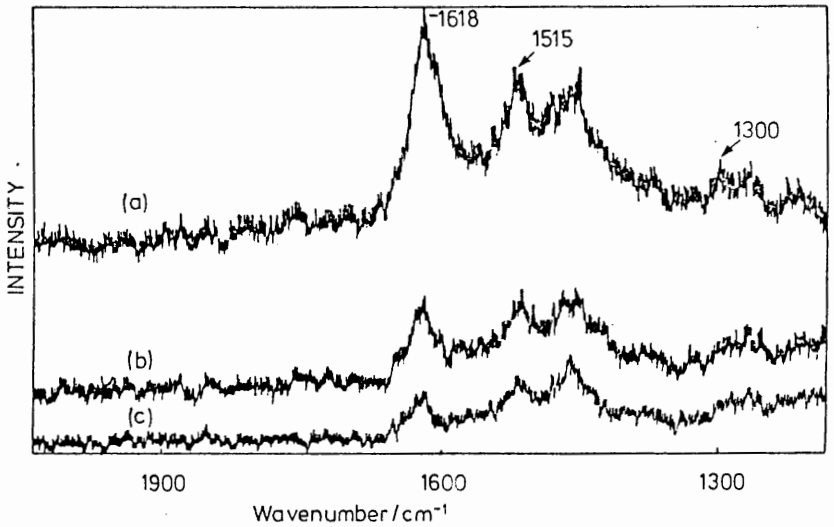


Figure C1.15 UQ (1.0 x 10^{-3} mol dm^{-3}) in ethanol pump 248 nm, probe 440 nm, time delays (a) 50 ns, (b) 500 ns, (c) 1000 ns.

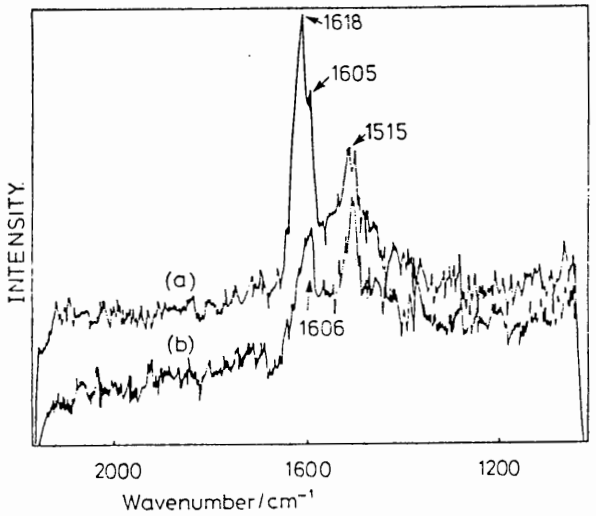


Figure C1.16 UQ (1.0 x 10^{-3} mol dm^{-3}) in ethanol, pump 248 nm, probe 440 nm, (a) no acid present, (b) small amount of H_2SO_4 added. Time delay 50 ns for both spectra.

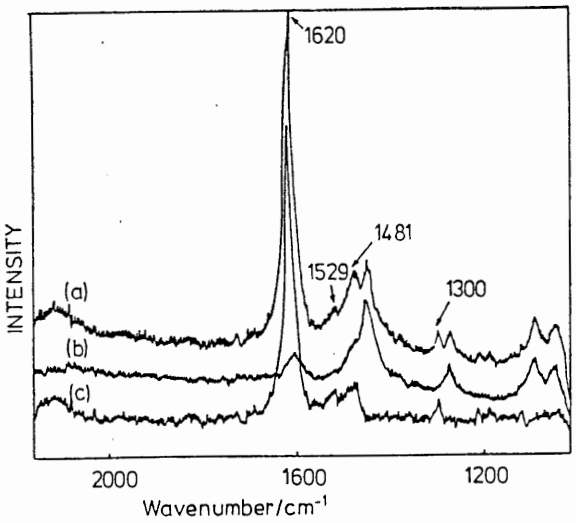


Figure C1.17 UQ (1.0 x 10^{-3} mol dm^{-3}) in ethanol saturated with $NaNO_2$, (a) pump 248nm, probe 440 nm, 100 ns delay, (b) probe 440 nm only, (c) result of a-b.

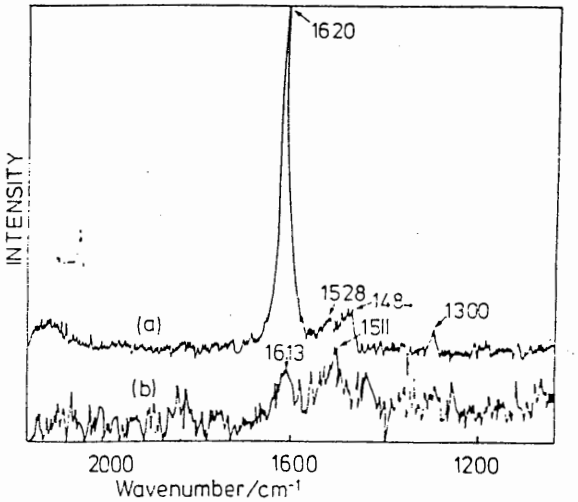


Figure C1.18 UQ (1.0 x 10^{-3} mol dm^{-3}) in ethanol saturated with $NaNO_2$, pump 248 nm, probe 440 nm, 100 ns delay, (a) no acid, (b) small amount of H_2SO_4 added to solution, time delay = 100 ns.

These reactions have been proposed for duroquinone by Scheerer and Grätzel[3] who concluded that the direct electron transfer process, equation (3), was operating.

Another route is also available for the generation of $\dot{UQ}H$ if $UQ^{\bullet-}$ is able to abstract a proton from ethanol, viz.

$$UQ^{\bullet-} + CH_3CH_2OH \rightarrow \dot{UQ}H + CH_3\dot{C}HOH$$

This possibility can be eliminated however because the NO_2^- saturated solutions show no 1511 cm^{-1} band, see below.

The evidence from our results indicates that ^3UQ reacts with ethanol by both electron transfer and hydrogen atom transfer mechanisms as shown in equations (1),(2) and (3).

The ubisemiquinone radical anion ($UQ^{\bullet-}$) can be produced by reacting ^3UQ with an electron donor, e.g.

$$^3UQ + NO_2^- \rightarrow UQ^{\bullet-} + NO_2$$

Ethanol solutions of UQ ($\sim$ 1.0 x 10^{-2} mol dm^{-3}) saturated with $NaNO_2$ gave the spectra shown in Figure C1.17. Kinetic analysis of the 1620 cm^{-1} band gave a lifetime of > 50 μs; the smaller peaks at 1528, 1481 and 1300 cm^{-1} were too weak for use in kinetic analysis.

These bands all are assigned to $UQ^{\bullet-}$ on the basis of the observation that the addition of a small amount of acid resulted in the disappearance of all four of the bands and in the formation of a new band at 1511 cm^{-1}, this being attributed to $\dot{UQ}H$ (see Figure C1.18) and is believed to be similar to the 1515 cm^{-1} peak shown in Figures C1. and C1. .

Aqueous Solutions of Ubiquinone

Pump (248 nm) and probe (440 nm) experiments on solutions of UQ (1.0 x 10^{-3} mol dm^{-3}) in water gave the TR^3 spectra illustrated in Figure C1.19. Comparison of these spectra with those of UQ in ethanol with added NO_2^- (Figure C1.17) shows the two sets of spectra to be similar. This evidence for the formation of $UQ^{\bullet-}$ indicates that ^3UQ is able to photo-oxidise water. The feasibility of this process may be calculated from the energetics of the electron-transfer step using equation (5)[4].

$$\Delta G = 96.48\ (E^\circ(D/D^{\bullet+}) - E^\circ(A^{\bullet-}/A) - e^2/\epsilon r) - E_T \qquad (5)$$

Where E° $(D/D^{\bullet+})$ and E° $(A^{\bullet-}/A)$ refer to the polarographic halfwave oxidation-reduction potentials for the electron donor, D, in this case water, $E^\circ(O_2/H_2O)$=0.81 V versus NHE, and electron acceptor, A, (UQ) respectively, $e^2/\epsilon r$ is a Coulombic term ($\sim$0.06eV) and E_T is the zero-spectroscopic energy of triplet ubiquinone.

A good estimate of the UQ reduction potential is the value obtained by Macus and Hawley[5] for Ubiquinone-1 of - 0.62 V versus NHE in acetonitrile. The triplet energy of UQ has been estimated by Bensasson et al[2] to be between 123 and 176 k J mol^{-1}. Substituting these values into equation (5) we find ^3UQ is able to photo-oxidise water (i.e. negative ΔG) provided its triplet is > 138 energy kJ mol^{-1}. Based on this observation, we reassign the triplet energy of UQ to be between 138 and 176 kJ mol^{-1}.

The fact that ^3UQ is able to photo-oxidise water is of great interest when compared with the triplet state reactivity of other quinone compounds of similar structure, namely duroquinone (II) and benzoquinone (III). The inability of triplet duroquinone to react with water is attributed to it possessing mixed Π,Π* and n,Π* character which is solvent dependent[6]. In water it is believed to have Π,Π* character[6].A Π,Π* triplet state does not possess

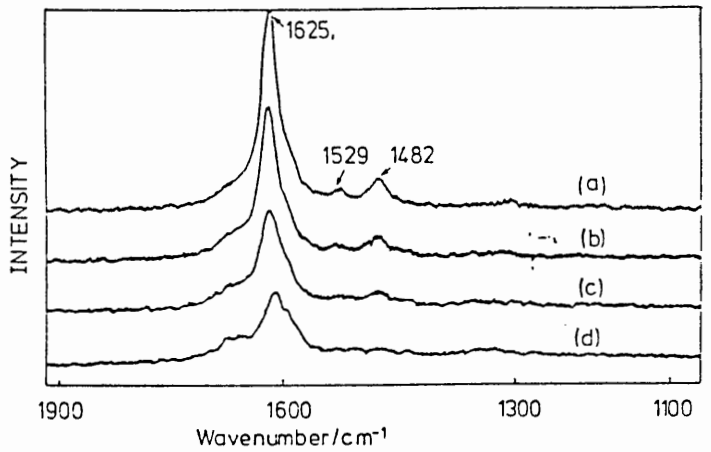


Figure C1.19 UQ (1.0 x 10^{-3} mol dm^{-3}) in water, pump 248 nm, probe 440 nm, time delays (a) 200 ns, (b) 1500 ns, (c) 80 μs, (d) probe only.

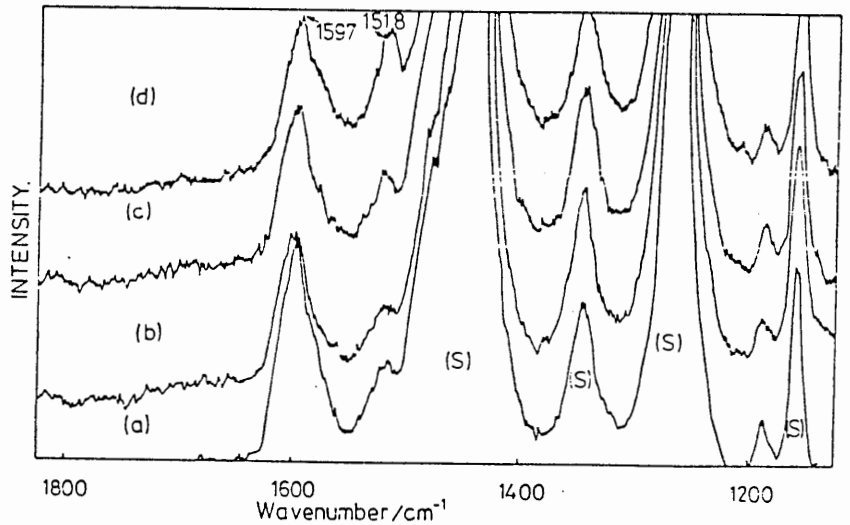


Figure C1.20 UQ (1.0 x 10^{-3} mol dm^{-3}) in cyclohexane, pump 248 nm, probe 440 nm, Δt delays (a) probe only, (b) 100 ns, (c) 50 ns, (d) 25 ns.

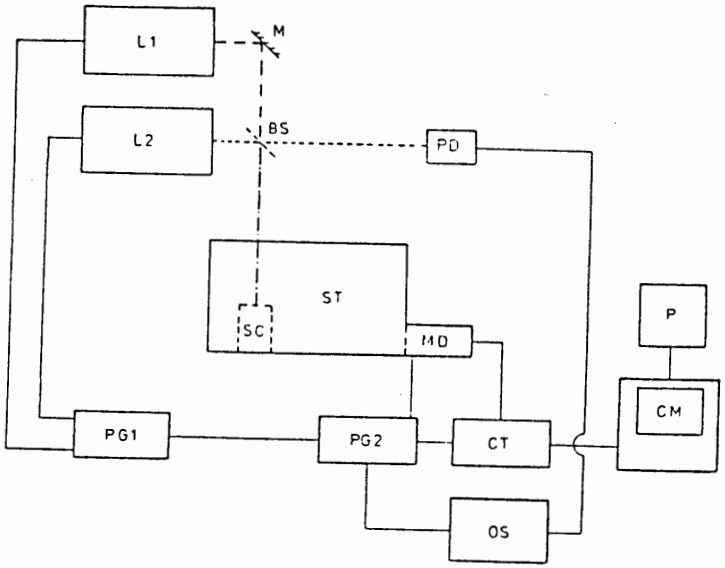


Figure C1.21 Experimental set-up used for TR3 spectroscopy. L1 and L2 = lasers, M = mirror, BS = beam splitter, PD = photodiode, ST = Spex Triplemate, SC = sample compartment, MD = multichannel detector, PG1 and PG2 = pulse generators, CT = controller (detector), OS = oscilloscope, P = plotter and CM = computer and monitor.

electron deficiency at the carbonyl oxygen, which is characteristic of an n,Π* carbonyl triplet state. This makes hydrogen abstraction or electron transfer less favourable for Π,Π* states. However, both benzoquinone and UQ triplet states have n,Π* character which would favour both species being able to react with water. Earlier work by Benssason et al[6] has shown that triplet benzoquinone can react with water, but more recent work using ethanol: water solvent mixtures has shown that for the mixed solvent the reaction of excited benzoquinone is by a two photon process[8]. Further work is required to confirm that our observations for the oxidation of water by ^{3}UQ is either a one or a two photon process.

The difference between the triplet state reactivities maybe due to the methoxy groups present in UQ. These groups exert an electron withdrawing effect (-I) which stabilises the formortion of the ion pair intermediate ($UQ^{\bullet-}$ - $H_2O^{\bullet+}$) and aids the charge separation leading to the solvated ion pair before back electron transfer can occur.

Ubiquinone in Cyclohexane

The ground state Raman spectrum of UQ in cyclohexane is shown in Figure C1.20a. Comparison of this with the spectra from the two-laser experiments shows a new band at 1518 cm^{-1} and bleaching of the 1597 cm^{-1} band. With increasing time delay between excitation and probe pulse the 1518 cm^{-1} band gets weaker. Kinetic analysis gives a transient lifetime of 40 ns. This is in fairly good agreement with the results of flash photolysis by Amouyal et al[9] (∿ 70 ns) and in view of this we ascribe the band to ^{3}UQ.

The 1597 cm^{-1} peak is assigned to both the C=C and C=O stretching modes for the ground state. In the spectrum of the triplet excited state the 1518 cm^{-1} band could arise either from the C=O or C=C stretching. The resonance enhancement will depend upon whether triplet ubiquinone has n,Π* or Π,Π* character. Previous work[7,10] tends to favour a n,Π* triplet state and if this is the case the C=O stretch in ground state UQ in the unresolved 1597 cm^{-1} doublet is bleached giving rise to the 1518 cm^{-1} (C=O) band for the triplet excited state.

Summary

The table summarises all the spectroscopic data and species assignments discussed.

Solvent	Band Wavenumber cm^{-1}	Species
Ethanol	1618	$UQ^{\bullet-}$
Ethanol	1515	$UQH^{\bullet}$
Ethanol with $NaNO_2$ addition	1620, 1528 1484, 1300	$UQ^{\bullet-}$
Water	1625, 1529, 1482	$UQ^{\bullet-}$
Cyclohexane	1518	^{3}UQ

References

1. J N Moore, D Phillips and R E Hester, J. Phys. Chem., (1988), 92, 5619; I McCubbin, D Phillips and R E Hester, J. Chem. Soc., Faraday Trans., 2, (1987), 83, 1519.

2. R Bensasson, C Chachaty, E J Land and C Salet, Photochem. Photobiol (1972), 16, 27.

2.a. J. Nafisi-Movaghar and F. Wilkinson, Trans. Faraday Soc. (1970), 66, 2257.

3. R Scheerer and Mr Grätzel, J. Am. Chem. Soc. (1977), 99, 865.

4. D Rehm and A Weller, Ber. Bunsenges. Phys., Chem., (1969), 73, 834; Isr. J. Chem., (1970), 8, 259.

5. M F Marcus and M D Hawley, Biochem. Biophys. Acta. (1971), 226, 234.

6. E Amouyal and R Bensasson, J. Chem. Soc. Faraday Trans. 1, (1976), 72 1274.

7. J C Ranford-Haret, R V Bensasson and E Amouyal, J. Chem. Soc., Faraday Trans. 1, (1980), 76, 2432.

8. R Rossetti and L E Brus, J. Am. Chem. Soc. (1986), 108, 4718.

9. E Amouyal, R Bensasson and E J Land, Photochem. Photobiol. (1974), 20 415.

10. D Kemp and G Porter, Proc. Royal Soc., (1971), A326, 117.

C1.9 INTERFACIAL CHARGE-TRANSFER STUDIES ON COLLOIDAL SEMICONDUCTORS BY TIME-RESOLVED RESONANCE RAMAN (TR3) SPECTROSCOPY

S Umapathy (Department of Chemistry, University of York)
A W Parker, (RAL)
R E Hester, (Department of Chemistry, University of York)

Introduction

Colloidal semiconductors have been used as microheterogeneous catalysts to mediate the water splitting photoredox reaction[1]. The efficiency of this catalytic action depends on the charge-transfer processes at the colloid/adsorbate interface. In order to improve the catalytic performance of colloidal semiconductors, it is important to understand the mechanism of this charge-transfer process. We present here the results of TR3 studies of a) photosensitization of colloidal titanium dioxide (TiO_2) and b) electron-transfer from photoexcited cadmium sulphide (CdS) to methylviologen (MV^{2+}).

Experimental

TiO_2 sol was prepared as described previously[2]. Complexes of ruthenium (II) tris (2,2'-bipyridyl 4,4'-diethyl carboxylate)(RB4ET) and ruthenium (II) cis-diaqua bis(2,2'-bipyridyl-4,4'-diethyl carboxylate)(RBDA) were kind gifts from Prof M Grätzel. CdS sol was prepared by mixing solutions of cadmium nitrate and sodium hydrogen sulphide. Cadmium nitrate, sodium hydrogen sulphide and methyl viologen were all used as received from Aldrich Co.

Time-resolved Raman experiments were performed using the set-up shown in Figure C1.21. Lasers L1 and L2 were excimer lasers (Lumonics Hyperex 460) pumping a dye laser (Lumonics FL3002). Appropriate selection of dyes (from Exciton Corp.) provided variable laser wavelengths for the experiments. Details of other components are described in the figure caption.

Results and Discussions

a) Photosensitization of colloidal TiO_2.

Photosensitization is achieved by adsorption of either RB4ET or RBDA. Both the complexes in their triplet excited state have sufficient energy to inject an electron into the conduction band of the TiO_2 semiconductor. The mechanism of photosensitization is as follows:

$$R \xrightarrow{h\upsilon} R^*$$

$$R^* + TiO_2 \longrightarrow R^{\cdot} + TiO_2\ e^-_{CB}$$

where R = RB4ET or RBDA
and CB = conduction band

In the case of RB4ET, the metal-ligand charge-transfer triplet excited state of the free (unadsorbed) complex was generated using

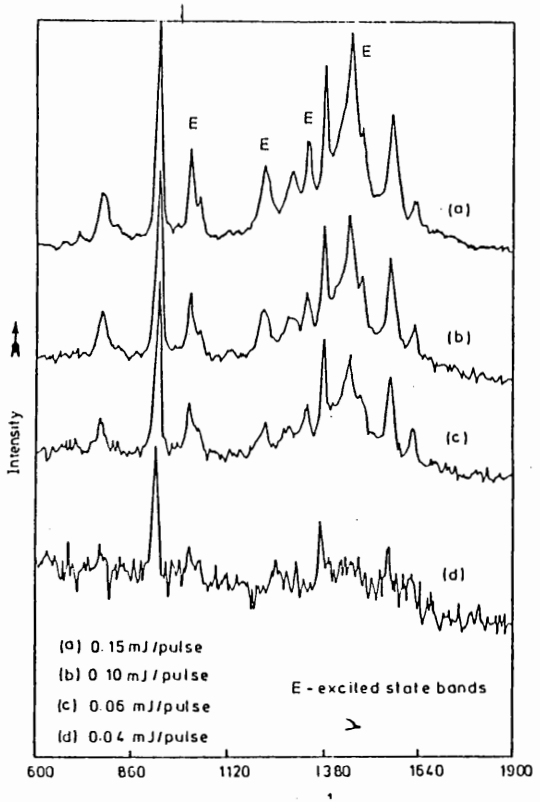


Figure C1.22 *Power dependent spectra of RB4ET.*

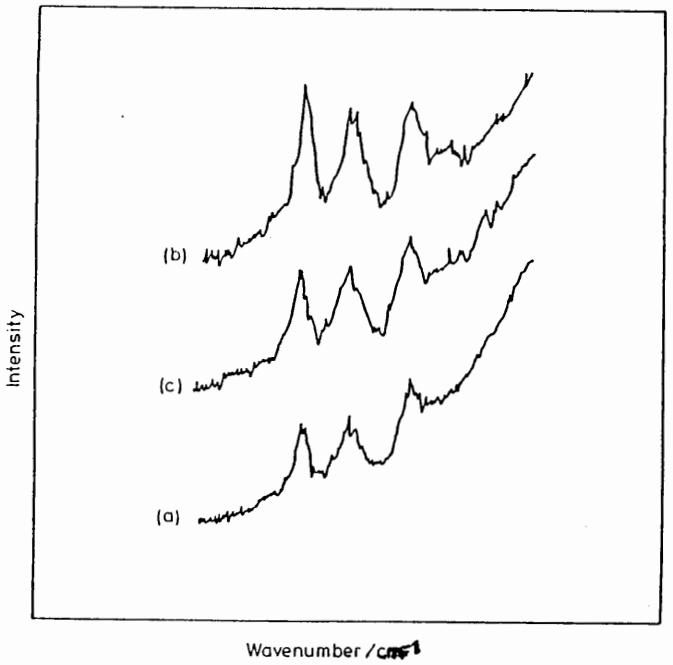


Figure C1.23

TR3 spectra of RB4ET adsorbed onto colloidal TiO_2 surface at various time delays between the pump and probe lasers a) 0 ns, b) 100 ns, and c) 1 μs.

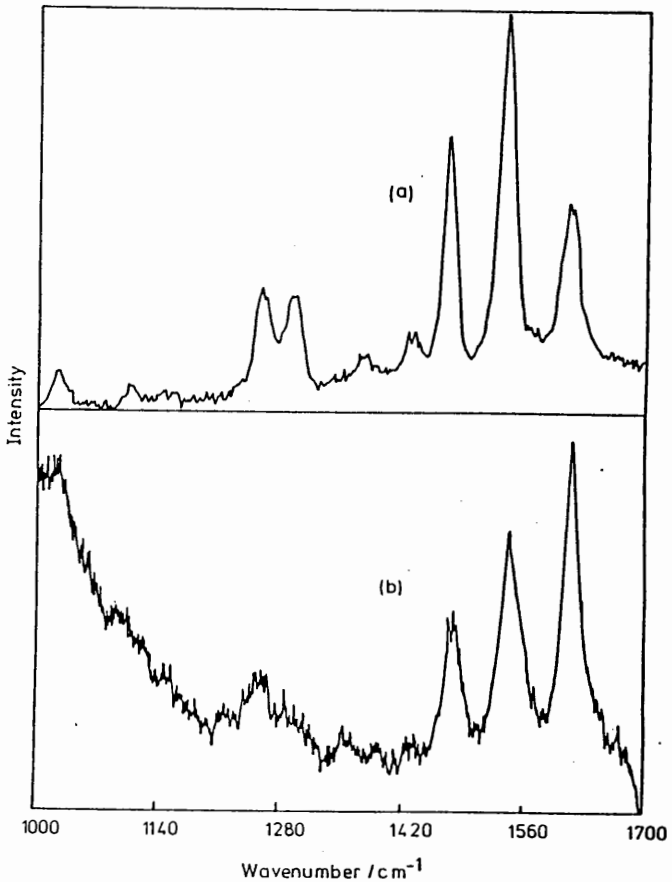


Figure C1.24

Spectra of RBDA adsorbed onto TiO_2 surface a) ground state RR spectrum, λ_{exc} = 488 nm (Ar^+ laser) and b) TR3 spectrum, λ_{exc} = 480 nm (pulsed dye laser).

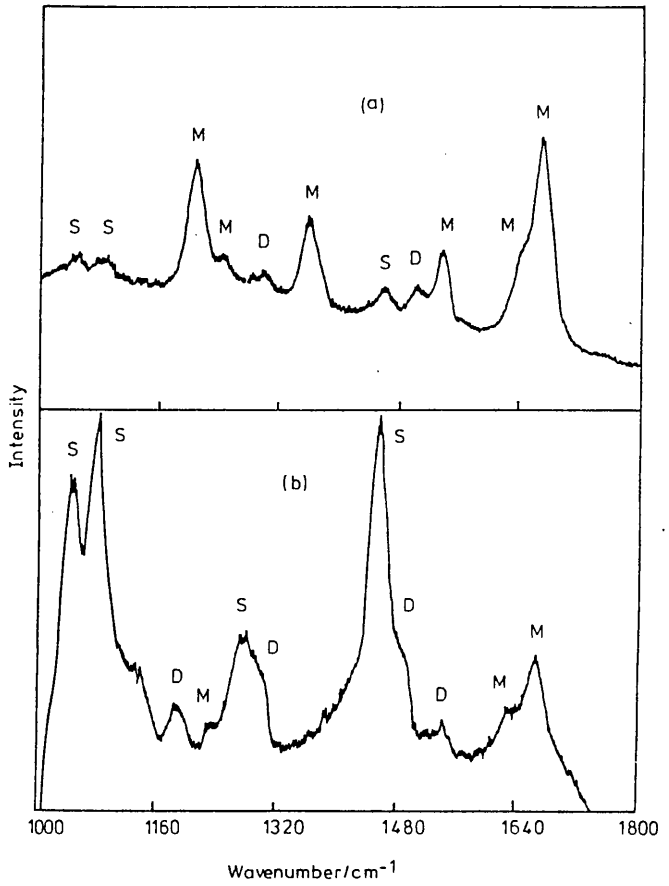


Figure C1.25 TR3 spectra of methylviologen adsorbed on colloidal cadmium sulphide as -
a) cation radical, λ_{exc} = 390 nm and
b) cation radical dimer, λ_{exc} = 540 nm. Bands are marked as S = solvent, M = monomer and D = dimer.

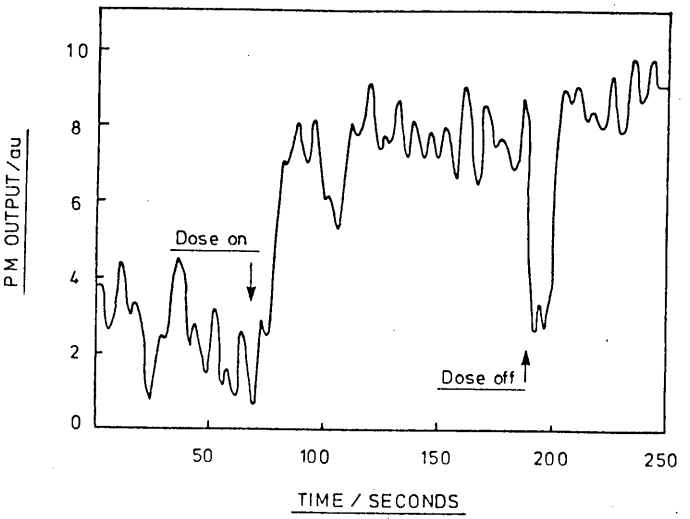


Fig. C1-26 Variation of second harmonic intensity (steady state photomultiplier current) with time from a GaAs (100) surface during dynamic exposure to triethyl gallium, (1 x 10^{-7} mbar) at 300K. $\lambda(1)$ = 1064nm, 5mJ $pulse^{-1}$, pulse duration 10ns, rep. rate 10 Hz, $\lambda(2)$ = 532nm.

a 410 nm dye laser pulse. The spectra recorded at various pulse energies are shown in Figure C1.22. Having established the transient Raman spectrum of the triplet state, a TR3 study of RB4ET adsorbed on TiO_2 was made. A 410 nm laser pulse was used to photoexcite RB4ET and a 480 nm laser pulse was used to probe the Raman scattering from the oxidized product of the complex. The spectra recorded at various time delays between the pump and probe pulses are shown in Figure C1.22. An analysis of these spectra reveals that the spectra recorded after a short delay (i.e. 0 - 800 ns) are due to the oxidized form of the complex. Longer delay times (≥ 1 μs) result in spectra which resemble the ground state, suggesting a probable recombination reaction of the oxidized state with the conduction band electrons. This observation is consistent with an earlier study by Grätzel et al.,(3), where the results were interpreted to show that electron injection occurs in a few nanoseconds and the recombination reaction occurs in microseconds.

In the case of RBDA, the excited state lifetime is expected to be a few picoseconds[4] (unlike the case of RB4ET, which has an excited state lifetime of 350ns) and therefore it is not possible to record the transient Raman spectra using the ns laser pulses. However, the TR3 spectrum of the longer lived oxidized form of the complex was recorded using a single laser pulse (which serves the purpose of simultaneous pumping and probing) as shown in Figure C1.24. This figure also shows the ground state spectrum of RBDA on TiO_2 for comparison.

b) Electron-transfer at the CdS colloid/methylviologen (MV^{2+}) interface.

Electron-transfer from photoexcited CdS to MV^{2+} results in the formation of MV^{+} (cation radical) as shown.

$$CdS \xrightarrow{h\nu} e^-_{CB} + h^+_{VB} + CdS$$

CB = conduction band
VB = valence band

$$e^-_{CB} + MV^{2+} \longrightarrow MV^{+}$$

Numerous groupsm[5-8], including ours[9], have demonstrated the above process using time-resolved absorption and Raman Studies. Although MV^{+} has been identified and characterized, recent reports[10,11] have suggested possible dimerization of MV^{+} to form $(MV^{+})_2$ at the CdS surface:

$$MV^{+} + MV^{+} \longrightarrow (MV^{+})_2$$

It has been shown that on excitation, the electron-transfer and dimerization both occur during the first few ns of the laser pulse, leading to formation of $(MV^{+})_2$ dimers[10,11]. These dimers absorb strongly at ca. 540 nm and have a lifetime of ∿ 100 ns. From these reports and earlier studies, it is known that the MV^{+} monomer absorbs strongly at 390nm and 600nm and the lifetime is ca. 500 μs. Thus by selecting the probe laser wavelength in resonance with the electronic transition of the dimer (λ_{exc} = 540 nm) and the monomer (λ_{exc} = 390 nm), we have been able to record the Raman spectra of both the dimer and monomer, respectively.

In Figure C1.25(a), the resonance Raman spectrum of MV^{+} adsorbed ion the CdS surface is shown. This spectrum is identical to that of MV^{+} given in earlier reports[8,9], except for the two bands at ca. 1300 and 1500cm^{-1}. A comparison of this spectrum with the other power dependent spectra recorded using a 390 nm pulse shows that these bands may be attributed to a short lived species, i.e. in this case probably the dimer[12]. We note here that since CdS itself absorbs very strongly at 390nm, a single laser pulse is sufficient to simultaneously pump the bandgap of the semiconductor and probe for the resonance Raman scattering from methylviologen cation radial.

In Figure C1.25(b), the $(MV^{+})_2$ RR spectrum recorded using a 540nm laser pulse is shown. Interestingly again, the single laser pulse had sufficient energy for simultaneous pumping and probing of the CdS/$(MV^{+})_2$ system. Attempts were made to perform a two laser experiment (by reducing the 540nm probe laser energy and using a 351nm laser pulse as a pump) so as to time-resolve the monomer

($\tau \approx 500$ μs) from the dimer ($\tau \approx 100$ ns), but with little success. The spectra recorded were all identical to that given by the single laser pulse experiment. The spectrum recorded using this 540 nm laser pulse was analysed along with the literature Raman data[13,14] on various electrochemically and chemically generated $MV^{\bullet}$ and $(MV^{\bullet})_2$ species. Based on this analysis, we tentatively assign the bands to the dimer. Further experiments are being carried out to confirm this assignment.

References

1. K Kalyanasundaram, M Grätzel and E Pelizzetti, Coord. Chem. Rev. 69, 57 (1986).

2. S Umapathy, G Lee-Son and R E Hester, J. Chem. Soc. Chem. Comm., 1841 (1987).

3. J Desilvestro, M Grätzel, L Kavan, J Moser and J Augustynski, J. Am. Chem. Soc., 107 2988 (1985).

4. P Liska, N Vlachopoulos, M K Nazeeruddin, P Comte and M Grätzel, Personal communication.

5. W J Albery, G T Brown, J R Darwent, E J Saiever-Iranizad, J. Chem. Soc. Fara. Trans. 1., 81 1999 (1985).

6. D Duanghong, J Ramsden and M Grätzel, J. Am. Chem. Soc., 104, 2977 (1982).

7. R Rosetti, S M Beck and L E Brus, J. Am. Chem. Soc., 104, 7322 (1982).

8. R Rosetti, S M Beck and L E Brus, J. Am. Chem. Soc., 106, 980 (1984).

9. K Metcalfe and R E Hester, J. Chem. Soc. Chem. Comm., 133 (1983).

10. Y Nosaka and M A Fox, J. Phys. Chem. 92, 1893 (1988).

11. J J Ramsden and M Grätzel, Chem. Phys. Lett., 132, 269 (1986).

12. S Umapathy, A W Parker and R E Hester, manuscript in preparation.

13. M Forster, R B Girling and R E Hester, J. Raman Spec., 12, 36 (1982).

14. T Lu, T M Cotton, J D Hurst and D H P Thompson, J. Phys. Chem., 92, 6978 (1988).

C1.10 IN-SITU MOVPE DIAGNOSTICS: OPTICAL SECOND HARMONIC GENERATION - A FEASIBILITY STUDY

D S Buhaenko, S M Francis, P A Goulding and M E Pemble*
Department of Chemistry, UMIST

Introduction

Metal organic vapour phase epitaxy (MOVPE) is a well-established method of growing epitaxial films of compound semiconductors such as GaAs, InP and GaAlAs on well-orientated substrates using metalorganic and hydride precursors[1-3]. Despite the success of these techniques, little is known regarding the chemical mechanisms involved in MOVPE reactions. Some suggested overall reaction schemes utilising common precursors for the growth of GaAs are,

$$(CH_3)_3Ga(g) + AsH_3(g) \rightarrow GaAs(s) + 3CH_4(g)$$

$$(C_2H_5)_3Ga(g) + AsH_3(g) \rightarrow GaAs(s) + 3C_2H_6(g)$$

$$(C_2H_5)_3Ga(g) \rightarrow (C_2H_5)_2\,GaH(s \text{ or } g?) + C_2H_4(g)$$

In order to improve the ability to control both growth rate and contamination levels together with the development of more

efficient growth schemes using safer, less toxic precursors there is currently much emphasis being placed on elucidation of the basic mechanistic pathways leading to the deposition of an epitaxial layer.

As part of our programme of work aimed at studying the basic surface chemistry of these processes, we at UMIST have for the first time applied the technique known as optical second harmonic generation (SHG) to the study of the interaction of a typical MOVPE group III precursors triethyl gallium (TEG) with a GaAs (100) surface prepared in UHV. In addition we have examined the dependence of the SH energy upon incident beam energy and as a result we are able to speculate on the nature of the SHG mechanism for the particular system under examination.

Theory

Optical second harmonic generation (SHG) is observed from a medium which possesses a centroasymmetric bulk structure since the presence of the resulting asymmetric charge distribution (dipole) produces significant higher order (non-linear) terms in the frequency dependent polarisability (susceptibility) function[4]. Thus for materials such as Si, which have centrosymmetric bulk structures, bulk SHG is forbidden. However, for a boundary between two phases, whatever their bulk structure, the 'dipole approximation' again becomes valid due to the lowering of symmetry produced by the interface. Thus for materials which have centrosymmetric bulk structures, SHG should be highly surface specific. This has been exploited in order to use SHG to monitor surface processes occuring on metals[5,6] and the semiconductors Si, Ge and GaAs[7-10]. That SHG is sensitive to surface processes may be seen in terms of perturbations to the surface electronic structure produced via processes such as adsorption, desorption, oxidation, melting etc. For reviews of the application of the SHG technique to the study of interfacial phenomena the reader is directed to the articles by Shen[11,12]. Thus the potential of the SHG technique in the monitoring of surface processes becomes obvious; since on a macroscopic scale the dipole approximation does not hold for gaseous species, SHG from such species is forbidden, ie. SHG is a surface sensitive technique that is independent of gas phase pressures. In addition, the use of pulsed laser primary sources means that it is possible to monitor dynamic surface processes such as adsorption, phase transitions etc. via the SHG technique.

However, for a material such as GaAs which possesses a centroasymmetric bulk structure, the dipole approximation predicts both surface and bulk SHG contributions with the bulk contribution possibly some three or four orders of magnitude larger than the surface contribution[10]. Indeed the aims of this present study were to determine firstly whether the extraction of the surface SHG from the surface and bulk SHG expected for GaAs was feasible and secondly if this proved feasible, to utilise SHG to monitor processes of relevance to MOVPE growth of GaAs.

Experimental

A previous report to the Laser Support Facility (1988) described the experimental arrangement in some detail[13]. Briefly the SHG experiments were performed using a primary beam of wavelength 1064nm from an Nd:YAG laser loaned from RAL. The laser was operated at 10Hz repetition rate with a pulse duration of 10ns, the energy of each pulse varying between 1mJ and 50mJ. The primary beam was incident on the GaAs (100) substrate mounted in UHV at an angle of 45 degrees. The specularly reflected component at the second harmonic wavelength of 532nm was detected using a conventional visible response photomultiplier tube (EMI 9217QB) after the colinear component of the primary beam at 1064nm had been filtered out using suitable dichroics.

The GaAs (100) substrate was prepared prior to the SHG experiment via annealing at 570-800 K in H_2 (1 x 10^{-6} mbar, 60 minutes) followed by annealing at 800 K in AsH_3 (1 x 10^{-6} mbar, 10 minutes). This procedure produces a surface which is free from contamination (Auger electron spectroscopy) and rich in As[14,15] and is believed to be analogous to the pre-growth substrate bake-out employed in MOVPE-growth on GaAs (100) substrates.

TEG (Epichem) was introduced via a passivated stainless steel gas handling system equipped with a leak valve to the UHV chamber. During exposure of TEG, great care was taken to minimise possible cracking of the TEG at filaments, pumps, etc. All exposures are quoted with respect to uncorrected ion gauge readings.

Results and Discussion

Figure C1.26 depicts the variation in SH intensity (at 532nm) from a GaAs (100) surface under dynamic exposure to TEG at 1 x 10^{-7} mbar. The incident laser energy was 5mJ per pulse, pulse duration 10ns, 10 Hz repetition rate. This figure illustrates that in accordance with previous data, the interaction of TEG with GaAs (100) produces a permanent increase in SH intensity[13]. Also of interest are the observations that

i) the increase in SH signal is large - comparable to the levels of background SHG observed prior to dosing TEG
ii) SHG from GaAs (100) is observed under conditions where the second order terms of the frequency dependent polarisability would be expected to be small for the bulk material (non-resonant process, $h\nu < E_g$, where E_g = bandgap energy).

It is believed that this is the first observation of apparently surface specific SHG from GaAs (100). Similar effects have been reported for Si surfaces[8] however bulk SHG would be disallowed from Si anyway due to the centrosymmetric crystal structure. Enhanced surface SHG from Si (111) surfaces has been attributed to a resonance process involving adsorption via low-lying surface states[8] such as have been suggested via surface structural calculations[16]. For GaAs (100), little data is available although for the c(2x8) As-stabilised surface, Neave et al have detected suitable states using UPS[17].

Alternative explanations discussed previously[13] include excitation of electron-hole pairs via laser induced surface heating and also multiphoton excitation, which might be expected to occur more readily for a direct bandgap material such as GaAs compared to an indirect bandgap material such as Si. Previously we noted that the surface heating mechanism was not favoured since it has been demonstrated that up to incident energies required to melt GaAs surfaces, little change in SHG is observed[9]. However we note here that these measurements were performed using a primary beam of wavelength 532nm, ie. under conditions where the bulk SHG contribution would be expected to dominate. For this reason it is not possible to dismiss the surface heating mechanism at this stage. The two-photon absorption mechanism is also a possibility that cannot be easily discounted. However, if such a mechanism were operating, it would presumably give rise to both surface and bulk SHG from GaAs whereas the data depicted in figure C1-26 would suggest that the signals observed here are largely surface in origin.

In investigating further the origins of the SH signal we have measured the dependence of the SH energy upon incident energy. Figure C1-27 depicts the variation of SH intensity as measured via the photomultiplier output current against incident pulse energy. From figure C1-27 it is clear that at incident pulse energies of approximately 5mJ, the resulting SH intensity saturates. Figure C1-28 is a log-log plot of SH energy against incident energy for the data points on the rising portion of figure C1-27 which was plotted in order to determine the order of the relationship between these two parameters. From this figure it would appear that there is a linear dependence of SH energy on incident energy. This result is surprising in that for 'normal' SHG from GaAs surfaces, a quadratic dependence is expected[9]. However, for a log-log plot the scatter of data points depicted in figure C1-28 is high. Indeed the best-fit straight line as calculated by linear regression has a correlation coefficient of only 0.89. It is believed that these measurements must be repeated allowing for

i) losses of both incident and SH intensity that occur at the windows
ii) pulse-to-pulse variations in the incident energy.

Only by using a more sophisticated experimental arrangement in which these factors can be adequately accounted for will it be possible to determine the true nature of the relationship between SH energy and incident energy in these experiments.

Despite the uncertainty in these data, it is believed that the saturation effect depicted in figure C1-27 is real. This observation is consistent with the concept of resonance via low-lying surface states since once sufficient energy to excite all available states is provided, further enhancement of the SH intensity would not be possible.

One final experimental result is worthy of mention here. On completion of the SHG vs incident energy measurements, the GaAs (100) substrate was annealed in 1 x 10^{-5} mbar O_2 for five minutes at 700K. Subsequent Auger analysis revealed that the surface was essentially oxidised. Following this treatment, no SHG signal was detected from the GaAs (100) surface. We interpret this observation as being further evidence in support of an SHG mechanism involving surface state resonances, since the electronic structure of the oxidised surface is likely to be completely different to that of the clean surface. Clearly the variation of the SHG with controlled oxidation should be the subject of further experimentation, although we note that Heinz et al also used the oxidation/disordering process to confirm that the SHG observed from Si surfaces was indeed surface specific[8].

The net increase in SH intensity upon exposure to TEG at 300K cannot be adequately accounted for at this stage. By analogy with measurements made on metal surfaces, an increase in SH intensity would be attributed to an increase in the second order surface susceptability arising from the presence of an electron donating adsorbate[18] ie. a decrease in surface work function. In terms of the physical processes occuring we have shown from other measurements (Auger electron spectroscopy, thermal desorption data) that TEG adsorbs on GaAs (100) at 300K[14]. However, it has not been possible to establish whether adsorption occurs molecularly or dissociatively. Very recently, McCrary and Donnelly have indicated that TEG dissociatively adsorbs on a somewhat ill-defined GaAs (100) surface used by these workers in experiments relating to the photo-assisted surface decomposition of TEG[19]. However, certain aspects of the experimental procedures used in this work cause us to question the validity of these observations in that there were apparently no precautions taken to avoid cracking the highly reactive TEG on hot filaments and ion pump electrodes within the reaction chamber.

Thus we feel that it is not yet possible to draw specific conclusions regarding the adsorption of TEG on GaAs (100). Experiments are underway in our laboratories in which a completely non-intrusive technique, IR spectroscopy, will be used to determine the mode of bonding of the TEG molecules to the GaAs surface.

Conclusions

Although this work has possibly raised more questions that it has answered, it has arguably been very successful. Specifically, it is possible that a method of measuring surface-specific second harmonic generation from GaAs (100) has been found. Also it has been possible to monitor in real time, the adsorption of a typical MOVPE reactant at a substrate surface. While the interpretation of the data is still open to question, the fact that some easily detectable variation in SHG occurs during adsorption of TEG is of note and suggests that SHG may become a useful in-situ surface diagnostic technique for use in the harsh environment of the MOVPE reactor.

Further Work

Future experiments will aim at reproducing the data described here, correlating changes in surface SHG with real surface chemical changes as characterised by other techniques and further investigations of the origins of the SHG observed from GaAs (100) under 1064nm illumination. In addition, one very exciting possibility will be explored. This approach will utilise the dependence of the surface SH signal on surface structure via the use of a polarised incident beam. Using this approach, it has been possible to monitor surface reconstructions using SHG since the second order surface susceptibility is highly anisotropic, dependent upon the symmetry properties of the surface layer[20].

Thus it may be possible to monitor the change from an amorphous deposit to an ordered overlayer using SHG. If this is the case,

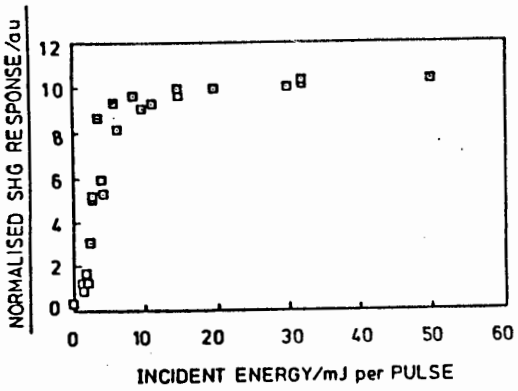
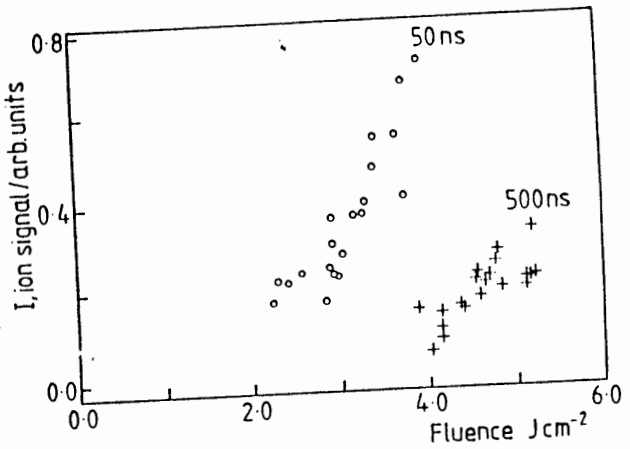


Fig C1.27 Variation of SH intensity (photomultiplier current) with incident pulse energy.



C1-29 Dependence of the $I(^2P_{3/2})$ signal, measured by MPI, on the laser fluence for the IRMPD of CF_3I at 1075cm^{-1} using square pulses of length 50 and 500ns. An intensity effect on the dissociation yield is clearly seen.

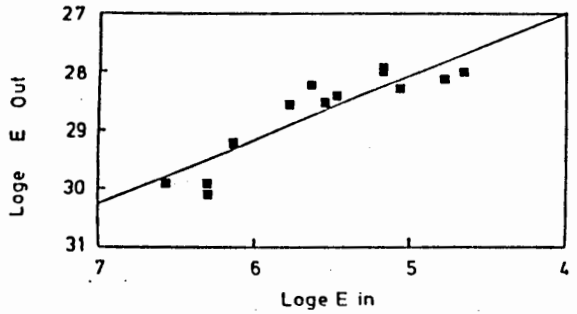
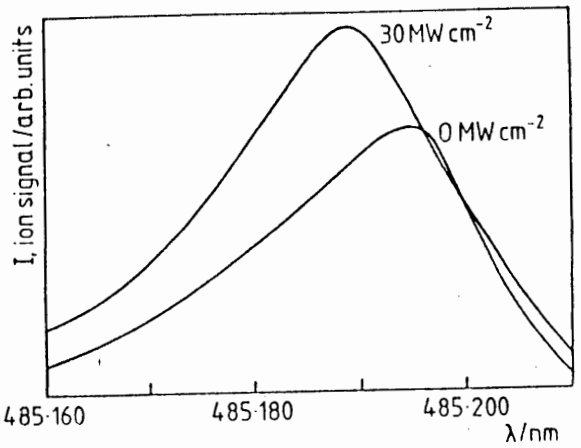


Fig C1.28 Log-log plot of SH energy against incident energy, C1-28 calculated assuming a photomultiplier gain of approx. 10^3. Also depicts best straight line as calculated using a linear regression routine. Regression parameters, slope = 1.06, correlation coefficient = 0.89.



C1-30 Measured MPI signal as a function of laser wavelength for detection of $I(^2P_{3/2})$ atoms with and without CO_2 laser radiation present. At a CO_2 laser intensity of 30 MWcm^{-2}, the resonance shifts to the blue due to the AC stark effect.

then SHG could conceivable become analogous to reflection high energy electron diffraction (RHEED) which is used in situ, to monitor semiconductor growth via molecular beam epitaxy. Here, oscillations in the RHEED intensity provide a real-time measure of growth. By analogy, oscillations in the surface SHG intensity may provide similar information not only for high vacuum growth techniques such as MBE but also for atmospheric pressure growth, ie. MOVPE.

Acknowledgments

The financial support of the SERC for the UHV system, funding for this feasibility study of SHG and studentships for DSB and PAG is gratefully acknowledged. In addition the support of the MOD (DCVD) for a postdoctoral research assistantship (SMF) pertaining specifically to the optical diagnostics is also gratefully acknowledged. Finally the authors would like to express their thanks to Dr A Langley and Ms S Tavender from RAL for assistance with the lasers and to Dr J McGilp, Trinity College Dublin for helpful correspondence.

References

1. H M Manasevit, Appl. Phys. Lett., 12, (1968), 136.

2. L Hollan, J P Hallais and J C Brien in 'Current Topics in Materials Science', vol. 5, Ed. E Kaldis, (North Holland) 1980, 155.

3. N J Mason in 'Chemistry of the Semiconductor Industry', Eds. S J Moss and A Ledwith, Blackie, 1987.

4. N Bloembergen and N Pershan, Phys. Review, 128, (1962), 6399.

5. H W K Tom, C M Mate, X D Zhu, J E Crowell, T F Heinz, G A Somorjai and Y R Shen, Phs. Rev. Lett., 52, (1984), 348.

6. H W K Tom and G D Aumiller, Phys. Rev. B, 33, (1986), 8818.

7. H W K Tom, X D Zhu, Y R Shen and G A Somorjai, Surface Science, 167, (1986), 167.

8. T F Heinz, M M T Loy and W A Thompson, Phys. Rev. Lett., 54, (1985), 63.

9. A M Malvezzi, J M Liu and N Bloembergen, App. Phys. Lett., 45, (1984), 1019.

10. D Guidotti, T A Driscoll and H J Gerritsen, Solid State Comm., 46 (1983), 337.

11. Y R Shen, J. Vac. Sci. Tech., A5, (1985), 1464.

12. Y R Shen, Nature, 337, (1989), 519.

13. D S Buhaenko, S M Francis, P A Goulding and M E Pemble, in Report to the Laser Facility Committee, RAL, 1988.

14. D S Buhaenko, S M Francis, P A Goulding and M E Pemble, to appear in Proceedings of the NATO Workshop on Reactions of Organometallics with Surfaces, St Andrews, 22-24 June 1988.

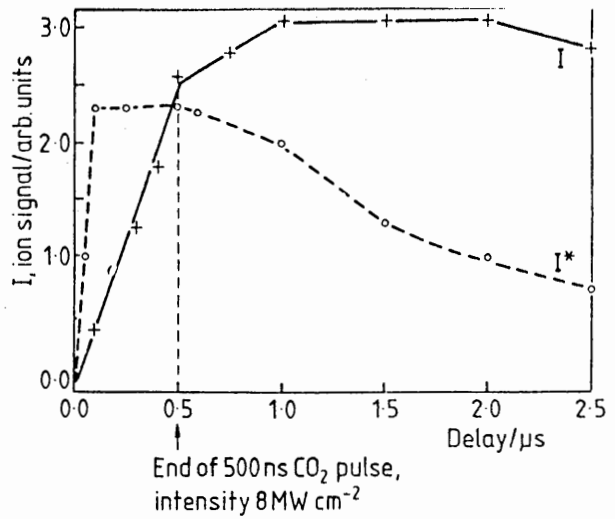
15. D S Buhaenko, S M Francis, P A Goulding and M E Pemble, J. Vac. Sci. Tech., B6, (1988), 1688.

16. R Del Sole and A Selloni, Phys. Rev. B, 30, (1984), 883.

17. P K Larsen, J H Neave and B A Joyce, 14, (1981), 167.

18. Z Rosenzweig and M Asscher, Surface Science, 204, (1988), L732.

19. V R McCrary and V M Donnelly, J. Phys. Chem., 93, (1989), 1148.



C1-31 Observations of $I(^2P_{3/2})$ and $I^*(^2P_{1/2})$ during and after the CO_2 laser pulse. Ground state I atoms grow in time during the pulse, and the rise after 500ns is due to unimolecular dissociation of CF_3I molecules excited above the dissociation threshold. Excited state I^* atoms are formed by photolysis of vibrationally hot CF_3I by the 477.8nm MPI beam. These species reach equilibrium during the IR pulse, and their decay after 500ns represents diffusional loss from the MPI probing volume.

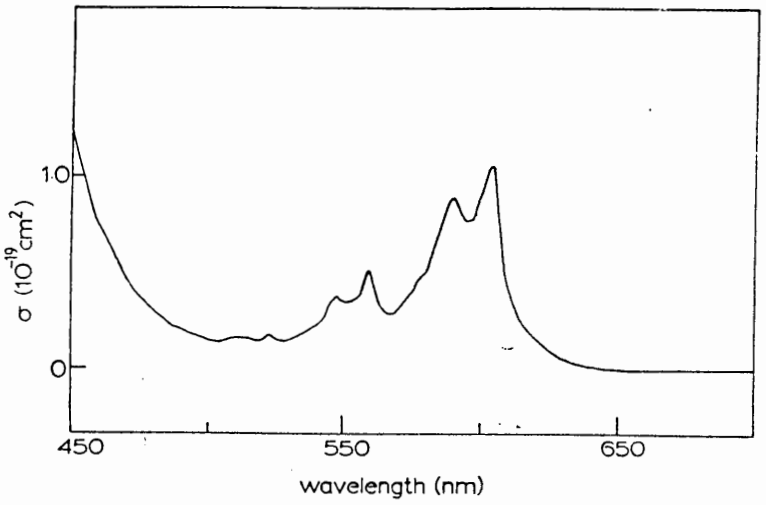


Fig C1.32 Electronic absorption spectrum of t-buSNO vapour at 300 K in the visible region.

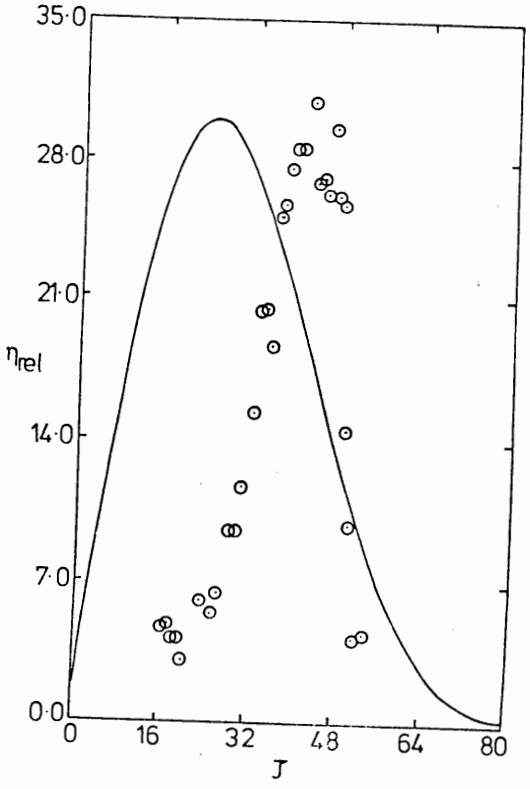


Fig C1.33 Comparison of observed and calculated statistical rotational distributions of nascent NO(v" = o, $\Pi_{\frac{1}{2}}$ - A") from the photodissociation of CH_3SNO at 355 nm.

20. J F McGilp, J. Vac. Sci. Tech., A5, (1987), 1442, and also refs. 6 and 8.

C1.11 IODINE ATOM DETECTION IN THE INFRARED PHOTODISSOCIATION OF CF_3I

G Hancock and P D Sutton
Physical Chemistry Laboratory, Oxford University

Infra-Red Multiple Photon Excitation and Dissociation (IRMPE/D) is a well established technique for radical generation and vibrational heating. Using shaped CO_2 laser pulses with flat intensity/time profiles[1], the dependence of photolysis yield and rate on CO_2 laser intensity (Wcm^{-2}) and fluence (Jcm^{-2}) can be investigated. IRMPD of CF_3I can be followed in real time by Multiple Photon Ionization (MPI) of the iodine atom, using blue radiation from an excimer pumped dye laser borrowed on the laser loan scheme.

For the IRMPD of CF_3I at 1075 cm^{-1},

$$CF_3I \xrightarrow{17\ h\nu} CF_3 + I(^2P_{3/2}),$$

Quack's Case C predicts[2] a dependence of yield on laser intensity. This is shown in Figure C1-29; for a given total CO_2 pulse energy the I atom signal is much larger for the 50ns pulse than for the 500ns, which has 1/10th the intensity. The measurements were made at the end of both pulses, and are unaffected by the AC stark shift (see Figure C1-30) associated with the electrical field produced by the CO_2 laser pulse.

Both ground state iodine $I(^2P_{3/2})$ and excited iodine $I^*(^2P_{1/2})$ are probed, at wavelengths 485.2nm and 477.8nm respectively. IRMPD produces only I but visible photolysis of vibrationally hot CF_3I produces I^*[3]. Figure C1-31 shows the time dependence of the two signals, during and after the CO_2 pulse. The I signal grows rapidly during the pulse due to fast dissociation and then decays much more slowly due to diffusion out of the probed region. The I^* signal represents hot CF_3I molecules. At the CO_2 intensities used in Figure C1-31 the IRMPD channel is not saturated and during the pulse hot CF_3I molecules are at steady state. The post pulse decay rate is much faster than diffusional and is virtually independent of pressure, so it is not collisional quenching of vibrationally hot CF_3I molecules left at the end of the pulse. It represents the slow unimolecular decay of threshold CF_3I molecules. Such decay has also been observed using cw IR probing of CO_2 excited CF_3I[4]. Threshold molecules are seen to decay in a unimolecular fashion after the photolysis pulse, with a pressure independent rate constant. The MPI signal at 485.nm suffers an AC stark shift to the blue during the CO_2 pulse. This is due to the high intensity, and is shown in Figure C1-30 for a pulse of 30 $MWcm^{-2}$, compared with the I signal after the pulse (zero CO_2 intensity).

References

1. M N R Ashfold, C G Atkins, G Hancock, Chem. Phys. Lett., 80, 1 (1981).

2. M Quack, J Chem. Phys., 69, 1282 (1978).

3. M Quack, E Sutcliffe, P Hackett and D Rayner, Far. Disc. Chem. Soc., 82, 229 (1986).

4. P Dietrich, M Quack, G Seyfan, Far. Disc. Chem. Soc., 82, 9 (1986).

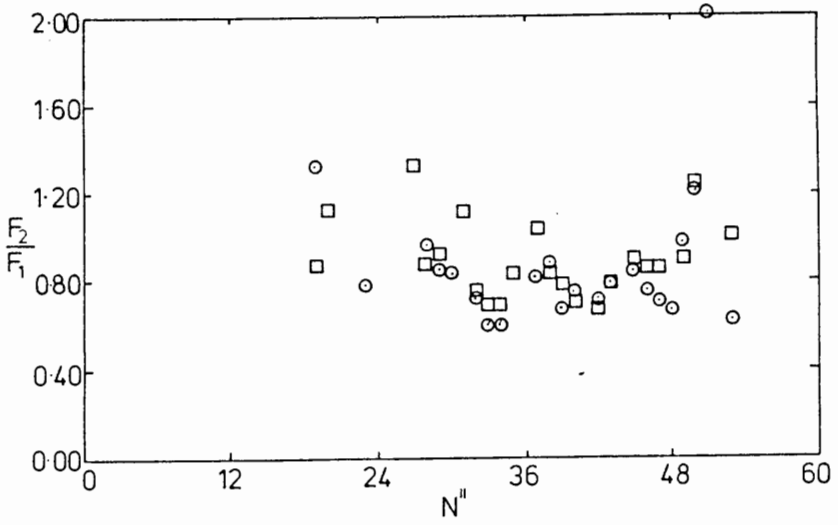


Fig C1.34 F_2/F_1 *spin-orbit ratio for NO (v" = 0, A") as a function of J from the photodissociation of* CH_3SNO(⊙) *and t-buSNO* (□).

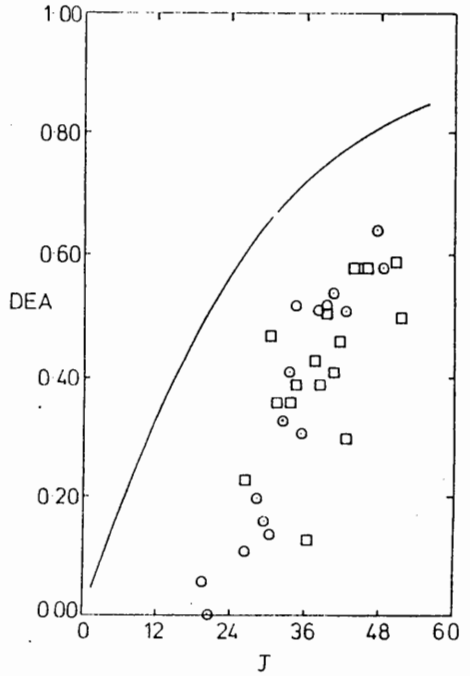


Fig C1.35 Degree of electron alignment (DEA) as a function of J for NO(v" = o, $\Pi_{3/2}$) *from the 355 nm dissociation of* CH_3SNO.

C1.12 PHOTODISSOCIATION DYNAMICS OF JET-COOLED ALKYL THIONITRITES

P A Giovanacci, M R S McCoustra, D M Wetzel, V M Young and J Pfab
(Dept of Chemistry, Heriot-Watt University)

Introduction

The photodissociation dynamics of the alkyl nitrates RONO (R = CH_3 and t-butyl) have been studied recently in several laboratories, and very detailed information is available from previous pulsed laser dissociation - LHF studies[1-3]. The photodissociation of the alkyl thionitrities RSNO, in contrast has remained virtually unexplored. Their electronic absorption spectra reveal weak structured predissociated continua between 500 and 600nm as shown in fig C1.32 for t-butyl thionitrite and strong continua centred near 350nm offering the possibility of studying very different dynamics in readily accessible wavelength regions. Of particular interest is the opportunity to probe the dynamics of the dissociation of the very weak S-N bond (D_0 ca 10000 cm^{-1}) to examine branching into alternate spin-orbit channels and to obtain Λ-doublet populations of the nascent NO.

We report here our results of the 355nm photodissociation of both CH_3SNO and t-buSNO, and of the 603nm photodissociation of the latter compound, and briefly describe results obtained very recently, that we have not yet analysed. They include LIF spectra of CH_3S, alignment and Doppler profile measurements of NO from the photodissociation of jet-cooled CH_3SNO near 550nm.

Experimental

The nascent NO fragment was characterised by two-photon LIF near 450nm for the 355nm experiments and by single-photon LIF near 225nm for the 603nm and 548nm dissociation experiments. The NO LIF transitions probed were $A^2\sum^+(v' = o) \leftarrow X^2\pi_i$. In the 355nm experiments the third harmonic output of the JK Hyper YAG 750 loan laser (ca 50mJ) was focused by a 50cm lens and optically bleached the parent thionitrite, thereby avoiding orientation and alignment effects in the photofragment distribution. Here nascent NO was probed by two-photon LIF. Experiments with 548nm and 603nm photolysis utilised probing by the more sensitive single-photon LIF technique, and optical saturation of the dissociation step was avoided. Jet-cooling of the alkyl thionitrites was performed by expanding 3 to 5% mixtures of the vapour with He at pressures from 300 to 800 Torr using either a pulsed nozzle with 0.5mm orifice or a continuous expansion from a 150μm glass nozzle. The jets were crossed 7 to 10mm downstream from the orifice by the counterpropagating colinearly aligned synchronised dissociation and probe laser beams. The loaned JK Hyper YAG 750/PDL-2 laser system provided between 5 to 50mJ pulse energy for photolysis in the 540 to 610nm region. The probe laser was an excimer pumped dye laser (Lambda Physik EMG 101/FL 3002) equipped with a BBO crystal for frequency doubling and an airspaced etalon for narrowing the linewidth of the dye laser. Delays of 20 to 50ns between dissociation and probe laser pulses were used. LIF spectra of the rotationally relaxed CH_3S fragment were recorded in the 370 to 410nm regions using a room temperature flow cell, 3 to 4% mixtures of CH_3SNO with Ar, and a Lambda Physik excimer pumped dye laser (EMG50/FL2002). For these experiments the probe laser was attenuated to ca 50μJ pulse energy and delayed by 1μs with respect to the dissociation laser (loaned JK Hyper YAG750/PDL2).

Results and Discussion

a. Photodissociation from the S_2-Continuum

A typical rotational distribution of NO(v" = o) in the $^2\pi_{1/2}$ state from the 355nm dissociation of CH_3SNO is shown in fig C1.33. The distribution peaks near J = 43½ and is hot and rotationally inverted. A calculated statistical distribution is shown for comparison by the solid curve in fig C1.34. It is clearly dynamical rather than statistical control that gives rise to the observed rotational distribution. Similar distributions have been measured for NO(v" = 1). The fraction of NO formed in v" = 1 is small (10%) for CH_3SNO and negligible (1%) for t-buSNO.

The spin-orbit distribution shown for NO(v" = 0) from both thionitrites as a function of J in fig C1.34 is also neither statistical nor thermal. There is a clear preference for the lower spin-orbit component ($F_1 = {}^2\pi_{1/2}$) with F_2/F_1 values of 0.7 ± 0.1 for CH_3SNO and 0.8 ± 0.15 for t-buSNO. Spin-orbit ratios serve as indicators of the correlation of parent and free fragment states and are frequently affected by surface crossings. An even clearer preference for one of two energetically close components is shown by the Λ-double populations, where the antisymmetric (A") component prevails. The same preference is shown for NO(v"=1) from the photodissociation of t-buONO from the S_2-continuum, where Doppler profile studies have established the symmetry of the upper state as A'[1,2]. Fig C1.35 summarises our results for NO(v"=o) in the form of plots of the degree of electron alignment (DEA) as a function of J and compares observed and calculated values using Andresens model[4]. We have analysed Doppler profiles of several LIF lines in the O_{12} - branches using an effective anisotropy parameter β_{eff} = 0 since any alignment of the parent in the lab frame should be absent in this experiment. We suspect that the linewidths measured are too narrow and may be affected by translational relaxation of the fragments in the jet. The energy balances derived from the results we have obtained thus far are summarised in tables 1 and 2. Note that any errors will accumulate in the values given for the internal energy of CH_3S and t-buS, which must be considered upper bounds.

Table 1

Energy balance for the 355nm photodissociation of CH_3SNO in cm^{-1} (E_{avl} = 17100 cm^{-1})

			$\%E_{avl}$obs.	$\%E_{avl}$calc.*
NO($^2\pi_{\frac{1}{2}}$)	trans	>2970	>17	32.5
	rot	2350	14	23.7
	vib	< 203	< 1.2	13.0
	el	56	0.3	-
$CH_3S(^2E_{\frac{1}{2}})$	trans	>1890	>11	20.7
	internal	<9625	<57	9.7

* Tuck's impulsive model (5)

Table 2

Energy balance for the 355nm photodissociation of t-buSNO in cm^{-1}

			$\%E_{avl}$obs.	$\%E_{avl}$calc.*
NO($^2\pi_{\frac{1}{2}}$)	trans	>4169	>25	32.5
	rot	2080	12	23.7
	vib	< 37	< 0.2	13.0
	el	55	0.3	-
t-bus $^2E_{\frac{1}{2}}$)	trans	>1405	> 8	10.9
	internal	<9350	<55	19.5

* Tuck's impulsive model[5].

b. Photodissociaton from the S_1-Continuum

Preliminary results of the photolysis of t-buSNO in cw jet on the origin of the $S_1(n,\pi^*) \leftarrow S_0$ transition near 603nm (fig C1.32) have been evaluated. Fig C1.36 shows the rotational population

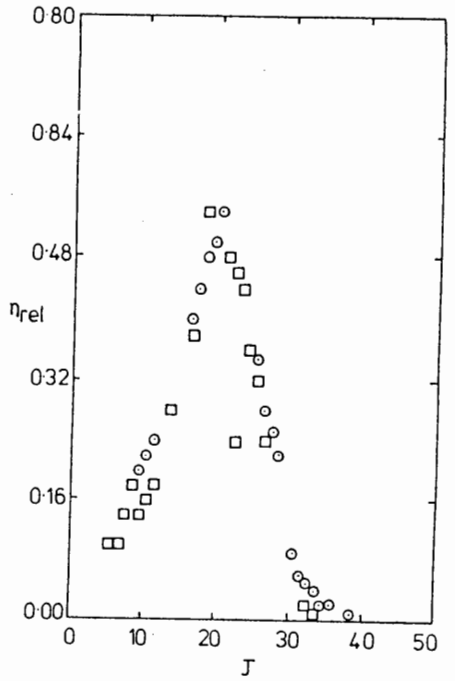


Fig C1.36 Rotational population distribution of NO(v" = o, A", $\Pi_{1/2}$o, $\Pi_{3/2}$) from the 603 nm photodissocation of t-buSNO.

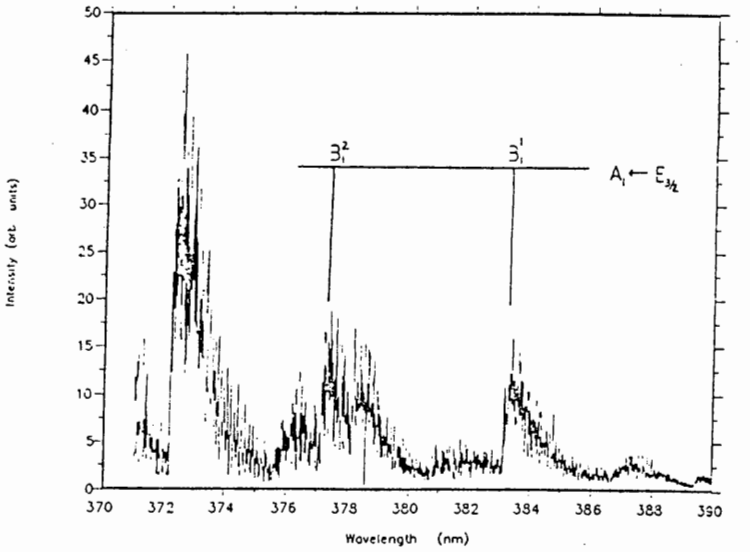


Fig C1.37 LIF excitation spectrum of rotationally relaxed CH_3S from the 560 nm photodissocation of CH_3SNO at 300 K.

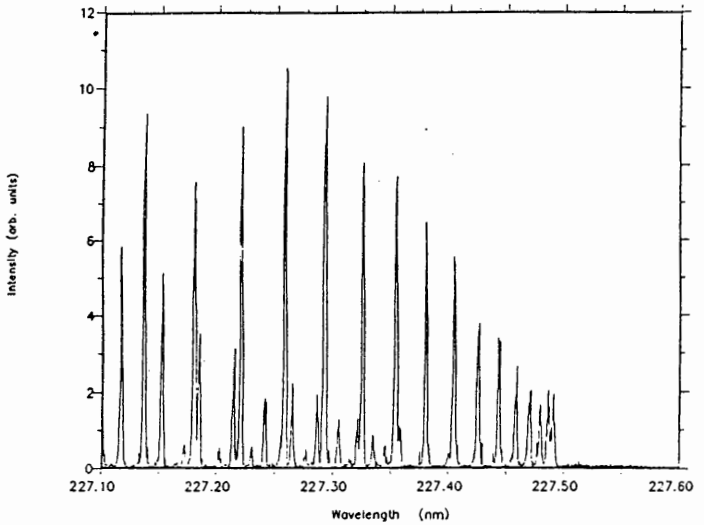


Fig C1.38 LIF excitation spectrum of NO(v" = o) from the 548 nm photodissociation of CH_3SNO.

distribution of NO(v" = o) deduced from single-photon LIF spectra that were partially saturated. The fraction of NO(v" = 1) was too small and was estimated from signal to noise ratios. The spin-orbit components of NO(v'= o) were found to be populated equally within experimental uncertainty. This behaviour clearly parallels the result for the vibrationally adiabatic dissociation of CH_3ONO, where excitation of the v' = o member of the parent's progression in the N = O stretching mode gives rise to NO(v' = o) with equal spin-orbit populations. The spectra obtained did not permit evaluation of reliable Λ-doublet ratios, and only the internal energy distribution of the NO fragment was obtained. There was insufficient time to complete this work, and we hope to return to it in the near future.

During our last, recent loan we succeeded in identifying and characterising the CH_3S radical in the 560nm dissociation of CH_3SNO. Part of its LIF spectrum is shown in fig C1.37. The complex progressions observed can be assigned to transitions from the $^2E_{3/2}$ and $^2E_{1/2}$ spin-orbit states to different levels of the ν_3' (C-S) stretching mode in the $^2A_1$ excited state. Fig C1.36 clearly shows evidence for significant population of the ν_3' = 1 mode. A more detailed analysis of the spectrum is in progress.

The 548nm dissociation of CH_3SNO in a pulsed expansion of He was studied in considerable detail using polarised photolysis and polarised LIF spectroscopy of NO with parallel and perpendicular relative polarisations of the colinear dissociation and probe laser beams. A portion of the ν(o,o) LIF spectrum of nascent NO(v" = o) is shown in fig C1.38. Preliminary analysis indicates that the NO fragment again is rotationally hot, but vibrationally cold. Doppler profiles of selected LIF transitions were recorded. Fig C1.39 shows the profile of the J" = 33½ transition of the Q_{11} and P_{21} branch of nascent NO (v" = o). We hope that these results will enable us to obtain information on the internal and translational energy of NO, on spin-orbit and Λ-doublet populations, some vector properties and the symmetry of the S_1 state.

References

1. R Lavi and S Rosenwaks, J.Chem.Phys., 89, 1416 (1988).

2. J August, M Brouard, M P Docker, C J Milne, J P Simons, R Lavi, S Rosenwaks and D Schwartz-Lavi, J.Phys.Chem., 92, 5485 (1988).

3. U Brühlmann and J R Huber, Chem.Phys.Lett., 143, 199, (1988).

4. P Andresen and E W Rothe, J.Chem.Phys., 82, 3634 (1985).

5. A F Tuck, J.Chem.Soc.Faraday 2, 73, 689 (1977).

C1.13 PHOTOFRAGMENTATION OF JET-COOLED CCl_3NO

A J Simpson, V M Young, P G Harper and J Pfab
(Dept of Chemistry and Physics, Heriot-Watt University)

Introduction

The objectives of this work are to recorded fluorescence and photofragment yield spectra of predissociating NO-containing molecules. The predissociation of jet-cooled C-nitroso compounds occurs on the nano- to microsecond time scale[1-2]. Most of these molecules reveal structured electronic spectra in the visible, emit fluorescence in the 650 to 900nm region and dissociate producing alkyl radicals and ground state NO($X^2\pi_{\frac{1}{2}}$). These molecules are unique in providing spectroscopic information on their S_1 and S_0 states via fluorescence excitation and dispersed fluorescence spectroscopy, fluorescence decay times of single vibronic levels and fragment yield spectra.

This report covers work carried out between January and February 1989 with the JK Hyper YAG 750/PDL2 loan laser. During this time we have recorded NO fragment yield spectra of jet-cooled CCl_3NO in

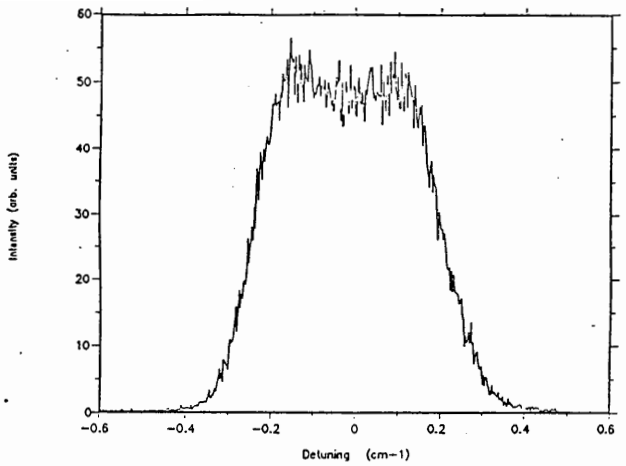


Fig C1.39 *Doppler profile of the J" = 33.5 transition of the Q_{11} + P_{21} branch of nascent NO (v" = o) from the 560 nm photodissociation of CH_3SNO.* $\hat{\epsilon}_p \parallel \hat{\epsilon}_a$.

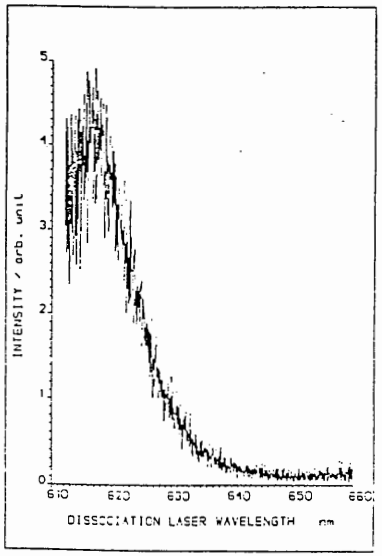


Fig. C1.40 Part of the NO photofragmetn yield spectrum of jet-cooled CCl_3NO (TCNM). The spectrum has been normalised to the power of the scanning dissociation laser.

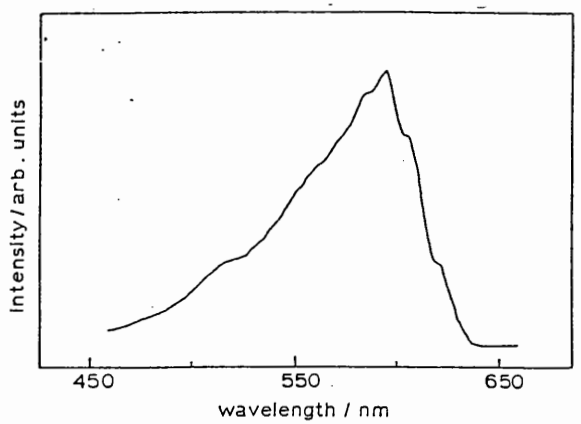


Fig. C1.41 Electronic absorption spectrum of TCNM in a hydrocarbon glass at 80 to 100K

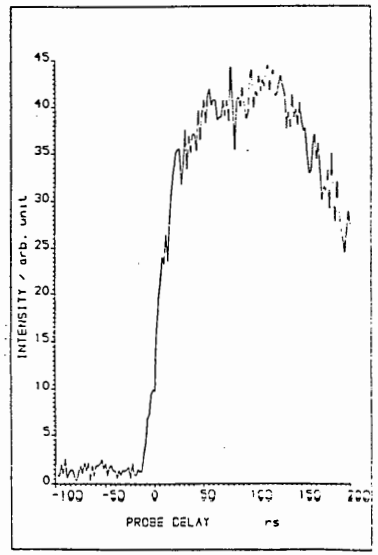


Fig. C1.42 Appearance curve of the NO fragment from the pulsed dissociation of jet-cooled TCNM at 620nm. The fast rise is due to the appearance of the nascent NO within the duration of the laser pulse while the slower decay is due to fly-out effects.

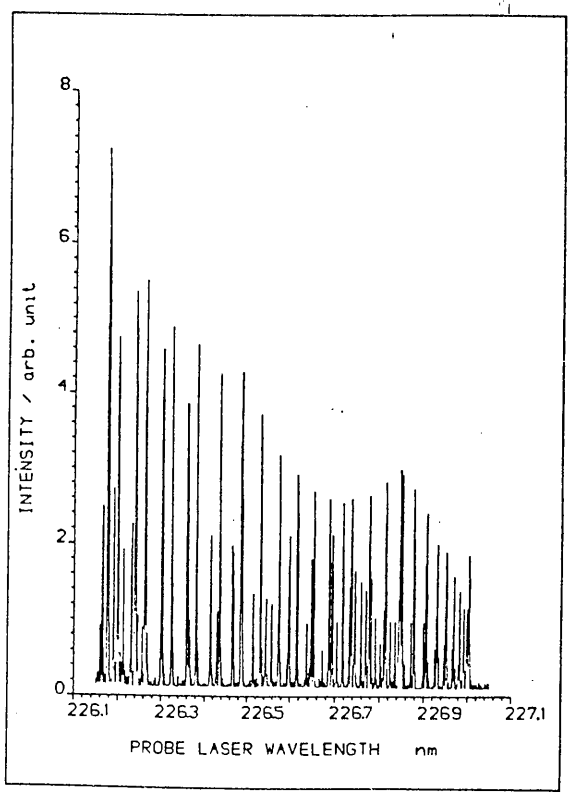


Fig. C1.43 Part of the v(o,o) LIF excitation spectrum of nascent NO from the photodissociation of jet-cooled CCl_3NO at 608nm ($\hat{e}_p \parallel \hat{e}_a$).

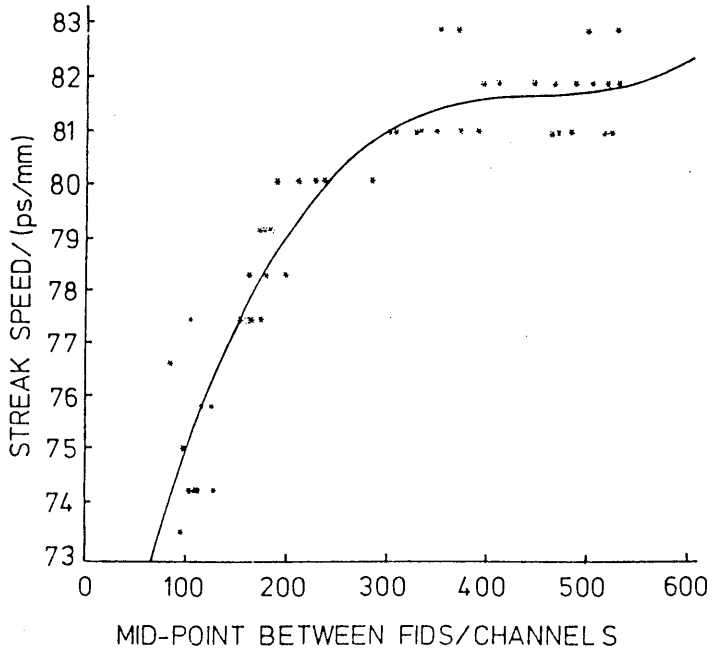


Fig. C1.45 Linearity of streak speed at 100ps/mm.

the range 555 to 670nm and LIF excitation spectra of nascent NO from the photodissociation of this molecule at several wavelengths. Results of appearance time measurement for nascent NO will also be reported briefly. The analysis of these results will take some time and will be reported later.

Experimental

CCl_3NO (trichloronitrosomethane, TCNM) was jet-cooled by pulsed expansion of 4% by volume mixtures of the vapour with He or Ar. The jet was crossed 10 to 30 nozzle diameters downstream of the orifice (0.5mm) of a commercial pulsed valve (NRC, model BV-100) by the counterpropagating colinearly aligned dissociation (loaned Nd-YAG pumped dye laser) and probe beams (frequency doubled excimer pumped dye laser, Lambda Physik EMG 101/FL3002). The photolysis beam was focused by a 30cm focal length lens. Typical pulse energies used were 5 to 15mJ in the range 560-570nm for photolysis and 10 to 20nJ in a 0.5 to 1mm beam for probing near 225nm.

Photofragment yield spectra of CCl_3NO were recorded by scanning the photolysis laser while exciting LIF of NO ($X\ \pi_i$) on a bandhead of the $A^2\Sigma^+(v'' = 0) \leftarrow X\ ^2\pi_i(v'' = 0)$ transition. The polarisation of the probe laser was rotated with a Fresnel rhomb, while the dissociation laser was kept vertically polarised. Fluorescence of the ν-bands near 250nm was collected by a doublet of planoconvex lenses and imaged onto the photcathode of a Hamamatsu R166Uh solar blind photomultiplier, using a Schott reflection filter.

Results and Discussion

Preliminary experiments with the dissociation laser tuned to 560nm indicated that CCl_3NO photodissociates readily, and nascent NO could be detected with good signal to noise ratio when the parent was jet-cooled by expansion with 200 to 400 Torr Ar. NO product yield spectra were obtained in the wavelength region 555-670nm with a delay of 100ns between photolysis and probe laser. These spectra showed no evidence of vibrational structure and were continuous even close to the long wavelength onset of the NO yield between 630 and 640nm. Under identical conditions CF_3NO provided structured, well resolved NO yield spectra. We also ruled out the possibility that lack of vibrational structure in the CCl_3NO spectrum was due to clustering or complexation of the parent under the mild expansion conditions used by substituting AR by He (4% TCNM in 400 Torr He). Figure C1.40 shows the long wavelength part of the NO yield spectrum. This can be compared with the electronic absorption spectrum of CCl_3NO in a hydrocarbon glass at 80 to 100K (Figure C1.41), which reveals evidence of faint vibrational failures. Preliminary attempts to see fluorescence in the red failed under conditions where CF_3NO emission was detected readily indicating that the quantum yields for emission must be much lower for TCNM. We conclude therefore that the $S_1(n\pi^*) \leftarrow S_0$ transition of TCNM in the visible is heavily predissociated and for all practical purposes continuous. This is confirmed by appearance rate measurements which have been made at several wavelengths. Figure C1.42 presents the results of a measurement of 620nm of the intensity of the NO LIF signal as a function of the delay time between photolysis and probe laser. The convolution the two laser pulses is expected to give a Gaussian with a half-width of about 25 to 30ns. Thus NO is clearly formed promptly within the duration of the laser pulse, and the lack of fluorescence of the $\tilde{A}(n,\pi^*)$ state of TCNM can be attributed to a rapid nonradiative transition leading to dissociation of the weak C-N bond.

We have then recorded LIF excitation spectra of the nascent NO photoproduct using photolysis at 608 and 620nm. Spectra recorded with parallel and perpendicular probe laser polarisation were identical leading us to conclude that the alignment of the NO fragment is not strong and that photodissociation occurs on the time scale of 1ps to 10ns. Figure C1.43 presents part of the LIF excitation spectrum of $NO(v^* = 0)$ from the photolysis of TCNM at 608nm. Spectra were recorded at nozzle distances from 3 to 13mm to ensure that relaxation did not affect the rotational distributions of the NO fragment. The analysis of these spectra is in progress and will provide rotational, spin-orbit and Λ-doublet populations of the NO fragment.

In conclusion, we have shown that the photochemistry and photophysics of TCNM is drastically different from the fluorine

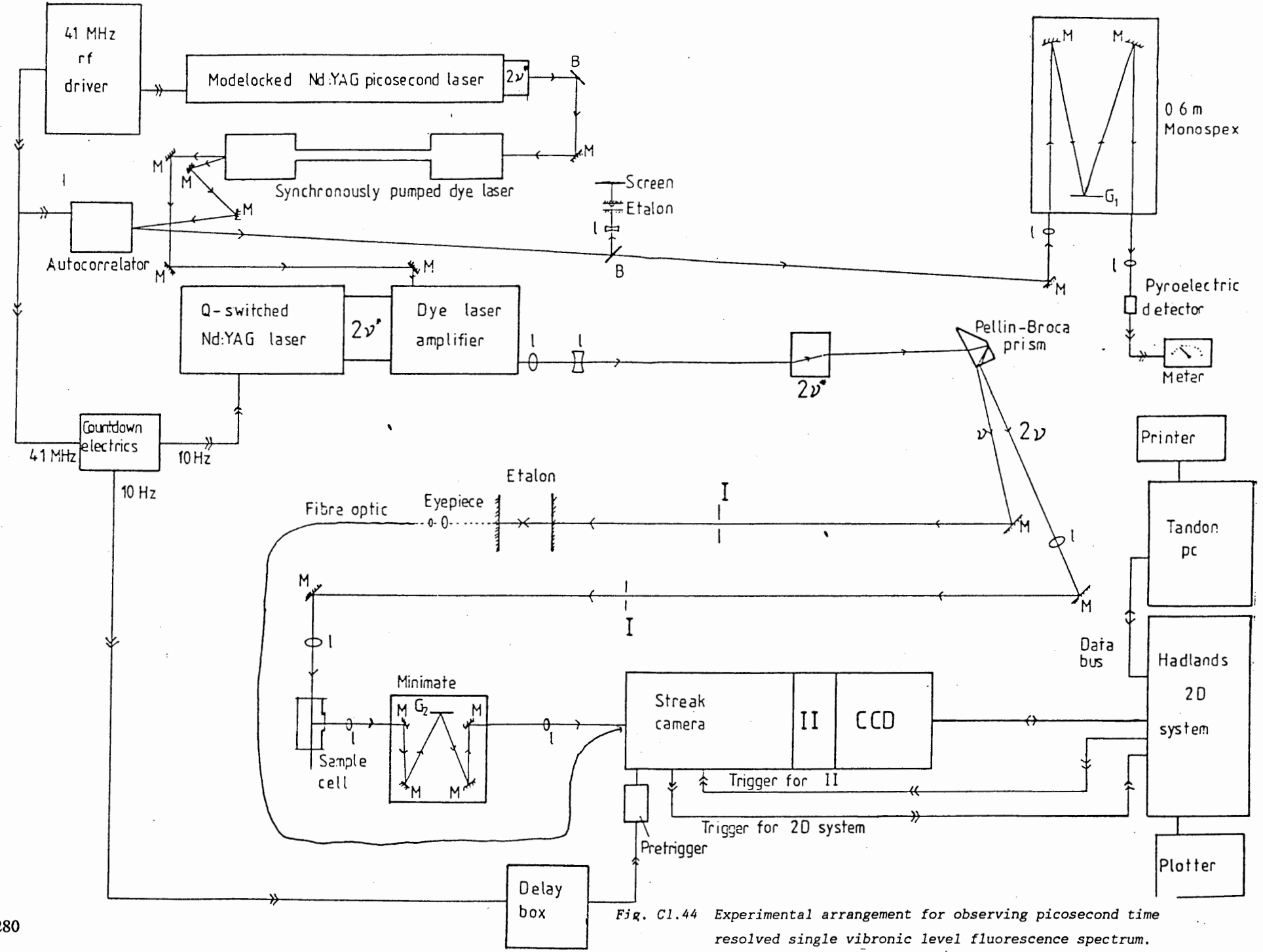


Fig. C1.44 Experimental arrangement for observing picosecond time resolved single vibronic level fluorescence spectrum.

containing nitrosomethanes we investigated earlier[1,2]. Photo-dissociation occurs much more rapidly, and the excited state no longer appears to support well defined vibronic structure. This indicates that the topology of the $\tilde{A}(n,\pi^*)$ state of CCl_3NO differs appreciably from that of the fluoronitrosomethanes.

References

1. J A Dyet, M R S McCoustra and J Pfab, J.Chem.Soc., Faraday Trans. 2, 1988, 84, 463.

2. M R S McCoustra, J A Dyet and J Pfab, Laser Chem., 1988, 9, 289.

C1.14 PICOSECOND SINGLE VIBRONIC LEVEL FLUORESCENCE SPECTROSCOPY

J M Hollas and P F Taday (University of Reading)
A J Langley, K Moore, W Shaikh and W T Toner (RAL)

Introduction

This report contains work done with the picosecond laser and the Imacon 500 streak camera, in sessions II and III in 1988 and session I in 1989, and is a continuation of the work reported in ref. 1.

We have chosen styrene, $C_6H_5HC = CH_2$, as the molecule we wish to study. This molecule has been well characterized in the ground, S_0, and excited, S_1, electronic states[2,3]. It is a characteristic of molecules which undergo intramolecular vibrational relaxation (IVR)[1] that the observed bands become more diffuse with increasing vibrational energy in S_1. Initially, work has been concerned with the excitation of the pure electronic transition in styrene to the zero-point level of S_1 which does not undergo IVR. Later work will be concentrated on exciting higher vibronic levels in S_1 in which IVR should be important.

Further Development of Experimental Method

Figure C1.44 shows the experimental arrangement used in these experiments. The Spectra Physics 3460 Nd:YAG picosecond laser synchronously pumps the dye laser. The wavelength of the dye laser is set using a 0.6m Spex monochromator with a 2400 lines/mm grating blazed at 250nm. This allows the wavelength of the dye laser to be set to within 25 cm^{-1} of a desired transition. The picosecond pulses from the dye are amplified by the Quanta-Ray Q-switched Nd:YAG pulsed dye amplifier system. The amplified radiation is then frequency doubled, the fundamental and doubled radiations being separated with the use of a quartz Pellin-Broca prism. This system produces 30-100μJ pulses at 287nm, but with a pulse-to-pulse variation of 20-40%. The visible radiation is used for timing fiducials for the streak camera. At first this was achieved by the use of an etalon consisting of two half-silvered mirrors of variable separation, with the reflection from the surfaces of the etalon being focused into a single-mode fibre optic, the end of the fibre being placed at the entrance slit of the streak camera. However, it was later found to be more convenient to use a Michelson interferometer and a multi-mode fibre to produce the required timing fiducials. The UV radiation is directed into a +-shaped cell containing styrene at its vapour pressure (10 Torr at 297 K). The fluorescence from the molecule is observed in two directions perpendicular to the laser beam and in a horizontal plane. In one direction the fluorescence is detected by an EMI 9789 QB photomultiplier tube which is used to fine tune the dye laser to the desired transition. In the other direction the fluorescence is focused into an f/4 Spex Minimate spectrometer, with either a 1200 or 2400 lines/mm grating, both blazed at 250nm. This dispersed spectrum is then focused onto the entrance slit of the streak camera. The streaked image is amplified by a factor of 1000 by an image intensifier (II) and detected by a charge-coupled device (CCD). The image from the CCD is read electronically to the Hadlands 2D microcomputer. The image can then be transferred to a Tandon pc where data reduction and analysis can take place. The synchronization between the arrival of the fluorescence pulse and the streaking of the camera is achieved electronically. The

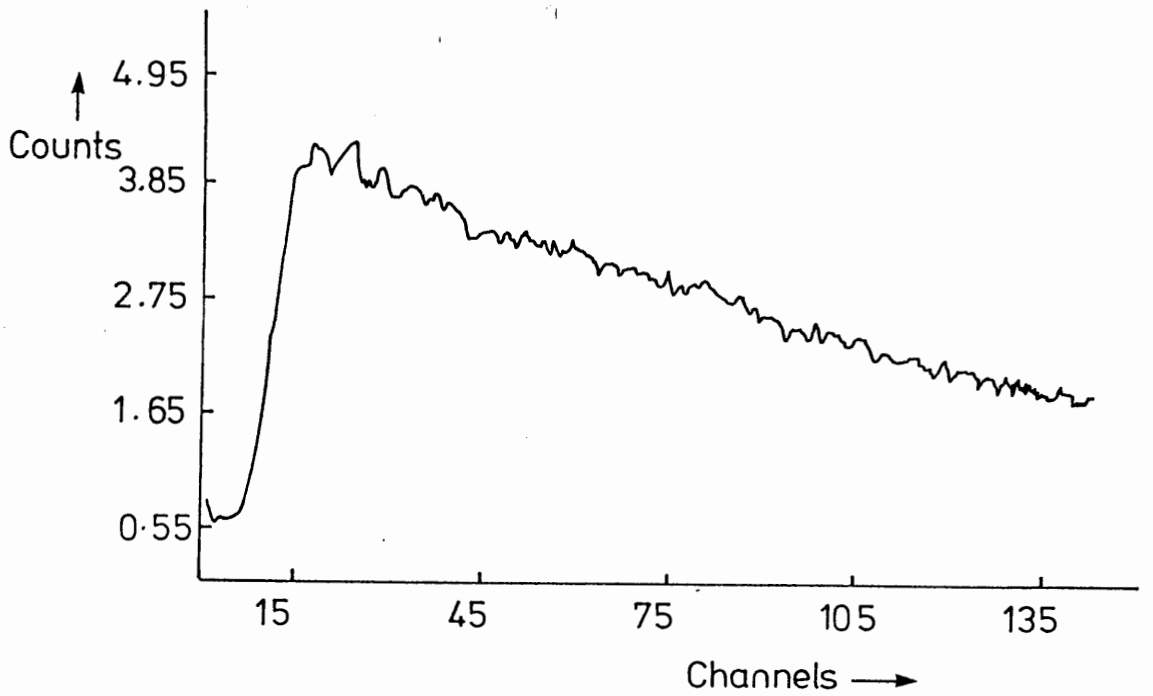


Fig. C1.46 Fluorescence decay from the zero-point level of the S_1 electronic state in styrene at 34 760 cm^{-1}. The lifetime of decay is 8ns.

initial electronic signal is obtained from the 41 MHz rf signal from the mode-locked driver. This is divided down into a 10 Hz signal which is used to trigger the Q-switched Nd:YAG laser and provide a trigger signal for experiments. Initially the pulse was taken directly from the countdown electronics box, amplified, and used to trigger the streak camera. But it was found that the time jitter between the arrival of the fluorescence and the streaking of the camera was about 100-150ps. This was later reduced to 50ps by the introduction of a constant fraction discrimination (CFD), which is used on the 41 MHz rf signal with the CFD gates with the 10 HZ signal from the countdown electronics.

Results

Linearity of streak rate

As is expected with most streak camera systems we observe a variation of streak speed across the streak image. Figure C1.45 was recorded with a camera slit width of 25μm, a streak speed of 100 ps/mm and a laser wavelength of 580nm. The fiducials were 313ps apart and the mid-point of the fiducials was moved by varying the delay on a delay box. From the graph it is possible to find the average streak speed $\frac{\Delta x}{\Delta t}$ at a particular channel of the CCD(x).

We can then deconvolute the signal obtained from the CCD to give the true fluorescence decay I(t) where

$$I(t)\Delta t = I(t)\,\frac{\Delta t}{\Delta x}\,\Delta x = i(x)\Delta x$$

Hence

$$I(t) = i(x)\,\frac{\Delta t}{\Delta x}$$

where i(x) is the measured fluorescence as a function of channel number and $\frac{\Delta t}{\Delta x}$ is the streak rate as a function of channel number x.

Fluorescence from the zero-point level of the S_1 electronic state of styrene

To allow for large amounts of data acquisition we are able to run the computer and CCD in a binning mode (see ref. 4 for a detailed description). Each framelet in a frame may then be added together, correcting for time jitter, background and sensitivity of the CCD. Figure C1.46 shows the fluorescence decay with excitation in the pure electronic transition, at 34 760 cm^{-1}. The lifetime of this decay was found to be approximately 8ns which is lower than the previously published value[5,6] of 20ns. This is due to the fact that our experiment is not done under collision-free conditions, and the lifetime of the state is limited by collisional deactivation. The high pressure of styrene (10 Torr at 297 K) must be used to obtain sufficient signal to observe a decay with the streak camera.

In addition to observing the temporal response of the styrene fluorescence, we are also able to observe the frequency response of the decay. If we integrate over all time we obtain the dispersed fluorescence spectrum in figure C1.47. This shows some rather broad features due to the decay from the excited state into vibrational levels in the ground state. The broadness of the spectrum is due to the resolution of the system being only about 2nm.

Time spread

The introduction of the Minimate spectrometer decreases the time resolution of the system[7-9]. The time spread T_s, due to the grating is given by

$$T_s = \frac{D\,m\lambda}{cd}$$

where D is the effective aperture of the grating, d^{-1} is the number of lines/mm, λ is the wavelength, m is the order, and c is the speed of light.

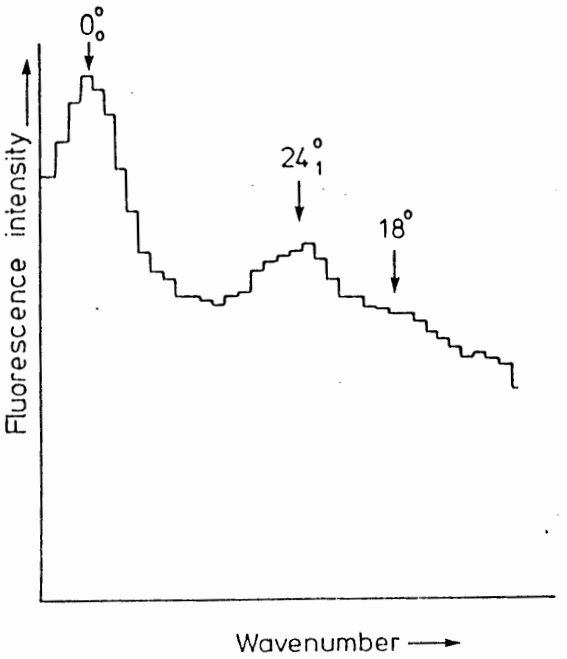
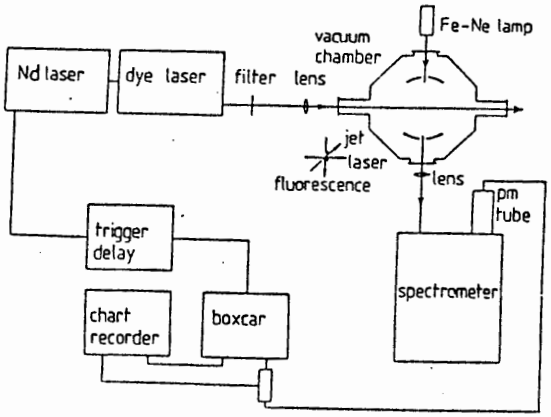


Fig. C1.47 *Dispersed fluorescence spectrum from the zero-point level of the S_1 electronic state in styrene.*



C1.48 *Experimental arrangement for fluorescence excitation and single vibronic level fluorescence spectra of molecules in a supersonic jet.*

For a 50mm, 1200 lines/mm grating working in the first order at a wavelength of 287nm, the time spread due to the grating is 57ps. This will limit the ultimate time resolution of the system

Conclusion

We have shown here that we are able to obtain a time and frequency resolved spectrum of excitation in the pure electronic transition in styrene in the vapour phase. In future experiments it is hoped to improve the time and frequency resolution of the system, as well as to excite into higher vibronic levels of the S_1 electronic state.

Acknowledgments

We would like to thank Dr A Beeby, of the Royal Institution, for his help with the development of the user software.

References

1. J M Hollas, P F Taday, A J Langley and W T Toner, Annual report to the Laser Committee 1988, paper B1-1, 155.

2. T R Gibson, J M Hollas, E Khalipour and J V Warrington, J.Mol.Spectrosc. 73, 234 (1978).

3. J M Hollas and T Ridley, J.Mol.Spectrosc. 89, 232 (1981).

4. A J Langley, D N Sansom and W T Toner, Annual report to Laser Committee 1988, paper B5-6, 270.

5. R P Steer, M D Swords, P M Crosby, D Philips and K Salisbury, Chem.Phys.Lett. 43 (3), 461 (1976).

6. M H Hui and S A Rice, J.Chem.Phys. 61 (3), 833 (1974).

7. Y Tsuchiya, IEEE J.Quantum Electron. QE20 (12), 1516 (1984).

8. P Saari, J Aaviksoo, A Fresberg and K Timpmann, Optics Comm. 39 (1,2), 94 (1981).

9. N H Schiller, Y Tsuchiya, E Inuzaka, Y Suzaki, K Kinoshita, K Kamiga, H Iida and R R Alfano, Optical Spectra, 55, June 1980.

C1.15 DISPERSED FLUORESCENCE AND FLUORESCENCE EXCITATION SPECTROSCOPY IN A SUPERSONIC JET

K H Hassan, J M Hollas, M Z bin Hussein and P F Taday

Introduction

The supersonic jet was first developed for use in spectroscopy by Klemperer et al. for studying rotational transitions, in the microwave and radiofrequency regions of the spectrum, of species such as van der Walls and hydrogen-bonded complexes. The techniques was extended for use in electronic spectroscopy by Levy et al[1].

In a supersonic jet a monatomic gas, such as helium or argon at typically a few atmospheres pressures is pumped through a nozzle containing a pinhole of the order of 100 μm in diameter. Collisions in the region of the pinhole convert the random motions of the atoms into directional flow with a much reduced velocity range. As a result the translational temperature T_r of the resulting jet is extremely low and can be less than 1K. Since the local speed of sound 'a' is given by

$$a = \left(\frac{\gamma k T_{tr}}{m}\right)^{1/2} \qquad (1)$$

where $\gamma = C_p/C_v = 5/3$, and the Mach number M is related to the mass flow velocity 'u' by

$$M = u/a \qquad (2)$$

the small value of T_{tr} results in high M, of the order of 100.

If a molecular gas is seeded into the atomic gas before the nozzle, it also is cooled to a similar transitional temperature. Cooling of the rotational degrees of freedom of the molecules is less efficient but rotational temperatures, T_{rot}, of about 10K are easily obtained. Vibrational cooling is still less efficient so that vibrational temperatures, T_{vib}, of about 100K are typical.

Fluorescence of the seeded molecules can be excited by intersecting the jet, which may be continuous or pulsed, with a laser beam. If the laser wavenumber is tuned continuously across the absorption spectrum, while detecting total, undispersed fluorescence, a fluorescence excitation (FE) spectrum is obtained which is similar to the corresponding absorption spectrum. An FE spectrum gives information regarding vibrational levels in the excited electronic state.

Because of the nature of the directed mass flow in a supersonic jet the conditions are virtually collision-free. In particular, there are not likely to be any atom-molecule collisions during the fluorescence lifetime of the molecule. Therefore, if the laser wavenumber is tuned to match an absorption band taking the molecule to a single vibronic level in the excited electronic state, fluorescence will occur from that level only and is known as single vibronic level fluorescence (SVLF). Such SVLF spectra provide vibrational information largely about the ground electronic state.

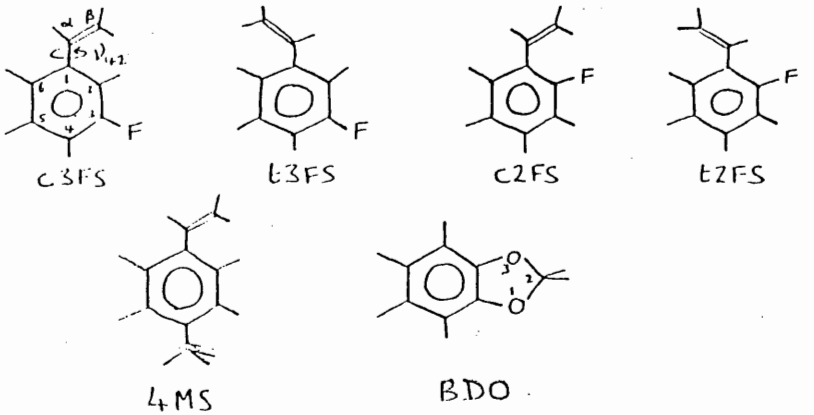
Experimental Method

For all the work reported here we have used the Quantel Datachrom Nd:YAG pumped dye laser, with frequency doubling and, for SVLF spectra, autotracking, from the Laser Facility Loan Pool.

The experimental arrangement is shown in Fig C1.48. The 0_0^0 bands (pure electronic transitions) of the spectra to be studied all lie in the region of 280 nm necessitating the use of frequency doubled dye laser radiation from rhodamine 590 or, for rather higher wavelengths, a 590/610 mixture. The supersonic jet, with helium as the carrier gas at a pressure of about 1.4 atm, is continuous and is directed vertically downwards into a 250 mm diffstak backed by a booster/rotary pump combination. Fluorescence is collected from the region of intersection of the jet and laser beam by four concave mirrors. For FE spectra, with the laser scanned across the absorption spectrum, the total fluorescence is collected with the spectrometer grating set to zero angle while, for SVLF spectra, the laser wavenumber is fixed and the spectrometer grating scanned. The signal from the PM tube is processed by an SRS boxcar averager.

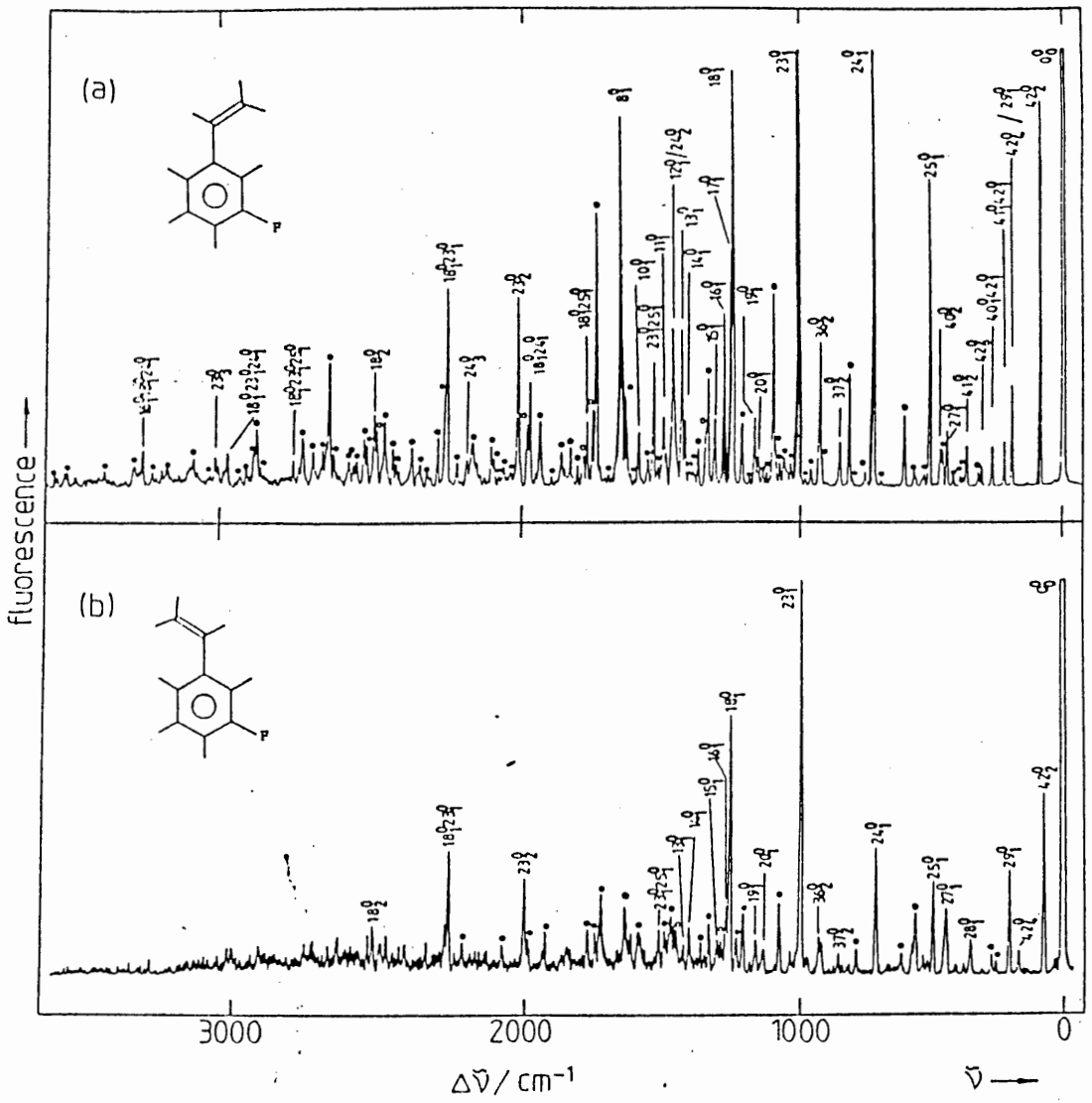
Results

In this work we have been concerned with the electronic transitions between the ground singlet state (S_0) and the first excited singlet state (S_1) of cis and trans 3-fluorostyrene (c3FS and t3FS), cis and trans 2-fluorostyrene (c2FS and t2FS), 4-methylstyrene (4MS) and 1,3-benzodioxole (BDO) which are shown below:

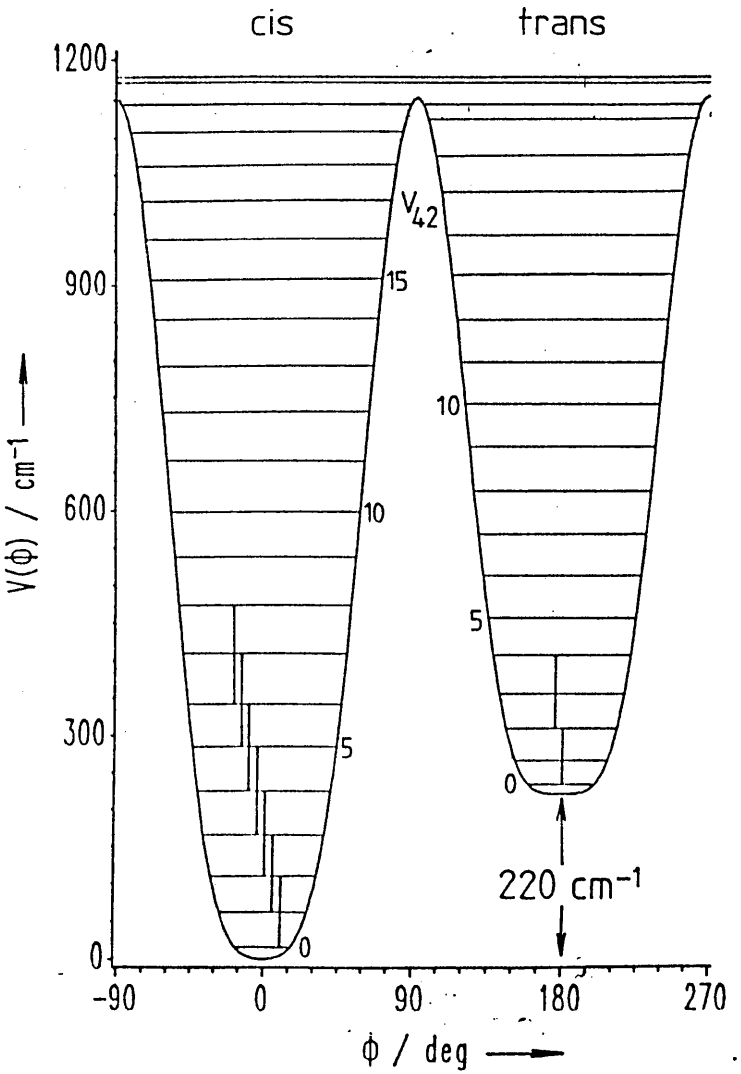


3-Fluorostyrene

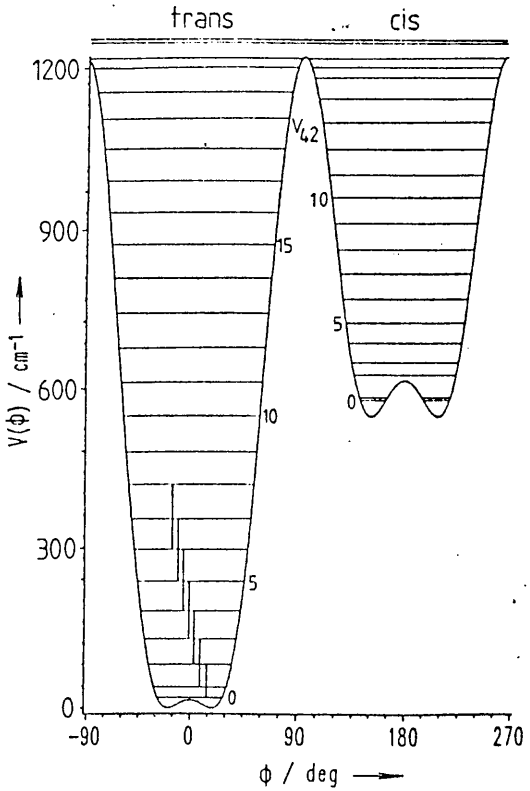
In principle 3Fs can exist as the cis and trans rotational isomers (rotamers) shown although, prior to our work, there was no evidence for two rotamers. Change from one to the other can be brought about by torsional motion about the C(1)-C(α) bond through the vibration ν_{42}.



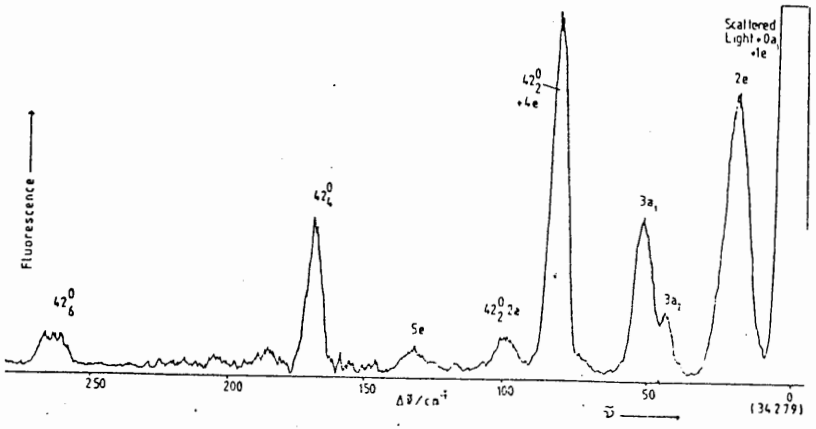
C1.49 Single vibronic level fluorescence spectra of (a) cis-3-fluorostyrene and (b) trans-3-fluorostyrene.



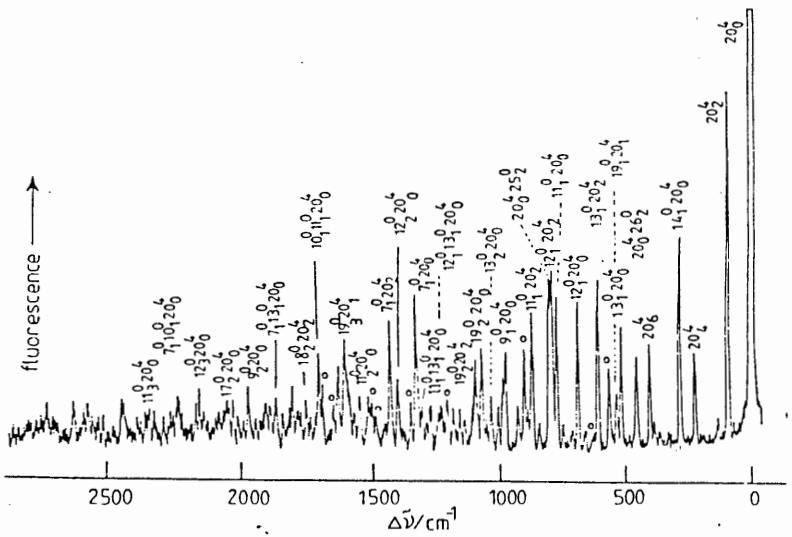
C1.50 Torsional potential function for 3-fluorostyrene.



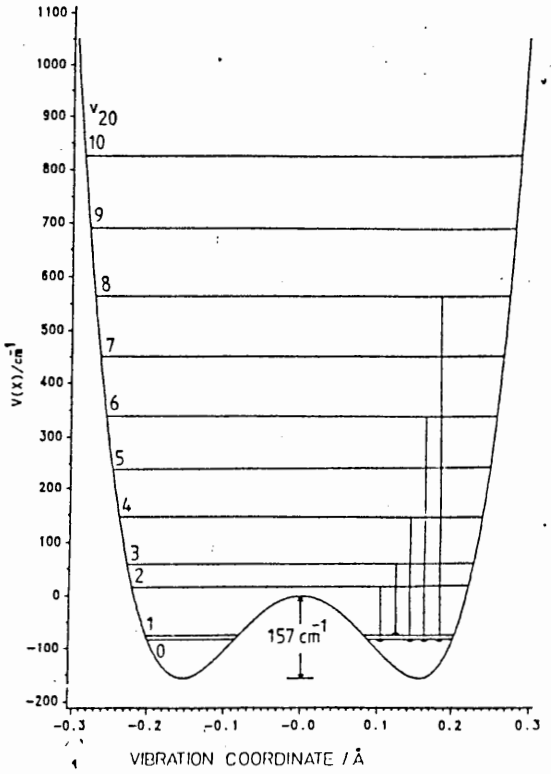
C1.51 Torsional potential function for 2-fluorostyrene.



C1.52 Single vibronic level fluorescence spectrum of 4-methylstyrene.



C1.53 Single vibronic level fluorescence spectrum of 1,3-benzodioxole.



C1.54 Potential function for a_2 oxygen-twisting vibration of 1,3-benzodioxole.

From the FE spectrum of 3Fs we found the 0_0^0 bands of the two rotamers. The bands are separated by 275 cm^{-1} and have an intensity ratio of about 3:1. The SVLF spectra with excitation in each of these bands is shown in Fig C1.49. From theses, and other SVLF spectra, we were able to observe progressions in ν_{42} up to ν_{42} = 8, in the more abundant, and up to ν_{42} = 4 in the less abundant rotamer with appreciably different intervals. The intervals were fitted to a torsional potential of the form

$$V(\phi) = \tfrac{1}{2}\,[V_1\,(1-\cos\phi) + V_2\,(1-\cos 2\phi) + V_4\,(1-\cos 4\phi)] \qquad (3)$$

where V_1 = 220±50 cm^{-1}, V_2 = 1040±80 cm^{-1} and V_4 = -247±10 cm^{-1}, shown in Fig C1.50. The value of V_1 represents the energy difference between the two rotamers and, assuming the room temperature ratio of the rotamers is maintained in the jet, leads to a 3:1, cis : trans ratio, as is observed. If the more stable rotamer is taken to be trans then we obtain V_1 = 467 cm^{-1} and an expected trans : cis ratio of 10:1. Therefore we conclude that cis is more stable than trans. The cis → trans barrier height is $V_2 + \tfrac{1}{2}V_1$ = 1150 cm^{-1}.

The large, negative value of V_4 leads to a very flat-bottomed minima for both rotamers, as in styrene itself[2]. Both rotamers are planar, but only just.

2-Fluorostyrene

As with 3FS, 2Fs may also exist as the cis and trans rotamers shown but steric hindrance by the fluorine atoms would seem to make t2FS much more likely.

From FE and SVLF spectra of 2Fs we have found one rotamer only, the trans form. Once again the C(1)-C(α) torsional potential function is of the form in eq.(3). We estimate that c2FS could be present as up to 5%, but escape detection, and this leads to $V_1 \geq 600$ cm^{-1}. We assumed V_1 = 600 cm^{-1} and fitted torsional vibrational levels of t2FS up to v = 8 to the potential function and obtained V_2 = 895±30 cm^{-1} and V_4 = -333±10 cm^{-1}. The potential function is shown in Fig C1.51. One of the most interesting features of this is that t2FS is non-planar. There is a barrier to planarity of 15±4 cm^{-1}. When this is just below the zero-point level, as is the case here, the molecule is referred to as quasi-planar. The potential function shows that c2FS is expected to be much more non-planar.

4-Methylstyrene

In 4MS there is, in addition to the C(1)-C(α) torsional motion, a torsional motion of the methyl group. In Fig C1.52 is shown part of the SVLF spectrum of 4MS with excitation in the almost coincident $0a_1$-$0a_1$ and 1e-1e bands, where a_1 and e refer to symmetry species of the methyl torsional levels. As well as a progression in the C(1)-C(α) torsional vibration ν_{42} up to v = 6 in S_0, there is a series of transitions to the methyl torsional levels 2e, $3a_2$, $3a_1$, 4e and 5e in S_0. Fitting of the C(1)-C(α) torsional levels to

$$V(\phi) = \tfrac{1}{2}[V_2\,(1-\cos 2\phi) + V_4\,(1-\cos 4\phi)] \qquad (4)$$

gives V_2 = 943 cm^{-1} and V_4 = -208 cm^{-1}. This is, again, a flat-bottomed potential due to the large negative value of V_4 but the barrier height of 943 cm^{-1} is less than that of 1070 cm^{-1} in styrene[2].

The methyl torsional levels have been fitted to

$$V(\phi) = \tfrac{1}{2}\,V_6(1-\cos 6\phi) \qquad (5)$$

with V_6 = 17 cm^{-1}, a considerably higher barrier than that of 10 cm^{-1} found for toluene[3].

Work is still proceeding with a view to observing more torsional levels (involving the methyl and vinyl groups) in S_0 and also more methyl torsional levels in S_1.

1,3-Benzodioxole

Previous work on the far infra-red spectrum of BDO[4] was concerned with whether the molecular skeleton is planar with respect to puckering of the carbon atom in the 2-position in the five-membered ring. It was concluded that it is planar and that the whole skeleton is planar also. But this conclusion is not consistent with the extreme vibrational complexity of the S_1-S_0 absorption spectrum in the gas phase[5].

We have obtained the S_1-S_0 FE spectrum in a supersonic jet and this shows a long progression indicating an important geometry change from S_0 to S_1. In Fig C1.53 is shown one of the SVLF spectra, obtained with the laser tuned to a band labelled 20_0^4 in the FE spectrum. The SVLF spectrum shows a progression 20_0^4, 20_2^4, 20_4^4, and 20_6^4 which is very anharmonic and which involves ν_{24} the a_2 out-of-plane twisting vibration of the oxygen atoms. The anharmonic behaviour indicates that the oxygen atoms are twisted out-of-plane in the ground electronic state, a structure which had not previously been suspected.

The energy levels in ν_{20}, up to $v = 8$, have been fitted to a W-shaped potential function

$$V(x) = Ax^2 + Bx^4 \qquad (6)$$

with $A = -13185$ cm^{-1} Å^{-2} and $B = 276106$ cm^{-1} Å^{-4} and shown in Fig C1.54. The barrier height is 157 cm^{-1} and the equilibrium out-of-plane distance of the oxygen atoms is 0.16 Å.

Acknowledgements

We are very grateful to Dr A J Langley and Mr W Shaikh for setting up and maintaining the Datachrom laser system.

References

1. R E Smalley, L Wharton and D H Levy, Acct.Chem.Res., 10, 139 (1977).

2. J M Hollas, H Musa, T Ridley, P H Turner, K H Weisenberger and V Fawcett, J.Mol.Spectry., 94, 437 (1982).

3. P J Breen, J A Warren, J I Seeman and E R Bernstein, J.Chem.Phys., 87, 1917 (1987).

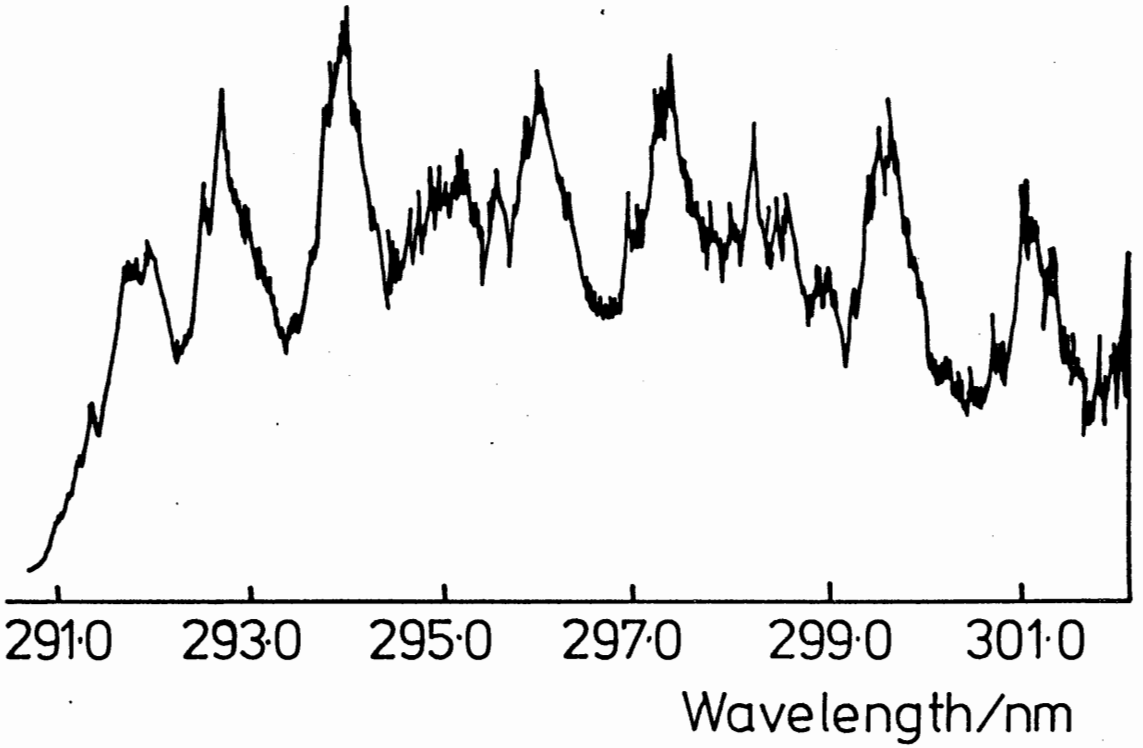
4. J A Duckett, T L Smithson and H Weiser, Chem.Phys.Lett., 64, 261 (1979).

5. A C P Alves, J M Hollas and B R Midmore, J.Mol.Spectry., 77, 124 (1979).

C1-16 LASER EXCITATION SPECTROSCOPY OF TRANSITION ELEMENT HALIDES IN SUPERSONIC BEAMS

F J Grieman, L R Zink and J M Brown (Oxford) T R Gilson and I R Beattie (Southampton)

Many first row transition element chlorides can be vaporized to give a few torr pressure at high temperatures below 1000°C. In our experiments, these molecules are seeded into a high pressure (several atmospheres) of an inert gas, followed by expansion through a jet into a rapidly pumped vacuum system. In this way the rotational and, to a lesser extent, vibrational energy is converted into translational energy. Such an isentropic expansion results in rotationally cold molecules (~ 10K). The jet is irradiated with the beam of a narrow band tuneable dye laser and the resultant fluorescence recorded (laser excitation spectroscopy). The excimer pumped dye laser at the LSF has been used in this way to record survey spectra of several species. It has even been possible to resolve rotational structure by the use of the intra-cavity etalon.



C1-55 Ultra-violet band system of $CoCl_2$

Three separate visits have been made to the LSF in the current year to carry out experiments of this type. Spectra for several molecules have been obtained including $NiCl_2$, CuCl, $FeCl_2$, $CoCl_2$ and InCl. To help the interpretation of these spectra, radiative lifetimes of each of these species have also been determined using a boxcar averaging system with a 10nsec gate.

Two experimental developments have enabled the first observations of the ultraviolet band systems of $FeCl_2$ and $CoCl_2$ to be made. First, the persistent clogging problems experienced in the past have been overcome with a new alumina nozzle system and specially prepared samples consisting of large, anhydrous crystals. Secondly, the use of the BBO crystal for frequency doubling with the pulsed dye laser has allowed observations to be made a shorter wavelengths (<340 nm) where the electronic transitions lie. Excellent resolution and signal-to-noise ratios have been obtained. The complete UV system of $CoCl_2$ (291 - 314 nm) has now been observed and is under analysis; part of the vibrational band structure is shown in figure C1.55.

The $FeCl_2$ system is more extensive ($\sim$ 260 - 295 nm) and quite likely consists of more than one electronic transition. Only a broad survey scan has been made so far. Some regular propressions can be identified but much further work, including dispersion of the fluorescence is needed. It is interesting to note that, although $CoCl_2$ can been formed efficiently from the reaction of CCl_4 with hot cobalt, the same is not true for $FeCl_2$

Most of the work has been on the electronic spectra of $NiCl_2$. A strong absorption system around 365 nm had been recorded previously but proved difficult to analyse. It was hard to pick out either vibrational propressions or chlorine isotope structure.

Some experiments have therefore been done using isotopically enriched ^{35}Cl and ^{37}Cl compounds to identify the bands concerned. Even with this help, the isotopic structure is far from obvious. It is nevertheless present and there is no real doubt that the transition involves $NiCl_2$. However, we have also been able to detect a weaker system in $NiCl_2$ at longer wavelengths around 460 nm (in the blue). This system shows a much more regular band structure arising we believe from vibrational and spin-orbit fine structure. Furthermore, it shows a comprehensive isotope structure, consistent with a linear structure in both upper and lower electronic states. Aided by dispersed fluorescence and lifetime studies, our understanding of this band system is now well-advanced. When the analysis is completed, we should stand a much better chance of sorting out the more complicated UV system since it appears that both involve the same lower state (presumably the ground state).

C1.17 LASER SPECTROSCOPY AND PHOTOPHYSICS OF INTRAMOLECULAR CHARGE TRANSFER SYSTEMS UNDER JET-COOLED CONDITIONS

B D Howells, T F Palmer, J P Simons and A Walters
(Dept of Chemistry, University of Nottingham)

Introduction

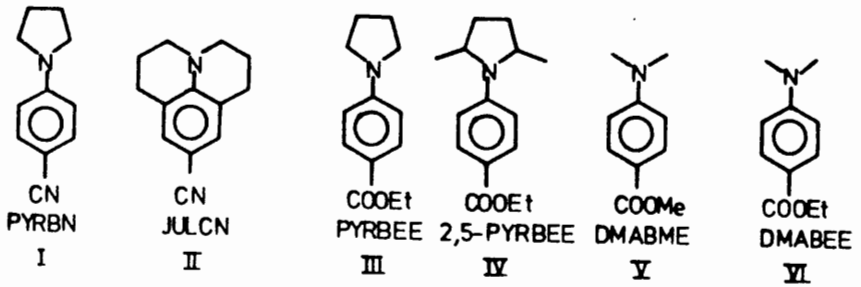
The advent of pulsed supersonic molecular beam expansion techniques has transformed the experimental study of molecular photophysics. The extreme cooling induced by this process results in very weak interactions such as van der Waals forces, becoming sufficient to prevent dissociation and allow nucleation to occur. Jet-cooling decongests otherwise impossibly dense molecular spectra enabling LIF or REMPI spectroscopies to probe the structures of molecular complexes, their state-selected intramolecular or inter-cluster dynamics and the dependence of 'solvent' spectral shifts on the nature and structure of the molecular complexes and the solute-solvent properties.

Gas phase solute-solvent clusters which form readily in jet expansions provide a direct link with solvation phenomena and have focused renewed attention on the role of solvent molecules in assisting the formation of charge-transfer (CT) states in a wide variety of molecular systems[1,2]. For example, aromatic amines endowed with electron withdrawing groups such as 4-N,N-dimethylaminobenzonitrile (4-DMABN), display a red shifted fluorescence ('A' band) in polar (or occasionally non-polar)

solvents which either completes or replaces the 'normal' ('B' band) fluorescence emission[1,2]. The anomalous bathochronic shift in emission has been associated with a twisted intramolecular charge-transfer (TICT) state accessed by torsion of the amino group about its bond to the aromatic ring. Many bichromorphic molecules with diverse structures such as amino-courmarins, N--phenyl carbasoles, symmetric di-aryls and unsymmetrical polyenes show similar dual fluorescence behaviour and the characteristic features of charge separation[2]. Common structural characteristics are electron donating chromophores connected by a single bond directly or indirectly to electron acceptor groups allowing (for most systems) full charge separation to be favoured in twisted configurations. Most investigations have been carried out in fluid or viscous solutions, where the behaviour is complicated by fluctuating solute-solvent interactions and the microscopic hindrance of intra-molecular mobility. Several investigations of the jet cooled excitation and emission spectra of the nitrile 4-DMABN have shown that neither the isolated molecule nor its monosolvated clusters exhibit dual fluorescence and that further solvation results in a drastic reduction in emission intensity. However, when mass resolved REMPI spectroscopy is substituted for LIF probing, two separate components can be detected in the polar, monosolvated cluster spectra of 4-DMABN, and also 3-DMABN. The first is very similar to that of the vibronically structured, bare molecule displaying only small spectral shifts, but the second component is displaced by $\sim$ 500-1000 cm^{-1} to lower frequency and is greatly broadened, with diffuse features superimposed on a broad background which bears no resemblance to the isolated, molecular spectrum. The strongly displaced system is attributed to the population of a low-lying charge transfer state, distant from the π-π^* state of the bare molecule. The low frequency vibronic structure is attributed to torsion of the dimethyl amino group in the π-π^* state[3-5]. For the corresponding esters, unlike the nitrile derivatives, there is evidence for direct charge transfer state formation (as well as torsional motion) even in the unsolvated, isolated molecule[6,7]. The difference has been attributed to a possible reversal in the ordering of these two low-lying excited singlet states: excitation of the "TICT fluorescence" correlates with the onset of a quasi-continuous component in the excitation spectrum. The present investigation focusses on the LIF excitation and emission spectroscopy of a wide range of isolated and solvated jet-cooled cyclic- and dialkyl-amino benzoic acid nitriles and esters seeking much needed insight into the photophysics of TICT state populations, its sensitivity to solvation solvate structure and site selectivity, and to the nature of 'donor-acceptor' substituents on the aromatic ring.

Experimental

Fully dispersed fluorescence and fluorescence excitation spectra were recorded under jet-cooled conditions for several, twisted intramolecular charge transfer (TICT) systems (I-VI).



A pulsed neodymium YAG Laser pumped dye laser (JK HY 750, Quanta Ray PDL 2) with wavelength extension (WEX) on loan from the Rutherford Appleton Central Laser Facility, provided frequency doubled excitation radiation (270 to 340nm) which intersected free jet expansions from a pulsed supersonic nozzle valve of aromatic amine vapours seeded in helium gas, a few mms downstream from the nozzle. LIF excitation spectra were generated by simultaneous recording of the incident laser intensity and that of total fluorescence along a perpendicular axis using photomultiplier/boxcar (Brookdeal 464, 465) combinations. Fluorescence spectra (FES) were recorded normalised to total

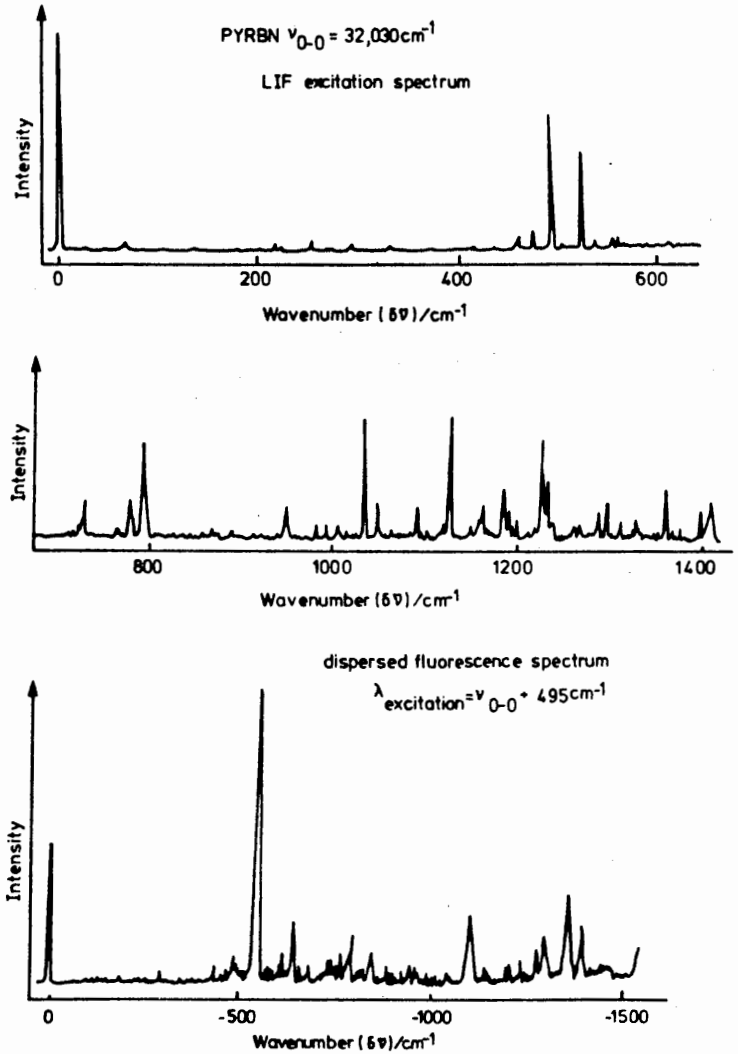


Figure C1.56

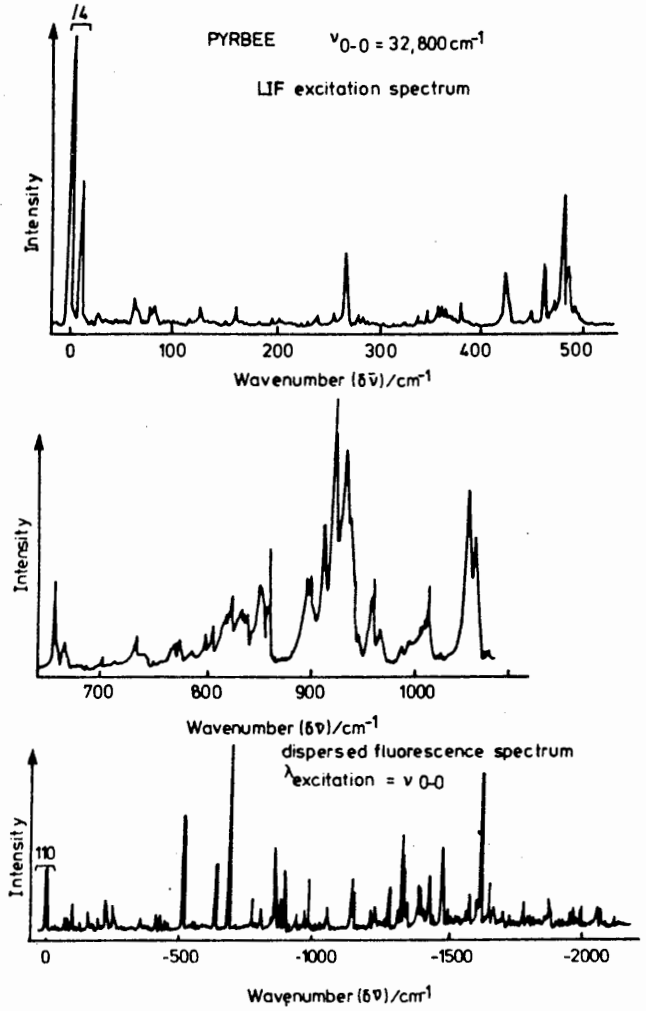


Figure C1.57

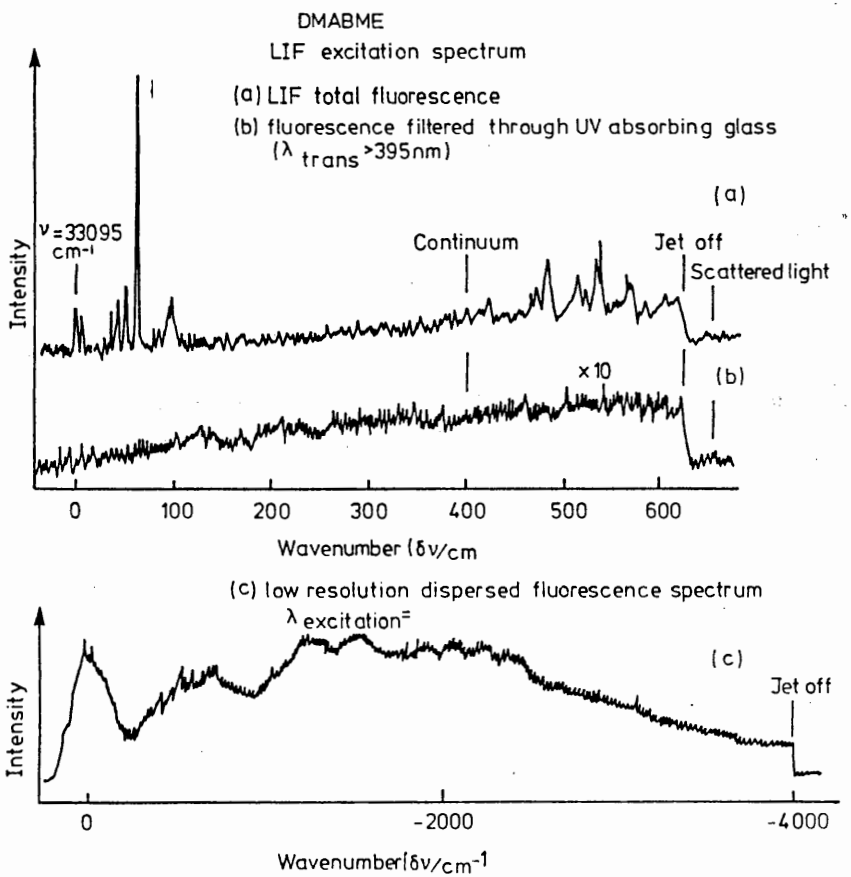


Figure C1.58

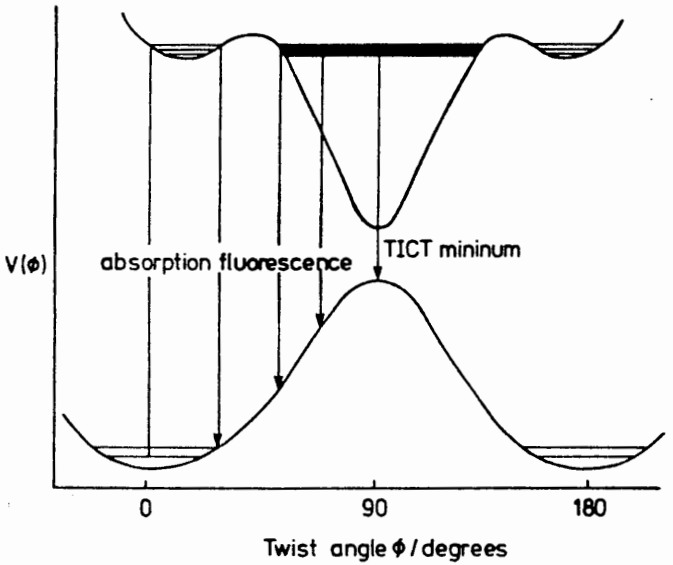


Figure C1.59

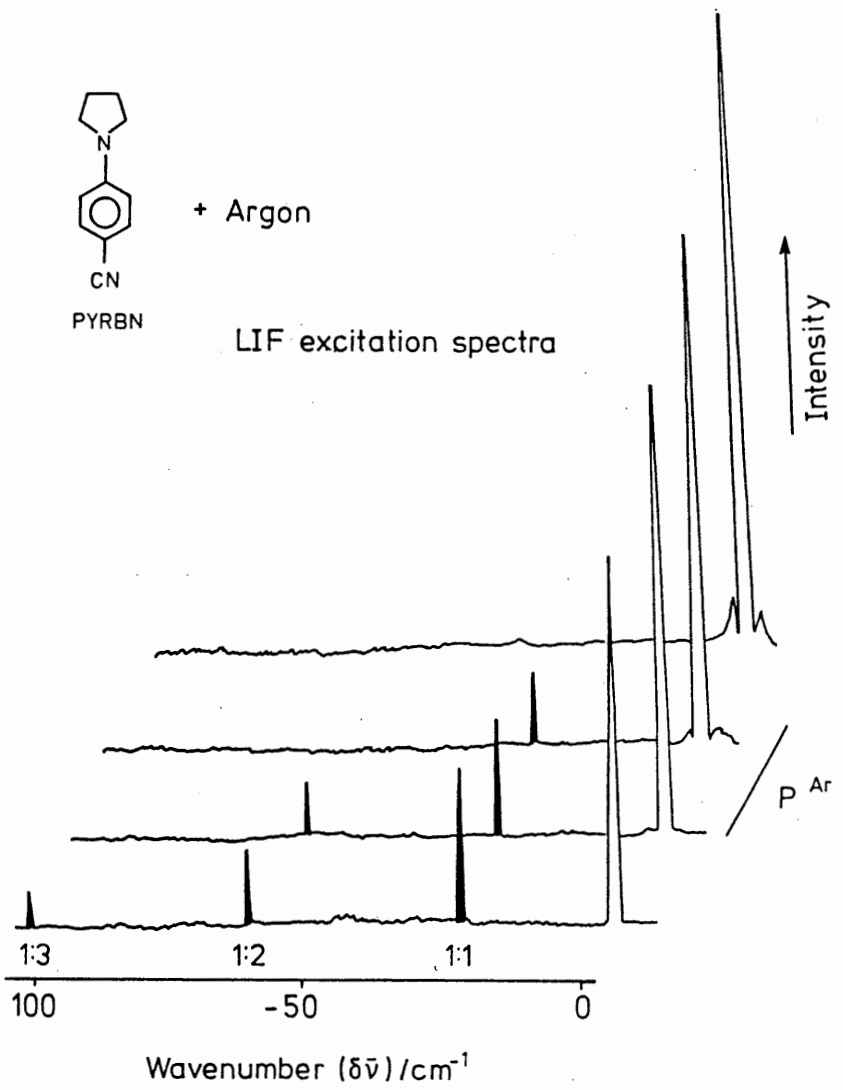


Figure C1.60

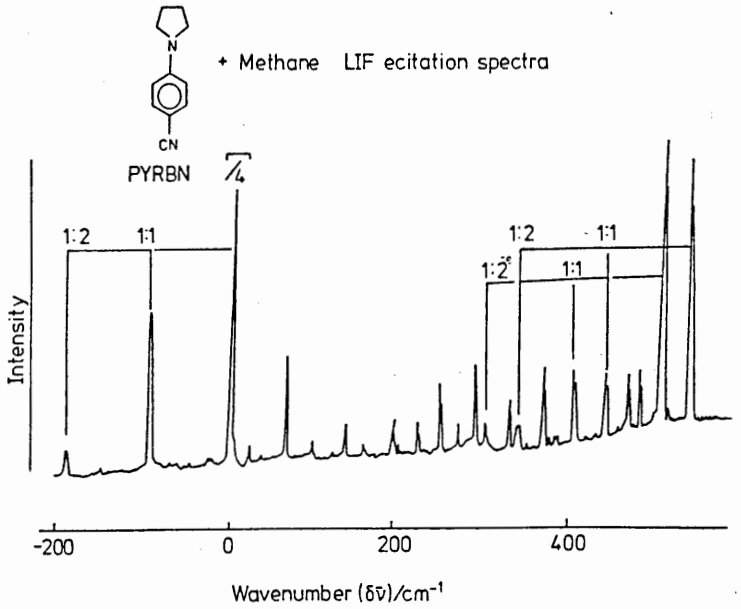


Figure C1.61

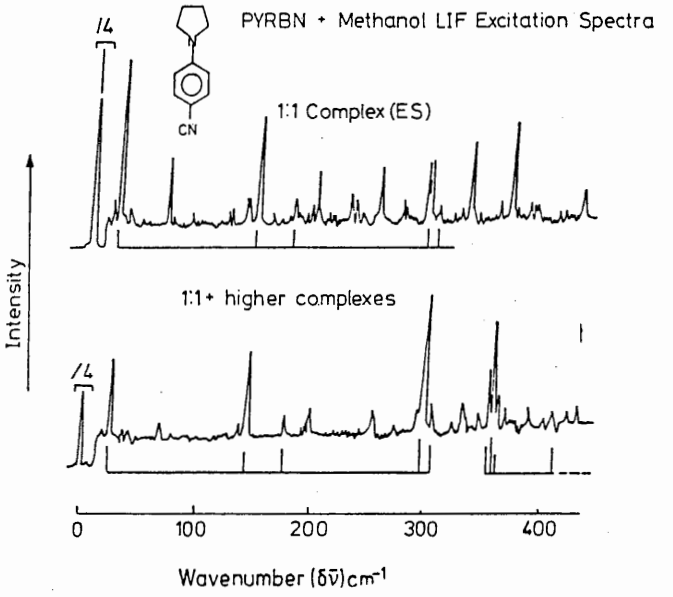


Figure C1.62

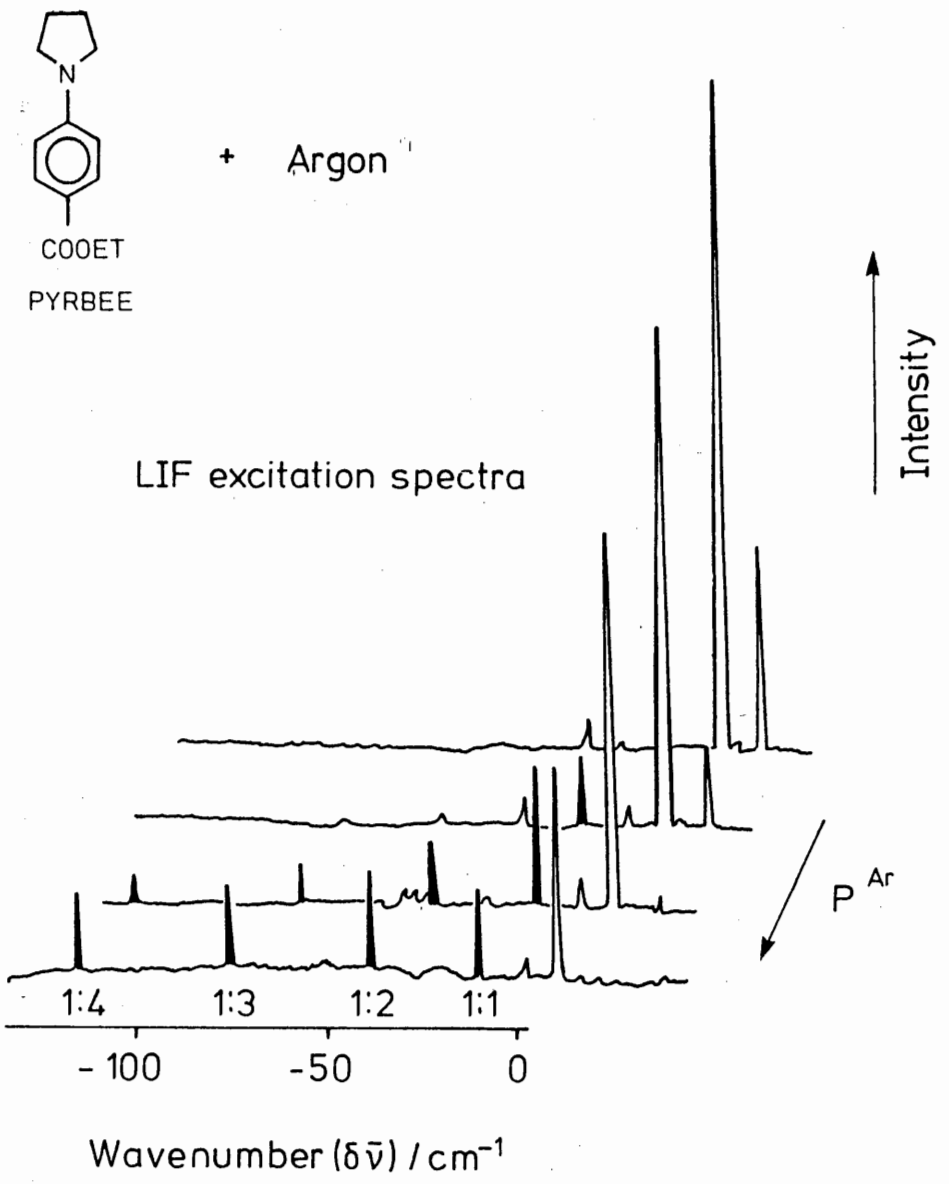

N
COOET
PYRBEE
+ Argon
LIF excitation spectra
Intensity
P Ar
1:4
1:3
1:2
1:1
- 100
-50
0
Wavenumber (δ ν̄) / cm⁻¹

Figure C1.63

fluorescence after dispersion through a monochromator (Spex minimate-reciprocal) dispersion 2nm/mm) and detection by an identical photomultiplier/boxcar combination. The quantities of the aminobenzonitriles and esters available were limited; rarely more than 0.5g and in some cases less than 100mg.

Results and Discussion

The isolated cyano compounds (Figure C1.56) displayed sharp, vibronically structure excitation spectra with no evidence of any broad shifted fluorescence component in emission spectra excited near the band origin. PYRBEE also displayed vibronically structure emission and excitation spectra (Figure C1.57) but the LIF excitation spectrum rapidly becomes increasingly broadened and congested. In contrast, the esters DMABME (Figure C1.58) and DMABEE displayed very broad, red shifted and nonstructured fluorescence continua at all excitation wavelengths. The structured components made only a very small contribution to the total spectrum.

The behaviour of the esters can be understood if there is a ready transfer into a quasi-continuous region of the TICT state across a low-lying torsional barrier even in the isolated molecule[6]. In the isolated molecular situation the notion of a two-state system, in which molecules are relaxed through vibrational energy transfer into local minima on the potential hypersurface, by collisions with neighbouring solvent, is inappropriate. In the absence of energy relaxation , IVR from locally excited levels near the potential barrier will allow access into a large volume of configuration space, and a broad fluorescence will result upon subsequent radiative decay (figure C1.59).

The lack of TICT emission from the cyano compounds (PYRBN and JULCN, parallels the behaviour found in other molecular analogues[5] (eg. ABN, DMABN). It has been suggested that in the cyano derivatives transfer across the barrier requires a solvent perturbation promoting a transition into the TICT state[2].

Solute-solvent van der Waals complexes of the aromatic amines formed readily under the jet-cooled conditions. For the cyano compound PYRBN, both bathochromic (with Ar (Figure C1.50), Dr, H_2, CH_4 (Figure C1.61)) and hypsochromic (with CH_3CN and CH_3OH (Figure C1.62)) shifts were observed; the methanol spectra being particularly rich in features attributable to 1:1 and higher complexation. For the ester, PYRBEE, where the split at the band origin may be associated with two alternative conformers, Figure C1.63 illustrates the changes effected by seeding the carrier gas with increasing partial pressures of Ar. As the proportion of Ar rises there are three distinct effects: a selective elimination of one component of the doublet, the appearance of successive, red-shifted satellite features associated with multiple complex formation and a general reduction in the overall fluorescence efficiency. The successive argon solvent shifts were not all the same: they were, respectively PYRBEE-Ar_1($-18cm^{-1}$), -Ar_2($-48cm^{-1}$), -Ar_3($-86cm^{-1}$), -Ar_4($-124cm^{-1}$); the spectral shifts only increased harmonically for the -Ar_3 and -Ar_4 clusters. Taken together with the selective quenching of one of the doublet components of the 'bare' molecular band origin, this implies **local site selectivity** by the individual Ar atoms initially complexed. A plausible speculation would place the first two near the substituent groups, and the third and fourth atoms at equivalent sites on each side of the aromatic ring.

When expanding PYRBEE/He or DMABME/He gas streams were seeded with polar solvents such as CH_3OH or CH_3CN, the vibronically structured features in the LIF excitation spectra were strongly quenched. No new features, assignable to solute-solvent complexes could be detected, but the underlying quasi-continua associated with a strongly red-shifted fluorescence increased in intensity. The formation of solvation clusters involving polar molecules does appear to promote transfer from the vertically excited, normal fluorescent state of the ester, into the twisted, intramolecular charge transfer state. Poster papers incorporating the results of this work have been presented at the CLF Review Panel Meeting at RAL in August; to the Farady Discussion No. 86: "Spectroscopy at Low Temperatures" at Exeter in September and the European Gordon

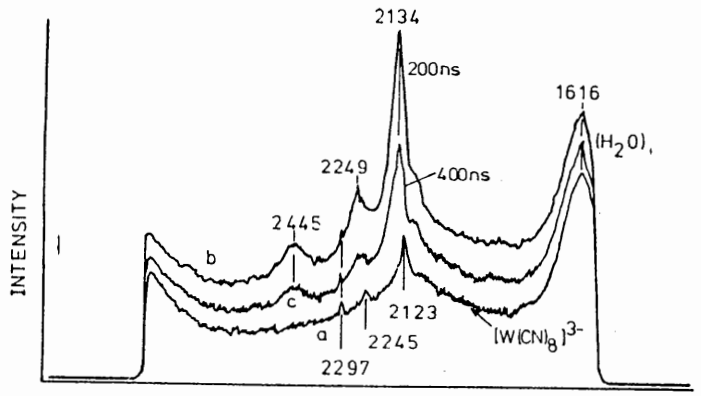


Figure C1.64 TR^3 spectrum of $[W(CN)_8]^{3-}$: pump pulse 249nm, probe 406nm.

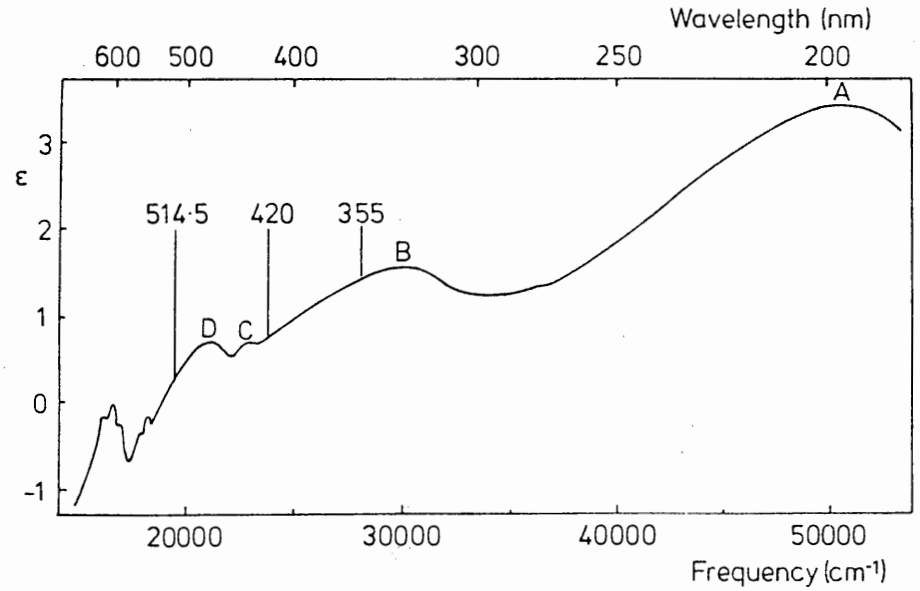


Figure C1.65 Gas phase UV absorption spectrum of NOCl, adapted from reference 7, showing some of the wavelengths used in this study.

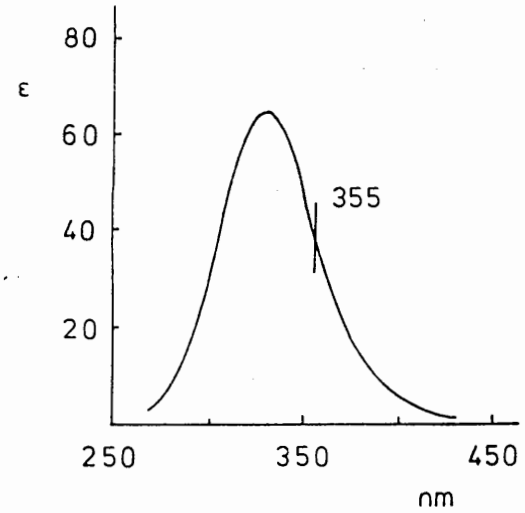


Figure C1.66 Absorption spectrum Cl_2.

Conference "Molecular Electronic Spectroscopy" at Ile d'Oleron, also in September.

We are most grateful to the Laser Support Facility for the loan of a tunable Nd YAG dye laser system. We are also grateful for helpful collaboration with Dr Christophe Jouvet (Laboratoire de Photophysique Moleculaire, Orsay) and with Dr W Rettig (Technishce Universitat, Berlin).

References

1. Z R Grabowski, K Totkiesicz, A Siemiarczuk, D J Cowley and W Baumann, Nouv. J. Chim., 1979, 3, 443.

2. W Rettig, Angew. Chem. 1986, 86, 969; Angew. Chem. Intern. Ed. ngl., 1986, 25, 971.

3. J A Warren and E R Bernstein, J. Chem. Phys., 1988, 88, 871.

4. T Kobayshi, J Futakami and O Kajimoto, Chem. Phys. Lett., 1986, 130, 63.

5. E m Gibson, A C Jones and D Phillips, Chem. Phys. Lett., 1987, 136, 454.

6. J August, T F Palmer, J P Simons, C Jouvet and W Rettig, Chem. Phys. Lett., 1988, 145, 273.

C1.18 TR3 SPECTRA OF OCTACYANOTUNGSTATE ION IN AQUEOUS SOLUTION

T J Kemp and L Vincze (Department of Chemistry, University of Warwick)

The aim of the experiment was to gain structural information about the 410 nm-absorbing transient ($\tau \sim 5$ms in H_2O at 293K) obtained on 249nm laser photolysis of $[W(CN)_8]^{3-}$ion.

A TR3 experiment was carried out on (aerated) aqueous $K_3[W(CN)_8]$ (concentration 10^{-3} mol dm^{-3}) using a pump pulse of 249nm and a probe pulse of 406nm (i.e. close to the λ_{max} of the transient under investigation).

Results

New peaks are shown at 2134, 2249 and 2445cm^{-1}. The first two are typical for $\nu(C\equiv N)$ but that at 2445 cm^{-1} is unusual (a) because of its very high frequency and (b) because of it breadth. It cannot be assigned to a free radical such as $^{\bullet}CN$ or $^{\bullet}CNO$ as these show $\nu(C\equiv N)$ elsewhere. The most likely candidate species is a hydrogen-bonded entity viz.

$$M - C \equiv N \ldots H - \overset{+}{N} \equiv C - M$$

which can have $\nu(C\equiv N-H)$ at ca. 2330-2500cm^{-1}.

The spectrum (Fig C1.64) was recorded at different time intervals after excitation and it appears that the lifetime of the 2445cm^{-1} species and the species with ν 2134cm^{-1} and 2249cm^{-1} are different, i.e. the TR3 experiment has generated a mixture of two transients. This was not clear from conventional UV flash photolysis experiments which showed a single-exponential decay of the 410nm band.
This work was reported as part of a general discussion of metal cyanide photochemistry in a plenary lecture at the Sixth Symposium on Photochemistry held at Eisenach (GDR) in September 1988, and will be published in an East German journal. It is hoped, in the event of a more definite assignment of the TR3 species, to publish a full account in a UK journal.

C1.19 RAMAN SPECTRA OF NOCl and Cl_2: PHOTODISSOCIATION DYNAMICS

A J Bell, P R Pardon and J G Frey (Department of Chemistry, University of Southampton)

Abstract

The resonance enhanced Raman spectra of NOCl and Cl_2 were recorded at a range of laser wavelengths from 514nm to 355nm, in both static and flow cells. A progression of overtone transitions (up to v"=13) were observed in the Raman spectrum of Cl_2 at 355nm. No overtones were observed for the NOCl dissociation at any of the wavelengths investigated. This suggests that the NOCl photodissociation may not be as fast as was previously thought.

Introduction

Resonance Raman scattering provides a means of probing the potential energy surface of a dissociative excited electronic state near the initial excitation point. In this method the spectrum of the radiation re-emitted during molecular photodissociation is recorded. The re-emission of a photon during dissociation is a highly unlikely event because the typical radiative fluorescence lifetime is of the order of 10^{-8}s whereas direct dissociation will occur within one vibrational period, typically less than 10^{-14}s. The expected quantum yield of fluorescence is thus very low (approximately 10^{-6}); despite this the spectrum can be observed, as has been demonstrated with ozone[1], methyl iodide[2], NO_2[3] and CH_2I_2[4].

The connection between the band intensities in the Raman spectrum and the dynamics of the dissociating molecule can be made with the time-dependent formulation of Raman scattering developed by Heler et al[5]. In this approach, the laser absorption is viewed as promoting a vertical excitation of the ground state vibrational wavefunction on to the excited state surface. The resulting wavepacket, in a non-stationary state, may subsequently move along a coordinate, q, due to a force given by the slope of the potential, $\partial V/\partial q$, along this direction. The spreading of the wavepacket is controlled by the second derivative of the potential, $\partial^2 V/\partial q^2$, along q. Both the motion and spreading of the wavepacket lead to overlap with various vibrational levels of the ground electronic state, and it is these overlaps that determine the Raman intensities of the fundamental, overtone and combination bands through a half-Fourier transform[5].

This time dependent approach is ideal for considering short time events such as direct photodissociation. If the excited state is longer lived then the wavepacket may return to the Franck-Condon allowed region of the excited state surface. In the time dependent formulation, it is the interference between the original wavepacket and the returned version which gives rise to the structure in the absorption spectrum and decreases the intensity of the Raman overtones.

Photochemistry of NOCl

The photo-decomposition of gas phase nitrosyl chloride has a quantum yield of $\phi_{NOCl}=2$ over the wavelength region 365-630nm[6]. The continuous nature of the absorption[7] (Figure C1.65) in this region is a consequence of the fast dissociation process, equation (1).

$$NOCl \longrightarrow NO(X^2\Pi) + Cl(^2P_{1/2,3/2}) \qquad (1)$$

The quantum yield $\phi_{NOCl}>1$ is due to the secondary reaction, equation (2).

$$Cl + NOCl \longrightarrow NO + Cl_2 \qquad (2)$$

The assignment of the bands in the UV absorption spectrum is shown in Table 1. The values obtained for the fragment anisotropy, β, are close to the maximum values possible ($\beta=-1$ for a perpendicular transition, and $\beta=2$ for a parallel transition), indicating that little or no rotation occurs between excitation and dissociation. In particular, Busch and Wilson[8] concluded from photofragment studies performed at 347.1nm, that the photodissociation proceeds from an excited state of A' symmetry and may occur within one vibrational period. This assignment is confirmed by subsequent MO calculations[9], and is consistent with the more recent experiments which probe the final state of the NO product in a cell[10,11] and in a molecular beam[12].

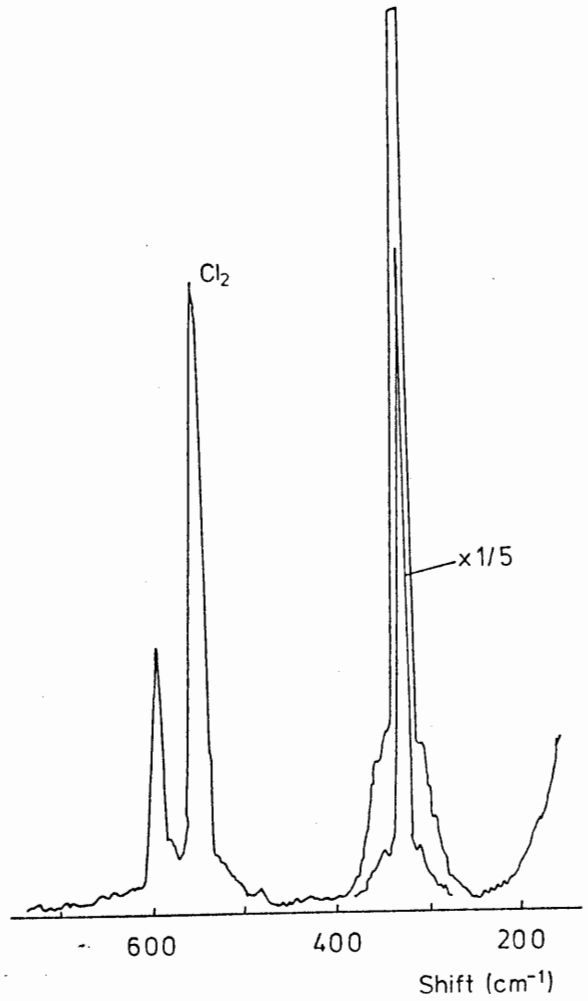


Figure C1.67

Raman spectrum of NOC1 at 514.,5mm (Coherent Ar⁺ Inovar 90) taken in a static cell.

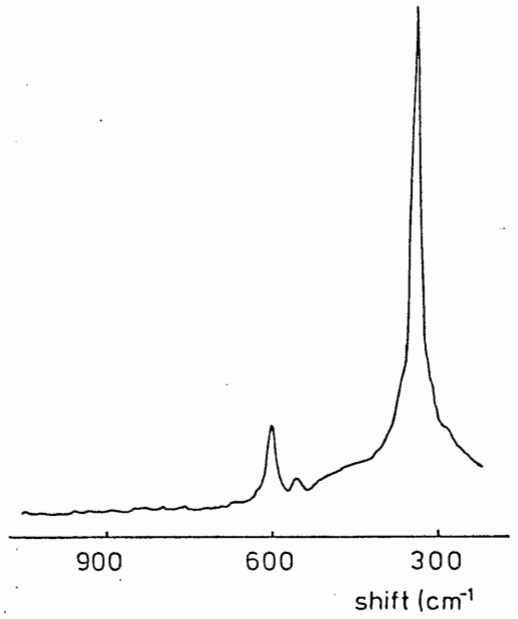


Figure C1.68 *Raman spectrum of NOC1 at 480nm (pulsed dye laser excitation) taken in a static cell and using an O-SMA intensified multichannel detector.*

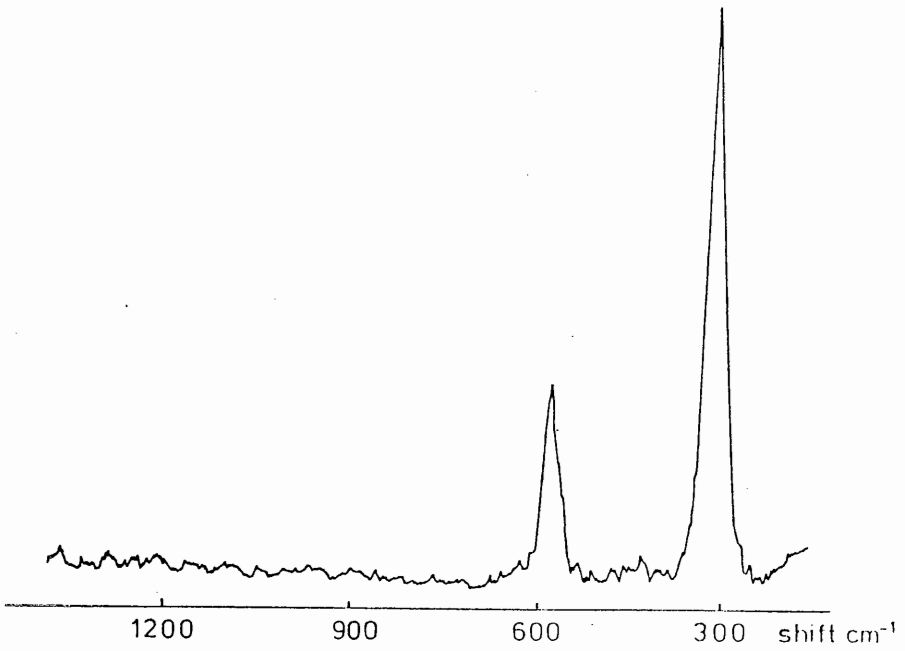


Figure C1.69 *Raman spectrum of NOCl at 355n (third harmonic of Nd:YAG, Quantel datachrome, flow cell).*

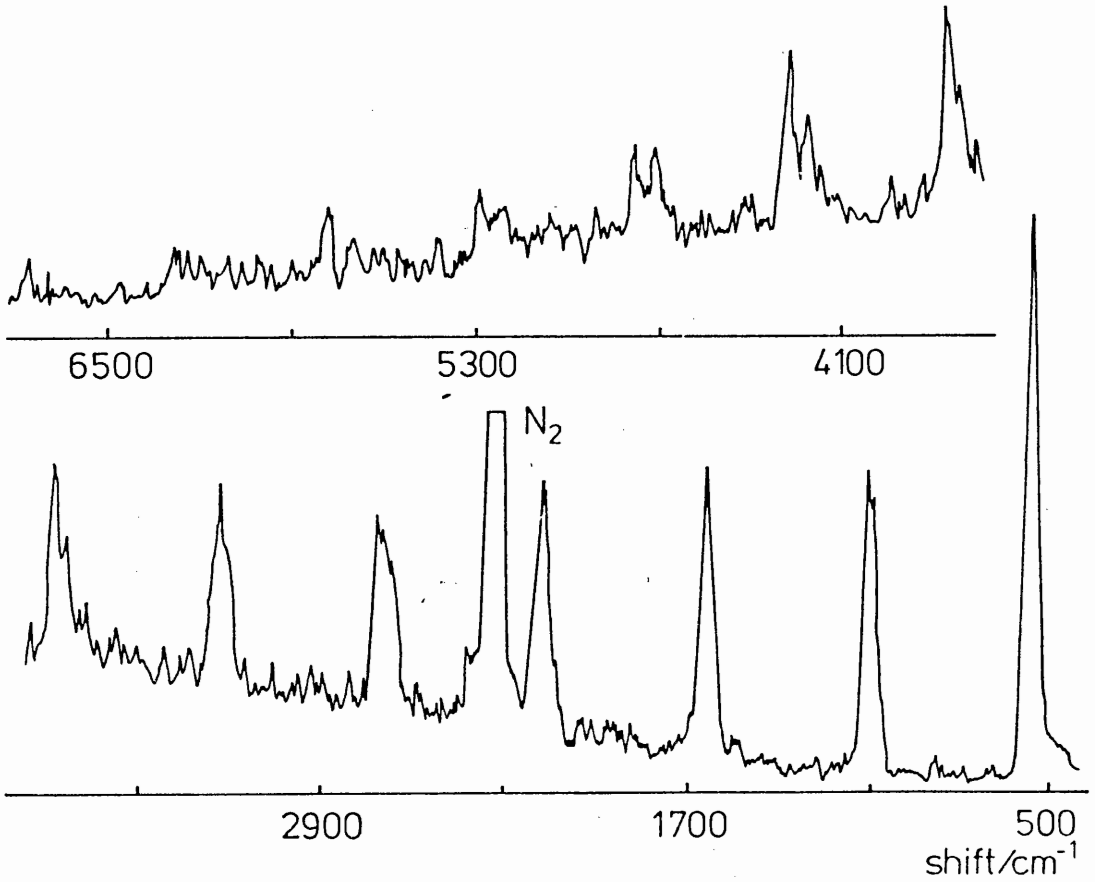


Figure C1.70 *Cl_2 Raman spectrum at 355nm (third harmonic of the Quantel Datachrome Nd:YAG laser) taken in a flow cell.*

Experimental

NOCl was prepared by reacting $POCl_3$(l) with $NaNO_2$(s). N_2 was passed through the reaction vessel and the resulting gas mixture flowed through a cold trap. Purification of the solid collected was achieved by trap to trap distillation, the major impurities being the more volatile oxides of nitrogen. Pure NOCl is a brown/orange gas at room temperature. Below-6°C (bp) it is a deep red liquid, which on solidification at -60°C (mp) turns pale yellow. After purification, the IR matrix isolation spectrum was recorded to check the purity of the sample.

The initial studies on the photodissociation of NOCl used a static fluorescence cell. Spectra were obtained with an Ar^+ laser (Coherent Inova 90) at 514.5, 488 and 458nm, scattered light being collected perpendicular to the incident radiation. The light was dispersed by a Cary 81 Raman spectrometer. Under the constant illumination of the cw laser, a new equilibrium NOCl concentration was established. There are a number of possible reactions occurring in this system and simulation of the reaction system is in progress.

The output of an excimer pumped dye laser (Lumonics, Lambda Physic FL2002) was used to record the Raman spectra at 480nm and 420nm. Dispersion of the emitted radiation was achieved by using a Triplemate monochromator (slit width 0.25mm), with a diode array (O-SMA) detector.

At 355nm (third harmonic of Nd:YAG, Quantel Datachrome) problems arise when using a static cell; the emission cannot be collected because complete laser absorption occurs too close to the cell window. A flow system was constructed such that the flowing sample gas is constricted by a buffer gas, N_2, to the centre region of the cell. The nitrogen Raman signal was used for calibration. A prism was used to ensure that only 355nm radiation entered the cell. The scattered light was collected at right angles to the laser beam and imaged onto the entrance slit of a monochromator (Spex 1401D operated in fist order) with a singlet lens (f=7.5cm). The dispersed light was detected with a photomultiplier tube (bialkali) and the signal integrated with a gate width equal to the laser pulse width, using a boxcar averager (SRS 250). For comparison the Raman spectrum of Cl_2 was obtained using this flow cell arrangement, with excitation at 355nm, near the 30500cm^{-1} absorption maximum (Figure C1.66).

Results

The Raman spectra of gaseous NOCl in a static cell, at wavelengths of 514.5 (Figure C1.67), 488 and 458nm showed the ν_2 and ν_3 fundamentals. A resonantly enhanced chlorine Raman signal was observed from chlorine formed by the dissociation of the NOCl. The Cl_2 signal was strongest at 488nm, where fluorescence from a high vibration-rotation state of the Cl_2(B) state to the ground electronic state was also seen, as was observed by Hwang and Chang[13]. The pulsed dye laser excitation spectra recorded at 480 and 420nm (Figure C1.68) showed similar features for the NOCl but a much smaller Cl_2 signal. At 355nm the flow cell was used owing to the much higher absorption coefficient of NOCl at this wavelength but once again the only observable features were the ν_2 and ν_3 fundamentals (Figure C1.69). The experimental ν_2 and ν_3 Raman shifts together with the ν_3/ν_2 intensity ratio at all the wavelengths studied are given in Table 2.

The difference in relative intensity of the chlorine fundamental taken in the static cell with the continuous and pulsed lasers was caused by each system establishing different steady state conditions. In the case of the flow cell, the Cl_2 peak is very small, the products of dissociation having been pumped away.

The flow cell arrangement was used to investigate the Cl_2 dissociation. The spectrum, following excitation at 355nm, is shown in Figure C1.70. A progression of overtones in the ground electronic state vibration were observed up to v"=13. The resolution used (entrance and exit slits 1000μm) was insufficient to resolve the chlorine isotope shift, however, transitions corresponding to v">6 were observed to be doublets. The component with the largest Raman shift has been assigned to Raman transitions

from v"=0, and the second component to hot band transitions from v"=1.

Discussion

Previous work on the photodissociation of NOCl using 347.1nm radiation[8] concluded that the dissociation occurred in under 80fs, probably within one vibrational period. This led us to believe that a time resolved spectrum, showing many overtones, would be observable at wavelengths approaching the B absorption maximum. NOCl is a bent triatomic molecule with 3 fundamental vibrations, shown in Table 3. All Raman transitions are allowed, however the intensity of the ν_1 signal is very weak[14]. Evidence that the NO is not vibrationally excited following NOCl dissociation at 355nm is given by Ogai et at[12] and so even if the ν_1 carried Raman intensity, one would not expect to see a progression in this vibration. Fission of the N-Cl bond would be expected to give rise to overtones of the ν_2 and ν_3 fundamentals (which both involve the N-Cl stretch and NOCl bend) as the excitation wavelength approached the B absorption maximum. As can be seen in the spectra, no overtones, within the limit of our signal to noise ratio, are observed for the ν_2 and ν_3 fundamentals. This would seem to indicate that the dissociation is not as fast as previously thought and that a predissociation mechanism may occur. The variation of the ν_3/ν_2 intensity ratio seems to be correlated with the formation of the different excited electronic states. Further work is needed to verify the findings at 335nm and we also hope to be able to probe the dissociative surface below 250nm (the A band).

The Cl_2 spectrum showed 13 overtones of the fundamental transition (ω_e=550cm^{-1}). The vibrational progression is not the same as that seen by Bondebey et al[15] following excitation of Cl_2 at 355nm in an argon matrix. The latter is at much longer wavelengths (Maximum at >900nm) and is due to fluorescence from the v'=1 level of a long-lived state assigned as the spin orbit component $^3\Pi(2_u)$, populated via a radiationless transition from the B state. The v"=14 vibrational state is only 9000cm^{-1} above the zero point level, while the Cl_2 dissociation energy is nearly 20,000cm^{-1}. Hence overtones would be expected to be seen much further out from the exciting line if a simple rapid dissociation process was occurring, for example in the REMPI spectrum of Cl_2[16]. The premature lowering of overtone intensity at v">8, is unexpected but may arise from a curve crossing to the B state or may simply be due to the initial excitation being away from the absorption maximum. The region around the 30500cm^{-1} absorption band of Cl_2 will be explored by this technique using a tunable laser source.

Conclusions

A long vibrational progression was observed following excitation to $Cl_2(^1\Pi_u)$ at 355nm. This is consistent with the rapid dissociation of this state. The reduction in the intensity of the overtones for v">8 may be due to a curve crossing. No progression in either ν_2 or ν_3 were observed for NOCl. This is taken as evidence that the excited state lifetime is longer than has been previously thought.

Acknowledgements

We acknowledge the help of the Laser Support Facility, Rutherford Appleton Laboratory in providing the use of the Lumonics and Lambda Physik excimer pumped dye laser combination and the loan of the Quantel Datachrome Nd:YAG laser. We would like to thank A K Brisdon and J S Ogden for the matrix infrared studies and T R Gilson for his co-operation in obtaining the Ar$^+$ laser Raman spectra. AJB would like to thank the SERC for a studentship.

References

1. D G Imre, J L Kinsey, R W Field, D H Katayama, J. Phys. Chem., 86, (1982) 2564.

2. D G Imre, J L Kinsey, A Sinha, J Krenos, J. Phys. Chem., 88, (1984), 3965.

STREAK CAMERA APPARATUS AT RUTHERFORD APPLETON LABORATORY

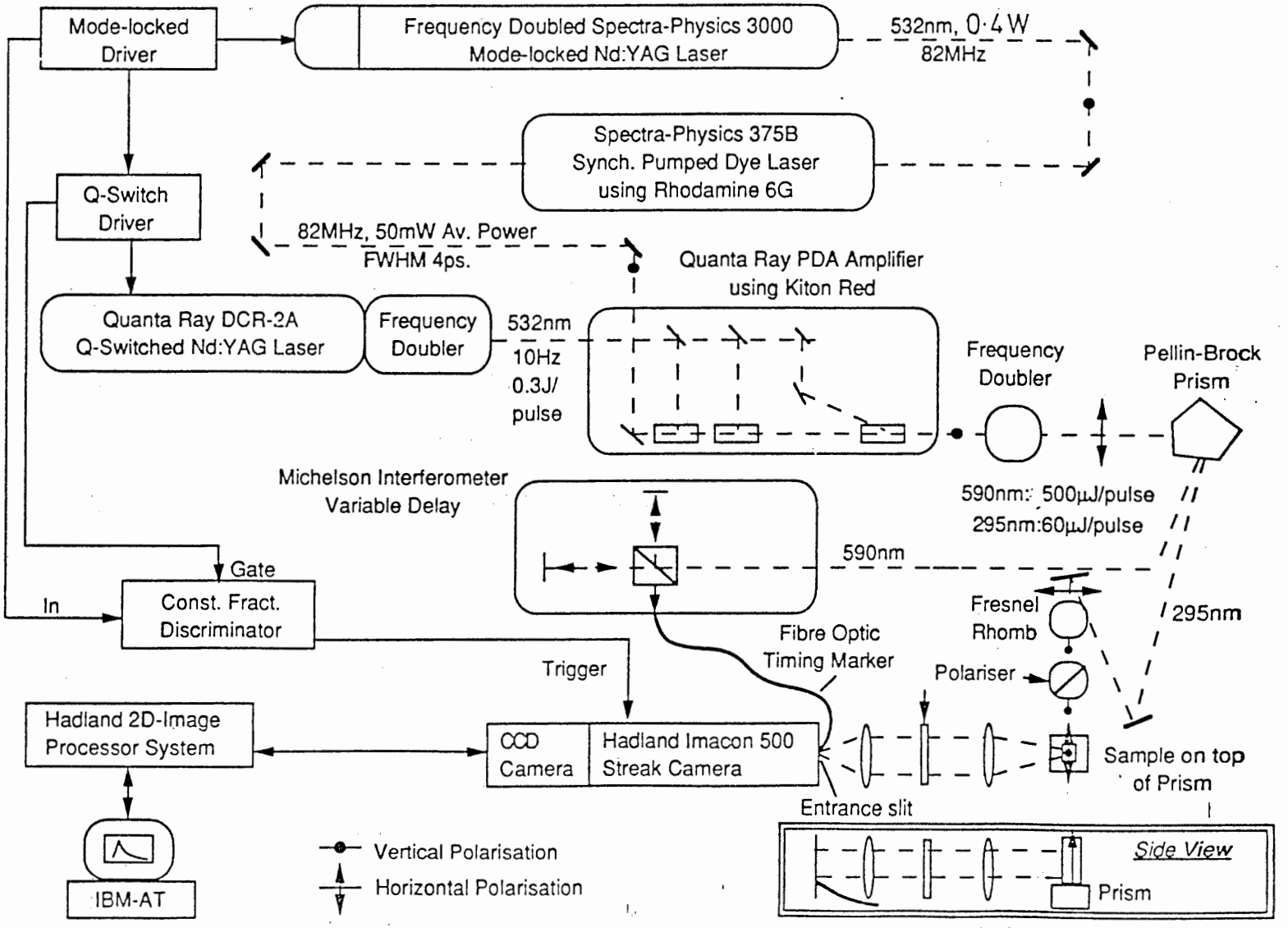


Fig C1.71 Picosecond laser and streak camera apparatus.

3. E A Rohlfing, J J Valentini, Chem. Phys. Lett., 114, (1985), 282.

4. J Zhang and D G Imre, J. Chem. Phys., 89, (1988), 309.

5. E J Heller, Acc. Chem. Res., 14, (1981), 386.

6. G B Kistiakowsky, J. Am. Chem. Soc., 52, (1930), 102.

7. C F Goodeve and S Katz, Proc. Roy. Soc. A. 172, (1939), 432.

8. G E Busch and K R Wilson, J. Chem. Phys., 56, (1972), 3655.

9. D Solgaid, F Lahmani, C Lardeaux and J P Flament, Chem. Phys., 79 (1983), 225.

10. A E Bruno, U Bruhlmann and J R Huberm, Chem. Phys., 120, (1988), 155.

11. A Ticktin, A E Bruno, U Bruhlmann and J R Huber, Chem. Phys., 125, (1988), 403.

12. A Ogai, C X W Qian, L Iwata, and H Reisler, Chem. Phys. Lett., 146, (1988), 367.

13. D M Hwang and H Chang, J. Molec. Spectr., 69 (1978), 11.

14. J K McDonald, J A Merritt, V F Kalasinsky, H L Heusel and J R Durig, J. Molec. Spectr., 117, (1986), 69.

15. V E Bondybey and C Fletcher, J. Chem. Phys., 64, (1976), 3615.

16. L Li, R J Lipert, H Park, W A Chupka and S D Colson, J. chem. Phys., 87, (1987), 6767.

C1.20 DEVELOPMENT OF A STREAK CAMERA SYSTEM AND DATA ANALYSIS SOFTWARE FOR THE MEASUREMENT OF TIME RESOLVED LASER INDUCED FLUORESCENCE

A Beeby, D Phillips (Royal Institution)
A J Langley, K Moore, W Shaikh, W T Toner (RAL)

The development of the streak camera with CCD readout and data analysis package has now largely been completed. This is the first stage of a development programme to provide a picosecond-laser user facility for the measurement of time-resolved laser induced fluorescence. In due course the facility will be enhanced by the addition of scheduled time-correlated single photon counting (SPC) experiments. The streak camera and SPC techniques are seen as complementary. SPC is a well proven technique producing reliable data of high statistical quality. Given the best commercially available multi-channel plate detectors time resolutions of $\sim$ 25 ps can be achieved. For faster processes however the streak camera has the advantage with a time resolution of $\leq$ 5 ps. Fluorescence data can be obtained from a few (and even single) laser shots so that measurements quite unobtainable with SPC on for example highly photo-degradable samples or species reaction kinetics can be made. Finally the ability to spread light collected from the sample along the streak camera slit so that time-resolved and wavelength or spatially resolved fluorescence can be processed in parallel offers a facility unique to the streak camera and its potential has yet to be fully explored.

A diagram of the apparatus used for streak camera experiments is shown in Figure C1.71. The acquisition of single laser-shot fluorescence decays and the approach to their addition and analysis has been described previously (1). Development work during the past year has concentrated upon overcoming two major difficulties associated with streak camera measurement of fluorescence:

a) The reduction of streak camera timing jitter.

b) Correction of the image distortion introduced by the streak camera and CCD readcut.

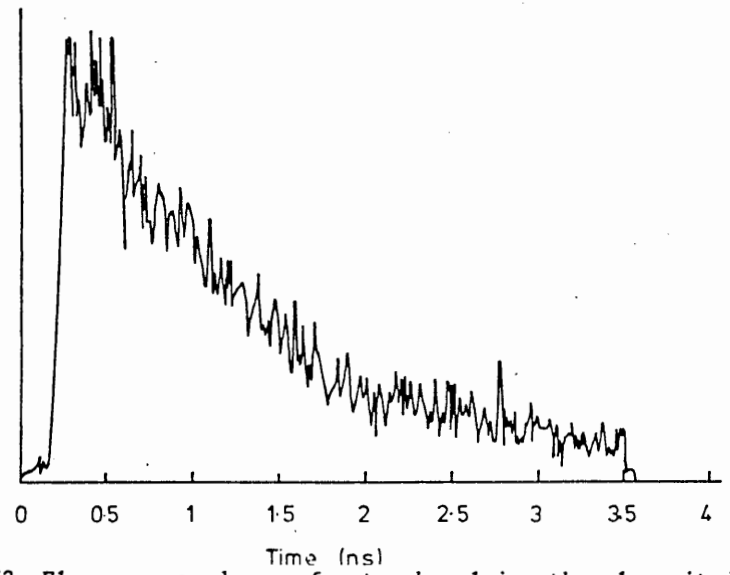


Fig C1.72 Fluorescence decay of p-terphenyl in ethanol excited at 290 nm obtained from a single laser shot.

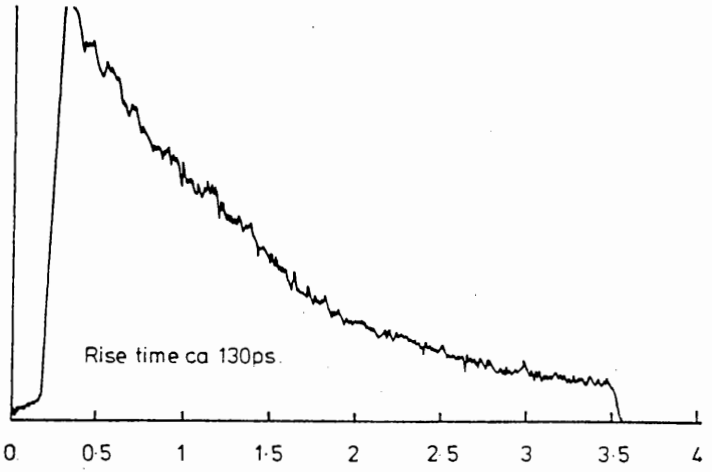


Fig C1.73 Fluorescence decay of p-terphenyl in ethanol obtained from 60 averaged laser shots but uncorrected for image distortion or time jitter.

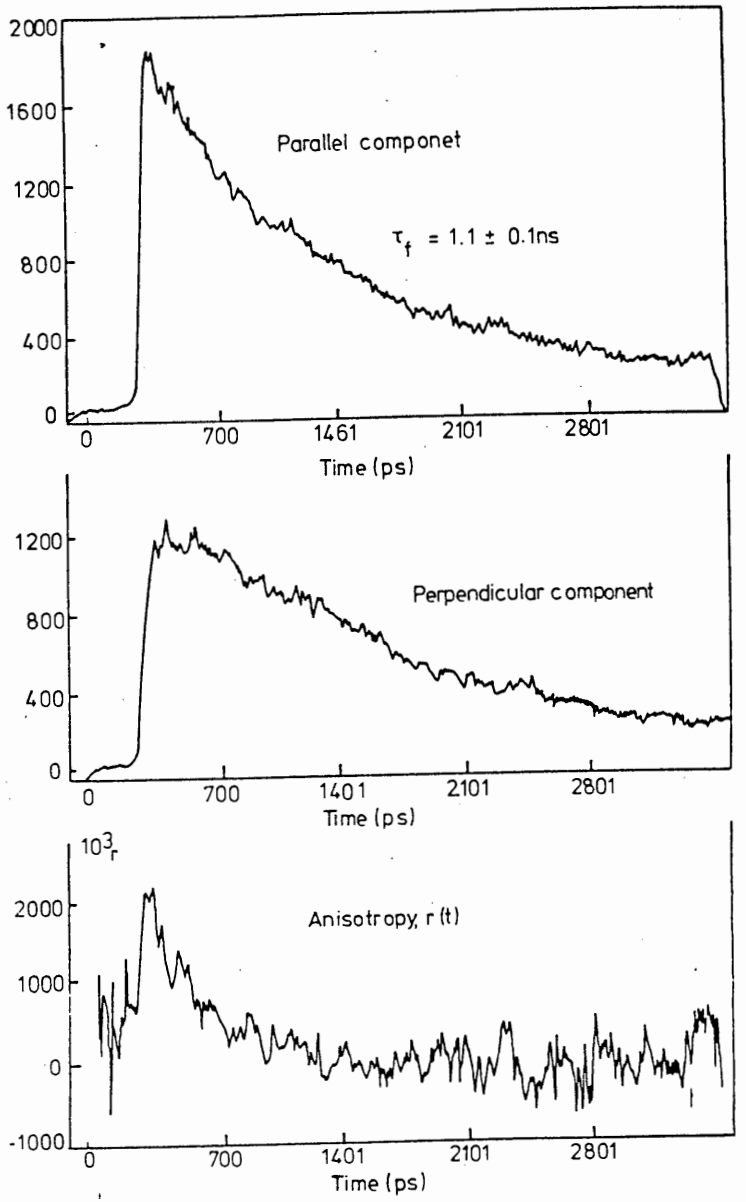


Fig C1.74 Fully corrected parallel and perpendicular fluorescence components together with the calculated anisotropy for p-terphenyl.

The approach to overcoming a) has been to acquire many single shot images each containing a timing marker which is then used to correct the position of the image before co-addition. For maximum streak speeds and timing resolution however a timing jitter of ca ± 50 ps is required. In early experiments the camera was triggered by the output of the Q-switch driver of the Nd:YAG pumped dye amplifier. This resulted in a jitter of ca ± 250 ps. A considerable improvement has been achieved by processing pulses from the mode-locker driver (fig C1.71) using a constant fraction discriminator CFD (Tennelec TC 454) gated by a pulse coincident with the train of amplified picosecond pulses at 10Hz. Triggering the streak camera with the CFD pulses results in a timing jitter of ≤ ± 50 ps. For software correction of this remaining jitter, timing marker fiducials derived from a Michelson type interferometer are introduced to the streak camera in a fibre optic.

Three major causes of fluorescence-decay image distortion are;

(i) CCD background count
(ii) variation of streak camera sensitivity across the time window, and
(iii) non-linearity of the streak speed.

The measured fluorescence decay is corrected by subtracting the averaged background gathered over many shots and then dividing by the measured fluorescence decay of a long lived fluorophore of known decay lifetime. The pair of fiducials derived from the interferometer serve to both calibrate the streak speed and measure its non-linearity which can then be corrected.

A software package has now been developed to correct for image distortion and for data analysis. This allows the transfer of data from the Hadlands 2D system to an IBM-PC compatible. The suite of programs available enables users to:

1) Gather, and transfer to the IBM fluorescence, background, characterisation (long lived fluorophore) and a set of many fiducial-pair images.

2) Subtract CCD background from fluorescence and characterisation images.

3) Divide the background subtracted fluorescence image by the characterisation image.

This results in a set of corrected single-shot fluorescence decay images which can be corrected for time jitter and then averaged. Commercial spread sheet or graphics packages are available (such as Lotus 123) for data presentation and subsequent analysis.

Results

To measure the performance of the streak camera system fluorescence images of the fluorescence standard p-terphenyl in ethanol were measured by excitation at 290 mm. Figure C1.72 shows a decay obtained from a single laser shot. The rise-time at the start of the decay is ca 50 ps and results from operating the camera at a slow streak speed (200 ps/mm) in order to display the decay out to 3.5 ns. Rise times of ca 5 ps are achievable at the fastest streak speeds. Figure C1.73 shows fluorescence decays of 60 averaged single-shot images but uncorrected for image distortion or jitter. The decay clearly appears non-exponential due to distortion and has a rise time of ca 130 ps. Figure C1.74 contains fully corrected parallel and perpendicular fluorescence components together with the calculated anisotropy. The measured lifetime of the fluorescence decay was 1.1 ± 0.1 ps. This however has to be corrected for the long lived life time of the characterisation fluorophore which in this case was fluoranthane. This was measured by SPC at the Royal Institution as 30 ps. When this correction is made the lifetime of fluorescence decay of p-terphenyl was

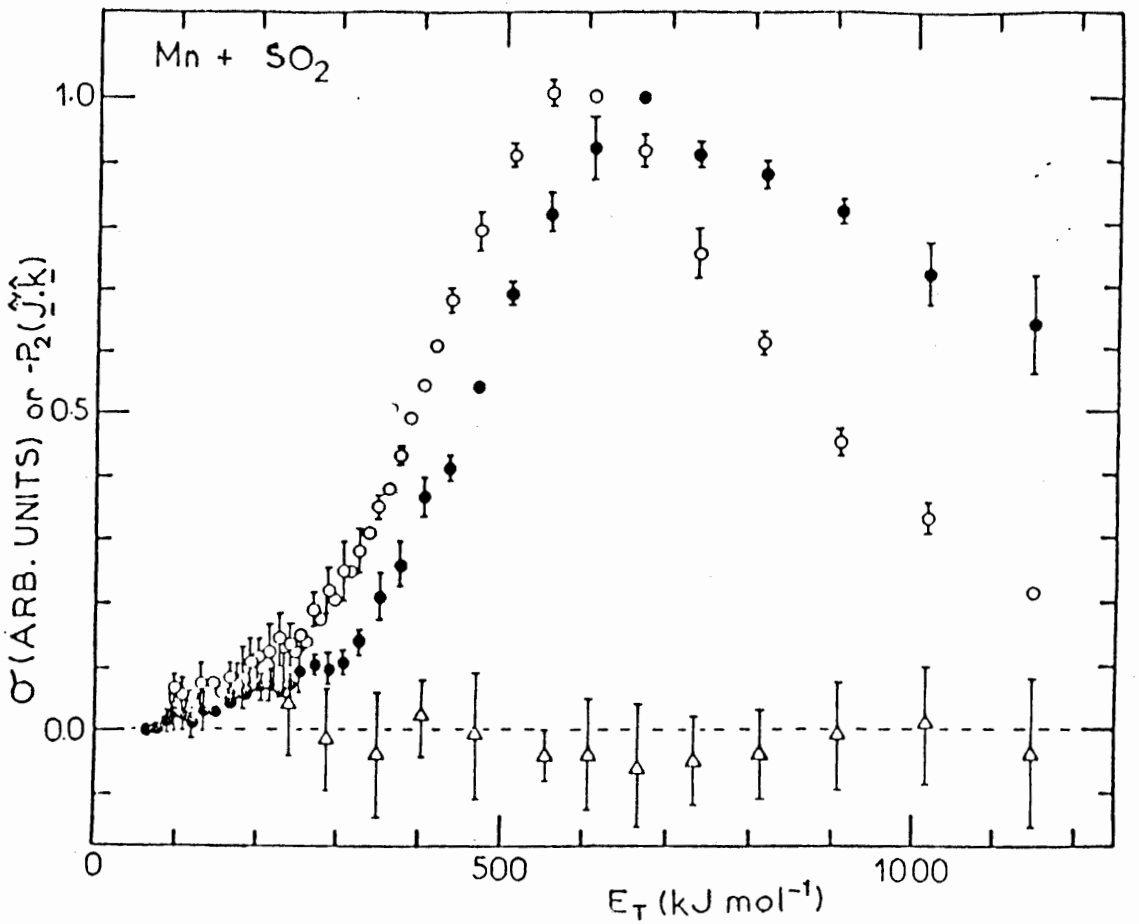


Figure C1.75 *Excitation functions for $MnO^*(A^6\Sigma^+)$ (O) and $Mn^*(z^6P_J)$ (•) production from $Mn+SO_2$. Also shown are $MnO^*(A^6\Sigma^+)$ polarisation measurements (Δ, see text).*

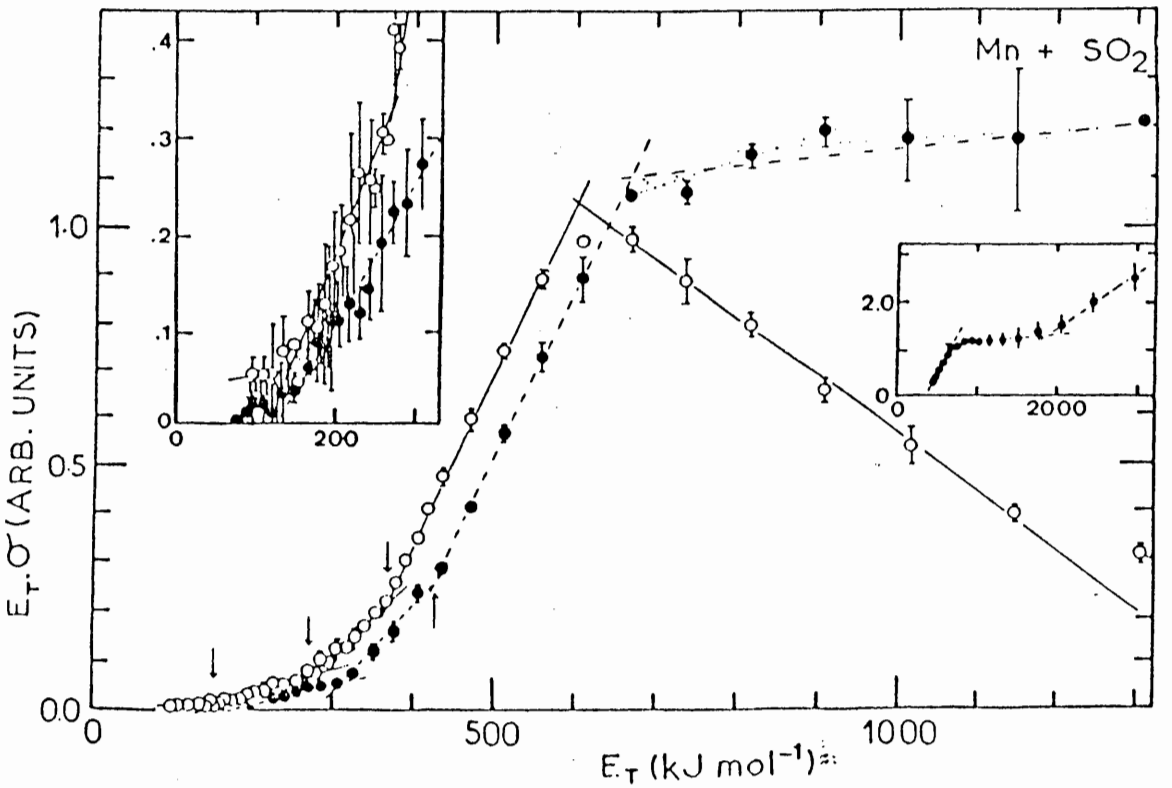


Figure C1.76 Plot of Eτ.σ against Eτ for the data of Figure C1.75.

τ = 1.3 ± 0.1 ps

r(t) = 360 ± 50 ps rotational correlation time.

These values are within 10% of values obtained by SPC measurements. Moreover the rise time of the averaged and jitter corrected images is ca 55 ps for the parallel component and compares favourably with single shot data. At the fastest streak speeds available with the Imacon 500 streak camera, rise times approaching the maximum time resolution of ∿ 5 ps should be achieved even with the co-addition of images.

C1.21 CHEMILUMINESCENCE AND ENERGY TRANSFER IN Mn ATOM REACTIONS

M R Levy (Dept of Chemical and Life Sciences, Newcastle upon Tyne Polytechnic)

Previous reports[1,2] have shown how pulsed laser ablation may be applied to the study of reactions of atoms of refractory elements. Briefly, a Nd:YAG laser (JK2000) is focused onto a solid metal target, to generate a pulsed atomic beam of wide velocity range and containing a number of metastable states in addition to the ground state. After a long flight path (≈ 280 mm) the beam interacts with a low pressure (≈ 10^{-4} torr) of reactant gas; and, at this point, both the beam, and any chemiluminescence from reaction products, are detected. Since the time-of-flight of the metal atoms determines the collision velocity, the ratio of the two flux-time distributions yields the translational excitation function (in arbitrary units) of the chemiluminescent process. Signal averaging (with the Biomation/Trachor Northern system) has been necessary as the pulsed beam is rather weak, has significant shot-to-shot variation, and falls off with target erosion and metal deposition on the mirror.

Initial measurements concerned the reactions Mn+RO (R=O, N_2, NO, SO, CO). This represented a suitable place to start because of the relative simplicity of both the Mn electronic structure and the MnO ($A^6\Sigma^+$-$X^6\Sigma^+$) electronic spectrum. In addition, the presence in the Mn beam of the Mn*(z^9P_J) atoms, with long radiative lifetimes, provided a useful means of detecting the pulses. Emission from both MnO*(A) (λ > 550 nm) and Mn* (z^6P_J) (λ = 403nm) was observed in these systems: Figure C1.75 shows the derived excitation functions for Mn+SO_2. Also shown are the measurements of the MnO* rotational polarisation, $P_2(j'k)$: these turned out to be essentially zero in all 5 cases, presumably because of strong interaction between the high spin magnetic moment of the MnO* and the earth's magnetic field.

In most cases <u>both</u> the chemiluminescent (MnO*) and energy transfer (Mn*(zP_1) processes are endothermic not only for ground state, $a^6S_{5/2}$, atoms of Mn, but even for the first excited state (a^6D_J multiplet). The contributions of the different atomic states to the measured relative cross-sections σ can thus be separated by application of the venerable 'line-of-centres' model

$$E\tau.\sigma(E\tau) = \sigma_0(E\tau-E_0) \qquad (1)$$

A multilinear plot of $E\tau.\sigma$ against $E\tau$ indicates the contribution of more than one atomic state and/or the opening up of different processes as $E\tau$ increases. Such multilinear behaviour has been found in all 5 cases: Figure C1.76 shows the plot for Mn+SO_2.

The analysis shows that MnO* is produced by only a very small number of Mn states: $a^6S_{5/2}$, a^6D_J and, for O_2 and SO_2 alone, z^8P_J and possibly a^4D_J. These results are entirely in accord with correlation diagrams based on l,j coupling, taking into account the known vibronic interaction between the $A^6\Sigma^+$ and $X^6\Sigma^+$ states of MnO[3]. The various chemiluminescence thresholds have allowed determination of a lower limit for the MnO bond energy, D_0=390±5kJ mol^{-1}, and an upper limit for the SO*($a^1\Delta$) excitation energy T_0≈100kJ mol^{-1}. The exothermic Mn+N_2O system shows significant excess barriers to chemiluminescent reaction, a feature which appears to be due to lack of appropriate <u>orbital</u> rather than state correlations. Total spin appears to be conserved for Mn*(z^6P_J) production, in all 5 cases.

A number of other systems have also been investigated: Mn+He, Ar, N_2, OCS, CS_2, CH_4, C_2H_6, $C(CH_3)_4$, C_2H_4, C_3H_6, C_4H_8, Br_2, SO_2Cl_2, PCl_3, $SnCl_4$ and SF_6. Although the data are still being analysed, some general points can be made:

(i) $Mn^*(z^6P_J)$ is produced in all cases, with $Mn(a^6S_{5/2})$ and $Mn^*(a^6D_J)$ being the only precursors (i.e. spin is again conserved). In some cases there are significant excess barriers, reflecting repulsive crossing of the potential surfaces, rather than an attractive long-lived complex interaction.

(ii) Mn+OCS yields MnS*, the less endothermic channel, but Mn+CS_2 gives no chemiluminescence.

(iii) Emission in the region of the MnH $A'\Pi$-$X'\Sigma$ bands occurs in all hydrocarbon reactions; again only a small number of Mn states seems to be responsible.

(iv) Among the halogen-containing molecules studied, only SF_6 gives significant chemiluminescence, again from reaction of only a small number of Mn states. This may reflect the spectroscopy of the manganese monohalides: only in MnF is there an overlap between the X and A vibrational manifolds[4].

References

1. M R Levy, Paper B.1.15, Laser Facility Committee Report 1987.

2. M R Levy, Paper B.1.12, Laser Facility Committee Report 1988.

3. A S-C Cheung, A M Lyra, A J Merer & A W Taylor, J. Mol. Spectrosc. 102, 224 (1983).

4. K Huber and G Herzberg, Constants of Diatomic Molecules, (Van Nostrand, New York, 1979).

C1.22 NON-THERMAL LASER INDUCED DESORPTION AND ENERGY TRANSFER FOR MOLECULES ADSORBED ON DI-ELECTRIC SURFACES

C J S M Simpson, C Minchington and C Kingsley (Physical Chemistry Laboratory, University of Oxford)

A W Parker (RAL)

Introduction

During the past year we have been studying both thermal and non-thermal laser induced desorption. This report will concentrate on the non-thermal desorption and energy transfer results.

Thermal desorption is a process which is not specific to particular molecules. It occurs for a wide variety of metal surfaces when they are heated using nano-second pulsed lasers in the visible or near UV. The temperature of the surface increases by about 200K at a rate of about 10^{10} Ks^{-1} and molecules, or atoms, are desorbed with temperatures less than those reached by the surface.

The objective in non-thermal desorption experiments is to excite the vibrations of a given molecule and not to heat the surface. If sufficient energy is given to the molecule this will cause it to be desorbed provided that the rate for desorption is greater than the rate of loss of energy to the surface. These experiments can be carried out using IR lasers to excite vibrations of the ground electronic state of the molecule, or using UV lasers to form electronically excited molecules.

The surfaces employed

The first requirement is to have a surface from which non-thermal rather than thermal desorption will occur. In general metal surfaces are unsuitable for two reasons. The first is that they are likely to be heated, especially if UV lasers are employed. The second is that they are likely to be efficient at deactivating

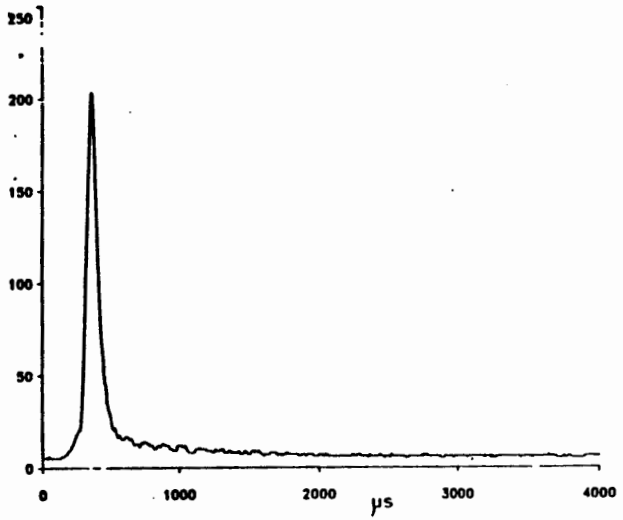


Fig C1.77 Explosive desorption of pyridine from Xe coated quartz.

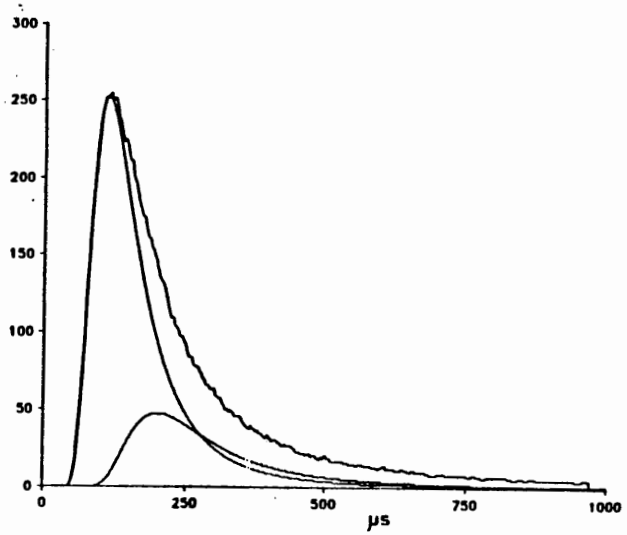


Fig C1.78 Pyridine desorbed from quartz at 20K by a 10 ns pulse at 270 nm. Temperatures of desorbed molecules 1020 K and 320K.

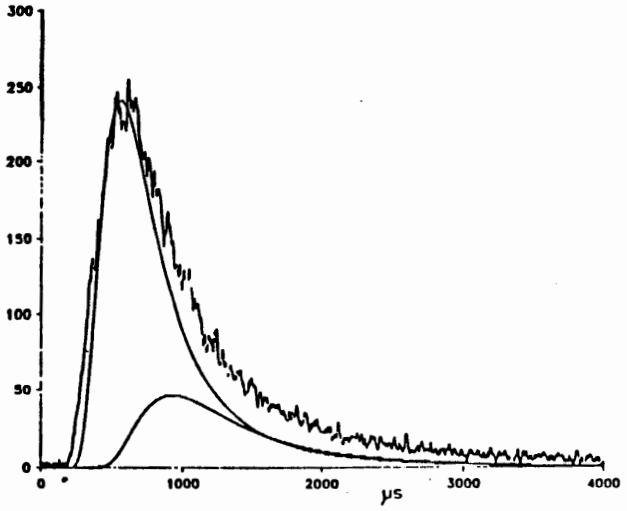


Fig C1.79 Pyridine desorbed from a surface of Xe coated quartz at 40 K following excitation by a 10 ns laser pulse at 255 nm. Temperatures of desorbed molecules 770 K and 240 K.

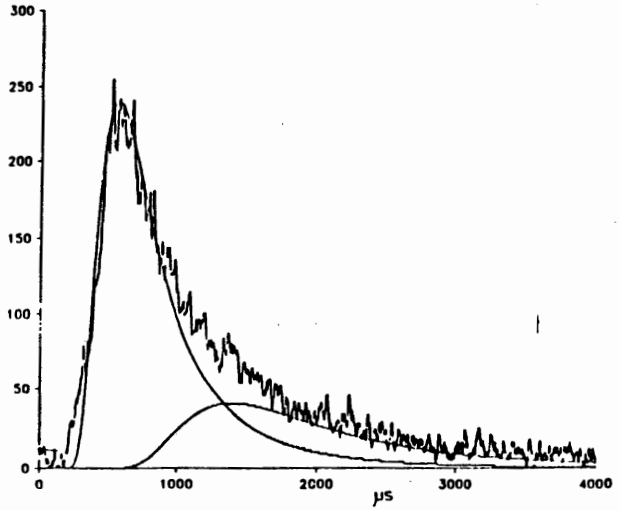


Fig C1.80 Cyclohexane desorbed from a surface of Xe coated quartz at 40 K following energy transfer from pyridine. Temperatures of desorbed molecules 780 K and 130 K.

vibrationally and electronically excited molecules when there have been produced by a pulsed laser. For these reasons we have worked with the dielectric surfaces MgF_2 and quartz. In all studies of processes on surfaces surface cleanliness is extremely important. It is well known that surfaces formed from freshly cleaved NaCl may be cleaned by modest heating under ultra-high vacuum UHV conditions. It is not easy to characterize dielectric surfaces and at present we do not possess the means of establishing the cleanliness of the surfaces which we have employed. Since the prime objective was to achieve non-thermal desorption from any surface this was not of paramount importance. However, once non-thermal desorption has been found to occur it becomes very important to know whether the results are affected by surface cleanliness. For this reason new surfaces were formed by firstly condensing Ar, Xe or O_2 onto quartz at 20K and then adsorbing the molecules to be studied onto these newly formed surfaces. We found that when the newly formed surface is firmly bound onto the quartz the non-thermal desorption results are the same as those from the uncoated quartz. This has removed the worry concerning surface cleanliness.

The characteristics of non-thermal desorption

There have been very few convincing results of non-thermal UV desorption. The large research group of Polanyi have used excimer lasers and LiF surfaces[1]. They have established that every species which is adsorbed onto the crystal is desorbed by the laser including Xe atoms, and concluded that colour centres are generated in the crystal producing shock waves which desorb everything. Ertl[2] has achieved good results for the non-thermal desportion of NO from a Ni (100)-O atom surface, but in the same experiments they also observe an equal amount of thermal desorption. For energy transfer studies it is necessary to completely eliminate thermal desportion. Domen and Chuang[3] have achieved specific non-thermal desportion of CH_2I from CH_2I_2 adsorbed on a sapphire surface using an excimer laser.

There is a great difference between thermal and non-thermal desorption of thin layers of molecules. For non-thermal desorption the temperatures of the desorbed species studied to date are much higher than those for thermal desorption being about 1000K instead of less than 400K.

Domen and Chuang also observed a new phenomenon for thick layers of CH_2I_2 on sapphire which they termed explosive desorption[3].

Results for non-thermal desorption

We also have found explosive desorption for thick layers of 1,3-cyclohexadiene adsorbed on MgF_2 and of pyridine adsorbed on quartz. This is illustrated in Figure C1.77.

Explosive desorption does not occur with thinner layers, but there is non-thermal desorption. This is illustrated for the desorption of pyridine from quartz in Figure C1.78.

Non-thermal versus thermal desorption

Clearly in order to study energy transfer from a donor molecule A to an unexcited acceptor molecule B it is essential that molecule B is not desorbed in the absence of A. The energy acceptor molecule will be desorbed if there is any significant thermal heating or if the laser directly excites both molecules.

The following results establish that within our experiments only non-thermal desorption is occuring,

1. Absorbed atoms of Ar, or Xe onto the dielectric surface are not desorbed by the laser.

2. Neither O_2, nor cyclohexane are desorbed when only these species are present on the dielectric surface.

3. Pyridine and 1,3-cyclohexane are only desorbed from the dielectric surface when the laser wavelength is tuned within the electronic absorption band of either molecules.

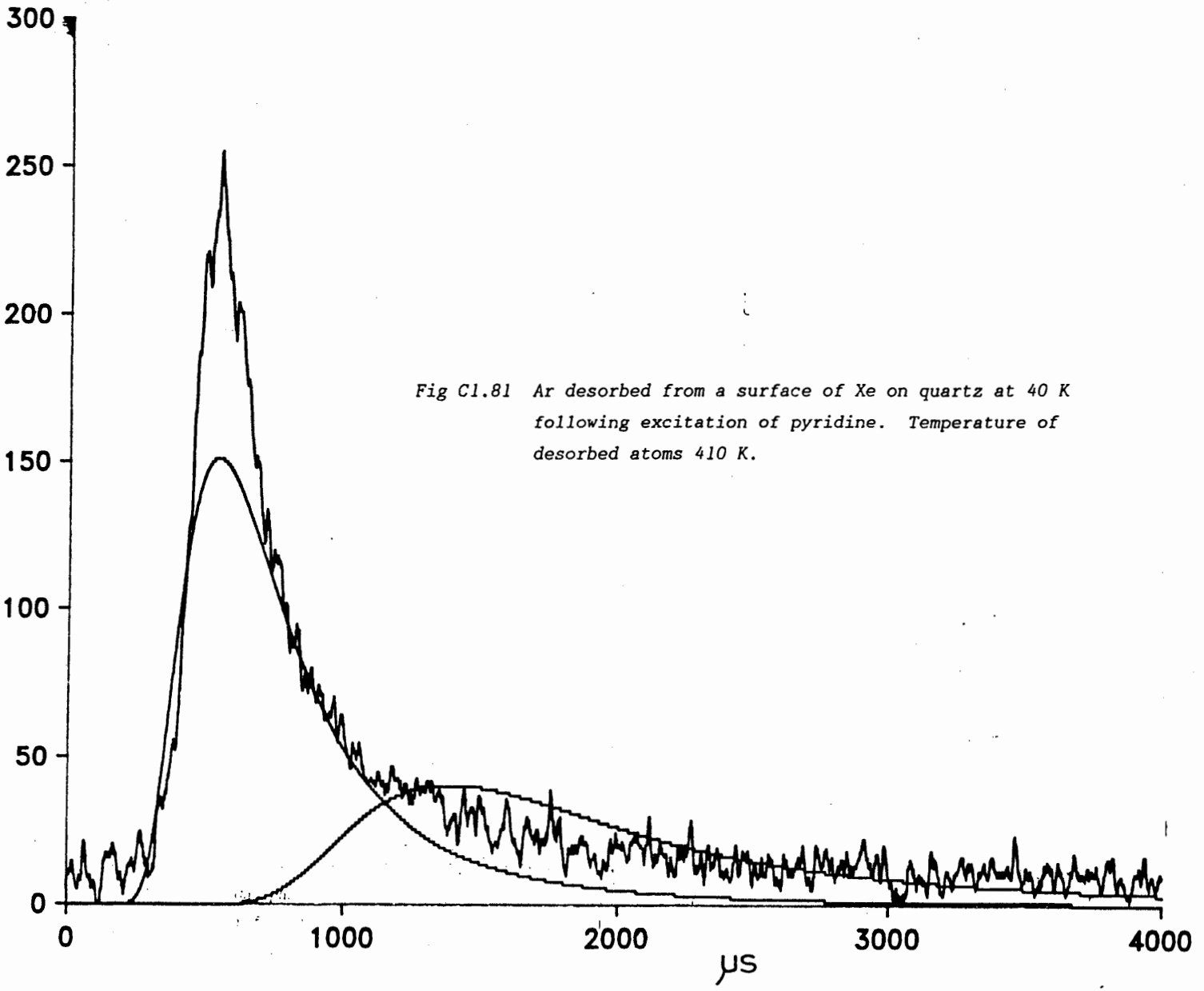


Fig C1.81 Ar desorbed from a surface of Xe on quartz at 40 K following excitation of pyridine. Temperature of desorbed atoms 410 K.

From 1 and 2 above it is concluded that heating of the surface by the laser is not taking place. Result 3 indicates electronic excitation to an upper electronic state must take place for desorption to occur.

Energy transfer

Firstly we established that cyclohexane is not desorbed from a quartz surface or from a surface of Xe on quartz at 20K when it is the only molecule adsorbed. We also have shown that pyridine is desorbed non-thermally for the same conditions.

For a three component mixture of pyridine, cyclohexane and argon adsorbed on a xenon surface adsorbed on quartz at 20K and at 40K both pyridine and cyclohexane are desorbed non-thermally with temperatures of about 800K, for the majority of the desorbed molecules, and about 200K for the minority of the molecules. This suggests that a small amount of thermal desorption is taking place. Further, a little Ar is also desorbed with a temperature of about 400K, and this is consistent with a small amount of thermal desorption occuring. These results are illustrated in Figures C1.79, C1.80 and C1.81.

Similar results were obtained for the desorption of pyridine/cyclohexane mixtures from quartz and of 1,3-cyclohexadiene/cyclohexane mixtures from MgF_2 giving further proof of energy transfer followed by non-thermal desorption of the acceptor molecule. These are the first results for the non-thermal laser induced desorption of polyatomic molecules which are not dissociated by the UV laser pulse. They are also the first results demonstating energy transfer on a surface between a molecule pumped by a UV pulsed laser and an initially unexcited molecule. They open the way to further studies of energy transfer between polyatomic molecules absorbed on surfaces. At present it is not known whether smaller molecules will also undergo energy transfer, or whether the originally pumped molecule will desorb too fast for energy transfer to take place.

References

1. E B D Bourdon, J P Cowin, I Harrison, J C Polanyi, J Segner, C D Stanners and P A Young, J Phys Chem **88** 6100 (1984).

2. F Budde, A V Hamza, P M Ferm, G Ertl, D Weide, P Andresen and H-J Freund, Phys Rev Letts **60** 1518 (1988).

3. K Domen and T J Chuang, Phys Rev Letts 59 1484 (1987).

C2	**BIOLOGY**	Pages
C2.1	UVRR STUDIES OF COENZYME BINDING TO DEHYDROGENASE ENZYMES	321-323
C2.2	TIME RESOLVED RESONANCE RAMAN STUDIES OF MODEL HEME SYSTEMS	323-326
C2.3	LASER-INDUCED TRAPPING OF BREAKS IN UV-DAMAGED MAMMALIAN CELLULAR DNA	326-331
C2.4	A REPETITIVE LASER-PLASMA X-RAY SOURCE FOR RADIOBIOLOGY RESEARCH	331-337

C2.1 UVRR STUDIES OF COENZYME BINDING TO DEHYDROGENASE ENZYMES

J C Austin*, R E Hester* and C W Wharton*
(* Chemistry Dept, University of York, * Biochemistry Dept, University of Birmingham)

Introduction

The coenzyme nicotinamide adenine dinucleotide (NAD^+) is essential to a large class of biological redox systems. The dehydrongenase enzymes and NAD^+ (or NADH) do not contain visible chomophores. However, the aromatic acids of the protein, NAD^+ and NADH absorb strongly in the UV (NAD^+ and NADH at 260 nm, aromatic amino acids at 200-220 and 250-280 nm). The UVRR investigation of dehydrognases can thus yield information relating to both the protein and coenzyme. We have demonstrated that UVRR spectroscopy (using 260 nm excitation) can be a sensitive probe of coenzyme binding to dehydrogenases, by comparing the UVRR spectra previously obtained from GAPDH[1] with those from other dehydrogenase enzymes. We have also investigated the effects of coenzyme binding on the enzyme GAPDH, by obtaining UVRR spectra with 220 nm excitation, where the aromatic amino acid residues of the protein are strongly resonance enhanced.

Experimental Details

Concentrations of enzymes and coenzymes for Raman experiments were in the range 4×10^{-5} to 6×10^{-6} M. UV radiation at wavelengths 220 and 260 nm was produced by frequency doubling the output from an excimer (Lumonics HX460) -pumped dye (Lambda Physik FL3002) laser using a β-barium borate crystal. (Laser Lines, Banbury, UK). The Raman radiation was collected in a Spex Triplemate spectrometer and detected using an OSMA intensified diode array (Spectroscopic Instruments). Enzyme spectra were collected for ca. 600- 1200 s, operating the dye laser at 25-30 Hz and less than 1mJ per pulse.

Results

UVRR spectra were obtained for the coenzyme NADH when bound to the enzymes liver and yeast alcohol dehyrogenase (LADH and YADH), lactate and malate dehydrogenase (LDH and MDH). The main results are summarised below; for further details see ref (2).

(1) The LADH and YADH enzyme-bound spectra are significantly different from those of free NADH and GAPDH-bound NAD^+. In particular, a strong band at 1325cm^{-1} appears in the alcohol dehydrogenase bound NADH spectra (see Figure C2.1 and spectra in previous report). The spectra obtained from LDH and MDH were of inferior quality, but show some differences in the main (ca. 1330cm^{-1}) NADH band.

(2) 220 nm RR spectra of holo- and apo- GAPDH are identical and show bands due to phe at 1001 and 1605cm^{-1}, trp at 1010, ca. 1355, 1460, and 1555cm^{-1}, and tyr at 1178cm^{-1} (see Figure C2.2).

Conclusions

Coenzyme binding: effects on coenzyme spectrum

The differences between the enzyme-bound and free coenzyme RR spectra may arise from one or more of the following factors.

(1) The extension of the coenzyme to an entirely 'open' conformation on binding to the enzyme. In solution the coenzyme is in equilibrium between two conformers: 'open' and 'stacked'.

(2) Adenine ring protonation on binding to the enzyme.

(3) Specific protein-coenzyme hydrogen bonding.

(4) Medium effects, i.e. general hydrophobicity of the coenzyme binding pocket; presence of charged groups.

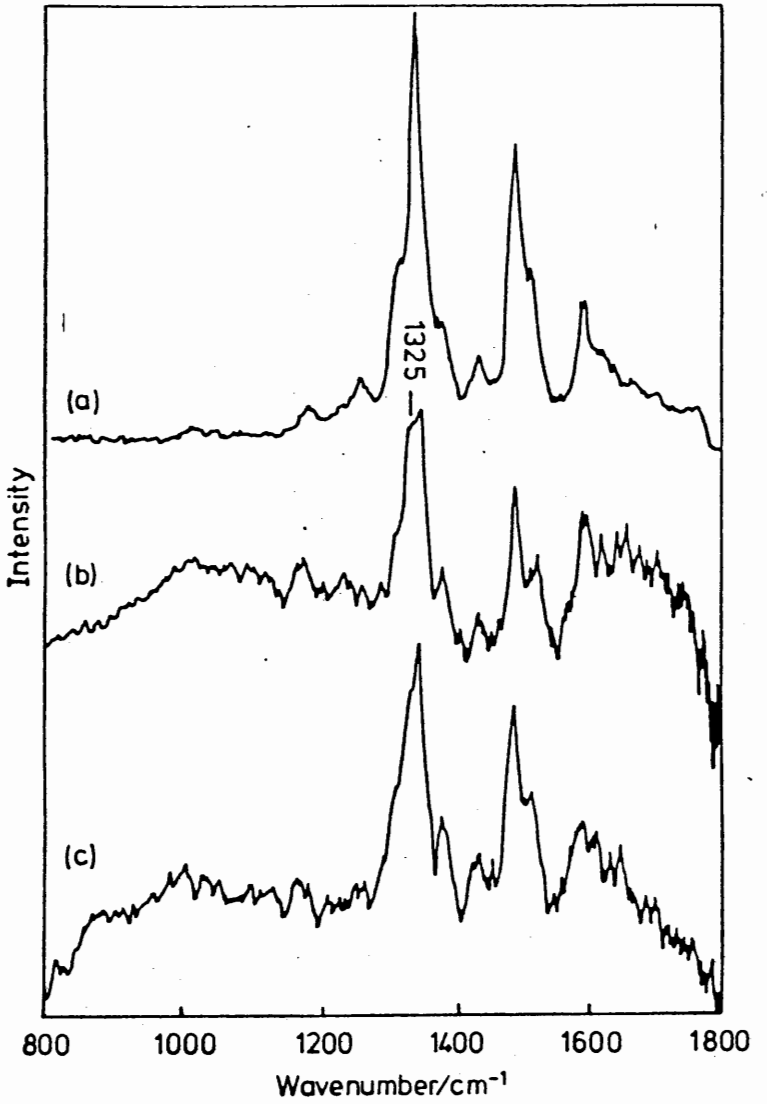


Figure C2.1 *260 nm RR spectra of*
(a) NADH; (b) Holo - Apo LADH difference;
(c) Holo - Apo YADH difference.
Enzyme bound NADH spectra given by (b) and (c).

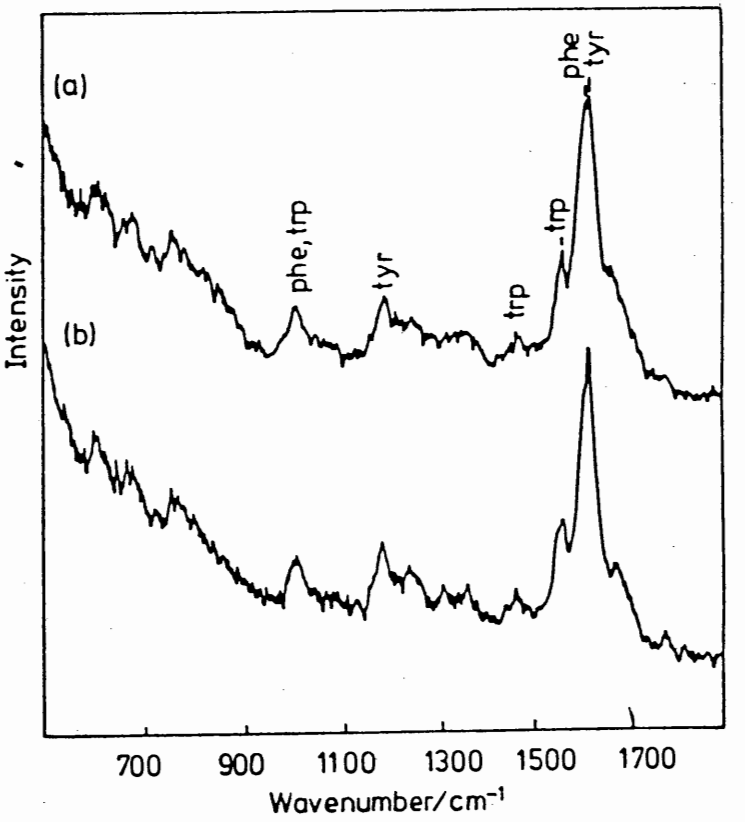


Figure C2.2 *220 nm RR spectra of*
(a) apo-GAPDH;
(b) holo-GAPDH.

Factor (1) affects all the enzyme spectra to the same extent. However, there is a conformational difference between the coenzyme when bound to GAPDH and when bound to LADH: a 180° rotation about the glycosidic bond of the nicotinamide ring. This results in a different stereochemistry of hydride transfer to the nicotinamide ring from the substrate: GAPDH is a 'B-type' dehydrogenase whereas LADH and YADH are 'A-type'. In fact, (1) is found not to be an important factor in determining the RR spectrum of NAD^+ or NADH. Furthermore, the A/B-type conformational difference did not appear to have a determining effect on the RR spectrum.

The changes in the coenzyme spectrum on binding to enzyme are not consistent with protonation of adenine, but may indicate strong hydrogen bonding to at least N_1 in the case of NADH bound to LADH (and YADH). However, in the hydrogen-bonded Watson-Crick adenine-thymine base pair, no changes were observed in the UVRR spectrum[3]. In the light of this result, it would be moderately surprising if, in this case, hydrogen bonding were the sole cause of the observed spectral changes.

LADH provides a generally more hydrophobic adenosine binding environment for the coenzyme that GAPDH. Consistent with this, the coenzyme spectrum when bound to GAPDH resembles the solution spectrum most closely.

The corresponding LDH and MDH spectra have been subjected to a less thorough analysis, but is appears that the spectral differences are consistent with a more hydrophobic coenzyme environment in LDH than in MDH.

Coenzyme binding: effects on GAPDH spectrum.

The lack of effects of coenzyme binding on the 220 nm-excitied RR spectra of GAPDH indicates that either the RR spectra are insensitive to this change, or that the aromatic amino acids are not greatly perturbed by the conformational change accompanying coenzyme binding. Two phe residues are involved at the coenzyme binding site, but there are 12 further residues in each subunit. Any perturbation of one of two phe residues would have to be large to affect the RR spectrum. A similar argument applies to the 9 tyr residues in each GAPDH subunit.

References

1. J C Austin, C W Wharton and R E Hester, RAL Annual Report (1988).

2. J C Austin, C W Wharton and R E Hester, Biochemistry, (1989), in press.

3. S P A Fodor and T G Spiro, J. Am. Chem. Soc., (1986), **108**, 3198.

C2.2 TIME RESOLVED RESONANCE RAMAN STUDIES OF MODEL HEME SYSTEMS

J C Austin, S E J Bell and R E Hester (Dept of Chemistry, University of York)

Introduction

The structural chemistry and dynamics of metalloporphyrins continues to be an active research area, due in part to their involvement in a wide range of biological systems, from redox enzymes to photosynthetic reaction centres. The model heme, iron(iii)tetraphenyl-porphyrin chloride (FeTPPCl) and its μ-oxo dimer $(FeTPP)_2O$), have been subjected to numerous studies, recently including transient absorption studies on the nanosecond (ns) and picosecond (ps) timescales[1-4]. These studies, whilst in some degree of conflict, indicate that for the μ-oxo dimer, photodisproportionation to Fe(IV) and Fe(II) porphyrins may take place:

$$(Por)Fe^{III}\text{-}O\text{-}Fe^{III}(Por) \longrightarrow (Por)Fe^{IV}{=}O + {}^{+}(Por)Fe^{II}$$

(Por)=porphyrin

Ferryl porphyrins (Fe^{IV}=O species) are known to exist as

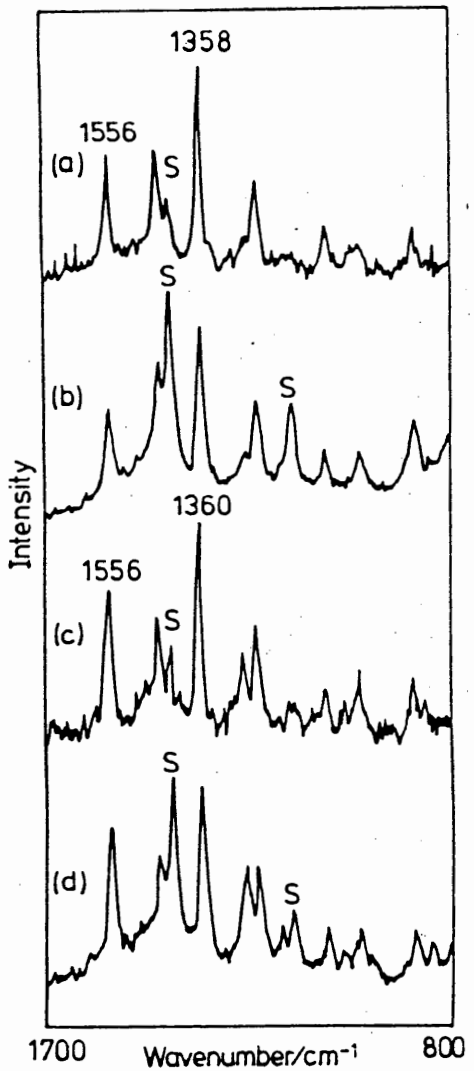


Figure C2.3 (a) $(FeTPP)_2O$ 408 nm-excited RR spectrum, low laser power.
(b) $(FeTPP)_2O$ 408 nm-excited RR spectrum, high laser power.
(c) FeTPPC1 408 nm-excited RR spectrum, low laser power.
(d) FeTPPC1 408 nm-excited RR spectrum, high laser power.

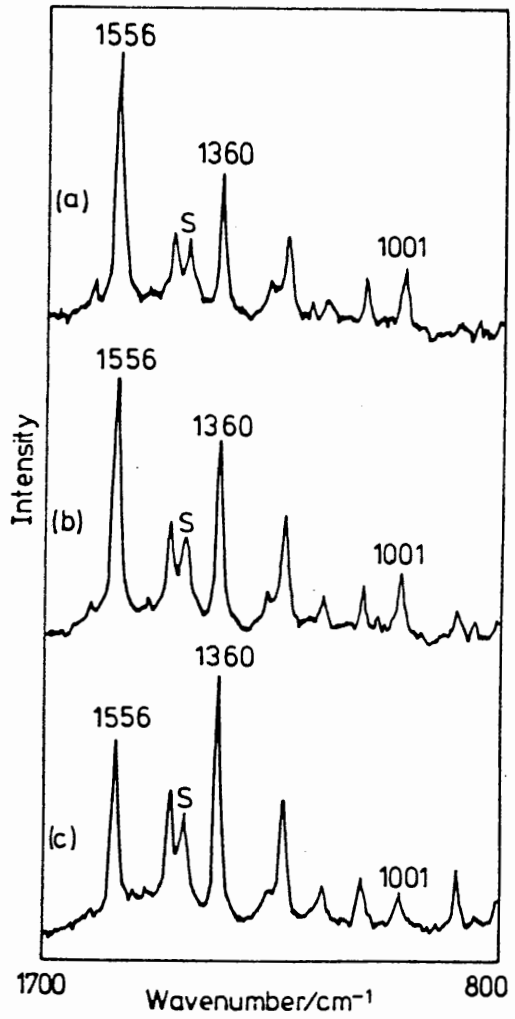


Figure C2.4 (a) 308 nm-photolysed dimer photoproduct RR spectrum, 424 nm excitation.
(b) FeTPPC1 424 nm-excited RR spectrum.
(c) FeTPPOH 424 nm-excited RR spectrum.

intermediates in numerous heme enzyme systems. Transient Raman spectra have been obtained for such ferryl intermediates in natural enzyme systems[5], but comparison of the data with data from model systems has been limited. The photodissociative method above could, in theory, yield a route to formation of model ferryl systems whose properties could be systematically varied. Thus, we have used time-resolved Raman spectroscopy, the photochemistry of both $(FeTPP)_2O$ and FeTPPCl on the ns timescale.

Experimental

Iron(III)tetraphenylporphyrin chloride was a generous gift from Dr J R Lindsay-Smith. The μ-oxo dimer was produced by reaction of the monomer FeTPPCl with sodium hydroxide. All spectra shown were obtained from solutions of porphyrins in dichloromethane.

Laser radiation of wavelength 408, 424 and 575 nm was obtained from a XeCl excimer (Lumonics HX460)-pumped dye laser (Lambda Physik FL3002). Laser radiation of wavelength 308 nm was split off from the XeCl excimer beam (most of the beam being used for dye pumping). Laser radiation of wavelength 411 nm was produced by Raman shifting the output of a XeF excimer (EMG-150) laser, using a hydrogen filled cell.

Raman spectra were obtained using conventional right angle scattering geometry. The Raman scattered light was collected with a Spex Triplemate spectrometer and detected using an OSMA intensified diode array.

Results

The Raman spectra of FeTPPCl and $(FeTPP)_2O$ shown in Figure B2.3 were obtained using single laser pulses of 408 nm (ca. 10 ns FWHM). The spectra in Figure C2.3 (a) and (c) show dimer and monomer, respectively, at low laser power. The corresponding spectra obtained at high laser power are shown in Figure C2.3 (b) and (d). At high laser powers, there appears to be a large degree of reversible photobleaching in both monomer and dimer samples, as judged by the relative intensities of the solvent bands (marked S). No new peaks were apparent in spectra (b) and (d).

Using laser pulses of wavelength 424 nm, bleaching at high laser powers was reduced (but still present). Using a pump pulse of 308 nm, and probing with the 424 nm pulse, a large background luminescence was observed when the pump-to-probe delay was ca. 0 ns, which completely masked the Raman spectrum. After 30-40 ns, this luminescence had almost completely decayed. However, no large bleaching effect was observed on this timescale, for either monomer or dimer. After some minutes of 308 nm irradiation, the Raman spectrum of the dimer sample changed irreversibly (see Figure C2.4 (a) and (b)). The uv-vis absorption and Raman spectra indicate that the dimer had been converted to FeTPPCl.

Using a 411 nm pump pulse, and probing with a 424 nm pulse, the large luminescence at 0 ns pump-to-probe time was avoided. However, no new features, or even significant bleaching was observed, even though large bleaching was observed for single (411 nm) pulse experiments. It is most likely that (despite much effort) the overlap of the two pulses both spatially and temporally was not sufficient.

Discussion

The results from the 408 nm single laser experiments on the dimer indicate that although significant bleaching of the ground state material can be induced, the species created is a weak Raman scatterer at this wavelength. Although it is conceivable that this bleaching is associated with photodissociaton of the dimer, it would be expected that the photoproducts (Fe=O and Fe complexes) would be strong Raman scatterers at 408 nm. In addition, photobleaching effects were also observed for the monomer FeTPPCl, which cannot undergo photodissociation. It seems probable in the latter case that the transient species formed is the triplet state of FeTPPCl, which has been found to have an absorption maximum at 440 nm, considerably to the red of our probe laser wavelength[1,2]. This triplet state may well be significantly populated by high irradiance 10 ns pulses despite its short (τ =30

ps) lifetime. Similar effects would also explain the bleaching but not photo- dissociation of dimer by 408 nm laser pulses.

From the experiments using 308 nm pump pulses (exciting into the Fe-O charge transfer band), some dimer disporportionation does seem to be taking place. Under our experimental conditions, recombination is in competition with other processes, leading to irreversible changes (Figure C2.4). Our difficulty in observing the primary products of the photodissociation may have been due to the 30-40 ns pump-to-probe delay that we were forced to adopt because of sample luminescence; the photoproducts may have considerably shorter lifetimes. Alternatively, secondary pumping by the 424 nm probe pulses may have photoexcited the fragments to upper electronic states. We expect that variation of probe pulse energy and/or wavelength should allow us to obtain spectra of the photofragments (and/or photoexcited species) produced by dissociation of the dimer complex.

References

1. P A Cornelius, A W Steele, D A Chernoff and R M Hochstrasser, Chem. Phy. Lett. (1981), **82**, 9.

2. Y. Liang, D K Negus, R M Hochstrasser, M Gunner and P L Dutton, Chem. Phys. Lett. (1981), **82**, 236.

3. M W Peterson, D S Rivers and R M Richman, J. Am. Chem. Soc. (1985), **107**, 2907.

4. C R Guest, K D Straub, J A Hutchinson and P M Rentzepis, J. Am. Chem. Soc. (1988), **110**, 5276.

5. T Kitagawa in "Spectroscopy of Biological Systems" Advances in Spectroscopy, Eds. R J H Clark and R E Hester (1986), **13**, 443.

C2.3 LASER-INDUCED TRAPPING OF BREAKS IN UV-DAMAGED MAMMALIAN CELLULAR DNA

R A Meldrum & C W Wharton (Dept of Biochemistry, University of Birmingham)

J Boon, W Lester & C Reason (RAL)

Automation of Break Trapping Experiments

The experimental procedure for the study of early and rapid events in repair of DNA breaks induced by UV-radiation damage has now been automated and experimental measurements may be made with much increased efficiency and rapidity. This has led to novel results which revise considerably current views on the mechanisms of the DNA repair process.

A machine built at the Rutherford Lab carries out the experimental procedure in the following way. A pipette delivers cells into quartz cuvettes on a rotating stage. The cuvettes are preloaded with the 351 nm-photoactivatable radioactive nick trapping agent (caged-α-^{32}P dideoxyadenosine triphosphate, see RAL report, 1986). After delivery of the cells into a cuvette the stage is moved on one place and electrodes are inserted into the cuvette, charged and fired to permeabilise the cells and allow entry of the radioactive agent. The "damaging" 248 nm laser pulse is fired and after a variable delay a 351 nm laser pulse is fired to photorelease (uncage) the break trapping agent. After a further delay which can be varied the cuvette is rotated on one place and a "quench" of sodium hydroxide delivered from a second pipette. At this stage precipitation of the acid insoluble fraction of DNA with TCA and filtration onto glass fibre filters for scintillation counting is carried out by hand.

Timecourses of DNA repair

Using the automated system timecourses of incorporation of α-^{32}P-ddATP and ^{3}H-TTP into DNA after damage by 248nm UV laser pulses have been measured. These show a rapid burst of DNA synthesis followed by a decrease which is indicative of enzymic excision of newly incorporated radiolabelled bases. Synthesis then

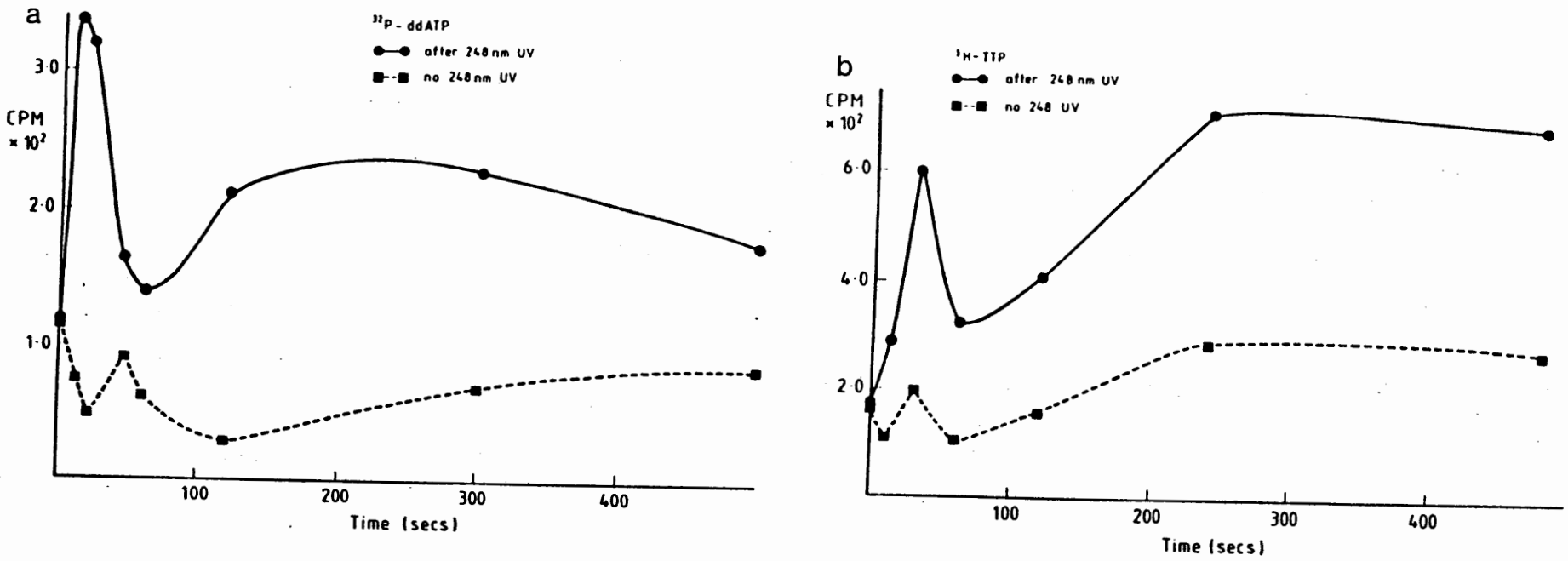


Fig C2.5 Timecourses of the incorporation of α-^{32}P dideoxyadenosine triphosphate and ^{3}H-thymidine triphosphate into HL60 cellular DNA after 248nm UV damage.

a) 1μCi α-^{32} ddATP was added to cuvettes followed by 0.8ml of cell suspension (ca. 10^6 cells).
Solid line - following permeabilisation cells were irradiated with 100 J/m² 248nm light and the incubations quenched at the times shown by addition of 0.5ml 5M NaOH.
Dashed line - control experiment with no UV irradiation.

b) 1μCi ^{3}H-TTP was added to cuvettes followed by 0.8ml of cell suspension (ca. 10^6 cells).
Solid line - following permeabilisation cells were irradiated with 100 J/m² 248nm light and the incubations quenched at the times shown by addition of 0.5ml 5M NaOH.
Dashed line - control experiment with no UV irradiation.

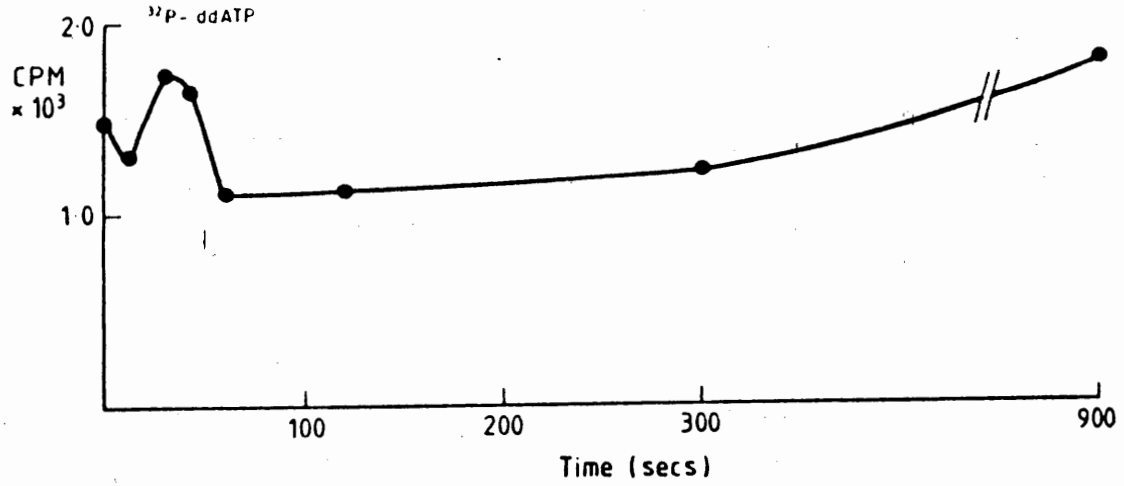


Fig C2.6 *Measurement of the rate of DNA repair at various times after UV-damage. 1μCi α-^{32}P ddATP was used essentially as in Fig. 1 except that permeabilisation was delayed for the times shown on the Fig following UV irradiation and the incubation was quenched 1 minute after permeabilisation.*

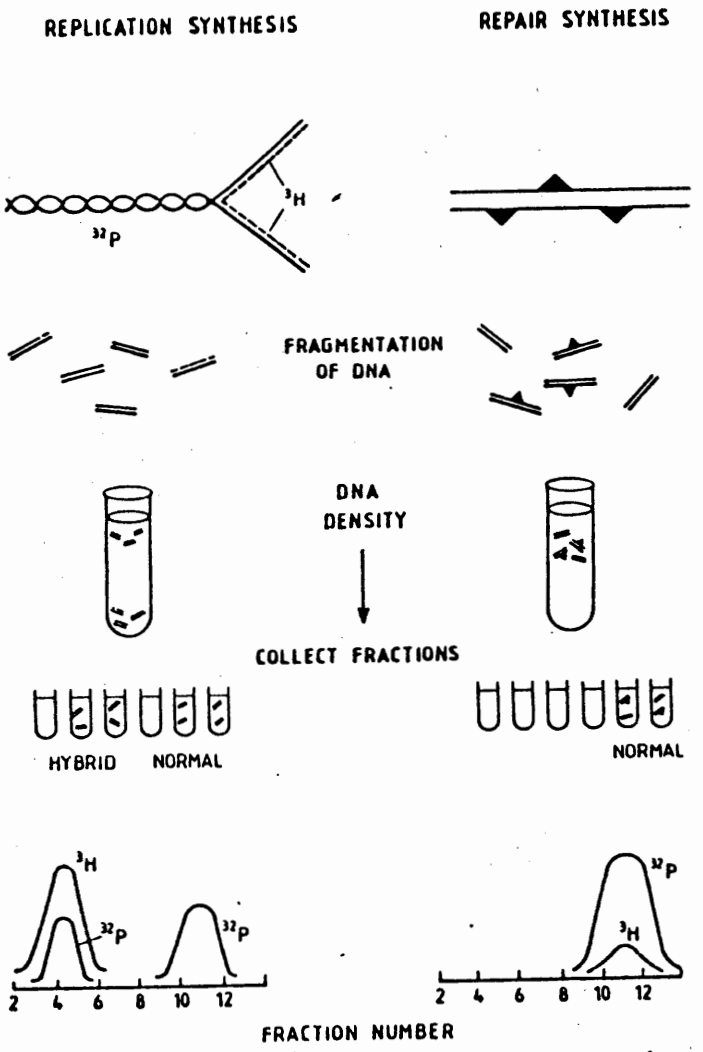


Fig C2.7

increases at a moderate rate and is maintained at a steady level up to 15 minutes.

The profile of the time course of incorporation of α-^{32}P-ddATP (Fig. C2.5A) is representative of the results of several identical experiments. It is notable that to our knowledge the burst of uptake in the early stages of DNA repair has not previously been observed; other workers have made their initial measurements several minutes after damage see eg. Squires et al, 1982. The time course for uptake of ^{3}H-TTP (Fig. C2.5B) which shows only one transient peak point is derived from a low number of replicate experiments. This transient peak of ^{3}H-TTP therefore cannot be regarded as real until more experimental data has been obtained.

The initial rapid rise and subsequent fall of α-^{32}P ddATP incorporation suggests that an enzyme with a specific affinity for the dideoxynucleotide, incorporates it in the DNA chain but that another enzyme readily recognises the dideoxynucleotide as an unnatural base and excises it. This all takes place within one minute. This excision enzyme activity is reduced or lost as incorporation of α-^{32}P ddATP then proceeds it at a moderately steady rate. The excision phase may thus be a special feature of the use of ddATP but the rapid incorporation phase is likely to be general.

Incorporation of ^{3}H-TTP, a natural base, shows a proportionately higher increase after 100 seconds than does incorporation of ddATP^{32}. The enzyme(s) active at this time may therefore have a higher specifity for ^{3}H-TTP.

An improved synthesis of cages α-^{32}P-ddATP

Considerable effort has been devoted to improving the preparation of radiolabelled caged-ddATP since the yield was previously ca. 10% (see RAL Reports, 1986, 1987). A microvolume methodology has been devised in which the volume of the aqueous phase is reduced from 1ml to 130µl and the volume of the organic phase from 2ml to 0.25ml (ie. the concentration of diazonium derivative is increased by a factor of 8). The yield is increased to 85%. ATP (0.25µmoles) added to the reaction mixture acts as a buffer, becomes caged and subsequently acts as a carrier in the HPLC purification. After this procedure the product is obtained in 98% caged form. Despite this high level of purity a recent batch showed anomalous photoactivation in that a threshold of 1 KJ/m² 351nm radiation was required to initiate photolysis. This behaviour is ascribed to the presence of a very low concentration of impurity which traps a photolytic intermediate. Since we have previously established that 1 KJ/m² is the optimal does for photoactivation of unlabelled caged compounds and this value was used in repair experiments insignificant incorporation of label was achieved.

Use of electropermeabilisation to start trapping experiments

Due to the fact that "caged" α-^{32}P ddATP did not photolyse optimally at 1kJ 351 nm UV laser irradiation permeabilisation of cells by electroporation was used as a method of instantaneous triggering of the break trapping process. The α-^{32}P ddATP is held outside the cells until allowed access by permeabilisation of the cells by an electric pulse. This is less satisfactory than employing a "caged" nucleotide which may be introduced into the cells before damage and be allowed to overcome diffusion limitations before being activated. The measurements of the enzyme rates of repair acquired by delayed permeabilisation after damage (ie. measurements of the rates of repair at these times) qualitatively support the conclusions derived from measuremnts made from overall (accumulated) repair. (Fig C2.6).

The effects of diffusion limitation were confirmed by an experiment where cells were electropermeabilised before and after 248nm UV damage and the incorporation of ^{3}H-TTP measured over 15 minutes. Enhanced uptake of ^{3}H-TTP after 248nm damage was seen in cells which were permeabilised before damage but not in cells permeabilised after damage.

This experiment also demonstrated that the incision process of UV repair in cells electropermeabilised before damage is still competent. The incision process is thought to be ATP dependent. During permeabilisation of cells by slower methods ATP is lost and

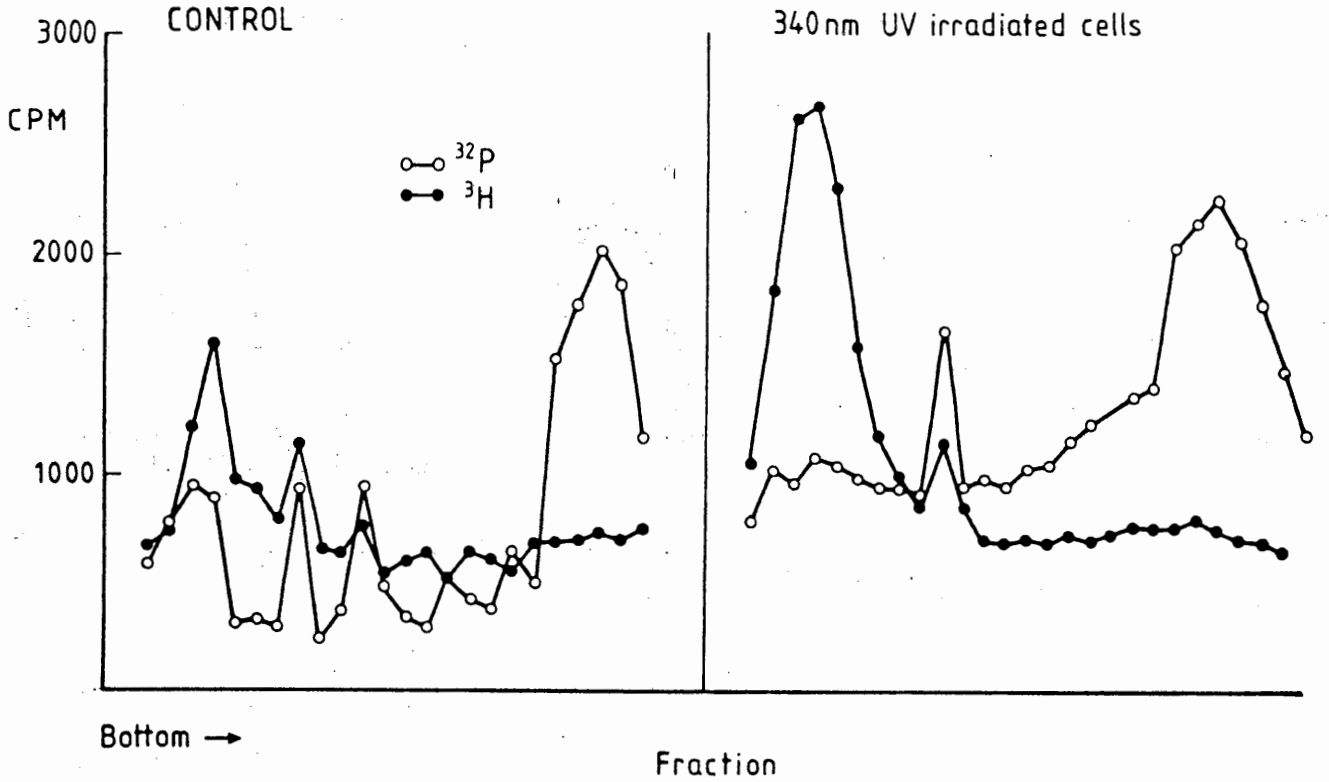


Fig C2.8 Alkaline caesium chloride gradients of DNA from untreated and irradiated (340nm UV) cells. Cells were prelabelled for 16 hours with 0.4uCi [^{32}P] orthophosphate. Cells were then irradiated with 1kJ/m^2 340nm UV (XeCl pumped dye laser) and both irradiated and control cells were incubated at 37°C for two hours with bromodeoxyuridine (10um), fluorodeoxyuridine (1uM) and 5uCi/ml ^3H-thymidine. The cells were then lysed in lysis buffer, digested with 50ug/ml proteinase K then layered on a caesium chloride gradient and centrifuged at 37000 rpm for 40 hours. Gradients were fractionated and counted for ^{32}P and ^3H.

the incision process impaired but when using fast time methods as described above ATP loss does not occur or take effect over the time period under study.

Stimulation of DNA synthesis by 351 or 340 nm UV laser irradiation

Previously we reported some stimulation of DNA synthesis by 351nm UV light. When an action spectrum of DNA synthesis activity after irradiation with laser pulses of wavelengths between 300 and 400nm at 1kJ/m² energy was determined, a peak of DNA synthesis stimulation occured at 340nm (RAL Report 1988). To determine whether this was due to induced repair synthesis or enhanced replication synthesis, cells were prelabelled with ^{32}P before irradiation with 340nm then incubated with 5-bromo deoxyuridine (BUdR) density label and ^{3}H-thymidine after irradiation (Smith et al, 1981). BUdR is a "heavy" analogue of thymidine, hence, when incorporated in long patches of replication DNA produces pieces of hybrid DNA with a greater density than normal. These may be separated from normal density DNA if the DNA is fragmented by shearing and sedimented on a caesium chloride gradient. If the short and the hybrid DNA density is not significantly different from the density of the normal DNA and sediments in the same fractions of the gradient. This strategy is illustrated in Fig. C2.7.

Fig C2.8B shows no peak of ^{3}H in the top fractions of the gradient where hybrid DNA containing patches of repair would equilibriate after cells have been irradiated with 340nm UV. It does however show an increased peak of ^{3}H, when compared to the control cells (Fig C2.8A), in the lower fractions of the gradient suggesting that the new DNA synthesised incorporated the BUdR in long stretches. This would confirm that enhanced DNA synthesis induced by 340nm UV light is enhanced replication synthesis.

Another explanation of enhanced ^{3}H-thymidine uptake after 340nm UV irradiation is that the nucleotide pool of the cells might be depleted in some way and so effectively increase the specific activity of the radioactively labelled thymidine. If this were the case, the ratios of ^{3}H to ^{32}P in all the fractions from the density gradient would be increased in DNA from irradiated cells when compared to control cells. The ratio $^{3}H/^{32}P$ is not increased in the fractions where normal density DNA equilibriates in the profile of DNA sedimented from irradiated cells so a depletion of the unlabelled nucleotide pool may be ruled out.

References

1. S Squires, R T Johnson and A R S Collins (1982) Mutation Research 95, 389-404.

2. C A Smith, P K Cooper and P C Hanawalt (1981) In DNA Repair - a Laboratory Manual E C Freidberg & P C Hanawalt Eds. Vol. 1, part B, 289, Dekker, New York.

C2.4 A REPETITIVE LASER-PLASMA X-RAY SOURCE FOR RADIOBIOLOGY RESEARCH

F O'Neill, I C E Turcu, G J Tallents, J Dickerson, T Lindsay (RAL)
D T Goodhead, A Stretch (MRC Radiobiology Unit)
C W Wharton, R A Meldrum (Birmingham University

Introduction

When soft X-rays are absorbed and deposit energy in biological material, effects such as cell-killing and DNA strand breaking are known to occur. The study of these processes is of fundamental biological interest as well as being of practical importance in relation to the clinical treatment of carcinoma using radiotherapy. Soft X-ray induced effects in biological specimens are also important in X-ray microscopy because in this technique the X-rays are typically used at high levels of illumination in order to make suitable images and radiation damage to specimens is certain to occur. Previous studies of the mechanisms of soft X-ray damage in biological cells have made use of essentially continuously emitting radiation sources such as X-ray tubes generating characteristic line radiation[1] or synchrotron radiation sources[2]. X-ray

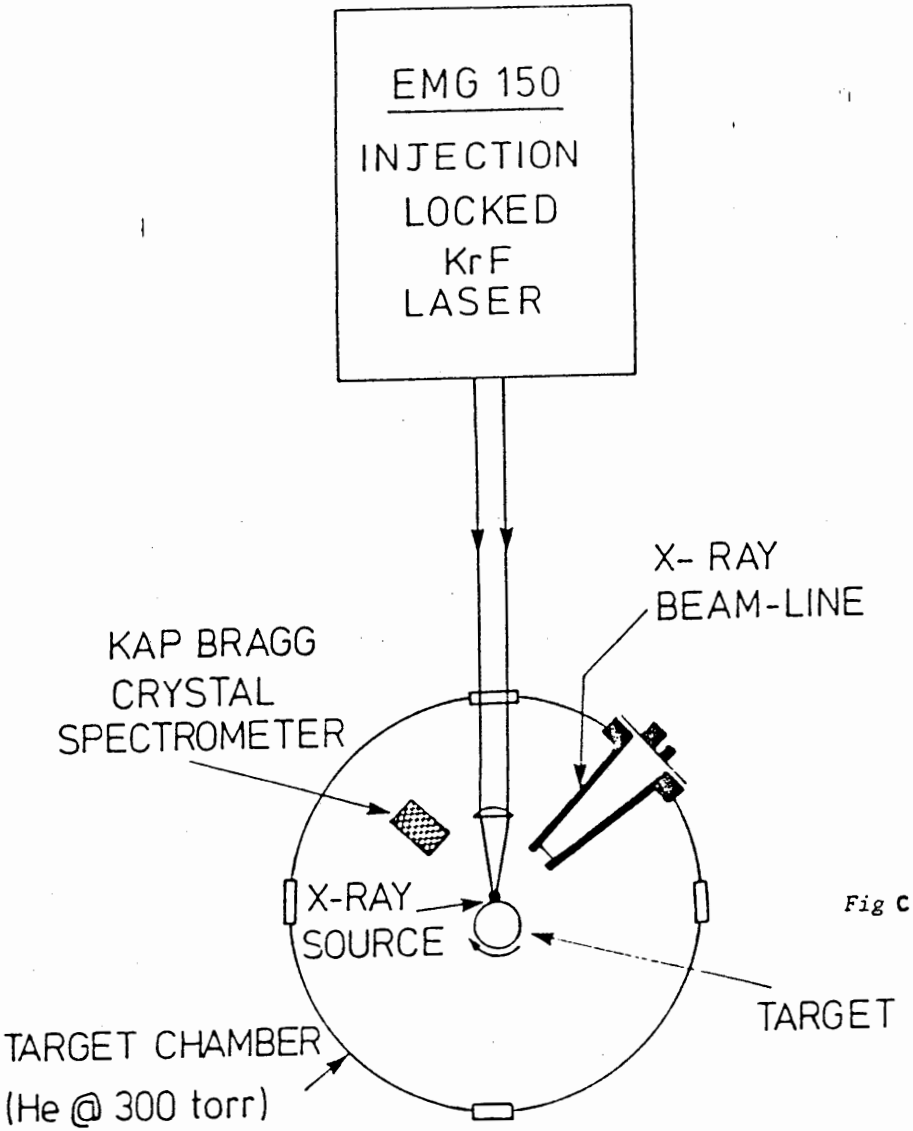


Fig C2.9 *Experimental arrangement.*

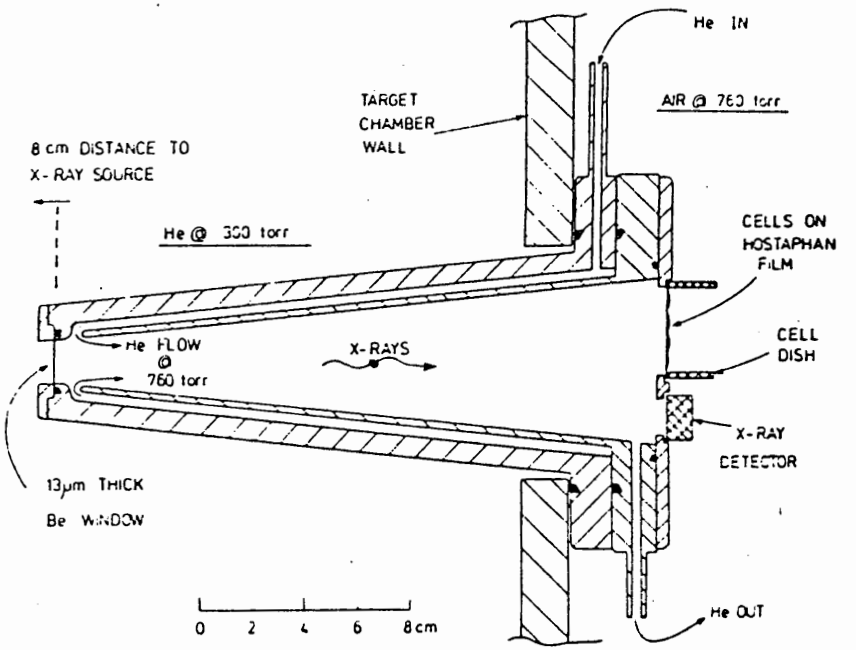


Fig C2.10 Details of X-ray beam-line on laser-plasma X-ray source.

tubes are low power laboratory-scale devices where the choice of X-ray wavelength is restricted by the availability of suitable electrode materials. Synchrotron sources are very powerful and can be tuned to any soft X-ray wavelength but to use this type of source the researcher typically has to travel to a distant site.

In the present paper we describe the first use of a repetitively pulsed laser-plasma soft X-ray source for radiobiology studies. This type of source is of interest because it is potentially a very powerful laboratory-scale device where wavelength tunability is feasible because of the comparatively free choice of target material. Another interesting characteristic is that the X-rays are delivered to the specimen in the form of intense short bursts of radiation so that at any instant during the pulse a number of X-ray photons are likely to be interacting with an individual biological cell nucleus. The experiments described here were performed mainly for calibration purposes and were designed to compare results obtained with a laser-plasma X-ray source with previous work using a cold-cathode discharge X-ray source.

The X-ray Source

A repetitive laser-plasma X-ray source at $h\nu \approx 0.85$ keV is generated by focusing laser pulses from the LSF Lambda Physik injection-locked EMG 150 KrF laser onto a rotating silver steel target in the experimental arrangement shown in Fig B2.9. The chemical composition of the target is ≥97.5% iron with traces of carbon (≈1%), silicon (≤0.5%), chromium (≤0.5%), and manganese (≤0.5%). The KrF laser is operated at 5 Hz repetition rate and produces an energy on target ≈0.3 J/pulse in a 25 ns pulse duration at a wavelength of 249 nm. The laser line-width is the normal free-running line-width ≈0.5 nm ($\Delta\bar{\nu} \approx 80$ cm^{-1}). Laser pulses are focused to a spot size ≈15 μm diameter on target using an aspheric lens of 9 cm focal length and the irradiance on target is estimated to be ≈ $0.5\text{-}1.0 \times 10^{13}$ W/cm^2. The target chamber is filled with helium gas at a pressure of 300 torr to reduce the rate at which target debris from the plasma coats the laser optics in the chamber whilst at the same time not attenuating the ≈1 keV X-rays in the beam line to the biological exposure station.

The pulses of X-rays from the laser produced plasma have a duration ≈ 5-10 ns and are emitted into the full 2π steradian solid angle in front of the rotating target. A $(\cos\theta)^{0.6}$ angular distribution of the radiation pattern can be assumed as has been measured in previous experiments using the same apparatus[3]. X-ray pulses from the plasma irradiate biological specimens through the conical beam-line arrangement shown in detail in Fig.B2.10. X-rays travel from the 300 torr He-filled target chamber through a 13 μm thick beryllium window into an atmospheric pressure region which is continuously flushed with He gas. The biological specimens are held in a specimen dish which is discussed below and which has been described in a previous publication[4]. A Si p-i-n diode X-ray detector is mounted in the exposure line beside the specimen dish to provide a continuous monitor of the X-ray pulses on an oscilloscope.

A Bragg crystal X-ray spectrometer (KAP crystal, 2d=26.63 Å) was placed inside the target chamber to record the X-ray spectrum from the plasma source. This information is necessary in order to be able to calculate the X-ray dose to the biological specimen as this dose is wave-length dependent. A 13 μm thick beryllium filter was placed over the spectrometer slit so the recorded X-ray spectrum was essentially the same as that incident on the biological specimen.

An X-ray spectrum of the plasma source recorded on Kodak Industrex film is shown in Fig.B2.11. To record this spectrum the laser was fired at 2 Hz repetition rate for 12 mins. The spectrum is seen to consist only of two groups of iron lines. The wavelengths of individual lines are noted on the microdensitometer trace of Fig.B2.11. The more intense lines are due to M to L shell (principal quantum number n=3-2) transitions of Ne-like (Fe XVII) and F-like (Fe XVIII) ions[5,6]. There are also some lower intensity lines which are dielectronic transitions in Na-like (Fe XVI) and Mg-like (Fe XV) ions[7] and one unidentified line at 14.030 Å (our measurement) frequently seen in iron spectra[8]. Other wavelengths in Fig.B2.11 are taken from references 5-7. The spectrum cuts off sharply on the long wavelength side due to the falling transmission of the 13 μm beryllium filter. The sharp

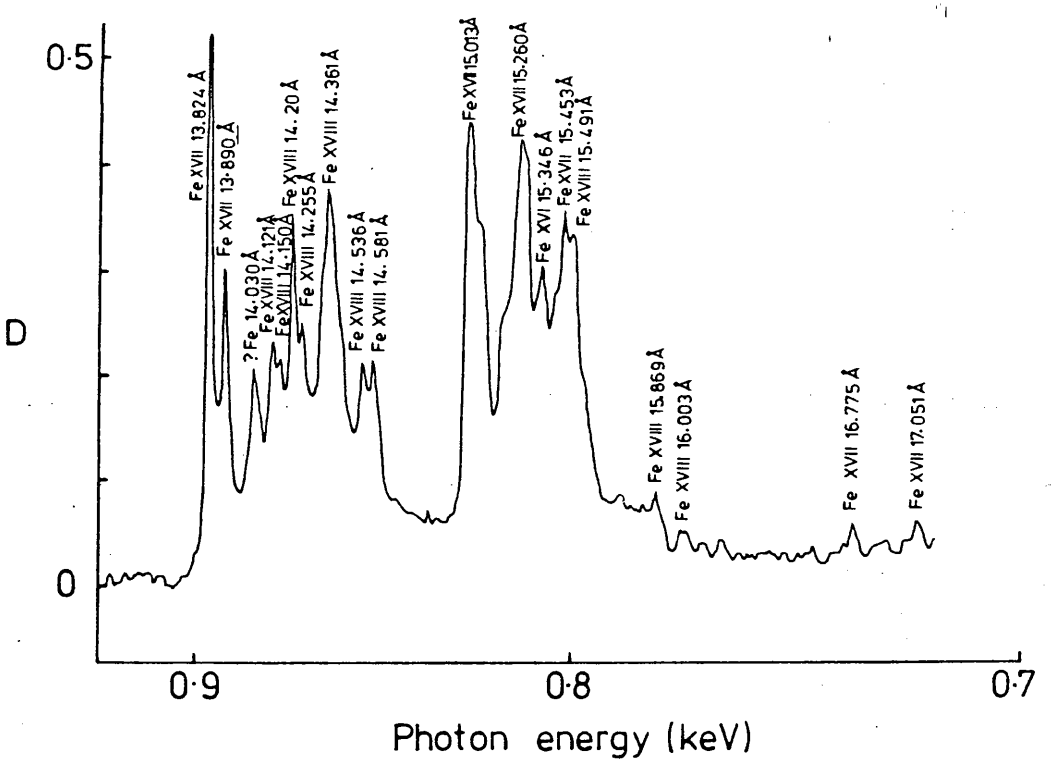


Fig C2.11 Microdensitometer trace of iron X-ray spectrum from steel target showing the wavelengths and identifications of the emitted spectral lines.

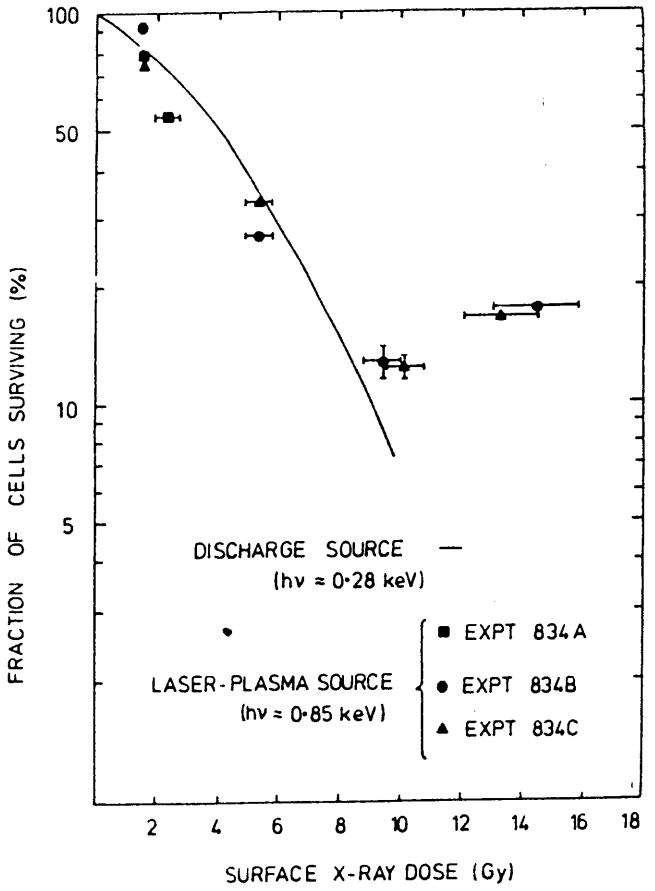


Fig C2.12 Survival of V79 hamster cells after irradiation with X-rays from the laser-plasma source. Different symbols are used for each of three experimental runs. For each point the standard deviation of the mean (vertical error bar) was calculated from the distribution of colonies on each of the five plates: these estimates of the uncertainties did not differ significantly from the alternative assessment based on Poisson distribution of total colonies. Where two different plating densities yielded countable results (ie, $\lesssim$ 700 colonies/dish) the mean is shown (weighted according to the uncertainties of the individual values). When not shown, the standard deviations are smaller than the size of the symbols.

fall-off on the short wavelength side with no lines at ≤ 13.82 Å is because the plasma is not hot enought to excite higher energy transitions of, say, O-like (Fe XIX) ions. There are however, some shorter wavelength lines of less intensity[8] beyond the range of the Fig.B2.11 exposure due to transitions originating from principal quantum number n=4, 5.... We could expect some low intensity emission from Fe XVII and Fe XVIII at wavelengths down to the series limits at 9.70 Å and 9,13 Å respectively.

The absolute intensity of the plasma X-ray source is deduced from the electrical signals generated by the Si p-i-n X-ray diode installed in the end of the X-ray beam-line. Knowing the source X-ray spectrum from Fig.B2.11 we have used the manufacturers data on sensitivity versus X-ray wavelength for the p-i-n diode to convert electrical signals into absolute X-ray flux. These measurements showed that at the source-specimen distance of 30 cm each plasma pulse delivered a maximum ≈20 nJ/cm² of X-rays which gives a dose of $\approx 2 \times 10^{-2}$ gray/pulse to the specimen. In practice when running at 5 Hz it was necessary to irradiate for 3-5 mins in order to achieve X-ray doses ≈15 gray for the highest X-ray exposures on the biological specimens.

Biological Cell Killing Experiments

The cell line and biological methods used in the present cell killing experiments are mostly the same as those used in a number of previous investigations into the effectiveness of monoenergetic ultrasoft X-rays[4,9], heavy ions[10,11] and other radiations. An ampoule of V79-4 Chinese hamster cells, which are held permanently as a large stock at liquid nitrogen temperature, was removed and the cells grown for 3 days. Approximately 40 hours prior to irradiation 5×10^4cells/dish were spread, with Eagle's Minimal Essential Medium plus 10% foetal calf serum, glutamine and antibiotics, into 3 cm diameter dishes (Fig.B2.10) each of which was constructed of a glass ring with a thin (2.5 µm) Hostaphan (Hoechst) polyester base[4]. The 40 hour growth period allowed formation of a non-confluent monolayer of well-flattened cells on the dish base, thereby minimising attenuation of the X-rays through the cells.

Prior to irradiation the cells were maintained in a 37°C incubator near the X-ray source. The cells were irradiated at room temperature without growth medium; immediately after irradiation fresh complete medium was added. For each dose point 5 dishes were irradiated sequentially and then together transported ≈1 km for replating. Individual dishes were without medium in the laser-plasma X-ray irradiation facility for times of about 2 to 6 minutes and were subsequently maintained with fresh medium and optimum pH for about 15 to 40 minutes before harvesting. For harvesting the medium was removed and the plastic dish base was cut out with a 3-bladed cutting device, leaving a 2 mm edge strip behind to avoid edge effects[4,9]. The cut out Hostaphan discs were transferred into trypsin-EDTA solution to remove the cells which were then collected by centrifugation, resuspended, counted and appropriately diluted before respreading at 200-50,000 per 9 cm dish. Alternative seeding densities (5 dishes each) were included to yield an estimated 200 surviving colonies, allowing for alternative possible survival curves. After 8 days growth the cells were stained, colonies containing ≥50 cells were counted and numbers expressed relative to the zero-dose controls. These methods were generally the same as those used previously to determine cell inactivation by carbon K characteristic X-rays[4]. The main difference in the present experiments was the slightly longer time interval between irradiation and respreading.

Fig.B2.12 shows the fraction of cells able to form colonies, as a function of the laser-plasma X-ray dose expressed as the absorbed dose in tissue at the incident surface of the cells (that is, at the Hostaphan/cell interface). Shown for comparison is the survival curve obtained previously when the same cell line was irradiated with monoenergetic 0.28 keV carbon K X-rays produced by a cold-cathode discharge source[4].

DNA Damage Studies

A clear stimulus of DNA synthesis as measured by uptake of tritiated thymidine was produced in V79 chinese hamster fibroblasts when the cells were subjected to a dose of approximately 2 gray of the X-rays. This stimulus almost certainly may be attributed to

induced DNA repair, since increase in uptake of tritiated thymidine is markedly reduced by the presence of 100 μM dideoxythymidine as indicated in the table below.

AVERAGE DOSE OF X-RAYS (Gy)	INHIBITOR	UPTAKE OF ^{3}-HTdR (cpm 10^4)
0	None	11.91(±2.01)
2.15	None	36.14(±3.56)
2.23	100 μM ddT	21.94(±3.03)

Dideoxythymidine is an inhibitor of polymerase beta and polymerase delta[12]. The enzyme polymerase beta is particularly active in catalysing DNA repair synthesis especially when "short patch" repair takes place[13] and therefore it is likely that these X-rays are inducing a considerable amount of "short patch" repair.

When AA8 chinese hamster ovary cell fibroblasts were irradiated with an average dose of approximately 2 gray no DNA repair synthesis was detected. AA8 cells do not adhere to the Hostaphan membrane as firmly as do V79 cells nor adopt such a spread geometry. The nuclei of the AA8 therefore are more distant from the Hostaphan membrane than those of the V79 cells. This suggests that the intensity of the X-rays that induce DNA damage is greatly reduced after 2 to 5 microns, the approximate distance a V79 cell nucleus lies from the Hostaphan membrane. This observation is in agreement with the estimated ≈2 μm e^{-1} attenuation length of 0.85 keV X-rays in biological cell tissue.

Discussion

The above results have shown that a repetitive laser-plasma soft X-ray source can be very effective in radiobiology research in particular for cell-killing studies. The main conclusions from the killing experiments with V79 cells are as follows:-

(a) As shown in Fig.B2.12 a 10-15 gray exposure delivered in a few minutes is sufficient to kill 80-90% of the cells. At this time it is not clear why ≈10-20% of the cells remain viable even at the highest exposures used but it could be due to this fraction being poorly adhered to the Hostaphan base of the exposure dish. Also it is not clear why slightly fewer cells appear to have been killed in the 13-15 gray exposures as compared to the 10 gray exposures. Another experiment would be necessary with more attention given to the 10-15 gray exposure range in order to clarify this point. Also in future experiments it should be possible to reduce the exposure times by supplying a higher X-ray dose-rate to the specimen. This will be achieved by using a higher repetition rate laser (≥50 Hz is easily possible) and by mounting the specimen closer to the source (dose at closer spacing increases according to the inverse square law).

(b) The pulse repetitive laser-plasma X-ray source has yielded similar results to a continuously emitting X-ray source. Thus there appear to be no special effects due to the X-ray photons being incident on the cell nucleus in bunches as compared to essentially one photon at a time.

(c) From the results displayed in Fig.B2.12 we can say that the cell killing effect of X-rays at hν≈0.85 keV is very similar to that of X-rays at hν≈0.28 keV. This is not too surprising because for each of these two photon energies the energy of the electrons released in the photoabsorption event will be similar[9]. The hν≈0.85 keV photons are mainly absorbed in oxygen atoms in biological H_2O thus generating a 0.52 keV Auger electron and a ≈0.33 keV photoelectron. The hν≈0.28 keV photons are also mainly absorbed in oxygen atoms thus generating 0.28 keV photoelectrons. These primary electrons cause the "radiation" damage in the biological cells with very similar effects due to the similarity of their energies.

The DNA damage studies with V79 and AA8 cells have not been as extensive as the cell killing experiments. It has been shown that higher energy X-ray photons would be more useful than the 0.85 keV photons used here. Photon energies ≈1.2-1.3 keV will approximately

double the penetration depth into the biological tissue which will allow proper irradiation of the nucleus of the AA8 cells which tend to have a rounder (and thicker) profile than the V79 cells.

References

1. D T Goodhead and D A Bance, Phys Med Biol 29, 535 (1984).

2. K Kobayashi, K Hieda, H Maezawa, M Ando, and T Ito, J Radiat Res 28, 243 (1987).

3. F O'Neill, G M Davis, M C Gower, I C E Turcu, M Lawless, and M Williams, X-rays from Laser Plasmas, ed. M C Richardson Proc SPIE 831, 230 (1988).

4. D T Goodhead, J Thacker, and R Cox, Int J Radiat Biol 36, 101 (1979).

5. R J Hutcheon, J P Pye and K D Evans, Astron Astrophys 51, 451 (1976).

6. U Feldman, G A Doschek, R D Cowan and L Cohen, J Opt Soc Am 63, 1445 (1973).

7. P G Burkhalter, L Cohen, R D Cowan and U Feldman, J Opt Soc Am 69, 1133 (1979).

8. G E Bromage, R D Cowan, B C Fawcett, H Gordan, M G Hobby, N J Peacock and A Ridgeley 1977 UKAEA Report CLM-R170 "The laser-produced spectrum of Fe XVII to Fe XXI below 18 Å".

9. D T Goodhead and J Thacker, Int J Radiat Biol 31, 541 (1977).

10. J Thacker, A Stretch and M A Stephens, Int J Radiat Biol 36, 137 (1979).

11. J Thacker, A Stretch and D T Goodhead, Radiat Res 92, 343 (1982).

12. S L Dresler, and K S Kimbro, Biochem 26, 2664 (1987).

13. A R S Collins, C P Downes, and R T Johnson in DNA Repair and its Inhibition (Eds A R F Collins, C P Downes and R T Johnson) IRL Press (Oxford) pp 1-11 (1984).

C3	PHYSICS	Pages
C3.1	NONLINEAR PROPERTIES OF SILICA AND AIR AT ULTRAVIOLET WAVELENGTHS	341-359
C3.2	MULTIPHOTON MULTIPLE IONIZATION OF N_2 PROBED BY COVARIANCE MAPPING	359-366
C3.3	CHARACTERISATION OF SOFT X-RAY EMISSION IN THE WATER WINDOW FROM A KrF LASER-GENERATED PLASMA	366-368

C3.1 NONLINEAR PROPERTIES OF SILICA AND AIR AT ULTRAVIOLET WAVELENGTHS

I N Ross (RAL)

Introduction

The current interest in excimer laser systems operating at terawatt power with picosecond or subpicosecond pulse durations has required an increasing attention to the nonlinear processes occuring in materials through which the laser beam travels. Ultimately the power and energy achievable from such systems is limited by these nonlinear processes. The materials of interest for these lasers are fused silica, fluoride crystal optics, the laser medium, air and other gases such as helium and Raman media. Several nonlinear processes must be considered and the dominant mechanism identified and this may vary from material to material and wavelength to wavelength. We can identify the competing nonlinear effects for picosecond pulses as: self-focusing (SF), Raman generation (RG), spectral broadening (SB) and continuum generation (CG), and nonlinear absorption (NLA). These processes have been considered both theoretically and experimentally but there is not sufficient experimental data in the ultraviolet or sufficiently well understood theory to enable a proper optimisation of high power excimer laser systems or to estimate the maximum achievable power from such a system.

This paper reports a number of measurements of the nonlinear properties of silica and air at ultraviolet wavelengths using short pulses lasers. There have been several measurements reported by other groups[1-6], notably the NLA measurements of silica and a number of other materials at 266 nm and 351 nm by Bloembergen et al and at 249 nm by Taylor et al, the n_2 and NLA measurements in silica at 351 nm by LLNL, the n_2 measurements and associated SB and CG in gases by Corkum et al and the NLA of silica fibres at all the main excimer laser wavelengths by Taylor and Leopold. To add to the available data we have measured both the NLA coefficient and n_2 in silica at 249 nm. We have also measured the threshold for nonlinear effects in air, at this wavelength and gained some insight into the processes occurring at this threshold. We also report measurements of NLA and CG in silica at 293 nm.

Theoretical Considerations

(a) Nonlinear Absorption (NLA)

There are a number of possible mechanisms for NLA, the most significant being two photon absorption, single photon absorption due to induced solarization following one or two photon absorption, and excited state absorption following two photon absorption. It has been shown possible to differentiate these processes (3) using particularly well controlled experimental techniques but for the most part it is sufficient to assume a two photon absorption process in which the absorption coefficient varies linearly with intensity and the intensity transmission T_I is given by :-

$$T_I = \frac{I_\ell}{I_0} = \frac{1}{1 + I_0 \beta \ell} \qquad (1)$$

where I_0, I_ℓ are the incident and transmitted intensities

β = two photon absorption coefficient

ℓ = path length in the nonlinear medium.

As the usual experimental parameter is energy the relation between energy transmission T_E and two photon absorption coefficient β must be found:

$$T_E = \frac{E_\ell}{E_0} = \frac{\iint^t I_\ell \, dt dA}{\iint I_0 \, dt dA} = \frac{\iint [I_0/(1+I_0 \beta \ell)] \, dt dA}{\iint I_0 \, dt dA} \qquad (2)$$

$$T_E = \frac{E_\ell}{E_0} = \frac{\iint^t I_\ell \, dt dA}{\iint I_0 \, dt dA} = \frac{\iint [I_0/(1+I_0 \beta \ell)] \, dt dA}{\iint I_0 \, dt dA} \qquad (2)$$

(b) Self-Focusing

The refractive index at high intensity is given by:

$$n = n_0 + n_2 \langle E^2 \rangle \qquad (3)$$

plus higher order terms which can usually be ignored. Since $\langle E^2 \rangle$ is proportional to intensity, this can be rewritten:

$$n = n_0 + \gamma I \qquad (4)$$

where $\gamma = 4.2 \times 10^6 (n_2/n_0)$ for I in GW/cm² and n_2 in ESU. The primary effect of n_2 is to introduce an intensity dependent phase on the transmitted beam given by:-

$$\text{nonlinear phase} = \frac{2\pi}{\lambda_0} \int_{\ell} \gamma I d\ell \qquad (5)$$

This integral is usually designated B and called the B-integral. In the presence of NLA, we can substitute (1) into (5) to obtain:

$$B = \frac{2\pi}{\lambda_0} \cdot \frac{\gamma}{\beta} \ell n \, (1+I_0 \beta \ell) \qquad (6)$$

Thus by time resolved or time integrated interferometry the intensity dependent phase can be measured and hence a value of n_2 obtained.

The most serious effect of n_2 is generally beam filamentation (or small scale self focusing) which leads to high peak intensity and reduction in focal intensity. An indirect but relevant method of measuring n_2 is to observe the growth of intensity modulation on an intense beam. For small modulation depth the growth G in modulation at a spatial frequency (w) has been shown[8] to be given by exp. $\int g d\ell$, the integral being taken down the beam propagation path, and where g is given by:

$$g = k\theta \sqrt{(\mu - \theta^2/4)} \qquad (7)$$

where $\mu = \frac{\gamma I}{n}$; $\theta = \lambda w$; $k = 2\pi/\lambda$

$\therefore$ spatial frequency exhibiting maximum growth is given by: $\theta = \sqrt{2\mu}$ and for this spatial frequency the growth is:

$$G = \exp \int k\mu d\ell = \exp B. \qquad (8)$$

Inclusion of nonlinear absorption in self-focusing analysis

The presence of NLA will tend to inhibit self-focusing effects in two ways. Filamentation will be inhibited through a damping term and the absorptive heating effect will lead to self-defocusing.

Filamentation

TPA can be included in the perturbation analysis through a complex nonlinear refractive index where we replace n_2 by n_2 (1 + iA) where $A = \beta/k_0\gamma$. The analysis assumes a strong beam travelling down the z-axis and a weak beam travelling at an angle θ to this z-axis; and the field vector can then be given by:-

$$E = E_0 \exp i\,(kz-\omega t) = C\,(1+b)\,\exp i\,(kz-\omega t) \qquad (9)$$

where C = constant
$b = a(z) \exp ik\theta x$

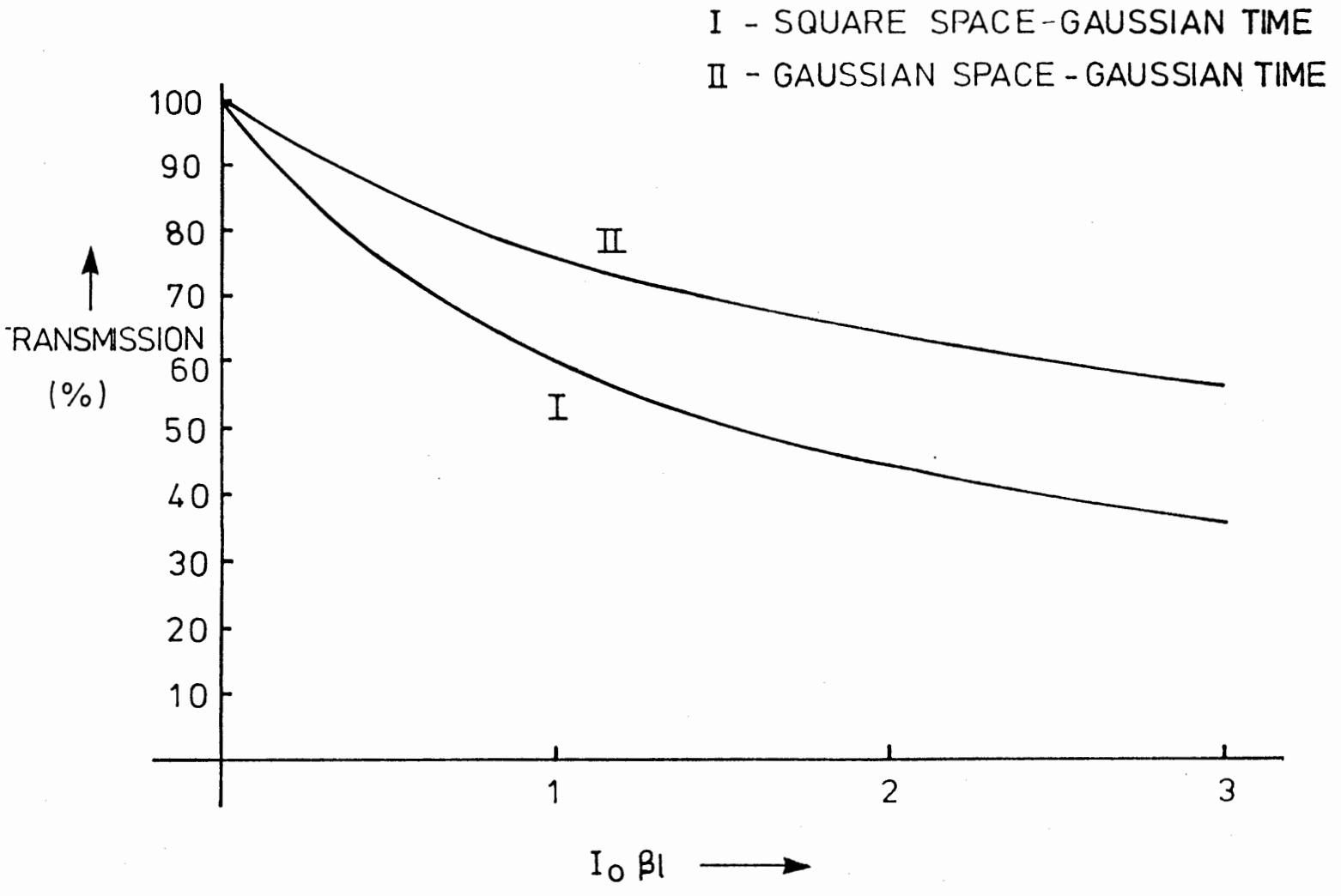
The paraxial approximation to the wave equation can be written:

$$\nabla^2 E_0 + 2ik \frac{\partial E_0}{\partial z} + k^2 \frac{n_2}{n_0} ([\mathrm{Re}E_0]^2 - C^2) E_0 = 0 \qquad (10)$$

where $\mathrm{Re}E_0$ = real part of $E_0 = \frac{1}{2}(E_0 + E_0^*)$.

Substituting for E_0 from equation (9) gives:-

$$-k^2\theta^2 b + 2ik \frac{\partial b}{\partial z} + 2k^2\mu\,(1 + iA)\,(b + b^*) = 0$$



CALCULATION OF TWO PHOTON ABSORPTION TRANSMISSION

Fig C3.1 Transmission curves in the presence of two photon absorption for two pulse shapes.

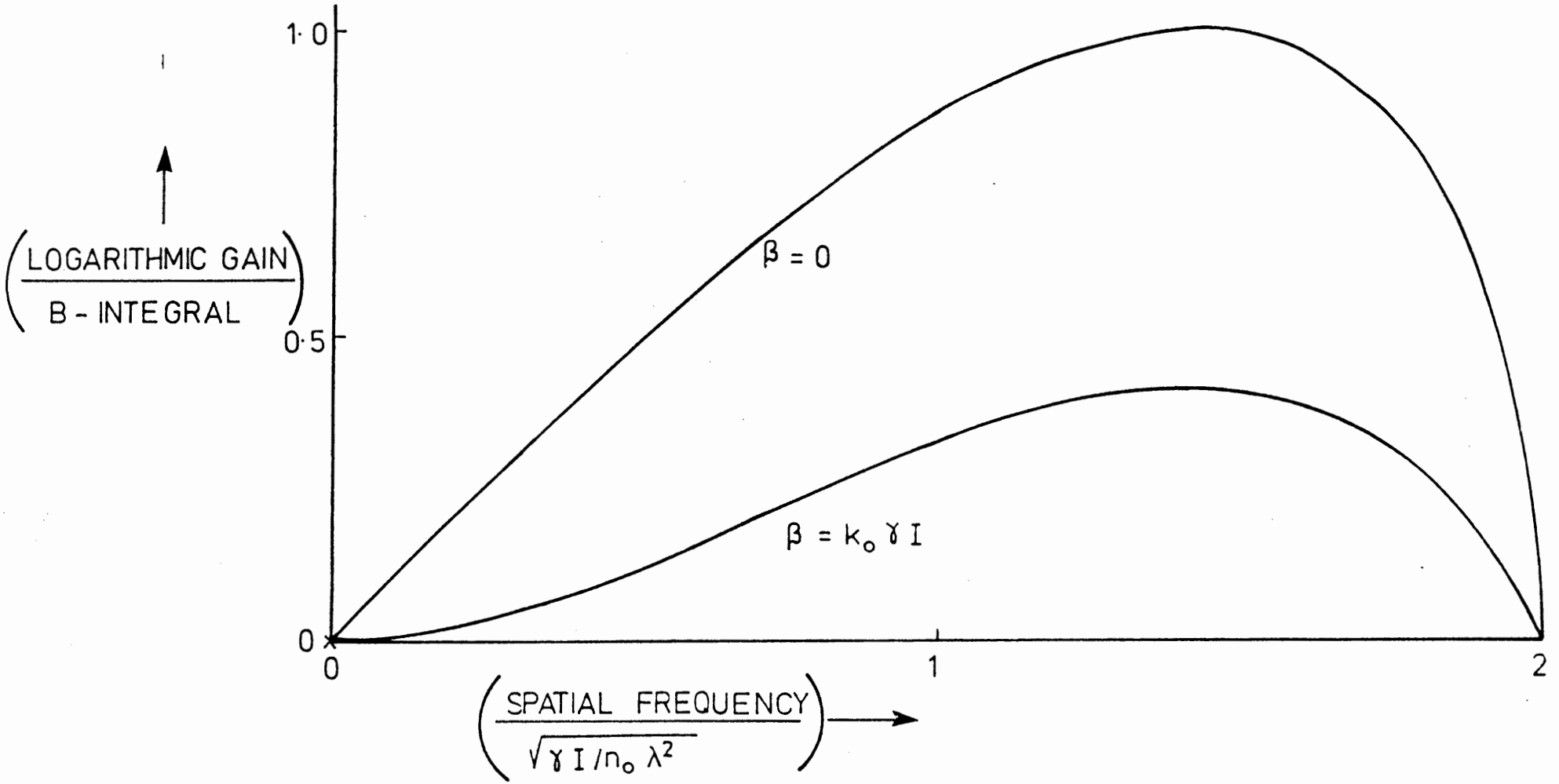


Fig C3.2 Effect on the filamentary gain of two photon absoption.

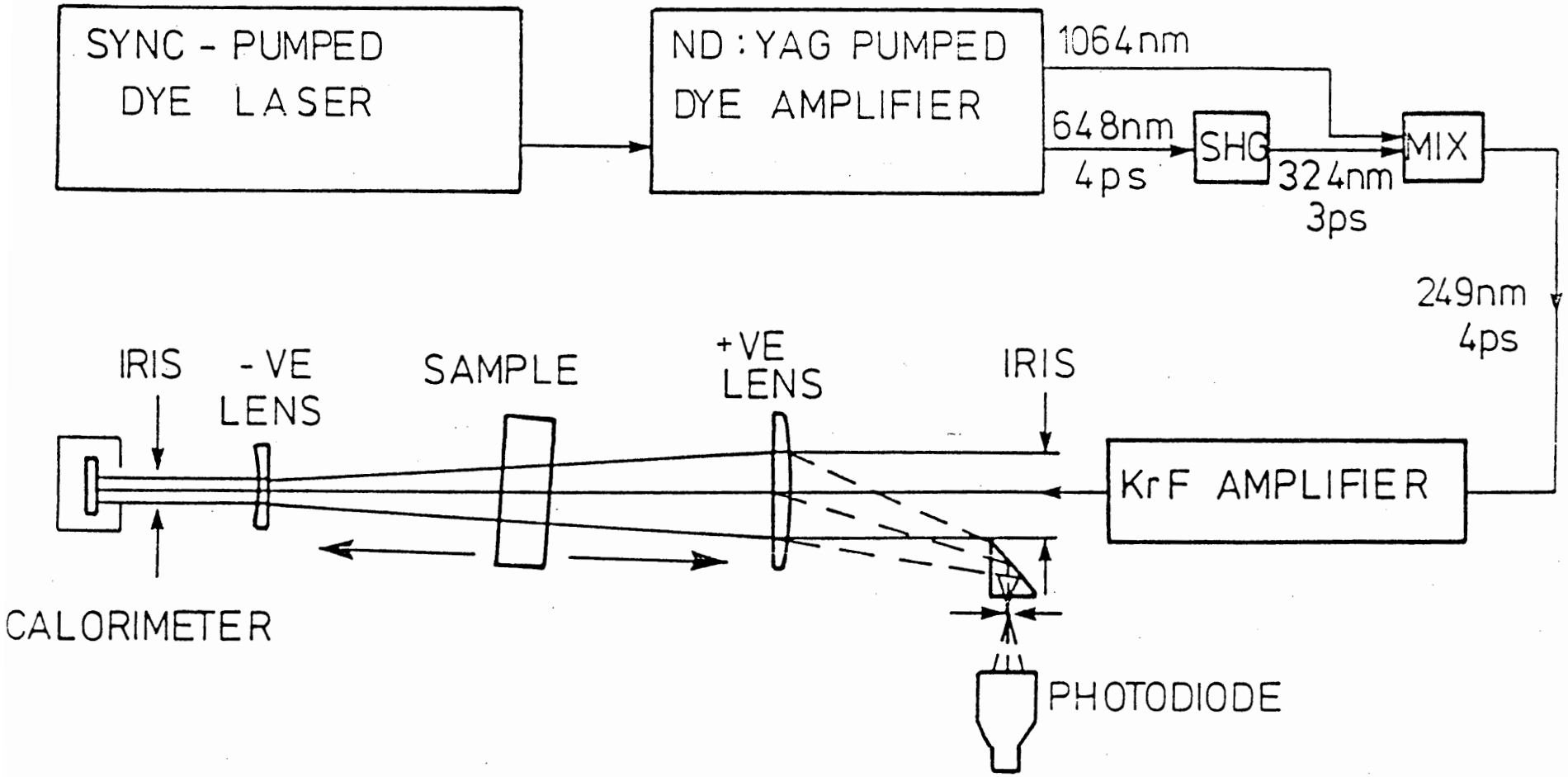


Fig C3.3 Measurement of nonlinear absorption at 249 nm.

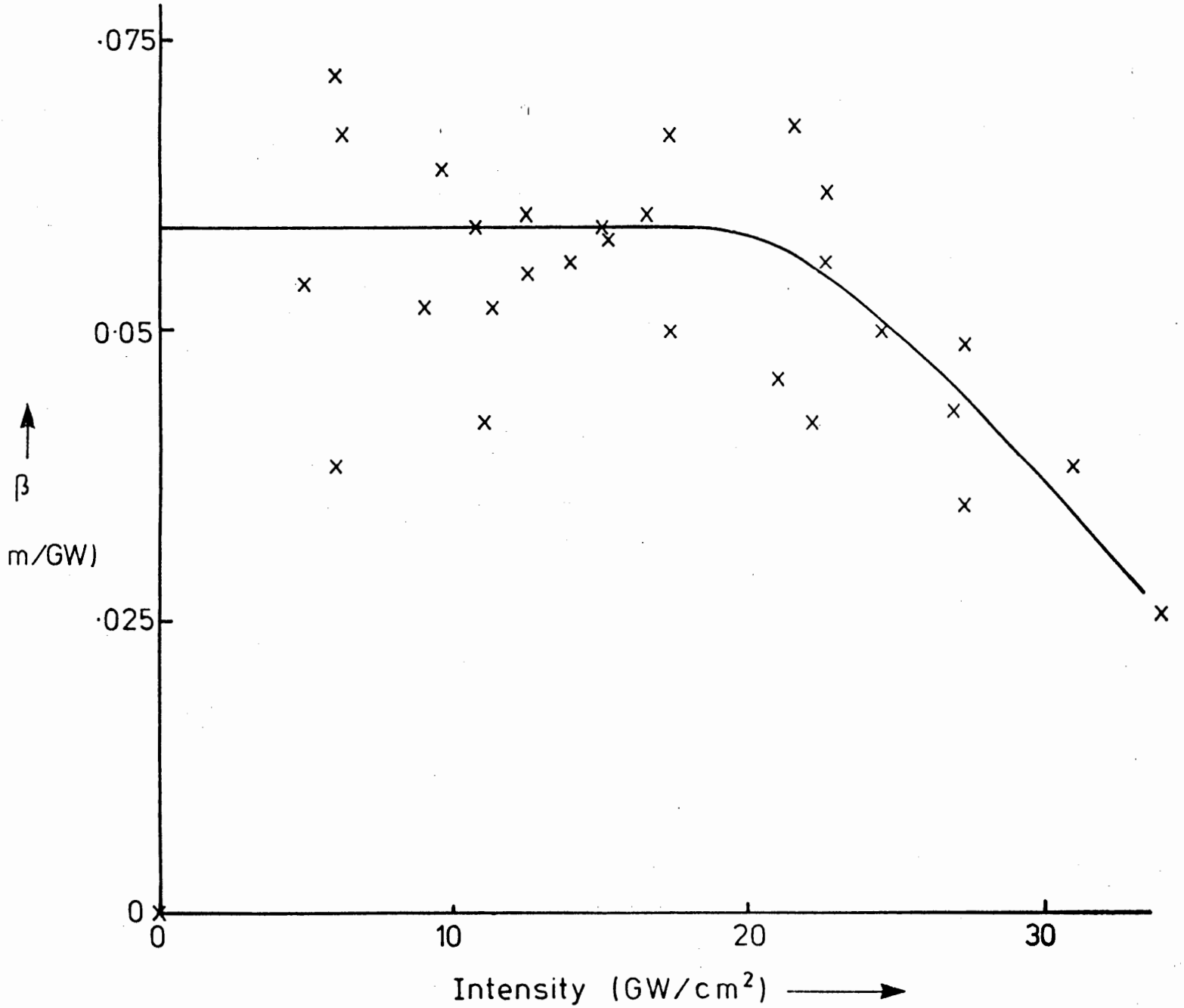


Fig C3.4 Measured values of the two photon absorption coefficient as a function of intensity.

where $\mu = (n-n_o)/n_o = n_2\langle E^2\rangle/n_o = n_2C^2/2n_o = \gamma I/n_o$

we now take the complex conjugate and eliminate b^* to give:

$$\frac{\partial^2 b}{dz^2} + 2\,k\mu A\,\frac{\partial b}{\partial z} - k^2\theta^2\,(\mu-\frac{\theta^2}{4})\,b = 0 \qquad (11)$$

The solution for this equation is:-

$$b = a_o \exp gz \exp ik\theta x \qquad (12)$$

where $g = -k\mu A \pm [k^2\mu^2A^2 + K^2\theta^2\,(\mu-\theta^2/4)]^{1/2}$

$$= -(\beta I) \pm [(\beta I)^2 + k^2\theta^2\,(\mu-\theta^2/4)]^{1/2}$$

Figure C3.2 plots g for β=0 (no NLA) and for $\beta = k_o\gamma$. The effect on the growth of filaments is plainly substantial.

At a spatial frequency given by $\theta = \sqrt{2\mu}$ the gain is maximised and is given by:

$$g_{max} = -\beta I + [(\beta I)^2 + (k_o\gamma I)^2]^{1/2}$$

$$= (-\beta+[\beta^2+(k_o\gamma)^2]^{1/2})I \qquad (13)$$

Thus the growth in modulation at the worst spatial frequency is given by:

$$G = \exp \int g\,d\ell$$

$$= \exp.\ fB \qquad (14)$$

Where B = B-integral = $\int k_o\gamma I\,d\ell$

and $f = -(\beta/k_o\gamma) + [(\beta/k_o\gamma)^2 + 1]^{1/2}$

We note also that due to NLA, the B-integral is reduced according to equation (6):

$$B = \frac{\ell n\,(1 + I_o\,\beta\ell)}{I_o\,\beta\ell} \cdot k_o\gamma I_o\ell = \frac{\ell n\,(1 + I_o\,\beta\ell)}{I_o\,\beta\ell} \cdot B_o. \qquad (15)$$

These equations enable calculation of n_2 from a measurement of the growth of spatial modulation on the beam.

Nonlinear Absorption Measurements

(a) Measurements at 249 nm

Figure C3.3 shows the arrangement used to measure the nonlinear absorption at 249nm. A uniform circular beam containing a few mJ in 4 ps was used, the target intensity being varied by axial movement of the sample in a long focus telescope. The incident beam energy was monitored using an integrating photodiode and the transmitted beam energy was measured using a calibrated calorimeter. Amplified spontaneous emission was measured without the short pulse and was below the 10% level even with a fresh fill in the KrF amplifier. Monitoring of amplified spontaneous emission at regular intervals enabled a correction to be made. Measurements of transmitted energy with an without the test plate gave a number of values for the plate transmission as a function of incident intensity. These transmission values when corrected for the Fresnel reflection loss were applied to the curve of Fig C3.1 to obtain values of $I_o\beta\ell$ and hence β. Fig C3.4 plots the values of β as a function of intensity. The averaged value of β for fused silica, was 0.06 cm/GW with an error of ±30%. We also note from Fig C3.4 the apparent saturation of the absorption process at high intensity. The saturation of a nonlinear process (n_2) has also been observed and commented on by Corkum[4] but may also be caused by increasing competition with other loss processes.

The pulse duration was measured before the final amplification stage by a cross correlation technique[9] in which the 249nm pulse was mixed with the 324 nm pulse in a KDP crystal to give a cross correlation signal at 1064 nm. Assuming a gaussian temporal profile, a mean pulse duration of 4 ps ± 1 ps was calculated. There is expected to be considerable variation of pulse duration with this non-transform-limited sync pumped laser system and our

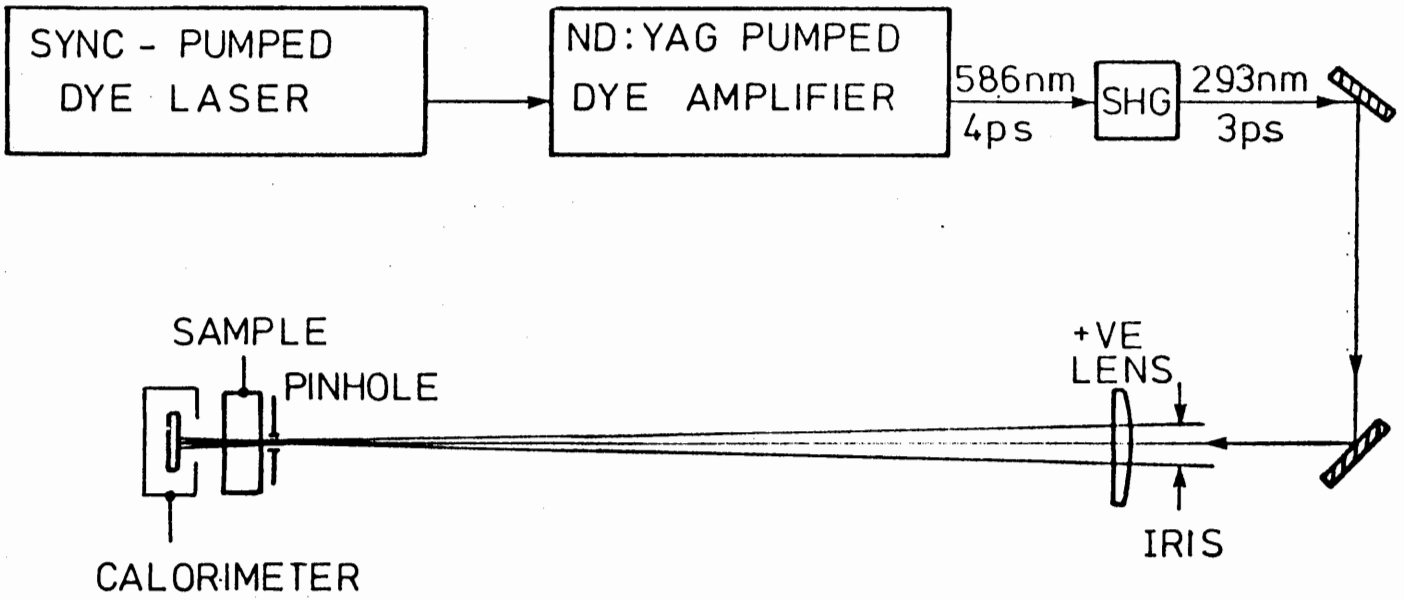


Fig C3.5 Measurement of nonlinear absorption at 293 nm.

COMMON PATH

INTERFEROMETER FOR MEASURING n_2

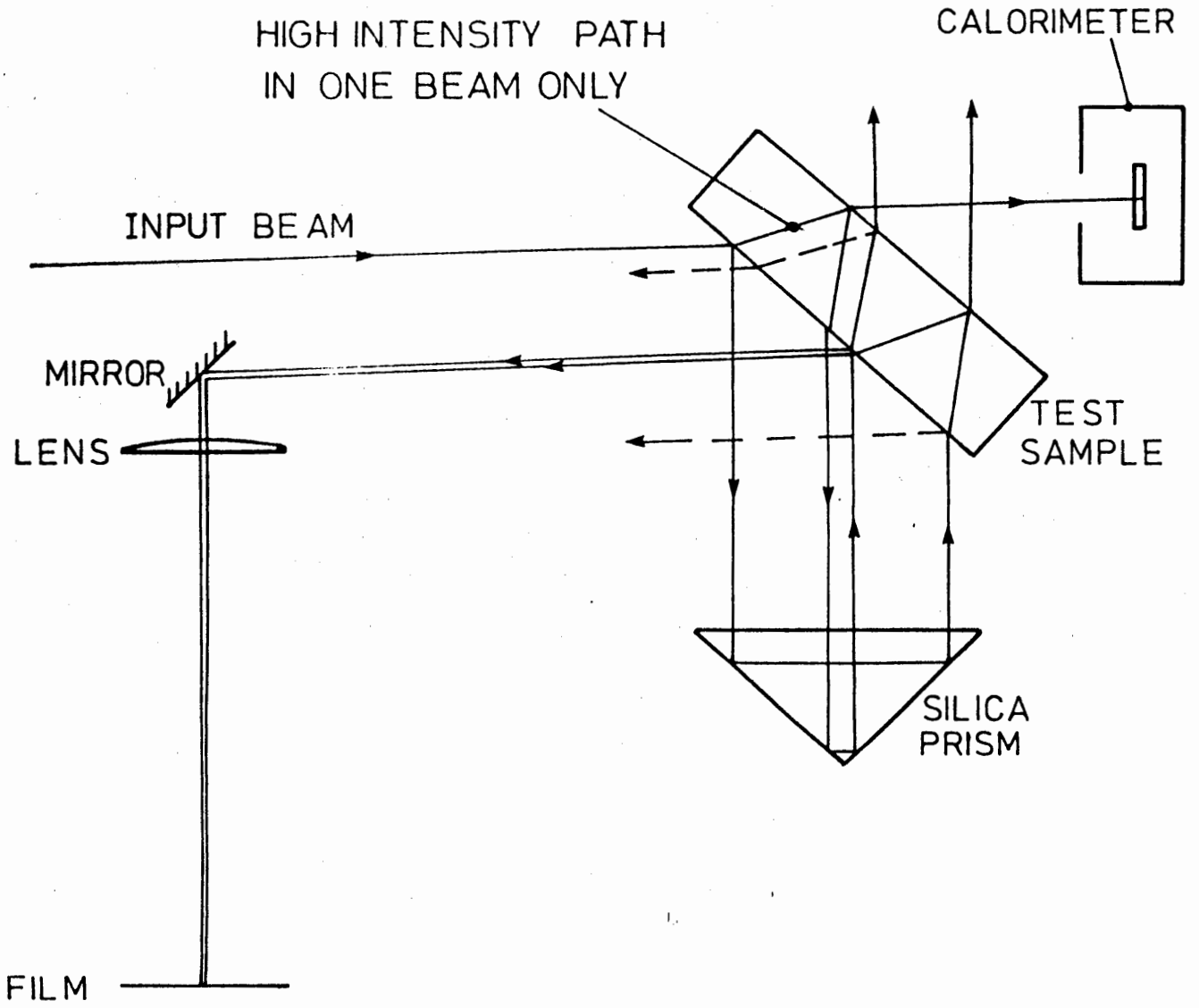
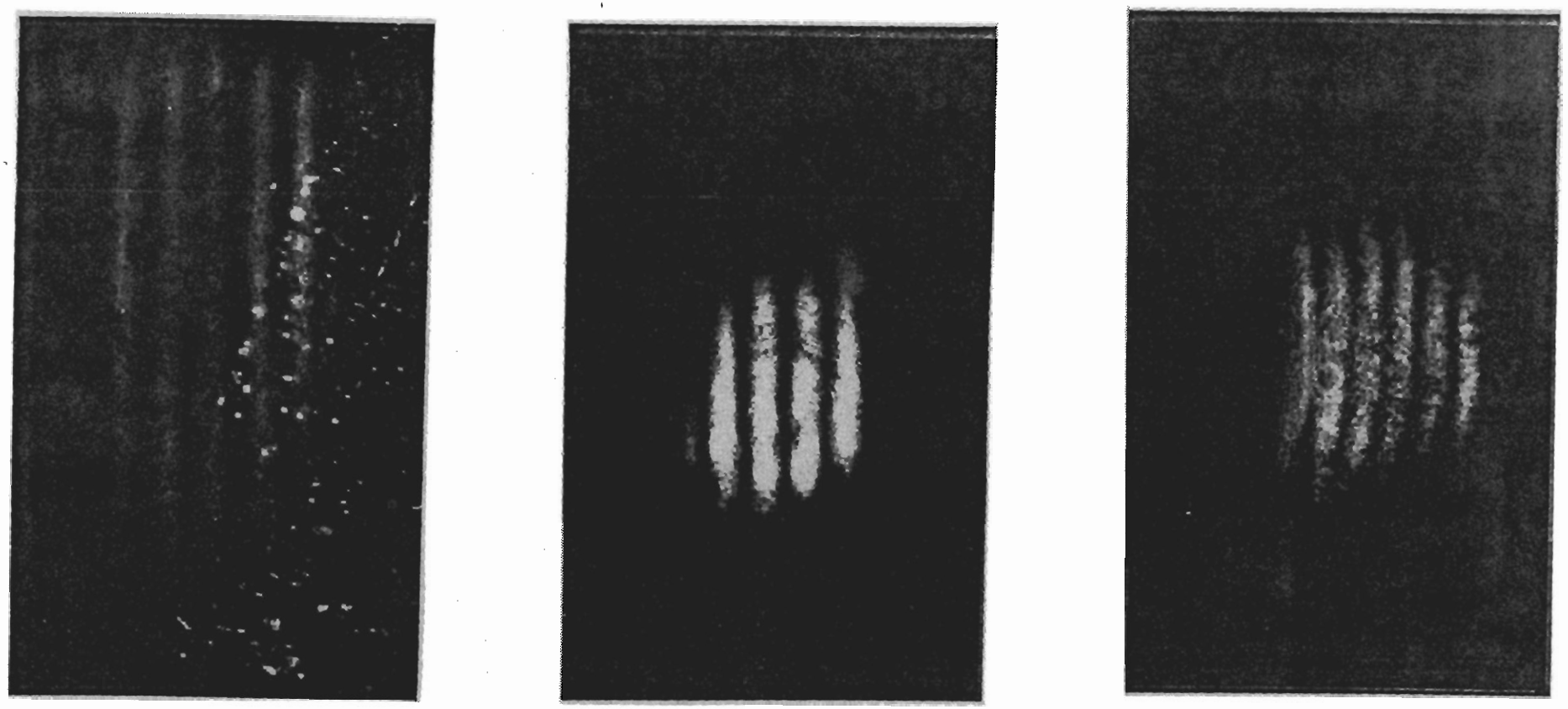


Fig C3.6 Common path interferometer for the measurement of nonlinear refractive index.

INTERFEROGRAMS RECORDED IN COMMON PATH INTERFEROMETER



Amplifier A. S. E. Only

Unamplified Oscillator $\int Idl = 0{\cdot}01\,GW/cm$

Amplified Oscillator $\int Idl = 10\,GW/cm$

Fig C3.7 Interferograms recorded a) using amplified spontaneous emission b) using low intensity beam c) using high intensity beam.

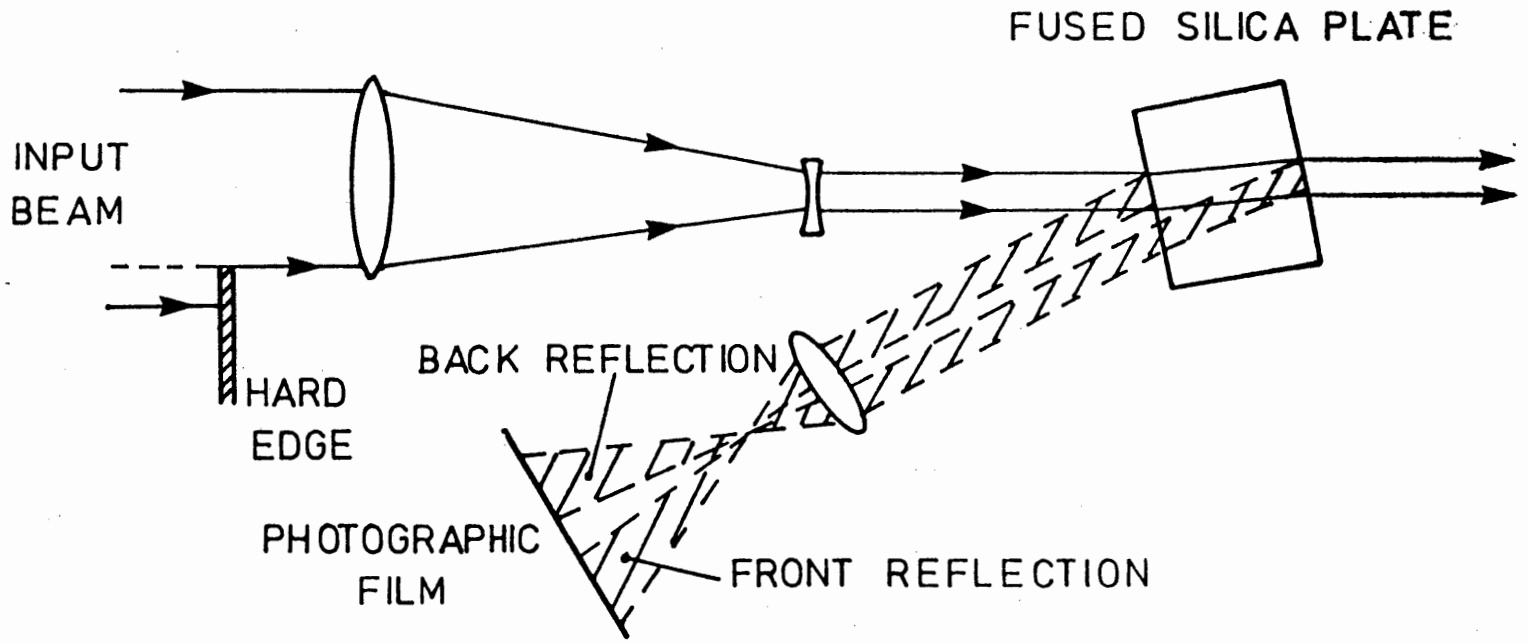


Fig C3.8 Arrangement for measuring filamentation.

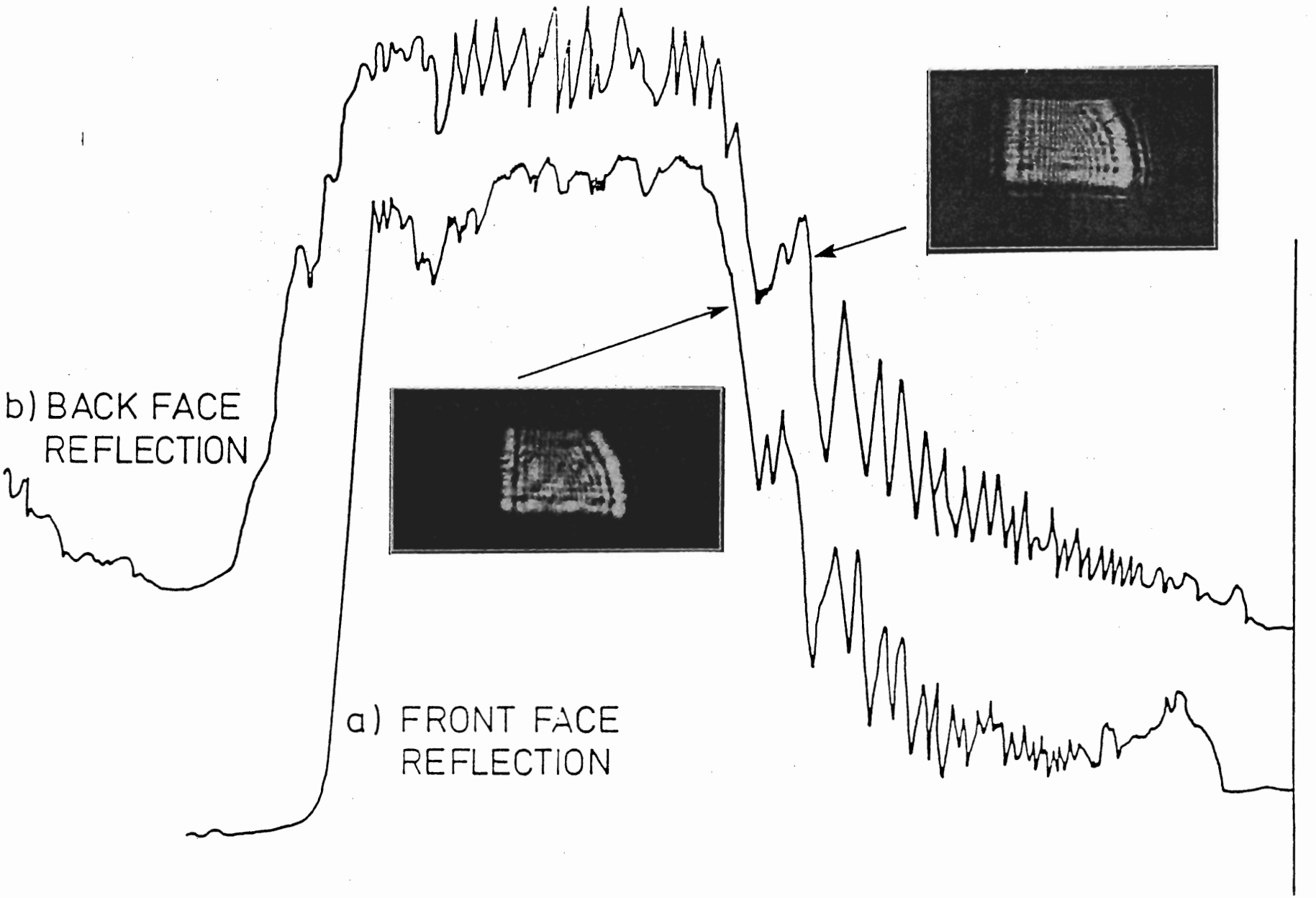


Fig C3.9 Measured intensity distributions before and after a sample showing filamentation.

overall error on the value of β of ±30% is largely due to uncertainties in the value of pulse duration.

(b) Measurements at 293 nm

Figure C3.5 shows the measurement arrangement for this wavelength. The technique was to measure the mean power transmitted to the calorimeter with and without the sample. This mean power was stable ±10% when averaged over a large number of pulses although there were much higher shot to shot variations (∿±30%). The use of this averaging technique gives an underestimate of β by only up to 4%, which is much smaller than the other inaccuracies in the measurement. The pinhole selected the central peak of the far field distribution and the value in β as a result of assuming the intensity constant over the pinhole aperture is overestimated but by no more than about 10%. For all samples tested in this arrangement the self-focus distance was larger than the thickness of the samples and no change in transmitted beam parameters were observed. The effect of self-focusing would be to give high values of β for thicker samples and this was not observed.

A number of samples of fused silica of different thicknesses and suppliers were tested and their values of β calculated as before from a value of transmission and using figure C3.1. No detectable difference between the different types of silica were observed and a mean value of β was 0.008 ± 0.004 cm/GW.

This value of β is almost certainly low because of the observed presence of strong forward scattering and broadband emission which will have reduced the beam's intensity as it propagated through the crystal and hence suppressed the NLA. A further discussion will be given in a later section.

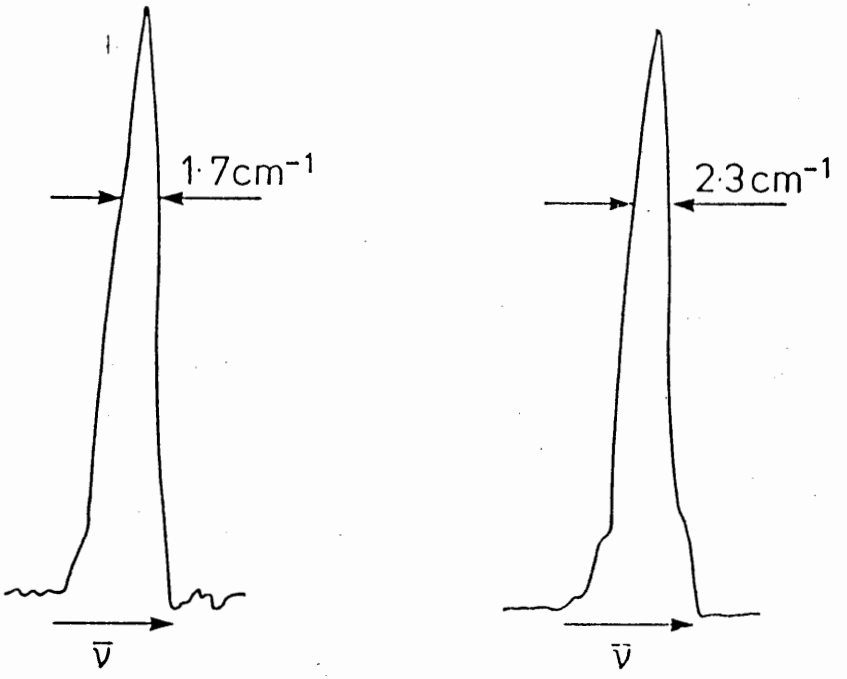
Measurement of nonlinear refractive index of silica at 249 nm

Two spatial techniques have been employed to make measurements of the nonlinear refractive index (n_2) of silica at 249 nm. A direct technique measuring the intensity dependent phase change and an indirect technique measuring the amplification of spatial intensity ripples on the beams. Although indirect the latter is very relevant in that it measures directly the most serious effect of n_2. Our methods follow previously developed techniques for visible and infra-red wavelengths[3].

(a) Figure C3.6 shows a 'common path' interferometer designed to give good contrast fringes of controllable spacing for broadband radiation at 249 nm. Figure C3.7(a) shows the fringe pattern recorded using the broadband amplified spontaneous emission output of the excimer amplifier, showing straight fringes across the entire beam. The interferometer is designed so that only one of the two counter propagating beams is at high intensity in silica and that only for a single pass in the sample. All other beams are reduced to the 4% level by Fresnel reflections. Figure C3.7(b) shows the fringe pattern for a low intensity beam and figure C3.7(c) the fring pattern at high intensity and the fringes can be seen to shift their phase according to the local intensity. Measurement of the fringe shift and fluence and assuming a Gaussian temporal pulse shape enabled a calculation of the phase shift for a particular peak intensity and hence a value for n_2 using equation (5). A mean value of 2.0×10^{-13} esu was obtained for n_2 with an uncertainty of 40% due primarily to the uncertainty in estimating the peak intensity from the measured fluence.

(b) The second technique is illustrated in Figure C3.8. Fringes of variable spacing and modulation depth were generated on the beam using Fresnel diffraction at a straight edge. Both front and back reflections from the test sample block were imaged onto film and simultaneously recorded. Figure C3.9 shows densitometer traces across images recorded in this way demonstrating the enhancement of some spatial frequencies. Measurement of the spatial frequency

SPECTRAL BROADENING DUE TO SELF PHASE MODULATION IN SILICA



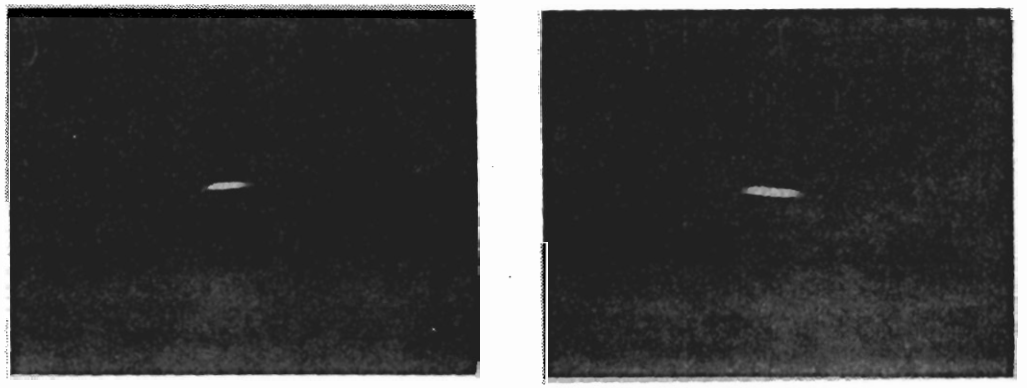


Fig C3.10 Spectral broadening in silica at 249 nm due to self-phase modulation.

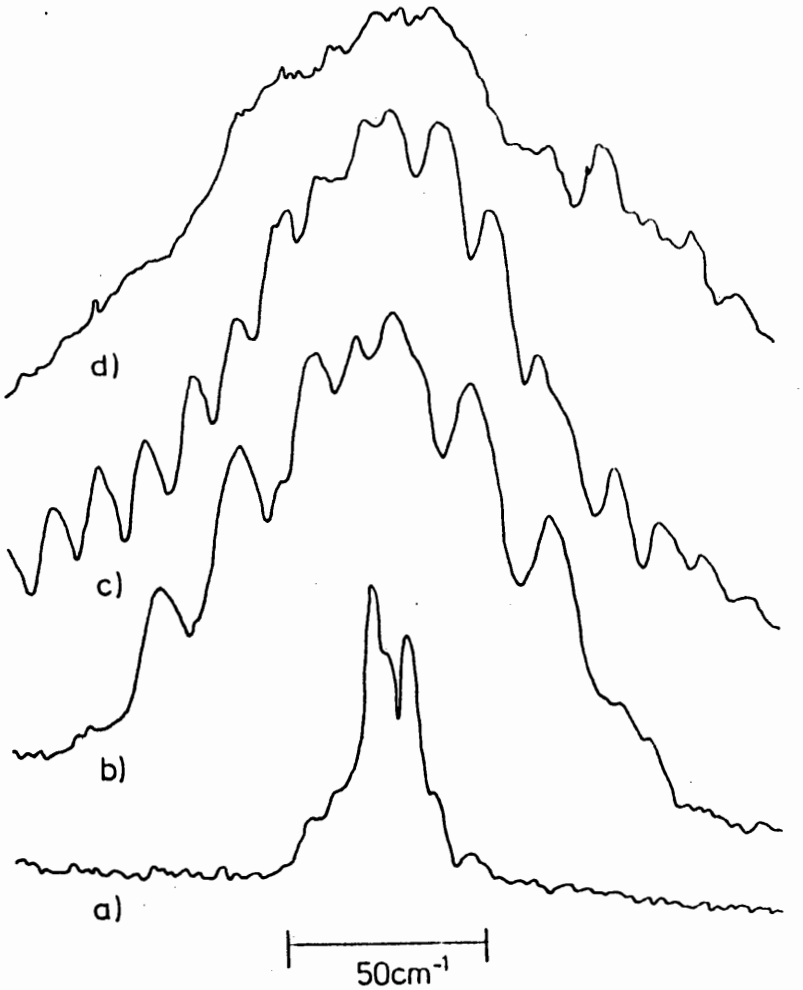


Fig C3.11 Spectral broadening in air at 249 nm at various intensities.

showing maximum enhancement and measurement of the magnitude of this enhancement enabled two values of n_2 to be derived using equation (13) and the two values obtained were 1.0 and 1.3 x 10^{-13} esu respectively with an uncertainty of ±0.5 x 10^{-13} esu. These values are lower than that derived by the direct technique, and this may be due to our limited understanding of the process of filamentation in these conditions.

Our measurements have given a value for n_2 up to twice that measured at visible wavelengths but suggest that, due to NLA, a higher B-integral than expected can be tolerated before serious deterioration of the beam through filamentation.

(c) A spectral technique has also been used to estimate n_2. Spectral broadening due to self phase modulation is a senstive way of detecting the onset of effects arising from n_2. An estimate of n_2 can also be made if assumptions are made as to the temporal profile and coherence of the laser pulse. For a transform limited pulse in a medium with low dispersion, the spectral broadening can be estimated from:

$$\frac{\text{Broadened linewidth}}{\text{Input linewidth}} - 1 \sim AB^n$$

where A and n are constants.

For a Gaussian temporal profile and square spatial profile, A ≈ 0.5; n ≈ 2. Figure C3.10 shows two spectra recorded from front and back reflections of a 20 mm thick sample of silica. The ratio of spectral widths gave a B-integral value of 0.8. But, for λ = 249 nm, B = 0.07 $n_2 \int I d\ell$, and in the experiment $\int I d\ell$ = 9 GW/cm. Hence n_2 = 1.3 x 10^{-13} esu which compares well with values obtained above.

Measurement of n_2 for air at 249 nm

This may be estimated by observing the threshold power at which a spatially coherent focused beam will exhibit spectral broadening. This power should then be close to the 'critical power' for self-focusing (P_{CR}) which is approximated by:

$$P_{CR} \approx \frac{\lambda^2}{n_2} \text{ for } \lambda \text{ in } \mu m,\ n_2 \text{ in esu x } 10^{13}$$

$$\text{Thus } n_2 = \frac{\lambda^2}{P_{CR}}$$

Experimentally P_{CR} was measured by reducing an iris diaphragm in the focusing beam until spectral broadening was no longer observed and at this point the energy transmitted through the focus was measured on a calorimeter. An energy threshold of 0.2 mJ was observed in a 2mm beam. This gave P_{CR} = 50 MW (for our 4 ps pulse length) and hence a value for n_2 of 1.2 x 10^{-16} esu. Threshold must also correspond to a significant B-integral (of the order of 1). Since, for an Airy distribution, $\int I d\ell = 2\pi P/\lambda$ through the focal region we can calculate the B-integral (= 0.07 $n_2 \int I d\ell$). This gave

$$B = 1.1$$

Earlier measurements of n_2 for air (10) gave

$$n_2 = 2 \times 10^{-16} \text{ esu for } \lambda = 694 \text{ nm.}$$

Broadband Generation

Nonlinear spectral changes can under some conditions be the dominant process and, even if it is not the dominant process, it may well affect beam propagation. The two principal spectral effects for short pulses are the generation of Stokes spectral sidebands due to Raman processes and spectral broadening due to self-phase modulation which is itself due to the nonlinear refractive index. The dominant process of the two is that requiring the lower value of $\int I d\ell$ at 'threshold'.

For Raman threshold

$$\gamma_t \int I d\ell = 25$$

where γ_t = transient Raman gain coefficient $\approx \gamma_s/[1 + 5.2\ T_2/t]$

$$\therefore \int I d\ell = (25 + \frac{130T_2}{t}) \frac{1}{\gamma s}$$

where γ_S = steady state gain coefficient in cm/GW
T_2 = dephasing time
t = pulse length

For self-focusing or self-phase modulation threshold (B = 1);

$$\int I d\ell = 60\lambda/n_2$$

where λ = wavelength in μm
n_2 = nonlinear index in esu x 10^{13}

Consequently, for n_2 effects to dominate:

$$\frac{60\lambda}{n_2} < (25 + \frac{130T_2}{t}) \frac{1}{\gamma s}$$

$$\therefore (0.43 + 2.2\ T_2/t)\ n_2 > \gamma s$$
$$> \gamma_0$$

where γ_0 = Raman steady state gain coefficient for λ = 1 μm.

(a) Experiments at 249 nm in air

The 4 ps amplified beam at 249 nm was focused in air using a 1 m focal length lens. A reflective grating working in 3rd order dispersed the spectrum and gave a resolution of 2 cm^{-1} for the full beam aperture. Figure C3.11 shows typical spectra at

a) low intensity

b) a little above threshold intensity, and

c) at high intensity.

For very short pulses vibrational Raman is stronger than rotational Raman by virtue of its very short T_2 time (≈7 ps). Since γ_0 = 0.95cm/TW for the vibrational line, our inequality shows that self-focusing effects dominate if $n_2 > 0.22 \times 10^{-16}$ esu. Since $n_2 \approx 2 \times 10^{-16}$, we would not expect to see any Raman effects in air with our short pules.

Experiment, as demonstrated in Figure C3.11(c), showed no evidence of Raman shifted spectral components.

As expected, Figure C3.11(c) shows that at well above threshold there is a rapid broadening of the spectrum, often called 'continuum generation'. Figure C3.11(b) provides some useful evidence of the process initiating this continuum generation. Since our source laser pulses were not transform limited the spectrum often contained a double line as seen in Figure C3.11(a). At just above threshold, sidebands were seen (Figure C3.11(b)) which enable energy to be efficiently coupled into an increasingly broader spectrum. Our present interpretation of this process is that there are efficient four wave mixing processes for pairs of wavelengths in the original spectrum according to:

$$2(\nu + \delta\nu) - \nu = \nu + 2\delta\nu \text{ and } 2\nu - (\nu + \delta\nu) = \nu - \delta\nu.$$

This process should depend upon the third order polarisabilities and be closely linked to similar processes such as self-focusing and self-phase-modulation. Indeed the observed thresholds are just those expected for n_2 effects and spectral broadening due to self-phase-modulation is generally seen as a precursor to 'continuum generation'.

However the dominance of continuum generation over other processes including self-focusing is surprising unless it is enhanced in some way. A possible enhancement process can come from the proximity of Raman transitions. This 'off-resonant' Raman enhancement of four wave mixing has been considered by Dangor et al

( ). For the generation of a 10% side-band from a two component spectrum:

$$\frac{1}{2}\,\gamma_s\,\frac{\Upsilon}{\sqrt{(\Upsilon^2+\Delta\omega^2)}}\,.\int I d\ell \approx \sqrt{0.1}$$

where γ_s = steady state Raman gain coefficient
Υ = Raman half-linewidth
$\Delta\omega$ = off-resonant displacement

$$\therefore\ \gamma_s \int I d\ell \approx 0.63 \times \frac{\Delta\omega}{\Upsilon} \text{ for } \Delta\omega >> \Upsilon$$

This is to be compared with the threshold for Raman generation of $\gamma\int I d\ell \approx 25$.

where γ = transient gain coefficient.

For rotational Raman transitions in air the strongest line is the S(8) line in nitrogen and for this line the Stokes shift is $\approx$ 76 cm^{-1} as compared to the separation of components in our ps system of $\sim$10 cm^{-1}, giving a value for $\Delta\omega$ of 66 cm^{-1}. Since γ_s = 13 cm/TW and Υ (rot) = 0.04 cm^{-1} for this line in nitrogen,

$$\Delta\omega/\Upsilon \approx 1650 \text{ and } \int I d\ell \approx \frac{0.63 \times 1650}{13} = 80 \text{ TW/cm.}$$

Since there are a number of rotational Raman transitions with appreciable gain, it is necessary to sum the gain over all these lines. Thus our threshold condition now becomes:

$$\int I d\ell .\ \sum_{\text{all lines}} \frac{\gamma_s \Upsilon}{\Delta\omega} = 0.63$$

Carrying out this summation over all rotational lines in nitrogen increases the calculated gain by a factor $\approx$10. Thus we estimate the threshold condition for sideband generation in air to be:

$$\int I d\ell = 8 \text{ TW/cm.}$$

as compared to the threshold for self-focusing of:

$$\int I d\ell = \frac{60\lambda}{n_2} \approx 12.5 \text{ TW/cm}$$

Thus the observed sideband generation leading to continuum generation appears to be explained by enhanced 4-wave mixing due to the proximity of rotational Raman transitions.

(b) Experiments at 293 nm in silica

The measurement of nonlinear absorption at 293 nm was hampered by the presence of a strongly competing process. The competing process was observed to scatter light into a forward cone such that the apparent NLA coefficient when measured well downstream (and including losses due to the scatter) was 0.03 cm/GW as compared to the true NLA coefficient of 0.008 cm/GW, measured close to the sample so as not to include scatter losses. The $\int I d\ell$ threshold for the conical scatter was $\approx$ 3 GW/cm and the scattered light was broadband covering typically a width of 5000 cm^{-1} at well above threshold.

Following the same mechanism as postulated in the previous section we calculate the threshold for Raman enhanced sideband generation to be:

$$\int I d\ell .\ \frac{\gamma_s \Upsilon}{\sqrt{\Upsilon^2+\Delta\omega^2}} = 0.63$$

Since $\gamma_s \sim 0.04$ cm/GW; $\Upsilon \approx 150$ cm^{-1}; $\Delta\omega = 400$ cm^{-1}

$$\int I d\ell = \frac{0.63 \times}{.04 \times} = 42 \text{ GW/cm}$$

while for a 10% loss from NLA;

$$\int I d\ell = 0.16/0.008 = 20 \text{ GW/cm}$$

This lower value suggests that NLA should be the stronger process. However, there is sufficient uncertainty in the values of parameters that the proposed mechanism may remain a possible explanation.

SUMMARY OF MEASUREMENTS ON SILICA.

Wavelength	249nm	266/268nm	293nm	308nm
β (RAL) cm/GW	0·06	(0·06)	0·008	
β (other labs.)cm/GW	0·045	0·02		0·007
$n_2 \times 10^{-13}$ e.s.u.	1·5 - 2·0			
B-INTEGRAL @ 20% Loss From Two-Photon-Absorption	0·6	1·5	3·0	3·0
$\int I\,dl$ LIMIT. in GW/cm	6	18	15	~45

The results of our measurements are summarised in Table I.

References

1. P Liu, L Yen, N Bloembergen, App Opt 18, 1979, 1015.

2. A J Taylor, R B Gibson, J P Roberts, Opt Lett 13 1988, 814.

3. Laser Program Annual Reports - Lawrence Livermore National Laboratory, 1978/1982, UCRL-50021-78/82.

4. P Corkum and C Rolland, Academic Press, R R Alfano (editor).

5. R S Taylor, K E Leopold, R K Brimacombe, App Opt 27, 1988, 567.

6. Y P Kim and M H R Hutchinson, Private Communication.

7. W E Martin and R J Winfield, App Opt 27, 1988, 567.

8. Laser Program Annual Report - Lawrence Livermore National Laboratory, 1973, UCRL-50021-73.

9. I N Ross, D Karadia and J M Barr, App Opt (submitted).

10. D V Vlasov, R A Garaev, V V Korobin and R S Serov, Sov Phys JETP, 49, 1979, 1033.

11. A E Dangor et al, J Phys B At Mol Opt Phys 22, 1989, 797.

C3.2 MULTIPHOTON MULTIPLE IONIZATION OF N_2 PROBED BY COVARIANCE MAPPING

L J Frasinski, K Codling and P A Hatherly,
(J J Thomson Physical Laboratory, University of Reading)

A novel covariance mapping technique has been employed to study the multiphoton multiple ionization of N_2 using an intense ($\sim 3\times10^{15}$W/cm^2) subpicosecond laser. The results are consistent with a simple field-ionization, Coulomb-explosion model of fragmentation. The prevalence of charge-symmetric dissociation processes such as $[N_2^{4+}] \rightarrow N^{2+}+N^{2+}$ is in sharp contrast to other recent experimental data.

In a recent publication, Frasinski et al[1] attempted to explain the results of their experiment on the multiphoton multiple ionization of N_2 in terms of a dynamic multielectron dissociative ionization process. A laser of wavelength 600nm, pulse length 0.6ps and repetition rate 10Hz was focussed down to a diffraction-limited spot to produce an intensity of about 3×10^{15} W/cm^2. This was used to ionize a beam of air molecules, producing a complex spectrum of atomic and molecular ions of various stages of ionization. A simple but well-characterised time-of-flight (TOF) mass spectrometer was used to determine the kinetic energies of the ions produced[2].

The use of air rather than pure N_2 created difficulties in interpretation but nevertheless the results were explained in terms of the following sequence of events:

$$N_2 \rightarrow [N_2^{2+}] \rightarrow N^+ + N^+ + 7(7.6)\text{eV}$$
$$\downarrow$$
$$[N_2^{3+}] \rightarrow N^+ + N^{2+} + 14(14.2)\text{eV}$$
$$\downarrow$$
$$[N_2^{4+}] \rightarrow N^{2+} + N^{2+} + 25(22.6)\text{eV}$$
$$\downarrow$$
$$[N_2^{6+}] \rightarrow N^{3+} + N^{3+} + 38(20\text{-}25)\text{eV}$$

The square brackets denote transient molecular ions. The round brackets are more recent values of kinetic energy release, see later discussion of the large change in value for the $N^{3+}+N^{3+}$ channel and the missing $N^{2+}+N^{3+}$ channel.

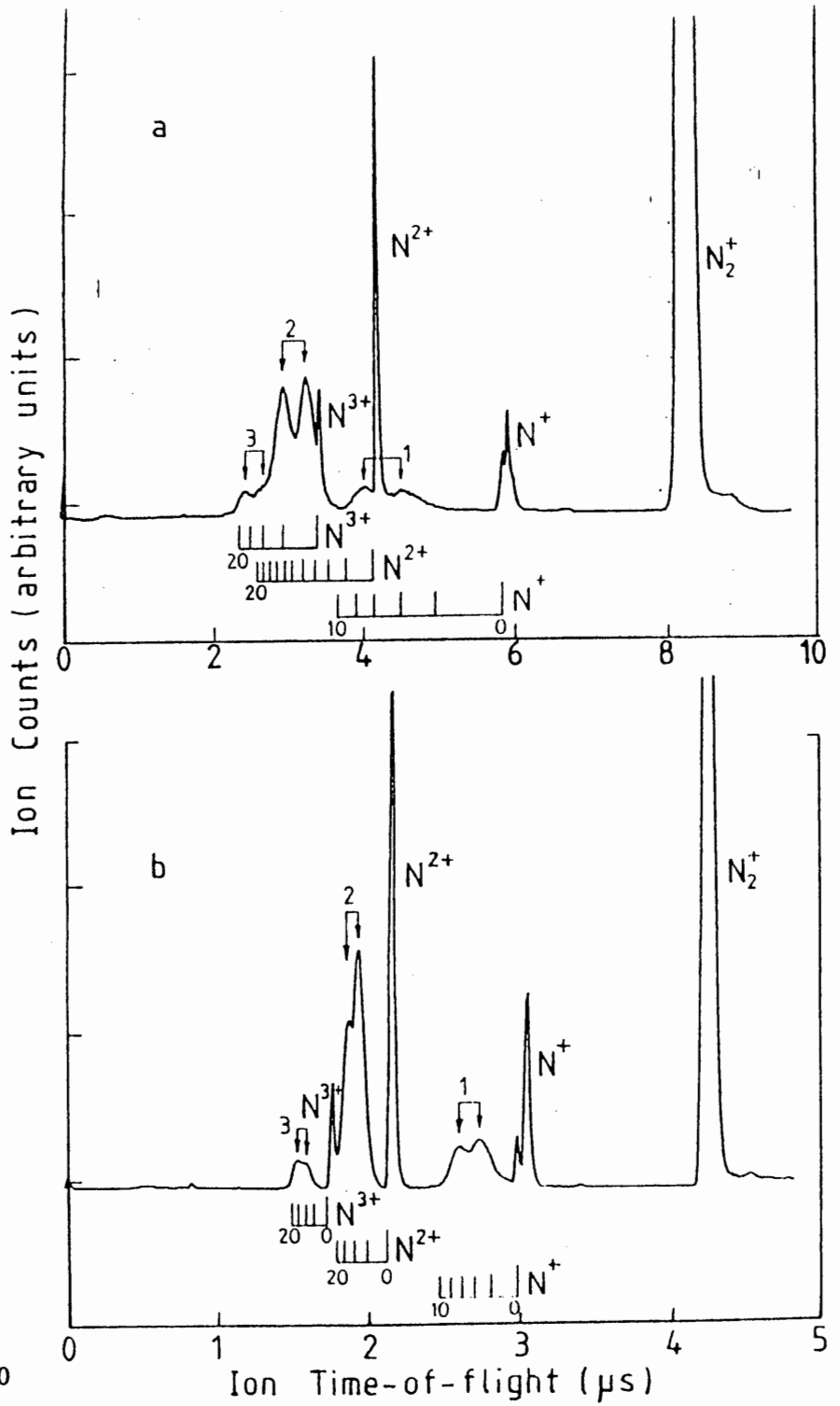


Fig C3.12 TOF spectra of N_2 with (a) 25V and (b) 100V across the interaction region. The arrows labelled 1, 2 and 3 denote N^+, N^{2+} and N^{3+} "forward" ions respectively. The scales alongside are the ion kinetic energies in eV.

It was suggested that, once the molecule is ionized beyond the single-ion stage, the fragment ions mutually repel in the Coulomb field. If additional electrons are stripped away as the molecule dissociates, the ions are now subjected to even larger Coulomb repulsion and hence gain energy. Thus the detailed dynamics of molecular multiphoton multiple ionization can be investigated on a time-scale of femtoseconds (the dissociation time-scale) even if a laser pulse of picosecond duration is used.

Two recent TOF spectra of pure N_2 taken directly from the digital oscilloscope are shown in Figure C3.12; these were obtained using 2000 laser pulses. The spectra consist, for each atomic ion, of a sharp "backward" peak and a two of broader "forward" peaks (arrowed). This structure is explained in the following way. The laser radiation is linearly polarised with its E-vector along the axis of the drift tube of the TOF spectrometer. Because of the molecule's elongated shape, the potential difference created by this laser E-field is larger along the molecular axis than at right angles to it. The potential barrier to electron emission is lower and therefore diatomic molecules much more easily ionized when their molecular axes lie along the E-vector. As there is no time for molecular rotation to occur, this leads to two groups of atomic ions, those ejected initially towards the detector ("forward" ions) which have TOF's that decrease almost linearly with their initial momentum and those that are ejected away from the detector. These "backward" ions, having necessarily the same range of momenta as the "forward" ions, arrive almost simultaneously at the detector to produce the sharp peaks at TOF's higher than those of zero energy ions. The kinetic energy scales for the "forward" ions shown in the figure were obtained by computer simulation.

These TOF spectra and others taken at different voltages across the interaction region appear to confirm the earlier analysis, although the kinetic energies obtained were slightly different (7.6eV, 14.2eV, 22.6eV and 35.0eV respectively with a 10% error on each). It was proposed that ionization could be viewed in terms of a classical field ionization process, rather than a multiphoton process[1,2]. It is important to appreciate that an intensity of 3×10^{15} W/cm^2 is equivalent to a laser E-field of almost 15V per Å. As the molecular ion dissociates, it inevitably increases in length. Thus the high E-field reduces even further the potential barrier to electron emission. In other words the E-field becomes more and more effective in field-ionizing the transient molecular ion.

However, the above model of sequential ionization was based solely on the measurement of the energies of the atomic ions and the only real justification of its validity lay in the fact that there were peaks in the N^+ and N^{2+} ion kinetic energy distributions at the same 7eV kinetic energy. The assumption was that they resulted from the same transient $[N_2^{3+}]$ ion, rather than from two totally uncorrelated processes. Unfortunately, no equivalent "peak" energy coincidences were observed between N^{2+} and N^{3+} ions to suggest the existence of transient $[N_2^{5+}]$ ions. What was required, then, was a method of unambiguously correlating the various atomic ion pairs with specific parent molecular ions.

We have devised a new experiment, based in part on our experience in triple-coincidence spectroscopy using synchrotron radiation[3]. In order to perform this experiment a completely new drift tube had to be designed and constructed, having the essential capability of a much greater collection efficiency. It was also important that the TOF should be a linear function of ion momentum component along the drift tube axis, for both "forward" and "backward" ions. (This is clearly not the case in Figure C3.12). In other words, one required that the two groups of ions should appear symmetrically disposed either side of the TOF corresponding to zero kinetic energy ions.

The idea behind the experiment is one of covariance mapping. This will be discussed more fully elsewhere, but the principle is the following. In a TOF spectrum from a single laser pulse, two particular atomic ions (e.g. N^+ and N^{2+}) may be correlated via a Coulomb explosion; in a second laser shot they may not. If only one molecule were to be in the laser focus at each pulse and if the collection efficiency were 100%, this correlation would be observable in a conventional coincidence experiment[3]. Here,

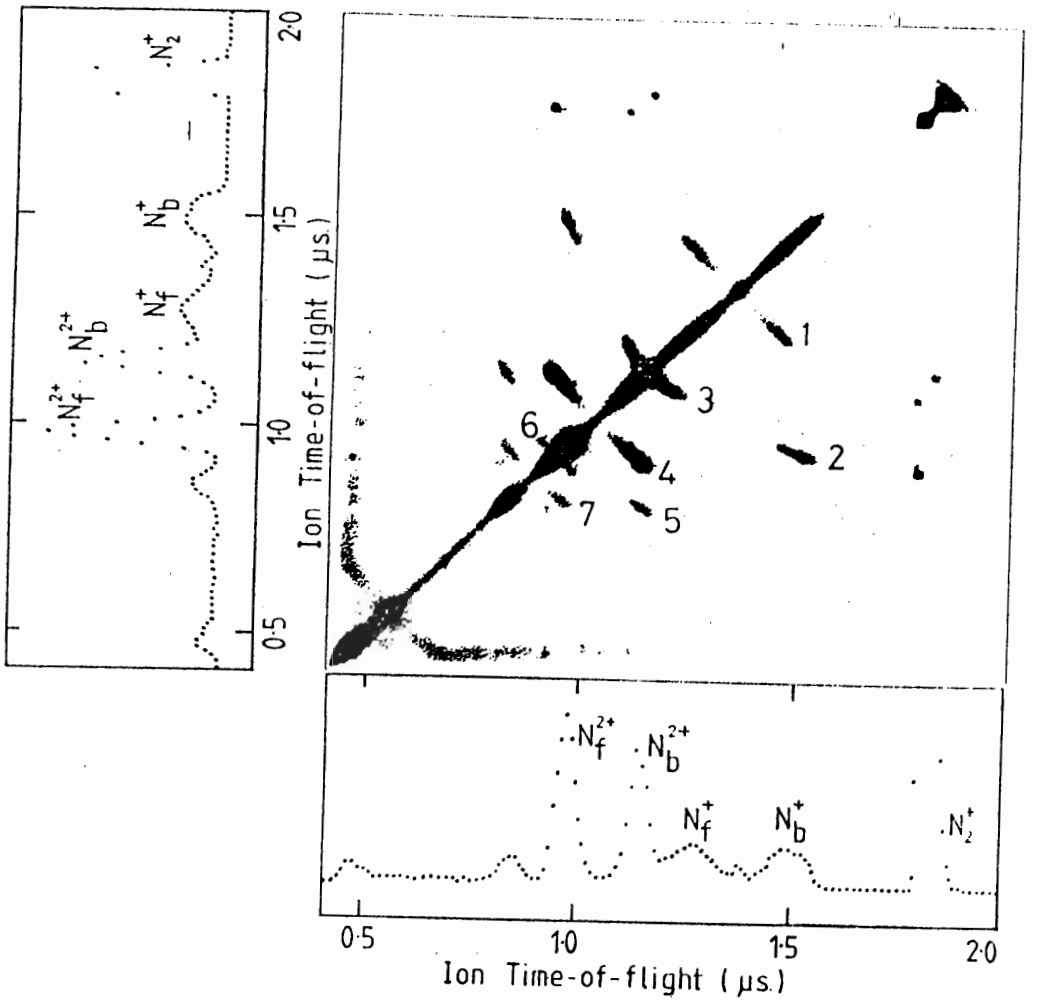


Fig C3.13 The covariance map of N_2. Along the x and y axes is placed the conventional, time-averaged, one-dimensional TOF spectrum. Subscripts f and b denote "forward" and "backward" ions. The correlation features 1-7 are discussed in the text. Note the strong autocorrelation line at 45°. (The unusual feature at low TOF is associated with protons from hydrocarbon impurity).

however, many ions may be produced per laser pulse and in some cases they may appear in the same channel of digital oscilloscope.

A conventional time-averaged, low-dispersion, one-dimensional TOF spectrum of N_2 is shown in figure C3.13 where there exists a considerable overlap of ions of differing charge states and kinetic energies. By using the TOF spectrum itself as both the x and y TOF axes and multiplying one by the other, channel by channel at each laser pulse, averaging the resulting two-dimensional array over many laser pulses and subtracting the product of the averaged one-dimensional TOF spectrum by itself, one obtains a map of correlations between ions resulting from the same parent molecular ion. What is determined, clearly, is a covariance map $\langle XY\rangle - \langle X\rangle\langle Y\rangle$, where the functions X(x) and Y(y) are the same set of one-dimensional TOF spectra. In general terms any statistical inter-dependence of X and Y will manifest itself as "hills" or "valleys", corresponding to correlated or anticorrelated parts of the X and Y functions. In this experiment we expect to see "hills" because pulse-to-pulse fluctuations in the number of parent ions create a positive correlation betwen the TOF peaks of the two charged fragments.

Figure C3.13 shows a typical covariance map of N_2 taken with 10,000 laser pulses. For clarity, the conventional time-averaged one-dimensional TOF spectrum X = Y is shown on both x and y axes, but it must be emphasised that the covariance is computed using the X and Y spectra acquired at each pulse. By creating such a map, one can determine the alternative dissociation channels.

The various features associated with energetic "forward" and "backward" ions are labelled from 1 to 7. There are two groups of N^+ ions (3.8 keV and 7.1 keV) which cannot be resolved in the one-dimensonal TOF spectrum. These are labelled N_b^+ and occur at about 1.5 μs on the x axis TOF spectrum. However, the island of covariance labelled 1 involves "backward" 3.8 eV N^+ ions correlating with "forward" 3.8 eV N^+ ions (labelled N_f^+ and occurring at about 1.3 μs on the y axis TOF spectrum), whereas the island labelled 2 relates to 7.1 eV N^+ ions correlating with 7.1 eV N^{2+} ions. This latter feature clearly involves "backward" N^+ ions correlating with "forward" N^{2+} ions, whereas island 3 involves "forward" N^+ ions correlating with "backward" N^{2+} ions, whereas island 3 involves "forward" N^+ ions correlating with "backward" N^{2+} ions. Zero energy N^+ ions would occur at about 1.4 μs on the one-dimensional TOF spectra but in fact the weak feature at that TOF is due to thermal energy N_2^{2+} ions. In a similar way island 4 indicates a $N^{2+} + N^{2+}$ correlation. Island 5 involves "backward" N^{2+} ions and "forward" N^{3+} ions, island 6 involves "forward" N^{2+} ions correlating with "backward" N^{3+} ions and finally island 7 is $N^{3+} + N^{3+}$ correlating resulting from $[N_2^{5+}]$ parent ions.

In summary, one sees that covariance mapping allows one not only to resolve structures that are unresolved in the one-dimensional TOF spectrum but more importantly to determine the parent molecular ions from which the atomic ions evolved. We note, also, that the covariance islands do not always correspond to peaks in the one-dimensional TOF spectrum. For example, island 7 ($N^{3+} + N^{3+}$) can be seen clearly on the covariance map, but is completely hidden in the wing of the N_f^{2+} peak seen in the x axis TOF spectrum.

At first glance this map not only confirms the earlier analysis but also adds the missing channel $[N_2^{5+}] \rightarrow N^{2+} + N^{3+}$. However, things are not quite so straight forward! From the location of the ions on the covariance map, one can determine the energies of the various atomic ions with moderate accuracy. There is, indeed, a correlation to confirm the $N^+ + N^+ + 7.6$eV step, a correlation to confirm the $N^+ + N^{2+} + 14.2$eV step and a major correlation to confirm the $N^{2+} + N^{2+} + 22.6$eV step. It is interesting to note that the kinetic energy released in the process $N^{2+} + N^{3+}$ (∿35eV) is greater than that associated with the process $N^{3+} + N^{3+}$ (in the range 20-25eV). This can be deduced from the fact that island 7 ($N^{3+} + N^{3+}$) lies at a longer y TOF than island 5($N^{2+} + N^{3+}$). This means that the sequence of Coulomb explosions is not as simple as that deduced from the earlier, one-dimensional TOF spectra.

With hindsight one can see that the higher energy (17.5eV) N^{3+} ion in Fig C3.12 was incorrectly assigned. This ion correlates with a 17.5eV N^{2+} ion and not with 17.5eV N^{3+} ion. It is the lower energy

(~11eV) N^{3+} ion of Figure C3.12 (not seen conclusively in the earlier TOF spectrum of air) that correlates with an identically charged N^{3+} ion. This essential reassignment indicates the power of the covariance mapping technique. If one retains the simple field ionisation, Coulomb-explosion model of multi-electron dissociative ionisation, one way that the $N^{2+}+N^{3+}$ pair might evolve is from a prior "two-electron" ejection from the transient $[N_2^{5+}]$ ion. The N^+ and N^{2+} ions would be about 3Å apart at the time of this two-electron emission. The two electrons may be removed from the N^+ ion but it is also possible that one electron is ejected from one ion, followed at least 1fs later (the laser E-field reversal time) by an electron from the other ion.

One knows that the 11eV N^{3+} ions must have evolved from a $[N_2^{5+}]$ parent molecular ion. This transient ion could not have been created instantaneously at the neutral molecule equilibrium internuclear separation of 1.1Å, since this would lead to a Coulomb energy of 118eV. It is just possible that the $N^{3+}+N^{3+}$ ion pair are created from two dissociating N atoms situated about 6Å apart (giving about 22eV Coulomb energy) but perhaps the simplest interpretation of the above observation is that the $[N_2^{5+}]$ transient ion is stripped of two electrons when the two N^{2+} atomic ions are far apart, yet still correlated. The additional Coulomb energy would be small and the kinetic energy releases almost identical for the $N^{2+}+N^{2+}$ and $N^{3+}+N^{3+}$ fragmentation processes.

In order to make further progress, one needs to study the one-dimensional TOF spectrum and the covariance map in conjunction. For example, one notes that the 7eV N^{2+} peak in the TOF spectrum,

Figure C3.12, is considerably larger than the 7eV N^+ peak with which it correlates. This may be due, in part, to a difference in detector efficiency. But it is also larger than the N^{2+} peak at 11eV, even though this 11eV peak is associated with the strongest correlation feature in Figure C3.13. This suggests that the process $[N_2^{5+}] \rightarrow N+N^{2+}+14eV$ may also be present.

In recent work on the multiphoton ionisation of N_2 using a 248nm, subpicosecond laser of focussed intensity $\sim 10^{16} W/cm^2$, Boyer et al[4] observe a distinct tendency towards charge asymmetric dissociation ($N+N^{2+}$; N^++N^{2+}; N^++N^{3+}). Their data are consistent with a simple picture of rapid molecular ionisation at an internuclear separation close to the equilibrium value of N_2 (1.1Å). They argue that this asymmetry is a natural consequence of a large induced dipole moment arising from the multielectron motion along the laser E-field. this large asymmetry leads naturally to a corresponding asymmetry in the dissociating products.

Boyer et al see no evidence for the charge symmetric dissociations $N^{2+}+N^{2+}$ and $N^{3+}+N^{3+}$. This is in complete contrast to the present data, where the symmetric channel $N^{2+}+N^{2+}$ is the most likely outcome. Moreover, the covariance map, Figure C3.13, gives unequivocal confirmation of the symmetric $N^{3+}+N^{3+}$ channel. We reiterate that the measured kinetic energy releases in these two processes are far too small to be the result of rapid ionisation at the N_2 equilibrium internuclear separation of 1.1Å. It is interesting to note that there is no sign of the asymmetric channel N^++N^{3+} in Figure C3.13.

Finally, such covariance maps allow one to determine the angular distribution of the various ions relative to the E-vector of the incident linearly-polarised laser radiation. In the earlier publication[1], we suggested that the ion emission was strongly peaked along the E-vector, although we could not be categorical because the ion collection efficiency of the longer drift tube was not high. We find here that for diatomic molecules such as N_2 and CO the angular distribution is approximately $\cos^2\theta$, where θ is the angle between the laser E-field and the direction of ion emission. We believe that such peaked angular distributions can be explained simply by the field ionisation model, although the multiphoton approach might well lead to similar results. Indeed, we are not suggesting that the multiphoton picture of multiple ionization of molecules is incorrect but that the field ionization approach may lead to simpler physical insights in situations where the laser E-field is high.

We are pleased to acknowledge the Science and Engineering Research Council (UK) for their financial support and the use of the Laser

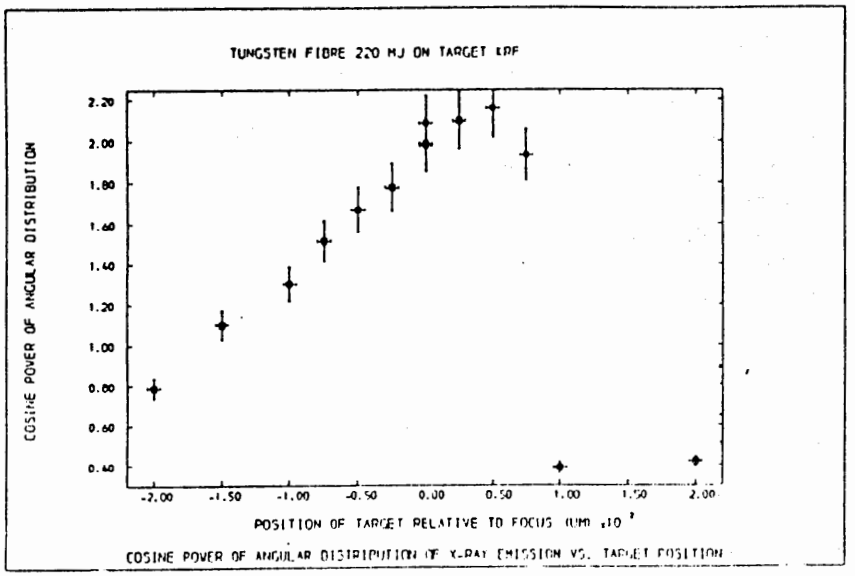


Fig. C3.14 Angular distribution of X-ray emission for a tungsten target.

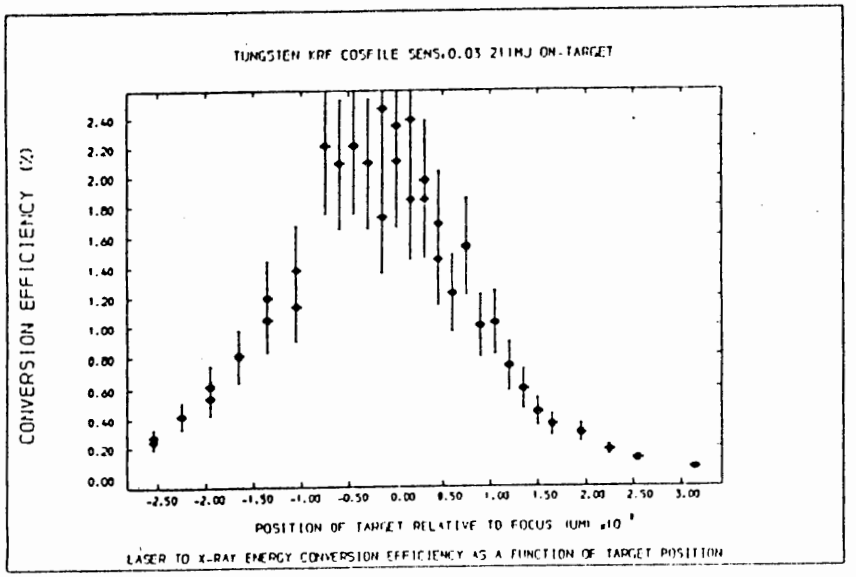


Fig. C3.15 Conversion efficiency for a tungsten target as a function of target position.

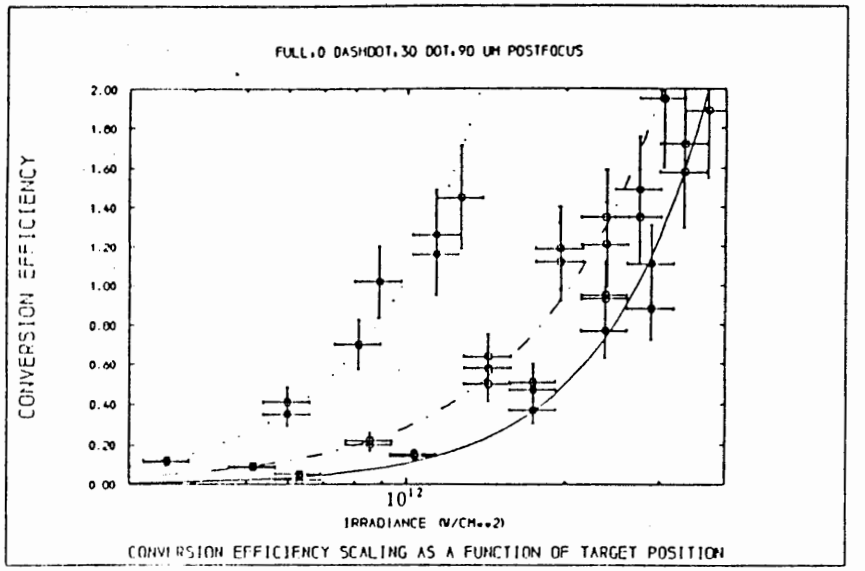


Fig. C3.16 Conversion efficiency as a function of irradiance. Three sets of data are given for a tungsten target positioned at focus, 30 and 90 microns post-focus.

Support Facility (LSF). We are particularly indebted to W T Toner of the Rutherford Appleton Laboratory (RAL) for his helpful comments about the covariance technique and his enthusiasm for the project and to Dr I N Ross (RAL) for providing the laser and focussing optics. Thanks are offered to M P Millard of Reading University for his excellent machining of the equipment.

References

1. L J Frasinski, K Codling, P Hatherly, J Barr, I N Ross and W T Toner, Phys Rev Lett 58 2424 (1987).

2. K Colding, L J Frasinski, P Hatherly and J R M Barr, J Phys B 20 L525 (1987).

3. L J Frasinski, M Stankiewicz, K J Randall P A Hatherly and K Codling, J Phys B 19 L819 (1986).

4. K Boyer, T S Luk, J C Solem and C K Rhodes, Phys Rev A submitted.

C3.3 CHARACTERISATION OF SOFT X-RAY EMISSION IN THE WATER WINDOW FROM A KrF LASER-GENERATED PLASMA

A M Rogoyski and A G Michette, (King's College London)
I C E Turcu and F O'Neill (RAL)

A series of experiments has been carried out towards the goal of characterising a laser-generated plasma source of soft X rays for applications in soft X-ray microscopy and lithography. The experiments involved a comparison of the emission characteristics of laser generated plasmas produced with a KrF laser with those produced using a Nd:YAG laser of comparable energy and pulselength. The experiments involving the latter system will not be detailed herein but may be found in (1).

The soft X-ray spectral region of most interest is that between the carbon K-edge and the oxygen K-edge, the so-called water window. The spectral region provides high contrast between water and carbon (a difference in absorption of approximately 10), the latter material being the main constituent of most biological structures of interest. Soft X-ray microscopy using radiation in this spectral region would provide a method of studying living, hydrated biological material at higher resolution than is possible with conventional optical microscopy and without the risk of introducing artefacts as may be found in the specimen preparation processes of electron microscopy.

The EMG-150 KrF excimer laser used at the Laser Support Facility at the Rutherford Appleton Laboratories provided an opportunity to investigate soft X-ray production using an ultra-violet driver laser. The laser delivered 250mJ on-target in a 25ns pulse at a wavelength of 248nm. This gave a range of irradiances of $5x10^{11}$-$5x10^{12}Wcm^{-2}$, which, using a 9cm focal length lens, corresponded to a range of focal spot sizes of 50-20 microns in diameter. The target chamber and target alignment system has been described previously[2]. Parameters under the experimenter's control such as the laser energy, focusing conditions and target material were varied in order to obtain optimum X-ray production in the water window. Several interesting results were obtained; the angular distribution of X-ray emission was measured using several silicon PIN diode X-ray detectors filtered with vanadium (the use of vanadium allows the peak response of the PIN diodes to be in the water window)[3]. It was found that the angular distribution of the X-ray emission was dependent on the size of the focused laser spot and the energy incident on target. Figure C3.14 shows a typical set of results obtained for a tungsten target where the angular distribution is given in terms of a $\cos^{n\theta}$ fit.

The steep angular distributions found for targets placed at the focus of the laser are thought to be caused by absorption of the X-rays in cooling, laterally expanding plasma. As the target is moved away from focus the angular distribution changes becoming less directional. At large distances away from focus (i.e. $\geq$200μm) the curvature of the target (a 250μm wire) produces an angular distribution that is less directional than a $\cos\theta$ distribution (which corresponds to the emission behaviour of an ideal Lambertian

source). Another interesting feature is the observed asymmetry in the dependence of the angular distribution on the target position. When the target is pre-focus the plasma expands into a region of continuously decreasing power density, however, post-focus the plasma expands into a region that has a higher irradiance near the optical axis while reducing the power incident on the plasma away from this region. The resulting difference in the heating and expansion dynamics of the plasma is thought to explain the different angular distributions measured. This angular distribution of X-ray emission is an important factor, not only in the proper calculation of the total X-ray emission produced by the source, but also as a design parameter of an X-ray microscope.

Data was also obtained for the laser energy to X-ray energy conversion efficiencies (η_{L-X}) as functions of target material (these materials included gold, tungsten, aluminium, copper, molybdenum and carbon) as functions of irradiating conditions. The latter parameter was varied by changing the focusing conditions of the laser and by changing the laser energy while keeping the focusing conditions constant. A typical set of results is shown in Figure C3.15.

The results of these experiments indicated that for optimum conversion of laser energy into water window X-rays, the target should not be placed exactly at focus (this depends on the maximum irradiance that the laser is capable of generating). Data was also obtained that provided the scaling of X-ray production with laser energy at constant focus spot size (carried out for several different spot sizes). Figure C3.16 shows the dependence of the conversion efficiency on the irradiance for a tungsten target for three different target positions, at focus, 30 and 90 µm post-focus.

Similar data was obtained for other target materials for some target positions. The following table lists the irradiance exponents (i.e. $\eta_{L-X} \alpha I^{n}$).

Target Material	at focus	30µm postfocus	60µm postfocus	90µm postfocus
Carbon	2.0	2.0	-	-
Copper	1.6	1.5	1.4	1.8
Tungsten	2.3	1.8	-	2.1

Irradiance exponents as a function of target position.

These figures have been used to estimate the conversion efficiencies of laser systems that are more powerful than the present system, allowing a proper specification for an LGP-based X-ray microscope to be made. Other results included time resolved measurements of X-ray production, again allowing the experimental parameters to be varied in order to maximise X-ray production.

These experiments were carried out for a variety of different target materials. The maximum conversion efficiency that was measured for any particular target material is given in the table below.

Z:	79	74	42	29	13	6
η_{L-X}(%)	3.5	2.6	2.4	0.9	1.4	0.7

Maximum conversion efficiencies as a function of target material

Similar experiments have also been carried out using the Nd:YAG laser based at KCL both before and after the KrF experiments. Generally, the conversion of laser energy into soft X-rays was poorer using the Nd:YAG laser because of the lower coupling of longer wavelengths into plasmas. Hard X-ray production was more easily measured using the Nd:YAG laser system. Optimum X-ray production was found to vary strongly with the focusing conditions of the laser with the least efficient conversion of laser to X-ray energy being found when the target was placed at focus. This effect is much more important with the use of the Nd:YAG system than was found for the equivalent KrF system. The angular distribution of X-ray emission was found not to be so strongly dependent on the irradiating conditions generated by the laser, behaving as a Lambertian source. Further experiments have also been carried out to investigate the production of debris from laser-generated plasmas.

The data presented is only a small part of the total data that was acquired during the course of these experiments. Further more detailed descriptions of these experiments will be given in future publications.

References

1. A M Rogoyski, PhD Thesis, University of London, 1989.

2. F O'Neill, G M Davis, M C Gower, I C E Turcu, M Lawless and M Williams in X-rays from laser plasmas, Ed. M C Richardson, Proc. SPIE 831, 230 (1987).

3. I Turcu, F O'Neill, V Zammit, Y Al-Hadithi, A Rogoyski, C Hills and A G Michette, Proc. SPIE 831, 1 (1987).

C4 **PLASMA X-RAY SOURCES/PSEC LASER DEVELOPMENT, NLO RESEARCH** Pages

C4.1 PLASMA X-RAY SOURCE GENERATION USING mJ-LEVEL 100psec XeCl LASER PULSES 371-373

C4.2 PLASMA X-RAY SOURCE GENERATED BY 30J, 30ns KrF LASER 373-377

C4.3 PLASMA X-RAY SOURCE GENERATION USING 20ns, 1.06μm Nd: GLASS LASER PULSES 377-379

C4.4 DEVELOPMENT OF A CCD DETECTOR/SPECTROGRAPH SYSTEM FOR PICOSECOND TIME-RESOLVED RESONANCE RAMAN (TR3) SPECTROSCOPY 379-382

C4.5 PICOSECOND PULSE DYE AMPLIFIER PUMPED BY A 6.7 KHz COPPER LASER 382-385

C4.6 EXCIMER LASER FABRICATION AND PATTERNING OF HIGH T_c SUPERCONDUCTING THIN FILMS 385-396

C4.7 EXPITAXIAL GROWTH OF THIN FILMS OF $BaTiO_3$ USING EXCIMER LASER ABLATION 396-400

C4.8 SIMULTANEOUS UV EXCIMER AND IR CO_2 LASER ABLATION OF PMMA 400-403

C4.9 WHITE LIGHT PHASE CONJUGATE LENSLESS IMAGE PROJECTION 403-408

C4.10 EXPERIMENTAL STUDIES OF SELF-PUMPED PHOTOREFRACTIVE RING RESONATORS 408-413

C4.11 MEASUREMENTS OF CW SBS GAIN IN FIBRE OPTIC RING RESONATORS 413-418

C4.1 PLASMA X-RAY SOURCE GENERATION USING mJ-LEVEL 100psec XeCl LASER PULSES

F O'Neill, I C E Turcu (RAL)
M H R Hutchinson, D Xenakis (Imperial College)

Plasma X-ray source generation using sub-nanosecond laser pulses is of interest for a number of reasons. For example by using pulses of duration ≈ 100 psec it is possible to achieve sufficient irradiance on target (≈10^{13}W/cm²) for X-ray generation by using tightly focused beams of only 1-10mJ energy/pulse. The plasma X-ray pulses produced by such a laser will be of short duration and will be useful for measuring the response time of X-ray detectors. Also the use of sub-nanosecond duration excimer laser pulses (instead of the normal 25ns pulses) might give improved X-ray generation at photon energies ≈1keV which is of interest for a number of applications.

In previous CLF Annual Reports (1987 and 1988) we have described the preliminary stages of a collaborative project to use a 100psec 308nm XeCl laser at Imperial College to generate laser-plasma sources of x-rays. In the present reporting period we have measured the conversion efficiency from laser energy to X-rays in the range hυ ≈ 0.7-0.9 keV (chromium and iron L-shell emission) using 500 μm diameter steel wire targets irradiated by single laser pulses of energy up to 8 mJ. The experimental arrangement is shown in Fig C4.1 and has been described previously in Section B4.4 of the CLF 1988 Annual Report. Quantitative measurements of the X-ray flux from the laser target were made using a silicon p-i-n diode X-ray detector filtered by a 1μm aluminium foil (e^{-1} transmission @ hυ = 0.65 keV).

Fig C4.2 shows a plot of the temporally and angularly integrated X-ray conversion efficiency at hυ > 0.65 keV as a function of laser energy on target. The main X-ray emission in this range is expected to be the multi-line L-shell emission from chrominum and iron in the steel target. The laser irradiance on target is ≈ 10^{13}W/cm² at the highest laser energy of 8 mJ where the X-ray conversion efficiency reaches ≈ 4%. This conversion efficiency is more than one order of magnitude greater than has been previously achieved[1] using 300 mJ, 25 ns KrF laser pulses focused at similar irradiances on copper targets and demonstrates the benefit of using short duration laser pulses for plasma X-ray generation. These efficiencies with 100 psec, 308 nm, mJ-level laser pulses are in fact comparable with previous X-ray conversion efficiency measurements reported[2] using 100-400 psec, 0.53 μm Nd: Glass laser pulses of up to 300J energy focused at an irradiance ≈ 10^{14}W/cm².

The results displayed in Fig C4.2 clearly demonstrate that higher keV X-ray conversion efficiency can be achieved from plasmas generated by excimer laser pulses of only 100 psec duration as compared to the 25 nsec pulses emitted by normal commercial discharge lasers. This improvement in X-ray efficiency is however obtained at the expense of laser efficiency since only a few nsec slice of stored optical energy is extracted from the excimer laser amplifier by a single 100 psec laser pulse because of the short storage time of the upper laser level. A possible solution to this energy extraction problem would be to amplify a train of 100 psec laser pulses lasting for ≈ 25 ns which are then focused onto target to produce X-rays. This would retain the benefit of the higher (∿2%) optical efficiency of the excimer laser whilst at the same time potentially achieving a high irradiance on target and the resultant high X-ray conversion efficiency. In previous experiments using a KrF laser[3] it has been demonstrated that a pulse train with an interpulse separation of a few nsec (< 4 nsec) can extract ≈90% of the available energy from an excimer amplifier. With the pulse train each pulse efficiently extracts a few nsec slice of the stored energy and the upper laser level population is repumped in the interpulse time in readiness for extraction by the next pulse in the train.

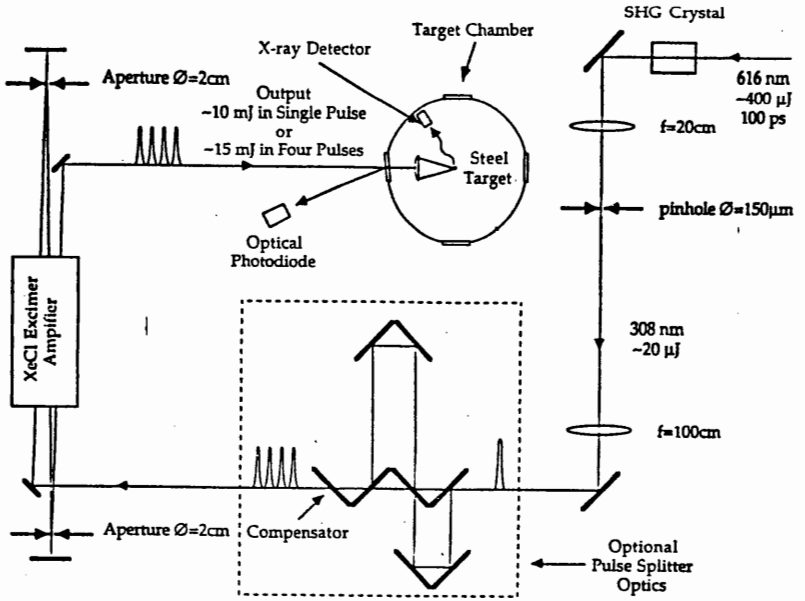


Fig C4.1 Experimental arrangement used to generate plasma X-ray source using mJ-level, 100 psec, 308 mm laser pulses.

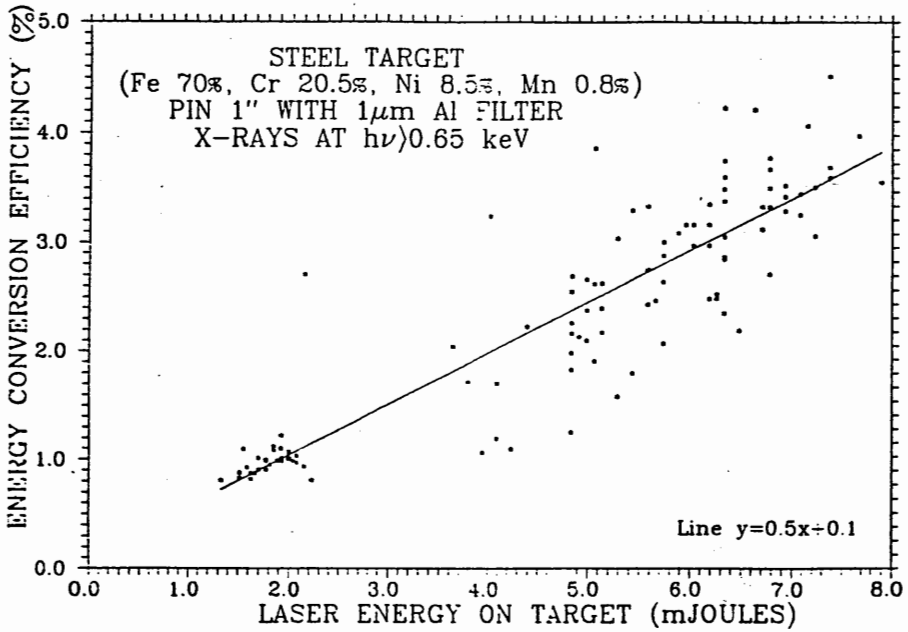


Fig C4.2 X-ray conversion efficiency versus laser energy on target for single pulse experiment.

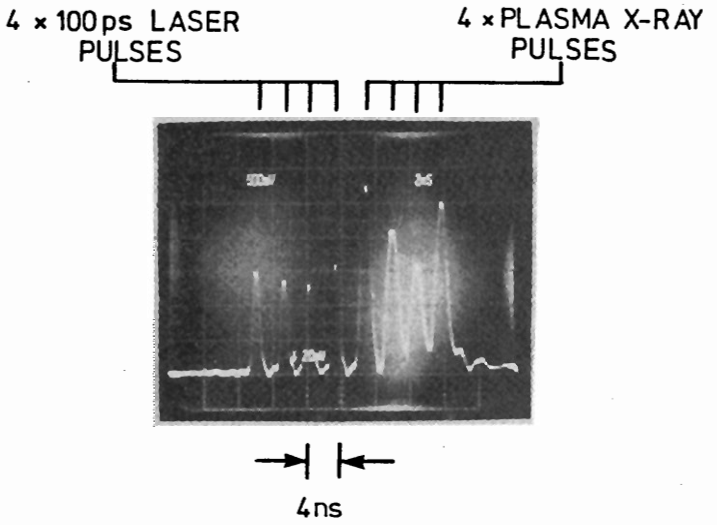


Fig C4.3 Four laser pulses on target and resultant four plasma X-ray pulses @ hν > 0.65 keV.

In the present project we have therefore carried out a preliminary experiment to test the suitability of an excimer laser pulse train for generating a laser plasma keV X-ray source. A 4-pulse train is generated from the present 100 psec single pulse oscillator using the passive pulse splitter arrangement[4] shown in Fig C4.1. After the pulse splitter array the four pulses are amplified in the XeCl laser amplifier and focused onto a steel wire target using the same arrangement as for the single pulse experiments described above. Fig C4.3 shows an oscilloscope trace of the four amplified laser pulses recorded by an optical photodiode and the corresponding four X-ray pulses from the target recorded by a Si p-i-n detector with a 1 μm Al filter. The optical and X-ray detectors each have sub-nanosecond response times. For this shot each laser pulse on target has an energy ≈ 1.5 mJ and the interpulse spacing is ≈ 3.1 ns. It can be seen that each laser pulse produces an intense X-ray pulse but there is some evidence of pulse-to-pulse variation in conversion efficiency. The conversion efficiency from optical energy to X-ray energy integrated over all four pulses is 1.2% for this particular laser shot.

It is interesting to note in Fig C4.3 that there is no marked drop-off in X-ray signal from the first pulse to the last pulse which is some 9 ns later. There appears to be no fall off of X-ray conversion efficiency with time in marked contrast to what has been observed (see section C4.2 below) in experiments using "normal" ≈ 25 ns duration excimer laser pulses.

References:

(1) G M Davis, M C Gower, F O'Neill and I C E Turcu, Appl Phys Letts 53, 1583 (1988).

(2) R Kodama, T Mochizuki, K A Tanaka and C Yamanaka, Appl Phys Lett 50, 720 (1987).

(3) T D Raymond et al in "Pulsed Single-Frequency Lasers: Technology and Applications" W K Bischel and L A Rahn, Editors, Proc SPIE 912, 122 (1988).

(4) C N Danson, C B Edwards and I N Ross, Opt and Laser Technol 17, 99 (1985).

C4.2 PLASMA X-RAY SOURCE GENERATED BY 30J, 30ns KrF LASER

G M Davis, M C Gower, F O'Neill and I C E Turcu (RAL)

This experiment was carried out in December 1987 using the SPRITE KrF laser and a preliminary description of the results was presented in Section A1-13 of the 1988 CLF Annual Report. The experiment was performed to assess the suitability of high energy long duration (≈25-30 ns) KrF laser pulses for generating plasma X-ray sources. We were particularly interested in measuring the scaling behaviour of conversion efficiency to plasma X-rays at hν≈1keV (Cu target, L-shell emission) as a function of laser energy on target up to ≈30J. X-ray sources in the ≈1keV photon energy range are of interest for applications such as X-ray lithography, X-ray microscopy, and DNA damage studies.

In a previous publication[1] we have described experiments to measure keV X-ray conversion efficiency from 25ns KrF laser pulses using a commercial repetitively pulsed laser which delivered energies up to 0.3J/pulse on target at a maximum irradiance (I) of $2 \times 10^{13} W/cm^2$. The best conversion efficiency from KrF laser light to keV L-shell X-rays from a Cu target was ≈ 0.2% which is much less than the 7-13% values reported using short pulse Nd lasers[2,3]. However in the KrF experiment it was observed that the X-ray conversion efficiency increased rapidly with laser irradiance (αI^2) up to the highest value used. Thus it is of interest to use more energetic pulses to produce higher irradiance on target and to investigate if this favourable scaling leads to

X-ray conversion efficiencies ≈10%. In the present paper therefore we describe experiments to measure keV X-ray production as a function of target irradiance using a low repetition rate oscillator-amplifier KrF laser delivering single shot pulses of ≈ 30ns duration and up to ≈ 30J energy on target at irradiances up to 2×10^{14} W/cm². This pulse length and energy have been chosen to simulate and exceed the highest performance likely to be achieved in the future from scaled-up commercial discharge-excited excimer lasers.

Low energy ≈ 30ns pulses from a discharge-excited unstable-resonator KrF laser oscillator (Lambda Physik model EMG 103) are amplified by multipassing them with appropriate beam expansion through two electron-beam- pumped amplifiers. The 80mm diameter high energy output beam from the final amplifier is focussed at normal incidence onto 500μm diameter Cu wire targets using a fused silica doublet lens of 27cm focal length. The targets are held in a vacuum chamber at 10^{-4} torr with the irradiated surface positioned in the plane of best focus of the laser beam. The intensity profile of the laser beam on target is obtained by measuring its intensity profile in the equivalent plane of a long focal length lens using a linear Si diode array. From these measurements we find that the focal spot size on target containing 90% of the laser energy is ≈ 23μm diameter. The maximum laser energy on target is 28.2 J which corresponds to an average irradiance ≈ 2.1×10^{14} W/cm². In order to measure X-ray conversion as a function of target irradiance the laser output energy and focal spot size were held constant and a variable pressure NO_2 gas absorption cell was placed in the 249nm laser beam just before the focusing lens to vary the energy on target.

Quantitative measurements of the X-rays emitted from the laser-produced plasma are made using a Si p-i-n diode detector placed in a horizontal plane at 45° to the laser axis. Charge signals from the p-i-n diode are displayed on an oscilloscope. To give the angular distribution of X-rays measurements were also taken on some laser shots with p-i-n detectors placed at angles of 17° and 76°. The X-ray signal was found to fall off approximately linearly with angle extrapolating to zero at ≈ 95° for low energy target shots (E ≤ 8J, I ≤ 6×10^{13}W/cm²) and at ≈ 115° for shots of higher energy than this. We have assumed these angular distributions to be symmetric about the laser axis. The p-i-n diodes are filtered by 6.2μm thick Be foils giving a detector plus filter response mainly in the range 0.9 keV ≤ hν ≤ 1.6 keV. When the detector plus filter response curve is multiplied with a Cu-plasma X-ray spectrum[2] generated using a frequency quadrupled Nd laser focused on target at an irradiance of 3×10^{14}W/cm² the resultant curve has a broad peak extending from 1.0keV to 1.4keV. It is this range of X-rays therefore that we are mainly detecting here. To calculate X-ray flux absolutely we assume that all the X-rays from the KrF laser-produced Cu plasmas are emitted at hν=1.2 keV. The manufacturers data on p-i-n diode sensitivity at hν=1.2 keV is then used to convert the detected electrical charge signals into incident X-ray flux. The total X-ray yield into the full solid angle of emission from the target is obtained from a time integration of the p-i-n diode charge signal integrated over the measured angular distribution. Energy conversion efficiency is defined as the total keV X-ray yield divided by the laser energy on target.

In Fig C4.4 we show our measurements of X-ray energy conversion efficiency as a function of the laser irradiance on target where we have also included data from Ref 1???? so that our present results from the high energy e-beam-pumped laser can be compared with data obtained previously using the low energy 0.3J discharge excited KrF laser. In the previous experiment focal spots of 9μm and 20μm were used and the p-i-n diode X-ray detectors were filtered with 10μm Be. The present results with the high energy laser show that energy conversion efficiency continues to increase rapidly with irradiance up to ≈ 3×10^{13}W/cm² (4.0 J on target). The conversion efficiency rises more slowly above this value of irradiance and reaches a maximum of 2.5% at 2×10^{14}W/cm².

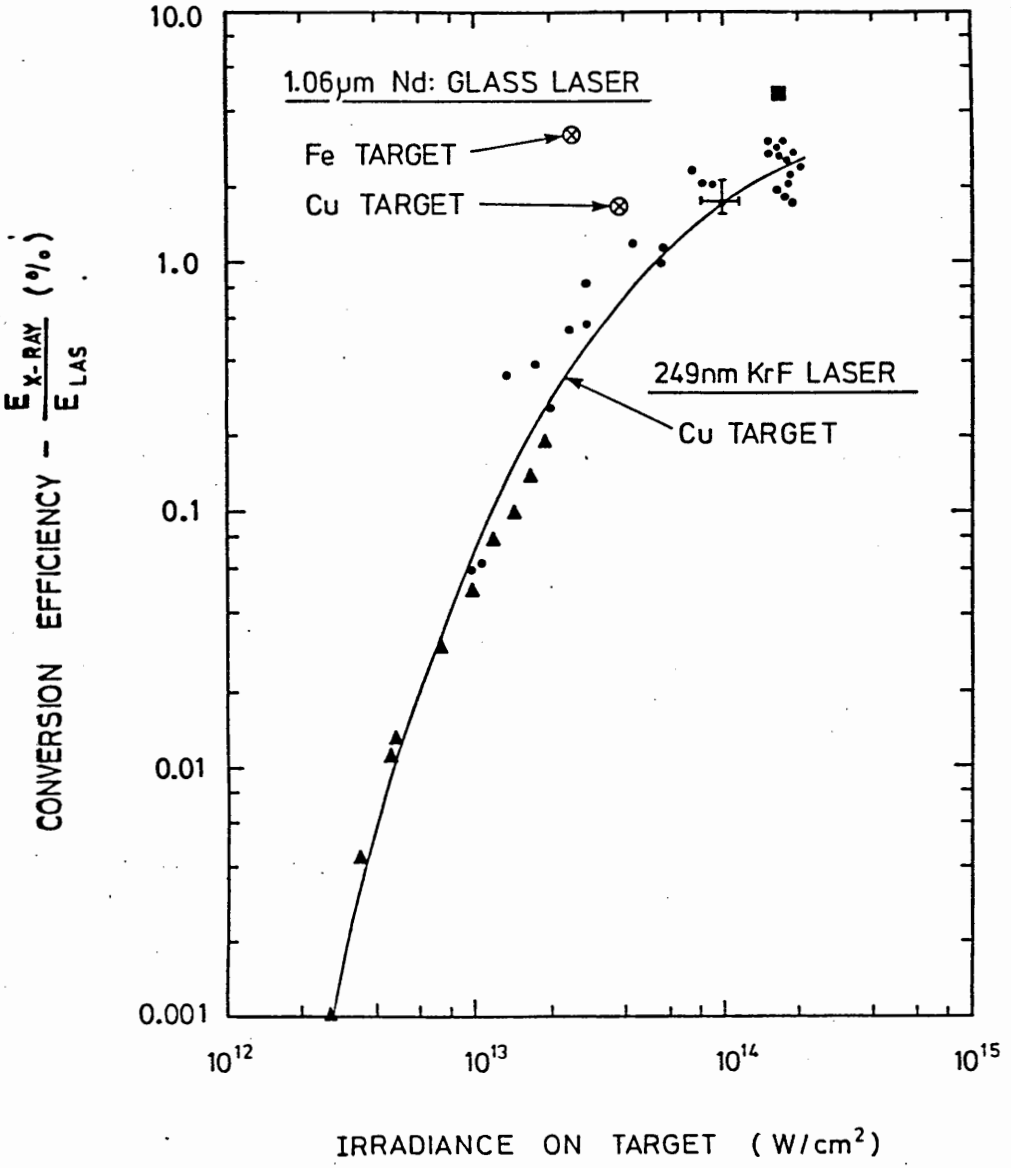


Fig C4.4 *X-ray energy conversion efficiency versus irradiance on Cu targets. The dots (•) are measurements in the present experiment and each dot represents one laser shot. Estimated error bars are shown. The square ( ) is one data point taken using a 10J KrF laser pulse of 14ns duration. The triangles (Δ) are data from Ref 1. The Nd: Glass laser data is discussed in Section C4.3.*

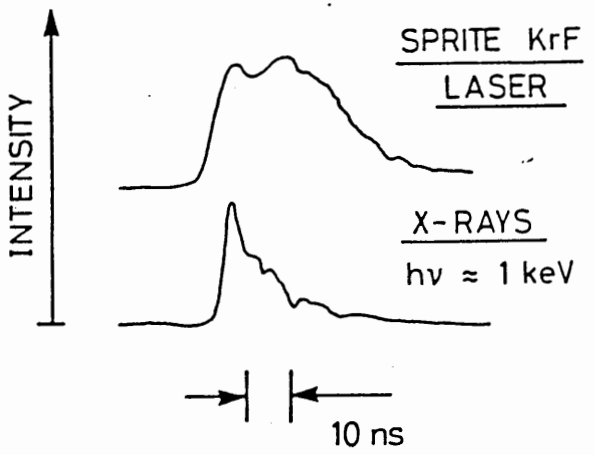


Fig C4.5 *Typical temporal shape of KrF laser pulse and ≈ 1 keV X-ray pulse. For this shot the laser energy on target was ≈ 25J. The two signals have a common time origin.*

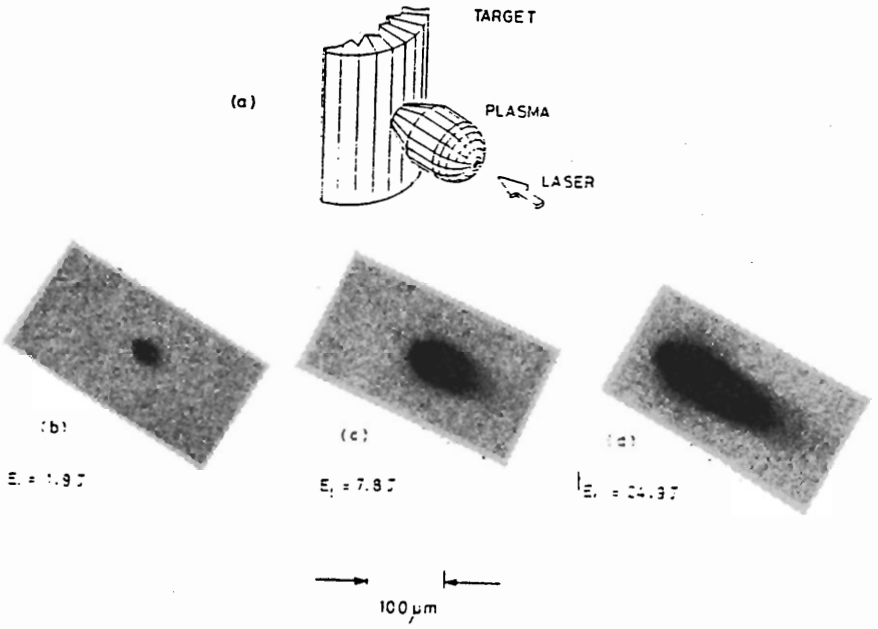


Fig C4.6 *X-ray pinhole camera pictures of the laser-produced plasma recorded on DEF film using single laser shots of energy E_1 on target as noted. (a) is a schematic diagram (not to scale) which represents the view of the plasma as seen by the pinhole camera. The pinhole was 4μm diameter filtered by 7.5μm Be foil. Note that the X-ray images (c) and (d) are overexposed*

The highest keV X-ray conversion efficiency of 2.5% achieved here with 30ns KrF laser pulses focussed to I = 2 x 10^{14}W/cm² is much less than the value of 13% obtained[2] using 0.5ns Nd laser pulses at I ≈ 10^{13}W/cm². Some but not all of the difference in efficiency is due to the fact that here we are measuring only X-rays in the range 1.0 - 1.4 keV whereas the Nd laser data covers the larger range of 0.75 - 2.0 keV. To help in understanding the reason for the lower efficiency with the long pulse KrF laser we have measured the temporal profile of the X-ray pulse using a vacuum X-ray diode (XRD) detector which has an estimated response time ≈ 100psec and is fitted with an Al photocathode filtered by a 6.2μm Be foil to give a peak spectral response at hν ≈ 1.0 keV. It was positioned in the target chamber to view the plasma at an angle ≈ 30° to the laser axis. The XRD is approximately four orders of magnitude less sensitive than the p-i-n diodes so it is only possible to record low noise traces of X-ray pulses when using laser energies ≥ 8J on target. Fig C4.5 shows the KrF laser pulse measured using an optical photodiode and 1 keV X-ray pulse recorded on a Tektronix 7844 dual-beam oscilloscope. It can be seen that the X-ray emission from the plasma peaks at the beginning of the laser pulse and the X-ray output falls off rapidly at later times with the result that only the initial part of the laser pulse is efficiently converted to X-rays. The full width half maximum duration of the X-ray pulse is 5ns and from the temporal shape of the two pulses we calculate that for an energy conversion efficiency of 2.5% the peak power keV X-ray conversion efficiency would be ≈ 7.5% which is in closer agreement with the values measured using the short pulse Nd:Glass laser.

The underlying physics mechanism which causes the early termination of the keV X-ray output from the plasma is uncertain. The effect occurred over the full range of irradiance used in these experiments although accurate X-ray pulse width measurements were not possible at low irradiances because the signals from the vacuum XRD were too noisy. It appears therefore that mechanisms such as target recoil out of the focus or laser back-scatter due to non-linear plasma interactions can be discounted. The reduction in 1 keV X-ray output during the latter stage of the laser pulse is most likely caused by a drop-off in plasma temperature due to the gradual expansion of the plasma volume into which the laser light is absorbed. Previous experimenters using 5ns Nd laser pulses focussed onto solid D_2 targets have reported just such a plasma temperature drop with time[4]. The extent of the plasma volume in the present experiments can be appreciated from the X-ray pin-hole camera pictures of the plasma displayed in Fig C4.6. Even though these are time integrated images they do show that particularly for high energy laser shots the plasma size is large in comparison to the 25μm size of the tightly focussed laser spot on target. The large plasma volume might also explain why long pulse laser irradiances ≈ 10^{14}W/cm² are needed for efficient X-ray generation compared to irradiances ≈ 10^{13}W/cm² for short pulse lasers. More experiments are needed to explain these plasma volume and X-ray pulse shortening effects with long pulse KrF lasers.

In conclusion we have measured the conversion efficiency from 249nm KrF laser light to X-rays at 1.0 keV ≤ hν ≤ 1.4 keV from a Cu laser-plasma source generated by 30ns pulses of energy up to ≈ 30J focussed at irradiances up to 2x10^{14}W/cm². The maximum time-integrated conversion efficiency is ≈ 2.5% but the peak of the X-ray emission occurs in the first few nanoseconds of the laser pulse where the peak power X-ray conversion efficiency is ≈ 7.5%. When the remaining part of the Cu-plasma X-ray spectrum[2] down to 0.6 keV is added in, the peak power conversion efficiency is estimated to be ≈ 15%. For the present type of experimental arrangement KrF laser pulses of 5ns duration and ≈ few joules energy would be the optimum choice for obtaining the maximum X-ray conversion efficiency from a plasma source at hν≈1keV. Laser pulses with these parameters could be generated from 25ns high energy discharge-excited excimer modules using efficient optical pulse compression techniques such as pulse stacking or backward Brillouin amplification. To show the beneficial effect of using shorter KrF pulses we were able to obtain a 14ns pulse from the

present laser by carefully adjusting the firing time of the master oscillator with respect to the two electron-beam-pumped amplifiers. This gave one data one data point (plotted in Fig C4.4) where the keV X-ray energy conversion efficiency increased to ≈ 5%.

References

1. E Turcu, G Davis, M Gower, F O'Neill and M Lawless, Microelectron Eng 6, 287 (1987).

2. M Chaker, H Pepin, V Bareau, S Boily, B Lafontaine, R Fabbro, I Toubhans, B Faral, J F Currie, D Nagel and M Peckerar, Proc Soc Photo-Opt Instrum Eng 733, 58 (1987).

3. K M Glibert, J P Anthes, M A Gusinow, M A Palmer, R R Whitlock, and D J Nagel, J Appl Phys, 51, 1449 (1980).

4. K Eidmann, M H Key and R Sigel, J Appl Phys 47, 2402 (1976).

C4.3 PLASMA X-RAY SOURCE GENERATION USING 20ns, 1.06μm Nd: GLASS LASER PULSES

F O'Neill (RAL)
C L S Lewis, D Neely (Queens University, Belfast)

In section C4.2 above we have described experiments to measure conversion efficiency from 249nm KrF laser light to ≈1keV plasma X-rays where 30ns laser pulses of energy up to ≈30J were focused onto Cu targets at irradiances up to 2×10^{14}W/cm². Energy conversion efficiencies ≈2.5% were achieved at the highest irradiance. It was noted however that the ≈1keV plasma X-ray pulses were of considerably shorter duration than the incident laser pulses (see Fig C4.5 of section C4.2). In particular after the first ≈5ns the power conversion efficiency to X-rays dropped rapidly to approximately zero. There are indications from previous experiments[1,2] on X-ray generation using longer wavelength lasers (eg Nd: glass operating at 1.06μm (ω) or 0.53μm (2ω)) that this premature termination of X-ray emission does not occur. An experiment has therefore been carried out using a Nd: glass laser at Queens University, Belfast to measure the temporal behaviour of ≈1keV X-ray emission from plasmas generated by 20ns, 1.06μm laser pulses. The main aim of the experiment was to confirm if plasma X-ray pulse shortening does or does not occur with long pulse IR lasers.

The Queens University Nd laser consists of a long pulse (≈80ns) Q-switched oscillator followed by a chain of glass amplifiers. A 20ns laser pulse is sliced from the 80ns Q-switched pulse and this 20ns pulse is amplified through the amplifier chain for target experiments using 1.06μm light. The laser pulse is focused to a ≈30μm spot on target and typical on-target energies were in the range 1-12J for a corresponding range of irradiances $\approx7\times10^{12}$ - 8.5×10^{13}W/cm². These experimental parameters are similar to those used for the KrF experiment described in section C4.2 above but with the laser wavelength changed from 249nm to 1.06μm. Plasma X-ray emission from Cu (L-shell emission at hν≈1.2keV) and Fe (L-shell emission at hν≈0.9keV) massive slab targets has been observed using the exact same detectors that were used in the KrF target experiments. In this way the results from this experiment should be directly comparable with the results of the KrF experiment described in Section C4.2.

Fig C4.7(a) shows the temporal shape of the 1.06μm laser pulse on target as measured using an optical photodiode and Fig C4.7(b) shows a typical soft X-ray pulse from a Cu plasma. The X-ray pulse is recorded using a fast vacuum X-ray detector with an Al photocathode filtered by 12.5μm Be. It is immediately obvious that no premature termination of X-ray emission is occurring. Fig C4.7(c) shows another pair of laser and X-ray pulses this time recorded on the same oscilloscope trace on the same shot. The shape of the laser pulse here is different from Fig C4.7(a) but

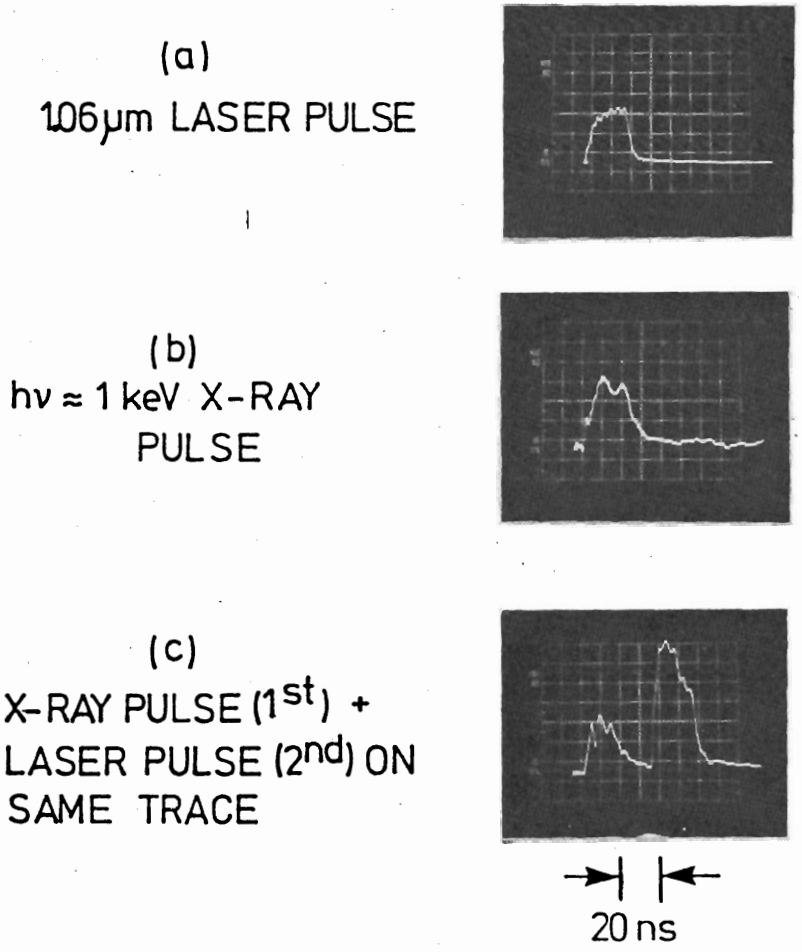


Fig C4.7 Typical 1.06μm laser pulses on target and 1 keV plasma X-ray pulses from Cu plasmas. Time-scales are all 10 ns/div. Optical and X-ray detectors have sub-nanosecond response times.

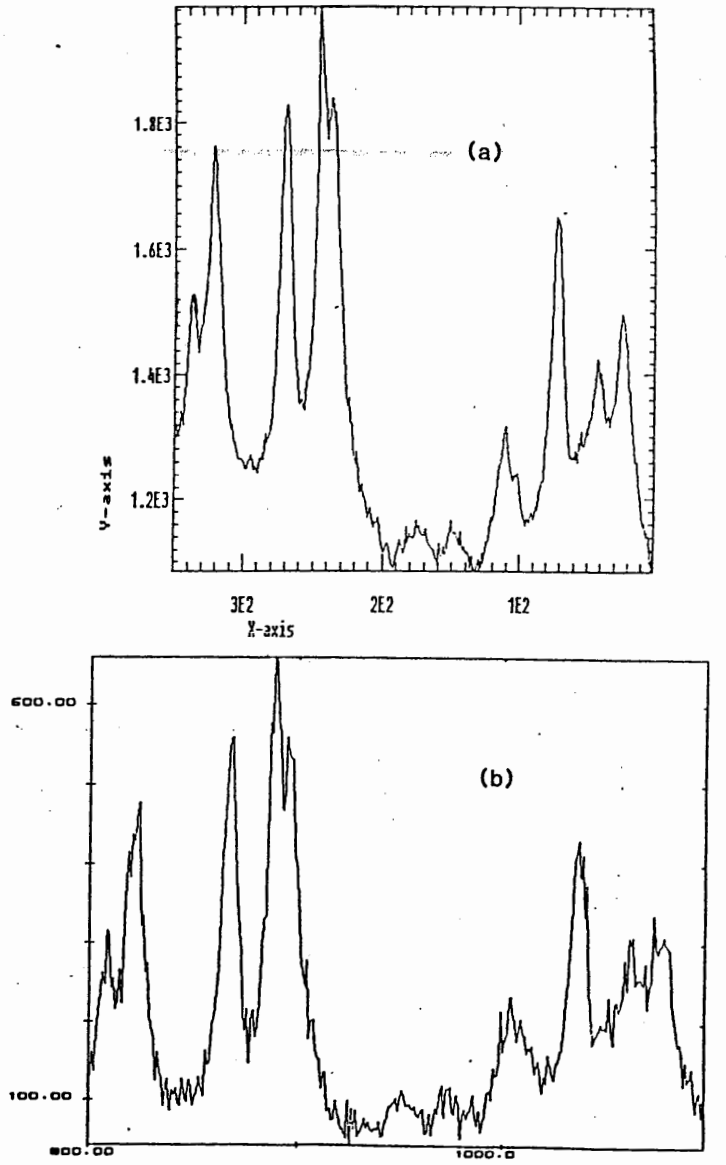


Figure C4.8 Raman spectra of n-hexane recorded in the range 800-1100cm⁻¹, λex = 514.5nm (a) using CCD/JY single spectrograph for 10 secs with 25mW and (b) using PMT/Spex double spectrograph for 150 secs with 50mW.

again the time history of the X-ray pulse approximately follows the laser but it appears that the small level of modulation of the optical signal is enhanced in the X-ray output. When these results are compared with the data presented in section C4.2 it is clear that there is a fundamental difference in the way in which long pulse IR and UV lasers interact with the laser produced plasma to generate ≈1 keV X-rays. More experiments will be needed to fully understand these temporal effects.

X-ray emission from Cu and Fe plasmas has also been observed using a Si p-i-n detector filtered by 6.4μm Be to give a quantitative measure of X-ray energy conversion efficiency. Two data points have been carefully analysed, one for each target material, and these are displayed in Fig C4.4 along with the long pulse KrF data for a Cu target. The data point for the Cu plasma emission (L-shell, hν≈1.2keV) shows that at $I \approx 4.1 \times 10^{13} W/cm^2$ (5.8J on target) the time integrated energy conversion efficiency is approximately the same for the 20ns, 1.06μm laser pulse and the 30ns, 249nm laser pulse. This implies that the power conversion efficiency is considerably higher for the 249nm KrF because with this laser it has been observed that most of the X-rays are emitted in a short 5ns burst at the beginning of the laser pulse. This confirms reports by previous authors[3-5] that short wavelength lasers can give higher levels of plasma X-ray emission than long wavelength lasers. To obtain full benefit of this effect using excimer lasers however it will be necessary to obtain pulse shortening to $\lesssim$ 5ns or perhaps mode-locked pulse trains will have to be used as discussed in section C4.1 above. One conversion efficiency point for the Fe plasma emission (L-shell, hν≈0.9keV) is also plotted in Fig C4.4 showing an efficiency of 3.3% at $I \approx 2.6 \times 10^{13} W/cm^2$ (3.8J on target). Thus Fe (or steel) is a better target for producing ≈1keV X-rays than Cu at least with a 1.06μm Nd laser.

References

(1) K M Glibert et al J Appl Phys 51, 1449 (1980).

(2) F Bijkerk (private communication).

(3) B Yaakobi et al Opt Commun 38, 196 (1981).

(4) R Kodama et al J Appl Phys 59, 3050 (1986).

(5) M Chaker et al Proc SPIE 733, 58 (1987).

(6) I C E Turcu et al Proc SPIE 831, 211 (1988).

C4.4 DEVELOPMENT OF A CCD DETECTOR/SPECTROGRAPH SYSTEM FOR PICOSECOND TIME-RESOLVED RESONANCE RAMAN (TR3) SPECTROSCOPY

S E J Bell, S Umapathy, J Austin and R E Hester (Dept of Chemistry, University of York)

Introduction

This report describes the development and characterisation at York University of a CCD and a single stage spectrograph for use as a low light level detection system. This set-up will be used in conjunction with the Laser Support Facility picosecond (ps) laser source and the copper vapour pumped dye laser amplifier described in Section C4.5 to perform ps TR3 experiments on a number of chemical and biochemical systems. Since the peak power levels of the ps laser pulses must be low, in order to avoid non-linear effects a low light level detection system such as a CCD and a high throughput single stage spectrograph are necessary.

Experimental Details

The CCD camera, acquired from Wright Instruments, contains a EEVP8603 chip mounted in a liquid nitrogen cooled cryostat. The chip has 385 x 576 pixels, each 22 x 22 μm giving a total imaging area of 8.5 x 12.7 mm. The CCD surface is coated with fluorescent

dyes to extend its sensitivity into the near UV. Such systems typically show quantum efficiencies >20% in the range from 800 to 300 nm.

Light absorption by the CCD chip substrate creates electron/hole pairs, the electrons and holes being stored and repelled respectively. The charge in each pixel is sequentially transferred to an amplifier so that a two-dimensional image of the light intensity at the focal plane of the spectrometer may be obtained. Alternatively, pixels may be "binned" into "superpixels", where the total charge in a group of pixels is summed before it is read from the detector. In practice, the CCD is used for Raman spectroscopy as a pseudo one-dimensional detector, adding the charge in each of the 385 separate columns before readout. This procedure minimises readout noise and gives a plot of light intensity against column number (385 channels) similar to that obtainable from other multichannel detectors. It would be desirable to disperse the spectrum across the longer dimension of the CCD (to give 576 channels), and bin along the shorter axis (385 pixels). This is prevented by the chip architecture, which does not allow full on-chip binning along the shorter axis. A comparison of the 385 channel display of the CCD with the 700 intensified channels of typical diode array detectors would suggest that under conditions of equal spectrograph resolution the CCD would cover a smaller spectral range. However, in a diode array "cross-talk" within the intensifier stage limits the resolution such that infinitely narrow spectral lines are 2-3 pixels FWHM. In the case of an unintensified CCD no such "cross talk" exists (FWHM measured as 1-2 pixels) and therefore the number of independent picture elements is near equivalent for the two systems.

The main advantage of the CCD for low light level detection is its inherent low level of thermally generated charge (dark noise), achieved by cooling the CCD to 140K. Because of this (unlike diode arrays) an intensifier is not necessary and the Raman scattering is read against essentially a zero background level. Dark noise in diode arrays is significant even when they are cooled to their minimum temperature (240K) and thus, at low light levels, the total accumulation times are limited by detector saturation due to thermal rather than photon events. In CCD's the major source of detector noise arises from the signal read out. This noise varies from chip to chip and in our CCD is approximately 10 e^-RMS. At low light levels the noise within the CCD remains at 10 e^-RMS, while statistical noise on the diode array increases as the square root of the total accumulation time. Hence, the use of a CCD gives a considerable improvement over a diode array. At high light levels (100's of photons per second), where signal accumulation times are short, the performances of the CCD and diode arrays are comparable. The only disadvantage of a CCD in comparison with a diode array is that it cannot be gated. This is irrelevant for our TR3 experiments due to the ultrafast time-scales involved, for which no electronic gating is feasible. We have compared the CCD mounted on a JY HR640 single spectrograph with a photomultiplier (PMT) coupled Spex double monochromator. The Fellgett (multiplex) advantage of the CCD would, of course, be expected to give better spectra than the scanning system even if each pixel within the CCD was inferior to that of the PMT. Figure C4.8 shows that the spectrum recorded using the CCD/single spectrograph has a better S/N ration than that of the PMT/double spectrograph system in spite of the necessary compensation made for the inherent superiority of the CCD based set-up. It is important to note that the multiplex advantage has been compensated for by reducing the accumulation time for the CCD by a factor of 15 (≈ square root of the number of pixels 385) and the throughput advantage of the single spectrograph has been compensated by reducing the power of the exciting laser by half.

The use of a single spectrograph requires considerable care, in both sample positioning and laser alignment in order to avoid stray and Rayleigh light scattering from entering the spectrometer. Figure C4.9 shows a spectrum of carbon tetrachloride from 800 down to 300 cm^{-1}. Additional use of narrow bandpass or cut-off filters should allow us to approach lower wavenumbers, if required. The

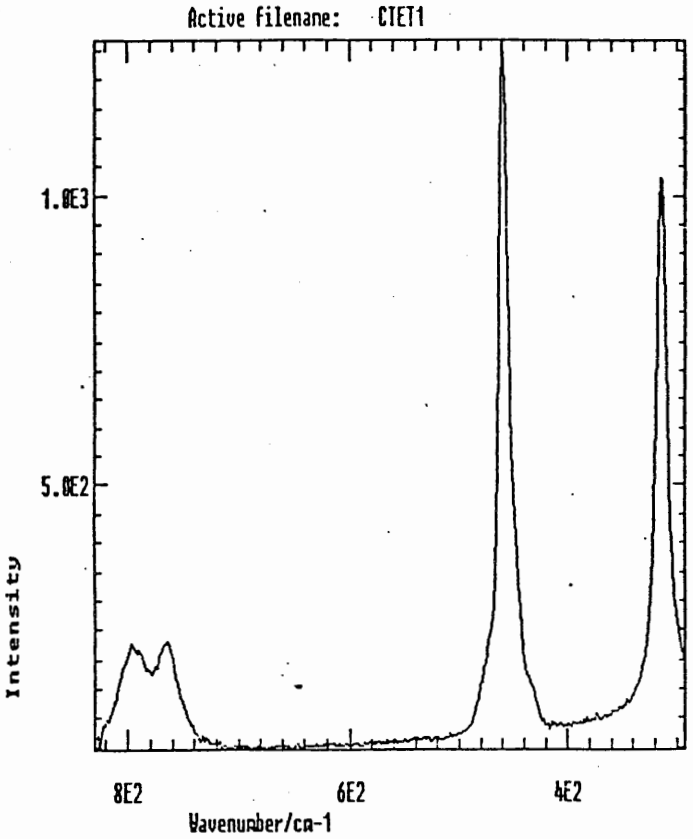


Figure C4.9 *Raman spectrum of carbon tetrachloride in the range 300-850cm⁻1 (λex = 406.7nm, 10 secs and 20mW).*

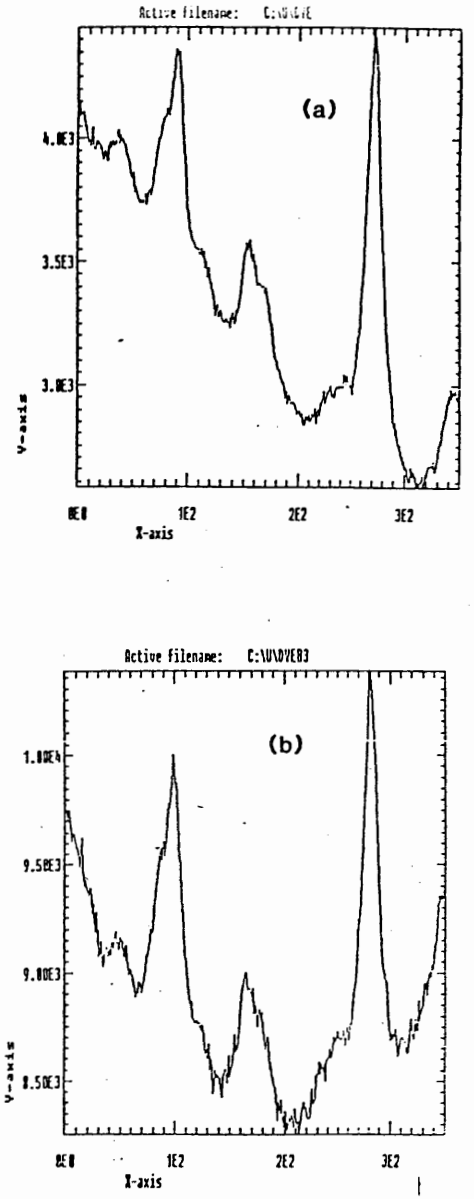


Figure C4.10 *Resonance Raman spectrum of red 2G dye solution, recorded (λex = 514.5nm, 10 secs and 25mW), (a) using 90° configuration and (b) using 180° configuration.*

spectra shown in Figures C4.8 and C4.9 were obtained with 90° sample illumination. To provide versatility in sample illumination, a 180° geometry has also been developed and tested. The back scattering arrangement (180°) is ideal for highly coloured samples. Figure C4.10 shows the spectra of a red dye obtained using both the 90° (Figure C4.10a) and 180° (Figure C4.10b) configurations. Based on the performance of this interim system a new sample compartment has been designed which allows easy switching between the two geometries. This is currently under construction.

The entire system has been designed to combine good light collection efficiency with easy sample handling and alignment. In particular, a set of procedures has been developed which uses a He-Ne laser mounted at one exit port of the spectrometer to define the optical axis of the light collection system. In addition,the detector may be used in image mode with the spectrometer set in zero order to ensure that the scattered light is focused and centred on the entrance slit of the spectrometer.

Summary

We believe the system described above is the best possible Raman set-up for ps TR3 experiments. The only serious drawback has been the limited software available with the Wright Instruments CCD camera for Raman data processing. However, improved software is expected from the manufacturers within the next few weeks.

C4.5 PICOSECOND PULSE DYE AMPLIFIER PUMPED BY A 6.7 KHz COPPER LASER

I C E Turcu, J Diggins, M Hannah, F O'Neill, I N Ross (RAL),
S Bell, R E Hester, S Umapathy (York Univ),
J M Barr (Southampton Univ)

A picosecond amplifier system has been built, to generate picosecond (3 - 10 ps) pulses with > 1 MW peak power at a repetition rate of 6.653 KHz. The pulse energy > 10 μJ will be sufficient to allow frequency doubling and the tunability around 610 nm makes it a useful tool for Raman Spectroscopy. Such a system was previously demonstrated[1] elsewhere.

A 3-10 ps pulse is generated by the Second Picosecond Dye Laser (LSF, LAB E) pumped by half of the 532nm output of the mode-locked YAG Laser[2]. A Cavity Dumper (CD) (Fig C4.11) switches pulses from the sync-pumped dye laser, yielding 5-10 nJ/pulse at a repetition rate of 6.653 KHz. This beam is injected into a Bethune Cell Dye Amplifier which is pumped by an Oxford Lasers, 40W Copper Laser (CVL). The CVL run in planar cavity configuration yields up to 6 mJ/pulse at a repetition rate of 6.653 KHz with peak power up to 135 KW. The beam is focused from 40 mm diameter to 8mm diameter by an f = 1.5 m lens. Both wavelengths emitted by the CVL (511 nm and 578 nm) are absorbed by the dye which is a 41:59 mixture by mass of Rh 6G (for green absorption) and Rh 640 (for yellow absorption). A 100 mg/ℓ (OD = 0.5 in 1 mm, at both λ = 511 and 578 nm) solution in ethanol was used as a result of optimisation of amplifier gain as a function of amplification wavelength and dye concentration. The 5 pass gain was strongly peaked at 615 nm.

We measured time dependence of the single pass gain in the Bethune cell amplifier, by running the cavity dumper at 41 KHz unsynchronised with the CVL and triggering the oscilloscope off the CVL pulses. Fig C4.12 shows the amplified injected pulses (lower trace) with a maximum net gain of 8 (transmission of the amplifier was ∿ 50%). The gain was strongly peaked on the peak of the CVL pump pulse. The maximum gain lasts for around 10ns. This sets a limit on the distance between the furthest turning mirrors in the 5 pass amplifier system (Fig C4.11). At present this distance is 64cm and the delay between the first and last passage of the injected pulse through the cell is 7.8 ns.

Both the cavity dumper and the CVL were externally triggered at a repetition rate of 6.653 KHz derived from and in synchronism with

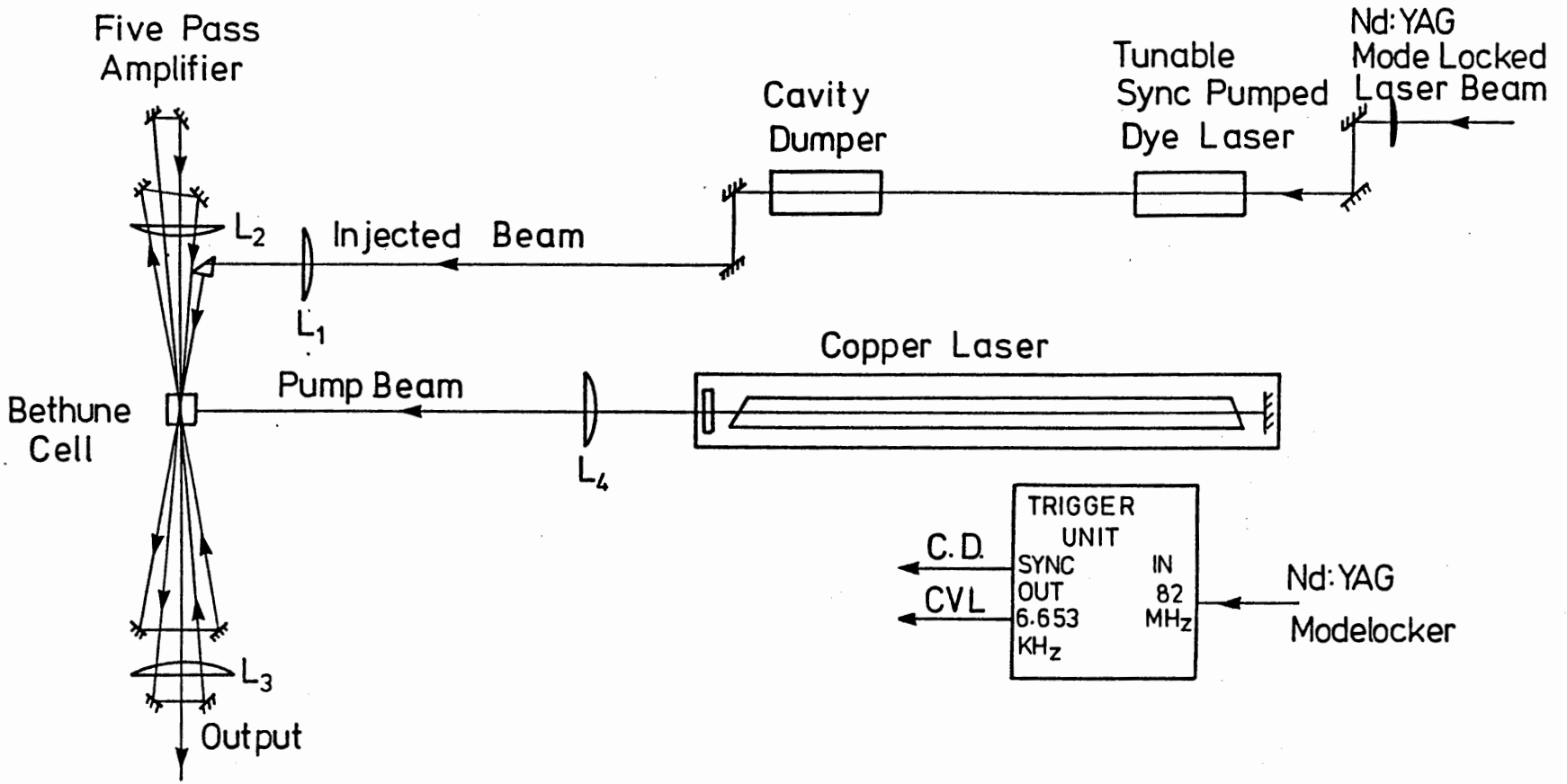


Fig C4.11 Picosecond Pulse Dye Amplifier System pumped by a 6.7 KHz Copper Laser.

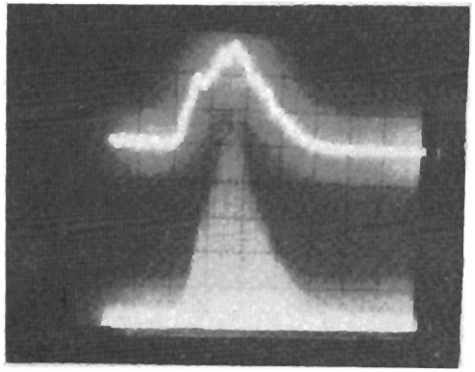


Fig C4.12 *Single pass gain time dependence (lower trace) versus CVL pulse (upper trace) for the Bethune cell dye amplifier. Time scale 20 ns/div.*

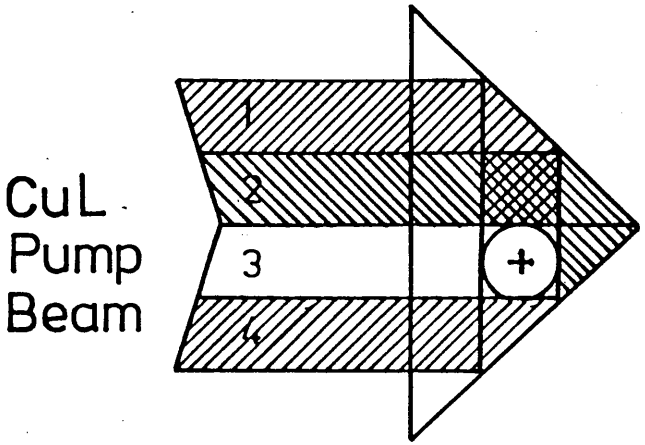


Fig C4.13 *End view of the "Bethune" dye cell prism. Copper laser pump light (ϕ = 8 mm) enters from left and due to total internal reflections in corner, equal segments (1 - 4) pump the top, back, front and bottom of the dye solution flowing through the ϕ = 2 mm cylindrical hole.*

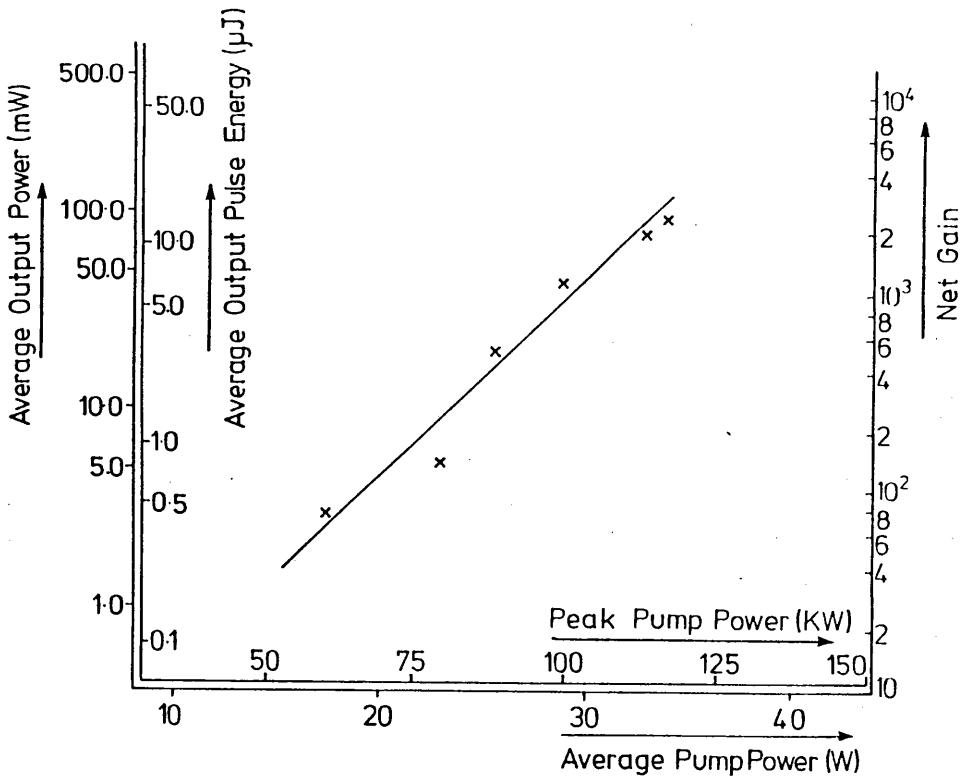


Fig C4.14 *Five pass amplifier net gain dependence on CVL pump power. No AR coating on 5 pass optics. System operated at 6.653 KHZ repetition rate. Injected beam power 38 μW (5.7 nJ/pulse) and wavelength 615 nm.*

the 82 MHz (÷ 2 ÷ 2 ÷ 3 ÷ 1024) signal of the YAG modelocker. Appropriate delays were provided for the two channels by a Digital Delay Pulse Generator (Model DG 535 - Stanford Research). The internal delays of both CVL and CD were around 250 ns.

The Bethune cell[3] used consists of a BK7 glass right angle triangle prism (10 mm long with a 10 mm hypothenuse) with a ϕ = 2 mm cylindrical hole through which the dye flows (Fig C4.13). By virtue of its geometry the pumping of the dye is uniform, hence multipass amplification of the injected pulse can be easily sustained. A number of problems had to be addressed:

i) in order to pass through the dye hole at different angles the injection beam had to be focused to diameters of 1 - 1.5 mm by lenses ($f_1 = f_3 = 500$ mm, $f_2 = 700$ mm);

ii) if the diameters of the beams are kept large ($\phi \sim 2$ mm) then the length of the multipass system increases and the time delay between the first and fifth passes will exceed the optimum 10 ns;

iii) the small size of the prism means that because of mechanical constraints on the mount and dye flow system the overall path travelled by the injection beam in dye is $\sim$ 30 mm/pass, ie the unpumped dye length is $\approx$ 20 mm/pass. This was reduced to 10 mm/pass by using re-entrant windows resulting in a 2 fold increase of the 5 pass net gain (due to increased transmission/pass of the dye cell).

The 5 pass net gain obtained so far, with re-entrant windows but without AR coated optics is 2.4 x 10^3 for 34 W (6.653 KHz) pump power on dye cell (Fig C4.14). With the CD injecting only 5.7 nJ/pulse this resulted in average output powers of 93 mW (at 6.653 KHz) or 14 µJ/pulse. The 5 pass net gain was measured to increase exponentially with the pump power (Fig C4.14). No saturation is observed up to average pump powers of 34 W (117 KW peak) on the amplifier. This implies that by AR coating the CVL focusing lens L_4 (Fig C4.11), the extra $\sim$ 4 W gained could increase the net gain considerably. The peak power for 40 W average power can be increased by decreasing the repetition rate at which the system works from 6.653 KHz (peak power 137 KW) to 5.339 KHz (peak power 171 KW). By AR coating the 5 pass system lenses L_1, L_2, L_3 and the outer surface of the insertion windows of the Bethune Cell a further increase in net gain could be obtained.

No saturation was observed in increasing the cavity dumper output from 3.3 nJ/pulse to 9.6 nJ/pulse, hence an increase to 20 nJ/pulse (as should be available from the dye laser) will also yield a higher amplified output. The calculated saturation energy for the present dye amplifier is 50 µJ/pulse (330 mW average power).

References

1. D B McDonald and C D Jonah, Rev Sci Instrum, 55, 1166 (1984).

2. J R M Barr, I M Ross, Li Ming Zang, CLF Annual Report C3.4 (1987).

3. D S Bethune, Appl Optics 20, 1897 (1981).

C4.6 EXCIMER LASER FABRICATION AND PATTERNING OF HIGH T_c SUPERCONDUCTING THIN FILMS

N Savva, K F Williams, G M Davis and M C Gower (RAL)

The ability to be able to rapidly pattern thin films of high temperature superconducting materials with high resolution is of paramount importance if these materials are to be used as interconnects in microelectronic circuits or to fabricate devices

such as Josephson junctions and SQUID's. Preferably such a patterning technique should involve a dry etching procedure that can rapidly reproduce patterned devices. A promising candidate for such a patterning procedure would be to use laser ablation of the film to remove the required regions. High resolution large field size imaging exposure of circuit mask patters could them possibly ablatively etch patterns cleanly into the film. Because of the large absorption coefficient in the ultra-violet spectral region of high T_c superconducting copper oxide materials such as $YBa_2Cu_3O_{7-x}$ (YBCO) and since the resolution of any optical imaging system depends directly on the wavelength of the illumination source, the laser of choice for high resolution ablative patterning would most likely be a pulsed excimer laser. Since the etch rate of the film per laser pulse can be very small (<0.1μm), such pulsed laser etching could possibly be used to etch multi-layer structures to the required depth in a controlled fashion. In this paper we report the ablative etch rates and quality of etch of YBCO thin films as a function of the incident laser fluence and number of pulses for each of the five excimer laser transitions ArF, KrCl, KrF, XeCl and XeF whose wavelengths are in the region 193 to 353nm.

Bulk Material Preparation

Thin films of YBCO were deposited onto a variety of substrates using excimer laser ablative sputtering of the bulk material. The bulk high T_c superconducting material was prepared by mixing, grinding and sintering techniques.

Firing of the ingredients was carried out by placing them onto an alumcna boat inside a fused silica tube furnace which could be heated to 1100°C and through which flowing oxygen was passed. The temperature of the furnace was programmed using an IBM PC to cycle at controlled heating and cooling rates. After trying many different 'shake and bake' procedures the following recipe was found to be the most successful in producing good superconducting material:

(a) Mix 1.13 gm Y_2O_3
3.95 gm $BaCO_3$
2.39 gm CuO

(b) Grind into fine powder using agate mortar and pestle. The use of an alumina mortar and pestle at this stage may introduce impurities into the superconductor which accumulate in grain boundaries.

(c) Bake in flowing dry oxygen at 950°C for 12 hours.

(d) Cool slowly at 100°C/hour.

(e) Regrind in mortar and pestle.

(f) Press into pellets using pressure of $\sim 10^4 kg/cm^2$.

(g) Rebake in flowing oxygen at 950°C for 12 hours.

(h) Cool slowly at $\lesssim$-100°C/hour.

The mixture should be a weakly fused black mass with the appearance of burnt toast. Any sign of green indicates a nonsuperconducting phase. The pellet can be tested for diamagnetism using the Meissner effect, i.e. the repulsion of magnetic flux lines due to the superconductor 'seeing' its mirror image of a like pole. This test can simply be carried out by observing the levitation of a small magnet above the superconductor as liquid N_2 is allowed to boil away from the base of the superconductor. For the photograph in Figure C4.15 the pellet was placed in a styrofoam coffee cup and the bottom covered with liquid N_2. Resistivity, AC susceptibility and critical current as a function of temperature of the bulk sample can be used to measure the superconducting characteristics

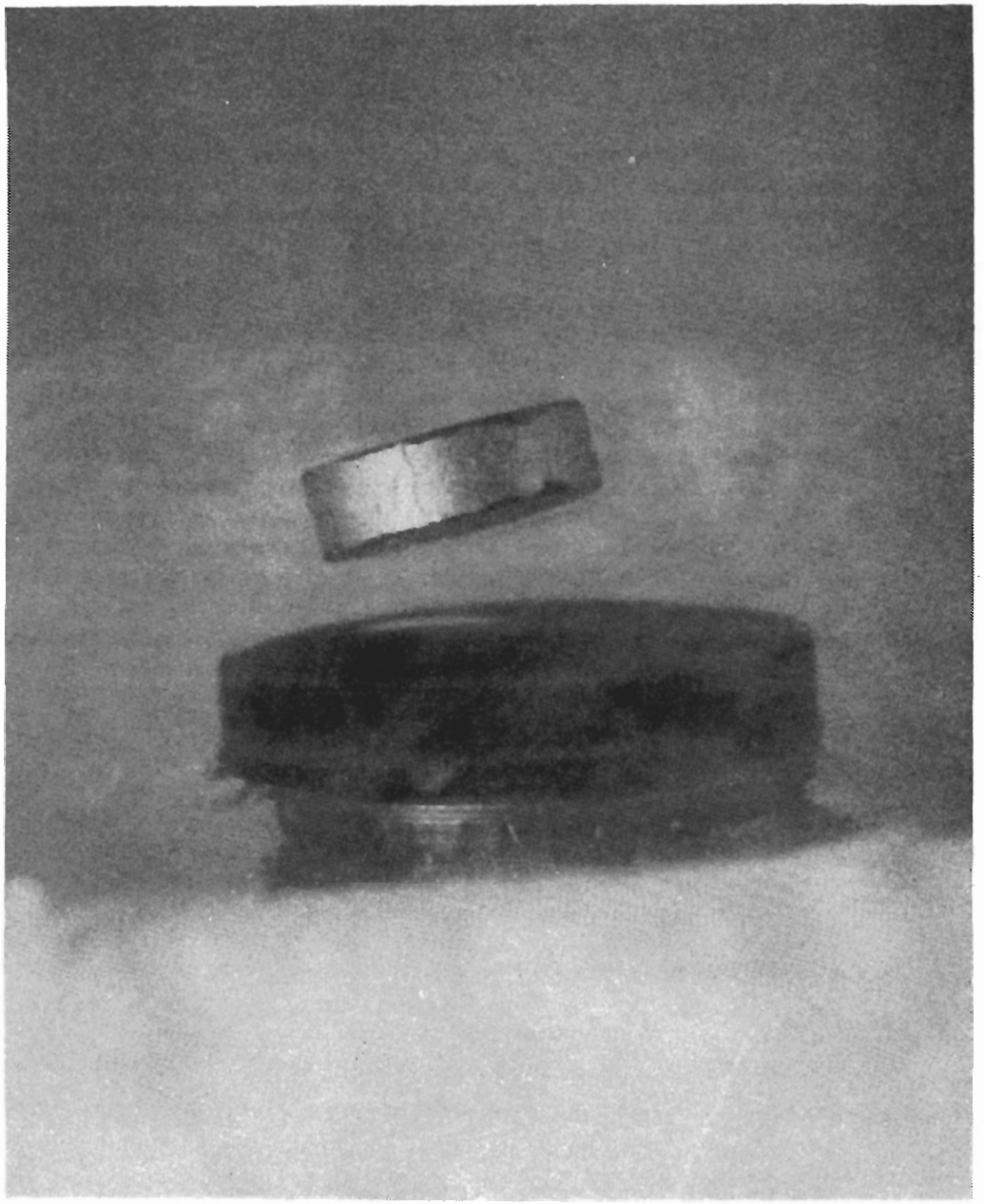


Fig C4.15

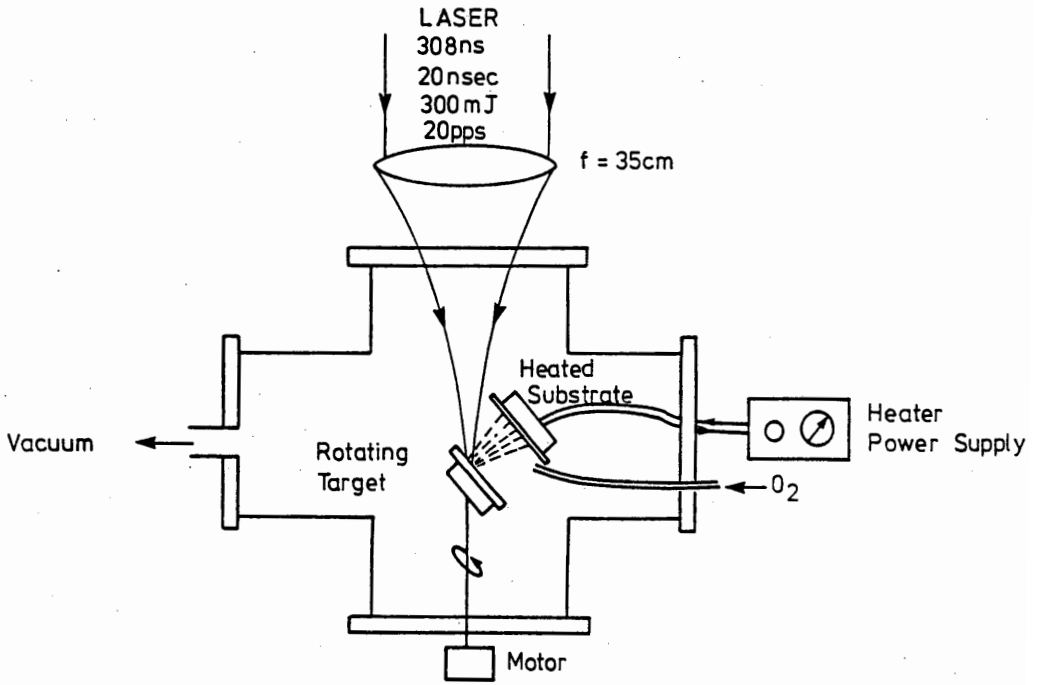


Fig C4.16

of the material produced. In the work reported here only the Meissner effect as a function the distance above the surface of liquid N_2 (i.e. of temperature) was used to assess the superconducting nature of the bulk material produced. Samples obtained from other sources (the Universities of Birmingham and Warwick and GEC) were also used and tested.

Film Fabrication

The setup sketched in Figure C4.16 was used to fabricate films by laser evaporation/sputtering of the bulk YBCO target material. A Lambda Physik EMG201MSC XeCl 308nm excimer laser which produced 300mJ of energy in a 20nsec duration pulse was focussed with a 35cm focal length lens onto the target pellet which was held by a rotateable holder inside a glass vacuum chamber. The base pressure inside the chamber achieved by the cryogenically trapped oil diffusion pump was $\sim 5 \times 10^{-4}$ mbar. The pellet was at an angle of 45° to the laser beam and the laser fluence at the pellet was $\sim 5 J/cm^2$. With the laser operating at 20 pulses per second the rotating target allowed spatial averaging effects to take place over any inhomogeneities which may be present in the constituent stoichometry, ablative efficiency, etc on the surface of the YBCO bulk material. Substrates were mounted parallel to the pellet at a distance of ~9cm. A quartz-halogen lamp situated inside a tubular copper substrate holder was used to heat the substrate to a temperature of ~500°C during film deposition.

During deposition the pellet was rotated at ~ 7 rpm, and oxygen gas was gently flowed across the substrate so that the chamber rose to a base pressure of 4×10^{-3}mbar. For a typical deposition duration of ~1hr, film thicknesses of 1-1.4μm were obtained. Various substrates including fused silica, glass, LiF, and MgO were investigated. For the majority of data described here (100) orientated polished MgO substrates were used. This material is known to be one of the least reactive of the above mentioned materials and its lattice parameter and thermal expansivity are well matched to the YBCO film. After deposition the film-coated substrates were allowed to cool at their natural cooling rate to room temperature in flowing oxygen.

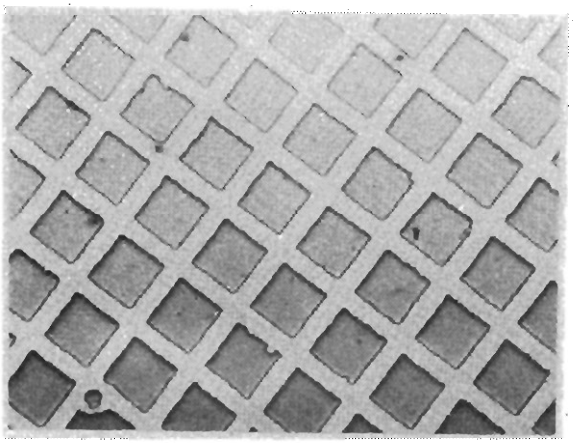
Film composition and quality were analysed by optical and electron microscopes, reflective Cu Kα X-ray diffraction (Siemens D500 powder diffractometer) and texture (GEC) cameras. A spectrophotometer (Shimadzu UV-160) was used to measure the transmission of the YBCO films on both fused silica and MgO substrates as a function of wavelength.

Figure C4.17 shows a 1.8μm thick YBCO film produced by depositing through a 86μm square hole 30μm line copper grid mesh placed in contact with the unheated glass substrate. While the glass substrate assured that this film was composed of amorphous material the smooth cosmetic nature of the film is immediately apparent. To obtain polycrystalline films of YBCO, single crystal MgO substrates were used at a temperature of 500°C during deposition. The 4.2 Å lattice parameter of this material is fairly closely matched to the ~3.8Å a,b lattice parameters of YBCO. After deposition, films were post annealed at 900°C for 1 hour in flowing oxygen followed by slow cooling. The diffraction pattern obtained using the X-ray surface texture camera set-up sketched in Figure C4-18(a) is shown in Figure C4.18(b). Diffraction from the crystalline planes of the YBCO film appears as horizontal lines which are indicative of the polycrystalline nature of the film. Diffraction spots arise from the MgO crystalline substrate.

Using the x-ray powder diffractometer set-up shown in Figure C4.19(a), the diffraction peak count obtained as a function of scattering angle at a fixed 8° incidence angle is shown for the YBCO film in Fig C4.19(b). Diffraction peaks from the YBCO lattice are marked on this figure. Unidentified impurity diffraction peaks are marked with a cross.

In order to characterise the electrical properties of the superconducting films extreme care must be taken in applying low

(a)



(b)

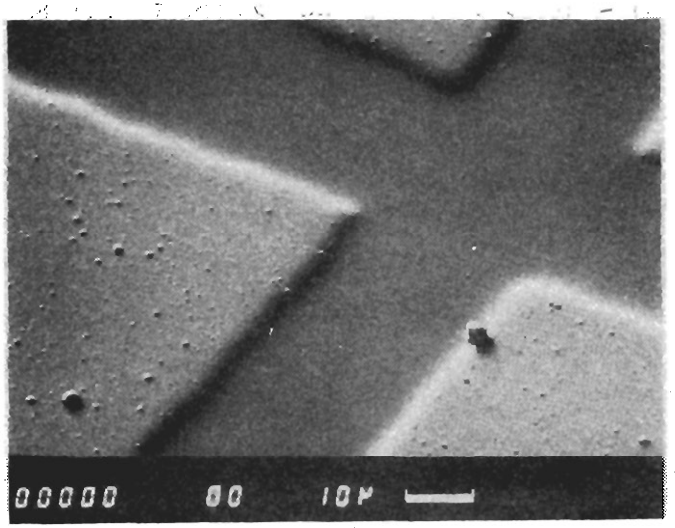
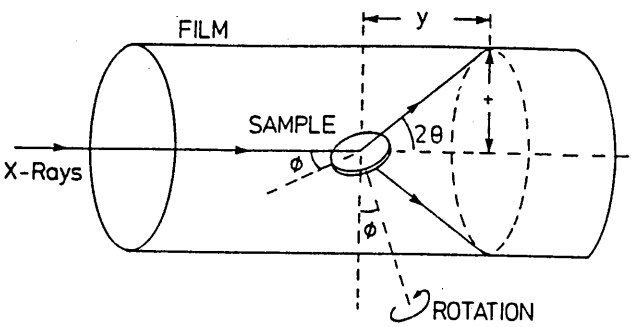


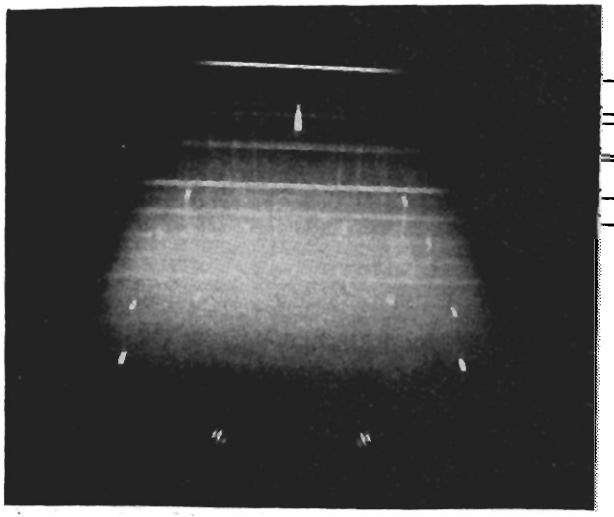
Fig C4.17

X-RAY SURFACE TEXTURE CAMERA



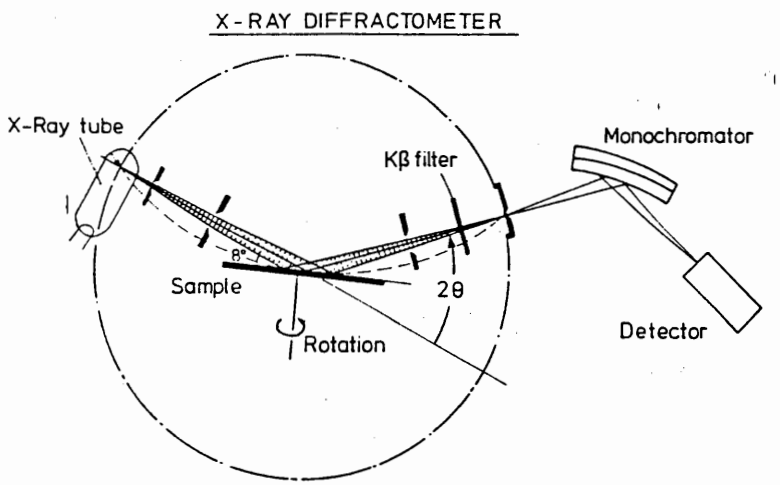
(a)

2θ

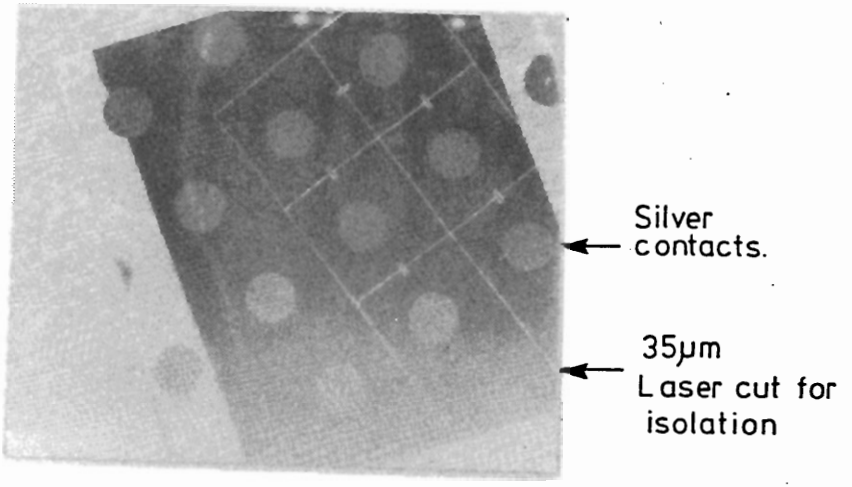


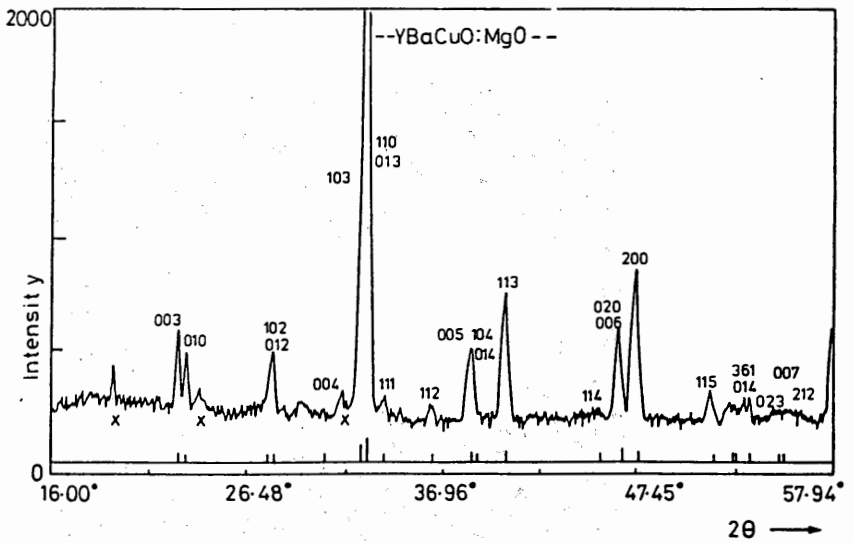
(b)

Fig C4.18



(a)





(b)

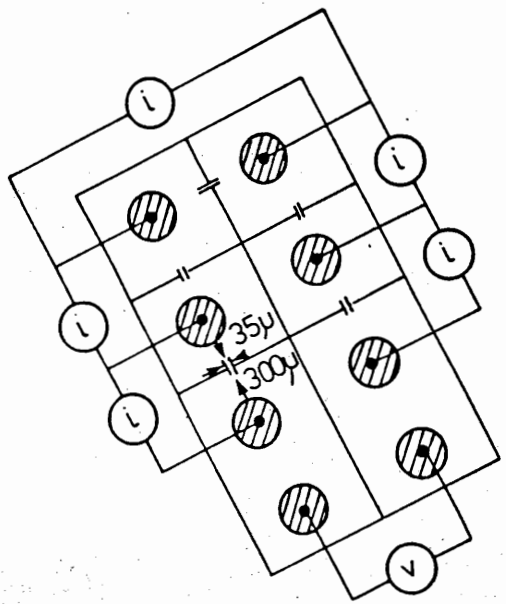


Fig C4.19

Fig C4.20

resistivity contacts and in the scribing of isolation tracks onto the film. The procedure adopted (see Figure C4.20) was to initially vacuum deposit through a contact mesh mask a matrix of ∿ 1mm diameter silver contact pads spaced 2.5mm apart onto the film. Two point probe measurements of resistance at room temperature between pads were then carried out to determine the spatial uniformity of the film over the substrate - the resistance between pads with this separation should be in the range 8-13 Ω for good quality superconducting films. Using a CW 60 mW visible Ar^+ laser focused with a microscope objective to produce a 3 μm diameter spot on the film, 35 μm wide and 300 μm long isolation channels between the contact pads were scribed onto the film by moving the substrate under the focal spot on a computer driven X-Y stage. Silver dag paint was then used to bond wires onto the pads.

The resistivity of the film was obtained by measuring the voltage and current characteristics between contacts. When placed in a variable temperature cryostat a resistivity measurement obtained as a function of temperature of the film is shown in Figure C4.21. These measurements show that the resistivity of this film started to fall at ∿ 80°K, with full superconductivity setting in at temperatures below a critical temperature of ∿40°K. The double peak in the resistivity curve and rather low critical temperature of this film may be due to the presence of impurities or to different structural phases of the deposited film.

Four point probe measurements of currents passed between any given pairs of contacts while simultaneously measuring the voltage between contacts of the circuit shown in Figure C4.20 allowed critical currents (J_c) to be measured in different X-Y directions of the film. Critical current measurements of the film as a function of temperature are shown in Figure C4.22 and as can be see, below T_c are in the range 10-100A/cm².

By placing the film and substrate between the primary and one of the secondary coils of a balanced double secondary transformer wound onto a Tufnel former, the real and imaginary components of the AC susceptibility of the deposited film were measured as a function of temperature. The temperature was varied by slowly raising the transformer and film above the surface of liquid helium contained in a cold finger cryostat. The results obtained are shown in Figure C4.21. The peak in the imaginary component of the susceptibility allows the critical temperature of the superconductor to be accurately measured.

Clearly these results have demonstrated that good polycrystalline uniform ∿1μm thick superconducting films can be fabricated by excimer laser sputtering of bulk superconducting material. The relatively low T_c of the YBCO films produced is expected to produce substantially different laser etching characteristics compared to higher T_c YBCO films. Since a study of the dry excimer laser etching characteristics of YBCO films was the major goal of this work no further work was carried out to increase the T_c of the films produced. More pure bulk laser target materials should produce higher T_c and J_c films. Initial indications at Siemens in W Germany have shown that when using much hotter substrates during deposition than those used here (up to 900°C) highly oxygenated stable unreactive films can be produced. Future work on the use of excimer laser ablative sputtering to fabricate thin superconductive films of copper oxide ceramic materials should concentrate on using high substrate temperatures in a relatively high (few torr) ambient oxygen pressure. A pulsed laser can not only efficiently ablate target material to deposit thin films on substrates placed near the surface plasma, but a UV excimer laser is also capable of photodissociating gaseous species such as oxygen to produce reactive species like atomic oxygen or ozone. If in the vicinity of the substrate, these species can then reactively impregnate the film.

Film Etching

Films were ablatively patterned and etched using an Oxford Lasers KX2, 2 pulses per second excimer laser which could operate on the

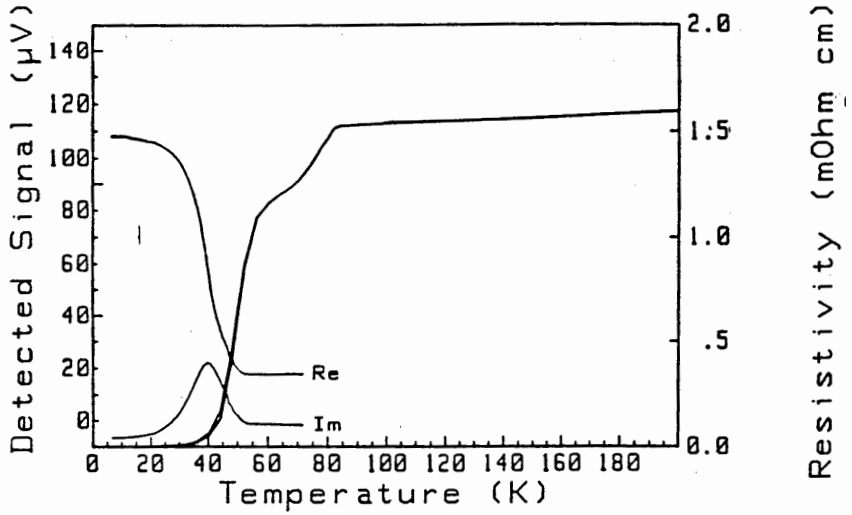


Fig C4.21

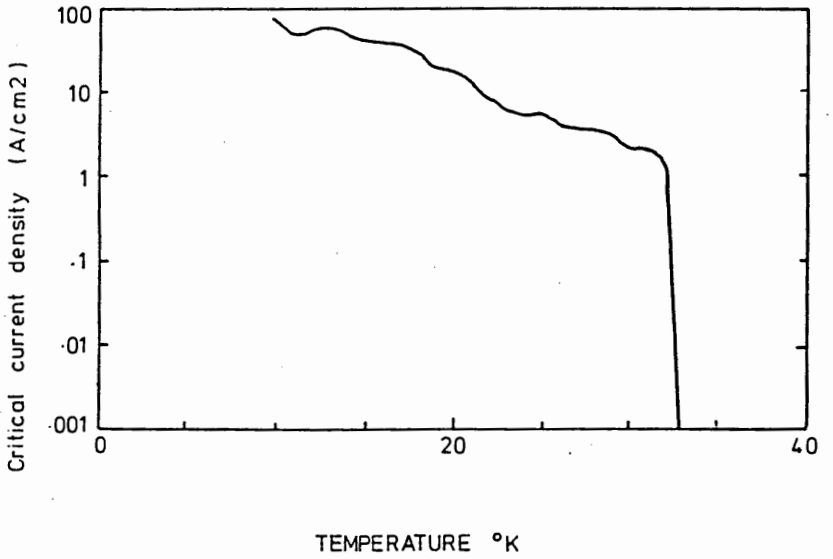


Fig C4.22

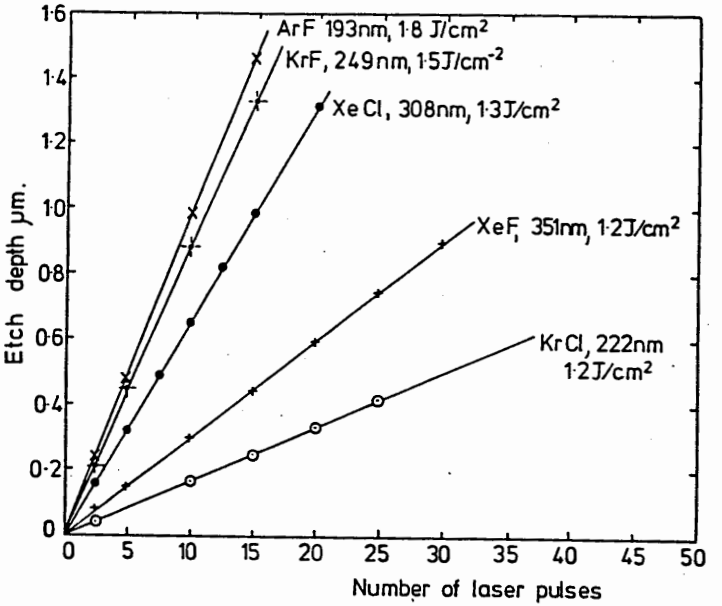


Fig C4.23

five principal rare gas halide transitions between 193 and 353nm (ArF, KrCl, KrF, XeCl and XeF). The laser output was reduced in size by a 35 cm focal length converging lens and made to overfill a 1mm diameter aperture drilled into a steel sheet against which the film and substrate were placed. The uniformity of the transmitted beam through the aperture was checked using burn patterns on Polaroid film. The transmitted energy through the aperture was measured with a cross-calibrated GenTec ED200 joulemeter. Apart from changing the fill gases in the laser, the system remained unchanged during measurement for different laser ablative wavelengths. Laser energy fluences incident upon the film were varied by changing the position of the aperture and film relative to the focal position of the focusing lens. All etching was performed in air. Measurements of ablatively etched hole depths in the film were made by gold coating the films subsequent to etching and using an interference microscope to count the number of fringe changes from the top of the film to the bottom of the etched region.

In Figure C4.23 we show measurements of the variation of the etch depth versus the number of exposure pulses for each of the excimer laser wavelengths. When using a fixed irradiation fluence of 500mJ/cm², in Figure C4.24 we show the etched depth per pulse of a thin YBCO film on a MgO substrate as a function of the ablative laser wavelength. For comparison, this graph also shows the measured absorption curve of a similar composition but thinner film before and after the post annealing process. Although the annealing process itself makes the film more absorbing in the ultraviolet, the measured etch depth per pulse does not follow the overall shape of the absorption curve of the film. In particular the etch rate showed a pronounced minimum at a wavelength of 222nm. This suggests that processes other than purely thermal ones are at least partially responsible for the ablative removal of material from the film.

For each excimer wavelength, comparison of the etch rate was also made as a function of the incident laser fluence. Typical etching data with these variable parameters are shown in Figure C4.25 when using a fused silica substrate. It is seen from these data that at each wavelength the etch rate of the film eventually saturates as the highest laser fluences studied are approached. Also, the threshold fluence for etching is highest for the shorter wavelengths and for 193nm is ∿200mJ/cm².

Contact printing of the etched pattern of a high resolution chrome-on-quartz test mask pattern is shown in the optical micrographs on Figure C4.26. This well defined pattern which covered an area of ∿ 1cm² was etched using a XeCl laser fluence of ∿ 200mJ/cm².

As shown in the scanning electron micrographs in Figure C4.27 features on the micron scale can be resolved. The fringes which arise from Fresnel diffraction of light at the edge of the mask are clearly etched into the film. It appears from these photographs that the etch quality is similar for all wavelengths and that the etching process itself produces considerable smoothening of the exposed film surface. While we have yet to measure if the remaining underlying material remains superconducting, if it does then it may be possible to use the laser itself to postanneal and oxygenate the film. From this work, it appears that on the surrounding unexposed regions there is only a small amount of redeposited debris from the etching process. This debris could possibly be reduced by performing etching in a flowing gaseous environment.

In conclusion, uniform superconducting thin films of $YBa_2Cu_3O_{7-x}$ have been fabricated using excimer laser ablative sputtering of the bulk material onto hot MgO substrates. The non-optimised films produced had a critical temperature and current of 40°K and 10-100 A/cm² respectively. Work in the future to improve these films should be aimed at using a more pure synthesis of the bulk target material as well as using hotter substrates - ideally in the range 900-1000°C - during deposition.

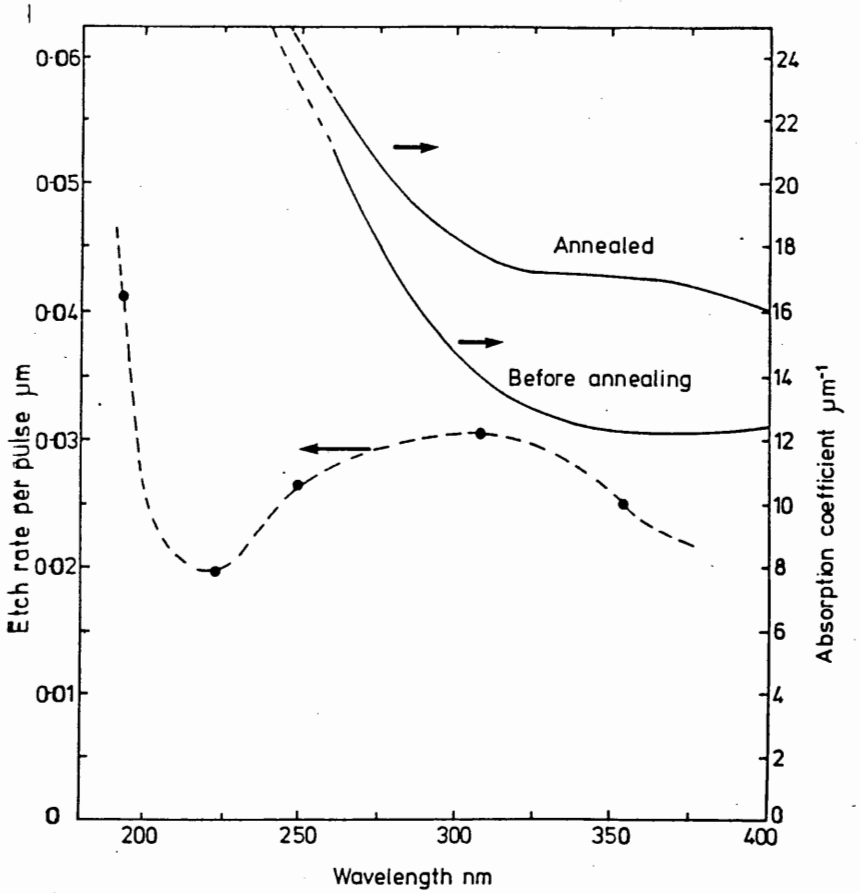


Fig C4.24

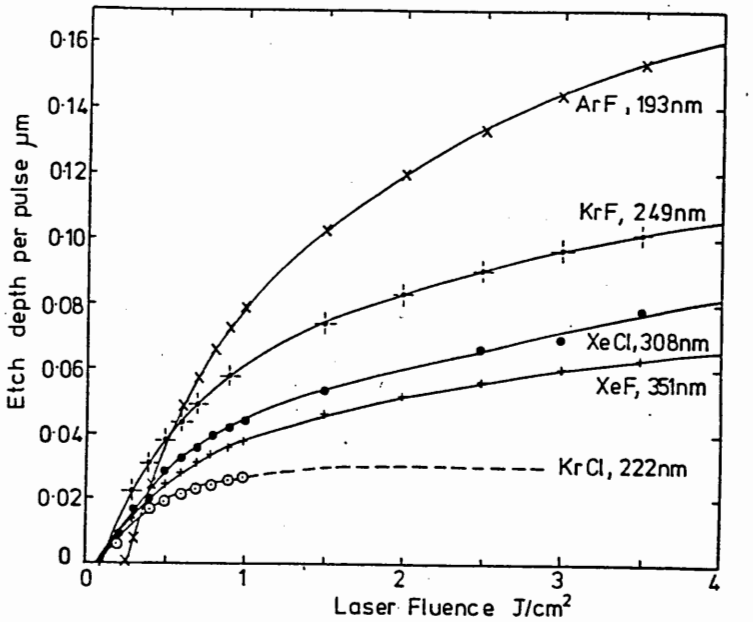


Fig C4.25

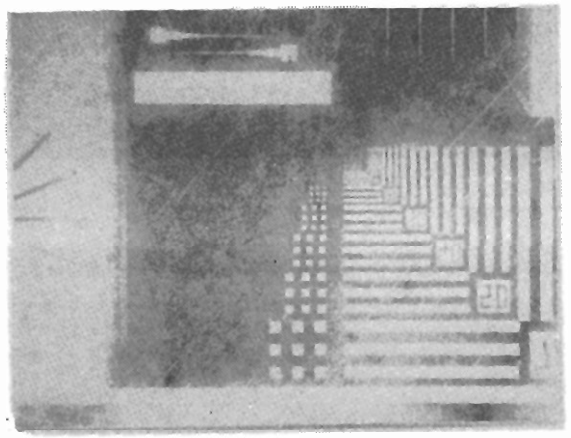


Fig C4.26

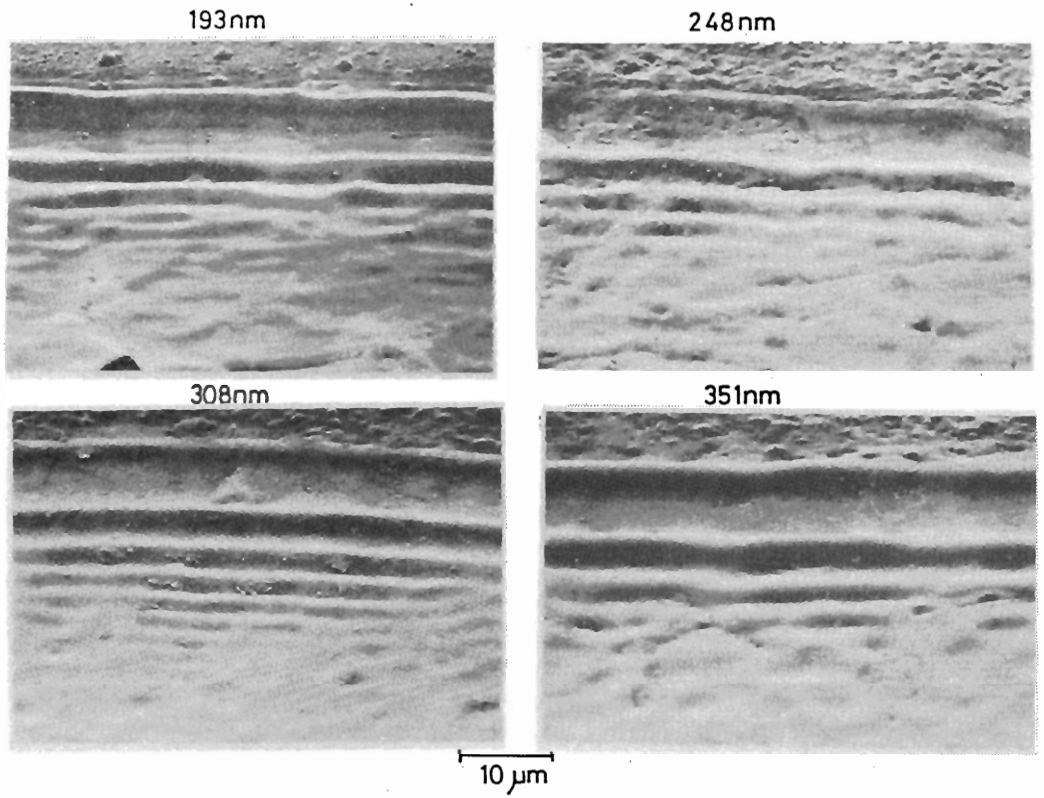


Fig C4.27

Measurements on polycrystalline superconducting films grown by ion beam sputtering have shown the top layer of the film not to be superconducting. The successful synthesis of good uniform quality epitaxially grown superconducting films may alleviate this problem, and must remain the goal of researchers working in the field.

We have shown that pulsed excimer laser etching can have micron scale resolution and may prove to be a viable technology for the dry patterning of thin superconducting ceramic films. This latter property is important since some of the superconducting copper oxide materials are known to be prone to attack by many common chemicals - including water. Thus a straightforward transfer of the well founded wet chemical etching procedures currently used in photolithography may not be appropriate for fabricating thin film superconducting devices of high T_c copper oxide materials.

C4.7 EXPITAXIAL GROWTH OF THIN FILMS OF $BaTiO_3$ USING EXCIMER LASER ABLATION

G M Davis and M C Gower (RAL)

Thin expitaxially grown films of the perovskite $BaTiO_3$ are of interest in the construction of devices such as thin film capacitors and pyroelectric detectors. The room temperature tetragonal phase of this material is ferro, pyro and piezoelectric. In addition, because of its large electro-optic coefficient in the tetragonal phase, epitaxial films of this material are of interest for various non-linear optical investigations and applications.

While a variety of methods have been used to grow thin films of $BaTiO_3$ often the films have either the incorrect composition, are amorphous or polycrystalline or can be of the non-ferroelectric cubic phase. The most successful methods to date for the fabrication of thin $BaTiO_3$ films are flash evaporation of the bulk $BaTiO_3$ material and co-evaporation of the metal oxides. In this section we report the use of excimer laser sputtering of sintered $BaTiO_3$ pellets to grow thin epitaxial layers of $BaTiO_3$ on hot LiF substrates. Such excimer laser ablation techniques are currently being studied as a method of depositing thin films of perovskite-like high temperature superconducting copper oxides such as Y-Ba-CuO and Bi-Sr-Ca-CuO (see previous section) as well as semiconductors such as CdS.

Sintered bulk pellets of $BaTiO_3$ were prepared from the dry powder (Aldrich, gold label with 99.995% purity) which was compressed at a pressure of $\sim 10^4 kg/cm^2$. The pellet was then placed in a fused silica tube furnace and heated to 1000°C at a rate of 400°C/hr. The temperature of the furnace was held at 1000°C for 2 hours. The oven was subsequently cooled at a rate of 200°C/hr to 140°C, at 1°C/hr near the $BaTiO_3$ cubic-tetragonal phase temperature of ~130°C down to 110°C, and finally at the natural cooling rate of the oven. The whole heating and cooling cycle was performed in the presence of a slow flow of O_2.

As for the work described in the previous section (see Fig C4.16) the sintered pellets were held on a motor driven rotateable (~7rpm) target holder inside a glass vacuum chamber which could be pumped with a cryogenically trapped diffusion pump to a base pressure of $3x10^{-4}$mbar. The output from a Lambda-Physik EMG201MSC XeCl excimer laser operating at a wavelength of 308nm was focused onto the pellet using a 35cm focal length lens at an angle of incidence of 45°. Laser fluences incident upon the pellet were varied by using altenuation filters and by changing the distance of the pellet from the focal position of the lens. Substrates such as fused silica, silicon, glass, MgO (100), $SrTiO_3$ (110) and LiF (100) were mounted on a heatable holder and were positioned parallel to the pellet at a variable distance away from it. For optimum film uniformity at a reasonable deposition rate over an area of ~1cm², the distance of the substrate from the focused laser beam on the pellet was fixed at between 6-8cm for the results reported herein. Deposited films were analysed by optical microscopy, reflective Cu Kα X-ray

diffraction (Siemens D500 powder diffractometer) and texture (GEC Model) cameras. Film thickness was measured by gold coating the film and using an interference microscope. For a fixed number of laser pulses, the thickness of the deposited film onto the substrate was found experimentally to be independent of the repetition rate of the laser up to the maximum value studied of 20pps. Furthermore, the thickness of the as-deposited film was found to be linearly dependent on the total number of laser pulses used during deposition and inversely proportional to the square of the distance of the substrate from the target.

In Figure C4.28 we show the $BaTiO_3$ film thickness deposited for a single laser pulse onto a fused silica substrate at room temperature as a function of the focused laser fluence incident upon the target pellet. It can be seen that for incident laser fluences greater than $\sim 2J/cm^2$ the deposition rate saturates at a value of ~ 0.3 Å/pulse. Below a threshold fluence value of $\sim 0.5J/cm^2$ there is negligible film deposition. To test the epitaxial and stoichiometric nature of the deposited films it is necessary to match the lattice spacing of the substrate material with that of tetragonal $BaTiO_3$ (a = b = 3.99Å, c = 4.04Å) and to use X-ray diffraction analysis of the films. Other requirements of the substrate are that it should have good adhesive properties for the deposited film, possess a similar thermal expansivity and be unreactive to it. Results of X-ray diffraction analysis for all of the substrates tested showed that well-ordered epitaxial films were obtained only on (100)-orientated LiF cubic crystalline substrates (lattice parameter 4.03Å) when depositing at substrate temperatures close to the maximum value of 620°C which could be achieved with the substrate heater. In general, $BaTiO_3$ films deposited onto $SrTiO_3$, MgO and Si at ~ 600°C and LiF substrates at temperatures between 300°C and 600°C showed polycrystalline structure with only partial preformed orientation. Deposited films on all of the other substrates studied, as well as on room temperature substrates of those already mentioned, were predominantly amorphous.

In Figure C4.29 we show an optical Nomarski micrograph of a $\sim 0.3\mu m$ thick epitaxially grown film of $BaTiO_3$ deposited onto a cleaved LiF (100) substrate which was held at a temperature of 617°C during deposition. The mosaic block structure is familiar in the epitaxial growth of $BaTiO_3$ films when using other deposition techniques such as flash evaporation. It may be caused by crystal growth from different nucleation sites, domain twinning in the films or, as observed in the epitaxial growth of CaF_2 on InP due to an increased lattice mismatch between the film and the substrate at room temperature compared to the growth temperature that causes the film to be stressed and to craze as the substrate cools to room temperature. The thermal expansion coefficients of polycrytaslline LiF and $BaTiO_3$ are ~ 33 and 6×10^{-6}/°K respectively. We note that when using substrates of bulk crystalline $SrTiO_3$ or $BaTiO_3$ and flash evaporation to deposit thin films of $BaTiO_3$, much higher temperatures of the substrates were required ($\gtrsim 900$°C) to observe epitaxial growth which are above the 848°C melting point of the LiF substrate used here.

The epitaxial nature of the film shown in Figure C4.29 was confirmed by X-diffractometer measurements using the set-up sketched in Figure C4.30(a) and an X-ray incident angle of 20° to produce the surface texture diffraction spots shown in Figure C4.30(b). The diffraction features arising from scattering with the lattice planes of $BaTiO_3$ are identified. Diffraction spots not identified arise from scattering from the cubic crystalline LiF substrate. For comparison in figure C4.30(c) we show the diffraction pattern observed from a $\sim 0.8\mu m$ thick film produced by depositing onto a polished (100) orientated substrate (latter parameter 4.2Å) at a temperature of 575°C. Horizontal diffraction lines of uniform intensity are characteristic diffraction features produced by a polycrystalline film. Since the lines have a nonuniform intensity, the diffraction pattern obtained with this film shows some degree of preferred orientation.

Using the setup sketched in Figure C4.31(a) the X-ray diffractometer picture of the film in Figure C4.29 is shown in

VARIATION OF DEPOSITION RATE WITH LASER FLUENCE

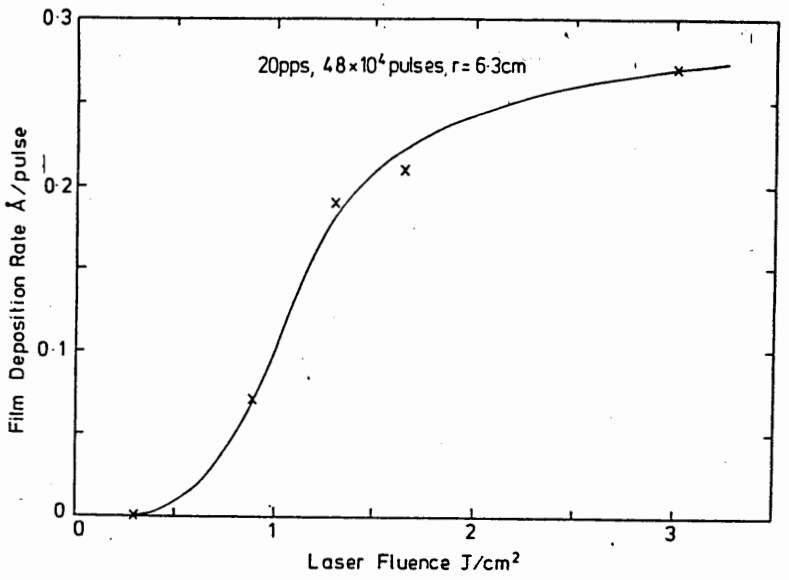


Fig C4.28

NOMARSKI OPTICAL MICROGRAPH OF ~0·3μm THICK EPITAXIAL $BaTiO_3$ FILM

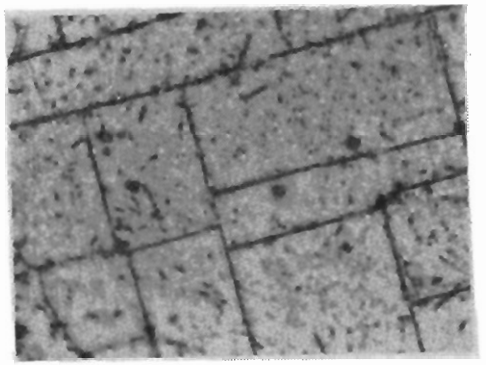
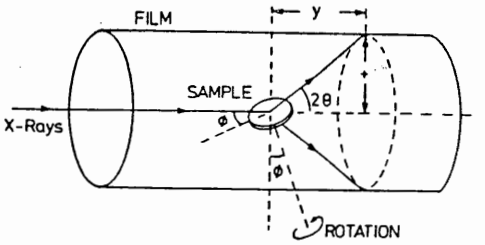


Fig C4.29

X-RAY SURFACE TEXTURE CAMERA



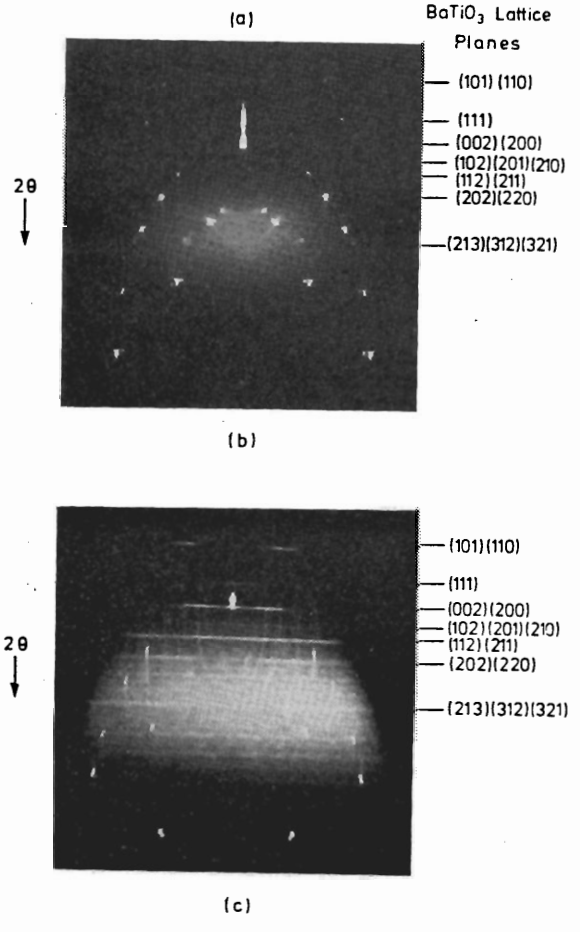
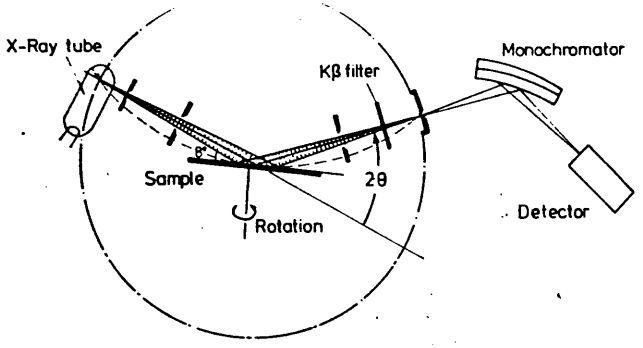
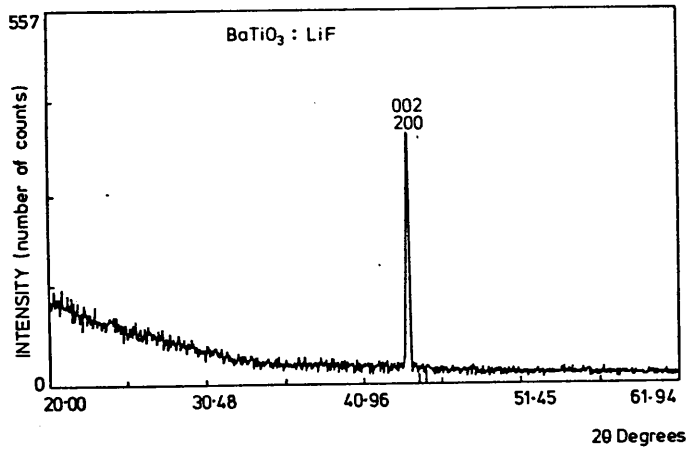


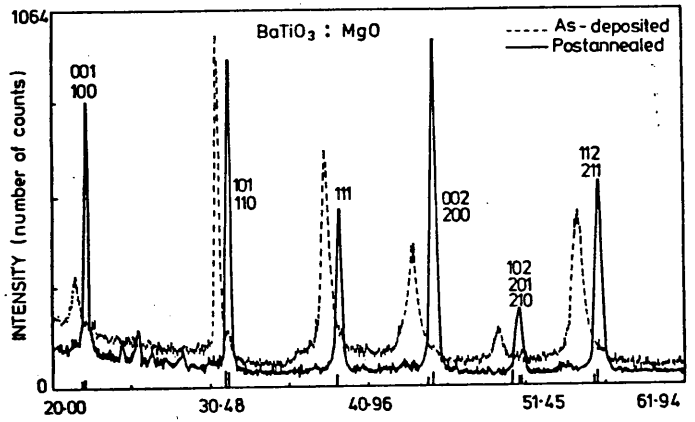
Fig C4.30



(a)



(b)



(c)

Fig C4.31

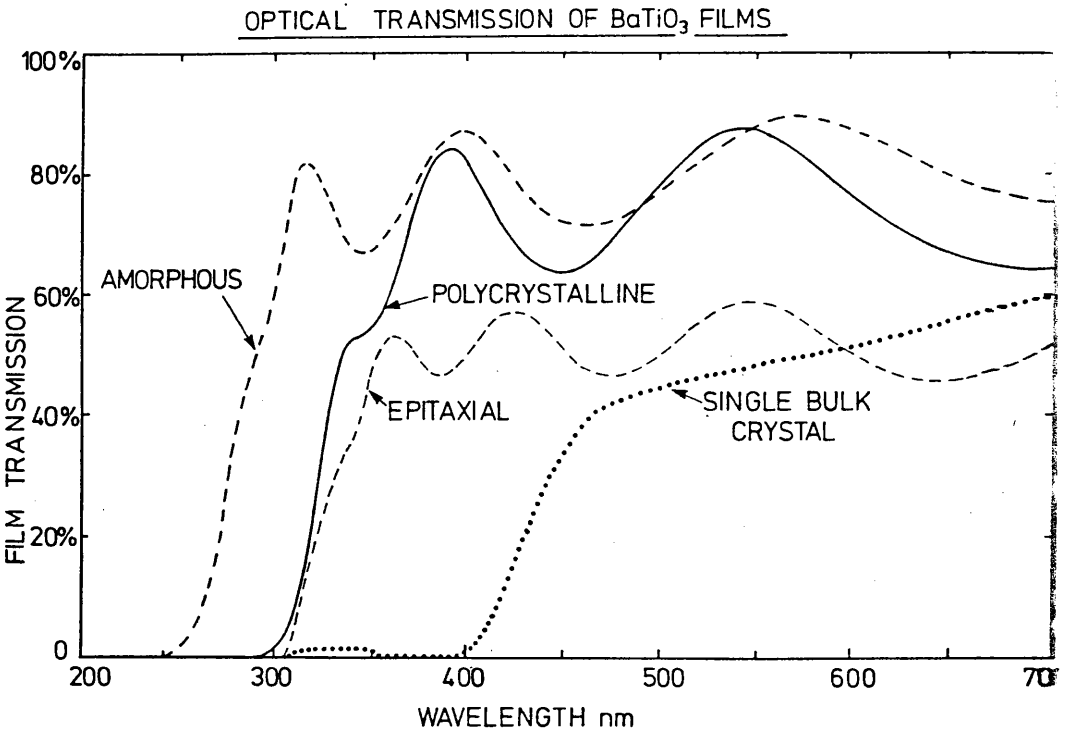


Fig C4.32

Figure C4.31(b). The single scattering peak observed in Figure C4.31(b) is characteristic of highly-ordered epitaxial film growth. For comparison, the dotted line in Figure C4.31(c) shows the multiple angle scattering from the as-deposited polycrystalline film on the MgO substrate used to obtain Figure C4.30(c). This latter film was subsequently annealed in an oven with flowing oxygen for 4 hours at 1100°C. The narrower diffraction peaks obtained after annealing are shown as the solid line in Figure C4.31(c) and closely match the calculated positions (shown as markers on the horizontal axis) of the expected scattering angles from polycrystalline $BaTiO_3$. The shifted and broader scattering peaks of the as-grown film are indicative of stress accummulation in the film. Since the expansion coefficient of MgO is only about twice that of $BaTiO_3$ this stress may be caused by the relative large lattice mismatch between the film and the MgO substrate. The shift of the peak in Figure C4.31(b) from the expected position is probably also caused by stress - perhaps as a result of the large mismatch in expansion coefficients of the epitaxially grown film and the LiF substrate. This shift prevents us determining if this as-grown expitaxial film is in a tetragonal or a frozen-in cubic phase.

The optical transmission of $BaTiO_3$ films on LiF substrates in the UV/visible region is shown in Figure C4.32 when the substrate is held at temperatures of 617°C (epitaxial growth), 480°C (polycrystalline) and 200°C (amorphous) during deposition. It can be seen from the data that the band edge absorption of $BaTiO_3$ at ∿4.5eV shifts to lower energies when the material is in the crystalline rather than the amorphous state. This shift may be due to a stress induced distortion of the band by the lattice-film interaction. For comparison, the measured transmission of a nominally pure single domain 5mm thick crystal of $BaTiO_3$ is also shown in Figure C4.32. Its band gap absorptive behaviour lies near 3eV.

In this section we have shown that thin epitaxial films of $BaTiO_3$ can be grown on hot LiF substrates using excimer laser ablative sputtering of pellets of bulk sintered $BaTiO_3$. The method is a convenient technique and can possibly be used to fabricate thin epitaxial layers of other mixed materials such as $LiNbO_3$, $KNbO_3$ and KDP which are also of great interest in nonlinear optics.

C4.8 SIMULTANEOUS UV EXCIMER AND IR CO_2 LASER ABLATION OF PMMA

A Jancarek and M C Gower (RAL)

Ablative photodecomposition (APD) to produce clean etching of polymers by pulses of light from UV excimer lasers is known to occur at least in part by photochemical processes by which the uv photons directly break the chemical bonds which hold the irradiated polymer together. This direct bond scission removes material as a result of the rapid rise in pressure at the irradiated site. The etching of the substrate material that results is extremely clean and usually shows little evidence of thermal effects such as melting or flow of the surrounding unirradiated polymeric material. Because of the likely photochemical nature of the process we have carried out a series of experiments which study the effect of populating the vibrational/rotational levels of the ground electronic state of polymethylmethacylate (PMMA) with a pulsed CO_2 laser prior to performing APD with ArF and KrF UV excimer lasers. We have studied the APD etching characteristics as a function of the energy fluence of the excimer laser.

The experimental setup is shown in Fig C4.33. A home-made CO_2 TEA laser operating in the TEM_{oo} mode at 10.6 μm produced a pulse shape consisting of a 80 nsec wide initial peak containing ∿ 10% of the energy followed by 1.8 μsec tail which irradiated the PMMA sample at a fluence of ∿ 260mJ/cm². The focussed 20 nsec duration output from a synchronised Lambda-Physik EMG150 excimer laser irradiated the sample at time delays after the arrival of the CO_2

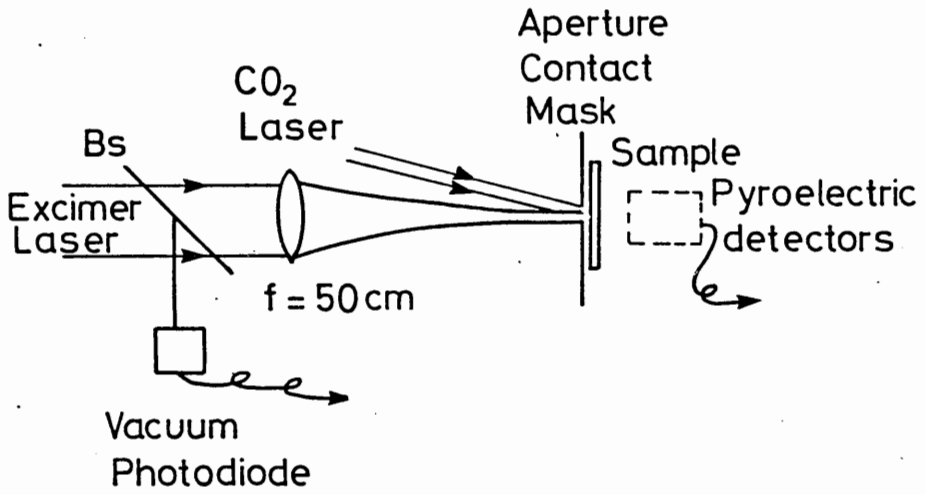


Fig C4.33

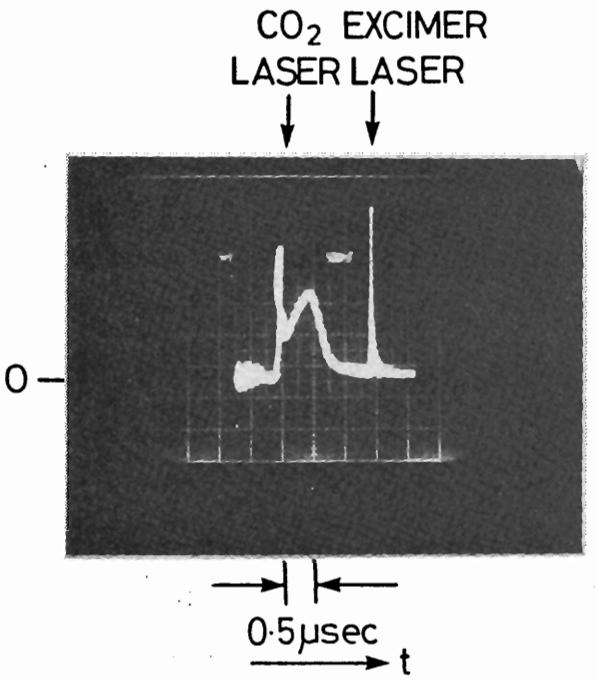


Fig C4.34

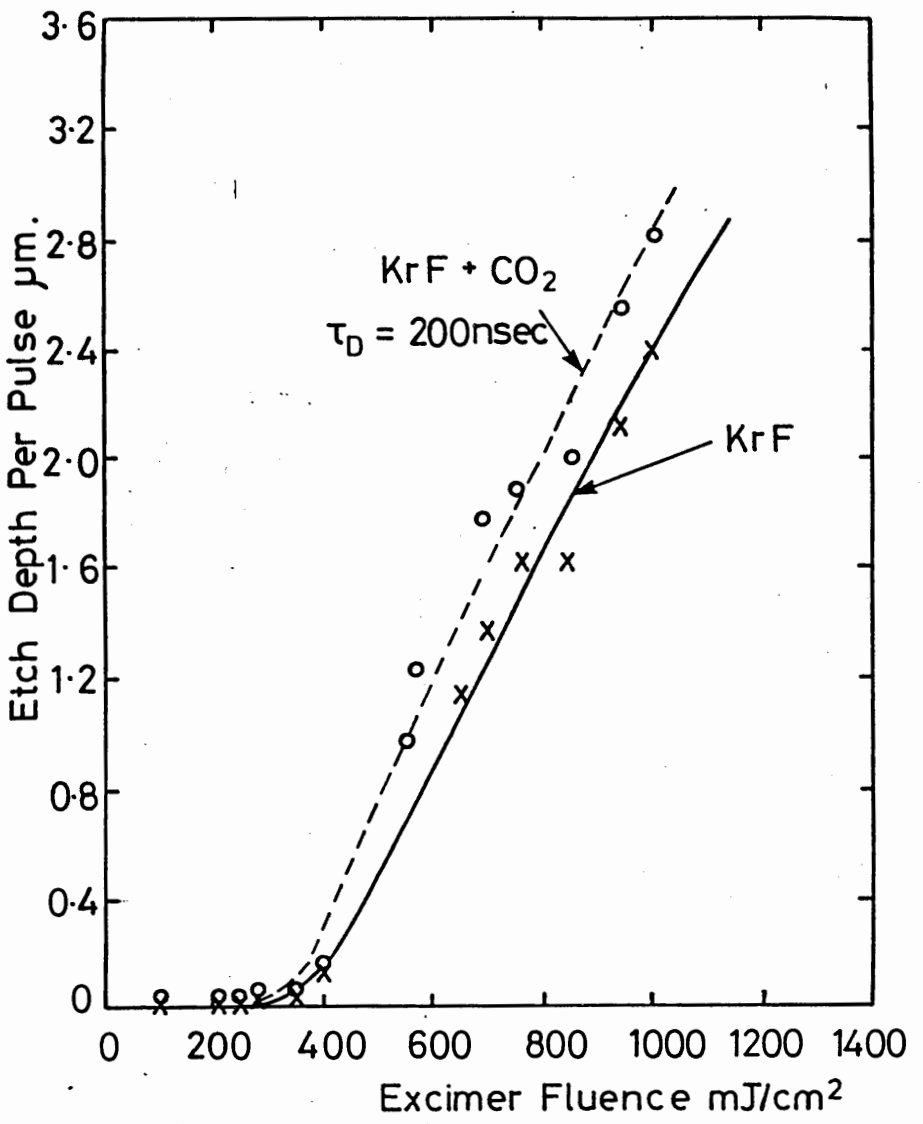


Fig C4.35

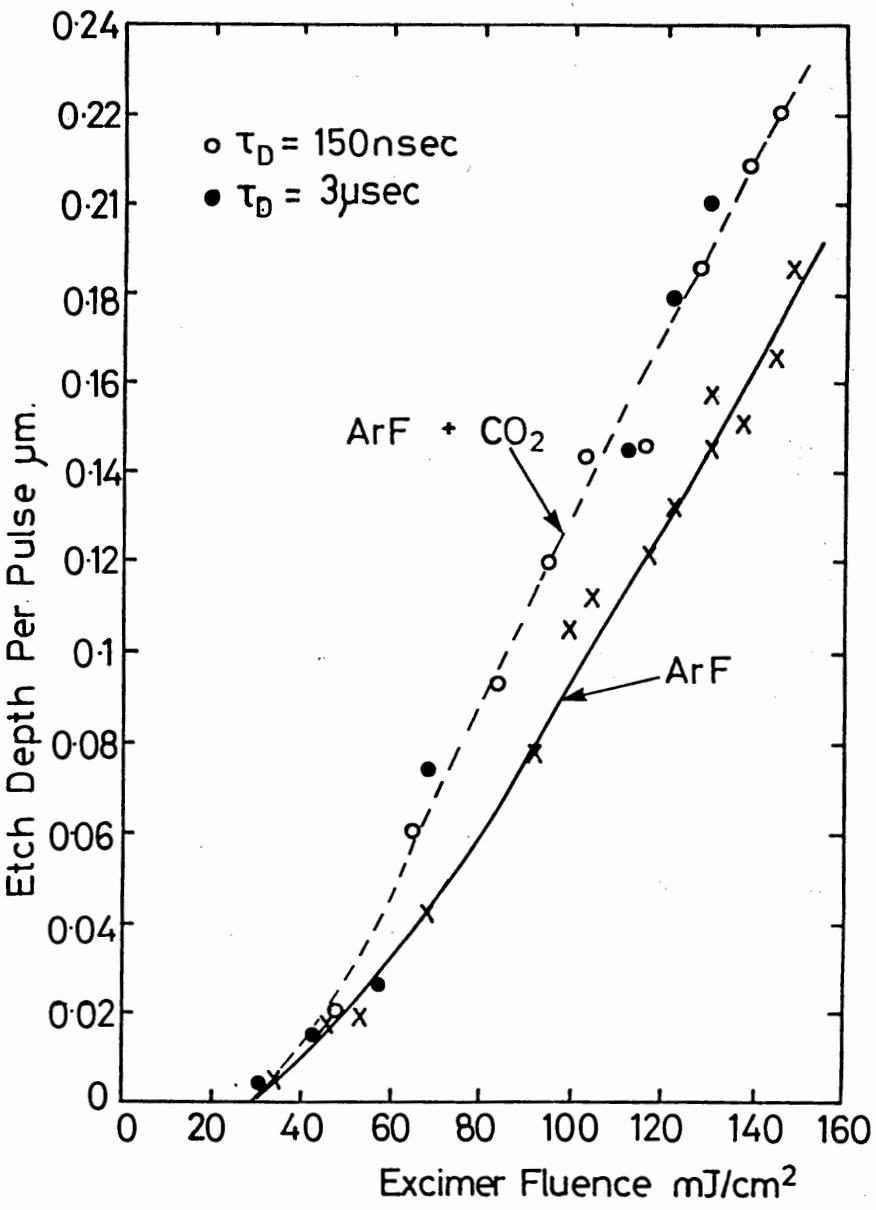


Fig C4.36

pulse variable between co-incidence and 3 µsec (see Fig C4.34). Circular aperture masks 2,1 and 0.5mm in diameter placed in contact with the 0.8mm thick samples of PMMA were used to define the irradiated area on the sample. Excimer laser fluences were varied by changing the distance of the substrate from the lens focal position. An ITL vacuum photodiode and a Molectron P5-01 fast pyroelectric detector were used to monitor the laser pulses temporal profiles and relative delays.

With different delays of the pulses from the ArF and KrF lasers relative to the CO_2 laser pulse, the etch rates measured as a function of the excimer laser fluence are shown in Figures C4.35 and C4.36 and are compared with the etch rates obtained using the excimer laser by itself. It can be seen from these data that for delays of arrival of the excimer laser pulse between 0.3 and 3 µsec, the CO_2 laser did not seem to change the threshold excimer laser fluence required to produce APD. However once above threshold at both uv laser wavelengths the etch rate obtained per pulse was enhanced by up to 60% by using the CO_2 laser to preheat the sample.

This behaviour leads us to conclude that initially populating excited vibrational/rotational levels of the ground electronic state of the polymer with the CO_2 laser produces larger photodissociation crossections in the ultraviolet spectral region which favour more efficient excimer laser APD. However higher probabilities for photodissociation do not appear to reduce the threshold excimer laser fluence required for initiating APD.

C4.9 WHITE LIGHT PHASE CONJUGATE LENSLESS IMAGE PROJECTION

P Hribek and M C Gower (RAL)

Four-wave mixing in non-linear optical media and in particular self-pumped phase conjugate emission (SPPCE) from crystals of $BaTiO_3$ can be used to perform lensless phase conjugate real-time imaging with high resolution. Using extremely simple beamsplitter/crystal experimental setups, projected images with resolutions of 0.5µm, and projector NA's close to unity are readily demonstrated with high efficiencies over field sizes of 3-4mm. Clearly a key requirement for visual observation of images created by any projector is the ability of the device to produce reproductions of the object in white light. Although an Ar^+ laser source has been used to perform multiwavelength phase conjugate imaging using four-wave mixing and self-pumped ring cavity geometries with photorefractive $BaTiO_3$ crystals, to our knowledge phase conjugate real time holographic white light imaging has yet to be demonstrated using any type of nonlinear optical material or interaction. In this section we report the use of simultaneous self-pumped phase conjugate reflections from a $BaTiO_3$ crystal of blue (442 nm), green (514 nm) and red (633 nm) laser light to project images in white light of objects having feature sizes as small as 30 µm.

The poled single domain 6 x 5.5 x 5 mm crystal of $BaTiO_3$ used for this work produced self-pumped phase conjugate reflections separately at each wavelength by internal 'cat-mirror' type reflections within the crystal. Self-pumped phase conjugate reflectivities (SPPCR's), uncorrected for Fresnel reflections, of up to 75% were measured in the red. The measured transmittance of the crystal as a function of wavelength is shown in Fig C4.37. The White light image projector setup is shown in Fig C4.38. The argon ion laser (Coherent Innova 90) operated on a single longitudinal mode and was isolated from back reflections by a Faraday rotator and polarisers. All beams entering the crystal were extraordinary polarised and had diameters of ∿2 mm. The He-Cd (Liconix 4240) and He-Ne (Spectra-Physics 107A) lasers operated multi-longitudinal mode and produced up to 35 mW of power. The three beams were combined and made to be colinear with an accuracy of 10µrad by the dielectric mirror M which at 45° transmitted 95% of p-polarised radiation at 442 and 514 nm and reflected 98% at 633 nm. The

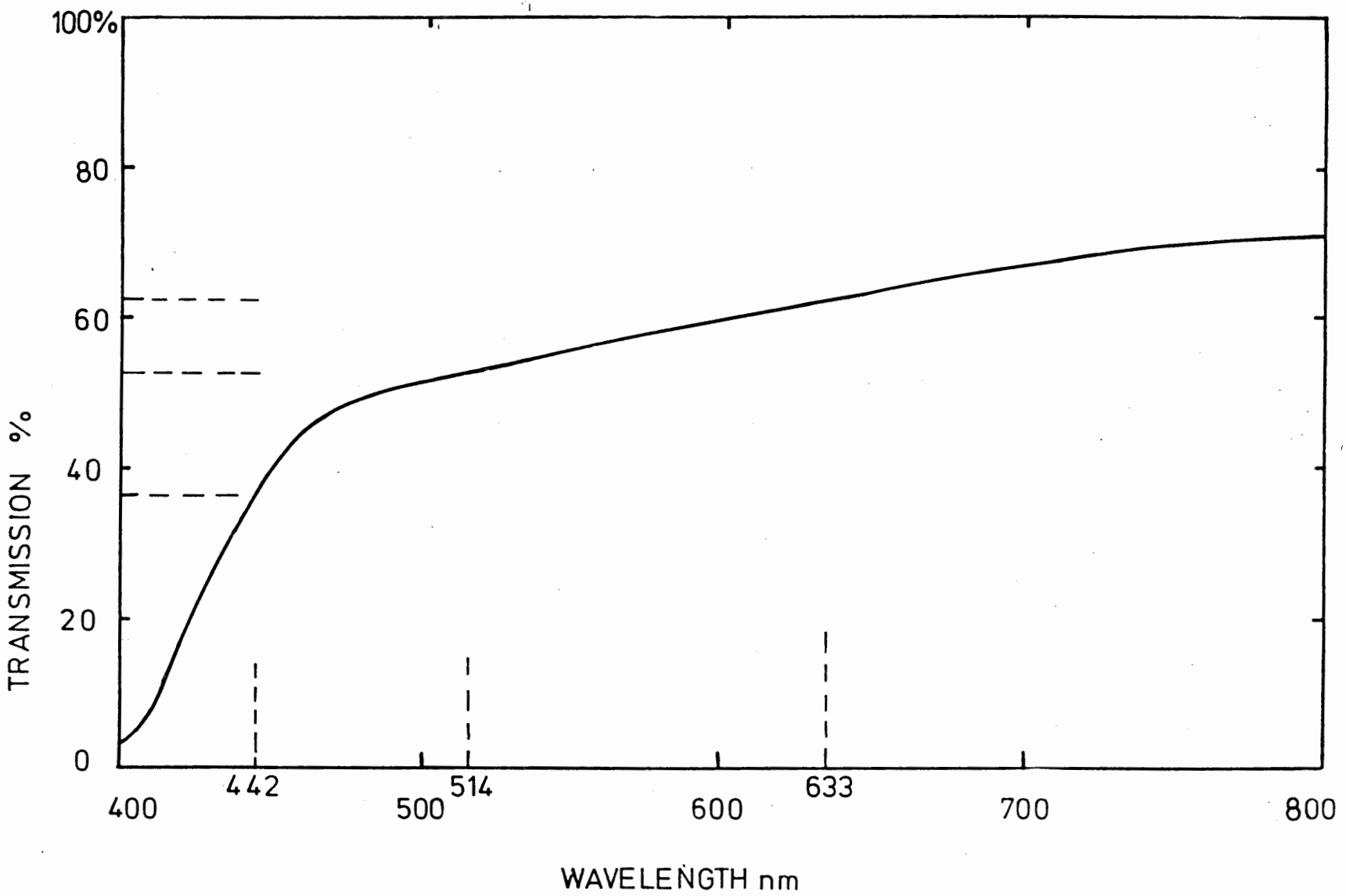

100%
80
60
40
20
0
TRANSMISSION %
400
442
500
514
600
633
700
800
WAVELENGTH nm

Fig C4.37

40°-50° angle of incidence into the crystal was the optimum found that produced stable self-pumped phase conjugate reflections of high reflectivity at all wavelengths.

In order to study the effects of possible grating erasure and crosstalk with multicolour illumination and to establish the conditions required for a satisfactory colour balance of the projected image, the SPPCR was measured without an object mask using two-colour operation at a fixed red incident laser power as a function of the blue and green incident powers. The results in Fig C4.39(a) and (b) show that as the power of either the He-Cd or Ar^+ lasers increases the SPPCR in the blue and green also increases while photoerasing gratings recorded in the red. The SPPCR in the red decreases from its single colour value of ∿65-72% when simultaneously illuminated with light at shorter wavelengths. For intensities in the red much larger than in the blue or green it is possible to observe SPPCE only in the red. Alternatively when blue or green intensities are much greater than in the red SPPCE is observed at the shorter wavelengths only. At either extreme the SPPCR for each colour is similar to that obtained for each colour only. The threshold power for SPPCE is higher at shorter wavelengths which is probably a result of the higher absorption experienced at these wavelengths (see Fig C4.37). Consequently, at 442 nm the beam diameter of the SPPCE was about half that of the input beam while at 633nm they had a similar size.

The SPPCR in the red is much more sensitive to variations of the incident power in the blue than in the green. This sensitivity is more easily appreciated in Fig C4.40 by replotting the data in Fig C4.39 as input and reflected power ratios normalised to the corresponding powers in the red. For example, at incident three colour powers used for projecting images which appear white to the eye (see below), a 10% change of the incident colour balance changed the projected colour balance by 27% in the green and 100% in the blue.

Stable simultaneous two and three colour SPPCE was observed only if the process was initiated in an illumination sequence starting with the longer wavelengths first. Unlike the case when mutually incoherent beams of the same wavelength pump a ring passive phase conjugate mirror, the startup ordering of input beams of different wavelengths pumping a 'cat' mirror are not interchangeable.

The imaging property of the projector were studied by placing a test mask (RC in Figure C4.38) 15 mm from the crystal and either viewing the expanded projected image from the beamsplitter directly on a screen or recording it with Polaroid colour film (Type 59). In Fig C4.41(a)-(d) we show the projected images recorded with simultaneous two and three colour illumination. It can be seen that two and three colour images can be obtained with a minimum of crosstalk between projected images down to a resolution of 30μm. Due to the sensitivity of the SPPCR to the illuminating colour balance (Fig C4.40), to obtain a stable projected image with a white appearance required careful balancing and stabilisation of the incident intensities at each wavelength. To create an image on a screen which appeared white to the eye required red, green and blue intensities incident upon the object mask of 14.0, 5.2 and 4.5 mW respectively. Compensation for the colour response of the Polaroid film required powers of 9.3, 4.4 and 3.1 mW respectively to record an image with a white appearance. The increase in crosstalk in the three colour compared to the two colour projections in Fig C4.41 is mainly in the horizontal direction and does not deter the clear observation of white light reconstructions of objects in the most intense region (middle) of the beams. Because of the differing sensitivities and speed of response of the eye compared to film, more satisfactory white light reconstructions than that shown in Fig C4.41, were obtained when viewing the images visually on a screen. By taking into account the relative spectral sensitivity of the eye and the different SPPCE beam diameters, we deduce that three colour illumination of the crystal at powers which produced images which appeared white reduced the reflected power ratios from the two-colour illumination values shown in Figure C4.40 and (b) by factors of about two and ten respectively.

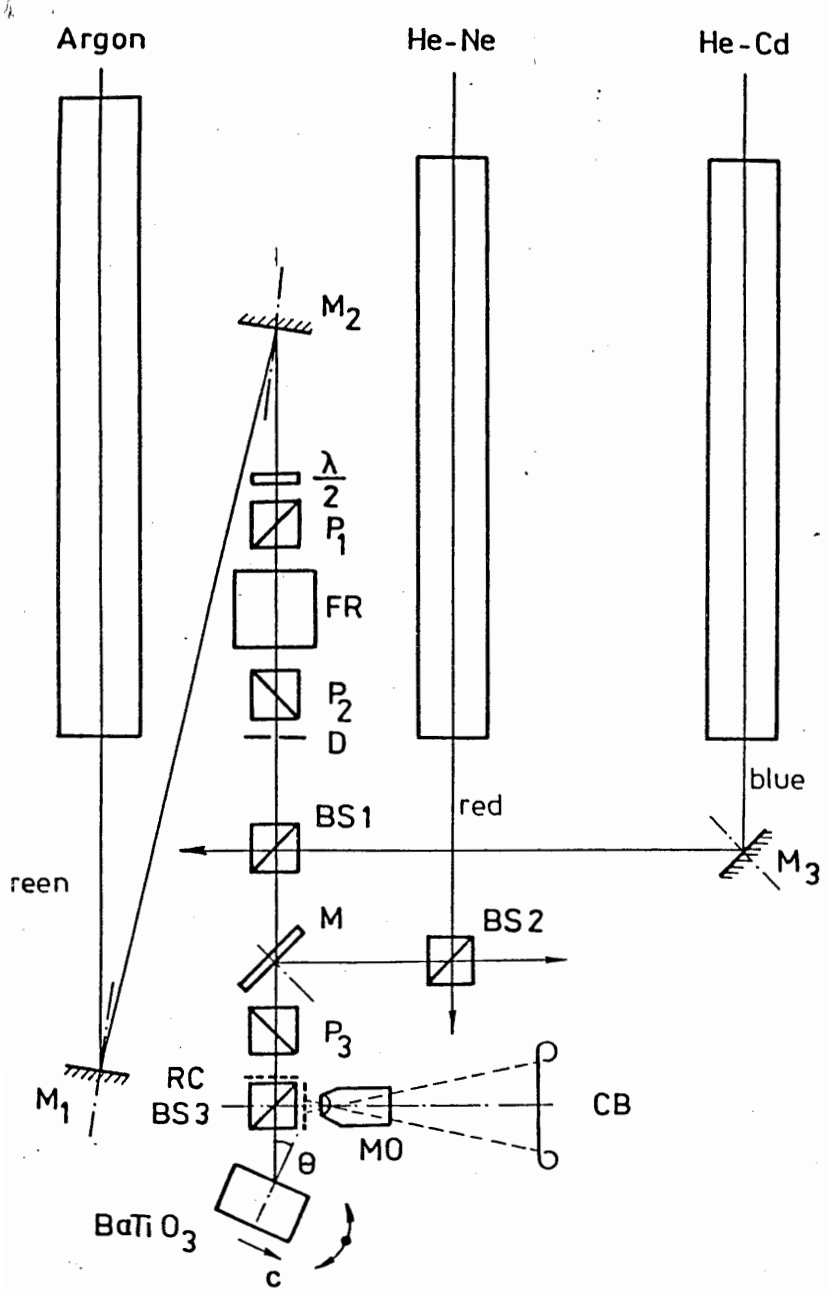


Fig C4.38

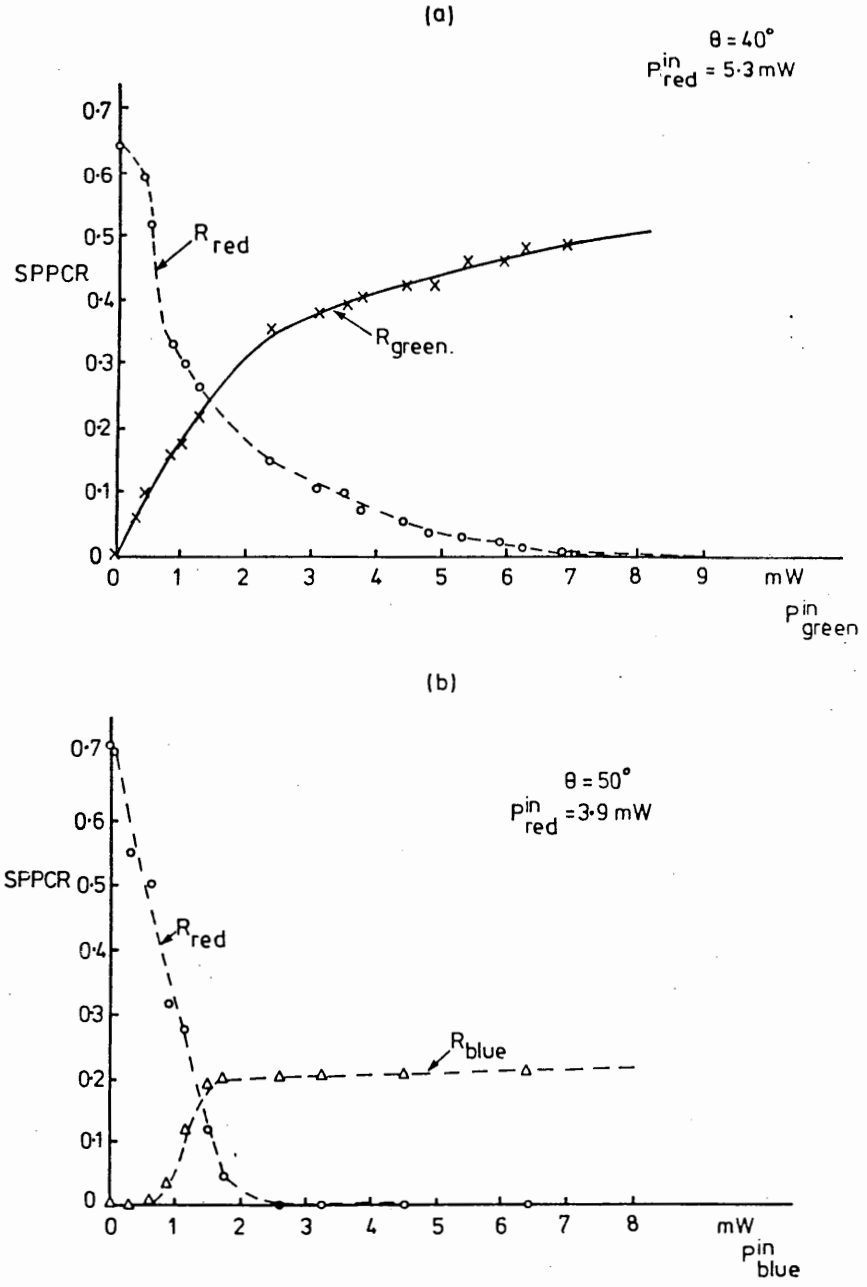


Fig C4.39

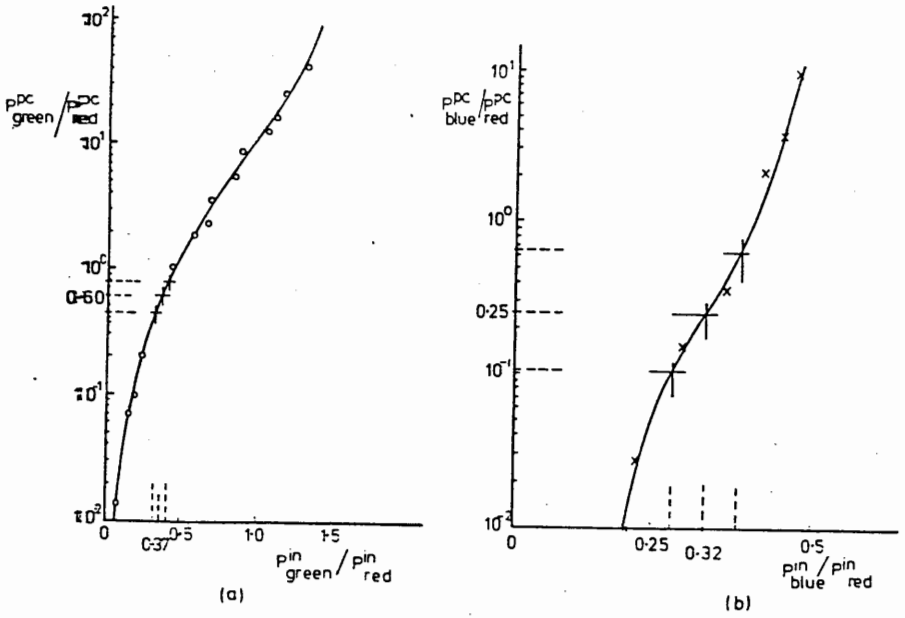


Fig C4.40

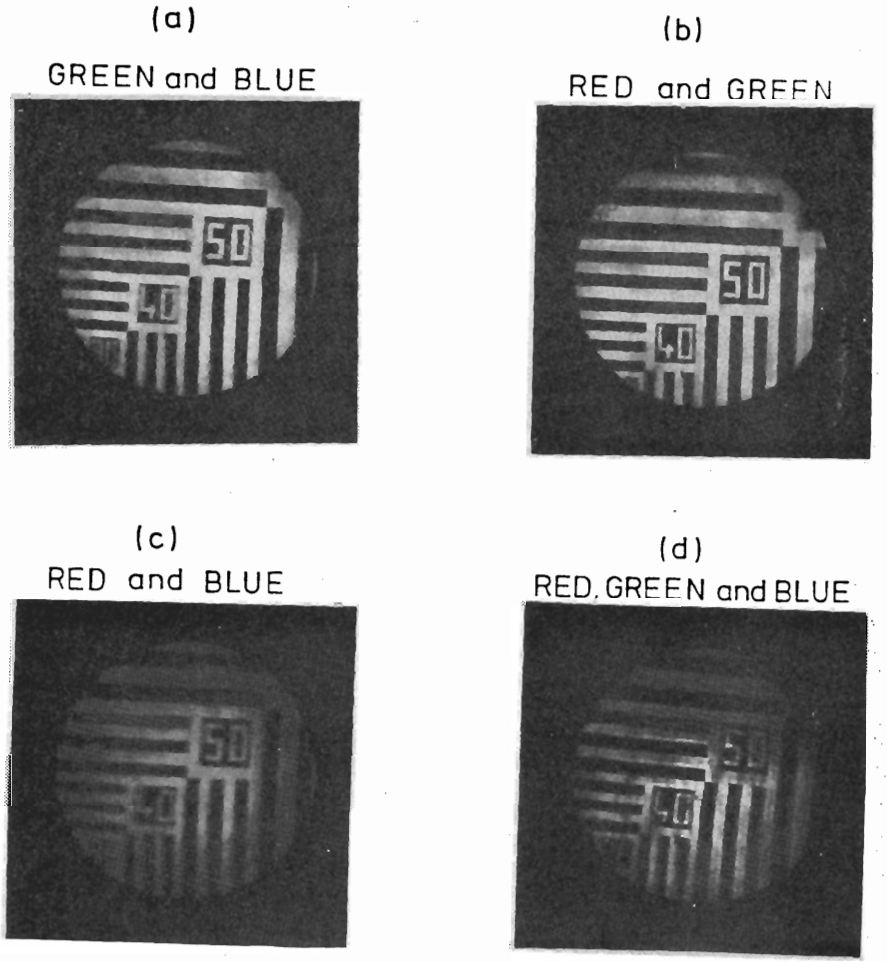


Fig C4.41

By using red and green illumination of **different** object mask patterns at intensities for which significant erasure of the red hologram does not occur, wavelength multiplexing of SPPCE holograms was investigated further . While good reconstruction of both images occurred simultaneously at each wavelength some crosstalk was evident. Features from one mask pattern at one wavelength were transferred to the reconstruction of the other mask at the other wavelength. This crosstalk could be minimised by careful optimisation of the relative incident intensities.

In conclusion, we have projected white light images using a phase conjugate mirror consisting of a $BaTiO_3$ photorefractive crystal simultaneously self-pumped with red, green and blue laser light. The resolution of the projected images was ~30μm with minimal crosstalk between images reconstructed at different wavelengths.

C4.10 EXPERIMENTAL STUDIES OF SELF-PUMPED PHOTOREFRACTIVE RING RESONATORS

P Hribek and M C Gower (RAL)

In the setup shown in Fig C4.42, two-beam coupling with undirectional oscillation in a ring resonator which contains a photorefractive $BaTiO_3$ crystal was used to create a new type of self-pumped phase conjugate mirror.

Initially the two-beam coupling efficiency and self-pumped phase conjugate reflection of the internal 'cat' mirror were investigated for the crystal. To measure the efficiency of two-beam coupling in the poled single domain 6 x 5.5 x 5mm $BaTiO_3$ crystal the set up in Fig C4.43 was used. The beams I_1 and I_2 interfere in the crystal to form a sinusoidally varying light interference pattern:

$$I(z)=I_0(1 + me^{ikz}) \qquad (1)$$

where $m = \frac{2(I_1 I_2)^{\frac{1}{2}}}{I_0}$ is the fringe modulation depth, the total intensity $I_0 = I_1 + I_2$, and k is the interference grating wavevector. This interference pattern is used to create space charge gratings which in turn induce refractive index variations in photorefractive media such as $BaTiO_3$. It can be shown that when $I_2 << I_1$, then I_1 and I_2 propagate with distance z according to:

$$I_1(z) = \frac{I_0(0)e^{\alpha z}}{1+(I_2(0)/I_1(0))e^{\Gamma z}} \qquad (2)$$

$$I_2(z)= \frac{I_0(0)e^{\alpha z}}{1+(I_1(0)/I_2(0))e^{-\Gamma z}} \qquad (3)$$

so that the beam I_2 will experience an exponential intensity gain, Γ, as it propagates through the length ,ℓ, of the crystal. As orientated in Fig C4.43.

$$\Gamma = -\frac{1}{\ell} \ell n \frac{I_1(0)}{I_2(0)} \left[\frac{I_0(0)e^{-\alpha \ell}}{I_2(0)} - 1 \right] \qquad (4)$$

where α is the absorption coefficient of the crystal. Using a single longitudinal mode Ar^+ laser operating at 514.5 nm and with an optimum beam crossing angle of $2\phi = 47°$ in Fig C4.43 we measured Γ in $BaTiO_3$ to be 9.0 cm^{-1}.

Two wave mixing was then used to couple light into and out of the ring resonator setup shown in Fig C4.42. The 0.5 mm diameter aperture D was used to force single mode oscillations in the ring resonator. For oscillation to occur within the ring cavity the

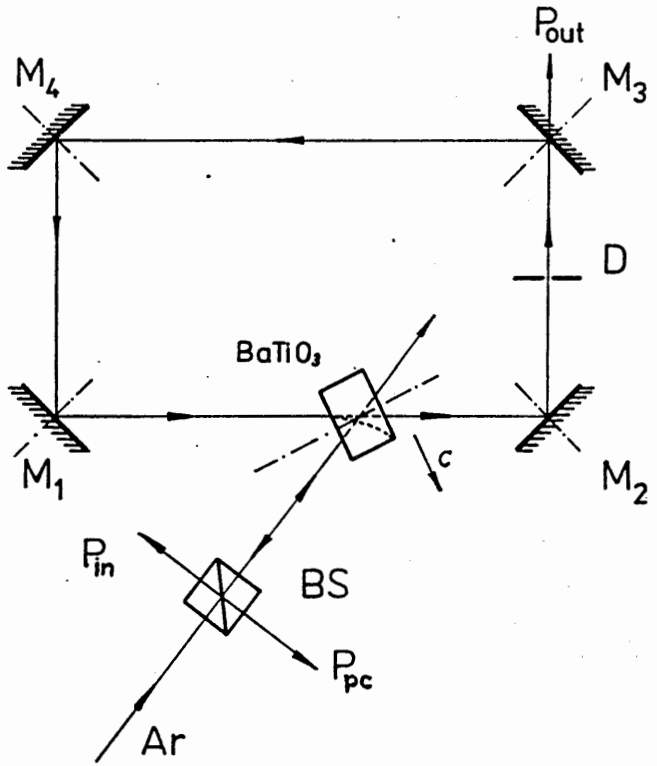


Fig C4.42

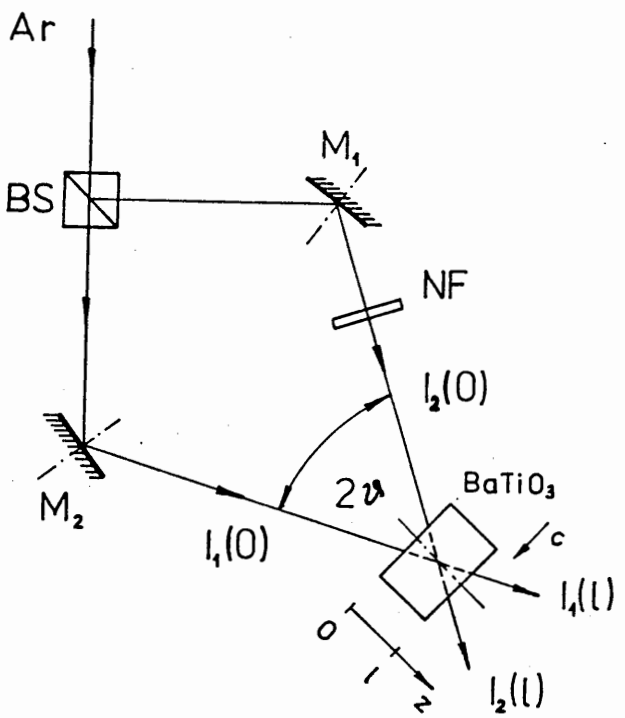


Fig C4.43

two-beam coupling gain $\Gamma\ell$ must exceed the cavity losses such that the threshold oscillation condition is satisfied:

$$(\Gamma\ell)_{th} = \alpha\ell - \ell nR \qquad (5)$$

where R is the product of mirror reflectivities. Since we measured $\Gamma\ell = 5.4$ and from Eq(5) $\Gamma\ell_{th} = 1.06$, undirectional oscillation readily occurs around the ring. For self-reproduction of the beam around the ring the round trip phase delay must be an integral multiple of 2π ie.

$$\Delta\psi + \int kds = 2N\pi \qquad (6)$$

where $\Delta\psi$ is a phase shift introduced by photorefractive coupling.

For this crystal the self-pumped phase conjugate reflectivity of the internal 'cat' mirror configuration was measured as a function of angle of incidence of He-Ne (633nm), Ar^+(514nm) and He-Cd (432nm) pump radiation. The results are shown in Fig C4.44. At the longer wavelengths pulsations of the SPPCE are observed at angles less than 20° while for angles greater than 65° the emission becomes unstable. In particular for this crystal from Fig C4.44 we see that the SPPCR can reach a stable value of $\sim$ 70% when using a He-Ne laser at an angle of incidence θ of $\sim$60°.

At sufficiently high powers, rotating the crystal from normal incidence ($\theta>0$) in fig C4.42 produces by internal reflections within the crystal a self-pumped phase conjugate reflection of the undirectional ring resonator beam that propagates around the ring in the opposite direction. The bidirectional oscillations in the cavity so produced can then generate by four-wave mixing with the pump laser beam a (self-pumped) phase conjugate reflection of the pump beam (P_{pc} in Fig C4.42).

If the pump beam enters the crystal at the position shown in Fig C4.45(a) (z +ive), light that is two-beam coupled into the resonator also fans out along the c-axis of the crystal and produces self-pumped phase conjugate emission due to internal resonators within the crystal. This process then causes a reduction in the forward going radiation intensity in the resonator. The four-wave mixing grating produces the stable phase conjugate reflection shown in Fig C4.45(b) which remains even after blocking the ring cavity resonator (fig C4.45(c)). Thus the ring cavity is necessary to make this kind of SPPCM self-starting. We found that when the beam crossing angle 2ϕ had its optimum coupling value of 47° and the angle of incidence θ = 10° then the phase conjugate reflectivity produced by this self-starting bidirectional ring cavity was $\sim$ 10% and was similar to that produced by the 'cat' mirror configuration (see Fig C4.44) for the same angle of incidence.

If the beam enters the crystals at the -ive z position (see Fig C4.45(a)) then the SPPCE produced by this resonator becomes unstable (Fig C4.46(b) and (c)) and can pulsate. As shown in Fig C4.46(a) this instability at this pumping position is probably caused by an overlap of the four-wave mixing grating with the internally generated diagonal loop resonator within the crystal responsible for producing the counter propagating light in the external ring. When the SPPCE reaches its maximum value then the maximum interference with the loop will occur and tend to destroy the counterpropagating light. This behaviour can be seen in Fig C4.47 which shows that as the counterpropagating light P_{out} in the ring builds up the intensity of the forward travelling light decreases and the SPPCE P_{pc} increases. At the point of maximum SPPCE the light in the ring reaches its minimum value.

In conclusion we have demonstrated a new type of self-pumped phase conjugate mirror which is based upon a ring cavity containing a $BaTiO_3$ crystal which is pumped by two-beam coupling of light into the ring. Counterpropagating light in the ring which is produced by SPPCE of the forward travelling light in the crystal then produces by a four-wave interaction with the pump beam SPPCE of the

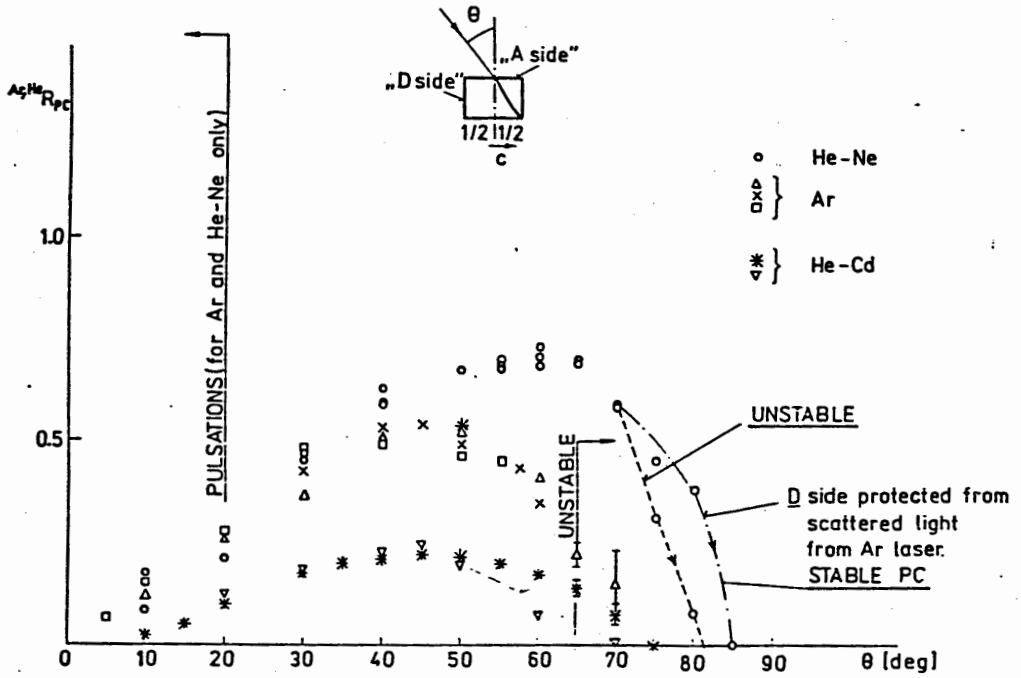


Fig C4.44

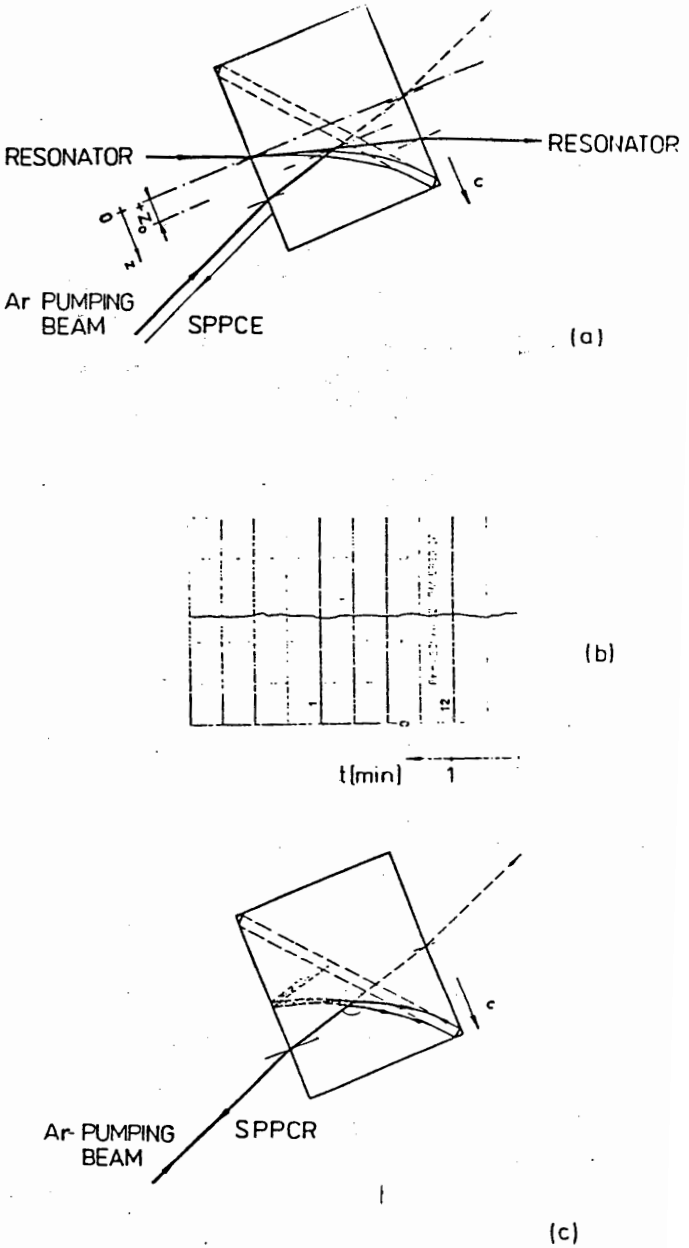
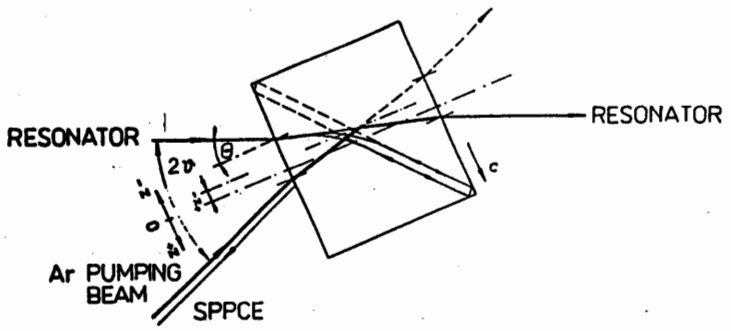
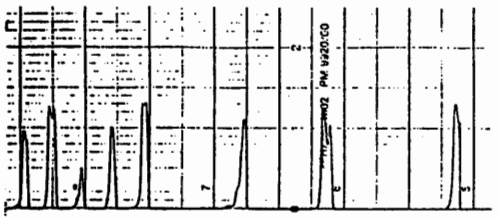


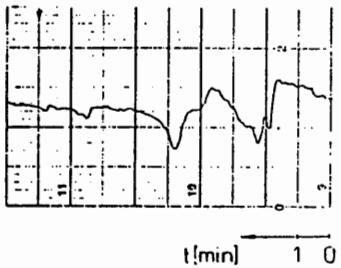
Fig C4.45



(a)



(b)



(c)

Fig C4.46

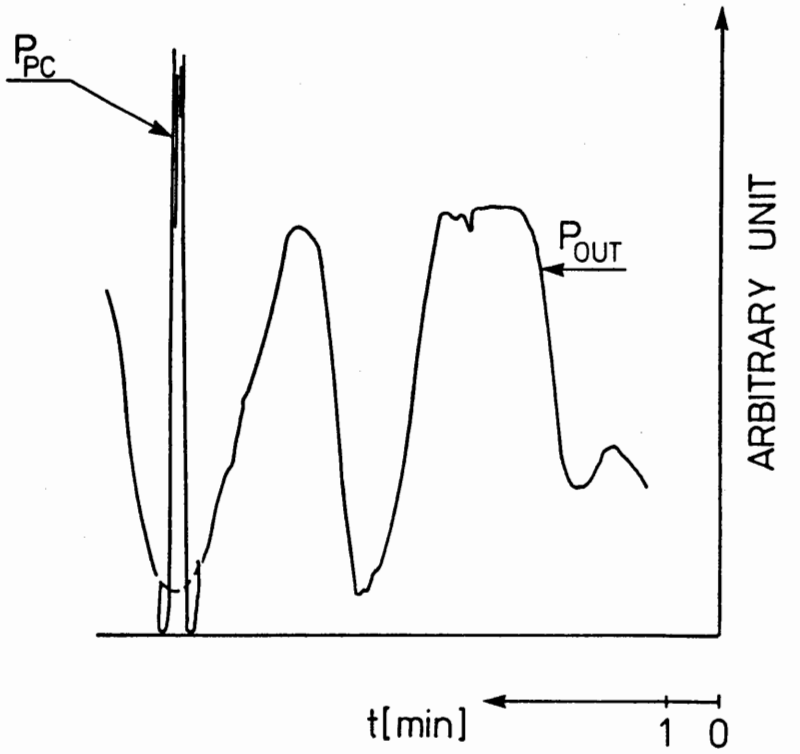


Fig C4.47

pump radiation. The device is self-starting and can produce stable SPPCE reflections which are those produced by similar in magnitude to other types of SPPCM's. Once initiated the ring cavity can be removed and stable SPPCE continues.

C4.11 MEASUREMENTS OF CW SBS GAIN IN FIBRE OPTIC RING RESONATORS

J F Massicott, G M Davis and M C Gower (RAL)

Stimulated Brillouin Scattering (SBS) in single mode optical fibres is regarded as a deleterious effect in fibre optic communication networks. Propagating the narrow bandwidth (<1MHz) single mode laser sources which are necessary for achieving high information carrier bit-rate over multikilometre optical fibre lengths at mw power levels efficiently generates a stimulated Brillouin backscattered signal which leads to a loss of the transmitted power, an intense backwardly propagating beam into the launching optics and a loss of carrier bandwidth.

The purpose of the work described in this section is to study the SBS generated in optical fibres by CW low-powered laser sources and to assess its potential as a method for producing phase conjugate reflections from low powered laser beams.

The small-signal (undepleted pump) backscattered SBS intensity, I_S, generated by a pump intensity, I_L, grows exponentially over an effective length

$$\ell = \frac{1-e^{\alpha\ell}}{\alpha} \quad \text{such that} \quad I_S = I_o e^{gI_L\ell}$$

where α is the optical attenuation coefficient of the fibre and the SBS gain g is given by:

$$g = \frac{2\pi n^7 p^2}{c\lambda^2 \rho V_a \Delta\nu_B} \qquad (1)$$

For silica we have:

n = refractive index = 1.46;
p = elastooptic coefficient = 0.271;
ρ = density = $2.21 \times 10^3 kgm^{-3}$;
V_a = acoustic wave velocity = $5960 ms^{-1}$;
$\Delta\nu_B$ = spontaneous Brillouin linewidth = 145MHz.

Thus g(silica) = 4.3×10^{-11} m/W with a Stokes shift of 34GHz.

The threshold for generating an intensity of SBS comparible to the pump intensity occurs when $gI_L\ell \sim 25$. On the other hand, seeding the fibre with radiation at the Stokes frequency can dramatically reduce this requirement. For example, a 100% increase in the seed signal occurs for $gI_L'\ell = 0.7$. Seeding of the fibre provides scope for generating SBS in larger diameter fibres in which, for the same pump power, the pump threshold intensity required to efficiently generate SBS is reduced by the ratio of the smaller to larger core cross-sectional areas.

Using a single-mode Ar^+ laser source, in initial experiments we have measured the SBS gain in fused silica fibres at 514 nm. Fibres with core diameters of 3.3 µm and 5 µm (York Technology types SM600 and SM1000 respectively) which had cut off wavelengths of 550nm and 840nm and measured attenuations at 514 nm of 32 dB/km ($\alpha = 7.3 \times 10^{-5} cm^{-1}$) and 112 db/km ($\alpha = 2.6 \times 10^{-4} cm^{-1}$) respectively were used for this study.

SBS in Single Mode Fibre

The arrangement shown in Figure C4.48 was used to observe SBS in a 250 m length of the 3.2µm core diameter fibre. Using a x10 microscope objective as a beam expander and a fused silica plate as

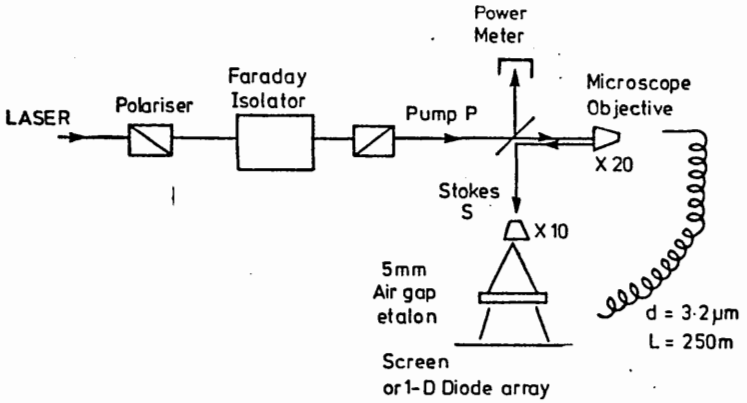
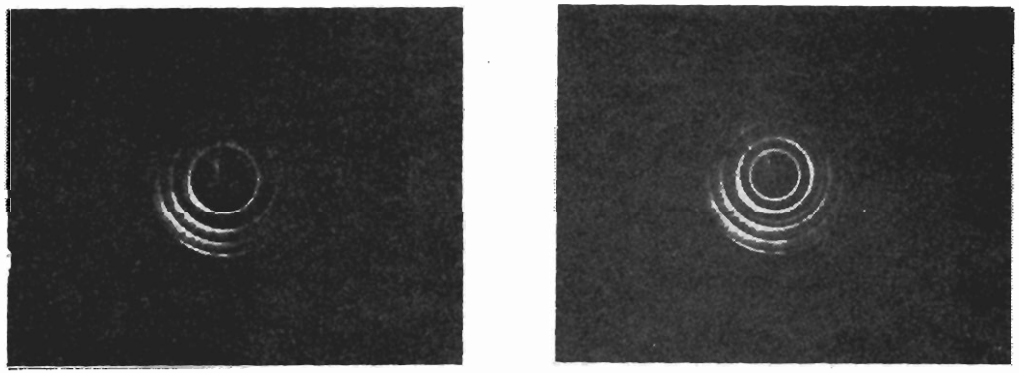


Fig C4.48



(a) (b)

Fig C4.49

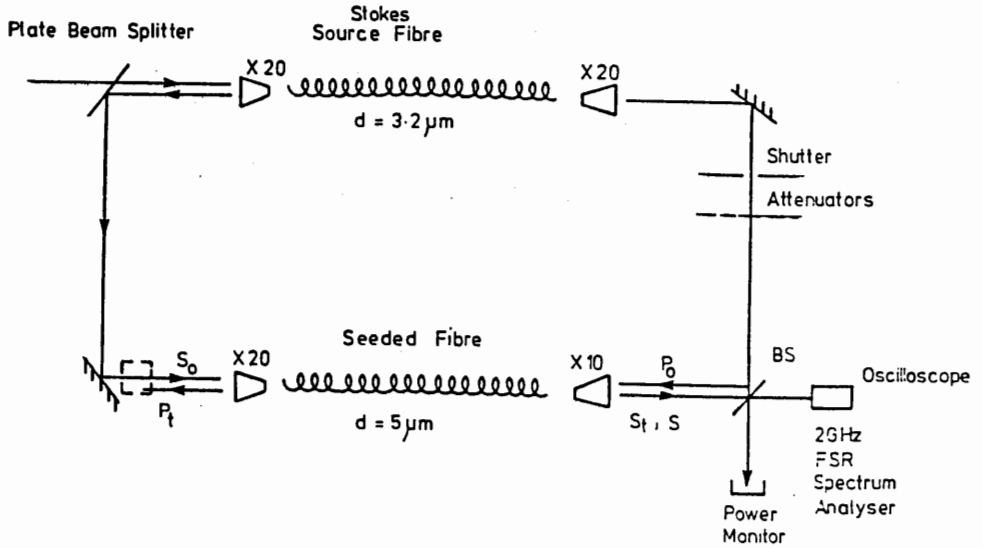


Fig C4.50

a beamsplitter, the frequency constituents of the backwardly propagating beams could be distinguished with a 5 mm fixed air gap Fabry-Perot etalon. Figure C4.49 shows the Fabry-Perot rings obtained from the pump due to reflection from the front surface of the fibre (a) and also the frequency shifted Stokes wave (b). Using a 2 GHz FSR scanning confocal etalon with a finesse of 200 the Stokes frequency shift in silica was measured to be 34 GHz.

SBS Amplification in Larger Diameter Fibres

The Stokes signal generated in the above fibre was used to seed a 5μm core diameter fibre in the ring resonator setup shown in Figure C4.50 The source fibre was pumped directly from the laser and used to produce the Stokes beam that was then fed into the back end of the larger core diameter fibre. The power transmitted through the source fibre was used as a pump beam for the seeded fibre. The laser pump intensity was varied by attenuating the beam with neutral density filters.

Using 250m and 280m lengths of source and seeded fibres respectively, the input and output Stokes signals detected by using a boxcar signal averager with a 15μsec gate width are shown in Figure C4.51. The Stokes signal S_t, transmitted through the fibre when it is unpumped is shown in (a) which upon pumping is amplified to S in (b). Gain measurements as a function of pump power of the seeded fibre are also shown in this figure. The higher gain was achieved when both the pump and seed signal propagated along the 5μm fibre in meridianal modes.

To reduce the power loss due to attenuation in the source fibre so that more pump power could be provided to the seeded fibre the experiment was repeated using shorter lengths of both source (100m long) and seeded fibres (125m). The SBS generated by the source fibre now became relatively unstable. Figures C4.52(a) and (b) show the amplified seed signal observed transmitted through the fixed air gap etalon as read out on a scanning 1-D EG&G Reticon Silicon diode array. The secondary peak in (b) in the pumped case is due to reflected pump light from the front surface of the fibre. The dependence of the measured Stokes gain on pump power is shown in Figure C4.52(c). From the slope of this graph the SBS gain for fused silica was measured to be $g = 3.5 \pm 0.7 \times 10^{-11}$ m/W if it was assumed that the effective interaction length over which Stokes amplification occured was the coherence length of the laser (36.5 m). This measurement of the SBS gain is close to the value calculated earlier using the linewidth and elasto-optic coefficient data and Equation (1).

The experimental setups shown in Fig C4.53 in which the fibres were pumped independently were also studied. The results obtained with the arrangement in Fig C4.53 were inconclusive. Detection of any amplified SBS was hampered by the transmitted seed signal making a second pass through the fibre. In the setup shown in Fig C4.53 all pump and SBS signals were isolated. Unfortunately, with this arrangement there was insufficient laser power to get above threshold in the source fibre.

An attempt to establish whether or not the amplified SBS was phase conjugate with the pump also proved inconclusive. Spatial information in the form of grids, wires, or knife edges, were introduced into the pump beam just before the beam splitter plate. Although the SBS beam sizes were rather too small for satisfactory conclusions to be made, visual examinations of the Brillouin backscattered beam showed no phase conjugation effects. Due to the low numerical aperture of the launched beam into the fibre, information which was contained in the higher order frequency Fourier components of the transmitted beam through the mask did not propagate into the fibre so that some spatial information of the mask pattern was lost. Furthermore, while the intensities in the principal Fourier maxima were in the SBS pump depletion regime, the pump intensities in the higher order components were low and probably not above threshold for backscsattering.

Future work to improve upon these results will concentrate on using low-powered pulsed laser sources with multimode and tapered fibres.

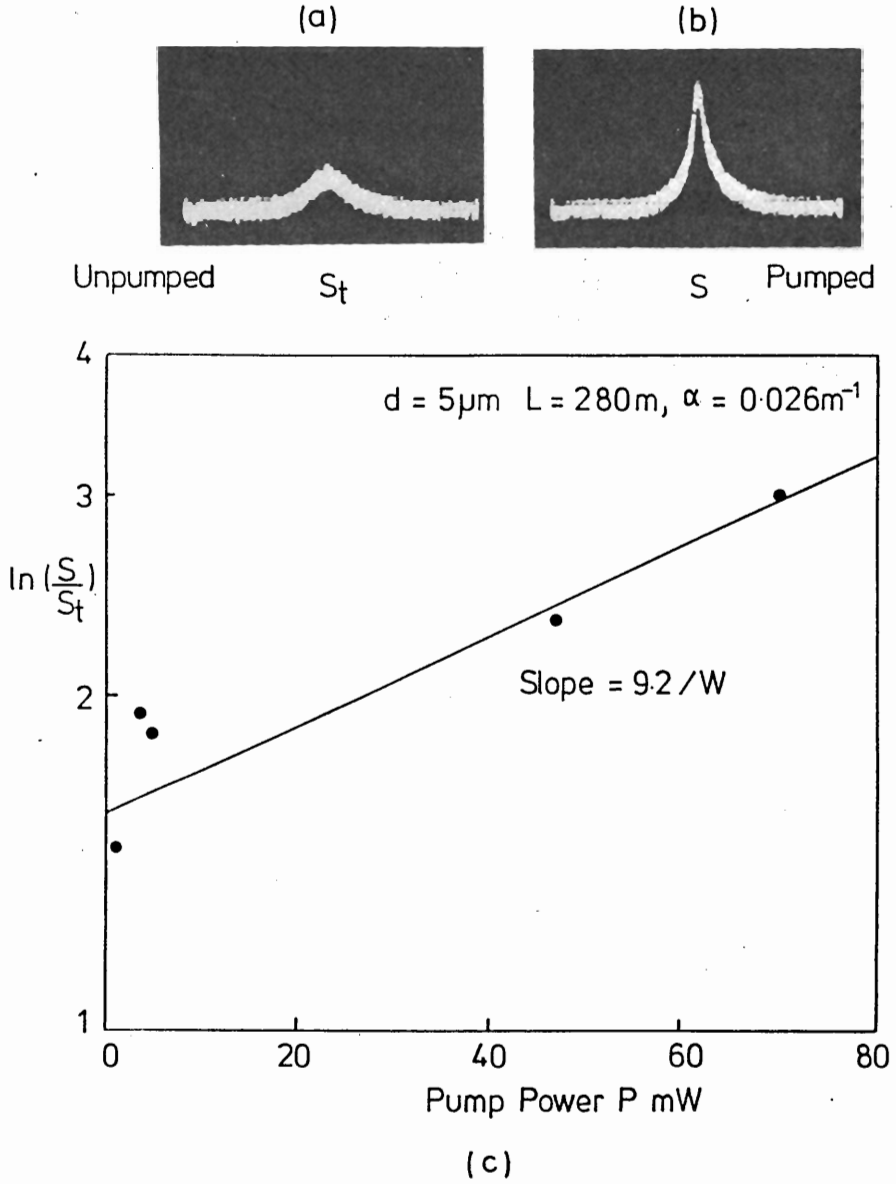


Fig C4.51

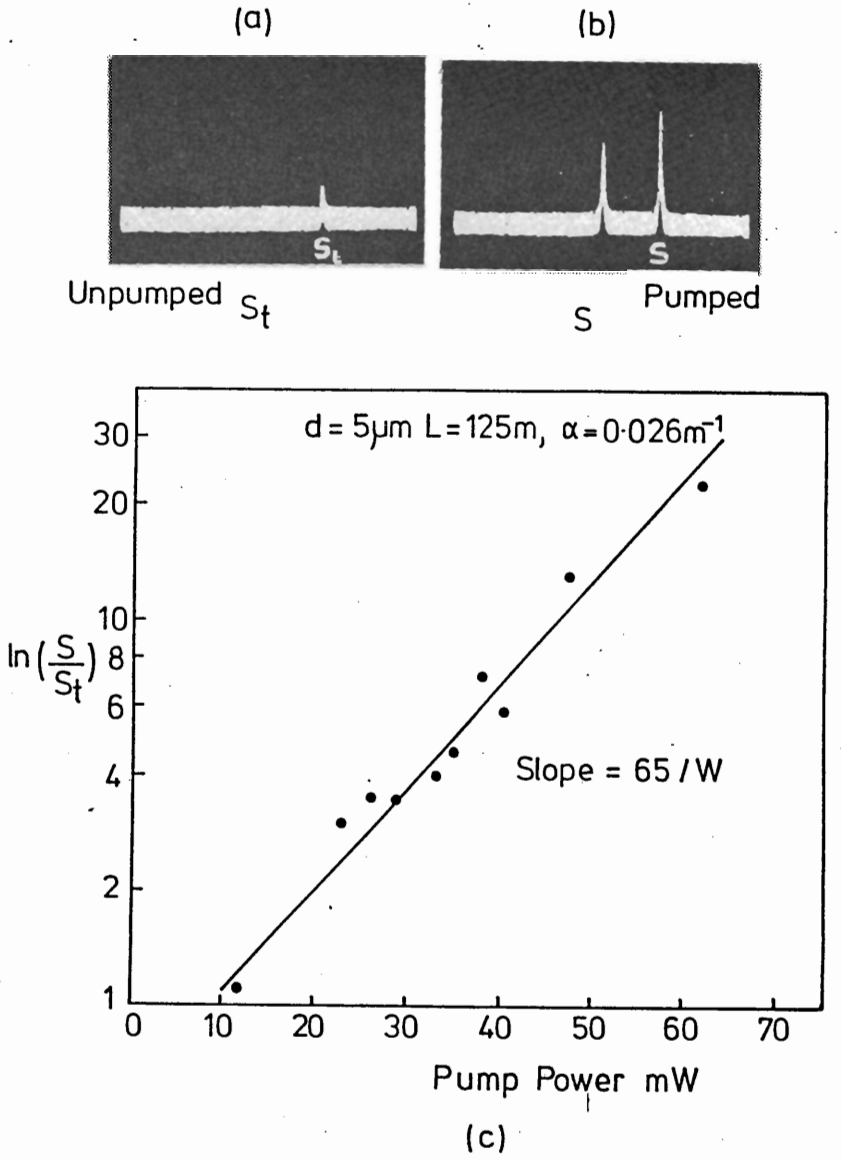
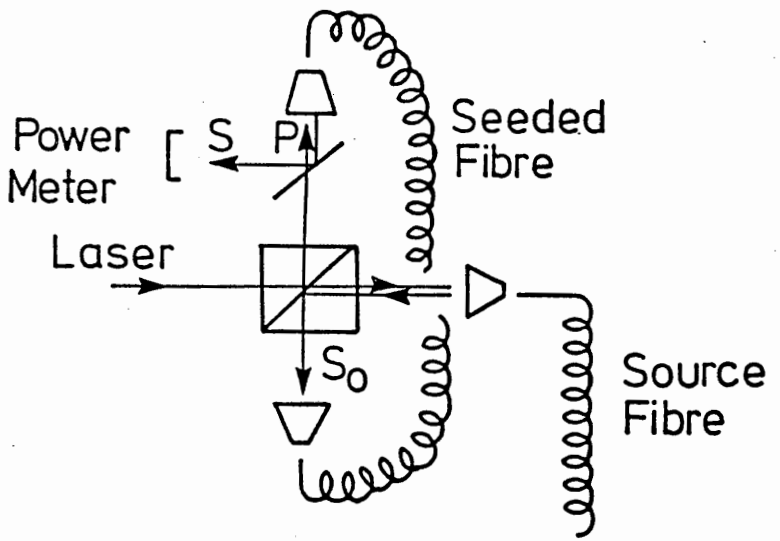
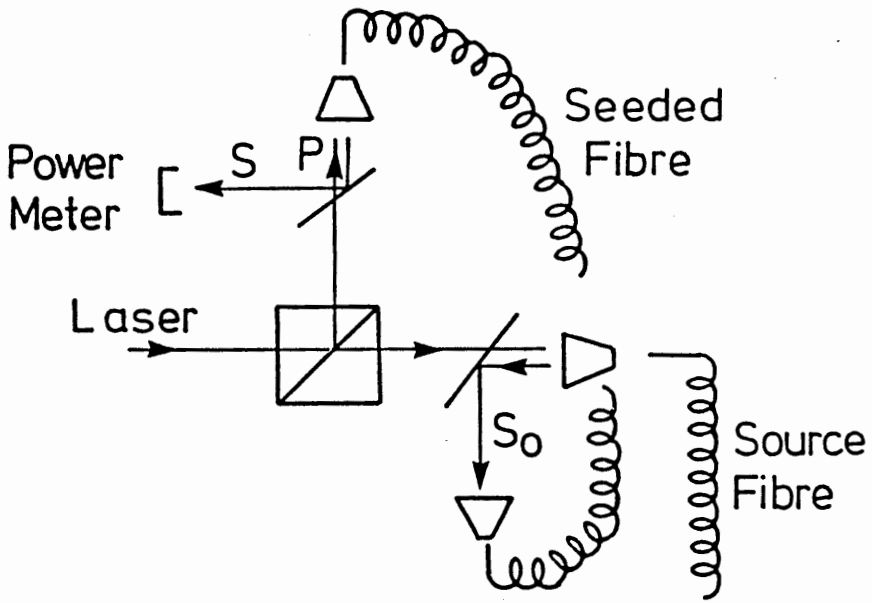


Fig C4.52


Power
Meter
S
P
Seeded
Fibre
Laser
So
Source
Fibre

(a)


Power
Meter
S
P
Seeded
Fibre
Laser
So
Source
Fibre

(b)

Fig C4.53

C5	**LASER SUPPORT FACILITY OPERATIONS**	Pages
C5.1	NANOSECOND PROGRAMME	421
C5.2	PICOSECOND PROGRAMME OPERATIONS	421
C5.3	LOAN POOL OPERATIONS	421

C5 LASER FACILITY OPERATIONS

C5.1 NANOSECOND PROGRAMME

A W Parker, S Tavender and W Shaikh (RAL)

The nanosecond facilities operated a full scheduled programme during the year. The new procedures for the maintenance and optimisation of the Raman Spectrometer led to a highly successful year in which all experiments obtained data of high technical quality.

This was aided by the use of $\beta BaBO_4$ for UV wavelengths and this is now the standard technique, replacing the line narrowed and Raman shifted excimer laser method in all but a few cases. The HX460/FL3002 XeCl-dye laser combination gave reliable operation throughout the year.

The programme of work using laser-plasma generated X-rays with the EMG 150 laser has expanded and the technique has now become standard. This laser, however, still gives problems due to its age. It proved impossible, for example to generate adequate line narrowed 193 nm output for a scheduled experiment. It is planned to replace this laser in the coming year.

C5.2 PICOSECOND PROGRAMME OPERATIONS

A J Langley and W Shaikh (RAL)

The start of the year was marred by the first significant breakdown of the laser since its installation in 1985 which resulted in the cancellation of a scheduled experiment. The problem arose during scheduled maintenance by the manufacturers. Since then operations have continued normally and a full schedule has been maintained. Development work using 50% of the output of the pump laser also continued throughout the year with the major programme being the commissioning of the copper vapour-pumped dye amplifier reported in Section C4.

C5.3 LOAN POOL OPERATIONS

A J Langley, S Tavender and W Shaikh (RAL)

During the period May 1988 to April 1989 14 laser and 6 diagnostic loans have been made to UK academic institution. Although the number of loans is less than in 1987/88 the average loan duration increased. Most of the Loan Pool users have been chemists, 17 in number, whilst 3 have been physicists. Work carried out using Loan Pool equipment has resulted in 20 publications during the period in journals, books and published proceedings.

The Loan Pool acquired an additional laser system during 1988 which, until recently, had been used in the Department of Chemistry at Edinburgh University. The system consists of a Spectron SL802 pulsed laser with doubling (532 nm) and tripling (355 nm) facilities together with a Quanta-Ray pulsed dye laser. Also acquired was a Quanta-Ray wavelength extension package for doubling and auto-tracking to the UV. The Nd:YAG laser is currently with the manufacturer receiving a full upgrade including new pumping chambers, avalanche chain switching and re-polished optical components. The system will become available in June 1989 and should provide 700 mJ at 1064 nm and $\sim$ 300 mJ at 532 nm.

The EMG101 received a full refurbishment at RAL in 1988 and despite some initial problems with performance the laser now functions well once again after a further strip-down and replacement of the internal heat exchanger. New UV tracking and etalon driver electronics were purchased for the FL3002 dye laser making the laser fully tunable through the UV (220- 400 nm).

The HE460 fluoride laser has also been refurbished at Lumonics Ltd in Rugby and has once again reached its specification. Gas lifetime measurements (with gas purifier) are currently being made.

D	**GENERAL FACILITY PUBLICATIONS**	Pages
D1	JOURNALS BOOKS AND PUBLISHED PROCEEDINGS	423-431
D2	CONFERENCE PRESENTATIONS AND UNPUBLISHED REPORTS	433-436
D3	PhD THESES	437

D1 JOURNALS, BOOKS AND PUBLISHED PROCEEDINGS

P Apte et al
Measurement of the uniformity of ablation for 0.53 μm laser irradiation of spherical targets
Optics Comms **67** 11 (1988).

J August et al
Intramolecular Charge Transfer in Jet-Cooled Aromatic Amines,
Chem Phys Letters, **145** 273 (1988).

J August et al
Photofragment vector correlations and dissociation dynamics in $HONO_2$
J Chem Soc Faraday Trans 2 **84** 587 (1988).

J August et al
Vector correlations in molecular photodissociation: $H_2O_2HONO_2$ and $(CH_3)_2COOH$
Ber Bunsenges **92** 264 (1988).

J C Austin et al
Structure and mechanistic studies of glyceraldehyde 3-phosphate dehydrogenase by UV resonance Raman spectroscopy in Spectroscopy of biological molecules - New Advances (Eds E D Schmid et al) Wiley, p121 (1988).

J C Austin, C W Wharton and R E Hester
An ultraviolet resonance Raman study of dehydrogenase enzymes and their interaction with coenzymes and substrates,
Biochem **28** 1533 (1989).

J C Austin, R E Hester
Surface-Enhanced Raman spectra of NAD$^+$ and related components
J Chem Soc Faraday Trans 1 (in press).

J E Baggott, et al
Absolute Rate Measurements for some Gas-phase Addition Rates of Dimethylsilylene
J Chem Soc Faraday Trans 2, 515 (1988).

K G H Baldwin et al
UV Thomson scattering in a dense z-pinch plasma
Plasma Phys Contr Fusion **30** 1141 (1988).

H C Barr et al
Studies of stimulated Raman scattering in a plasma filament
Phys Fluid **31** 641 (1988).

H C Barr et al
Nonlocal effects and the Raman instability
Phys Rev Lett **58** 1950 (1988).

H C Barr et al
Raman scattering from parabolic density profiles
Bull Am Phys Soc **33** 1919 (1988).

J R M Barr et al
High energy amplification of picosecond pulses at 248 nm
Opt Comm **66** 127 (1988).

J R M Barr et al
Picosecond Raman pulse combining and compression in light guides for ultra-high laser systems
Proc SPIE **874** 60 (1988).

A R Bell et al
Collisionless shocks in laser-produced plasma
Phys Rev A **38** 1363 (1988).

A R Bell, P Gibbon
Electronic nonlinearities in Langmuir waves with aplication to beatwave experiments
Plasma Phys Contr Fusion **30** 1319 (1988).

S E J Bell, K C Gordon, J J McGarvey.
Time-resolved resonance Raman spectroscopy and solution kinetics of photogenerated transients in the metal-carbene complex $(OC)_5W{=}C(OMe)Ph$
J Am Chem Soc **110** 3107 (1988).

J P Booth, G Hancock.
The radiative lifetime of $CF(A^2\Sigma^+)^1$,
Chem Phys Lett **150** 457, (1988)

T J M Boyd, R D Lonsdale, J J Sanderson.
Electron thermal transport in laser-target plasmas on the basis of Grad's 13-moment transport equations
J Plasma Physics **39** 115 (1988)

T J M Boyd, D Cooke
Morphology of self generated magnetic fields
Phys Fl **31** 651 (1988).

T J M Boyd et al
Some anomalies in the Raman spectrum from laser-produced plasmas
Laser and Particle Beams **6** 287 (1988).

T J M Boyd et al
Absolute Raman scattering from rippled density profiles
Bull Am Phys Soc **33** 2075 (1988).

T J M Boyd, H C Barr
New perspectives on Raman scattering from laser plasmas
Laser Plasma Ints, to be published.

D S Buhaenko et al
The dynamic interaction of triethylgallium with GaAs (100) surfaces monitored using optical second harmonic generation. Presented at ISSC-8 Liverpool, March 1989; to appear in J Condensed Matter.

D S Buhaenko et al
Surface studies during growth of GaAs in Mechanisms of reactions of organometallic compounds with surfaces
in Proceedings NATO Workshop, 1988, Plenum p 145 (1989)

R S Chittock et al
UV resonance Raman studies of glyceraldehyde 3-phosphate dehydrogenase
Biochem Soc Trans **13**, 930 (1988)

K Codling et al
Multiphoton ionisation of H_2 and D_2 using an intense sub-picosecond laser
J Phys B **21** L433 (1988).

S E Coe et al
Study of shock coalescence in laser-irradiated targets
Appl Phys Letts, to be published.

A Collins et al
Resonant excitation of the GR centre in diamond
J Phys C Solid State Phys **21** L161 (1988).

N P J Cotton et al
The coupling between protonmotive force and the pyridine nucleotide transhydrogenase in chromatophores from photosynthetic bacteria
European J Biochem, to be published.

A E Dangor, A K L Dymoke-Bradshaw, A Dyson.
New techniques for laser scattering in plasmas
J Appl Phys **64** 6182 (1988).

A E Dangor et al
Forced Raman scattering in nitrogen of a two frequency laser beam,
J Phys B, 797 (1989).

S J Davidson et al
Investigation of the opacity of hot, dense aluminium in the region of its K-edge
Appl Phys Letts **52** 847 (1988).

G M Davis et al
Excimer laser direct etching of GaAs
J Phys D: Appl Phys **21** 683 (1988)
Eng Optics, August 333 (1988).

G M Davis et al
Plasma X-ray source for lithography generated by a ∿ 30 J, 30 ns KrF laser
Appl Phys Lett **53** 1583 (1988).

A Djaoui et al
Interpretation of EXAFS data from laser-shock compressed plasmas
Plasma Phys and Controlled Fusion **31** 111 (1989).

J A Dyet, M R S McCoustra and J Pfab
The spectroscopy, photophysics and photodissociation dynamics of jet-cooled CF_3NO
J Chem Soc Faraday Trans 2, **84** 563 (1988).

A Dyson et al
Measurements of the heat flux, inverse bremsstrahlung absorption and equilibration in an under-dense laser heated plasma.
Plasma Physics and Controlled Fusion **30** 1259 (1988).

A E Dyson, A E Dangor, A K L Dymoke-Bradshaw.
Sideband generation by coherent Raman scattering in quartz of an intense two frequency laser.
J Phys B (1989) (In press).

E M Epperlein et al
2-D non-local electron transport in laser-produced plasmas
Phys Rev Lett **61** 2453 (1988).

E M Epperlein et al
A code for the solution of the Vlasov-Fokker-Planck equation in 1-D or 2-D, Comp Phys Comm, to be published.

E H Evans et al
Picosecond absorption measurements of photosystem 1 from the cyanobacterium, Chlorogloea Fritschii.
Presented at 5th European Bioenergetics Conference, Aberystwyth UK, 1988, EBEC Reports **5** 174, (1988).

T W Ford et al
Comparision of soft X-ray contact microscopy with other microscopical techniques for the study of the fine structure of plant cells, X-ray microscopy II (D Sayre et al, eds), Springer-Verlag 403 (1988).

E Gamaly et al
Physics of Laser Driven Implosions
Sov Phys Uspekhi (to be published).

T Garvey et al
The SERC plasma beatwave experiment, in High Brightness Accelerators, Ed. Hyder, Rose, Guenther, Plenum Press, New York and London 755 (1988).

P Gibbon, A R Bell
Cascade focusing in the beatwave accelerator
Phys Rev Lett **61** 1599 (1988).

M Gower, P Hribek
Mechanisms for interally self-pumped phase conjugate emission from $BaTiO_3$ crystals
J Opt Soc Am **5** 1750 (1988).

M Grande et al
Assessment of multilayer mirror for XUV use - X-ray Multilayer Mirrors
Proc SPIE **913** (1988).

M Grande et al
Twenty-fold increase in thermonuclear yield in laser driven compression, Las Part Beams, to be published.

T A Hall et al
Experimental observation of ion correlation in dense laser-produced plasma
Phys Rev Lett **60** 2034 (1988).

K H Hassan and J M Hollas.
Supersonic jet fluorescence spectroscopy of 1,3-benzodioxole: a non-planar (C_2) structure in S_0, Chem Phys Lett, in press.

P A Hatherly, L J Frasinski, K Codling.
Multiphoton ionisation of n-alkanes using an intense sub-picosecond laser
Chem Phys Lett **149** 477 (1988).

R E Hester et al
Ultraviolet resonance Raman spectra of an enzyme-substrate intermediate of papain
J Raman Spectrosc **18** 211 (1988).

R E Hester et al
Functional activity of haemoglobins adsorbed on colloidal silver: a surface-enhanced resonance Raman study
J Phys Chem **92** 2044 (1988).

R E Hester, H R Virdee
In situ resonance Raman investigation of a polypyrole-modified electrode
Croatica Chimica Acta **61** 355 (1988).

C Hills et al
Laser plasma soft X-ray sources; overcoming the debris problem by means of relay optics X-ray Microscopy II
(D Sayre et al, eds) 50 (Springer, Berlin 1988).

J M Hollas and M Z bin Hussein.
The C(1)-C(α) torsional potential function of 2-fluorostyrene from S_1-S_0 fluorescence in a supersonic jet
Chem Phys Lett **154** 14 (1989).

J M Hollas and M Z bin Hussein.
The C(1)-C(α) torsional potential function of cis- and trans-3-fluorostyrene by supersonic jet spectroscopy
Chem Phys Lett **154** 228 (1989).

J M Hollas and M Z bin Hussein
The 291 nm band system of 3-fluorostyrene: ground state vibrational assignments for the cis and trans rotamers from their supersonic jet spectra,
J Mol Spectroscopy, in press.

B Howells et al
'Spectroscopy at Low Temperatures'
J Chem Soc Faraday Discuss **86** (1988).

T J Kemp
New insights into a clasical problem: the photochemistry of $[Mo(CN)_8]^{3-}$ and $[W(CN)_8]^{3-}$ ions
J Int Rec Mat, to be published.

M H Key et al
Review of progress at the UK Central Laser Facility in developing XUV lasers based on recombining laser-produced plasmas,
SPIE Proc **913** (1988).

M H Key et al
Twenty fold increase in thermonuclear reactions yield in laser driven compression
Opt Comm to be published.

M H Key
Energy transport in laser produced plasmas, Handbook of Plasma Phys III, S Witkowski, A Rubenchick eds, North Holland Phys, to be published.

M H Key
XUV Lasers
Phys Bull **344** (1988).

M H Key et al
XUV lasers - a survey of progress
UV and X-ray Spectr of Astrophysical and Lab Plasmas
J Physique Colloque, **C1 49** 185 (1988).

M H Key
Some recent progress at the SERC Central Laser Facility in high power laser development and experimental applications to X-ray lasers short pulse energy transport and implosions
Las Part Beams, to be published.

M H Key
XUV and X-ray spectroscopy of laser produced plasmas in Astrophysical and laboratory plasma spectroscopy,
D Brown and J Lang Eds, Publ Edinburgh Univ (1988).

M H Key
XUV lasers
J Mod Opt **35** 575 (1989)

A Kvaran et al
Vibrational relaxation in KrF and XeCl by rare gases
Appl Phys **B46** 95 (1988).

M R Levy
Chemiluminescence and energy transfer in Mn + N_2O collisions at high translational energy
J Phys Chem (1989) (In press)

C L S Lewis et al
Status of soft X-ray research at RAL
Plasma Phys Contr Fusion **30** 35 (1988).

J P Marangos et al
HeII Balmer series line shifts in a dense z-pinch plasma
J Phys **B21** 3357 (1988).

M R S McCoustra, J A Dyet and J Pfab
The state-selected predissociation dynamics of $CC1F_2NO$
Laser Chem **9** 289 (1988).

J J McGarvey, S E J Bell, K C Gordon.
Single- and two-color pulsed laser resonance Raman spectroscopy of excited states of Bis(2,9-dimethyl-1,10-phenanthroline)copper(I) in Solution
Inorganic Chemistry, **27** 4003 (1988).

A G Michette et al
The potential of laser plasma sources in scanning X-ray microscopy,
X-ray Microscopy II,
(D Sayre et al, eds), 59 (Springer, Berlin 1988).

A G Michette et al
A laser-generated plasma source for X-ray lithography and VLSI
J Phys E: Sci Instrum **21** 959 (1988).

J N Moore et al
Time resolved resonance Raman spectroscopy applied to the photochemistry of the sulphonated derivatives of 9, 10-anthraquinone
J Phys Chem **92** 5619(1988).

B A Omar et al
The application of doped fluorescers to the recording of pulsed UV laser beam profiles,
Optics Laser Tech **20** 193 (1988).

D Phillips
Applications of lasers in photobiology and photochemistry
Radiation Measurements in Photobiology, ed B L Diffey, Academic Press (London) to be published.

D Phillips, G Rumbles
Time-resolved laser spectroscopy, Nanosecond and picosecond techniques, principles, devices and applications.
Applications of Lasers in Polymer Science and Technology, eds J P Fouassier and J Rabek, CRC press, to be published.

F O'Neill et al
Plasma X-ray sources for lithography generated by a 0.5 J KrF laser,
Proc SPIE **831** 230 (1988).

F O'Neill et al
KrF laser-plasma X-ray sources for lithography
IPO Short Meetings **10** 31 (1988).

R S Richards et al
X-ray contact microscopy, using synchrotron and laser sources, of ultra-sectioned, heavy metal contaminated earthworm,
X-ray Microscopy II, Springer series in Optical Sciences **56** 343 (1988).

R S Richards et al
Comparison of synchrotron and laser sources in X-ray contact microscopy of metal-contaminated biological tissue
Nucl Instr Meth **A272** 889 (1988).

I N Ross et al
High resolution holographic image projection at visible and ultraviolet wavelengths
Appl Opt **27** 967 (1988).

A M Rogoyski et al
Characterisation and optimisation of a laser generated plasma source of soft X-rays
Laser Part Beams **6** 225 (1988).

B A Shiwai et al
Experimental observation of ion correlation in high density plasmas
SPIE Proc **913** 91 (1988).

J P Simons.
Solvation,
J Chem Soc Faraday Discuss **85** (1989) in press.

A D Stead et al
Soft X-ray contact microscopy of botanical material using laser-produced plasmas or synchrotron radiation
X-ray microscopy II (eds D Sayre et al) Springer-Verlag 433 (1988).

G J Tallents et al
The production of hot above critical density plasmas by thermal and superthermal electron energy transport
Las Part Beams, to be published.

P Thomas, M Key
Plasma set to ignite?
Phys World **1** 20 (1988).

I C E Turcu et al
A M Rogoyski, C P Hills and A G Michette
Calibration of a KrF laser-plasma source for X-ray microscopy applications
Proc SPIE **831** 211 (1988).

C W Wharton et al
Vibrational spectroscopy of atomic interactions in enzyme-substrate intermediates, Spectroscopy of biological molecules - New Advances (Eds E D Schmid, F W Schneider and F Siebert) Wiley, 95 (1988).

L R Zink et al
The Dispersed Fluorescence of Nickel Dichloride under Molecular Beam Conditions: a Determination of Ground-State Vibrational Intervals. Chem Phys Lett, **146** 501, (1988).

D2 CONFERENCE PRESENTATIONS AND UNPUBLISHED REPORTS

19th European Conf Laser Interaction with Matter (ECLIM), Madrid (1988):

J E Andrew
Multiplexed picosecond pulse amplification in KrF followed by Raman beam combining for ultra-high power laser systems.

H C Barr et al
Global modelling of stimulated Raman scattering from inhomogeneous plasmas.

A Dajoui, T A Hall
Calculations of X-ray absorption structure above the K-edge of hot compressed aluminium.

S Davidson et al
K-shell absorption spectra from a dense aluminium plasma.

G M Davis et al
Plasma X-ray source at 1.0 keV ≤ hν ≤ 1.4 keV generated by = 30 J, 30 ns KrF laser pulses.

E Fabre et al
Implosion experiments at 0.26 μm.

A Giulietti
Study of stimulated Raman and brillouin scattering of an intense laser beam smoothed by a random phase plate or flye-eye lens in millimetre sized plasmas.

M Grande, A Ridgeley
Comparison of electronic array devices with X-ray film as detectors of X-rays in the 1 keV region.

M Grande et al
Twenty-fold increase in thermonuclear reaction yield in laser driven compression.

T A Hall et al
Experimental measurement of electrical conductivity of a dense plasma using a skin depth technique.

T A Hall et al
Improved EXAFS studies of shock compressed dense plasmas.

T A Hall, L M Newell
Rapid growth of filamentation in an overdense plasmas.

M H Key et al
Some recent progress at the SERC Central Laser Facility in laser development and experimental applications to X-ray lasers, short pulse energy transport and implosions.

M H Key et al
The production of hot above-critical density plasma by thermal and superthermal electron energy transport

C L S Lewis et al
Time-resolved gain measurements on Li-like Al transitions between 10.3 and 15.4 nm.

G J Rickard et al
Fokker-Planck simulations of short-pulse laser-plasma experiments

R Brown
Time-resolved spectroscopy of photosynthesis systems. Presented at 2nd Biophysics and Synchroton Radiation Conference, Chester UK. 1988.

G M Davis et al
Excimer laser direct etching of GaAs
3rd BACG Photochemical Processing Workshop, Heriot Watt Univ (1988).

XVI Int Conf Quantum Electronics, Tokyo, Japan
Japan Soc Appl Phys, July 18-21, 156 (1988):

J E Andrew et al
Multiplexered picosecond pulse amplification in KrF followed by Raman beam-combining for ulta-high-power laser systems.

G M Davis, M C Gower
Experimental investigation of the properties of stimulated Brillouin scattering of a variable coherence length KrF excimer laser.

Y Kato et al
Extension of recombining plasma laser with Balmer-α transition to shorter wavelength.

18th Anomalous Absorption Conf, L'Esterel
Quebec, Canada (1988).

H C Barr et al
Raman scattering from a paraboloid density profile.

A Dyson et al
Heat flux inverse Bremsstrahlung and equilibration in underdense plasmas.

European Gordon Conf "Molecular Electronic Spectroscopy", Ile D'Oleron (1988).

M Brouard et al
Photofragment vector correlations in vibrationally mediated photodissociation: a new angle on intramolecular vibrational redistribution

M Brouard et al
Photofragment vector correlations in single photon and vibrationally mediated photodissociation
7th European Conf Dynamics of Molecular Collisions, Assissi (1988).

Proc 35th Scottish Univ Summer School in Physics "Laser-plasma Interactions 1988", ed M B Hooper, SUSSP, Edinburgh (1989):

M H Key
Introduction to the physics and applications of laser produced plasmas.

C L S Lewis
Plasma-based soft X-ray lasers

F O'Neill
Laser-plasma XUV sources.

S J Rose
Dense plasma physics.

M H Key
Physics and applications of laser produced plasmas
Baghdad Symp Plasma Physics (1988), to be published.

K S Richards et al
Soft X-ray contact imaging of biological material, both living and sectioned, using synchrotron and laser sources
2nd Int Conf Biophysics and Synchrotron Radiation, Chester (1988).

2nd European Conf Spectroscopy of Biological Molecules, Freiburg (1987):

J C Austin et al
Raman studies of glyceraldehyde-3-phosphate dehydrogenase

J de Groot et al
A surface enhanced resonance Raman study of the functional activity of haemoglobins adsorbed at a colloidal silver surface.

R E Hester, J C Austin
Spectroscopic studies of biological systems.

Proc 11th Conf Raman Spectroscopy, Wiley (1988):

J C Austin et al
UV resonance Raman studies of the enzyme glyceraldehyde-3-phosphate dehydrogenase.

S E J Bell et al
Resonance Raman spectroscopy of a water-soluable cytochrome P450 model system.

J J McGarvey
Time-resolved Raman spectroscopy using single and two-colour pulsed laser techniques

S Umapathy et al
Raman spectroscopic studies of species of semiconductor surfaces

S Umapathy et al
Time-resolved resonance Raman spectroscopy of photosensitizers

J P Marangos
VUV measurements of plasma line shapes
9th Int Conf Spectral Line Shapes (1988)

10th Int Symp Gas Kinetics, Swansea (1988):

J E Baggott et al
Time resolved studies of the kinetics of the reactions of Dimethyl silylene.

M Brouard et al
Photofragment vector correlations in single photon and vibrationally meduated photodissociation.

P A Giovanacci et al
Photodissociation of jet-cooled NMCA in the near-uv

P A Giovanacci et al
The 35 nm photodissociation of jet-cooled alkyl thionitrites.

K Codling, L J Frasinski
Laser-molecule interactions at high intensities
NATO ASI Meeting on Atoms in Strong Fields, Kos (1988).

N H Rizvi et al
A laser plasma X-ray source, Presented at Lasers 88, Lake Tahoe (1988).

International Quantum Electronics Conference (IQEC) (1988)

J E Andrew et al
Multiplexed picosecond pulse amplification in KrF followed by Raman beam combining for ultra-high-power laser systems.

M H Key
Laser sources of XUV and VUV, Third European conference in atomic and molecular physics, Bordeaux (1989).

M H Key
XUV lasers, CERN School of Synchrotron and Free electron lasers, Chester (1989).

M H Key et al
X-ray laser research at the Rutherford Appleton Laboratory, International Congress on Optical Science and Engineering, Paris 1989.

M H Key
A physical model of the scaling to short wavelength of XUV lasers operating by recoimbination to hydrogenic ions
Rutherford Appleton Laboratory Report (in press).

M H Key
Design constraints for Raman amplifiers in high power KrF laser systems with optical multiplexing and Raman beam combining Rutherford Appleton report (in press).

J J McGarvey.
Intramolecular rearrangements versus solvent interactions in photogenerated transients in metal carbene complexes, Annual Meeting of Fast Reactions in Solution Group 1988 at Bielefeld.

D3 PhD THESES

A E Dyson.
Measurements on under-dense plasmas with intense lasers and experiments on the laser-plasma beat wave, PhD, University of London, 1989.

A M Ellis
Some Studies of the Electronic Structure of Small Molecules and Solid Metal Oxides, PhD, University of Southampton, 1989.

I T F Gillan.
Laser frequency up-conversion schemes in vibrationally inverted molecular systems, PhD Queen's University Belfast, 1988.

M J McAllister.
Photoacoustic spectroscopy of colour centres in crystals, PhD, Queen's University Belfast, 1988.

I Burghardt
A high resolution study of the D-state of Cu Cℓ, Diploma Thesis, University of Bonn, 1988.

E **APPENDICES**

A1.8 INTENSITY MEASUREMENTS OF A MONOCHROMATIC X-RAY BEAM FORMED BY A SPHERICALLY BENT CRYSTAL

A1.9 MEASUREMENT OF X-RAY SPECTRAL LINE WAVLENGTHS BY USING DOUBLE BRAGG REFLECTION

A2.4 BEAT-WAVE EXPERIMENT

A3.3 LASER COMPRESSION OF HIGH ASPECT RATIO DEUTERIUM TRITIUM FILLED SHELLS

A3.4 HOT MATTER STOPPING POWER

A3.5 ALPHA PARTICLE RADIOGRAPHY OF RAYLEIGH-TAYLOR INSTABILITY

C2.5 INVESTIGATION OF FAST ABSORBANCE CHANGES IN PHOTOSYSTEM I

APPENDIX

A1.8 INTENSITY MEASUREMENTS OF A MONOCHROMATIC X-RAY BEAM FORMED BY A SPHERICALLY BENT CRYSTAL

A Ridgeley, C Danson, N Rizvi, R Bann (RAL)
A M Maksimchuk, A V Rodé, G V Sklizkov (PN Lebedev Physical Institute, USSR)
E Forster, I Ushmann (Friedrich-Schiller-University Jena, GDR)

Introduction

The usefulness of using a monochromatic X-ray backlighting beam for the diagnostics of dense laser-produced plasmas has already been demonstrated[1,2].

In order to conduct experiments on active X-ray diagnostics the transmitted beam flux in the registration plane must exceed that of the self-emitted plasma radiatoin within a given wavelength range.

A specific scheme to form a monochromatic transmitted X-ray beam has been proposed by Kalashnikov et al[3] and is reproduced in Fig A1.30. By inserting the pinhole apertue P at the image plane of the backlighting source (the aperture size must not be larger than the backlighting source image) the energy demands of the backlighting source can be reduced considerably. When the spectral reflection bandwidth of the focussing crystal coincides with spectral line emission from the backlighter source there exists the possibilities of measuring laser intensity, short timescale effects and high spatial resolution effects in the dense plasma.

The analysis of absorption and refraction of the X-ray transmitted beam in the dense plasma[3] indicates that the spectral range 7-10 Å is optional for diagnostics of the plasma regions with the highest dnesity. A transmitted beam of wavelength = 10 Å is essentially not absorbed in a plasma with density 10^{22}-10^{23} cm^3 but refraction is considerable and may reach 0.1°.

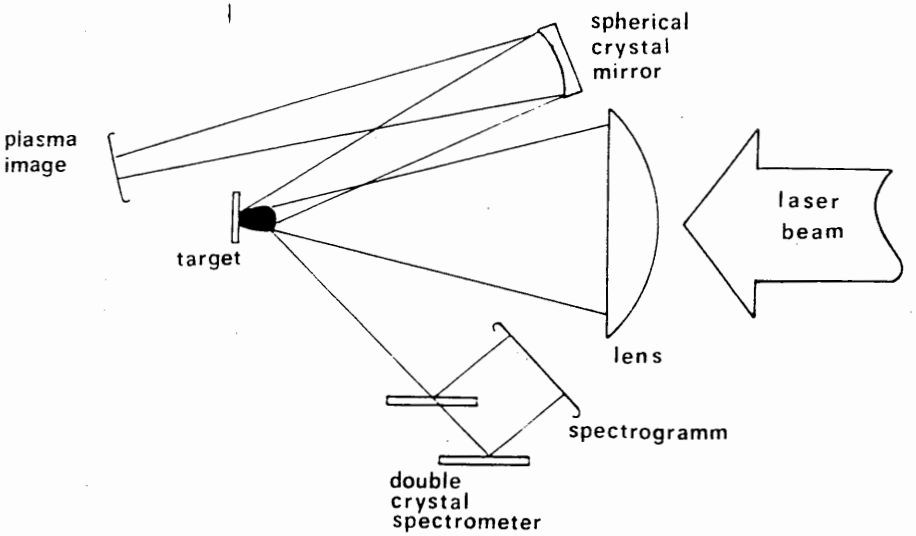
The aim of experiments carried out in Target Area 4 target vessel of the Central Laser Facility, RAL, was the optimisation of the system "focusing crystal - X-ray backlight source" by selecting the target material in the backlighting scheme. A comparison of K-, L-, M-spectrum intensities of the plasma radiation in the narrow spectral range was made. The brightness of an X-ray monochromatic beam formed by the spherically-bent focusing crystal was determined.

Experimental conditions

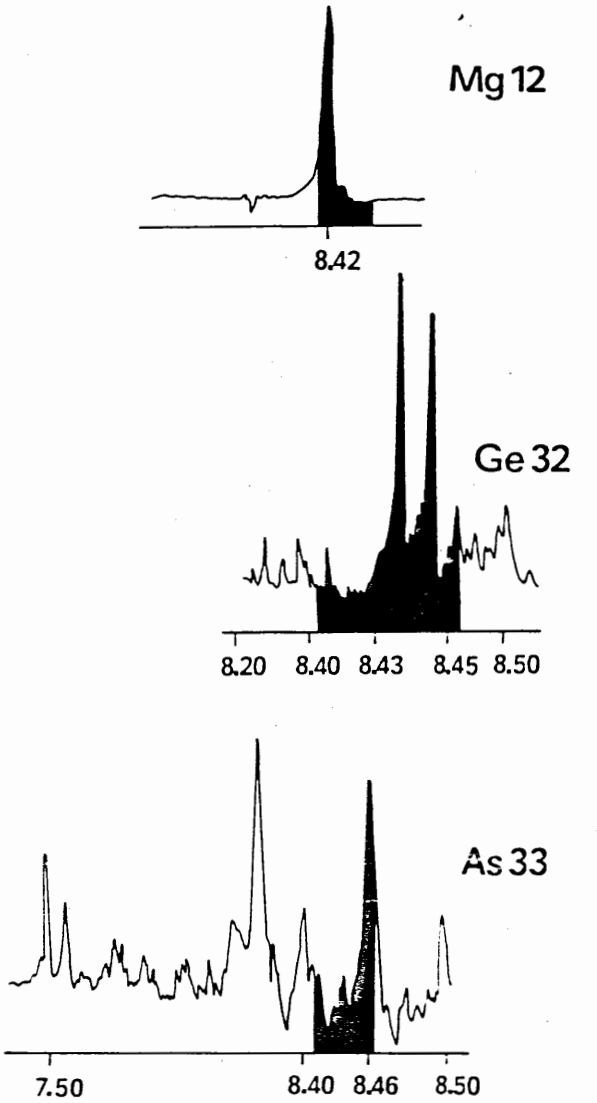
The experimental scheme is given in Fig A1.31. The radiation from a Nd:laser with energy of 10 J, duration of 0.6 ns, is focused on the target surface, the flux density being 5.10^{13} W/cm^2.

The X-ray quantum monochromatic beam is formed by a spherically-bent crystal of Q[1010], 2d = 8,509 Å, with diameter of 24 mm and curvature radius of 300 mm. The spectral range of X-ray radiation reflected at a crystal and then focused depends on the crystal curvature radius, crystal diameter, the magnification of the scheme and radiation incident angle[4]. To measure the beam brightness in the image plane and compare the different target radiation intensities the range of 8.41-8.46 Å is chosen. The Ly_α Mg(XII) lines and the corresponding dielectronic satellites are in this range, the incident Bragg angle is 82°, and the magnification is equal to 2.

The control of spectral line alignment in the focusing cyrstal reflection range is realised by the double-crystal quartz spectrometer which offers the possibility of the absolute measurements of X-ray spectral wavelengths[5]. For instance, Fig A1.31 shows the K-spectrum of magnesium and the L-spectrum of germanium and arsenic, in which is marked the spectral width of the monochromatic beam obtained. The plasma radiation lines contained in the given range are clearly seen. The specral interval positon



A1.30 The experimental scheme.



A1.31 X-ray spectrum of magnesium, germanium and arsenic. The spectral range of 8.41 Å - 8.46 Å, where the X-ray quantum monochromatic beam is formed, is marked. Intensity scale on the spectra is different.

may be changed[4] by scanning the focusing cyrstal Bragg angle and its width is varied with the aperture diaphragm or by changing the magnification.

The intenstiy measurements are carried out in the soure image plane with the help of DEF-2 film which was developed in a standard developer Kodak-D19.

Results

Fig A1.32 shows the results of intensity measurements of a monochromatic beam in the laser plasma image plane when different materials are used as a target. The targets irradiated K-spectrum (magnesium, aluminium, silicon), L-spectrum (copper, germanium, arsenic, selenium, bromine) and M-spectrum (samarium, europium, gadolinium, terbium, dysposium, holmium, erbium) are compared.

Based on the results mentioned above the following conclusions are made concerning the intensity of different target radiation within the range of 8,41-8,46 Å:

1. The X-ray intensity of magnesium K-spectrum is twice or three times as much as that of aluminium and silicon, because the Mg(XII) Ly_{α}-line is aligned in the spectral range registered, whereas aluminium and silicon form a beam only in the continuum radiation.

2. The beam intensity when L-spectra of elements with Z = 29-33 and M-spectra with Z = 64-68 are used is higher than that of a beam with the Mg(XII) K-spectrum by an order of nearly as the spectral lines are in this spectral range.

3. The continuum recombination K-, L-, M-radiation of different element ions is practically similar as seen form the comparison of intensities of Al13, Si14, Br35, Sm62, Eu63, for which spectral lines are not in the range of the monochromatic beam formation.

Thus, as the results given show, the use of line emission in L- and M-spectra coincident with the wavelength band of a backlighting scheme comprising an X-ray monochromatic beam formed by a focusing crystal enables one to improve the beam brightness by nearly an order of magnitude.

References

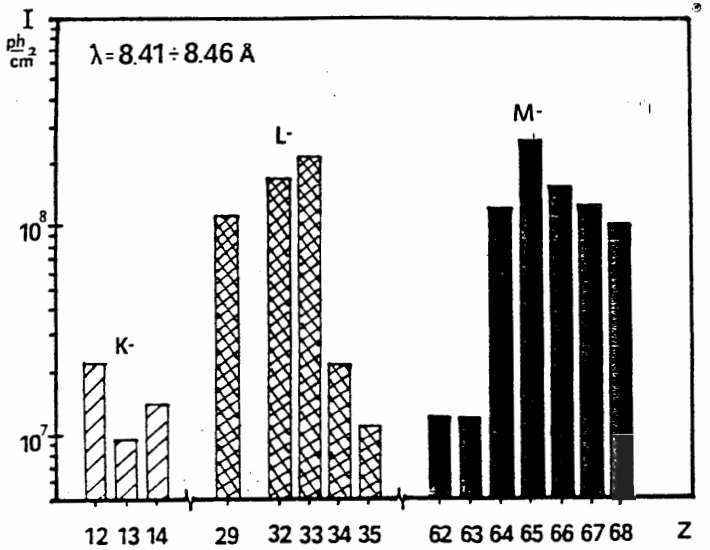
1. C L S Lewis, J McGlinchey
"Quasimonochromatic projection radiography of dense laser driven spherical targets", Opt Comm **53** no 3, 179 (1985).

2. "X-ray radiography of Laser Fusion Targets" in
H G Ahlstrom "Physics of Laser Fusion" **II** Univ of California LLL, UCRL-53106, 129 (1979).

3. M P Kalashnikov, G Korn, M Yu Mazur et al
"Images of shell targets laser-produced plasma in the light of intrinsic and backlight X-ray radiation", Prepring Lebedev Physical Inst, no 70, 48 (1989).

4. N G Basov, Yu A Mikhailov, A V Rodé, G V Sklizkov
"Spherically bent crystals for X-ray diagnostics" Laser Division Annual Report 1988, A7-4, 149 (1988).

5. A Ridgeley et al
"Measurements of X-ray spectral line wavelengths by using double Bragg reflection", Laser Division Annual Report 1989.



A1.32 The intensity of an X-ray quantum monochromatic beam in the plasma image plane, different materials are used as a target.

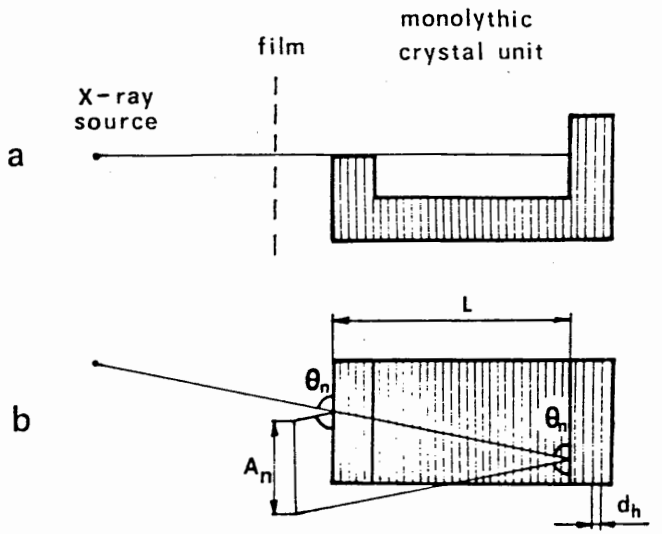


Fig A1.33 Scheme of a monolithic crystal for absolute wavelength measurements, (a) side-view, (b) top-view, (d is not in scale, h characterises orientation of net planes).

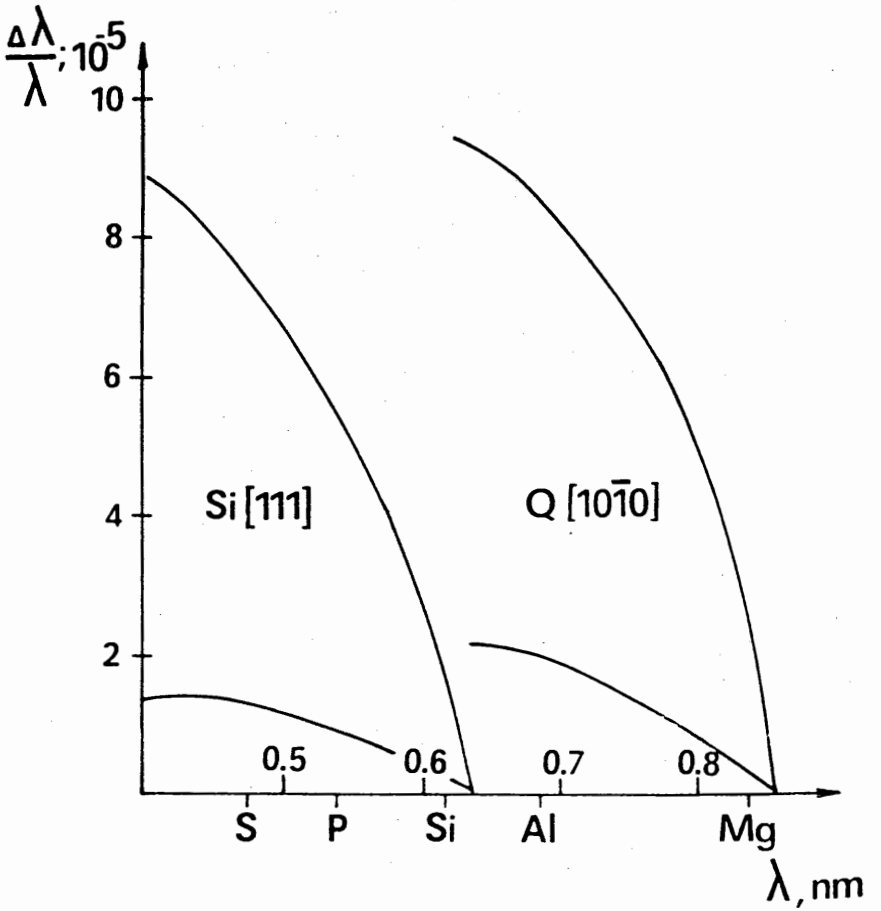


Fig A1.34 Accuracy of wavelength measurements for Si and Q monolithic crystal units depending on wavelength and measuring errors of parameters (position of Ly_α lines is shown, explanations are in the text).

APPENDIX

A1.9 MEASUREMENT OF X-RAY SPECTRAL LINE WAVELENGTHS BY USING DOUBLE BRAGG REFLECTION

A Ridgeley, C Danson, N Rizvi, R Bann (RAL)
A M Maksimchuk, A V Rodé, G V Sklizkov (PN Lebedev Physical Institute, USSR)
E Forster, K Goetz, I Ushmann (Friedrich-Schiller-University Jena, GDR)

Introduction

The absolute values of X-ray spectral line wavelengths are traditionally determined by comparison with reference line wavelengths being used as standards. Problems can arise connected with the fact that both the characteristic lines of neutral atoms and the spectral lines of multicharged ions may be shifted or broaden asymmetrically due to either the Doppler effect plasma effects (the Stark effect, the plasma polarisation).

In this paper the feasibility of making laser plasma X-ray spectral line measurements not using standard wavelengths is discussed. The Bragg reflection at two crystal planes parallel to each other and which have the same orientation is proposed. The first measurements of the Mg (XII) Ly_α doublet with accuracy $\Delta\lambda/\lambda \cong 5.10^{-5}$ show that the method proposed may be used to diagnose dense laser plasmas.

The Measuring Method

Fig A1.33 shows the wavelength measuring scheme by using monolithic or crystal block, with parallel reflecting planes disposed etalon fashion. The crystal surfaces should be parallel to the reflection planes and similar in orientation as well as in space.

In this way, X-ray wavelength of pulse sources can be evaluated from accurate measurements of three distances:

1. atomic planes, d_h,
2. distance between the reflecting surfaces L, and
3. shifts of corresponding lines on film A.

From the geometry of Fig the Bragg angle may be determined

$$\cot \theta_n = \frac{A_n}{2L} \qquad (1)$$

hence X-ray wavelengths

$$\lambda_n = 2d_n, \; \mathrm{Sin}\theta_n = 2d_n, \; [1 + (\frac{A_n}{2L})^2]^{-\frac{1}{2}} \qquad (2)$$

The reflection correction of the Bragg's law has to be applied to eq 2, especially, if softer X-rays (which are typical for laser-produced plasmas) are analysed. This leads to

$$\lambda_n = 2d_n, \; \{[1 + (\frac{A_n}{2L})^2]^{-\frac{1}{2}} - \delta \; [1 + (\frac{A_n}{2L})^2]^{\frac{1}{2}}\} \qquad (3)$$

Here $\delta \cong 10^{-5} - 10^{-4}$ is the deviation of the X-ray refraction index from unity.

In practice the effect of the small angular deviation α between crystal surfaces and atomic planes has to be considered. In this case eq 1 is modified to a more complicated form

$$\mathrm{cat}\,(\theta_n - \alpha) + \mathrm{cat}\,(\theta_n - \alpha) = \frac{A_n}{L} \qquad (4)$$

The accuracy of wavelength measurements is mainly determined by measuring errors in the distances d_h, L, A_n. Due to the small

values of the errors their influence on deviations α, δ can be neglected. Thus the influence of d_h, L, A_n on $\Delta\lambda$, $\Delta\lambda/\lambda$, respectively, can be obtained by differentiating Eq 2:

$$\left|\frac{\Delta\lambda}{\lambda}\right| = \left|\frac{\Delta d_n}{d_n}\right| + \frac{(\frac{A_n}{2L})^2}{1+(\frac{A_n}{2L})^2}\cdot\left(\left|\frac{\Delta L}{L}\right| + \left|\frac{\Delta A_n}{A_n}\right|\right) \qquad (5)$$

Fig A1.34 shows this dependence for monoliths using Si (111) and Q (1010) reflections, respectively.

The factor $(\frac{A_n}{2L})^2/[1+(\frac{A_n}{2L})^2]$ is equal to $\cos^2\theta_n$, consequently, the two left curves drop down to $\lambda = 2d_{Si} \cong 0.627$ nm and the two right ones to $\lambda = 2d_Q \cong 0.851$ nm. The upper Si curve corresponds to $\Delta A_n = 10$ μm, $\Delta L = 5$ μm, $\Delta d = 2.10^{-7}$ nm and the lower one to $\Delta A = \Delta L = 1$ μm, $\Delta d = 2.10^{-7}$ nm. The assumed errors for the quartz curves are calculated with $\Delta L = 1$ μm, $\Delta d = 5.10^{-7}$ μm, $\Delta A_n = 10$ μm and $\Delta A_n = 1$ μm for the upper and lower curve, respectively.

One can see that with possible measuring errors $\Delta L = \Delta A = 1$ μm an accuracy $\Delta\lambda/\lambda = 2.10^{-5}$ is obtained in spectral interval from 0.4 to 0.85 nm. Even when errors are 5-10 μm a resulting $D\lambda/\lambda \leq 10^{-4}$ is obtained in this interval. But, this is true only if d is known with the accuracy $Dd/d = 10^{-7} - 10^{-6}$ [1], as in our case.

Fabrication of Monoliths

Quartz and Silicon crystals are applicable for fabrication of monolithic blocks due to their high lattice perfection over a large crystal volume. As a first step wafers were cut from some silicon blocks to select the block with the highest perfection. X-ray topography, accurate determination both of lattice parameters and angular deviation of the surface from the atomic planes were used to provide this selection [ ].

The two-plate quasimonolithic quartz crystal was fabricated in a different way. Several plates of quartz were carefully cut from one block, grinded, polished and investigated by all the X-ray methods. All plates had only small deviations (within 10 seconds of arc from Q [1010] atomic planes. A pair of Quartz plates with the least deviation from each other (2 sec) was selected. These crystal plates were brought into optical contact at either side of a quartz glass spacer having well-polished parallel surfaces. These two plates were fixed so that the front plate is shifted downward and to the left in order to allow absolute wavelength measurements over a wider λ-range. The distance L amounts to (3,2485 ± 0,0002) cm and atomic planes spacing is $d = (0,4254895 \pm 5.10^{-7})$ nm.

Thus, the fabrication of crystal monolithic blocks includes thorough steps such as precise cutting and etching, selection of the suitable plates and fixing them by optical contact. However, by comparing the wavelength measuring results obtained using different monoliths in the same experiment one can get for wavelength which are similar within a given accuracy.

Wavelength measuring experiments

The absolute method of measurement of spectral line wavelength considered is applicable to both CW and pulsed sources.

Laser generated plasma experiments were carried out with the following parameters of the neodymium glass laser: E = 10 J, $\tau = 0.6$ ns, $q = 5.10^{13}$ W/cm². Distances between the lines on the film are measured with the accuracy of ± 5 μm. The double monolithic block is disposed with respect to a target so that the dispersion direction is parallel to a target plane, the Doppler shift of lines registered is minimum.

The wavelength measurement of Ly_α doublet of Mg(XII) H-like ions gave the following results: $\lambda_{3/2} = 8,4193 \pm 0,0002$ Å for

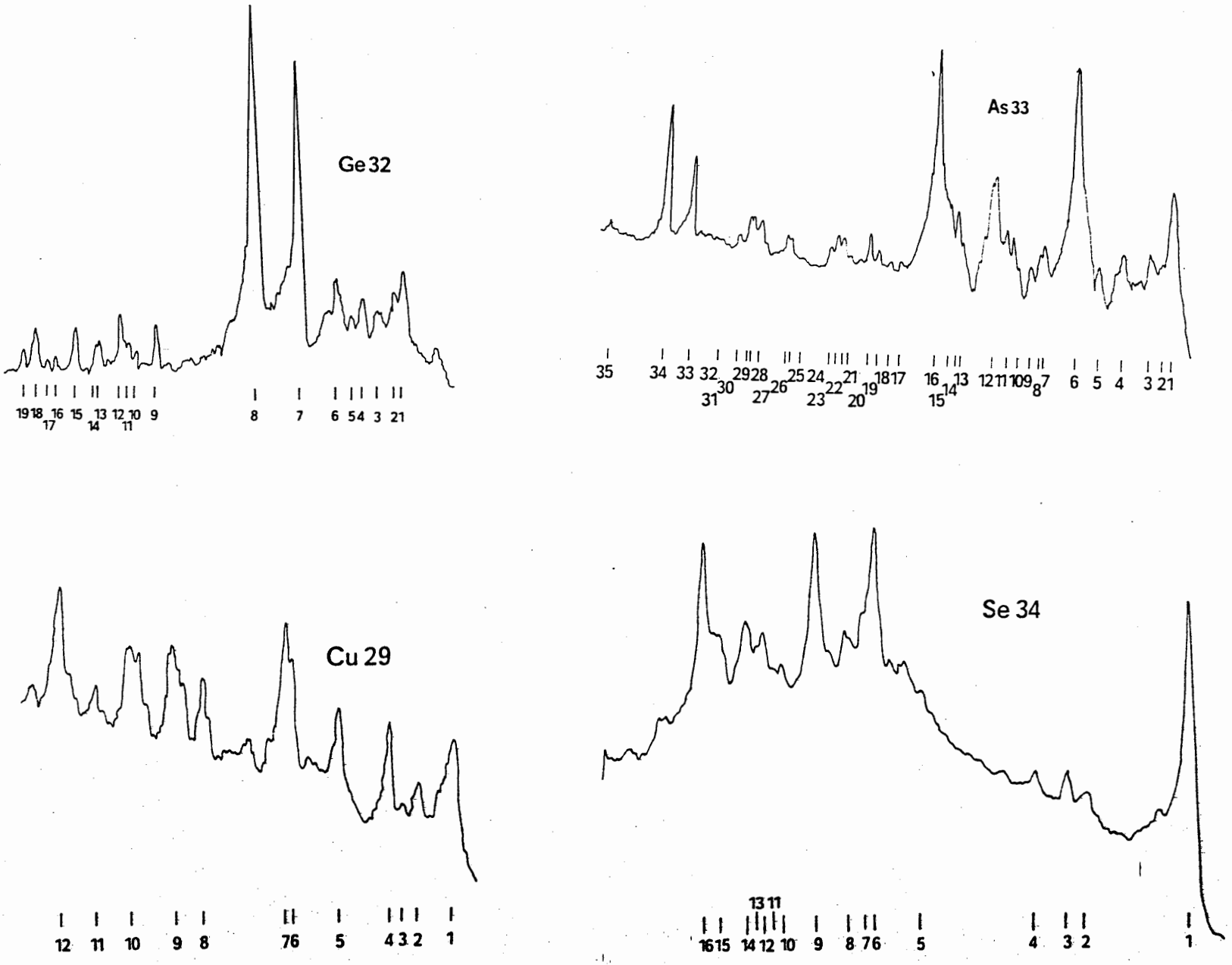


Fig A1.35 Copper, germanium, arsenic, selenium L-spectrum in the range of 7,5-8,5 Å, figures correspond to the line number from Tables 1-4.

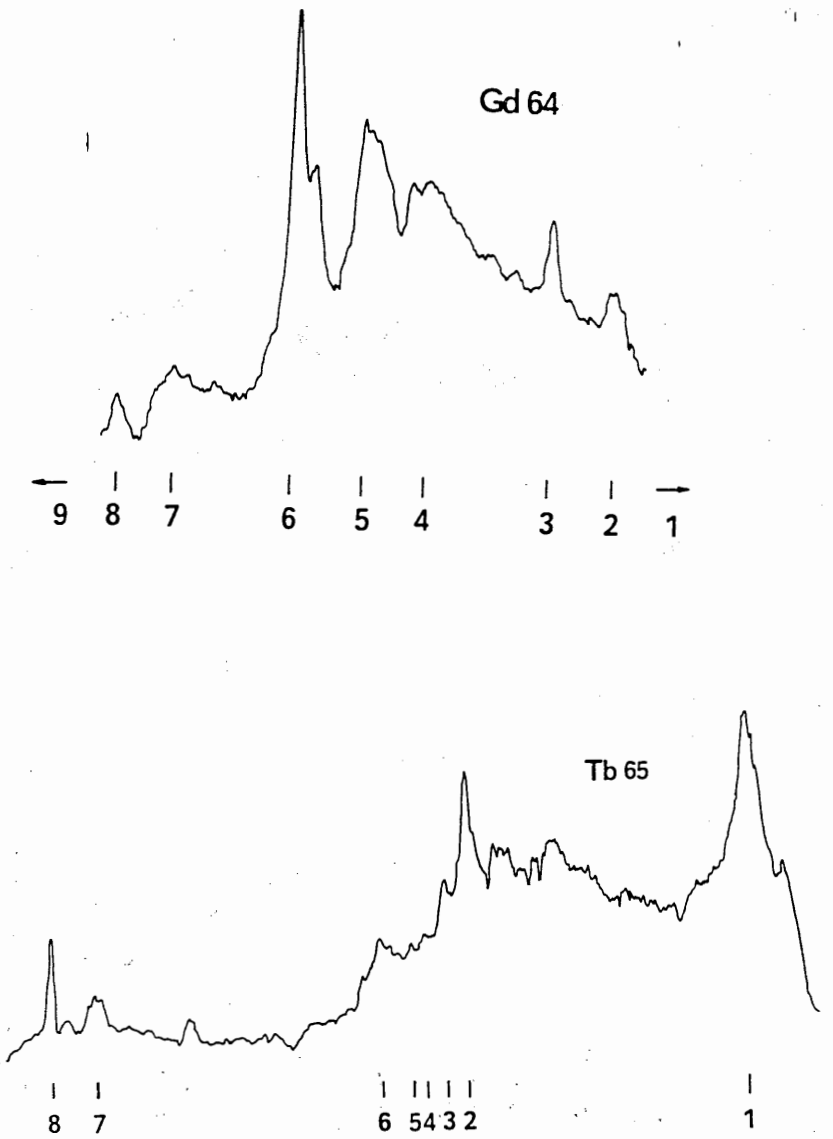


Fig A1.36 Gadolinium, terbium M-spectrum in the range of 7,5-8,5 Å, figures correspond to the line numbers from Table 5 and 6.

Table 1 Copper L-spectrum in range 8 - 8,5 Å. λ_{exp}-this work, λ_{theor}-(5)

No	λ_{exp}	λ_{theor}	Ion	transition	J_o-J_1
1	8,4556	-		?	
2	8,4166	-		?	
3	8,4003	-		?	
4	8,3856	8,385	[O]-	$2p^4\ ^3P - 2p^3(^4S)4d\ ^3D$	1-2
5	8,3371	8,333	[O]-	$2p^4\ ^1D - 2p^3(^2P)4d\ ^3F$	2-3
6	8,2981	-		?	
7	8,2929	8,281	[O]-	$2p^4\ ^3P - 2p^3(^4S)4d\ ^3D$	2-2
8	8,2365	-		?	
9	8,2266	-		?	
10	8,2209	8,222	[O]-	$2p^4\ ^1D - 2p^3(^2P)4d\ ^3F$	2-3
11	8,2082	-		?	
12	8,2044	-		?	

Table 2 Germanium L-spectrum in range 8 -8,5 Å
λ_{exp}-this work, λ_{theor}-(5, 8)

No	λ_{exp}	λ_{theor}	Ion	transition	J_o-J_1
1	8,5265	-		?	
2	8,5264	-		?	
3	8,5080	8,507	[F]-	$2s^22p^5\ ^2P$-$2s^22p^4(^1D)3d\ ^2P$	3/2-1/2
4	8,4937	-		?	
5	8,4813	-		?	
6	8,4648	-		?	
7	8,4237	8,4180	[O]-,	$2p^4\ ^1D - 2p^3(^2D)3d\ ^1F$	2-3
8	8,3728	8,3720	[O]-,	$2p^4\ ^1D - 2p^3(^2D)3d\ ^3F$	2-3
9	8,2444	8,2452	[O]-,	$2p^4\ ^3P - 2p^3(^2D)3d\ ^3D$	2-3
10	8,2162	8,212	[F]-,	$2s2p^5\ ^2P - 2s2p^5(^1P)3p\ ^4D$	3/2-5/2
11	8,2071	-		?	
12	8,1959	8,1944	[O]-,	$2p^4\ ^3P - 2p^3(^2D)3d\ ^1F$	2-3
13	8,1668	8,176	[F]-,	$2s2p^5\ ^2P - 2s2p^5(^3P)3p\ ^2D$	3/2-5/2
			[F]-,	$2s2p^5\ ^2P - 2s2p^5(^3P)3p\ ^2D$	1/2-3/2
			[F]-,	$2s2p^5\ ^2P - 2s2p^5(^3P)3p\ ^4D$	3/2-3/2
14	8,1614	-		?	
15	8,1326	8,136	[F]-,	$2s2p^5\ ^2P - 2s2p^5(^3P)3p\ ^2P$	3/2-3/2
16	8,1047	8,099	[F]-,	$2s2p^5\ ^2P - 2s2p^5(^3P)3p\ ^4D$	3/2-5/2
17	8,0923	-		?	
18	8,0760	8,068	[F]-,	$2s2p^5\ ^2P - 2s2p^5(^3P)3p\ ^2D$	1/2-3/2
19	8,0577	-		?	
20	7,9350	-		?	

Table 3 Arsenic L-spectrum in range 8 -8,5 Å
λ_{exp}-this work, λ_{theor}-(5, 6, 7)

No	λ_{exp}	λ_{theor}	Ion	transition	J_o-J_1
1	8,4931	8,5036	[O]-	$2p^4\ ^3P - 2p^3(^4S)3s\ ^3S$	0-1
2	8,4921	-		?	
3	8,4910	-		?	
4	8,4877	-		?	
5	8,4788	-		?	
6	8,4652	8,460	[Ne]-,	$2s^22p^6\ ^1S - 2s^22p^53d\ ^3D$	0-1
7	8,4399	8,4360	[O]-,	$2p^4\ ^1S - 2p^3(^2P)3s\ ^1P$	0-1
8	8,4533	8,4328	[O]-,	$2p^4\ ^1D - 2p^3(^2D)3s\ ^1D$	2-2
9	8,4355	8,4290	[O]-,	$2p^4\ ^3P - 2p^3(^2D)3s\ ^3D$	1-1
10	8,4055	-		?	
11	8,3977	8,3971	[O]-,	$2p^4\ ^3P - 2p^3(^4S)3s\ ^3S$	2-1
12	8,3822	8,385	[F]-,	$2s^22p^5\ ^2P - 2s^22p^4(^3P)3d\ ^4P$	1/2-3/2
13	8,3323	8,3368	[O]-,	$2p^4\ ^1D - 2p^3(^2P)3s\ ^3P$	2-1
14	8,3231	8,325	[F]-,	$2s^22p^5\ ^2P - 2s^22p^4(^1S)3s\ ^2S$	3/2-1/2
15	8,3113	-		?	
16	8,2884	8,2809	[O]-,	$2p^4\ ^3P - 2p^3(^2P)3s\ ^3P$	1-0
		8,266	[Ne]-,	$2s^22p^6\ ^1S - 2s^22p^53d\ ^1P$	0-1
17	8,2181	8,211	[F]-,	$2s^22p^5\ ^2P - 2s^22p^4(^3P)3d\ ^2P$	1/2-3/2
18	8,1938	8,1922	[O]-,	$2p^4\ ^1D - 2p^3(^2P)3s\ ^3P$	2-2
		8,195	[F]-,	$2s^22p^5\ ^2P - 2s^22p^4(^3P^o3d\ ^4P$	3/2-1/2
19	8,1665	8,1784	[O]-,	$2p^4\ ^1D - 2p^3(^2P)3s\ ^1P$	2-1
		8,167	[F]-,	$2s^22p^5\ ^2P - 2s^22p^4(^1D)3d\ ^2S$	1/2-1/2
20	8,1465	8,1302	[O]-,	$2p^4\ ^3P - 2p^3(^2P)3s\ ^3P$	1-2
		8,150	[F]-,	$2s^22p^5\ ^2P - 2s^22p^4(^1D)3d\ ^2P$	1/2-3/2
21	8,0980	8,098	[F]-,	$2s^22p^5\ ^2P - 2s^22p^4(^1D)3d\ ^2P$	1/2-1/2
22	8,0792	-		?	
23	8,0628	-		?	
24	8,0442	8,042	[F]-,	$2s^22p^5\ ^2P - 2s^22p^4(^1S)3d\ ^2D$	1/2-3/2
25	7,9665	7,968	[F]-,	$2s^22p^5\ ^2P - 2s^22p^4(^1D)3d\ ^2S$	3/2-1/2
26	7,9317	-		?	
27	7,9194	7,915	[F]-,	$2s^22p^5\ ^2P - 2s^22p^4(^1S)3d\ ^2D$	1/2-3/2
		7,912	[F]-,	$2s^22p^5\ ^2P - 2s^22p^4(^1S)3d\ ^2D$	3/2-3/2
28	7,8359	7,820	[Nd]-,	$2s^22p^6\ ^1S - 2s^22p^53p\ ^3P$	0-1
29	7,8080	-		?	
30	7,7979	-		?	
31	7,7580	-		?	
32	7,6920	-		?	
33	7,5834	-		?	
34	7,4855	-		?	
35	7,2409	-		?	

Table 4 Selenium L-spectrum in range 8 - 8,5 Å
λ_{exp}-this work, λ_{theor}-(6, 8, 9)

No	λ_{exp}	λ_{theor}	Ion	transition	J_o-J_1
1	8,3857	8,3860	[Ne]-	$2s^22p^6\ ^1S - 2s^22o^53s\ ^1P$	0-1
2	8,2673	8,261	[F]-	$2s^22p^5\ ^2P - 2s^22p^4(^3P)3s\ ^4P$	3/2-5/2
3	8,2457	-		?	
4	8,2057	-		?	
5	8,0630	-		?	
6	7,9754	7,9759	[Ne]-,	$2s^22p^6\ ^1S - 2s^22p^53s\ ^3P$	0-1
7	7,9799	7,983	[F]-,	$2s^22p^5\ ^2P - 2s^22p^4(^1D)3s\ ^2D$	3/2-5/2
8	7,9565	-		?	
9	7,9168	-		?	
10	7,8741	7,8788	[Ne]-,	$2s^22p^6\ ^1S - 2s^22p^53s\ ^3D$	0-1
		7,8750	[O]-,	$2p^4\ ^3P - 2p^3(^2D)3s\ ^3D$	1-2
11	7,8576	-		?	
12	7,8417	-		?	
13	7,8331	-		?	
14	7,8218	7,8295	[O]-,	$2p^4\ ^3P - 2p^3(^4S)3s\ ^3S$	2-1
		7,821	[F]-,	$2s^22p^5\ ^2P - 2s^22p^4(^3P)3s\ ^4P$	1/2-3/2
15	7,7875	-		?	
16	7,7777	7,7760	[O]-,	$2p^4\ ^1D - 2p^3(^2P)3s\ ^3P$	2-1

transition $^2S_{1/2}$ - 2p $^2P_{3/2}$ and $\lambda_{1/2}$ = 8,4244 ± 0,0002 Å for transition $^2S_{1/2}$ - 2p $^2P_{1/2}$. These values are in a good agreement with theoretical calculations( ): $\lambda_{3/2}$ = 8,419203 Å, $\lambda_{1/2}$ = 8,424612 Å.

The absolute measurements of X-ray spectral line wavelengths within the range of 8-8.5 Å are carried out by means of the quartz monolithic block. In this case the measuring accuracy is the maximum that offers the possibility to identify the complicated L-, M-spectra by comparing measured and calculated wavelengths.

L-spectrum wavelengths of Cu, Ge, As, Se ions and possible line identification are given in the Tables 1-4, the spectra are presented in Fig A1.35. M-spectrum wavelengths of Gd, Tb ions are in the Tables 5 and 6, and the spectrta in Fig A1.36.

Conclusions

A crystal spectrograph has been developed to measure the absolute values of X-ray spectral line wavelengths using a double Bragg reflection. Preliminary results indicate that a wavelength accuracy of $\Delta\lambda/\lambda \cong 5.10^{-5}$ is obtained. The measuring method does not need reference spectral lines. The spectrograph is used in conjunction with a monocrystal one for wavelength identification purposes. These advantages make possible the successful use of the spectrograph not only for wavelength measurements but also for the laser-generated dense plasma diagnostics, for instance, to measure shift and line broadening as a result of the plasma effects[3,4].

Acknowledgment

The authors are grateful to M Key and C Edwards for their help in organisation of the laser-produced plasma experiments. We would like to thank B Hoffman and K Korbs for their support in the fabrication of crystal units. The advice of S Grosswig and R Kittner in the conduction of lattice-parameter measurements is greatly appreciated.

References

1. S Grosswig, J Hartwig, K H Jackel, R Kittner, W Melle, Nauch apparat - Sci Instrum **1** no 4, 29 (1986).

2. V A Boiko, V G Palchicov, I Yu Skobelev, A Ya Faenov "X-ray spectroscopy of multicharged ions", Moscow, Energoatomizdat (1988).

3. S Skupsky, Phys Rev A **21** 1316 (1980).

4. N G Basov, K Goetz, M P Kalashnikov, Yu A Mikhailov, A V Rode, G V Sklizkov, S I Fedotov, E Forster, Nucl Instrum and Meth in Phys Res B9, 773 (1985).

5. H Gordon, M G Hobby, N J Peacock, J Phys, VB13, No 12, 1985 (1980).

6. P O Bogdanovich et al, "Spectroscopic constants of atoms", Report of the Spectroscopy Committee of the USSR Academy of Sciences, Moscow (1977).

7. R J Hutcheon, L Cooke, M H Key et al, Phys Scripta **31** no 1, 89 (1980).

8. V A Boiko, S A Pikuz, U I Safronova et al, J Phys **B12** 1927 (1979).

9. L A Vainshtein, U I Safronova "Spectroscopic constants of atoms", Report of the Spectroscopy Committee of the USSR Academy of Sciences, Moscow (1977).

APPENDIX

A2.4 BEAT-WAVE EXPERIMENT

A E Dangor, A K L Dymoke-Bradshaw, A Dyson (Imperial College)
T Afshar-Rad, C N Danson, C B Edwards (RAL)
T Garvey (CERN)
F Amiranoff, G Mattieussent (Ecole Polytechnique)

Introduction

The aim of this experiment is to study the generation of plasma waves by the laser beat-wave process. In this process the plasma wave is excited by the beat between laser beams whose frequency difference $\Delta\omega = \omega_1 - \omega_2$ is equal to the plasma frequency ω_p. The electric field associated with the plasma wave can be very large, and if the laser beams are copropagating and have frequencies $\omega_1 = \omega_2$ $(= \omega) > > \omega_p$ the plasma wave has a phase velocity $v_p = c[1 - (\omega_p/\omega)^2]^{1/2}$ which is close to the speed of light. This is the basis of the plasma beat-wave accelerator (PBWA) proposed by Tajima and Dawson[1]. It is of interest to note that the energy gain is proportional to γ^2 where $\gamma = [1 - (v_p/c)^2]^{-1/2}$ is the relativistic factor associated with the phase velocity v_p of the plasma wave. Substituting for v_p, $\gamma = \omega/\omega_p$.

Plasma waves excited by the beat-wave process using carbon dioxide lasers operating at 90.6 μm and 10.6 μm have been reported[2,3]. Relative plasma wave amplitude $\delta n/n$ of 1-3% have been observed. In our experiment we use the Vulcan laser system operating at 1.053 μm (YLF) and 1.064 μm (YAG). Thus the relativistic factor associated with the wave $\gamma = \omega/\omega_p$ is about 100. In the experiments with carbon dioxide lasers γ = 10. Since the energy-gain is proportional to ν^2 our experiment is more relevant to particle acceleration. However, at intensities available from the Vulcan system the larger value of ω/ω_p imposes the requirement that the plasma density be very close to the resonant density corresponding to $\omega_p = \omega_1 - \omega_2$. Calculations[4] show that the density deviation Δn that can be tolerated from the critical density n at exact resonance has to be such that $\Delta n/n < 0.2\%$ if the plasma wave amplitude is to be within one half of the relativistic saturation value. This requires that a plasma with a precise density be produced and that the plasma be extremely homogeneous and very reproducible.

In a previous experiment[5] we showed that a fully ionised plasma can be generated by multiphoton ionisation in hydrogen with a frequency doubled YFL laser at an irradiance of about 10^{14} Wcm^{-2}. The plasma was found to be uniform within the measurement error over a length of at least 8 mm using f20 optics. Thus by changing the ambient pressure of the gas it is possible to scan through the resonant plasma density. This is the technique we employed in the experiment reported here to generate the plasma.

Experimental Arrangement

Figure A2.13 is a schematic of the experiment. The experiment was conducted in TA2 with the 50 cm radius target chamber. Four laser beams, all copropagating and focused at the centre of the target chamber, were used:

(a) A beam to generate the plasma. This was a frequency doubled, λ = 0.526 μm, 5 J energy, 200 ps pulse length, 100 mm diameter beam focused with a 2.3 m lens.

(b) The two pump beams, λ_1 = 1.053 μm and λ_2 = 1.064 μm, to excite the plasma wave. Each beam was about 50 J energy, 200 ps pulse length, 100 mm diameter and focused with a 2 m lens.

(c) A probe beam to diagnose the plasma wave. This was a frequency doubled, λ = 0.526 μm, 5 J energy, 200 ps pulse length, 100 mm diameter beam focused with a 2.3 mm lens.

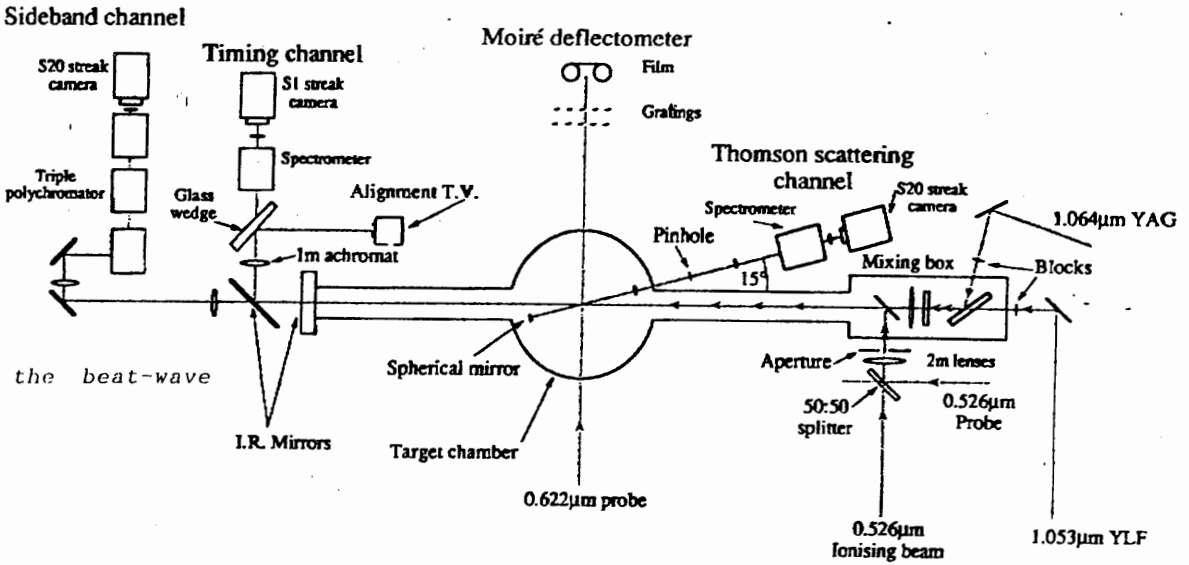


Fig. A2.13 The experimental arrangement for the beat-wave investigation.

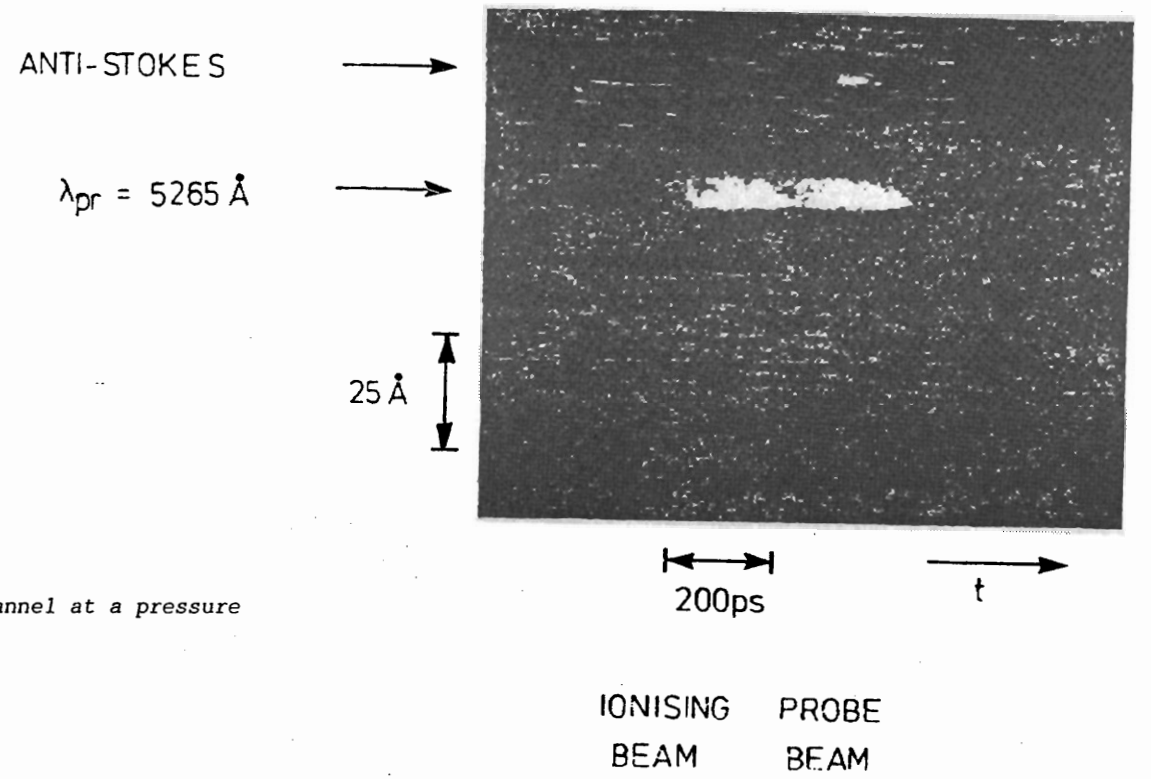


Fig. A2.14 Streak photograph of the sideband channel at a pressure close to resonance.

The frequency separation of the 1 μm pump laser beams is nearly coincident with a rotational transition in nitrogen (J = 11 and J = 13 at 99 cm^{-1}). Thus there will be forced Raman scattering in air leading to large Stokes and anti-Stokes sidebands[6]. To avoid this the two pump beams were generated in separate oscillators and made to follow separate air paths to the target area. A dielectric polariser and high order waveplate positioned in the mixing box was used to combine the beams with little loss. The mixing box was evacuated and filled with hydrogen at the same pressure as in the target chamber. However, there is still come coherent Stokes and anti-Stokes scattering in the optical components[7] which gives rise to sideband generation at a level greater than that generated by the expected plasma wave. Hence a separate green beam is used to probe the plasma wave. This beam and the beam used to generate the plasma (the ionising beam) were introduced into the target chamber using a dichroic mirror situated in the mixing chamber.

The radiation dimension was measured and the spatial coincidence of the four laser beams checked with an equivalent focal plane monitor using the 1.0 m focal length achromat shown in the figure. The relative timing of the four laser beams was checked with a spectrometer and streak camera. The ionising beam was adjusted to be 200 ps before the pump beams; the timing of the probe beam was adjustable. A Moire deflectometer system using a transversely propagating low energy probe laser pulse, frequency doubled and Raman shifted to 0.622 μm, was used to determine the axial length of the plasma generated by the ionising beam. With the deflectometry it was established that the 1 μm pump lasers were by themselves capable of ionising the hydrogen. Thus the deflectometry served as an additional check of the spatial coincidence of the laser beams. Thomson scattering of the two green beams was observed at two angles by monitoring the direct and complementary scattered beams as shown in the figure. This determined the plasma temperature and density at the time of the ionising and probe beams.

The magnitude of the excited plasma wave was determined by measuring the relative amplitude of the sidebands generated on the probe beam by interaction with the plasma wave. The sidebands are of very low intensity and for this reason it was necessary to use a triple polychromator with a high rejection ratio to disperse the light. A streak camera differentiated between the ionising and probe beams and the 1 μm beams were rejected by the dielectric mirrors at the output. Despite these precautions, sidebands generated by interaction of the probe with phonon generation associated with Raman scattering of the pump beams in the quartz in various optical components were observed[7]. To reduce these to an acceptable level a 20 mm diameter aperture was placed in the probe beam and a central 20 mm diameter section of the pump beams removed with a block as shown in Fig A2.13.

Results and Discussion

Figure A2.14 is a streak photograph of the sideband channel at a pressure close to resonance. This shows the ionising and the probe laser beams at λ_{pr} = 0.5265 μm and a sideband coincident with the probe. The sideband is shifted by $\Delta\lambda$ = 2.8 nm which is in agreement with the expected shift ($= \lambda_{pn}^2[\lambda_1 - \lambda_2]/\lambda_1\lambda_2$). The Stokes sideband was blocked in the triple monochromator to maximise the rejection ratio. Figure A2.15 is a microdensitometer trace of the streak photograph showing the time history of the sideband. The sideband shows a peak close to the maximum of the probe beam and has a FWHH of 50 ps which is equal to the time resolution of the channel. Thus the lifetime of the sideband is less than 50 ps.

The variation of the ratio of the anti-Stokes sideband to the probe intensity is a function of the hydrogen gas pressure is shown in Fig A2.16. Clearly there is an enhanced sideband at a fill pressure which is close to the resonant density. This is at 1.08×10^{17} cm^{-3} for the YLF and YAG pump beams and corresponds to a fill pressure of 1.662 torr at 26°C. The residual sideband

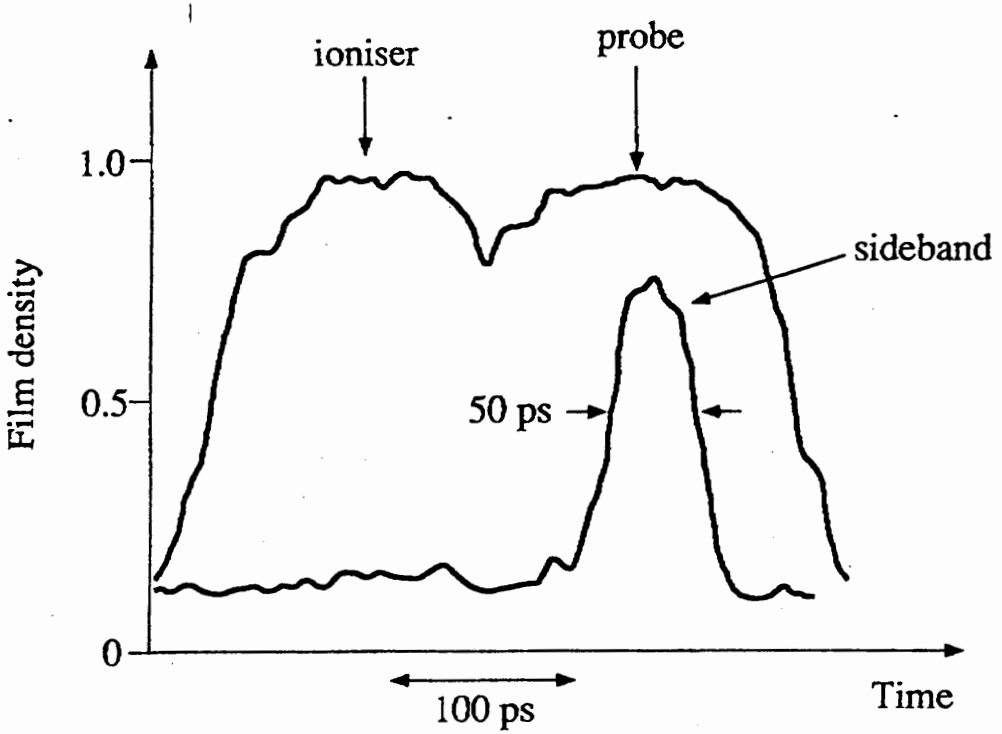


Fig. A2.15 Microddensitometer trace showing the time history of the sideband relative to the ioniser and probe beams.

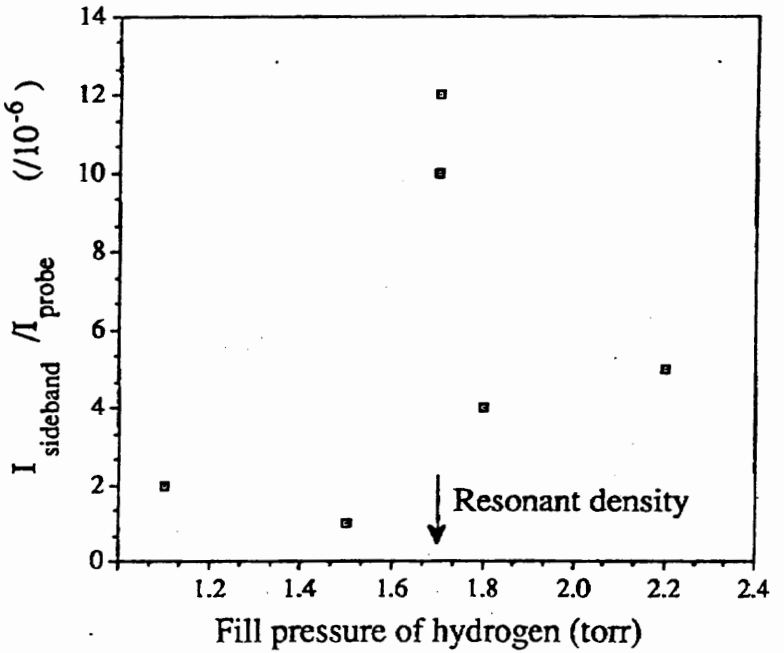


Fig. A2.16 The ratio of sideband to probe intensities as a function of filling pressure.

observed above and below the resonant density is presumably due to Raman scattering in quartz.

The relative plasma wave amplitude δn/n is related to the sideband ratio I_s/I_{pr} by

$$\frac{I_s}{I_{pr}} = [\frac{\pi L}{2 \lambda_{pr}} (\frac{\omega_p}{\omega_{pr}})^2 \frac{\delta n}{n}]^2$$

where L is the interaction length and the subscript pr refer to the probe laser beam. The observed ratio close to resonance is 1.2×10^{-5}. Using an estimated interaction length L of 5 mm the expression gives δn/n ≈ 1%.

Calculations show that at the estimated pump intensities of 2×10^{14} Wcm^{-3} at a δn/n of 9% can be expected due to saturation by relativistic nonlinearity. Here Gaussian profiles are assumed for the pump laser beams with FWHH of 200 ps. Further, the calculations show that the plasma wave amplitude saturates near the peak of the pump beams and remains at this value for a long time. This is not in agreement with the observed 50 ps lifetime of the sideband.

Lower values of δn/n can be expected due to collisional effects and deviation of the density from exact resonance. At the assumed intensities of the pump beams the quiver velocity of an electron in the laser field is substantially higher than the electron thermal velocity corresponding to the measured electron temperature of 25 eV. Thus saturation of the plasma wave due to collisional effects is unlikely. A density detuning of 1% from exact resonance does give a δn/n close to the observed lifetime. This indicates that there is some additional mechanism which is limiting the plasma wave amplitude.

A possible candidate which may be responsible for the low value of δn/n observed is the modulational instability[8,9]. Here the plasma wave generated by the beat wave process couples with a low frequency ion oscillation which destroys the coherence of the plasma wave and limits δn/n to a low value. For the parameters of our experiment the growth time of the modulational instability is about 4 ns. A particle simulation by A R Bell at Imperial College predicts a δn/n between 1-2% which is close to the observed value in our experiment. A more detailed comparison between the experiment and simulation is in preparation.

References

1. T Tajima and J M Dawson, Phys Rev Lett 43, 267 (1979).

2. C E Clayton, C Joshi, C Darrow, D Umstradter, Phys Rev Lett 54, 2343 (1985).

3. N A Ebrahim et al in Proc 1986 Linear Accelerator Conf (Stanford Accelerator Center, Stanford, CA) June 2-6 1986.

4. S J Karttunen and R R E Salomaaa, IEEE Trans on Plasma Science PS15 134 (1987).

5. A E Dangor et al, IEEE Trans on Plasma Science PS-15 161 (1987).

6. A E Dangor et al, J Phys B At Mol Opt Phys 22, 797 (1989).

7. A Dyson et al, to be published in J Phys B At Mol Opt Phys.

8. P Mora, Phys Rev Lett 61, 1611 (1988).

9. D Pesme et al, Laser and Particle Beams 6, 199 (1988).

C2.5 INVESTIGATION OF FAST ABSORBANCE CHANGES IN PHOTOSYSTEM 1

R Sparrow, E H Evans and R G Brown (Lancs Poly)
R S Chittock and W T Toner (RAL)
M C W Evans (UCL)

Introduction

We have continued our characterisation of absorption transients in Photosystem I (PSI) excited by a short laser pulse. Last year we reported the presence of two saturation transients measured at 705 nm and a non-saturating component at 670 nm[1]. We attributed the saturating component with a slower recovery time, to the reaction centre chlorophyll P700, and the transient at 670 nm to light harvesting chlorophyll[2]. Our further interpretation of the data awaited transient spectra at various time intervals after excitation, although we proposed that the shorter lived component of the 705 nm transient was on a common pathway with P700.

Our ability to change the measuring wavelength with ease and consistency has been facilitated by pulse shortening to 1 ps by adding a saturable absorber, enabling us to excite a stable continuum. Light is monochromated by using interference filters of 10 nm bandwidth. These filters are our major limitation in wavelength discrimination.

Results and Discussion

Figure C2.13 shows a spectrum of the saturating absorption transient measured 100 ps after excitation, under conditions where the reaction centre chlorophyll P700 was chemically reduced or fully oxidised. Under the former condition two spectral features could be identified, a broad peak with its maximum at 690 nm and a smaller peak at 705 nm. Both these features were absent in oxidised samples. Our current interpretation of this spectrum is that it represents the reaction centre state $P700^{+}\ A_0^{-}$, with P_{700}^{+} responsible for the feature at 705 nm, and A_0^{-} at 690 nm. This interpretation would be consistent with the assignment of an absorbance change at 690 nm with A_0^{-} by Nuijs et al[3]. Figure C2.14 shows a spectrum of the maximum of the absorbance transient attained approximately 7 ps after excitation. Under conditions where the reaction centre chlorophyll, P700 was oxidised, a saturating absorbance transient was still observed, consistent with our previous analysis, of a chlorophyll molecule in a common energy transfer pathway with P700. The absorption spectrum of this chlorophyll appears to be further to the red than P700, possibly maximal at 710 nm. Such a chlorophyll originally identified by Butler[4] as that contributing the long wavelength fluorescence of PS1. We would suggest that this chlorophyll, on a common pathway with P700, could act as a 'funnel' between the bulk light-harvesting chlorophyll and P700. Figure C2.15 shows the spectrum of the transient maximum under conditions where P700 is chemically reduced. This spectrum is more complex than that in Figure C2.14. If it is assumed that the 'funnel' chlorophyll spectrum is unchanged from that shown in Figure C2.16, then the additional features appear at 690-700 nm (Figure C2.16) from that shown in Figure C2.14, then the additional features appear at 690-700 nm (Figure C2.16). Without further data it is difficult to interpret the reactions causing these fast absorbance changes. One interpretation would be that the formation of $P700^{+}\ A_0^{-}$, to which we have already assigned peaks at 690 nm at 706 nm, has already taken place within 7 ps.

Experiments are currently under way to improve the spectral resolution and statistics of the data to facilitate interpretation.

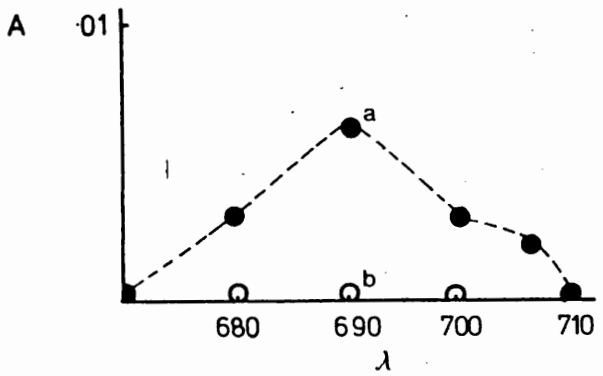


Fig. C2.13a Absorption spectrum of transient measured 57 ps after excitation of PS1 in the presence of DCPIP (50 μM), solium ascorbate (100 mM) and sodium dithinite.

Fig. C2.13b As a) but with potassium ferricyanide (5 mM).

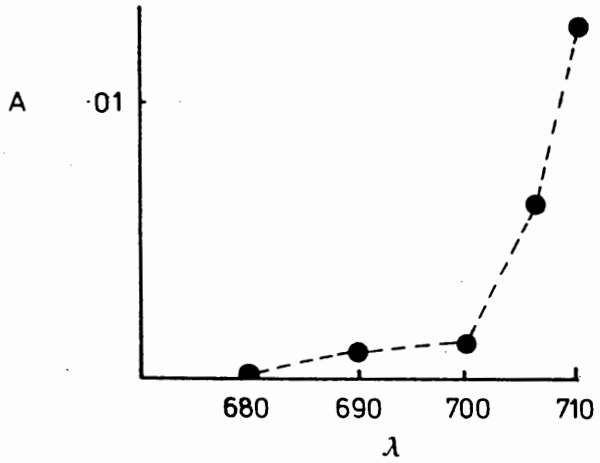


Fig. C2.14 Absorption spectrum of the transient measured 7 ps after excitation of PS1 in the presence of potassium ferricyanide (4 mM).

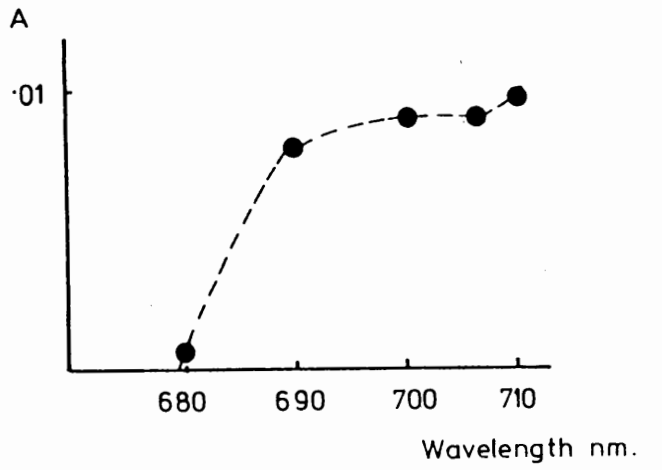


Fig. C2.15 As Figure C2.14 but in the presence of DCPIP (50 μM), sodium ascorbate (100 mM) and sodium dithionite.

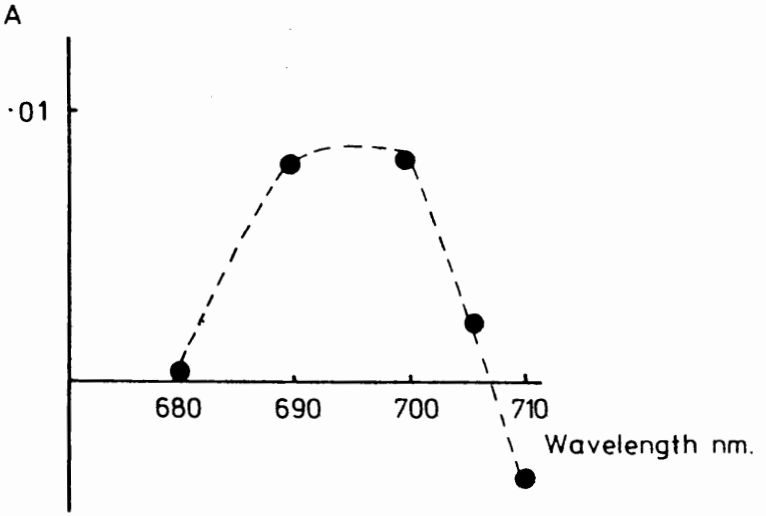


Fig. C2.16 The spectrum resulting from subtracting the spectrum in Figure C2.14 from that in Figure C2.15.

References

1. R Sparrow, R Brown, E Evans, R Chittock, W Toner and M Evans Annual Report to LFC, CLF, RAL p 204-208 (1988).

2. R Sparrow, R Brown, E Evans, R Chittock, W Toner and M Evans EBEC Reports, 5, 174 (1988).

3. A M Nuijs, V Shuvalov, H van Gorkom, J Plijter and L Duysens, Biochem Biophys Acta 850, 310-18 (1986).

4. B Wittmershaus, D Brns and C Huang Biophys J, 52, 829-836 (1987).

APPENDIX

A3.3 LASER COMPRESSION OF HIGH ASPECT RATIO DEUTERIUM TRITIUM FILLED SHELLS

M J Lamb, M Savage, S Davidson (Queens University, Belfast)
A P Fews, M L Williams (University of Bristol)
A V Rode, A I Nititenko (Lebedev Physical Institute)
M Grande, A Ridgeley (RAL)

Last year we reported on a new mode of laser driven implosion (NUHART) in which twelve laser beams are focused in a dodechedral pattern of spots on the surface of a high aspect ratio (≈400) glass shell[1]. Such non-uniformly irradiated targets, filled with deuterium, produced neutron and proton yields of 3×10^7, a factor of twenty higher than the yield which could be obtained from similar uniformly irradiated targets using the same laser energy.

This year further compression experiments have been carried out using deuterium-tritium filled shells, and yields of 5×10^8 have been obtained. These high yields implosions have been used as alpha-particle sources for particle radiography experiments on hot matter stopping power and on Rayleigh Taylor instability. These experiments will be described in later sections. Here we concentrate on general implosion related measurements.

Glass shells of diameter 500-800 μm, with wall thickness 0.7-1.9 μm and aspect ratio in the range 200-400, filled with ∿1.5 atmospheres of D-T, were irradiated with up to ∿800 J, 600 ps of frequency-doubled light from VULCAN focused to a D/R of +1. During the hot matter stopping power experiment (Nov 88) eleven drive beams were used instead of twelve. The targets were supplied by the Lebedev Physical Institute, Moscow.

A plastic scintillator/photomultiplier detector monitored the neutron yields, and the alpha-particles and protons were recorded by CR39 plastic track detector. The latter permitted absolute yield determination and measurement of core temperature and shell $\rho\Delta r$. Time-resolved hard x-ray emission was recorded on an x-ray streak camera to monitor the implosion time and the hot core lifetime (figure A3.14).

A variety of time-integrated x-ray images were also recorded. Orthogonal filtered (> 10 keV) pinhole cameras monitored implosion symmetry and x-ray core size (figure A3.15). Note that despite the non-uniformity of the irradiation core sizes of ∿100 μm were obtained, but with some structure (figure A3.16). Monochromatic (λ = 0.425 nm, $\lambda/\Delta\lambda$ = 800) x-ray images were recorded at seventeen times magnification by reflection from a spherically bent quartz $(10\bar{1}0)$ crystal. These images, have a resolution < 15 μm, also in some cases showed multiple structure within the implosion core which had a overall size of ∿100 μm. Thirty times magnified images were also recorded using a spherical quartz $10\bar{2}0$ crystal (λ = 0.491 nm, $\lambda/\Delta\lambda$ = 1400). These had a demonstrated resolution of 8 μm but, being sensitive to helium-like silicon emission, were dominated by coronal emission and showed no strong core features. A space resolving minispectrometer recorded 1:1 monochromatic 'images' of the H-like and He-like silicon line emission.

Alpha particle penumbral images were also recorded on CR39. These indicated source dimensions comparable to those of the hard x-ray cores obtained from the pinhole cameras.

The alpha particle yields obtained in the two experiments (Nov 88, 11 beams; Jan 89, 12 beams) are shown in figure A3.17 together with the proton yield data from the original NUHART experiment (Sept 87). Here the yields have been normalised for target size and aspect ratio according to the scaling

$$Y \propto r^4.(r/\Delta r)^5$$

The normalisation parameters were r = 303 μm and $r/\Delta r$ = 400.

The normalisation yields were typically thirty times less than the

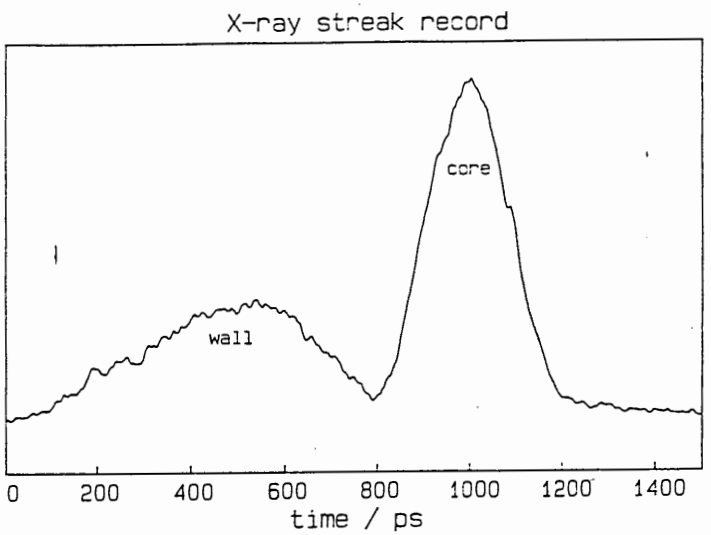


Fig A3.14 Time-resolved X-rays showing wall and core emission.

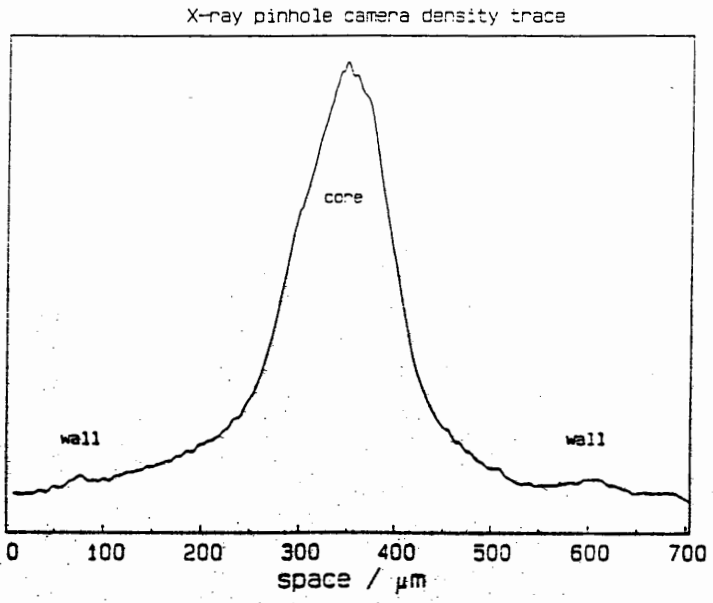


Fig A3.16 Densitometer scan through X-ray pinhole camera image.

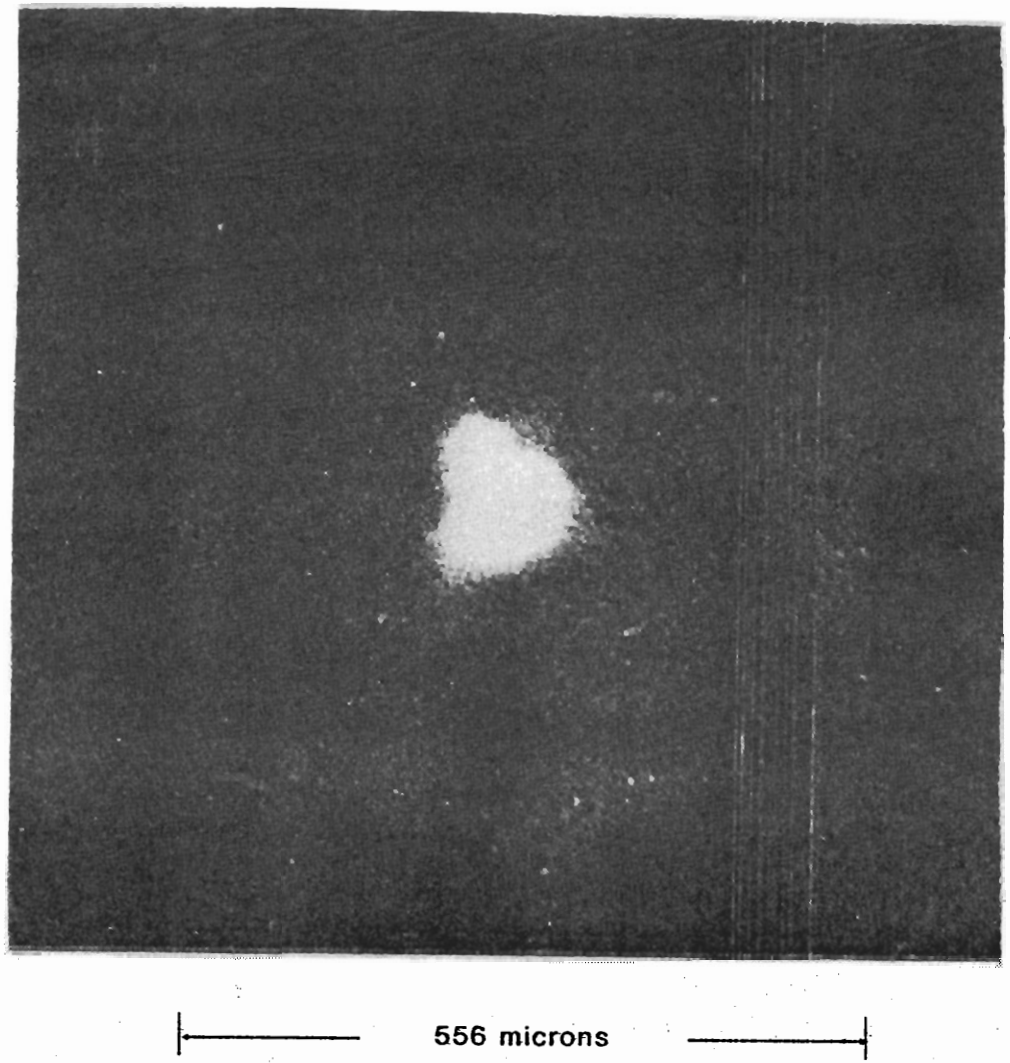


Fig A3.15 X-ray pinhole camera photograph.

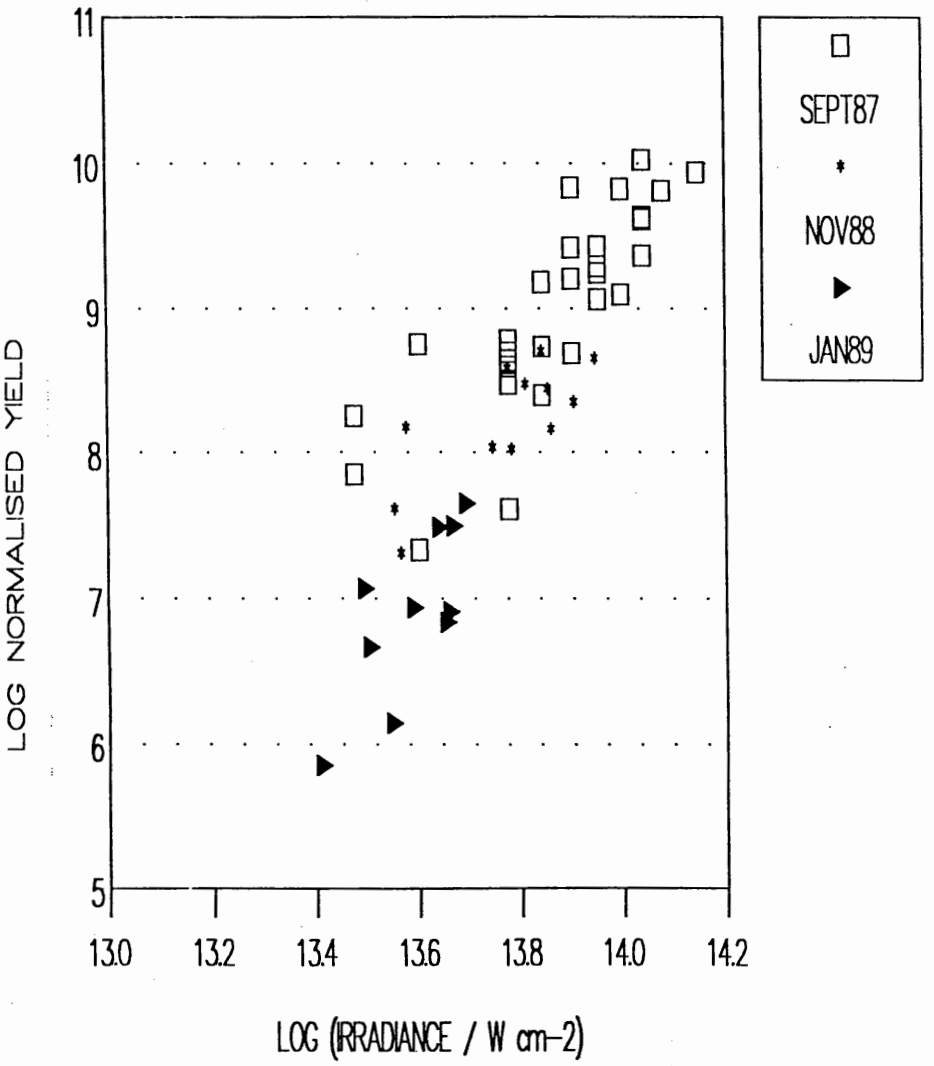


Fig A3.17 Normalised alpha (Nov 88, Jan 89) and proton (Sept 87) yields plotted against average irradiance.

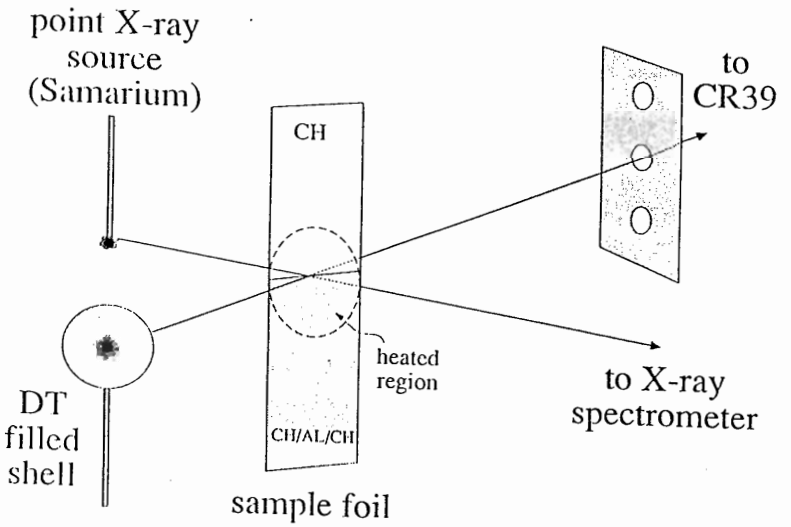


Fig A3.18 Experimental layout for hot matter stopping power.

alpha particle yields for the same shot indicating that the D:T mixture was not equimolar; (a yield ratio of > 100 would be expected). The core temperature estimated from the width of the proton energy spectrum was typically 5 keV. However in some shots the alpha particle data indicated higher temperatures (up to 2 to 3 times greater than that determined from the proton data). This is unrealistic and must be due to an additional broadening of the alpha particle energy spectrum in passing through the shell as a result of shell breakup.

References

1. M H Key, M J Lamb, A P Fews et al, to be published in Optics Communications.

A3.4 HOT MATTER STOPPING POWER

A P Fews, M L Williams (University of Bristol)
M J Lamb, M Savage, S Davidson (Queens University Belfast)
A V Rode, A I Nikitenko (Lebedev Physical Institute)
M Grande, A Ridgeley (RAL)

NUHART implosions of DT filled shells have been used as a source of fusion alpha particles in a recent experiment to measure the stopping power of an aluminium plasma produced by x-ray radiative heating.

The experimental layout is shown in figure A3.18 Glass shells of approximately 600 μm diameter and 0.8 μm wall thickness, filled with ≈ 1.5 atmospheres of DT, were driven by ≈ 500 Joules of 0.53 μm, 600 ps laser light using just eleven of Vulcan's twelve main beams. The twelfth beam (≈ 50 J, 600 ps) irradiated a gold coated foil target to provide x-rays to radiatively heat a nearby sample foil which contained two regions. One region consisted of 0.5 μm of aluminium sandwiched between two 0.3 μm layers of CH plastic, whilst the other was a single 0.6 μm thick region of CH plastic. The tamping effect of the plastic layers helped to reduce density gradients in the heated aluminium plasma, and the plastic-only part of the sample provided a comparison region.

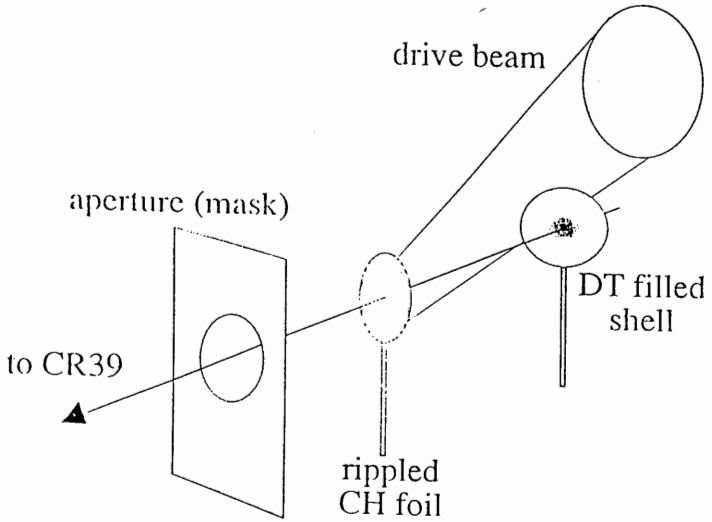
Alpha particles from the implosion core, having passed through the various sample foil regions and an array of penumbral apertures, were recorded on CR39 plastic track detector and their residual energy thus determined[1]. Determination of the stopping power of the test plasma requires a knowledge of the source energy spectrum, and, because of the need to unfoil penumbral images of the radiograph, also a knowledge of the spatial structure of the particle source. Hence direct alpha particle penumbral images of the implosion core were also recorded on CR39. A detailed analysis of this data is in progress.

The ionisation state of the test plasma at the instant of thermonuclear particle probing was measured using the technique of point projection x-ray absorption spectroscopy[2]. A samarium-coated fibre target, irradiated with a synchronised laser beam, provided a short-pulse point-source (100 ps, 10 μm) of x-rays to probe the foil simultaneously with the alpha particles, and aluminium 1s-2p absorption features recorded on a Bragg crystal spectrometer. Nitrogen-, oxygen-, and fluorine-like absorption lines were observed corresponding to a temperature of 20-25 eV. However numerical simulations indicate that under the experimental conditions used only half of the sample may have been heated.

References

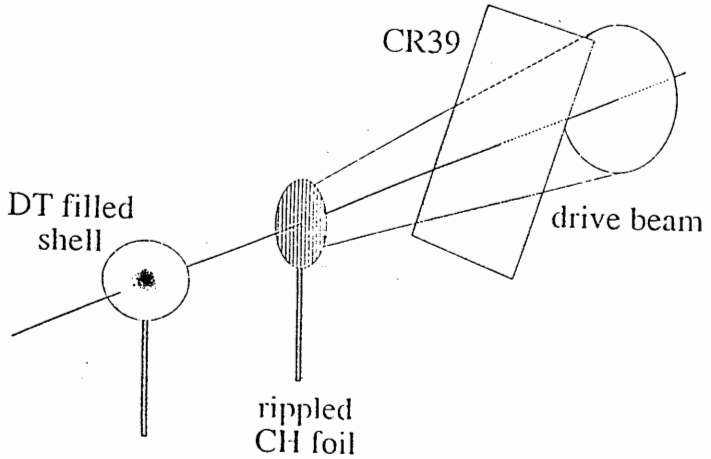
1. Fews and Henshaw, Nuc Instr Meth 197, 517-529 (1982).

2. Davidson et al, RAL-88-042 25-27 (1988).



Configuration A

Fig A3.19 Experimental configuration A for alpha particle radiography of Rayleigh Taylor instability.



Configuration B

Fig A3.20 Experimental configuration B for alpha particle radiography of Rayleigh Taylor instability.

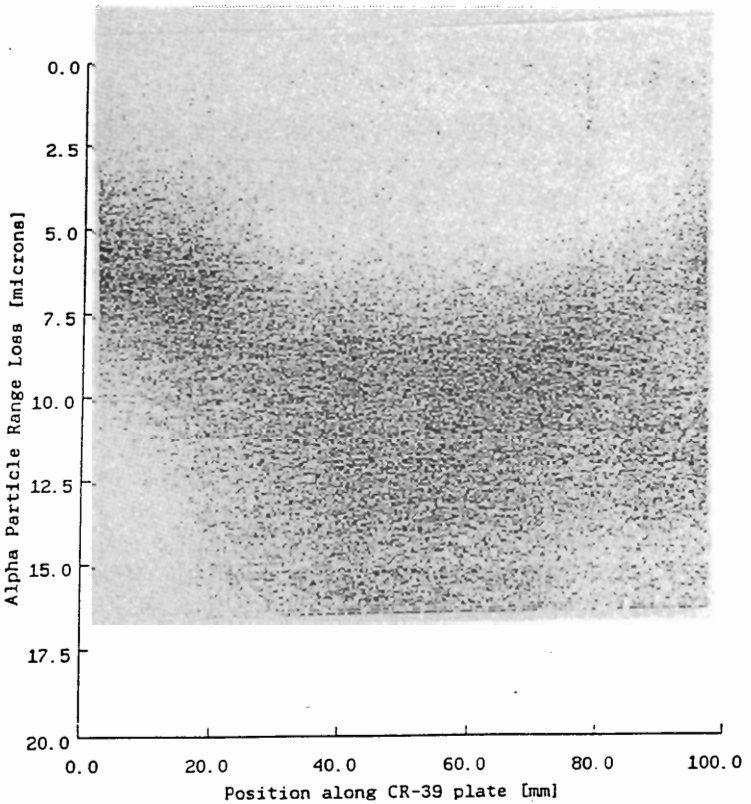


Fig A3.21 Range loss distribution through a section of an alpha particle radiography of an accelerated foil.

A3.5 ALPHA PARTICLE RADIOGRAPHY OF RAYLEIGH TAYLOR INSTABILITY

A P Fews, M L Williams (University of Bristol)
M J Lamb, M Savage (Queen's University Belfast)
M Grande, M H Key, A Ridgeley (RAL)

Fusion alpha particles from DT filed NUHART implosions have been used to radiograph laser accelerated planar foils to measure the growth of Rayleigh Taylor instability.

The experimental arrangements used are shown in figures A3.19 and A3.20. The DT shells were driven by twelve beams (800 J, .53 μm, 600 ps) and produced a maximum of 5.3×10^8 alpha particles. The sample foils consisted of 550 μm diameter disks of CH, 8 μm thick, with 1 μm deep grooves having a spatial period of 20 μm. These were driven by 70 J of 0.53 μm laser light in a pulse of 2 ns. The synchronisation between this drive beam and those driving the implosion was varied so that the foil was probed at times of 1, 1.5 and 2 ns into its acceleration. Alpha particles having passed both around and through the foil were either imaged (configuration A) or cast a direct shadow (configuration B) on to CR39 plastic track detector.

The information on mass redistribution within the target resulting from Rayleigh Taylor instability is obtained from the broadening of the alpha particle energy spectrum. Figure A3.21 shows the alpha particle range loss distribution derived from a cross-section through a shadowgram recorded in configuration B (probe time 1.5 ns), plotted as a function of position along the CR39 plate. At the edges of the plate we see particles which have passed around the foil and so the range loss here is characteristic of the source. In the central region corresponding to the shadow of the foil, and also the width has increased due to a mass redistribution resulting from the instability. This experiment has only just be completed and analysis is in progress.